

Deformation and Failure Behaviour of Self-reinforced Polypropylene and Self-reinforced Polypropylene/steel Fibre Metal Laminate

Jae Young Nam

March 2020

A thesis submitted for the degree of Doctor of Philosophy of The Australian National University.

© Copyright by Jae Young Nam, 2020

All Rights Reserved

*To my grandmas who never gave up on me,
and to my late grandpas who would have been proud of me.*

Declaration

This thesis presents findings from research undertaken at the Research School of Electrical, Energy and Materials Engineering, College of Engineering and Computer Science, Australian National University, Canberra, Australia.

I certify that this thesis does not incorporate without acknowledgement any material previously submitted for a degree or diploma in any university, and that, to the best of my knowledge, it does not contain any material previously published or written by another person except where due reference is made in the text.

Acknowledgement

First and foremost, I would like to thank my supervisor, Assoc. Prof. Shankar Kalyanasundaram. His guidance over the many years I have known him has given me the opportunity to learn, experiment and grow as a researcher and as a person.

I would also like to thank Prof. Wesley Cantwell, Assoc. Prof. Raj Das and Assoc. Prof. Adrian Lowe for being on my supervisory panel, and Adj. Prof. Zbigniew Stachurski for his occasional advice and friendly conversations which I enjoyed immensely.

This research was made possible with scholarships and grants from the Australian Government and the Research School of Electrical, Energy and Materials Engineering (RSEEME) at Australian National University. Facilities and equipment were provided by RSEEME, John Curtin School of Medical Research and School of Art and Design at Australian National University, and University of Auckland Faculty of Engineering.

I thank my fellow researchers in my group, Anthony, Seb, Nima, Wentian, Davood, Mendy, Lu, Youssef, and John, for the stimulating discussions, good laughs and a helping hand in setting up the equipment. I am also indebted to my officemates and the regular members of the unofficial Shut Up and Write group for their companionship through good and hard times, and the quiet pressure and support to charge ahead with my thesis.

I am very grateful to my wonderful friends in Canberra and around the world who have supported me throughout the PhD journey. A special thanks go to Nate, who I can always depend on for moral support in times of need.

Finally, I would like to express my deepest gratitude to Mum, Dad and Harrison, without whose unending encouragement, love and support I would not have gotten this far. You raise me up, so I can stand on mountains. You raise me up to walk on stormy seas. You raise me up to more than I can be.

Publications

J. Nam, W. Cantwell, R. Das, A. Lowe, and S. Kalyanasundaram, "Deformation behaviour of steel/SRPP fibre metal laminate characterised by evolution of surface strains," *Advances in Aircraft and Spacecraft Science*, vol. 3, pp. 61–75, 2016.

X. C. Dou, S. D. Malingam, J. Nam, and S. Kalyanasundaram, "Finite Element Modeling of Stamp Forming Process on Thermoplastic-Based Fiber Metal Laminates at Elevated Temperatures," *World Journal of Engineering and Technology*, vol. 3, pp. 253–258, 2015.

X. C. Dou, S. D. Malingam, J. Nam, and S. Kalyanasundaram, "Finite Element Modeling of Stamp Forming Process on Fiber Metal Laminates," *World Journal of Engineering and Technology*, vol. 3, pp. 247–252, 2015.

J. Nam, W. Cantwell, R. Das, A. Lowe, and S. Kalyanasundaram, "Evolution of meridian strains in stamp forming of steel-based fibre metal laminate," In Proc. 8th Australasian Congress on Applied Mechanics, Melbourne, Australia, 2014.

J. Nam, W. Cantwell, R. Das, A. Lowe, and S. Kalyanasundaram, "Effect of blank holder force on strain evolution of forming of steel/SRPP fibre metal laminate," In Proc. 8th Australasian Congress on Applied Mechanics, Melbourne, Australia, 2014.

J. Nam, W. Cantwell, R. Das, A. Lowe, and S. Kalyanasundaram, "Effect of blank holder force on draw forming of steel/SRPP fibre metal laminate," In Proc. 16th European Conference on Composite Materials, Seville, Spain, 2014.

J. Nam, R. Das and S. Kalyanasundaram, "Damage development and failure behaviour of self-reinforced polypropylene and self-reinforced polypropylene/steel fibre metal laminate under tensile loading," *Composites Part A: Applied Science and Manufacturing*. Manuscript in preparation.

J. Nam, R. Das and S. Kalyanasundaram, "Damage development and failure behaviour of self-reinforced polypropylene and self-reinforced polypropylene/steel fibre metal laminate under tensile loading," *Composites Part B: Engineering*. Manuscript in preparation.

J. Nam, R. Das and S. Kalyanasundaram, "Damage development and failure behaviour of self-reinforced polypropylene and self-reinforced polypropylene/steel fibre metal laminate under tensile loading," *Journal of Composite Materials*. Manuscript in preparation.

Abstract

This thesis discusses material behaviours related to the failure of woven self-reinforced polypropylene (SRPP) and a fibre metal laminate (FML) based on SRPP and mild steel. Single polymer composites such as SRPP are relatively new, as compared to the traditional fibre-reinforced composites, and while there have been studies that investigate the optimal manufacturing methods, there are relatively few that look at the failure behaviour of SRPP in depth. On top of this, SRPP exhibits behaviours that are quite different from most traditional fibre-reinforced polymers due to its unique construction. As a result, there is also limited knowledge of the behaviour of SRPP-based FMLs, except under impact. A better understanding of these materials will be valuable, given that they have a lot of potential uses in many applications, especially for those that can benefit from recyclability, high impact resistance and weight reduction. For this reason, failure, and related deformation behaviours of SRPP and SRPP/steel FML, were investigated.

The material behaviours were studied using different reinforcing directions under uniaxial tension, and different specimen geometries under combined in-plane biaxial and out-of-plane bending deformations, for both the SRPP and FML. In addition, specimens of different thicknesses were studied for SRPP under uniaxial tension, which behave differently and give important insights into the failure mechanisms. Analyses were carried out using a combination of microscopy and surface strain analysis, which can effectively be used to study various damage types in SRPP and their relation to the failure of SRPP and FML.

In this research, various types of damage and related mechanisms were uncovered, some of which have not been previously reported in the literature. One of the most important aspects was that the critical damage mechanisms that cause failure in the materials were identified for different material and loading conditions. This includes a particular type of matrix damage in SRPP which was found to cause an unusually high strain concentration and, as a result, lead to material failure in some cases. It was found that failure from such damage can be suppressed in some specimens which exhibit mechanisms that can impede damage growth.

It was found that the process of damage development, and how this relates to the failure behaviour, can depend on one or more of the following factors, some of which are related: damage type, presence (or

lack) of toughening mechanisms, mode of crack propagation, reinforcing direction, weave geometry, sensitivity to local damage, loading condition, material thickness, and consolidation quality. Some of these factors can influence the failure behaviour to the point that the same type of specimen, subjected to the same loading condition, can fail from different regions of the material, under different failure mechanisms. In the course of the analysis, it was found that, in many cases, the surface strains captured during the deformation process can indicate where, and under which conditions, failure occurred.

The findings from this research highlighted the importance of understanding the exact mechanisms behind the failure of SRPP, SRPP-based FML and similar materials, since they can vary significantly depending on numerous factors. It is anticipated that the findings from this study will lay the groundwork for future research on developing failure criteria for such material systems for the benefit of researchers and designers using composite and hybrid materials.

Nomenclature

AE	Acoustic emission
ARALL	Aramid fibre-reinforced epoxy/aluminium alloy FML
CFRP	Carbon fibre-reinforced polymer
DIC	Digital image correlation
DP steel	Dual phase steel
DSC	Differential scanning calorimetry
FEA	Fibre metal laminate
FLC	Forming limit curve
FLD	Forming limit diagram
FML	Fibre metal laminate
FRP	Fibre-reinforced plastic
GFRP	Glass fibre-reinforced polymer
GFRPP	Glass fibre-reinforced polypropylene
GLARE	Glass fibre-reinforced epoxy composite/aluminium FML
HSCP	High-strain concentration point
IBD test	Induced-biaxial deformation test
iPP	Isotactic polypropylene
OPIM	Oscillating packing injection moulding
PE	Polyethylene
PEEK	Polyether ether ketone
PP	Polypropylene
SiC	Silicon carbide
SPC	Single polymer composite
SRPE	Self-reinforced polyethylene
SRPP	Self-reinforced polypropylene
UD	Unidirectional
WWFE	Worldwide Failure Exercise
0°/90°	Uniaxial tensile test specimens with reinforcements oriented at 0° and 90° to the loading direction

2-phase FRP	Fibre-reinforced polymer with chemically different reinforcement and matrix phases
30°/60°	Uniaxial tensile test specimens with reinforcements oriented at ±30° and ∓60° to the loading direction
± 45°	Uniaxial tensile test specimens with reinforcements oriented at +45° and −45° to the loading direction
[deg]	In-plane shear strain in degrees (°)
[log.]	Logarithmic (true) strain, given in mm/mm
$BC_{\parallel}^{0^{\circ}}$	Boundary or boundary crack oriented at 0° to unidirectional tensile load, between two 0°-tapes.
$BC_{\perp}^{0^{\circ}}$	Boundary or boundary crack oriented at 0° to unidirectional tensile load, between orthogonal tapes where the 90°-tape weaves under the edge of a 0°-tape.
$BC_{\parallel}^{90^{\circ}}$	Boundary or boundary crack oriented at 90° to unidirectional tensile load, between two 90°-tapes.
$BC_{\perp}^{90^{\circ}}$	Boundary or boundary crack oriented at 90° to unidirectional tensile load, between orthogonal tapes where the 0°-tape weaves under the edge of a 90°-tape.
d	Punch depth in IBD test
E^{chord}	Chord modulus of elasticity between 0.1–0.3% strain
$E^{tangential}$	Tangential stiffness above 1% strain
P	Applied load
s_{ε_t}	Standard deviation in strain to failure
t	Specimen thickness
α	Stress ratio, $\sigma_{p2} / \sigma_{p1}$
β	Strain ratio, $\varepsilon_{p2} / \varepsilon_{p1}$
γ_{12}	In-plane shear strain about reinforcing directions
γ_{xy}	In-plane shear strain about x and y directions
ε_1	Strain in the reinforcing direction 1
ε_2	Strain in the reinforcing direction 2
$\varepsilon_{applied}$	Strain applied to the specimen
ε_{avg}	The average strain of the specimen
ε_{HSCP}	Strain at a high-strain concentration point
ε_{max}	Maximum strain in the specimen
ε_{p1}	First principal strain
ε_{p2}	Second principal strain
ε_x	Strain in the x -direction
ε_y	Strain in the y -direction
ε_z	Strain in the z -direction

ε_t	Tensile strain to failure
$\varepsilon^{transition}$	Transition strain
θ	Angle to the loading direction
ι	The ratio between ε_{max} and $\varepsilon_{applied}$ or between ε_{max} and ε_{avg}
σ_1	Stress in the reinforcing direction 1
σ_2	Stress in the reinforcing direction 2
σ_{p1}	First principal stress
σ_{p2}	Second principal
σ_x	Stress in the x -direction
σ_y	Stress in the y -direction
σ_z	Stress in the z -direction
σ_t	Tensile strength
σ_y	Upper yield strength
$\sigma^{transition}$	Stress at transition strain
τ_{12}	In-plane shear stress about reinforcing directions
τ_{xy}	In-plane shear stress about x and y directions
Γ	The gradient of strain increase

Table of Contents

1	Introduction	1
1.1	Background	1
1.2	Aims	4
1.3	Thesis outline	5
2	Literature Review	6
2.1	Introduction	6
2.1.1	Background	6
2.2	Failure behaviour in fibre reinforced plastics.....	9
2.2.1	Thermoset-based FRP	9
2.2.2	Thermoplastic-based FRP	13
2.3	Self-reinforced polypropylene.....	15
2.3.1	Composite structure and failure behaviours	15
2.3.2	Matrix microstructure and interfacial strength	23
2.3.3	Reinforcement microstructure and behaviours.....	29
2.4	Fibre metal laminate.....	34
2.4.1	Steel-based FML	34
2.4.2	Thermoplastic-based FML	35
2.5	Summary	39
3	Materials and Methods	40
3.1	Introduction	40
3.2	Materials.....	40
3.2.1	Steel.....	40
3.2.2	SRPP.....	42
3.2.3	FML.....	42
3.3	Experimental methods.....	48
3.3.1	Uniaxial tension tests.....	48
3.3.2	Induced-biaxial deformation tests	51
3.3.3	Real-time surface strain analyses	54

3.4	Summary	59
4	Failure Behaviour Under Uniaxial Tension (On-axis)	61
4.1	Introduction	61
4.2	Deformation and failure behaviour of self-reinforced polypropylene.....	61
4.2.1	Stress-strain and macroscopic failure behaviour	62
4.2.2	Microscopic analysis of damage mechanisms.....	66
4.2.3	Failure behaviour.....	89
4.2.4	Summary of failure behaviour of SRPP	124
4.3	Deformation and failure behaviour of self-reinforced polypropylene/steel fibre metal laminate.....	125
4.3.1	Stress-strain behaviour and damage characteristics	125
4.3.2	Surface strain analysis	128
4.3.3	Summary of failure behaviour of FML	136
4.4	Summary	137
5	Failure Behaviour Under Uniaxial Tension (Off-axis).....	139
5.1	Introduction	139
5.2	Deformation and failure behaviour of off-axis self-reinforced polypropylene	140
5.2.1	Stress-strain and macroscopic failure behaviour	141
5.2.2	Microscopic damage mechanisms.....	148
5.2.3	Failure behaviour.....	168
5.2.4	Summary of failure behaviour of off-axis SRPP.....	185
5.3	Deformation and failure behaviour of off-axis self-reinforced polypropylene/steel fibre metal laminate.....	186
5.3.1	Stress-strain behaviour and microscopic damage in the SRPP layer	186
5.3.2	Surface strain analysis	191
5.3.3	Summary of failure behaviour of off-axis FML.....	197
5.4	Summary	198
6	Failure Behaviour Under Biaxial Deformation	200
6.1	Introduction	200
6.2	Deformation and failure behaviour of circular specimens	202
6.2.1	SRPP.....	202
6.2.2	FML.....	218
6.3	Deformation and failure behaviour of hourglass specimens	236
6.3.1	SRPP.....	236
6.3.2	FML.....	240
6.4	Summary	248
7	Conclusion and Future Work.....	250

References	257
Appendix A – Collano® 22.100 datasheet	276
Appendix B – Lap shear test summary	277
Appendix C – Finite element analysis setup.....	278
C.1 Material modeling	278
C.1.1 Steel	278
C.1.2 SRPP.....	278
C.1.3 FML.....	280
C.2 Elements and Mesh	280
C.3 Model setup.....	282

List of Figures

Figure 1.1	a) Commercial GLARE® Laminate (glass fibre-reinforced epoxy composite/aluminium FML) [3] and b) its application in Airbus A380. [4]	1
Figure 1.2	Carbon fibre-reinforced composite component in the body of McLaren 720S. [8].....	2
Figure 1.3	Volvo XC90 body structure with steel parts highlighted (green part represents aluminium). [9]	3
Figure 2.1	Example applications of Curv®, a commercial SRPP: a) anti-ballistics (e.g. helmets, protectors, and military vehicle armour); b) sports helmet; and c) automotive components [22].	7
Figure 2.2	Fibre–matrix debonding in a polyester resin/glass fibre-reinforced composite [47].	9
Figure 2.3	Schematic showing of damage events leading to final failure of a UD composite due to increase of the applied tensile load [48, Fig. 3].	10
Figure 2.4	Different types of cracks observed in textile composites loaded in tension. From top to bottom in left column: transverse matrix cracks inside yarns, transverse cracks at yarn boundaries (b), debonding of yarns and local delaminations inside yarns (I), transverse cracks in the matrix pockets, shear matrix cracks. From top to bottom in right column: splitting of the yarns, cracks on the boundary of or inside Z-yarns, longitudinal cracks in the matrix pockets, delaminations. Taken and modified from [24, pp. 43–44, Tab. 3.1].....	11
Figure 2.5	Schematics of the hot compaction process [62].	15
Figure 2.6	a) Diagrams of SRPP made by the hot compaction process; and (b) a scanning electron micrograph at the section indicated in (b) [63].	16
Figure 2.7	Illustration of a) Mode I fracture – tensile opening and b) Mode II fracture – in-plane shear.	22
Figure 2.8	Scanning electron micrograph of an etched longitudinal section of a hot compacted SRPP showing lamellar growth between interfibrillar boundaries [65, Fig. 8b].	24
Figure 2.9	Polarised optical microscopy of the fibre–matrix interface of an SRPP formed by introducing fibre into a molten matrix at 167°C [121, Fig. 2a].	24
Figure 2.10	Schematics for a typical polymer a) spherulite [122, Fig. 14.13]; and b) lamella with conventional crystallographic directions and planes.	25
Figure 2.11	Schematics of shish-kebab structures a) formed in polymers under shear stress [123, Fig. 1], and in SRPP during consolidation, illustrated in b) [124, Abstract] and c) [95, Fig. 12].....	26
Figure 2.12	Crazing observed in polypropylene during a tensile test [133]. The tensile load is vertical in this image.	27

Figure 2.13	Deformation modes in the amorphous phase of semi-crystalline polymers: a) interlamellar slip; b) lamellar separation; c) rotation of stacks of lamellae [109, Fig. 2]. d) rotation of crystal fragments due to slip, marked by arrows. The resolving of the shear on a plane due to simple tension or compression is also illustrated [109, Fig. 4].	28
Figure 2.14	Behaviour of the different sectors in PP spherulites under uniaxial tension and simple shear [133, Fig. 13]. The black arrows represent the applied stresses and the white arrows the locally active deformation mode.	29
Figure 2.15	Stages in the plastic deformation of a semi-crystalline polymer [122, Fig. 15.13].	30
Figure 2.16	Molecular model of the transformation into the microfibrillar structure by fracturing in the initial lamellae in blocks which are then incorporated into microfibrils [120, Fig. 8].	31
Figure 2.17	Formation of 'skewed' microfibrils by shearing of a stack of parallel lamellae: a) stack before shearing, b) after shearing by one lamella thickness per block width, c) after shearing by two lamellae thicknesses per block width [119, Fig. 1].	31
Figure 2.18	Drawing of microfibrillar structure. The centres of mass of the fibrils are displaced linearly as in an affine transformation (a), the fibrils are sheared (b), the electron density difference between crystal blocks and amorphous layers between them is smeared out (c) [120, Fig. 12].	32
Figure 3.1	Measured stress–strain curves of steel, 1.0 mm SRPP, and SRPP/steel FML.	41
Figure 3.2	2/2 twill weave pattern on the SRPP: a) photograph, b) diagram with smallest repeating unit outlined in red.	42
Figure 3.3	Stacking sequence of a SRPP/steel FML.	43
Figure 3.4	Temperature profile during the manufacture of FML.	44
Figure 3.5	Lap shear test specimen. All dimensions are in mm, not to scale. SRPP is shown in black and steel is shown in grey.	46
Figure 3.6	Examples of failed lap shear test specimens, with layers peeled apart and bent to show damaged surfaces.	46
Figure 3.7	Steel tensile test specimen. All dimensions are in mm, not to scale.	50
Figure 3.8	SRPP tensile test specimen with aluminium tabs. All dimensions are in mm, not to scale. Gauge length (l) is 44 mm for 0.3 mm specimens in $30^\circ/60^\circ$ and $\pm 45^\circ$ directions and 66 mm for all other samples. Thickness (t) is 0.3 mm, 0.6 mm or 1.0 mm. Direction of reinforcement in SRPP is $0^\circ/90^\circ$, $30^\circ/60^\circ$ or $\pm 45^\circ$.	50
Figure 3.9	FML tensile test specimen. All dimensions are in mm, not to scale. SRPP is shown in black and steel is shown in grey. Gauge section is indicated by dotted lines. Direction of reinforcement in SRPP is $0^\circ/90^\circ$, $30^\circ/60^\circ$ or $\pm 45^\circ$.	50
Figure 3.10	Deformation modes in sheet metal forming indicated on the a) strain diagram and b) stress diagram with contours of equal effective stress (yield loci). Principal directions are indicated by 1 and 2 in the diagrams. Yield loci for [214, pp. 33, 39].	51
Figure 3.11	Induced-biaxial deformation test setup; a) a 300 kN double-action mechanical press with hydraulic ram used in the test, and b) a cross-sectional schematic diagram. All dimensions are in mm, not to scale.	53
Figure 3.12	Induced-biaxial deformation test specimen geometries. Tape orientations are indicated by directions 1 and 2. All dimensions are in mm except the angle.	54
Figure 3.13	ARAMIS, a commercial digital image correlation system provided by GOM GmbH [218].	55

Figure 3.14	Example of facets in ARAMIS – a) 15×15 pixel facets with a facet step of 13 pixels [219, Ch. D, p. 3], b) facets shown on images captured by left and right cameras at a deformed state (green solid lines), with undeformed state shown as reference (white dashed lines) [219, Ch. A, p. 6].	55
Figure 3.15	Stochastic pattern spray-painted on specimens for uniaxial tensile tests.	56
Figure 3.16	3D DIC system setup for induced-biaxial deformation tests. The digital cameras are behind the support structure of the press machine.	58
Figure 3.17	Examples of DIC images for a deformed circular SRPP specimen, showing a) a digital image from the left camera, b) strain grids superimposed on a digital image from the right camera, and c) computed surface strains.	58
Figure 3.18	Stochastic pattern spray-painted on specimens for induced-biaxial deformation tests.	59
Figure 4.1	Tensile stress-strain curves of 0.3 mm, 0.6 mm and 1.0 mm SRPP samples. Failure strains portrayed are sample averages. Stress values are based on the averages of specimens that have not failed at given strains, and error bars indicate sample standard deviations.	63
Figure 4.2	Typical specimen failure in a) 0.3 mm, b) 0.6 mm and c) 1.0 mm SRPP tensile samples. Spray painted sides are also shown for (b) and (c) for clarity.	64
Figure 4.3	Optical micrograph showing different types of damage in a 0.3 mm SRPP tensile specimen. Dotted lines divide regions where surface tapes are at 0° and 90° to the applied load.	67
Figure 4.4	Optical micrograph of tape-splits in a 0° -tape and a 90° -tape on the surface of a 0.6 mm SRPP tensile specimen.	68
Figure 4.5	Optical micrograph of aligned crazes forming on the surface of a 0.3 mm SRPP tensile specimen.	69
Figure 4.6	Optical micrograph of aligned crazes forming on the surface of a 0.6 mm SRPP tensile specimen.	70
Figure 4.7	Optical micrograph of crazing on a surface exposed from a split in a 90° -tape of a 0.3 mm SRPP tensile specimen.	72
Figure 4.8	Optical micrographs of fibril pull-outs in a 1.0 mm SRPP tensile specimen.	73
Figure 4.9	Optical micrograph of a fibril pull-out from a 0° -tape in a 0.6 mm SRPP tensile specimen.	73
Figure 4.10	Optical micrographs of fibril pull-outs in a 1.0 mm SRPP tensile specimen.	74
Figure 4.11	Optical micrographs of a 0° -tape of a 0.6 mm SRPP tensile specimen, showing different modes of crack propagation, indicated by the different crack tips.	75
Figure 4.12	Optical micrograph of a fracture surface of a 0.3 mm SRPP tensile specimen. The direction of the applied load is orthogonal to the page.	76
Figure 4.13	Optical micrograph of a fracture surface of a 0.3 mm SRPP tensile specimen, showing boundaries between 90° -tape and the matrix (A and B) and a fibril pull-out (C).	77
Figure 4.14	Optical micrograph of microfibrillar crack bridging in a 90° -tape of a 0.6 mm SRPP tensile specimen.	78
Figure 4.15	Scanning electron micrographs of microfibrillar crack bridging in 90° -tapes of 0.6 mm SRPP tensile specimens. Magnification = 200x (a), = 20,000x (b). EHT = 1.00kV.	79

Figure 4.16	Micrographs of a) 1.0 mm and b) 0.6 mm SRPP tensile specimens showing smaller microfibrils from crack bridging attached around larger fibril pull-outs.....	80
Figure 4.17	Different fibrils in SRPP according to the lateral dimension. The relationship to Peterlin's model [120, Fig. 12] is shown.	80
Figure 4.18	Crazing fibrils in polyethylene, reproduced from [132, p. 405]. The applied load is vertical in this image.....	81
Figure 4.19	Crack bridged by single fibres and ligaments consisting of several fibres in a unidirectional carbon-fibre/epoxy composite. Reproduced from [229, p. 224].....	81
Figure 4.20	Optical micrograph of tape kinking in a 0.6 mm SRPP tensile specimen.	82
Figure 4.21	Optical micrograph of a 0.6 mm SRPP tensile specimen showing oblique crack initiation and propagation in a section of a 0°-tape.	83
Figure 4.22	Possible deformation gradient and shear stress created around fibril pull-outs in an SRPP tape.	84
Figure 4.23	Optical micrograph of a 0.6 mm SRPP tensile specimen, showing a section of a 0°-tape that has been delaminated from the 90°-tape on the surface.....	85
Figure 4.24	Optical micrograph of a 1.0 mm SRPP tensile specimen, showing a section of a 90°-tape that has delaminated from the 0°-tape on top.....	87
Figure 4.25	Example of shear flow in the matrix at a boundary crack between orthogonal tapes.....	87
Figure 4.26	Illustration of the four types of boundaries and boundary cracks.....	90
Figure 4.27	Boundary cracks between parallel tapes in a 0.6 mm SRPP tensile specimen, exhibiting matrix damage similar to tape-splits.....	91
Figure 4.28	Boundary cracks between orthogonal tapes in 0.3 mm SRPP tensile specimens, depicting the process of the matrix damage development.	91
Figure 4.29	Cross-sections of boundary cracks on the surface that are oriented at 90° to the loading direction, a) between two 90°-tapes ($BC \parallel 90^\circ$), and b) between 0° and 90°-tapes ($BC \perp 90^\circ$).....	93
Figure 4.30	Optical micrograph of 0.3 mm SRPP tensile specimen, showing a crack propagating from boundary cracks.	94
Figure 4.31	Optical micrograph of a boundary crack propagating into the tape in a 0.6 mm SRPP tensile specimen.....	95
Figure 4.32	First principal strain of a 0.3 mm SRPP tensile specimen at applied strains of a) 4.38% and b) 17.9%.....	96
Figure 4.33	First principal strain on the front surface of a 0.3 mm SRPP tensile specimen at an applied strain of 19.4% (left) and a photograph of the back of the specimen after failure (right). Arrows and dotted lines indicate corresponding sections along the edges of 90°-tapes.....	96
Figure 4.34	First principal strain on a surface of a 0.3 mm SRPP tensile specimen at an applied strain of 13.3%, showing an example of a high-strain segment and sections along the edge and the middle of a 90°-tape.	97
Figure 4.35	Possible locations where high-strain segments (red lines) occur, in relation to the weave structure.	98
Figure 4.36	Plot of first principal strain (ϵ_{p1}) on sections along the edge and middle of a 90°-tape of a 0.3 mm SRPP specimen (bottom), and a diagram of the corresponding weave structure (top).....	99

Figure 4.37 Cause of the textured surface strain according to [183, p. 202, Fig. 6.19], reproduced from the same literature.	99
Figure 4.38 First principal strains of a 0.3 mm SRPP tensile specimen at applied strains of a) 5.0%, b) 10.0%, and c) 13.3% (last stage before specimen failure). Points A and B are points of maximum strain at different stages of deformation. Failure occurs along the dotted line in (c).	102
Figure 4.39 First principal strain (ϵ_{p1}) against the applied strain for points A, B and the average strain of the specimen in Figure 4.38.	102
Figure 4.40 First principal strain (ϵ_{p1}) against the applied strain for a maximum strain point, failure point and the average strain in a 0.3 mm SRPP tensile specimen.	104
Figure 4.41 First principal strain (ϵ_{p1}) against the applied strain for maximum strain points and the average strain in a 0.3 mm SRPP tensile specimen.	105
Figure 4.42 Strain paths of points A, B and the average strain of the specimen in Figure 4.38, a) up to failure, and b) up to 6% applied strain. Strains are given in first (ϵ_{p1}) and second (ϵ_{p2}) principal strains.	106
Figure 4.43 First principal strains of a 0.3 mm SRPP tensile specimen at applied strains of a) 4.99%, b) 15.0% and c) 19.4% (last stage before specimen failure). Points A, B, and C are points of maximum strains at different stages of deformation. Failure occurs along the dotted line in (c).	107
Figure 4.44 Strain paths of points A, B and C and the average strain in the 0.3 mm SRPP tensile specimen in Figure 4.43. Strains are given in first (ϵ_{p1}) and second (ϵ_{p2}) principal strains.	107
Figure 4.45 First principal strains of a 0.3 mm SRPP tensile specimen at applied strains of a) 5.0% and b) 7.8% (last stage before specimen failure). Points A and C are points of maximum strain at different stages of deformation, and point B is an HSCPs. Failure occurs along the dotted line in (b).	108
Figure 4.46 Optical micrograph showing brittle fracture in a 0.3 mm SRPP tensile specimen. A and B indicate crack branching.	110
Figure 4.47 Optical micrograph of a 0.3 mm SRPP tensile specimen showing brittle fracture.	110
Figure 4.48 Optical micrographs of a) brittle and b) ductile fracture surfaces of 0.3 mm SRPP tensile specimens. The direction of the applied load is orthogonal to the page.	111
Figure 4.49 Optical micrograph of fracture in a 0.3 mm SRPP tensile specimen, showing both brittle and ductile characteristics. (a) is focused on the upper surface, (b) is focused further from surface, and (c) shows an area in (b) at a higher magnification.	112
Figure 4.50 Optical micrograph of a 0.3 mm SRPP tensile specimen, pointing out brittle failure in 90°-tape and ductile failure in 0°-tape along the fracture path.	113
Figure 4.51 Optical micrograph of the 0.3 mm SRPP tensile specimen in Figure 4.50, showing propagation of a crack in the same brittle or ductile mode into 0° and 90°-tapes.	114
Figure 4.52 Optical micrograph of a 0.6 mm SRPP tensile specimen, showing crack tip blunting.	116
Figure 4.53 Optical micrograph of a 0.6 mm SRPP tensile specimen, showing crack arresting in a 90°-tape by developing tape-splits at local zones ahead of the cracks.	118
Figure 4.54 Cook and Gordon's crack deflection mechanism, showing interaction between an advancing crack and a plane of weakness under various conditions. Reproduced from [235, Fig. 8–12].	118

Figure 4.55	Growth of an oblique crack in a 0°-tape of a 1.0 mm SRPP tensile specimen, which does not lead to an immediate failure of the specimen. The applied strain at failure was 15.9%.....	120
Figure 4.56	First principal strains of a 0.6 mm SRPP tensile specimen at the last stage just before specimen failure (15.1% applied strain).	122
Figure 4.57	Digital image (left) and surface strain (right) of a section of a 1.0 mm SRPP tensile specimen, showing limitation in strain computation around large damages for a high-precision measurement.	123
Figure 4.58	Digital image (left) and first principal strain (right) of a 0.6 mm SRPP tensile specimen, showing reduced accuracy of strain computation along the edge of the specimen.	123
Figure 4.59	Photographs (a) and scanning electron micrographs (SEM) (b) showing typical damage in the SRPP layer of SRPP/steel-FML tensile specimens. SEM magnification = 5,000x (left), 20,000x (right), EHT = 1.00kV.	128
Figure 4.60	First principal strain of a SRPP/steel FML tensile specimen at the applied strains shown. The last image shows the stage just before failure and regions of higher strains are indicated. Scales have been manually adjusted to show strain patterns.	129
Figure 4.61	First principal strain (ϵ_{p1}) and shear strain (γ_{12}) in an SRPP/steel FML tensile specimen at 0.612% applied strain. Scales have been manually adjusted to emphasise strain patterns.....	130
Figure 4.62	First principal strain (ϵ_{p1}) against second principal strain (ϵ_{p2}) for steel, SRPP and SRPP/steel FML tensile specimens.	131
Figure 4.63	First principal strain of the SRPP/steel FML tensile specimen shown in Figure 4.60 a) before, b) during and c) after failure. Scale has been manually adjusted to show strain patterns.	132
Figure 4.64	First principal strain (ϵ_{p1}) along a section of the SRPP/steel FML tensile specimen in Figure 4.63a, at different stages of deformation.	133
Figure 4.65	First principal strain of a SRPP/steel FML tensile specimen a) before, b) during and c) after failure. Scale has been manually adjusted to show strain patterns.	133
Figure 4.66	a) First principal strain (ϵ_{p1}) in the SRPP/steel FML tensile specimen in Figure 4.65a. ϵ_{p1} against b) the applied strain and c) the second principal strain (ϵ_{p2}), at strain concentration points shown in (a). Average strain in the specimen is also given for comparison.....	134
Figure 4.67	Comparison of strain growth at HSCPs in a) 0.3 mm, b) 0.6 mm, c) 1.0 mm SRPP and d) SRPP/steel FML specimens. Images on the left represent strains at the last stage before the specimens fail.	135
Figure 5.1	Shear strain (γ_{12}) definition. Dotted lines indicate the undeformed state, and solid lines indicate the deformed state.....	140
Figure 5.2	Tensile stress-strain curves of 0.3 mm SRPP loaded at 0°/90°, 30°/60° and ± 45°. Failure strains portrayed are sample averages, stress values are based on the average of specimens that have not failed at given strains, and error bars indicate sample standard deviations. Point of failure for each sample is indicated with a cross.....	141
Figure 5.3	Tensile stress-strain curves of 0.6 mm SRPP loaded at 0°/90°, 30°/60° and ± 45°. Failure strains portrayed are sample averages, stress values are based on the average of specimens that have not failed at given strains, and error bars indicate sample standard deviations.	142

Figure 5.4	Tensile stress-strain curves of 1.0 mm SRPP loaded at 0°/90°, 30°/60° and ± 45°. Failure strains portrayed are sample averages, stress values are based on the average of specimens that have not failed at given strains, and error bars indicate sample standard deviations.	142
Figure 5.5	Tensile stress-strain curves of 0.3mm, 0.6 mm and 1.0 mm SRPPs loaded at a) 30°/60° and b) ± 45°. Failure strains portrayed are sample averages and the stress values are based on the average of specimens that have not failed. The error bars indicate sample standard deviations.	144
Figure 5.6	Photographs of 0.3 mm (a–c), 0.6 mm (d) and 1.0 mm (e) 30°/60° SRPP tensile test specimens at failure.	145
Figure 5.7	Photographs of 0.3 mm (a–c), 0.6 mm (d) and 1.0 mm (e) ± 45° SRPP tensile test specimens at failure.	146
Figure 5.8	Delamination shown in a 1.0 mm ± 45° SRPP tensile test specimen after failure. The direction of the applied load is horizontal in this image.	146
Figure 5.9	Separation of a 0.6 mm 30°/60° specimen after failure.	147
Figure 5.10	Optical micrograph of a boundary crack between two 60°-tapes in a 0.3 mm 30°/60° SRPP tensile test specimen, indicated with an arrow.	149
Figure 5.11	Optical micrograph of boundary cracks between 30° and 60°-tapes in a 0.3 mm 30°/60° SRPP tensile test specimen.	149
Figure 5.12	Optical micrographs of boundary cracks in 0.3 mm ± 45° SRPP tensile test specimens.	150
Figure 5.13	Optical micrographs showing ductile damage in a) 0.3 mm 30°/60°, b) 1.0 mm ± 45°, and c) 0.3 mm ± 45° SRPP tensile test specimens.	150
Figure 5.14	Optical micrograph of a curved edge of a 30°-tape in a 0.6 mm 30°/60° SRPP tensile test specimen.	151
Figure 5.15	Tape-splits in a 0.6 mm 30°/60° SRPP tensile test specimen.	152
Figure 5.16	Optical micrograph of tape-splits in a 1.0 mm ± 45° SRPP tensile test specimen.	152
Figure 5.17	Optical micrograph of matrix crazing between neighbouring 60°-tapes in a 0.3 mm 30°/60° SRPP tensile test specimen.	153
Figure 5.18	Optical micrograph of surface matrix crazing in a 0.3 mm ± 45° SRPP tensile test specimen.	154
Figure 5.19	Optical micrograph of a 0.3 mm 30°/60° SRPP tensile test specimen near a slit, showing a mixture of crazing on the surface matrix and shear flow and ductile failure in the tape.	155
Figure 5.20	Optical micrograph of a delaminated tape in a 1.0 mm ± 45° SRPP tensile test specimen. Direction of the applied load is 45° to the horizontal direction.	157
Figure 5.21	Optical micrograph of delamination occurring from a boundary between 30° and 60°-tapes in a 0.6 mm 30°/60° SRPP tensile test specimen.	157
Figure 5.22	Comparison of tape orientations in regions of small and large amounts of damage in a 0.6 mm 30°/60° SRPP tensile test specimen.	158
Figure 5.23	Optical micrograph of the edges of a) 0.6 mm 30°/60° and b) 0.3 mm ± 45° SRPP tensile test specimens.	159
Figure 5.24	Pull-outs and fracture of tapes and fibrils in a 1.0 mm ± 45° SRPP tensile test specimen after failure. Examples of fractured tapes and fibrils are highlighted. Direction of load is horizontal in the image.	160

Figure 5.25	End of a fibril that has fractured in a brittle manner in a 0.6 mm 30°/60° SRPP tensile test specimen.....	160
Figure 5.26	Optical micrographs of the end of a fibril pull-out in a 1.0 mm ± 45° SRPP tensile test specimen at different magnifications.	161
Figure 5.27	Optical micrograph of a tape section in a 0.6 mm 30°/60° SRPP tensile test specimen, exhibiting both brittle and ductile failure.....	161
Figure 5.28	Optical micrograph of a fibrillar crack bridging in a tape-split of a 0.6 mm 30°/60° SRPP tensile test specimen.	162
Figure 5.29	Scanning electron micrographs of fibrillar crack bridging in a tape-split of a 0.6 mm 30°/60° SRPP tensile test specimen. Magnification = 5,000x (top), 20,000x (bottom), EHT = 1.00kV. Direction of the load is at 60° to the tape orientation shown.	163
Figure 5.30	Optical micrograph of fibrillar crack bridging in a tape-split of a 1.0 mm ± 45° SRPP tensile test specimen.	163
Figure 5.31	Scanning electron micrograph of fibrillar crack bridging in a tape-split of a 1.0 mm ± 45° SRPP tensile test specimen. Magnification = 5,000x, EHT = 1.00kV. The tape is orientated along the arrows in the image.	164
Figure 5.32	Optical micrograph of fibrils bridging inter-tape delamination in a 0.6 mm 30°/60° SRPP tensile test specimen.	164
Figure 5.33	Scanning electron micrographs of matrix damage at a boundary between + 45° and - 45°-tapes of a 0.6 mm ± 45° SRPP tensile test specimen. Magnification = 5,000x (top), 20,000x (bottom), EHT = 1.00kV.....	165
Figure 5.34	Optical micrograph of a tape-fold in a 0.6 mm ± 45° SRPP tensile test specimen.....	166
Figure 5.35	Optical micrograph of a fractured tape section in a 0.6 mm 30°/60° SRPP tensile test specimen.	167
Figure 5.36	Failures along a boundary between 30° and 60°-tapes in a 0.3 mm 30°/60° SRPP tensile test specimen. White lines indicate boundaries between 30° and 60°-tapes and red lines on either side of the damage represent the same tape boundary.	169
Figure 5.37	Optical micrograph of a slit at a boundary between 30° and 60°-tapes in a 0.3 mm 30°/60° SRPP tensile test specimen. Solid lines indicate boundaries between 30° and 60°-tapes and dotted lines indicate boundaries between tapes oriented in the same direction. Arrows indicate tape orientations.	169
Figure 5.38	Slits occurring away from fracture sites and not along tape boundaries in 0.3 mm SRPP tensile test specimens tested at a) ± 45° and b) 30°/60°. Nearby tape boundaries between weft and warp tapes are indicated with dotted lines for clarity.....	170
Figure 5.39	Optical micrograph of a possible crack tip blunting in a 0.3 mm ± 45° SRPP tensile test specimen.....	171
Figure 5.40	Optical micrographs of fractured edges of a 0.3 mm 30°/60° SRPP tensile test specimen.	171
Figure 5.41	Fractures in 0.3 mm SRPP tensile test specimens with failure along the indicated tape boundaries, tested in a) 30°/60° and b) ± 45° directions.....	172
Figure 5.42	Crack propagation and coalescence in a 0.3 mm ± 45° SRPP tensile test specimen.	173
Figure 5.43	a) First principal strain (ϵ_{p1}) and b) shear strain (γ_{12}) in a 0.3 mm ± 45° SRPP tensile test specimen just before fracture.	174
Figure 5.44	a) Photograph and b) first principal strain (ϵ_{p1}) in a 0.3 mm 30°/60° SRPP tensile test specimen at an applied strain of 41.5%.....	174

Figure 5.45	a) Shear strain (γ_{12}) before failure in a 0.3 mm $\pm 45^\circ$ SRPP tensile test specimen. Fracture paths are indicated by red lines in (a) and a photograph of the specimen after failure is shown in (b) for reference.	175
Figure 5.46	Fracture along tape boundaries (encircled) in the 0.3 mm $\pm 45^\circ$ SRPP tensile test specimen in Figure 5.45. Fracture along the boundary labelled ‘slit’ indicates the slit at B in Figure 5.45a.....	176
Figure 5.47	First principal strain (ϵ_{p1}) against the applied strain for points A, B, C and the average strain in the 0.3 mm $\pm 45^\circ$ SRPP tensile test specimen in Figure 5.45.....	177
Figure 5.48	Strain paths of points A, B, C and the average strain in the 0.3 mm $\pm 45^\circ$ SRPP tensile test specimen in Figure 5.45.	177
Figure 5.49	First principal strain (ϵ_{p1}) against strain ratio ($\beta = \epsilon_{p2}/\epsilon_{p1}$) for points A, B, C and the average strain in the 0.3 mm $\pm 45^\circ$ SRPP tensile test specimen in Figure 5.45.	178
Figure 5.50	Strain behaviour for points A, B, C and the average strain in the 0.3 mm $\pm 45^\circ$ SRPP tensile test specimen in Figure 5.45. a) Shear strain (γ_{12}) against applied strain and b) γ_{12} against strain ratio ($\beta = \epsilon_{p2}/\epsilon_{p1}$).....	178
Figure 5.51	a) First principal strain (ϵ_{p1}) in a 0.3 mm $30^\circ/60^\circ$ SRPP tensile test specimen before fracture. Points A and B indicate strain concentration points along the fracture path. ϵ_{p1} against b) applied strain and c) strain ratio ($\beta = \epsilon_{p2}/\epsilon_{p1}$) for strain concentration points and the average strain in the specimen.....	179
Figure 5.52	Progression of damage until failure (a–c) and after failure (d–f) in a 0.6 mm $30^\circ/60^\circ$ SRPP specimen.	181
Figure 5.53	First principal strain (ϵ_{p1}) in a 0.6 mm $30^\circ/60^\circ$ SRPP tensile test specimen at applied strains of a) 17.5% and c) 17.8%, showing strain concentration at the edge of a tape which pulls out from the edge of the specimen.	182
Figure 5.54	0.6 mm $\pm 45^\circ$ SRPP tensile test specimens at failure.	183
Figure 5.55	Tape pull-outs in a 1.0 mm $30^\circ/60^\circ$ SRPP tensile test specimen at failure.	184
Figure 5.56	0.6 mm $\pm 45^\circ$ SRPP tensile test specimen with (a) and without (b) a translucent layer of first principal strain (ϵ_{p1}) transposed on top, at 17.7% applied strain. (Applied strain at failure = 19.2%).	185
Figure 5.57	Tensile stress-strain curves of $30^\circ/60^\circ$ and $\pm 45^\circ$ SRPP/steel FMLs in comparison to $0^\circ/90^\circ$ FML.	187
Figure 5.58	Tensile stress-strain curves of a) $30^\circ/60^\circ$ and b) $\pm 45^\circ$ SRPP/steel FMLs in comparison to steel and 1.0 mm SRPPs of corresponding orientations.....	188
Figure 5.59	Buckled steel layers in an unloaded $30^\circ/60^\circ$ SRPP/steel FML tensile test specimen, post-failure. Direction of the applied load is horizontal in the image.....	189
Figure 5.60	Delamination within the SRPP layer of a $\pm 45^\circ$ SRPP/steel FML tensile test specimen caused by out-of-plane bending in the steel layers. Direction of the applied load is horizontal in the image.	190
Figure 5.61	Scanning electron micrograph of the surface of a delaminated SRPP layer in a $\pm 45^\circ$ SRPP/steel FML tensile test specimen. Magnification = 500x, EHT = 1.00kV.....	191
Figure 5.62	First principal strain (ϵ_{p1}) of a $30^\circ/60^\circ$ SRPP/steel FML tensile test specimen at applied strains shown. The final image shows strains just before failure.....	192
Figure 5.63	First principal strain (ϵ_{p1}) of a $\pm 45^\circ$ SRPP/steel FML tensile test specimen at applied strains shown.	193

Figure 5.64	First principal strain (ϵ_{p1}) of the 30°/60° SRPP/steel FML tensile test specimen in Figure 5.62 at applied strains of a) 5.53% and b) 29.4%, showing strain localisation bands, tape directions and the fracture band.	194
Figure 5.65	Example of localised necking and failure occurring in the steel layer of a $\pm 45^\circ$ SRPP/steel FML tensile test specimen, where the surface strain is highest. (First principal strain is shown).	194
Figure 5.66	First principal strain (ϵ_{p1}) of a $\pm 45^\circ$ SRPP/steel FML tensile test specimen at an applied strain of 34.2%, showing strain localisation bands and tape directions.	195
Figure 5.67	a) Applied strain in the loading direction ($\epsilon_{applied}$) and b) maximum shear angle (γ_{12}) at failure of 1.0 mm SRPP and SRPP/steel FML specimens, tested at 30°/60° and $\pm 45^\circ$ to the applied load.	196
Figure 6.1	Local x - y coordinates and tape orientations 1 and 2 in the undeformed state, for a) circular and b) hourglass specimens in induced-biaxial deformation tests. Dotted perimeters represent approximate boundaries for areas visible to the DIC system. c) Outer and inner surfaces or layers shown on a cross-section of a deformed specimen.	201
Figure 6.2	Inner surfaces of failed circular SRPP induced-biaxial deformation test specimens. Corners of the images are located on the die bend. Stages of critical failure initiation (1) and propagation (2 – 5) are indicated in (e).	203
Figure 6.3	Close up of failure at the centre of the specimen shown in Figure 6.1e.	204
Figure 6.4	Combination of deformation in the tape directions and in-plane shear deformations at locations diagonal to the tape direction from the centre.	205
Figure 6.5	Fibril pull-outs along a diagonal failure path from the centre of a specimen.	205
Figure 6.6	Propagation of failure in the direction of tape orientation.	206
Figure 6.7	Larger amount of tape and fibril pull-outs occurring on the outer surface (a) of a specimen compared to the inner surface (b), in same regions (A and B).	206
Figure 6.8	Side-view of the outer surface of a specimen, showing fibril pull-outs.	207
Figure 6.9	Comparison of circular SRPP induced-biaxial deformation test specimens that exhibit different amounts of damage before failure.	207
Figure 6.10	Fibril pull-out process in circular SRPP induced-biaxial deformation test specimens.	209
Figure 6.11	Digital image of a region in a circular SRPP induced-biaxial deformation test specimen before failure. Red lines indicate large tape-splits, yellow lines indicate boundary cracks and white lines indicate fractures across fibrils. Fibril fractures that triggered fibril pull-outs are numbered in the order of appearance.	211
Figure 6.12	Digital image of a circular SRPP induced-biaxial deformation test specimen before failure, showing a critical fibril pull-out near the centre (A) and a non-critical fibril pull-out away from the centre region (B).	212
Figure 6.13	a) Strain in x -direction (ϵ_x), b) strain in y -direction (ϵ_y), and c) shear angle about x - y directions in a circular SRPP induced-biaxial deformation test specimen before failure.	213
Figure 6.14	Comparison of strains underneath fibril pull-outs in the centre region of the specimen (A) and outside the centre region (B), in the direction of tape orientation, of a circular SRPP induced-biaxial deformation test specimen.	214
Figure 6.15	Strain in x -direction (ϵ_x) in a circular SRPP induced-biaxial deformation test specimen: a) ϵ_x distribution after a fibril pull-out occurs in the x -direction at point A	

	at a punch depth (d) of 34.0 mm, b) plot of ϵ_x against d at points A and B, c) ϵ_x distribution after the fibril pull-outs propagate further and the fibrils unload ($d = 36.9$ mm).	215
Figure 6.16	First principal strain directions in a circular SRPP induced-biaxial deformation test specimen indicated with arrows, before (a) and after (b) a fibril pull-out.	216
Figure 6.17	Typical curves of applied load (P) against specimen depth (d) of circular induced-biaxial deformation tests specimens for steel, SRPP and SRPP/steel FML.	218
Figure 6.18	a) Punch depth (d), b) average first principal strain (ϵ_{p1}) and average strain in x -direction (ϵ_x) in circular induced-biaxial deformation tests specimens for steel, SRPP and SRPP/steel FML before failure.	219
Figure 6.19	Circular SRPP/steel FML induced-biaxial deformation test specimens that have failed a) along meridian lines or b) partially along the meridian lines. Corners of the images are located on the lock-ring. Horizontal and vertical lines marked on the inner surface depict tape directions in the SRPP layer, not meridian lines.	220
Figure 6.20	Circular SRPP/steel FML induced-biaxial deformation test specimens that have failed in the side-wall regions. Corners of the images are located on the lock-ring. Horizontal and vertical lines marked on the inner surface depict tape directions in the SRPP layer, not meridian lines.	221
Figure 6.21	Comparison of first principal strains in circular induced-biaxial deformation test specimens for steel (left), SRPP (centre) and SRPP/steel FML (specimen in Figure 6.19a, right), at punch depths of approximately a) 0 – 1 mm, b) 10 mm, c) 20 mm, and d) 30 mm.	222
Figure 6.22	Comparison of strain in the y -direction in circular induced-biaxial deformation test specimens for steel (left), SRPP (centre) and SRPP/steel FML (specimen in Figure 6.19a, right), at punch depths of approximately a) 10 mm, b) 20 mm, and c) 30 mm.	223
Figure 6.23	First principal strains in circular SRPP/steel FML induced-biaxial deformation test specimens that fail along the meridians (left) and in the side-wall region (right), a) at a punch depth of 35.7 mm and b) just before failure (punch depths of 36.2 mm, 36.0 mm). Digital images of specimens after failure are shown for reference in (c).	225
Figure 6.24	First principal strain (ϵ_{p1}) of a circular steel/SRPP FML induced-biaxial deformation test specimen at punch depths of a) 35.7 mm, b) 35.8 mm, c) 35.9 mm, and d) 36.0 mm (last stage before failure). Images on the left depict surface strain distributions. Plots on the right depict strains along a horizontal section through the point of maximum strain ($\epsilon_{p1, \max}$), with red lines indicating strains at the stage corresponding to the left image.	226
Figure 6.25	Failure in a circular steel induced-biaxial deformation test specimen: a) first principal strain distribution and maximum strain point ($\epsilon_{p1, \max}$) at the last stage before failure, b) tearing (left) and propagation of crack (right) upon failure.	227
Figure 6.26	First principal strain (ϵ_{p1}) and strains in x and y directions (ϵ_x , ϵ_y) in a circular steel/SRPP FML induced-biaxial deformation test specimen that fails along the meridian lines, at the last stage before failure. Points in ϵ_y distribution that are highlighted in a translucent grey colour represent strains above 20.0%. ϵ_x in an SRPP specimen at the last stage before failure is given for comparison.	228
Figure 6.27	First principal strain (ϵ_{p1}) and strains in x and y directions (ϵ_x , ϵ_y) in a circular steel/SRPP FML induced-biaxial deformation test specimen that fails in the side-wall region, at the last stage before failure (left). Points in ϵ_x and ϵ_y distributions that are highlighted in a translucent grey colour represent strains above 20.0%. ϵ_{p1} in a steel specimen at the last stage before failure is given for comparison (right).	229

Figure 6.28	Inner surface of a circular steel/SRPP FML induced-biaxial deformation test specimen, showing propagation of failure in the constituent layers.	230
Figure 6.29	Comparison of first principal strain in circular steel/SRPP FML induced-biaxial deformation test specimens that fail at the side-wall (left) and along the meridians (right), and in FML specimen simulated using finite element analysis (right), at punch depths of approximately a) 10 mm, b) 20 mm, c) 30 mm, and d) 35 mm (close to failure).	232
Figure 6.30	Comparison of strain in the y-direction in circular steel/SRPP FML induced-biaxial deformation test specimens that fail at the side-wall (left) and along the meridians (right), and in FML specimen simulated using finite element analysis (right), at punch depths of approximately a) 10 mm, b) 20 mm, c) 30 mm, and d) 35 mm (close to failure).	234
Figure 6.31	a) Shear angle about tape orientations (γ_{12}), b) first principal strain (ϵ_{p1}), and c) second principal strain (ϵ_{p2}) in an SRPP hourglass induced-biaxial deformation test specimen before failure.	237
Figure 6.32	Damage in an SRPP hourglass induced-biaxial deformation test specimen shown after failure.	237
Figure 6.33	Development of a critical tape pull-out in an SRPP hourglass induced-biaxial deformation test specimen at punch depths of a) 22.5 mm, b) 24.4 mm, c) 26.8 mm, d) 34.3 mm (last stage before failure), and e) after failure. Photographs are shown on the left and ϵ_{p1} are shown on the right. The dotted lines indicate areas where the strain cannot be computed.	238
Figure 6.34	Damage in SRPP/steel FML hourglass induced-biaxial deformation test specimens shown after failure.	240
Figure 6.35	Failure in the outer steel and SRPP layers in an SRPP/steel FML hourglass induced-biaxial deformation test specimen.	241
Figure 6.36	Comparison of first principal strains in steel (left), SRPP (centre) and SRPP/steel FML (right) hourglass induced-biaxial deformation test specimens, at punch depths of approximately a) 0 – 1 mm, b) 10 mm, c) 20 mm, and d) 30 mm, except for the steel specimen at a punch depth of around 30 mm.	242
Figure 6.37	a) Comparison of strain paths in steel, SRPP and SRPP/steel FML hourglass induced-biaxial deformation test specimens, in a plot of first principal strain (ϵ_{p1}) against second principal strain (ϵ_{p2}). For each material, the maximum ϵ_{p1} point (ϵ_{max}) and the average strain in the centre region (ϵ_{avg}) are given, where the centre region is the top 1 mm of the final punch depth (example given in b).	243
Figure 6.38	Comparison of shear angles in SRPP (left) and SRPP/steel FML (right hourglass induced-biaxial deformation test specimens in Figure 6.36, at punch depths of approximately a) 0 – 1 mm, b) 10 mm, c) 20 mm, and d) 30 mm.	244
Figure 6.39	Comparison of first principal strain (ϵ_{p1}) and shear angle (γ_{12}) in SRPP and SRPP/steel FML hourglass induced-biaxial deformation test specimens shown in Figure 6.38, at a punch depth of 30 mm. Average strains in the centre regions (ϵ_{p1} , γ_{12}) and maximum strains ($\epsilon_{p1, max}$, $\gamma_{12, max}$) are given, where the centre region is the top 1 mm of the punch depth.	245
Figure 6.40	Comparison of first principal strain (ϵ_{p1}) and shear angle (γ_{12}) in steel (left), SRPP (centre) and SRPP/steel FML (right) hourglass induced-biaxial deformation test specimens at the last stage before failure.	246
Figure C.1	Mesh patterns tried on full-circle blanks in FEA models. Only a quarter of the blanks are shown.	281

Figure C.2	FEA model geometry for a circular FML induced-biaxial deformation test.....	282
Figure C.3	Half-section of an FEA model with lock-ring.....	283
Figure C.4	First principal strain in a SRPP hourglass test specimen prior to induced-biaxial deformation test, induced from fixing the convex edges with a lock-ring.....	283

List of Tables

Table 1.1	Thesis chapter summaries.	5
Table 3.1	Tensile properties of steel and SRPP.	41
Table 3.2	Average thickness and density of SRPP/steel FML and its component materials.	43
Table 3.3	Parameters varied to determine optimal conditions for consolidating SRPP/steel FML.	45
Table 3.4	Modified parameters for SRPP and FML tensile tests.	49
Table 3.5	Brief explanation of deformation modes and the corresponding principal strain and stress ratios shown above in Figure 3.10.	52
Table 3.6	DIC system measuring volume, facet size and facet step for uniaxial tensile tests.....	57
Table 4.1	Summary of mechanical properties of 0.3 mm, 0.6 mm and 1.0 mm SRPP tensile test samples. Tensile failure strain (ϵt), strength (σt), chord modulus of elasticity (<i>Echord</i> , stiffness between 0.1–0.3% strain), tangential stiffness (<i>Etangential</i> , stiffness above 1% strain), transition strain ($\epsilon transition$), and stress at transition strain ($\sigma transition$) are given.	63
Table 4.2	Plane stress and plane strain conditions and the associated modes of crack propagation and failure.	92
Table 4.3	Sample statistics of 0.3 mm SRPP on possible indicators of failure.....	103
Table 4.4	Tensile failure strain (ϵt), strength (σt) and upper yield strength (σy) or stress at transition strain ($\sigma transition$) of steel, SRPP and SRPP/steel FML samples.....	126
Table 5.1	Tensile failure strength (σt), strains (ϵt) and relative standard deviation in failure strain ($s\epsilon t$) of 0.3 mm, 0.6 mm and 1.0 mm SRPP specimens oriented at 0°/90°, 30°/60° and $\pm 45^\circ$ to the loading direction.....	143
Table 5.2	Tensile failure strains (ϵt), strengths (σt) and upper yield strength (σy) or stress at transition strain ($\sigma transition$) of steel, 0°/90°, 30°/60° and $\pm 45^\circ$ SRPP/steel FMLs, 30°/60° and $\pm 45^\circ$ 1.0 mm SRPP specimens.	188
Table 5.3	Approximate angles of tape orientations, strain localisation bands and fracture bands to the loading direction in 0°/90°, 30°/60° and $\pm 45^\circ$ tensile SRPP/steel FML specimens.....	195
Table 6.1	Punch depth (d), load (P) and strains in circular SRPP induced-biaxial deformation test specimens. For strains, average (avg.) and maximum (max.) values are given for	

	first principal strain (ϵ_{p1}), second principal strain (ϵ_{p2}), strains in x and y directions ($\epsilon_{x,y}$), and shear angle (γ_{12}).	217
Table 6.2	Sample statistics of circular induced-biaxial deformation tests specimens for steel, SRPP and SRPP/steel FML before failure: applied load (P), depth (d), average first principal strain (ϵ_{p1}), and average strain in x -direction (ϵ_x).....	218
Table 6.3	Comparison of punch depth (d), average and maximum first principal strains (ϵ_{p1}) and shear angles (γ_{12}) in steel, SRPP and SRPP/steel FML hourglass induced-biaxial deformation test specimens before failure. Average strains are based on the centre region, in the top 1 mm of the punch depth.	246
Table B.1	Lap shear test configurations and resulting maximum loads, used to determine optimal conditions for consolidating SRPP/steel FML.....	277

1 Introduction

1.1 Background

Fibre metal laminate (FML) is a hybrid material system consisting of fibre-reinforced plastic (FRP) and metal sheets in a laminate structure. As with any composites and hybrid material systems, FML combines the desirable characteristics of its constituents to the benefit of its targeted use. The system originated at Fokker Aircraft in the 1950s when they were investigating the idea of bonding aluminium sheets together to improve fatigue performance, which later transitioned into metal/composite hybrids during research at the Delft University of Technology in the 1970s. Its core benefits include higher impact, fire [1] and corrosion [2] resistance, and better fatigue tolerance [1], compared to aluminium, and with a lower density than the metal it would replace.

To highlight some of the benefits of FMLs, one can refer to GLARE[®] (Figure 1.1), which is one of the earliest FMLs, made out of a glass fibre-reinforced epoxy composite and aluminium, and used in

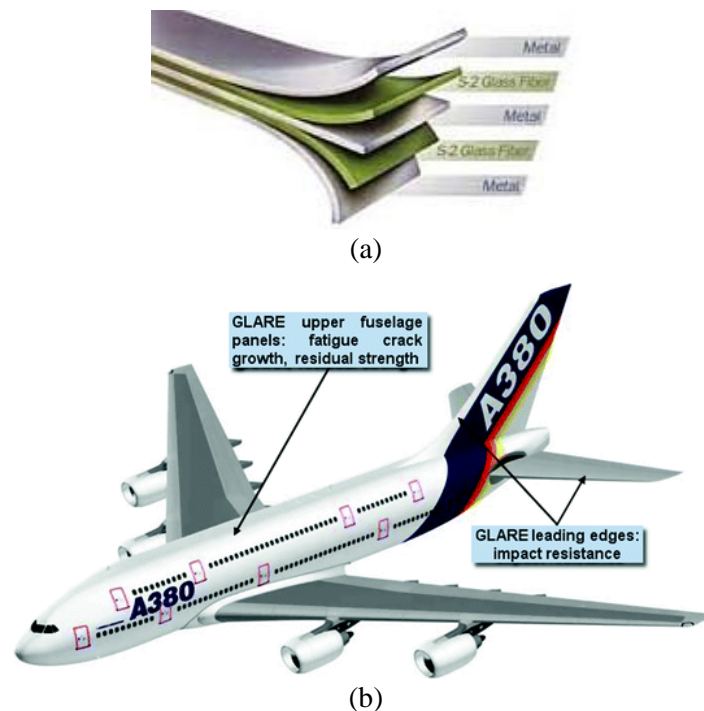


Figure 1.1 a) Commercial GLARE[®] Laminates (glass fibre-reinforced epoxy composite/aluminium FML) [3] and b) its application in Airbus A380. [4]

numerous aircrafts such as the C5-A Galaxy in the US Air Force, the Boeing 777 and the Airbus A380 [5]. Its impact resistance (specific first cracking energy) was found to be up to 3.6 times higher than aluminium in a high-velocity impact [6, Tab. 3.2]. This characteristic was effectively used in designing a lightweight luggage container that can contain a bomb detonation larger than the one used in the 1988 Lockerbie disaster [7].

Due to such characteristics, the use of FMLs can potentially benefit industries beyond just aerospace, as well as the wider society. For example, if used in vehicles to replace steel components of a similar thickness, it may help reduce fuel consumption and therefore help meet the target greenhouse gas emission levels. In road crash scenarios, a significant improvement to impact resistance may help reduce fatalities. Of course, such improvements must be achieved without compromising other important features such as stiffness, strength, and corrosion and fatigue resistance that relates to vehicle safety and performance. FMLs, in fact, would improve these properties by significant margins.

A question may arise, at this point, regarding other materials that could replace some of the steel parts in automotive vehicles. Indeed, there is a clear appetite in the automotive industry to use materials such as aluminium and composites. (See Figure 1.2 for an example.) These materials are used mainly for reducing vehicle weight and, in some cases, for additional improvements in other properties. However, this has brought to light several challenges, such as the lower formability of aluminium alloy compared to steel, and composites requiring processing (e.g. manual hand layup) that are not suitable for existing mass manufacturing techniques. Also, composites require significant modifications to joining and surface painting techniques traditionally utilised for steel parts. While this is not a major barrier for luxury car manufacturers with relatively small production volumes, it poses a considerable challenge for companies that are reliant on mass production with high rates of output and lower unit production costs. As such, steel remains the primary material used in the automotive industry, as exemplified by the extensive use of steel in the body of the Volvo XC90 (Figure 1.3).



Figure 1.2 Carbon fibre-reinforced composite component in the body of McLaren 720S. [8]

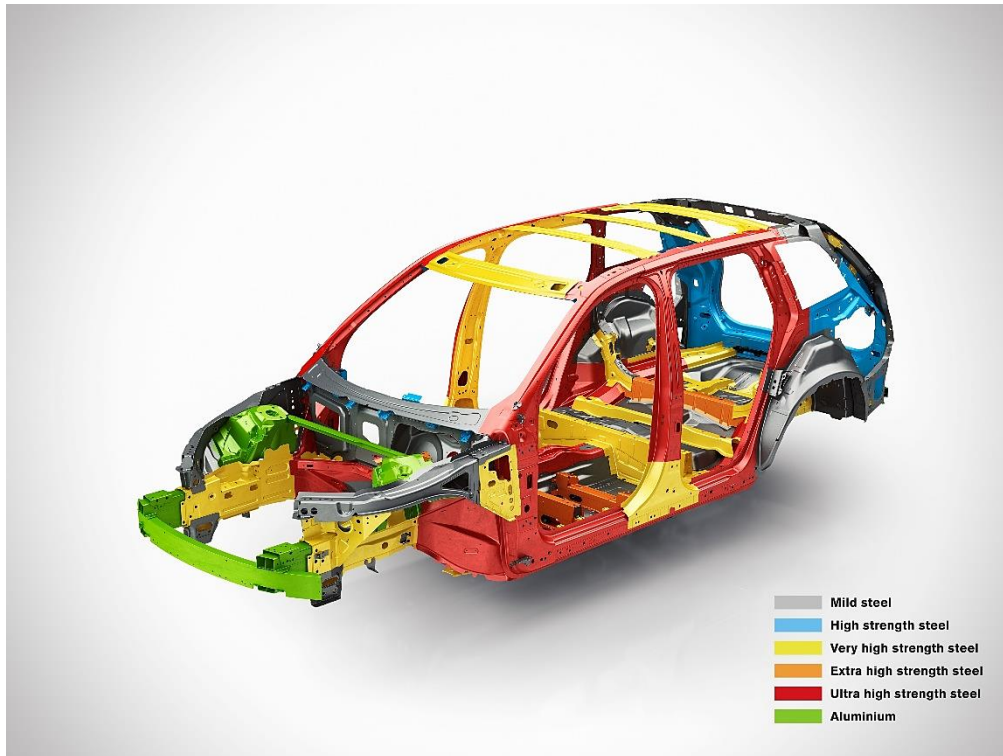


Figure 1.3 Volvo XC90 body structure with steel parts highlighted (green part represents aluminium). [9]

The viability of FMLs in the automotive and other industries is undeniably limited at this time, not least by the cost of manufacturing the materials. Traditional FMLs mostly require costly manual layup processes, followed by the curing of thermosetting resins under heat to consolidate into the desired, permanent shape. In attempting to reduce costs, some researchers have investigated the potential of stamp forming FRPs and FRP-based FMLs by using a thermoplastic polymer matrix [10–15]. The use of thermoplastic FRPs allows FMLs to be pre-consolidated into sheets and then be formed subsequently in similar ways to standard metal stamp forming. By minimising the required changes in tooling and manufacturing processes, this would lower the main barrier for use in industries depending on mass production. Thermoplastics are also highly recyclable, impact resistant, lightweight, and more ductile than thermosetting polymers such as epoxy.

The use of steel instead of aluminium in an FML system can potentially offer greater stiffness, strength, toughness, and manufacturability, as well as reduced material and manufacturing costs. Obviously, this would be at the expense of higher weight compared to aluminium-based FMLs, rendering it inapplicable in aerospace applications. However, steel-based FMLs may be useful in mass production industries such as the automotive sector. With this in mind, this research investigates a steel based FML system.

This research investigates the behaviour of self-reinforced polypropylene (SRPP) and an SRPP-based FML out of a variety of thermoplastic-based FRPs, as it maximises the aforementioned benefits over

thermoset FRPs. SRPP is a single polymer composite (SPC) which has chemically identical components for the reinforcement and matrix phases, as the name suggests. Due to this, it is fully recyclable and lighter than the more commonly used thermoplastic-based FRPs. Also, considerably higher fibre content (70–90% fibre volume fraction) and excellent adhesion between the reinforcement and the matrix can be achieved due to the nature of its unique manufacturing process. This is a significant advantage over most composites where good interfacial adhesion between the fibre and the matrix is difficult to achieve.

Despite the benefits, there has been relatively little focus on the failure behaviour of SRPP in the existing studies of the material. In addition, it has a unique structure that makes it behave quite differently to typical FRPs that have different reinforcement and matrix phases. Due to this, assumptions cannot be carelessly applied to the material behaviour of SRPP based on the existing knowledge of FRPs. The same applies to SRPP-based FML, since its behaviour can largely depend on the behaviour of the SRPP layer.

Furthermore, this study will demonstrate the necessity of understanding the physical damage characteristics that develop under different loading conditions, and how they contribute (or do not contribute) to the failure of SRPP and SRPP-based FML, before it can be said that these materials are well understood for wider use.

1.2 Aims

FMLs were initially developed for applications in the aerospace sector, and they have been widely studied. Hence, extensive research exists on aluminium FMLs but there is limited research on FMLs based on steel or SRPP, especially beyond impact applications. While there is currently a limited understanding of the material behaviour of SRPP, it should be mentioned that the failure behaviour of FRPs themselves is still not fully understood due to their variety and complexity, and a significant portion of the existing research uses epoxy resin-based composites rather than thermoplastic composites. It is not surprising, then, that even less is understood about woven SPCs such as SRPP, which is a subcategory of thermoplastic FRPs.

Such a knowledge gap is hindering their full exploitation in industries, outside a few high-end applications, despite the many benefits they can offer. To help bridge the gap, this research aims to deliver insights into the behaviour of woven SRPP and SRPP/steel FML. More specifically, it will focus on the failure and deformation behaviour relevant to the failure of SRPP and SRPP/steel FML when subjected to the following conditions: 1) uniaxial tensile load along one of the reinforcing directions, 2) uniaxial tensile load applied at off-axis angles to the reinforcing directions, and 3) combined in-plane biaxial and out-of-plane bending deformations. In a broader context, this study aims to contribute to our

understanding of how and why woven thermoplastic SPCs and FMLs based on such composites would deform and fail in the way they do.

1.3 Thesis outline

Table 1.Error! Bookmark not defined. Thesis chapter summaries.

Chapter	Title	Summary
1	Introduction	Describes the motivation behind studying the material deformation and failure behaviour of SRPP and SRPP/steel FML and the overarching aim of this thesis.
2	Literature Review	Reviews existing studies that are relevant to understanding the deformation and failure behaviour of the SRPP and SRPP/steel FML discussed in the thesis.
3	Materials and Methods	Details the materials made and used, the setups for the experiments and the subsequent analyses so that the results in this study can be reproduced by a third party.
4	Failure Behaviour Under Uniaxial Tension (On-axis)	Discusses the findings from analysing the behaviour of SRPP and SRPP/steel FML when subjected to uniaxial tensile load along one of the reinforcing directions of the SRPP (layer).
5	Failure Behaviour Under Uniaxial Tension (Off-axis)	Discusses the findings from analysing the behaviour of SRPP and SRPP/steel FML when subjected to uniaxial tensile load at off-axis angles to the reinforcing directions of the SRPP (layer).
6	Failure Behaviour Under Biaxial Deformation	Discusses the findings from analysing the behaviour of SRPP and SRPP/steel FML under induced-biaxial deformation tests (as described in Chapter 3), which induce in-plane biaxial deformation and out-of-plane bending in the materials.
7	Conclusion	The concluding chapter reflects on the significance of the findings set out in this thesis.

2 Literature Review

2.1 Introduction

This chapter reviews relevant literature on the behaviours of self-reinforced polypropylene (SRPP) and SRPP/steel FML. It is not the aim of this literature review to provide a comprehensive and critical review of studies on FRPs that are based on different reinforcement and matrix phases, as these behave considerably differently to SRPP. Instead, studies are presented in this chapter with more focus on behaviours specific to SRPP and SRPP-based FML which are necessary for understanding the results and discussions of this research.

2.1.1 Background

SRPP has the benefit of being more recyclable, lightweight ($0.8\text{--}0.9\text{ g/cm}^3$) [16], having higher fibre volume fraction (70–90% or higher in some cases [17]), and higher strain to failure ($\approx 20\%$), in comparison to thermoset-based FRPs and even 2-phase thermoplastic FRPs such as carbon fibre or glass fibre-reinforced polymers (GFRP)¹. It also has high impact resistance – in multiple cases outperforming glass fibre-reinforced thermoplastics [18–21] – allowing it to be commercially exploited in applications such as anti-ballistics, automotive components, and sports equipment (see Figure 2.1). In some cases, SRPPs have comparable stiffness and strength values (6–8 GPa, 200–250 MPa) compared to GFRP (4–5 GPa, 80–100 MPa) [16].

The properties mentioned above are attributed to the fact that both the reinforcement and matrix phases in SRPP are made of polypropylene (PP), as the name suggests. It falls under a category of polymers called single polymer composite (SPC), also known as a self-reinforced polymer, single-phase composite, homocomposite, homogeneous composite, or all-polymer composite (i.e. all-PP). In comparison to 2-phase composites, SPCs have almost perfect adhesion between fibre and matrix due to mutual diffusion between the two chemically identical components creating strong chemical bonds [23]. This characteristic is a significant improvement because strong interfacial bonding is crucial for the

¹ For comparison, GFRP has a density of around $0.94\text{--}1.2\text{ g/cm}^3$, fibre volume fraction of 20–30%, and failure strain of 2–5 %.

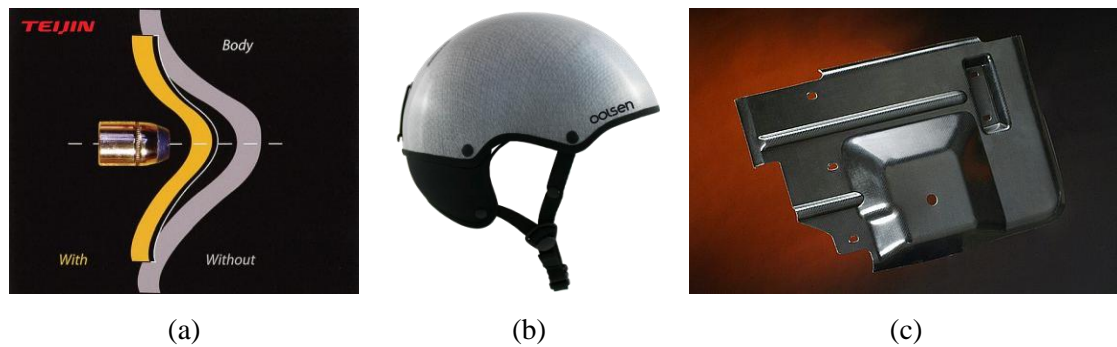


Figure 2.1 Example applications of Curv®, a commercial SRPP: a) anti-ballistics (e.g. helmets, protectors, and military vehicle armour); b) sports helmet; and c) automotive components [22].

fibre–matrix load-transfer mechanism, and hence in providing composite shear, transverse, and fatigue strengths. However, good adhesion in composites is very difficult to achieve, often causing fractures to initiate at the interface [24]. This is especially true for PP-based 2-phase composites because the polymer has low surface free energy and bonding or interfacial adhesion is usually weak [25, p. 2049].

Fibre Metal Laminate (FML) is a material system that combines FRP and metal layers in laminate forms with many benefits. An example of its benefits is its high impact performance. In comparison to the plain composite material, Reyes Villanueva and Cantwell [26] found the sandwich structure of glass fibre-reinforced polypropylene (GFRPP)/aluminium/aluminium foam had higher high-velocity impact resistance due to several energy-absorption mechanisms, including the fracture of the aluminium, longitudinal splitting, and fibre fracture. Fan, Cantwell and Guan [27] also found that an FML based on glass fibre-reinforced epoxy/aluminium alloy had specific perforation energy that could be more than twice that of the plain composite in quasistatic and low-velocity impact perforation tests, depending on the thickness of the composite. Another critical benefit of FML over metal is better fatigue resistance due to a possible fibre-bridging effect [28–30]. Crack growth in ARALL, an aramid fibre-reinforced epoxy/aluminium alloy FML, exhibited crack growth 10–100 times slower than in aluminium and fatigue damage never occurred in realistic conditions in riveted lap joints [1].

Before proceeding into an analysis of deformation and failure of SRPP and SRPP-based FML, it is imperative to understand that there are several factors about these materials that make the vast proportion of existing research in composites inapplicable.

FMLs based on steel or thermoplastic composites are relatively new classes of materials: FML itself was first patented in 1984 and most studies since then have focused on FMLs based on aluminium alloys and FRPs based on aramid, carbon, and/or glass fibre reinforcements. As Alderliesten [31] mentions, most research on FMLs are on thermosetting resins which are widely accepted in the aeronautical industry (with applications in the Airbus A380), while research on thermoplastic-based FMLs has developed only recently.

This is also the case beyond FMLs: coverage of thermoplastic-based FRPs is much smaller than those based on thermosets. For instance, Worldwide Failure Exercises (WWFEs) [32–37] conducted over many years assessed how well leading failure theories predict composite failure via test cases based on glass and carbon fibres and resin matrices. Moreover, as commented in Reeder’s study [38] of delamination failure of thermoset epoxy- and PEEK-based composites, different criteria are suitable for thermoset and thermoplastic polymers. No one criteria can cover all because they behave quite differently. Even with thermoset-based composites, findings from the first WWFE [32] resulted in 50% of 19 leading failure theories being modified, demonstrating the complexity of the field.

Not only that, SPCs form only a part of thermoplastic-based composites and are structured and behave quite differently to the traditional 2-phase FRPs. Fibres are less stiff and more ductile compared to the well-established glass or carbon fibres, and the fibre–matrix interface is stronger than typical composites. The first concept of SPC was introduced in 1975 [39], and while there is some literature on processing techniques, basic properties, and impact performance, limited knowledge exists on the failure behaviour of SPCs outside general damage characteristics. Also, the amount of literature on SPCs pales in comparison to those on 2-phase FRPs. On top of this, SRPP only forms a subset of the knowledge pool on SPCs.

SRPP exhibits multiple damage mechanisms that occur simultaneously, ranging from brittle fibre or tape fracture, longitudinal crack or splitting, transverse cracks, matrix thinning, delamination, ductile fibre–matrix splitting, to fibrillation. Regarding fibrillation, some authors attribute it to good consolidation whereas some attribute it to the exact opposite [40–44].

Studies of deformation and failure of FRPs are traditionally based on unidirectional (UD) lamina or cross-ply UD laminas, as was the case for WWFEs. Woven composites again behave differently from UD laminas. In general, the mechanics of woven composites is more complicated than UD laminates due to the curvatures in reinforcements and ply nesting, factors which lead to different types of damage including: matrix fracture causing delamination between yarns, matrix fracture within yarns, interlaminar delamination, and fibre fracture [45]. Even for the same woven FRP, damage development and propagation under impact can differ depending on the reinforcement architecture [46].

This literature review is divided into three sections that describe the behaviours of FRPs, SRPP, and FMLs in relation to their failures. It covers SRPP before FMLs, given that failure of FML should first be understood at the level of its constituents. (It does not cover steel as its behaviour is very well known in comparison.) SRPP is covered extensively, given that it is relatively less well known, but the section on FMLs is shorter because the concept of this laminate system is well known (although research on FMLs based explicitly on steel or thermoplastic FRPs is lacking). Before the SRPP section, typical failure behaviours of FRPs are also briefly described to give context to the class of SRPPs materials. These sections are further divided into parts relevant to thermoset FRPs, thermoplastic FRPs, the

structure and behaviour of SRPPs at the composite- and component- (matrix and reinforcement) levels, steel FMLs, and, finally, FMLs based on thermoplastic FRPs including SRPP.

2.2 Failure behaviour in fibre reinforced plastics

2.2.1 Thermoset-based FRP

In many cases, cracks in 2-phase FRPs initiate from micro-debonding at the fibre–matrix interface, as shown in Figure 2.2, under the high tensile and shear stress concentrations caused by high mismatch in stiffness between the two phases. This is usually the case in thermoset-based composites. This can occur in fibres perpendicular and parallel to the loading direction. The growth of the latter case is usually seen under fatigue loading at the end of a broken fibre rather than under quasi-static loading. Debonding then leads to larger scale fibre–matrix debonding or, less frequently, matrix fracture [24, pp. 12–56]. An illustration of damage development where fibre breakages lead to interface debonding and matrix cracks is shown in Figure 2.3.

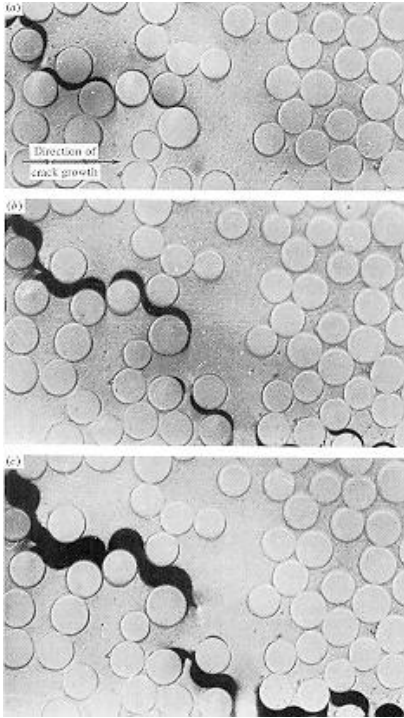


Figure 2.2 Fibre–matrix debonding in a polyester resin/glass fibre-reinforced composite [47].

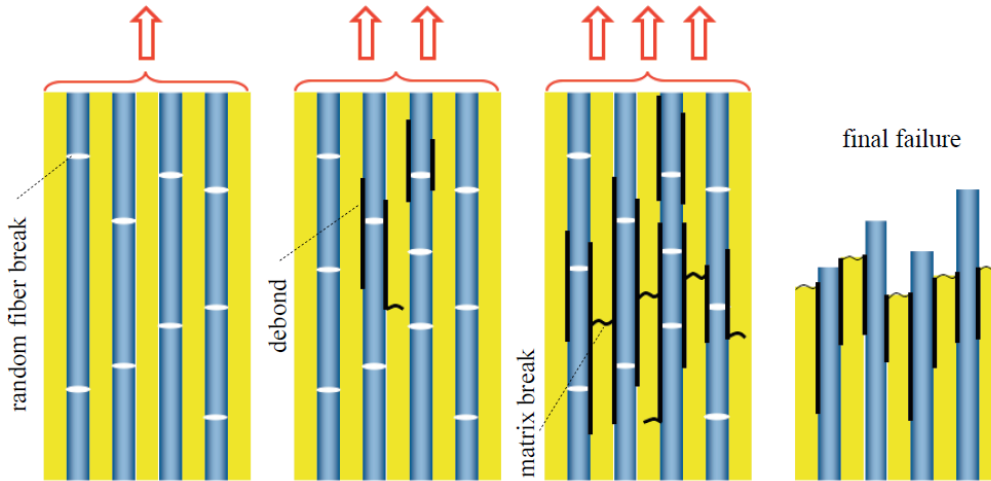


Figure 2.3 Schematic showing of damage events leading to final failure of a UD composite due to increase of the applied tensile load [48, Fig. 3].

Matrix fracture often initiates at the free edges and leads to interlaminar delamination and localised fibre fractures in adjacent plies [24, pp. 12–56]. Matrix cracks can propagate in all directions but often propagate along fibre directions under quasi-static loading [49]. Examples are transverse cracks in transverse plies and splitting in longitudinal plies where the propagation is driven by a mismatch in the Poisson’s ratios of differently oriented adjacent plies. When the matrix tensile strength is high enough to resist the stress concentration, shear yielding can also occur instead of propagating in a brittle manner [48].

In composites with woven structure, there are additional ways in which damage can occur. Typical examples are illustrated in Figure 2.4. Failure in a woven thermoset composite often initiates by fibre–matrix debonding, preferentially at the yarn boundaries normal to the loading direction. The initial boundary cracks do not necessarily develop into large cracks, depending on the stress distribution which is affected by the weave architecture. Micro-debonding forms transverse matrix cracks within or on the yarn boundaries. Unlike in UD cross-ply, the length and spacing of cracks are initially limited by crimp boundaries, then at higher load propagate along the yarn. When cracks have developed to a certain level (e.g. if crack saturation exists), shear stresses between the transverse cracks and longitudinal layers trigger local delaminations that are confined to crimp boundaries. These can lead to an onset of fibre failure in surrounding bundles, as well as transition to interlaminar delaminations at a stage which depends on interlaminar fracture toughness. Longitudinal yarns can also split due to transverse tensile stresses created in the longitudinal yarns from Poisson’s effect and constraint from transverse yarns. Final failure occurs with longitudinal fibre breakages at strains below the failure strain of fibres due to fibre crimp and delaminations that reduce efficient load transfer inside the fibre bundles.

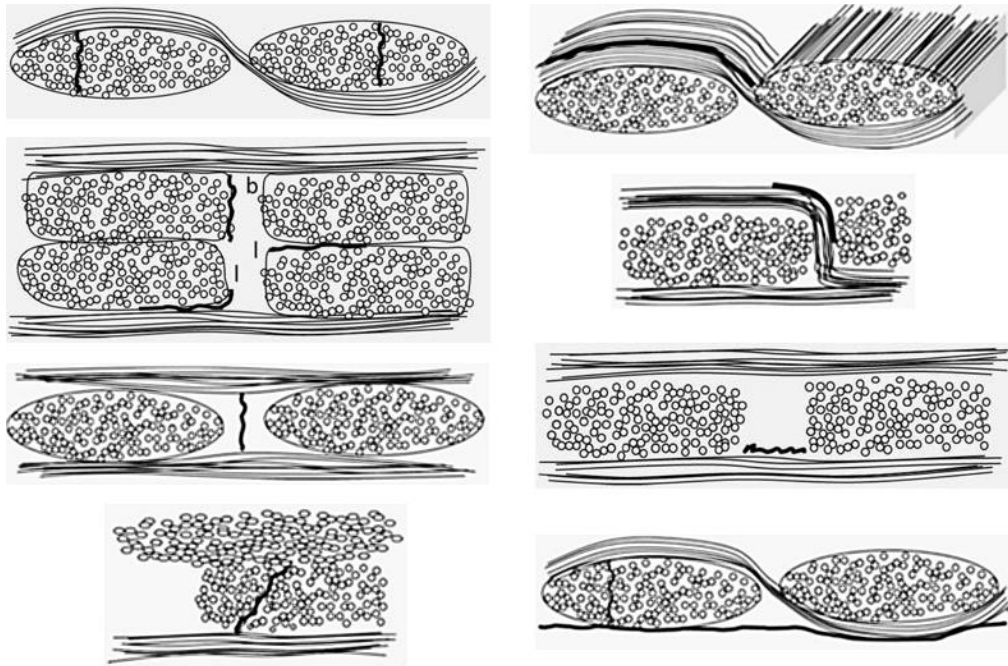


Figure 2.4 Different types of cracks observed in textile composites loaded in tension. From top to bottom in left column: transverse matrix cracks inside yarns, transverse cracks at yarn boundaries (b), debonding of yarns and local delaminations inside yarns (I), transverse cracks in the matrix pockets, shear matrix cracks. From top to bottom in right column: splitting of the yarns, cracks on the boundary of or inside Z-yarns, longitudinal cracks in the matrix pockets, delaminations. Taken and modified from [24, pp. 43–44, Tab. 3.1].

Similar micro-debonding, typically at yarn boundaries, is also seen in the woven composite when loaded off-axis [24, pp. 41–56]. These then form matrix cracks inside yarns which indicate high shear deformation in the matrix and ductile failure, in contrast to brittle fracture surfaces formed under transverse cracks. Debonding and fibre pull-outs are also often observed. In a study of tensile behaviour of glass-reinforced/epoxy composite under off-axis loading [50], woven FRP fractured at varying angles to the reinforcement and the load, which also changed with weave patterns. In contrast, UD laminate of the same material failed at fracture angles consistent with the fibre direction regardless of the angle to the tensile load.

2.2.1.1 World-wide failure exercises

Given its impact in the space of composite failure studies, WWFEs are briefly described in this subsection.

The first WWFE [32] initiated in 1996 tested the ability of 19 existing failure theories to predict the response of classical FRP laminate of unidirectional (UD) lamina under in-plane, biaxial loading, using 14 test cases. It concluded in 2004 that only a few theories gave an acceptable correlation with test data

for 75% of the test cases. As a result, some 50% of the theories were modified, with some being modified for the first time in over 40 years.

The organisers then moved on to finding out the maturity of failure criteria in predicting the behaviour of FRPs under triaxial stresses. This Second WWFE [33–35] tested 12 participating theories using FRP UD lamina and multi-directional laminates based on various fibres and resins. The results showed that only a few theories gave acceptable correlation with experimental data (within $\pm 50\%$) for about 75% of the test cases.

The third WWFE focused on judging the predictive capabilities of the 12 participating theories (summarised briefly and referenced in [36, 37]) on a variety of in-plane loading or combined 3D loading conditions, sometimes in the presence of stress concentration, under thermal load, or for different laminate thicknesses. These required predictive outputs in the forms of stress–strain curves, crack density variation, failure stress and strain envelopes, delamination level and location, loading/unloading curves, strengths versus hole diameter, or laminate thickness. Its test cases were based, again, on laminates of UD laminas based on epoxy material (carbon and E-glass fibres). Below are notable points from the concluding remarks [37]:

- There is a general lack of consensus between theories and the models are broadly immature from manufacturing and design perspectives with regards to:
 - Effects of ply thickness and lay-up sequence.
 - Size effects, such as the effect of hole diameter to thickness ratio.
 - Effects of unloading and reloading.
 - Interaction between cracks in adjacent layers of different orientation.
 - Matrix cracking and delamination under pure bending.
 - Delamination driven by matrix cracking.
- There were large differences in models, even in predicting the strength and failure strains where failure is controlled by tensile failure in fibres.
- No two models gave the same predictions for any of the test cases.
- Ratios between the highest and lowest predictions were as high as 20 in some test cases.

The WWFEs show that predicting FRP failures is still far from being mature and demonstrates the level of complexity of damage that can occur in these composite materials. It also suggests there is a requirement to better understand their failure behaviours. The same is true for thermoplastic FRPs, which behave differently but are often designed based on criteria that have been developed for thermoset FRPs. At the very least, such criteria should be used in conjunction with a good understanding of failure behaviour of thermoplastic FRPs so that designers can understand where the failure criteria cannot apply, on top of the limitations highlighted above.

2.2.2 Thermoplastic-based FRP

Nishida et al. [51] presented a comparison of mechanical properties between woven thermoplastic and thermoset-based carbon fibre-reinforced polymer (CFRP) and concluded that thermoplastic matrix provided better performance. Compared to their thermoset-based counterparts, thermoplastic-based samples exhibited similar interfacial shear strength, tensile strength, and elastic modulus; they also had higher interlaminar shear and impact strengths and almost double the interlaminar fracture toughness. Thermoplastic-based CFRP had slower interlaminar crack development, fewer and shorter cracks, and better energy absorption under impact due to its ability to deform plastically compared to the brittle thermoset matrix.

This illustrates the advantages of using thermoplastic-based composites, on top of longer shelf-life and ease of manufacturing, although it has disadvantageous creep behaviour [52]. In fact, in some cases, the interlaminar fracture toughness of thermoplastic FRPs were found to be at least one order of magnitude higher than thermoset FRPs, which is affected by matrix toughness and fibre–matrix interfacial strength [53, 54]. However, it must be noted that the mechanical performances depend on the specific materials used and testing conditions, such as environmental conditions, presence of notches, different joint types [55], and fibre impregnation quality [56].

Under a three-point bending test of a GFRPP, Wafai et al. [49] observed load drops related to 1) initiation and propagation of cracks in transverse plies via fibre–matrix debonding in fibre-rich areas ahead of the crack tip, and 2) coalescence of cracks in matrix-rich areas at a later stage. Transverse cracks grow quite quickly before the stiffness recovers at the end as they transition to interlaminar delamination, which then propagates along the boundary between longitudinal and transverse plies. The difference to thermoset FRP was that the crack opening was bridged by matrix fibrillation, probably indicating that the cracks formed by crazing. Delamination was characterised by microcracks in matrix-rich areas, fibre–matrix debonding, and shear-induced microcracks with internal micro-fibrillation, indicating a combination of Mode I (tensile opening) and Mode II (in-plane shear) fractures. The latter depends on the thickness of the matrix interlayer and the distribution of adjacent fibres. Despite being chemically identical, different grades of PP also exhibit significantly different interlaminar fracture toughness due to differences in ductility and toughness. Matrix deformation strongly affects energy dissipation, especially in the delamination phase.

At low shear strains, thermoplastic-based FRPs show similar behaviour under shear to that of thermoset-based FRPs [57]. However, at larger strains the response varies significantly with regards to matrix damage, and thermoplastic FRPs exhibit delayed failure due to higher shear strength in the matrix.

Bourmaud et al. [58] describes damage mechanisms in injection moulded short flax fibre-reinforced/PP composite under tension, and they mention how similar mechanisms are seen in glass and natural fibre-

reinforced composites. The damage initiates and propagates preferentially through transverse fibre bundles, showing that its middle lamella interface is weaker than the fibre–matrix interface. In areas without fibre bundles, microvoids and microcracks initiate at fibre tips, then a large number of fibres break, after which the shear stress causes microcracks to propagate along the sides of the fibres. Brittle cracks propagate transversely between these points in the matrix, bringing about a final fracture with fibre pull-outs. The authors conclude that, despite some debonding, there is no major fibre–matrix weakness, counter to common thinking, although they suggest that increasing interface bonding is necessary for improving composite quality.

Hufenbach et al. [59] explain that textile composites have a combination of both discrete and diffuse damage characteristics². In addition, in composites such as GFRPP (which are dominated by diffuse damage² such as interface failure, ductile matrix, void growth, or whitening, instead of discrete damage such as fibre or inter-fibre failure and delamination), there is no clear separation of damage mechanism related to load history. The result is that identification of separate damage phases is impossible. Critical damage can arise before the appearance of discrete damage, and multiple damage mechanisms can occur simultaneously in different directions.

In a study by Wang [60] of the failure behaviour of flax fibre-reinforced/PP under stretch forming, it was found that because the matrix is much more ductile in comparison to the thermoset resin, composite failure is clearly driven by fibre fracture. Because of the dominance of fibre failure as the primary failure mechanism, the author found that load path dependency in leading to failure can be eliminated by using maximum strain in the fibres as the indicator rather than using the composite's strain state. This theory was applied in another study involving a woven GFRPP [61] where it was shown that failure was mostly affected by fibre strain, regardless of strain paths or fibre orientation. Thus, in most cases strains in the glass fibres were a more consistent and straightforward predictive indicator as to the final failure location and fibre strain level. However, it can be questioned whether the same theory applies to SRPP, even though it is also based on a PP matrix. Being PP, its reinforcement phase is much more ductile, and does not have the same level of inextensibility as glass or flax fibres. As opposed to the failure being dominated by fibre fracture, multiple damage mechanisms occur in SRPP.

² Discrete damage can be quantified on meso- or microscale with justifiable effort, such as fibre failure, interfibre failure, and delamination. Diffuse damage mechanisms exhibit no local character or cannot be quantified with justifiable effort, such as interface failure, ductile matrix, void growth, or whitening [59].

2.3 Self-reinforced polypropylene

2.3.1 Composite structure and failure behaviours

Understanding the structure of SRPP and SPCs is essential to understanding their behaviours. This is true of any material, but because SPCs are quite different from conventional 2-phase FRPs, caution must be exercised to not use similar assumptions in cases where they may not apply.

A commercially produced SRPP called Curv was used in this research. It is manufactured using the hot compaction method in which highly-drawn PP tapes are woven together and then selectively melted on the surfaces to form a matrix between the tapes. Schematics of the hot compaction process and a scanning electron micrograph of SRPP section are shown in Figure 2.5 below and Figure 2.6 in the next page. Curv has a 70% tape fraction which is the optimum ratio for the composite [21, 64]. Due to the stretch in the tapes, these are highly oriented and act as reinforcement that gives the composite its strength and stiffness. Although the tapes act like fibres, they are geometrically different from fibres or filaments which have matrix joining together each strand separately.

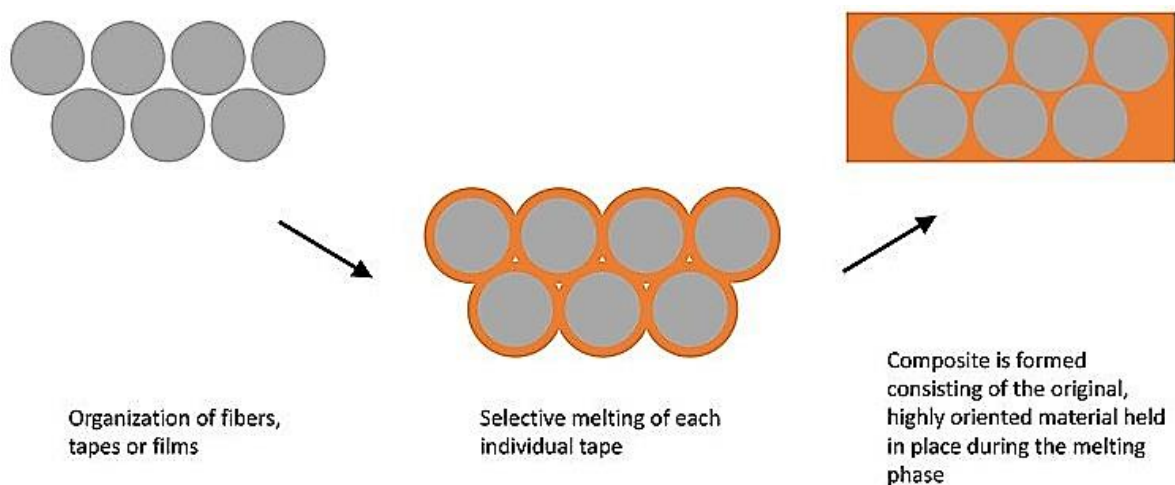


Figure 2.5 Schematics of the hot compaction process [62].

The hot compaction method was developed in 1989 by researchers at the University of Leeds [21]. Since then, researchers – notably, Ward, Hine, Swolfs and their colleagues – have carried out multiple studies on hot compacted SRPP. These have mostly focused around the effect of varying processing parameters on the composite’s mechanical properties and morphology [21, 41, 64–73]. Influential parameters, some of which depend on each other, were: the molecular weight of PP, quality of transcrystalline layer between the reinforcement and the matrix, processing temperature, and form factor of the fabric reinforcement.

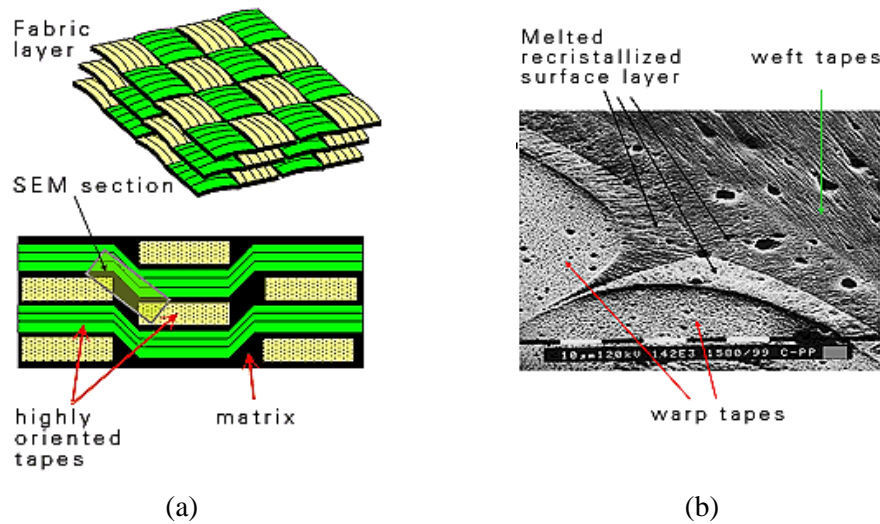


Figure 2.6 a) Diagrams of SRPP made by the hot compaction process; and (b) a scanning electron micrograph at the section indicated in (b) [63].

The hot compaction process is one of three main industrial methods of producing SPCs [74]. Other processes are: 1) the coextrusion method, where reinforcements are coextruded with a surface layer that melts at a lower temperature to form the matrix; and 2) the film stacking method, where reinforcement and matrix-giving layers are sandwiched together and heated for consolidation. These methods use different polymer grades (for example, homopolymer for fibres and copolymer for the matrix) or different polymorphs (for instance, using a lower melting modification for the matrix). Some notable studies on coextruded SRPPs include those by Cabrera, Alcock, Barkoula, and their colleagues, and a few others [17–19, 40, 74–81], and on film-stacked SRPPs, by Bárány, Karger-Kocsis, Izer, and their colleagues, Kitayama, Houshyar, and his colleagues, and a few others [82–97]. The primary focus of these studies is often on finding the optimal parameters for a particular processing technique.

There are SRPPs made using less well known techniques, such as introducing fibres into supercooled matrices [98–100], or using oscillating packing injection moulding (OPIM) [101–104]. While the SRPP made by OPIM is technically an SPC, it is quite different from SPCs made from methods that produce flat sheets using explicit control over the direction and continuity of the reinforcements. Commercial SRPPs include Pure [105], Tegriss [106], and Torodon [107].

It should be noted that SRPP can exhibit slightly different mechanical properties and failure characteristics depending on the method used. For example, the relationship between impact resistance and the material thickness in hot compacted woven SRPP [69] were reported to be different to that of coextruded woven SRPP [18]. In addition, the form factor, processing conditions, loading conditions, and reinforcing directions in relation to the load can affect the mechanical properties and failure behaviour, as will be explained in the following sections. Although this thesis investigates the material behaviour of one type of SRPP (hot compacted woven SRPP with tape reinforcements), it is important

to lay out the similarities and differences between different types of SRPP, so that the findings from this research can be used in future works on SRPP and SPCs with the understanding of how certain behaviours might vary depending on the manufacturing conditions.

2.3.1.1 Form factor

In studies of hot compacted SRPP and self-reinforced polyethylene (SRPE), the flat rectangular tape was determined to be the better choice of reinforcement geometry compared to multifilament bundles of circular fibres or fibrillated tapes [41, 68]. Flat tapes gave the least crimping, were easier to weave into a balanced style, and had the least internal free space, which provided a larger surface area for direct adhesion between the tapes. Indicatively, peel tests by Jordan et al. [68] showed that, when using fibre bundles, critical cracks propagated along the boundary of transcrystalline matrices, whereas when tapes were used, cracks propagated within the tapes as well as in the matrix. This correlated with the superior mechanical properties observed with tape-type reinforcement. This conclusion must be addressed with some caution; it may be that the tape is actually weaker than fibre bundles and this causes cracks to preferentially propagate through the tapes than at the interface. However, this is less likely, given that the peel strength increased by a factor of 9 when using tapes instead of fibre bundles.

Justification for the woven style of the commercial hot compacted SRPP stems from one of the earliest studies on the hot compaction process. Hine et al. [66] found hot compacted UD SRPE to be limited by the transverse strength of individual fibre, with transverse failure occurring within the fibres. This led to studies based on woven structures so that the transverse strength of reinforcement was not directly relevant to the composite. Ward and Hine [21] found a balanced weave pattern to be best for practical use, although an earlier paper from the group [41] noted that this reduces the stiffness by half compared to a UD arrangement because the reinforcement's transverse stiffness is comparable to that of the matrix.

Swolfs et al. [70] showed that arrangements which gave smaller voids between the tapes resulted in better compaction quality, such as a 2/2 twill weave pattern which gave less crimping than a plain weave; moreover, overfeeding of tapes or adding interleaved films increased the matrix content by filling in voids. Voids can lead to early damage initiation, and the additional matrix can reduce debonding and delaminations in tensile, peel, and impact tests. It was noted that impact resistance is dominated by tape fracture and fibrillation, rather than debonding and delamination, and is therefore mostly unaffected by weaving style. This was slightly different to the observations by Alcock et al. [18] who reported that, depending on the processing temperature, the impact property of coextruded tape-reinforced woven SRPP correlated in varying degrees with delamination and tape fracture. The authors also noted this difference and suggested that hot compacted SRPP is less prone to delamination than other SRPPs.

2.3.1.2 Processing conditions

Failure behaviours of SRPPs can differ due to different processing parameters. In a study on SRPP made with quasi-unidirectional carded mats by film stacking at 150–175°C [84], samples consolidated at lower temperatures exhibited mainly delamination and fibre pull-outs under tension, whereas samples processed at higher temperatures exhibited fibre fracture as the dominant failure mode. When consolidated at higher temperatures, interlaminar strength, tensile modulus, tensile strength, and peel strength were increased, while dynamic impact perforation energy was decreased [84, 86].

Similar observations were made for a woven SRPP made with coextruded tapes [40]. When compacted at a somewhat higher temperature (160°C compared to 140°C), tape pull-outs and delaminations, which previously occurred over the length of specimens, disappeared. Instead, localised tape fractures occurred with micro-fibrillations. Since a change in processing temperature gave a negligible change in tensile strength in a UD version of the SRPP [17], the authors concluded that the sensitivity in the woven SRPP was due to higher processing temperature which resulted in increased interlaminar strength, allowing stress to reach the longitudinal tensile strength of the reinforcement.

However, unlike the film-stacked SRPP, an increase in tensile strength with processing temperature was almost negligible in a study of coextruded SRPP, although a direct comparison between the two studies is difficult because there are large discrepancies in strength and stiffness. For example, the maximum tensile strength of a coextruded woven SRPP (269 MPa) [40] was about twice that of a film-stacked SRPP (120 ~ 130 MPa) [84]. It is clear that the properties of SRPP depend on both processing method and parameters.

As described above, the general trend in the literature is that higher processing temperatures result in the localisation of fractures and delaminations, reduced pull-outs, increased fibrillation, improved interlaminar and tensile properties, and a decrease in impact properties (due to the overall reduction in delamination which absorbs large amounts of energy, although this can vary depending on whether the impact type is penetrative or not [71]). It is often explained that these are related to improved reinforcement–matrix interfacial bonding. It must be noted that these observations only apply below the temperature that causes substantial melting of the reinforcement phase. Above such temperature (e.g. 190°C), both tensile and impact properties are reduced from reduction or disappearance of load-bearing capacity, delamination, and fibrillation, despite the fact that interfacial bonding is improved [97].

2.3.1.3 Damage accumulation under uniaxial tensile load

The mechanical properties of tape-reinforced woven SRPP and GFRPP can be comparable, but their damage mechanisms are very different [40]. Acoustic emission (AE) events, signalling the occurrence of damage, occur at higher stresses in SRPP than in GFRPP for several reasons: 1) PP tapes have higher

strain to failure and smaller scatter in strengths compared to glass fibres, 2) interfacial failures and fibre breakages occur earlier in GFRPP since SRPP has better interfacial strength, and 3) the cross-section of PP tapes is larger than glass fibres by more than 500 times, and hence, the smaller number of reinforcements per volume in SRPP lead to fewer fibre failures than in GFRPP. This is despite the reinforcement volume fraction in SRPP being higher.

SRPP sustains multiple forms of damage before fracture. In an AE study by Izer et al. [42], damage in tape-reinforced film-stacked SRPP included tape fractures close to tensile failure, microscopic debonding during alignment of reinforcement towards the direction of the load, fibre–matrix debonding, fibrillation, and delamination. In poorly consolidated samples, the latter three occurred in higher proportions, and the total number of AE events indicated that damage was higher, with the damage accumulating from early stages of deformation. This is similar to observations made by Swolfs et al. [70] on hot compacted SRPP, where the lower quality of consolidation resulted in earlier damage initiation, as well as more damage.

In Izer et al.'s study, it was reasoned that no AE events were detected during testing of pure PP matrix, and thus all AE events are expected to be due to fabric or reinforcement–matrix interactions [42]. Venkatesan, who studied a tape-reinforced hot compacted woven SRPP, also found that no failure was initiated in the matrix [108, p. 207–209]. Instead, failure of the composite was caused by [tape] breakage which led to subsequent matrix failure from the dissipated energy. However, this does not strictly mean there is no damage in the SRPP matrix prior to fibre fracture. It will be seen in Section 2.3.2 and Chapter 4 that the matrix in hot compacted SRPP exhibits damage characteristics that are somewhat different to pure PP, probably due to its transcrystalline microstructure and existing in regions where tapes have not fractured. It should also be noted that Venkatesan's findings were derived from visual observations (there was no microscopy) in a study that did not focus primarily on damage characteristics.

Hine et al. [41] have suggested that matrix failure occurs around the yield point, such that the resulting reduction in stress transfer reduces the stiffness. Note that the yield point in an SRPP occurs at a similar strain as the yield in the matrix, i.e. pure PP ($\approx 2\%$). Thus, what the authors refer to as matrix failure must really be a non-critical type of damage in the matrix. Another possible explanation of the yielding behaviour is that tie molecules, which connect crystals across the amorphous phase, start to flow at the yield point [70, 109]. A further increase in stress after yielding occurs reflects the fact that the tie molecules gradually align to the tensile load.

The behaviour of matrix yielding *before* the yielding of reinforcement in SRPP is quite unusual among composites. The difference may be that a typical FRP has stiff, brittle, and inextensible fibres embedded in a more ductile matrix, in comparison to SRPP which has reinforcement that is highly ductile and extensible. It is, therefore, preferable to have a matrix that remains ductile until failure of the reinforcement, and this is reflected by higher resistance to peeling when the matrix is more ductile [41].

2.3.1.4 Damage accumulation under non-uniaxial tensile loads

Zanjani and his colleagues [44, 110–112] studied the behaviour of tape-reinforced hot compacted woven SRPP during stretch forming. At failure, SRPP was described as failing catastrophically, with a complex mixture of longitudinal cracks propagating in tape directions along and between the tapes, yarn ruptures (fibrillation and fibril fractures), fibre pull-out, matrix shearing, delamination, and transverse cracks throughout the thickness. In some locations, fibre kinking due to localised compressive strains was also observed. This was contrasted to GFRPP, which had one dominant failure mode – gradual and localised fibre fracture due to inextensible and brittle nature of glass fibres.

It was also shown in their study [111] that, depending on the aspect ratios of the specimens, SRPP can exhibit different failure mechanisms due to different in-plane deformation modes. For a specimen with high aspect ratio, SRPP failed transversely to the first principal strain, with a jagged surface showing yarn rupture, fibre pull-outs, and delamination. With a decrease in the aspect ratio, the fracture propagated at 45° to the first principal direction, showing a bridging effect which delayed the final fracture. With a further decrease in aspect ratio, the bridging effect became more pronounced and the failure mechanism also included matrix shear failure.

It is also possible for none of the above forms of damage which are seen under stretch forming to occur under draw forming, at least before forming limit is reached by wrinkling, as shown in Venkatesan's work [108]. This occurred in the absence of a lock-ring which prevented specimens from being drawn in, and depending on the level of the blank holder force and the preheat temperature.

Under compression, UD SRPP was reported to fail by micro-buckling, with a maximum compressive strength of around 56 MPa (in the longitudinal direction at high compaction temperatures) [17]. This is closer to that of bulk PP (~ 50 MPa) and much lower than the tensile strengths of the composite. In woven SRPP, compressive failure occurred similarly by buckling, and it was noted that the bending stiffness must contribute to the compressive strength of the composite [40]. Delamination was also observed under compression, with some fibrillation occurring where cohesive tape failure occurred. This led to the conclusion that the increase in compressive strength that occurs when the compaction temperature is increased (from 140°C to 160°C) must be due to increased fibre–matrix interfacial strength, which prevents such failures.

In tensile tests, more consolidated samples having higher strength and stiffness typically exhibit less delamination and tape debonding, since they are concentrated over a smaller area (around the fracture site). However, in impact tests, these failure modes are preferential since they are highly energy consuming processes, as with fibrillation and tape pull-outs. Due to this, impact performance can be improved by lowering consolidation quality and thereby interfacial strength [18], or by using a multilayered SRPP instead of a monolithic one to induce more delamination [113]. This demonstrates that designs with SRPP must be tailored according to the intended application.

2.3.1.5 Crack propagation

Romhany et al. [43] studied crack growth in single-notched tensile samples of hot compacted woven SRPP by tracing the movement of AE events. As monitored by AE events, the crack did not grow until the load approximately reached a plateau, after which the crack started to slowly propagate. Shortly before fracture, fast crack growth occurred at points where the load exhibited sudden drops. The cause of the load drops has not been fully understood, although some researchers explain it in terms of crack bifurcation [114]. Romhany and colleagues conclude that voids in poorly consolidated samples are responsible ([43, Fig. 3]). However, in a study of film-stacked SRPP, Izer et al. [42], from the same group, later observed a similar phenomenon with a single tape and reinforcement fabric and thought it was due to fibre cracks and breakage.

Interestingly, the SRPP studied by Romhany et al. [43] was Curv, which is the same commercial product studied in this research, but similar pop-ins were not observed, as will be shown in Chapter 4. The difference is possibly due to the different thicknesses and the manner of crack initiation. This research studied 0.3–1.0 mm-thick tensile specimens, whereas Romhany et al. used 3 mm-thick specimens with cracks initiating at the notch on one edge.

Romhany et al. [43] also found that the initial damage zone was initially larger in poorly consolidated samples and then became smaller. This was attributed to the crack propagating too fast for stress to be redistributed in voided areas. This agrees with the observation mentioned previously by Swolfs et al., that voids can cause early damage under tension [70]. Similarly, Alcock et al. [40] mention that mechanical properties are negatively affected by voids, but also that voids have been reported to increase failure strain by a crack-arresting mechanism [115]. It should be noted that the study which showed that voids arrest cracks was conducted on FRP made from glass fibres and vinyl ester, a thermosetting resin.

2.3.1.6 Fibrillation and interfacial strength

Most papers report observing fibrillation at failure in SRPP depending on processing parameter. Typically, fibrillation is observed more extensively in reinforcements that are perpendicular to the load. A possible exception is the study by Romhany et al. [43] who reported that rovings aligned to tensile load showed brittle fractures, while fibrillation occurred in rovings perpendicular to the load.

In a study of coextruded tape-reinforced UD SRPP, Alcock et al. [17] observed fibrillation in conjunction with no single fracture surface. This behavior was attributed to the transverse strength of the tapes being so weak that cracks propagated rapidly along the tape direction, causing intra-tape fibrillation as well as inter-tape debonding. The failure under tension is then more likely due to delamination rather than tensile fracture of the reinforcement, which may explain the tensile strength of single tape being higher than that of the composite.

The explanation that fibrillation is due to transverse cracks travelling along the tape direction and causing delamination is likely to be true, especially given its agreement with Peterlin’s model of the molecular structure of drawn PP [116–120], which will be described later. The description that fibrillation appears because “the transverse strength of the tapes is so poor” needs to be carefully explained. The description may lead the reader to imagine intra-tape splitting under Mode I fracture (tensile opening), which is illustrated in Figure 2.7a. But it will be explained in Section 2.3.3 that cracks and fibrillation along the tape direction are likely to begin from microscopic voids which cause tensile strain in the microfibril to be lower compared to the surrounding microfibrils. The resulting shear between the microfibrils causes them to debond. Therefore, at a *microstructural scale*, fibrillation arises from intra-tape fracture in Mode II (in-plane shear), which is illustrated in Figure 2.7b.

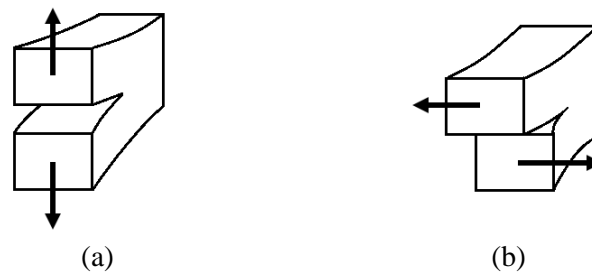


Figure 2.7 Illustration of a) Mode I fracture – tensile opening and b) Mode II fracture – in-plane shear.

Some researchers have related the fibrillation in SRPP to its interfacial strength. Jordan et al. [68] observed extensive fibrillation in peel tests of tape-reinforced hot compacted woven SRPP samples and stated that fibrillation might merely be easier in tapes, or alternatively, that it is a reflection of better bonding. The higher energy required to induce extensive fibrillation would correlate with the observed higher peel strength. In a tensile test of notched samples of a similar SRPP, Romhany et al. [43] also observed fibrillation in which the fibres and their bundles split from the matrix in a very ductile manner; they said this was a clear indication of good interfacial adhesion.

On the other hand, Izer [93, p. 68] stated that in typical tensile failures of film-stacked SRPP, well-consolidated samples fail by fibre breakage, while fibrillation is prevented by strong interfacial adhesion. However, looking at pictures of failed samples from Izer [93, pp. 66–67], it is possible the author was referring to the total volume of fibrillation, with delamination decreasing with processing temperature due to damage occurring over shorter lengths of the specimens, rather than any decrease in the extent of fibrillation (by larger extent I mean a larger number of thinner fibrils across the lateral section). In any case, from the pictures, which show the edge side of the specimens, it is difficult to discern fibrillations from delaminations. It is also possible, of course, that the different failure behaviours observed in this research is due to a difference in the type of reinforcement or manufacturing parameters.

It should be noted that the aforementioned correlation between the higher degree of fibrillation and a higher interfacial adhesion in [43] and [68] seems to apply only to specimens that exhibit macroscopic fibrillation and high strength. It will be shown later, in Section 4.2.1, that thin SRPP specimens exhibit a very small amount of fibrillation which can only be observed under the microscope, whereas thicker specimens exhibit much more fibrillation which can be observed without microscopy, similar to the studies above. However, the thin specimens that exhibit no macroscopic fibrillation are conjectured to have a higher level of bonding than the thicker specimens, based on the evidence from the current study and a few others [41, 70, 71, 97], which will be explained in more detail in Section 4.2.1.

2.3.1.7 Reinforcement orientations

In a study of the mechanical properties of coextruded tape-reinforced UD SRPP, tensile strengths at different angles between reinforcement and load were predicted using Tsai–Hill and maximum stress criteria [17]. The values were in good agreement with measured data, although their data show just one data point between $0^\circ < \theta < 30^\circ$, where the change in curvature of the criterion is most dramatic. Regarding fracture characteristics, failure of the UD SRPP was dominated by tape strength between $0^\circ < \theta < 2^\circ$, by shear between $2^\circ < \theta < 23^\circ$, and by transverse strength of the tape above this angle. Fracture dominated by tape strength at small angles showed extensive fibrillation.

In a study of coextruded woven SRPP, samples oriented at $\pm 45^\circ$ to the tensile load exhibited evident intraply shearing, or a trellis effect, where the reinforcing tapes rotated by as much as $\pm 27^\circ$ to the direction of the tensile load [40]. Tensile strain to failure at $\pm 45^\circ$ is much higher ($\approx 40\%$) due to this and more tape debonding occurs than at $0^\circ/90^\circ$ ($\approx 10\%$). When consolidated at a lower temperature, but still above adequate pressure, failure strain was further increased due to lower interfacial strength, leading to greater tape debonding and pull-outs. At higher processing temperature, micro-fibrillation and tape breakage occurred instead of tape debonding and pull-outs. The increase in strength and decrease in failure strain with an increase in processing temperature was much more pronounced than the changes observed for $0^\circ/90^\circ$ samples.

2.3.2 Matrix microstructure and interfacial strength

While it can seem like a good idea to take the properties of PP or melted SRPP as the properties of the matrix in SRPP, this is not exactly accurate because the structure of the matrix in SRPP is different from that of the amorphous PP spherulites. In SPC, the matrix phase recrystallises into lamellae, growing epitaxially from the surface of the fibrillar reinforcement (as was shown in Figure 2.6, and also in Figures 2.8 and 2.9). Figure 2.9 shows both the lamellae that recrystallised epitaxially to the fibre and those that recrystallised into spherulites from the molten PP away from the fibre. These lamellae meet regions that recrystallised from adjacent reinforcements, effectively forming the matrix phase. In hot

compacted SPCs such as those shown in Figures 2.6 and 2.8, the reinforcement and matrix originate from the same material, in comparison to SPCs that have chemically identical but structurally different materials for their reinforcement and matrix (e.g., different polymer grades).

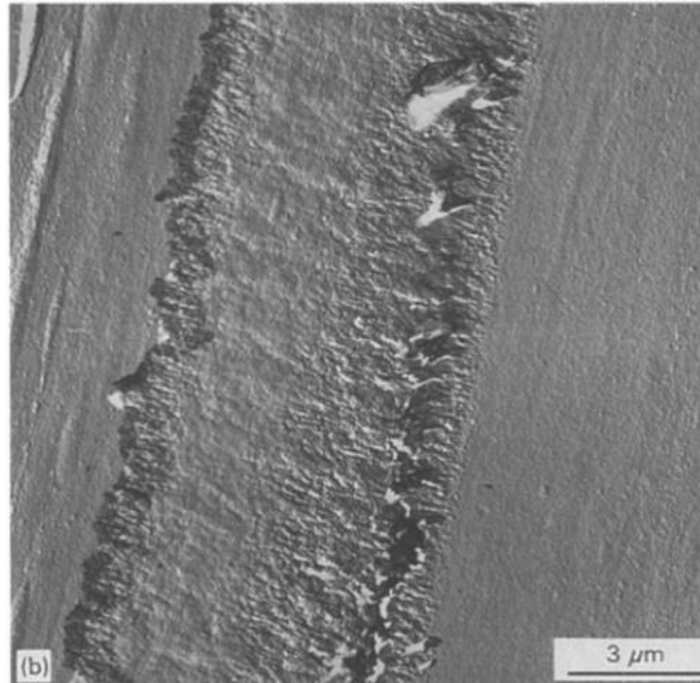


Figure 2.8 Scanning electron micrograph of an etched longitudinal section of a hot compacted SRPP showing lamellar growth between interfibrillar boundaries [65, Fig. 8b].



Figure 2.9 Polarised optical microscopy of the fibre-matrix interface of an SRPP formed by introducing fibre into a molten matrix at 167°C [121, Fig. 2a].

The microstructure of the transcrystalline layers in SPCs are formed as follows. (For reference, schematic of spherulites, lamellae, and crystallographic orientations of polymers are shown in

Figure 2.10 with the axes-naming convention.) During recrystallisation, the direction of lamella growth (*b*-axis) is perpendicular to the tape orientation. The mechanism may be somewhat similar to the ‘shish-kebab superstructure’ formed during flow-induced crystallisation of polymers [123], depicted in Figure 2.11a. In this analogy, highly oriented molecules on the surface of the reinforcement material serve as the ‘shish’ and the lamellae in the epitaxial layer as ‘kebabs’. The oriented chains in the shish can act as row nuclei for the growth of kebabs, with the lamellar molecular orientation (*c*-axis) aligned in the same direction as the shish. Interestingly, it has been reported that microstructures similar to this can also be formed in non-SPCs under certain conditions³.

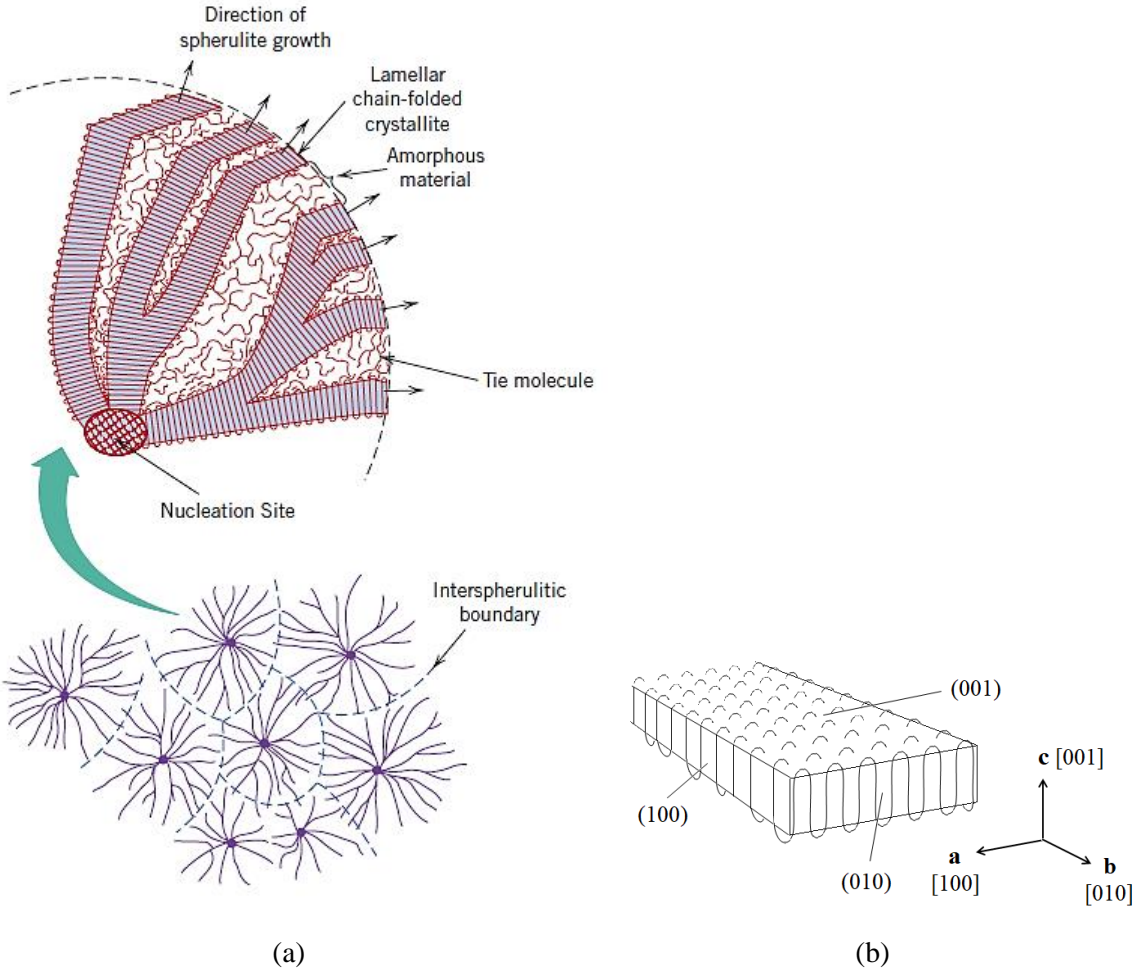


Figure 2.10 Schematics for a typical polymer a) spherulite [122, Fig. 14.13]; and b) lamella with conventional crystallographic directions and planes.

³ Microstructures similar to SPC can be formed in non-SPCs, for instance, in injection moulded GFRP when polymer matrix is recrystallised in presence of shear [125], or in FRPs with polymer fibres where there is a composite of liquid crystalline polymer fibres and PP matrix [126].

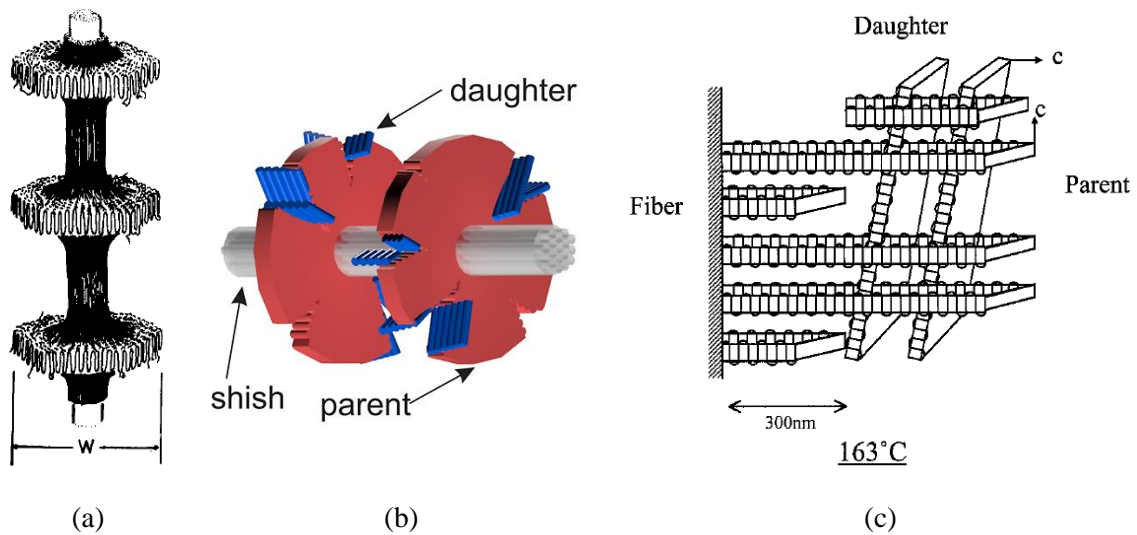


Figure 2.11 Schematics of shish-kebab structures a) formed in polymers under shear stress [123, Fig. 1], and in SRPP during consolidation, illustrated in b) [124, Abstract] and c) [95, Fig. 12].

In SRPP, there are two forms of kebabs, as shown in Figures 2.11b and c. ‘Parent’ kebabs form first as described, and then ‘daughter’ kebabs nucleate from the (010) lateral surface of parent kebabs, such that the *a*-axis of the daughter kebab is aligned to the molecular orientation of the shish and the *c*-axis is perpendicular to it. Kitayama et al. [95] studied morphologies and mechanical properties of the fibre–matrix interface of SRPP. They found that transcrystalline regions close to the fibre were densely packed with lamellae of the parent kebab, and daughter kebabs started to appear at a distance away from the fibre, as shown in Figure 2.11c. This agrees with other observations in the literature.

Kitayama et al. also reported strong interfacial adhesion, with no debonding occurring under tensile stress transverse to the fibre. Interestingly, the authors stated there are different arguments on whether the transcrystalline layer in PP improves or reduces interfacial adhesion. However, this observation was based on research on 2-phase FRPs with PP matrix and different fibres, such as cotton cellulose fibres [127] and glass fibres [128–130]. Given research on SRPP and other SPCs showing evidence from SEMs of mechanically loaded samples, the more convincing argument is that the interfacial adhesion is improved by the described structure in the transcrystalline layer.

For example, a well-compacted UD SRPE exhibited transverse failure within the fibres when subjected to bending loads, not at the fibre–matrix interface [66]. Similarly, [68] showed that for SRPPs made with high molecular weight PP tapes, peeling forces tend to disrupt the reinforcement itself. Even for SRPPs made with lower molecular weight PP multifilament bundles, which exhibited poorer mechanical properties, cracks propagated through boundaries between transcrystalline layers within the matrix. Therefore, the limiting component in the fracture of the SRPP studied in this research is unlikely to be the interface. As such, excellent load transfer is expected due to strong interfacial bonding.

As can be seen, the microstructure of the matrix in an SRPP is incongruent with that of a plain PP. However, to help illustrate the characteristic damage of SRPP in comparison to PP in Chapter 4, the mechanism of craze-crack occurring in PP is briefly described here. Crazes are highly localised zones of plastic dilatational deformation that initiate on the surface [109] and form microvoids, and the material between the microvoids extends into fibrils ($< 1 \mu\text{m}$) under further local strain. These fibrils are aligned with the tension and can support a load. Microcracks initiate and propagate perpendicular to the tension, with fibrils progressively breaking under further stress and causing the microvoids to coalesce. This is called a craze-crack mechanism and eventually leads to brittle fracture [131, 132]. An example of craze-crack propagation in PP is given in Figure 2.12. The white in micrographs derives from stress whitening, which is a generic term for different microscopic phenomena that cause light scattering due to localised changes in the polymer's refractive index [132].

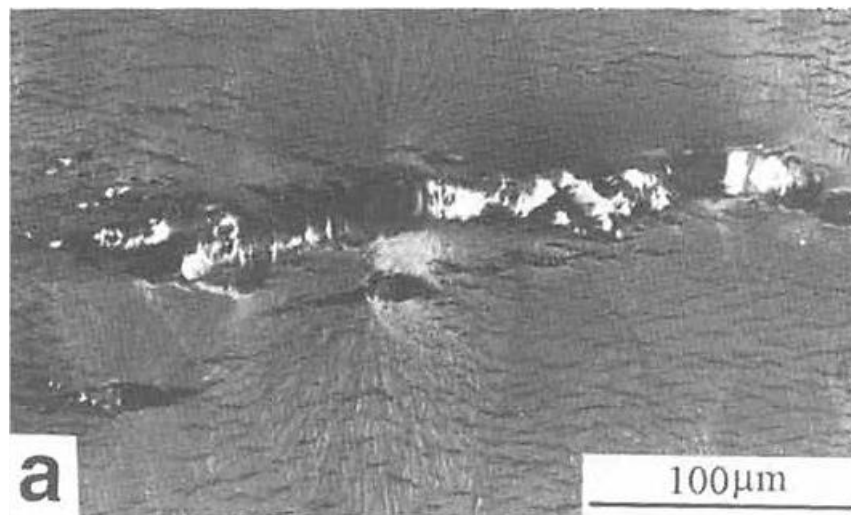


Figure 2.12 Crazing observed in polypropylene during a tensile test [133]. The tensile load is vertical in this image.

In understanding deformations in the matrix of SRPP it is also helpful to visualise the deformations of plain PP at different orientations with respect to the lamellae. Plastic deformation in semi-crystalline polymers can be divided into two parts – deformations in the amorphous phase and polymer crystals, as illustrated in Figure 2.13 [109]. In the amorphous phase (Figures 2.13 a–c), the primary deformation modes are induced by a) interlamellar slip, where chains are sheared as attached neighbouring lamellae slip past each other; b) interlamellar separation, where tension or compression causes lamellae to separate from each other and the attached chains between the lamellae to unravel and straighten; and c) stack rotation, where both the lamellae and the amorphous chains rotate.

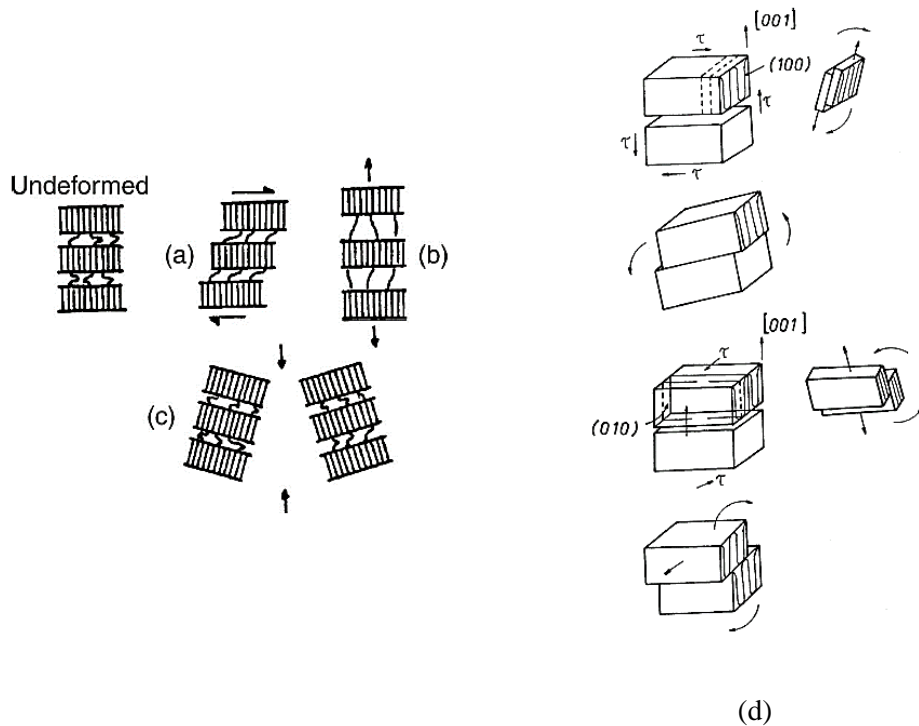


Figure 2.13 Deformation modes in the amorphous phase of semi-crystalline polymers: a) interlamellar slip; b) lamellar separation; c) rotation of stacks of lamellae [109, Fig. 2]. d) rotation of crystal fragments due to slip, marked by arrows. The resolving of the shear on a plane due to simple tension or compression is also illustrated [109, Fig. 4].

In the crystalline phase, plastic deformation occurs by crystallographic slip (Figure 2.13d), twinning, and by martensitic transformation, without destroying the crystalline order at low to moderate amounts of deformation. Of these, the slip mechanism can produce the largest plastic strains. The slip planes and directions in PP are (010)[001], (110)[001], and (100)[001], in the order of lowest critical resolved shear stress (easiest slip mechanism) to highest. (The lowest and average critical shear stresses in iPP are 22.6 MPa and 25 MPa, respectively.) [109, 134]

Also, Aboulfaraj et al. [133] describe the behaviour of lamellae and linked amorphous regions at different lamellar orientations when subject to uniaxial tension and shear, as shown in Figure 2.14.

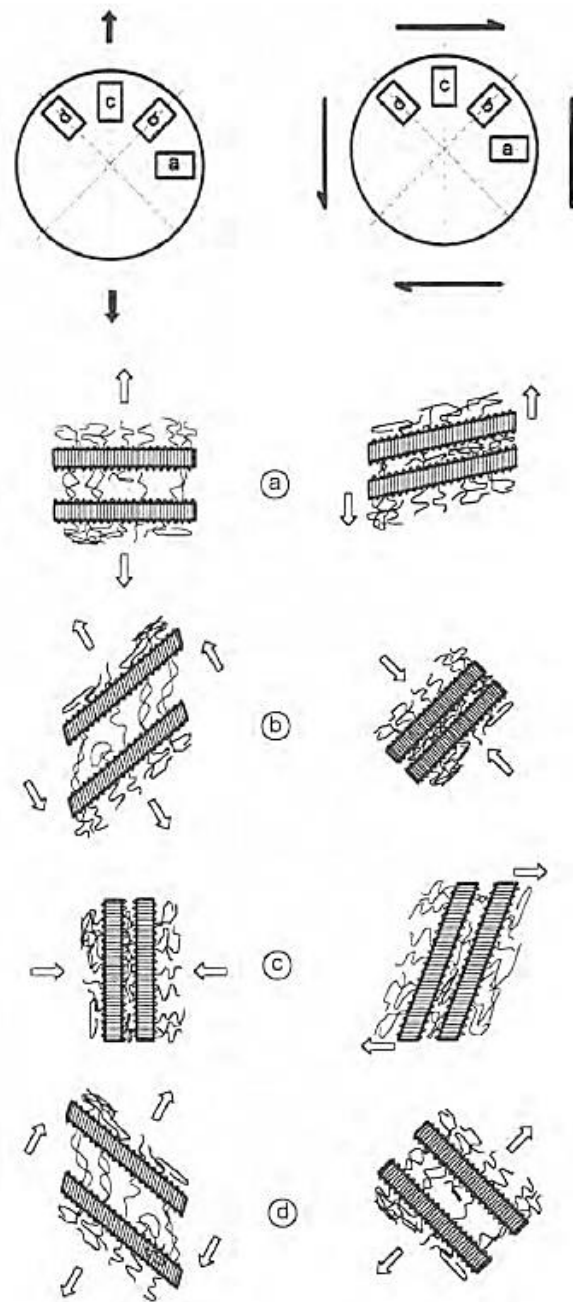


Figure 2.14 Behaviour of the different sectors in PP spherulites under uniaxial tension and simple shear [133, Fig. 13]. The black arrows represent the applied stresses and the white arrows the locally active deformation mode.

2.3.3 Reinforcement microstructure and behaviours

Other than those mentioned already, there is limited literature specifically on reinforcements in SRPP. However, the drawing of PE and PP has been studied in depth, although there still are differing hypotheses on the exact microstructure and deformation processes that give rise to the structure.

There are two notable theories describing the deformation mechanism in semi-crystalline polymers. One is the crystallographic slip theory described previously, based on works by Bowden and Young [135–139], where plastic deformations derive from dislocations travelling along slip planes (similar to crystal plasticity in metals). This is widely accepted, although there are doubts about how the dislocations are generated [109]. The other is by Peterlin [116–120] which describes destruction of crystals and formation of microfibrillar structures *at large deformations*. Current theories are largely based on the works of these authors, and some good reviews are provided in [109] and [140], authors who, with their colleagues, have carried out substantial studies on the subject. Crystallographic slip theory is more relevant to deformations at small ($> 1\%$ [119]) and intermediate strains, while Peterlin's theory is more appropriate in describing the microstructure and characteristics of drawn semi-crystalline polymers such as PP tapes in SRPP.

Callister [122] refers to the classic plastic deformation model shown in Figure 2.15, where the lamellae and tie molecules rotate such that the chains (*c*-axis) are oriented towards the tensile axis and then broken into smaller crystalline blocks and connecting tie molecules. However, Peterlin suggests a different model based on the observation that lamellae disappear and fibrillar structure grows *concurrently* at high strains. He suggests that lamellae are destroyed in 'micronecks' and the broken-off crystal blocks are incorporated into the newly arranged microfibrillar structure, as illustrated in Figure 2.16 [120]. He also hypothesised that lamellae or crystal blocks which are more aligned with tensile stress exert strong shearing forces on other lamellae (due to their higher strains providing a shear component to the adjacent lamellae stacks) [119]. This is illustrated in Figure 2.17. The final structure of drawn semi-crystalline polymer consists mostly of microfibrils which are tens of microns in length and a few hundred angstroms laterally [116]. Peterlin claimed this is generally applicable to all polymers that are at least partially crystalline in the unoriented state [120].

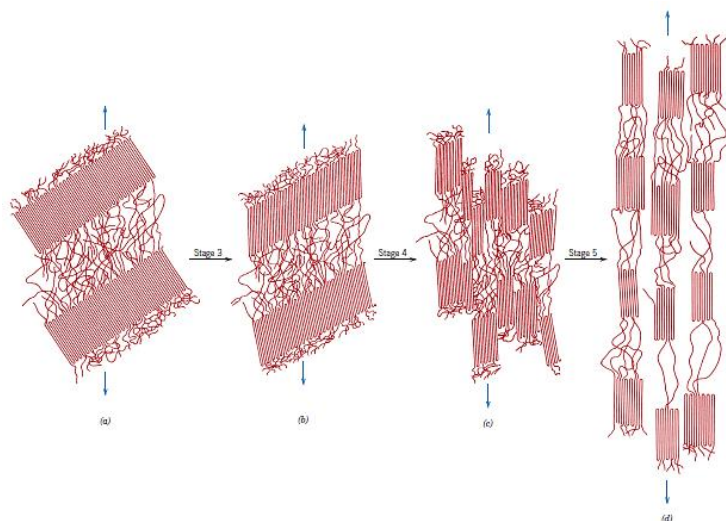


Figure 2.15 Stages in the plastic deformation of a semi-crystalline polymer [122, Fig. 15.13].

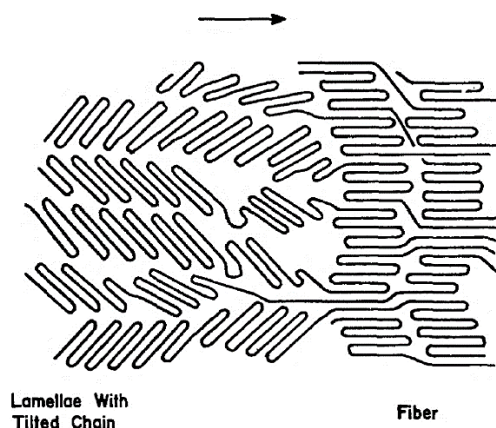


Figure 2.16 Molecular model of the transformation into the microfibrillar structure by fracturing in the initial lamellae in blocks which are then incorporated into microfibrils [120, Fig. 8].

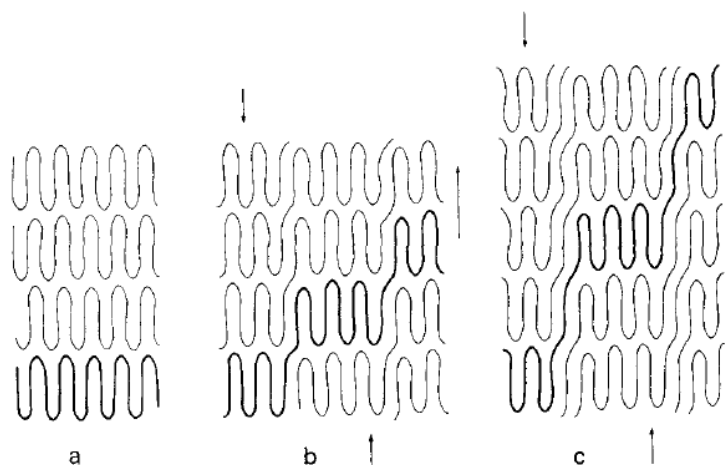


Figure 2.17 Formation of 'skewed' microfibrils by shearing of a stack of parallel lamellae: a) stack before shearing, b) after shearing by one lamella thickness per block width, c) after shearing by two lamellae thicknesses per block width [119, Fig. 1].

Peterlin's model has been generally well received and, despite criticisms, is widely acknowledged [141]. The specific mechanism involved during stretching is still disputed. A more recent study [142], using synchrotron radiation and small and wide angle x-ray scattering measurements, showed that the structure of drawn PP differs depending on the processing temperature. It has been hypothesised that oriented lamellae, microfibrils, or fibrillar crystals are formed when stretched at 50–80°C, 90–120°C, or 120–150°C, respectively. Fibrillar crystals are described as well-packed periodic lamellae inside fibrils oriented in the meridional direction (*c*-axis), in comparison to microfibrils where no lamellae with good periodicity exist.

Properties of drawn PPs differ depending on whether or not they were formed under a positive normal stress component that allows it to be cavity-free. Cavitations can be formed during necking without pressure and can later induce crazing or shear yielding. Visually, this can manifest in the form of whitening. The strength of a PP is restricted to 120 MPa when it is drawn without a cavitation control mechanism. In such case, fracture initiates in microfibrils one by one, whereas a PP drawn to the same ratio under compression in a channel-die can have a strength of up to 300 MPa. It has been reported that rolltrusion can produce PP with a tensile strength of 524 MPa [109]. Note that a cavity-free, die-drawing process was elaborated in the 1980s by researchers at the University of Leeds who also developed Curv. Interestingly, some studies [23, 143, 144] have found that fibrillar structures on a nanoscale can be achieved in some SPCs ('nanocomposites') if the starting material is neat nanofibrils instead of highly oriented strips (as in hot compaction).

Mechanisms involved during drawing of the already drawn microfibrillar structure is different from the way it forms from the lamellar structure. Peterlin [120] explains that most deformation comes from axial translation of the centres of mass of the fibrils, as shown in Figure 2.18a. In this case, the cross-section and length of the fibrils remain practically unchanged, but the number of fibrils per cross-section, and therefore the actual cross-section of the specimen, decrease. This is accompanied by a change in shape of the fibril due to shear stress on the fibrils, causing shear displacements between the microfibrils within, as shown in Figure 2.18b. This, in turn, causes irregular displacements of crystalline blocks and amorphous portions, as shown in Figure 2.18c. Under large displacements of the fibrils, and resulting shearing between microfibrils, tie molecules connecting different fibrils become more extended and taut. These taut tie molecules contribute to the high axial elastic modulus of drawn PP [119].

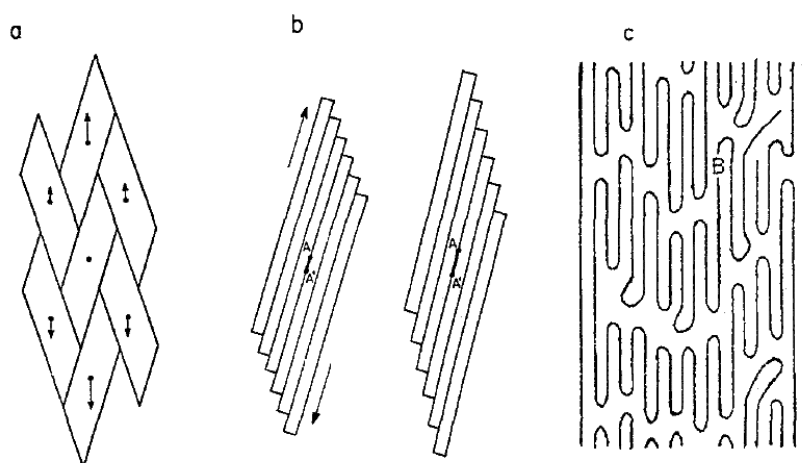


Figure 2.18 Drawing of microfibrillar structure. The centres of mass of the fibrils are displaced linearly as in an affine transformation (a), the fibrils are sheared (b), the electron density difference between crystal blocks and amorphous layers between them is smeared out (c) [120, Fig. 12].

Well before fracture, point vacancies from ends of microfibrils, usually at the boundary of the fibrils, can, under stress, open and form microcracks. At such point defects, stress concentrations are created due to reduced force transmission in the axial direction and reduced friction between microfibrils at the abrupt discontinuity [119]. From this, longitudinal cracks can propagate along the boundary between adjacent microfibrils. Coalescence of microcracks by radial and axial growth can then reach a critical value and grow catastrophically, leading to fracture. Where longitudinal growth is sufficiently enhanced, the fracture is fibrous [118]. This aligns very well with observations of fibrillation in SRPP mentioned earlier.

According to Galeski [109], fracture in rolled samples initiates under tension by longitudinal delamination of layers parallel to the rolling plane, which then spread to the entire gauge length. Microfibrils are formed in the final stage of delamination and initiate propagation of fracture in other microfibrils, leaving the sample looking like an open book with free-standing pages.

As explained by Peterlin [116], fibrillation involves microfibrils having different draw ratios and, as a consequence, having poor adhesion or bonding between the fibrils. This leads to longitudinal voids and longitudinal slips of fibrils, resulting in the tendency for drawn PE and PP to fibrillate. If microfibrils are at an angle, especially perpendicular to the tensile stress, these can very soon separate, with fibrillar elements peeling off the bulk of the undeformed proportion. In such a case, crazes and cracks are almost parallel to the microfibrils [119].

According to Peterlin's model, the basis of a drawn semi-crystalline polymer is folded chain crystal blocks which are incorporated into microfibrils and aligned with taut tie molecules connecting the different blocks. Therefore, the strong unit is the microfibril, not the lamellae, and the former determines the stiffness and strength [116].

Shinozaki and Groves [145], who studied the plastic deformation of oriented PP and its tensile and compressive yield criteria at different angles, state that the Hill–von Mises model of plasticity in metals has been successfully applied to polymers, but that it is unsuitable for PP. Their critique is that researchers incorrectly fit this criterion with a non-zero slope at $\theta = 0^\circ$, which makes the model false between $0^\circ < \theta < 10^\circ$, for which, unfortunately, reproducible experimental data is very difficult to obtain. They found Kelly and Davies' criterion [146] to be more suitable, according to which there are different modes of failure at different angles between the applied tensile load and the reinforcement directions. However, looking at their results, the model does not appear to give a significantly better fit than does the Hill–von Mises criteria for approximately $\theta > 40^\circ$.

According to observations by [145], a drawn PP subject to tension at small angles to the drawing direction ($0^\circ \leq \theta \leq 10^\circ$) fails by brittle, fibrous fracture with a jagged fracture surface. At intermediate angles ($20^\circ \leq \theta \leq 80^\circ$), large plastic deformations occur until ductile shear failure. At these angles, deformation bands appear, with increasing sharpness as the angle increases. It is also mentioned that the

mechanism operating at $\theta = 30^\circ$ is simple shear parallel to the molecular orientation. At large angles ($85^\circ \leq \theta \leq 90^\circ$), fibre–matrix interface failure, crazing, and a smaller number of bridging fibrils were observed. In other words, drawn PP fails by molecular fracture at small angles between the molecular orientation and the loading direction, by intermolecular or interfibrillar shear at intermediate angles, and by molecular or fibrillar separation at large angles.

2.4 Fibre metal laminate

2.4.1 Steel-based FML

Only a few studies exist on steel-based FMLs because mainstream research on FMLs is geared towards lightweight aerospace applications. As of yet, only ARALL and GLARE are commercially used, and both are based on aluminium alloys. Nevertheless, there are benefits to considering the use of FMLs based on steel for applications that do not depend critically on weight. For instance, Hoo Fatt et al. [147] suggest that the ballistic performance of FMLs can be improved by using ductile metals which undergo large deformation since 84–92 % of the energy absorbed by GLARE in ballistic deformation is from panel deformation, only 2–9 % from delamination, and 7% from tensile fracture. In a study of impact failure of GLARE, Vlot, Vogelesang, and Vries [1] found that failure of the aluminium had caused failure of the FML, with results showing that the composite had matrix cracking and delamination but no fibre failure. Stainless steel-based FMLs show improved tensile and fatigue properties compared to aluminium FMLs, and offer significant benefits in terms of high stiffness and failure strength [31, p. 22].

Langdon and Rowe [148] investigated bonding of woven GFRPP/steel FML and its response under blast loading. A single-step process of pre-stacking all layers and consolidating them under heat, pressure, and rapid cooling gave the best bonding when tested under bending (in comparison to consolidating the GFRPP plies first and then bonding the steel layers using polymer interlayers or adhesives). The FML exhibited a similar response as GFRPP/aluminium FML under blast loading, with multiple forms of damage: pitting, pedalling, and plastic deformation of the metal layers; matrix cracking, fibre fracture, and fibre pull-through in the GFRPP; and debonding between layers. Debonding and plastic deformation of the metal panel on the opposite side of the impact increased with magnitude of the loading, and was found to be lower than that of GFRPP/aluminium FML but higher than monolithic aluminium.

Reyes and Gupta [149] investigated dual phase (DP) steel FMLs based on GFRPP and SRPP. Using modified polyolefin (PP/PE) adhesives, the authors reported good adhesion between the hot-dip zinc surface of the DP steel and the FRPs, despite the fact that polyolefins like PP are difficult to bond. Tensile stress–strain curves of FMLs were similar in curvature to that of DP steel. Strength of the SRPP-based FML was much higher (464 MPa) than that of SRPP (86 MPa) but lower than that of DP steel

(620 MPa), whereas GFRPP-based FML had a strength (351 MPa) that was slightly higher (252 MPa) than the GFRPP and slightly lower (470 MPa) than the DP steel at failure.

The strengths of the FMLs could be predicted using the rule of mixtures. A modified version gave better predictions, where the metal strength at failure strain of the composite was used if the metal layer had not reached its maximum strength at the failure point of the FML, as in the case of GFRPP/DP steel FML. The modification was not needed for SRPP/DP steel FML, which failed at around 28% (from their graph), close to the failure strains of steel ($\approx 31\%$) and SRPP ($\approx 30\%$); thus, when the FML failed the metal layer had been strained past its maximum strength. This failure strain is much higher than that of GFRPP-based FML which appeared to have failed around 6–7%, close to the failure strain of the GFRPP used ($\approx 5\%$). The demonstrated dependency of tensile properties of those FMLs on their constituent materials is in line with behaviours commonly observed in FMLs from other literature, for example, in Carrillo and Cantwell's study of SRPP/aluminium FML, which will be described in Section 2.4.2.1 [150].

On a side note, there have been only a few studies of FMLs based on other metal alloys, such as titanium, magnesium, and stainless steel [31, pp. 21–22]. Stainless steel-based FMLs provide a closer point of comparison to steel-based FMLs than do the others. However, stainless steel is harder, stronger, less malleable, more brittle, and more expensive than mild steel, and is therefore less utilised in manufacturing [151]. Studies using stainless steel in FMLs are mostly concerned with thermoset-based FRPs, impact performance, fatigue characteristics, or improvement of laminate adhesion [152–157]. Beyond FML systems, Harhash and his colleagues [158–161] have studied the forming of a polymer–metal laminate system based on thermoplastic polymers and steel for potential use in the automotive industry.

2.4.2 Thermoplastic-based FML

Thermoplastic polymer matrix-based FMLs have been developed recently and most FMLs, including commercial ones, are thermosetting epoxy-based. It is mentioned in [31, Ch. 2.4, p. 23] that one of the problems identified earlier with thermoplastic-based FML is that the high temperature required for 'curing' is detrimental to most high-strength aluminium alloys in terms of their mechanical and fatigue properties, as discovered in [162]'s preliminary study. (Note the term 'curing' is not really accurate for thermoplastic.) Alderliesten outlines that, for this reason, most studies on thermoplastic-based FMLs are focused on titanium and carbon fibre-based FMLs, notably their basic mechanical properties and initial manufacturing trials [163] but mostly on their impact properties [26, 148, 164–167].

In general, FMLs based on thermoplastic-based FRPs exhibit higher impact resistance compared to FMLs based on thermoset-based FRPs. For example, a study by Cantwell et al. [164] has shown that four thermoplastic-based GFRPs/aluminium FMLs had higher specific perforation energies under high

impact compared to aluminium and a thermoset-based GFRP/aluminium FML. In particular, a cross-ply of UD GFRPP/aluminium FML had a specific perforation energy that was more than 60% higher than that of thermoset-based FML and almost double that of aluminium.

As an example of tensile fracture behaviour, an FML based on cross-ply carbon fibre-reinforced/polyether ether ketone (PEEK)/titanium FML was found to fail under tensile loads with fibre fracture along the fibre direction and fibre–matrix interface debonding for fibre directions larger than 15° [168]. For this specific FML, Tsai–Wu failure criteria can predict its first ply failure reasonably well, but the maximum stress criterion was less successful.

Hou and Friedrich suggested [169–172] that thermoplastic-based FML can be pre-consolidated into sheets and then subsequently formed using similar tools and methods typically employed in sheet metal forming. This is possible because thermoplastics have thermally reversible properties, unlike thermosets which form permanent cross-linking during curing and therefore cannot be melted and then reformed. This means thermoplastic FRPs, and by extension, thermoplastic FRP-based FMLs, can be pre-consolidated under elevated temperature, cooled, and then subsequently (thermo-)formed at a later stage. Several studies have confirmed the forming capabilities of GFRPP/aluminium FML and SRPP/aluminium FML under various parameters, as will be described in the next section.

2.4.2.1 SRPP-based FML

The good impact property of SRPP has been mentioned earlier. Similarly, SRPP/aluminium FMLs have favourable impact properties, with the specific perforation energy being twice or more than FMLs based on Kevlar or even glass-reinforced thermoplastic FRPs [173]. In a study by Cantwell et al., described in the previous section, the latter was shown to have higher impact resistance than a similar FML based on a thermoset FRP [164]. This high impact property of SRPP-based FML is mostly due to the high failure strain of the SRPP reinforcement [173].

Carrillo and Cantwell [150] studied the properties of an SRPP/aluminium FML. Mixed-mode (I and II) interlaminar fracture resistance of the FML was found to initially increase linearly with crack length, during which extensive fibre bridging was observed. The fracture toughness of the metal–composite interface was higher than between the SRPP layers (which delaminated), although this may have been because the consolidation pressure of FML (0.7 MPa) was lower than that of the SRPP (3 MPa). The FML's low consolidation pressure was also suspected to have caused premature failure in the SRPP layers under tension by causing relaxation in the reinforcement phase, despite the fact that SRPP has a higher failure strain than aluminium.

The tensile properties of $0^\circ/90^\circ$ and $\pm 45^\circ$ FMLs lie between those of aluminium (stronger, stiffer, less ductile) and SRPP, except that the failure strain of $0^\circ/90^\circ$ FML is slightly higher than that of SRPP. The

reported stress–strain behaviours of the constituents and the SRPP/aluminium FML were different to those of SRPP/steel FML, as reported by Reyes and Gupta [149] and described earlier. However, both studies show that, in general, the behaviour of the FML lies between those of its constituents.

FML behaves similarly to SRPP in that it is weaker and more ductile when loaded off-axis, with strengths and failure strains of 131 MPa and 27% at $\pm 45^\circ$, and 154 MPa and 23% at $0^\circ/90^\circ$. The $0^\circ/90^\circ$ and $\pm 45^\circ$ laminates failed in the aluminium at approximately $\pm 5^\circ$ to the dislocation band of aluminium, which is around 65° to the load. The $0^\circ/90^\circ$ laminate showed extensive debonding between the SRPP layers along the entire length of the specimens, whereas the $\pm 45^\circ$ laminate showed localised, less extensive debonding in the SRPP layers due to rotation of the fibres.

The FML's flexural strengths were higher than its tensile strengths, as is the case for most materials. Under bending, a change in the fibre orientations did not lead to any significant difference in stress–strain behaviours. Failure occurred throughout its volume due to intralaminar delamination within the SRPP laminae, with no metal–composite debonding or fracture. Under low-velocity impact loading, the FML went through considerable plastic deformation, varying levels of thinning in the metal, and, depending on the level of impact, localised fracture in the composite and metal layers without any interlaminar debonding.

There are a number of studies on pre-consolidated, woven SRPP/aluminium FMLs in terms of its behaviour during various forming methods, such as channel forming [174–177], rectangular cup forming [177, 178], hemispherical draw forming [179–182], and stretch forming [183, 184], mostly comparing them with GFRPP/aluminium FMLs. Compston et al. [174] found that, during channel forming at a raised temperature, putting aluminium in an FML with SRPP reduced strains in the aluminium, which improved forming limits through delay of necking and tearing in the aluminium.

Mosse and colleagues carried out the first comprehensive study of the stamp formability of pre-consolidated aluminium FMLs based on GFRPP and SRPP, investigating their formability during channel and rectangular cup forming and the effects of varying process temperatures [175, 178], feed rates, blank holder force, and tool radius [176, 177]. They found that an increased preheat temperature changed the deformation mode and improved formability in general, except that cracks propagated faster and caused damage in the composite layer. Shape errors in forming of FMLs were found to be sensitive to feed rate, but overall significantly fewer than in aluminium (by around 75%), especially in the SRPP-based laminate (80–90% less). Blank holder force and tool radii were found to have effects on the shape error but were secondary to feed rate.

Dhar Malingam [179] conducted a comprehensive study on the effects of processing parameters on the draw forming behaviour of SRPP/aluminium and GFRPP/aluminium FMLs. Blank holder force and preheat temperature significantly affected the deformation behaviour of the FMLs, but the feed rate had no significant effect on the SRPP-based FML. The most substantial effect of temperature occurred at

the melting point of the adhesive, where the individual layers deformed independently of each other. FML had more uniformly distributed strains with a reduced maximum strain in comparison to aluminium, and reached higher forming depths, especially at higher temperatures. Common failure mechanisms in SRPP-based FMLs were matrix cracking, delamination, and laminate debonding. GFRPP-based FML was unable to be deformed without incurring damage, typically longitudinal matrix cracking, interlaminar delamination, fibre fracture, and fibre–matrix debonding.

In a study of draw forming by Gresham et al. [181], varying degrees of tearing in aluminium and fracture in SRPP were observed, increasing with a decrease in the blank holder force or an increase in the preheat temperature. Wrinkling and delamination also occurred in both material layers. Interestingly, increasing the temperature increased formability at lower blank holder forces but decreased formability at higher blank holder forces, with the latter also showing no damage in the core composite layer. This shows interdependency of the parameters that affect the onset of failure.

On the other hand, a similar study investigating effects various processing parameters showed that the preheat temperature and the blank holder force were the two factors significantly affecting the first principal strains and deformation modes – but not their interdependency, blank holder force, or feed rate [182]. In terms of the effect of temperature, the state of the adhesive was found to significantly affect forming characteristics by allowing layers to slide over each other in the melted state.

Sexton et al. [183, 184] investigated the deformation and failure limits of woven SRPP/aluminium and woven GFRPP/aluminium FML under stretch forming. It was shown that the addition of SRPP improved the failure limits of the aluminium and the FML did not undergo localised necking, whereas the GFRPP-based FML exhibited reduced failure limits. In the SRPP/aluminium FML, the optimal preheat temperature was 120°C, which is high enough to increase the failure strain in the composite layer but not so high as to melt the adhesive and cause the layers to deform independently. In this case, failure initiated from fibre fracture in the SRPP layer, whereas around and above 140°C, the adhesive melts and failure can initiate from the aluminium. This is opposite to GFRPP-based FML, which shows higher stretch formability when the adhesive melts and allows the layers to form independently.

Sexton also showed that different strain states could be induced by altering specimen shapes and fibre orientations. The complexity in establishing failure limits in principal strain space was demonstrated, where samples failed below the limiting surface strains of other samples, greatly influenced by the strain states of the composite layer. It was suggested that failure limits of SRPP/aluminium FML should take into consideration the amount of shear, fibre locking under intra-ply shear, and therefore fibre orientations, all of which play a role in the failure of SRPP. This reinforces the well-known fact that intra-ply shear is the most dominant deformation mode in woven FRPs [185].

The elastic and damping properties of a cross-ply SRPP/aluminium-based FML under different frequencies were studied recently by Iriondo et al. [186]. The FML was found to have greater damping

capacity than GLARE of similar configuration and containing aluminium alloy. The FML had a loss factor in the damping model that was higher by more than 10 times than the other two, which can be attributed to the composite layer being thermoplastic.

It is also worth mentioning that there are other types of hybrid material systems based on SRPP, other than SRPP-based FMLs, which can exhibit similar mechanical properties to those seen in the SRPP/steel FML studied in this research, although the failure mechanisms themselves are mostly different. An example of such a hybrid material system is where different fibres are combined with the SRPP, most notably the carbon fibre/SRPP hybrid materials studied by researchers at KU Leuven and their collaborators [187–201]. This particular hybrid was shown to exhibit a high strain to failure while increasing the stiffness, as compared to SRPP, when produced under certain manufacturing parameters. This is noteworthy, considering that many studies on composites focus on achieving high strength and stiffness while sacrificing material toughness, despite the importance of the latter property [202]. It will be shown in Section 4.3.1 that the hybridisation of SRPP with steel panels in the SRPP/steel FML also has the effect of increasing the stiffness and strength, while maintaining a high strain to failure. It will be shown that, in fact, the FML exhibits a slightly higher failure strain than the SRPP.

2.5 Summary

For an informed and widespread usage of SRPP and SRPP-based FMLs, an understanding of their failure behaviours is necessary. Many failure analyses on thermoplastic FRPs use existing failure theories that have been developed for thermoset FRPs, whose limitations have been highlighted by the WWFEs. Also, SRPP behaves differently to 2-phase thermoplastic FRPs, not to mention thermoset-based composites. If a woven structure is used, this will add more complexity to failure analysis.

A natural progression in future research will lead to the development of failure theories of SPCs, such as SRPP, that physically account for their unique damage characteristics. However, this literature review also indicates that there is a need for a better understanding of the damage and failure characteristics themselves, *before* failure theories can be developed.

Therefore, in an effort to partially fill this knowledge gap, this thesis will investigate the deformation and failure behaviours of SRPP and SRPP/steel FML. It is hoped this will help generate future studies that will make use of the findings here, so that such materials can be utilised in different applications with more ease and understanding. The methods adopted in this research in order to achieve this aim are outlined in the next chapter.

3 Materials and Methods

3.1 Introduction

This research examines the multiple damage components that develop during quasi-static deformations and their role concerning failures in SRPP and SRPP/steel FML. This is done by studying the materials' behaviour under different loading conditions, specifically:

1. Uniaxial tensile loading along one of the reinforcement directions.
2. Uniaxial tensile loading at off-axis to the reinforcement directions. This induces in-plane stresses and strains that are different from 1. above, offering a deeper insight into the materials' in-plane shear behaviour.
3. Combined in-plane biaxial and out-of-plane bending loading. This induces different states of stresses and strains at different points in the material. This is done by employing an experimental methodology that has traditionally been used for studying failure limits of metallic alloys.

This chapter outlines the materials and the methods used to study the above. The subsections on materials briefly summarise the basic properties of steel, SRPP and SRPP/steel FML. It also includes a description of the process and parameters used for making the FML specimens, along with methods and justifications on how the processing parameters were obtained. The subsections on the experimental methods outline the equipment and experimental setups, and the methods of analyses with relevant parameters, so that they can be reproduced as required.

3.2 Materials

3.2.1 Steel

The SRPP/steel FML specimens were made using a low-carbon (0.035–0.070% carbon content), commercial forming steel. It is a cold-drawn, hot-dipped zinc-coated steel called GALVABOND G2, provided by BlueScope Steel. It is suitable for moderate drawing applications, with tensile mechanical properties shown in Figure 3.1 and Table 3.1. This information was obtained from the manufacturers'

specifications and values measured according to the ASTM A370 standard [206]. Thicknesses specified by the manufacturers for the steel and zinc coatings are 0.40 ± 0.04 mm and 0.04 mm respectively, with variations on the actual product. The measured thicknesses of the metal sheets are 0.45 mm on average, and this value is used throughout the analyses.

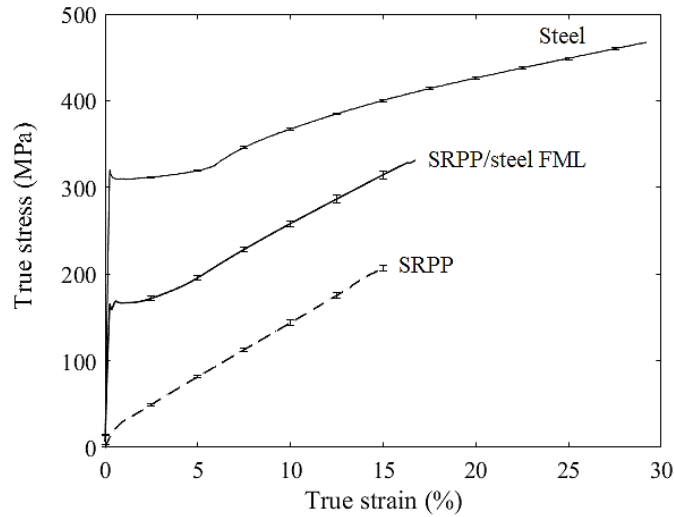


Figure 3.1 Measured stress–strain curves of steel, 1.0 mm SRPP, and SRPP/steel FML.

Table 3.1 Tensile properties of steel and SRPP.

Properties	Steel (from datasheet) ¹	Steel (measured)	SRPP (from datasheet) ²	1.0 mm-thick SRPP (measured) ³	SRPP/steel FML (measured)
Yield strength, σ_y (MPa)	350–390	331 ± 2	n/a ⁴	n/a	176 ± 4
SRPP transition strain, $\varepsilon^{transition}$ (%)	n/a ⁴	n/a ⁴	not available	0.73	n/a ⁴
SRPP stress at transition strain, $\sigma^{transition}$ (MPa)	n/a ⁴	n/a ⁴	not available	21 ± 1	n/a ⁴
Failure strain, ε_t (%)	27–41	29.2 ± 0.8	20	15 ± 1	17 ± 1
Failure strength, σ_t (MPa) ⁵	370–430	462.6 ± 0.8	120	210 ± 3	332 ± 3

¹ From ranges specified for 0.35 and 0.5 mm (ranges inclusive of both) in manufacturer’s datasheet [203].

² The manufacturer’s datasheet for Curv, the SRPP used in this research, for thickness 0.3–3.0 mm [204]. Values in the datasheet are from tests performed by the University of Kassel and the University of Leeds on materials produced on a pilot line and are ‘for guidance only’.

³ The following properties for SRPP were calculated according to the ASTM D3039 standard [205]: $\varepsilon^{transition}$, $\sigma^{transition}$, σ_t , tensile chord modulus of elasticity, E^{chord} .

⁴ Not applicable.

⁵ Measured tensile strength is given at sample average stress at the sample average of failure strains, in order to reflect a more accurate view of the stress-strain relation, rather than the sample average of ultimate tensile stress.

⁶ Not specified in datasheet. Values shown are typical known values for steel that were cross-checked with manufacturers.

3.2.2 SRPP

Propex Fabrics GmbH produced Curv [62], the SRPP used in this research, from a single component of PP through hot compaction. PP tapes are woven, compacted and heated to a temperature close to the onset of melting to selectively melt every surface which, on recrystallisation, forms the matrix. The tapes are manufactured from PP films by stretching or drawing. This process produces a highly oriented microstructure which gives the material its stiffness and strength [74]. The tapes are woven in a balanced 2/2 twill pattern as shown in Figure 3.2 and tensile properties are shown in Figure 3.1 and Table 3.1 above.

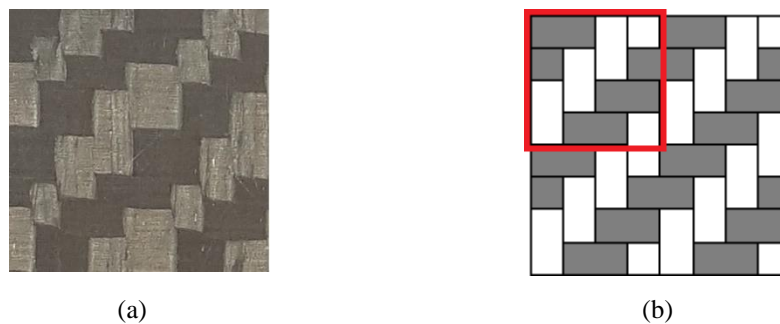


Figure 3.2 2/2 twill weave pattern on the SRPP: a) photograph, b) diagram with smallest repeating unit outlined in red.

The SRPP used in the FML is of 1.0 mm thickness. However, in an effort to fully understand the deformation and failure behaviour of SRPP, 0.3 mm and 0.6 mm-thick specimens were also studied under uniaxial tension. To establish a framework of understanding failure of the FML, an approach was taken to analyse the failure of SRPP ranging from the thinnest available specimens (0.3 mm), to thicker specimens (0.6 mm and 1.0 mm). This study was carried out due to the fact that the failure in the SRPP/steel FML is largely influenced by the failure in the composite layer. This approach helped isolate different aspects of deformation and failure behaviour of the SRPP. By considering the thickness effects, a comprehensive understanding of factors leading up to the failure of SRPP and SRPP/steel FML can be ascertained.

3.2.3 FML

SRPP/steel FML was prepared by bonding two steel sheets on either side of a 1.0 mm SRPP sheet using three layers of hot-melt adhesive films between steel and SRPP, as shown in Figure 3.3. The adhesive used (Collano 22.100 [207], 0.35 mm thickness, datasheet given in Appendix A) is a thin thermoplastic film based on modified polyolefines with the minimum bonding temperature of 140°C and a density of

0.92 g/cm³. The thickness and density of the FML and its constituents are presented in Table 3.2, and the measured tensile mechanical properties are shown in Figure 3.1 and Table 3.1 above.

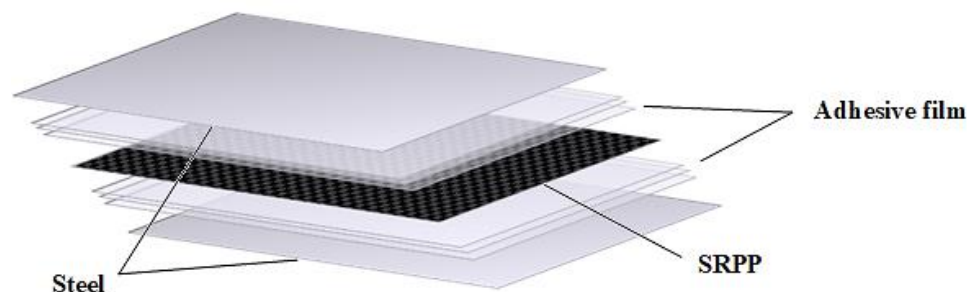


Figure 3.3 Stacking sequence of a SRPP/steel FML.

Table 3.2 Average thickness and density of SRPP/steel FML and its component materials.

	Steel	1.0 mm SRPP	SRPP/steel FML
Thickness, t (mm)	0.45	1.00	1.92 ± 0.02
Density, ρ (g/cm ³)	7.85 (see note ¹)	0.92	4.20 (see note ²)

¹ Not specified in datasheet. Values shown are typical known values for steel that were cross-checked with manufacturers.

² Average value.

3.2.3.1 Parameters for manufacturing FML

FML was prepared using the following procedure.

1. Surfaces of the steel and SRPP sheets are degreased with acetone.
2. Surfaces of the steel, SRPP and adhesive films are cleaned with isopropanol, using lint-free tissues in a dust-free environment.
3. SRPP is abraded with an 80-grit silicon carbide (SiC) sandpaper and any resulting residue from the surfaces are cleaned.
4. The steel sheets are stacked on either side of an SRPP sheet using three adhesive films at each interface, as shown in Figure 3.3, ensuring no dust gets trapped between the layers.
5. The laminate is consolidated in a preheated hot platen press at 170°C and 4–4.2 MPa for 1 minute. The pressure increases slightly due to in-plane shrinkage and a slight increase in thickness in the SRPP layer in the early stage of heating.

6. The laminate is cooled to room temperature using water cooling system circulating through the platen press, while maintaining the pressure to prevent shrinkage in the SRPP layer. The temperature profile during processing is given in Figure 3.4.
7. The final laminate is checked to ensure shrinkage in the SRPP layer has been prevented.

This manufacturing procedure was derived by varying parameters and obtaining optimal conditions as summarised in Table 3.3 in the next page.

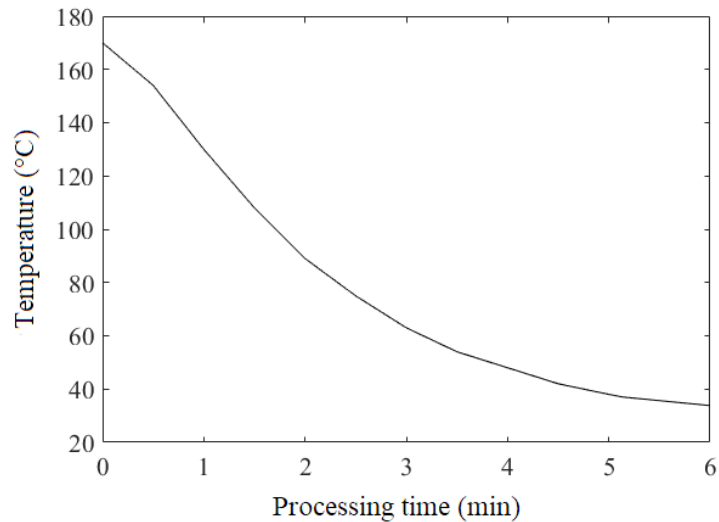


Figure 3.4 Temperature profile during the manufacture of FML.

Initial assessments were carried out to determine acceptable temperature ranges, pressures, heating and cooling methods, type of surface treatment, and adhesive film, based on three criteria:

1. There is no obvious visual damage to the material.
2. The laminates need to pass a simple peel test. The adhesive films are cut in half and used to consolidate the laminate partially. The unconsolidated end of the laminate is peeled apart by slip-joint pliers. The laminate should be able to withstand the force without peeling.
3. Able to achieve batch consistency with respect to the above two criteria.

After the initial assessments, lap shear tests were carried out to determine the optimal temperature, number of adhesive films and the grit size of the SiC used for surface abrasion. Lap shear tests were designed based on the ASTM D5868 standard [208]. The thickness, gauge length and joint type were modified to account for the additional layer and the actual thickness of the constituent parts of the FML.

Table 3.3 Parameters varied to determine optimal conditions for consolidating SRPP/steel FML.

Parameter	Variation	Optimal condition
<i>Part A – Initial assessment</i>		
Temperature (°C)	$140 \leq T \leq 190$, in increments of 10	$165 \leq T \leq 180$
Pressure (MPa)	$1 \leq p \leq 5$	$p \geq 1.2$ ¹
Heating	<p><i>Option A:</i> Insert the laminate into the platen press at room temperature, and leave it in to heat up in sync with the press. (Approximately 1.5 hours.)</p> <p><i>Option B:</i> Insert the laminate after the platen press has stabilised at the desired temperature and leave in place for 1 minute.</p>	<i>Option B</i> ^{2,3}
Cooling	<p><i>Option A:</i> Cool by natural convection.</p> <p><i>Option B:</i> Cool by water cooling system running through the plates of the press. (Approximately -40 – -15 °C/min, with a higher cooling rate occurring at higher temperatures.)</p>	<i>Option B</i> ⁴
Material surface treatment	Chemical etching, annealing (steel only), bead blasting, abrasion with steel wool or silicon carbide (SiC) sandpaper.	Abrasion with sandpaper ⁴
Type of adhesive films	Collano 23.351, 23.110, 22.010, 22.100 [207]	Collano 22.100 ⁵
<i>Part B – Parameters for the lap shear test</i>		
Temperature (°C)	$165 \leq T \leq 180$, in increments of 5	170
Number of adhesive films	1 – 3	3
Surface abrasion	<ul style="list-style-type: none"> ○ No abrasion ○ Abrasion with SiC – grit size: 80, 120, 320 	No abrasion on steel, 80-grit SiC abrasion on SRPP

¹ 1.2 MPa is the minimum pressure required to prevent shrinkage in SRPP. 4–4.2 MPa was used for the sake of prudence.

² *Option A* induced degradation in SRPP with prolonged heat exposure.

³ Too much melting of the surface occurred at higher temperatures due to fluctuations in the press temperature until stabilising at the desired temperature.

⁴ Other options were inadequate due to difficulties in achieving even surface treatment and batch consistency, material damage resulting in degradation in mechanical properties, flexural plastic deformation, and/or no improvement in adhesion.

⁵ Collano 22.010, an earlier version of Collano 22.100, is also acceptable.

During the lap shear tests, specimens with dimensions shown in Figure 3.5 were loaded in tension at 0.13 mm/minute until failure occurred. Damage typically occurred in SRPP where some parts remained attached to the steel, as shown in Figure 3.6. In Figure 3.6a, the steel layers have been peeled further and bent away from the SRPP layer to show more clearly the damage to the SRPP and the remaining attachment to the steel, whereas the layers in Figure 3.6b have been peeled apart completely. A summary of variations and optimal parameters are shown in Part B of Table 3.3. More detail on the configurations and resulting maximum load are given in Appendix B.

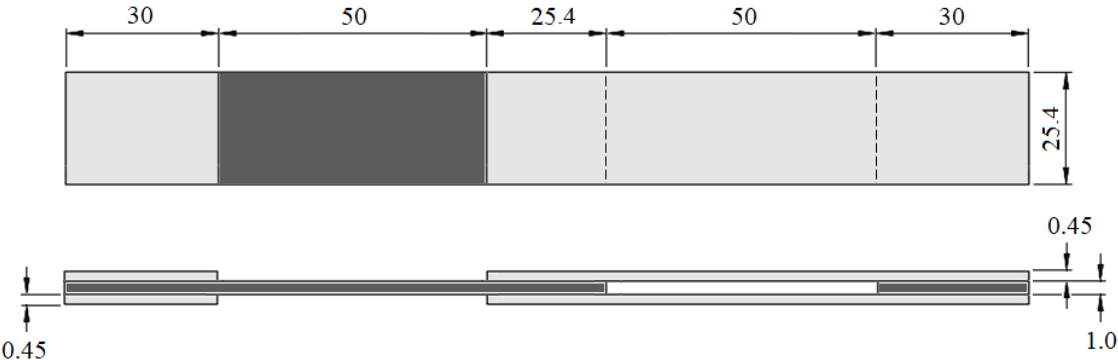


Figure 3.5 Lap shear test specimen. All dimensions are in mm, not to scale. SRPP is shown in black and steel is shown in grey.

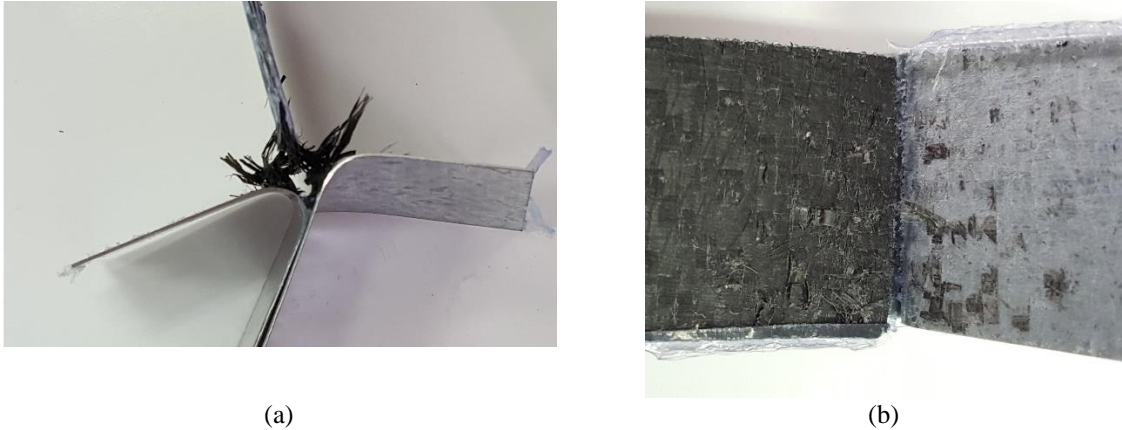


Figure 3.6 Examples of failed lap shear test specimens, with layers peeled apart and bent to show damaged surfaces.

Good adhesion is vital to the overall mechanical properties of the FML but was also found to be quite difficult to achieve for SRPP/steel FML. Three parameters that influence the quality of adhesion are discussed below:

Temperature

Some researchers found that the best adhesion of PP-based surfaces is achieved at the melting temperature of the matrix [157]. Due to the highly oriented nature of the tapes, hot compacted SRPP has two endotherms in differential scanning calorimetry (DSC) corresponding to the higher melting temperature of tapes and the lower temperature for the recrystallised matrix [67]. This means SRPP has a small window of processing temperature and time, where the lower limit is the melting temperature of the matrix which forms molecular continuity with the polymer adhesives on melting. The upper limit is determined by molecular relaxation of highly oriented fibres which accelerates exponentially around its melting temperature (close to hot compaction temperature), above which tensile properties decline [84]. Also, [21], who produced the prototype of Curv, suggested post-forming SRPP between the melting points of the matrix and the tapes, at around 170°C. As such, it was decided that, although the best adhesion in the FML occurred at 175°C, it is best practice to keep the consolidation temperature at 170°C so as to:

- 1) not approach too closely the softening temperature specified in the datasheet (175°C) in order to minimise the risk of reducing the mechanical properties of the SRPP layer, and
- 2) minimise the risk of temperature overshooting in the platen press (which never realistically stabilises to a single temperature but constantly fluctuates), especially as the shear strength of the interface declined sharply between 175°C and 180°C.

Pressure

Pressure can be a sensitive parameter in consolidating FMLs. A non-SPC composite material such as GFRPP has the danger of the matrix flowing out of the composite above a certain pressure and are typically bonded at a lower pressure (≈ 0.5 MPa). SRPP sheets required higher pressures in comparison because it exhibited substantial in-plane shrinkage ($> 50\%$) and an increase in thickness when subjected to elevated temperatures at low pressure. In-plane shrinkage appears to be due to shrinkage in the PP, which can occur at temperatures 100°C below the melting range of the PP [21], and tensile relaxation of the drawn tapes. In a study investigating bond strength between SRPP and mild steel, the authors noted that the peel strength increased by 100% when the pressure was increased from 0.02 MPa to 0.2 MPa [209]. For the SRPP used in this research, it was found that a minimum pressure of 1.2 MPa was required to avoid shrinkage. During rapid cooling, pressure can drop due to thermal contraction in the metal plates in the press if not carefully controlled. Hence, a pressure of 4–4.2 MPa was used to ensure that the applied pressure is maintained well above the required minimum throughout the consolidation process.

Surface treatment

The best surface treatment was found to be abrasion using silicon carbide (SiC) sandpaper on SRPP only. There are various means of surface treatment based on traditional FMLs as summarised by [210] but these have limited applicability when bonding thermoplastic polymer and metal surfaces which have a low bonding compatibility. There were instances where grit blasting was found to be effective on stainless steel and silane pre-treatment on galvanised steel in the adhesion of epoxy surfaces or coatings [156, 211, 212]. For the hot-dipped zinc-coated steel used in the present research, a number of methods were tested including chemical etching with hydrochloric acid, sulphuric acid, annealing, bead blasting, and abrading with steel wool, all of which were found to be inadequate due to difficulties in achieving even surface treatment and batch consistency, material damage resulting in degradation in mechanical properties, flexural plastic deformation, and/or no improvement in adhesion. As for SRPP, chemical or strong mechanical surface treatment beyond solvent degreasing and abrading with sandpaper was found to be inadequate due to it creating too much visible damage to the PP tape. From lap shear tests on specimens prepared using different grades of SiC sandpapers, it was found that the best adhesion is achieved with a combination of no abrasion on steel and light abrasion of SRPP using coarse sandpaper (80-grit, SiC).

As a final note, mechanical and laser cuttings are inadequate for SRPP and FML due to mechanical or thermal damage to the SRPP and adhesive layers. Waterjet cutting is recommended, as was used in this research. The edges of metal specimens need to be deburred using a round file.

3.3 Experimental methods

This section outlines experiments and analyses carried out in this study. Uniaxial tensile tests, induced-biaxial deformation tests, microscopic analyses, and real-time surface strain analyses have been used to study the material behaviours. The aim here is to give sufficient details to enable future replication by other researchers; the exception is the microscopic analyses, which do not require extra explanation. For microscopic examinations, optical and scanning electron microscopes were used, typically on specimens after tests have been carried out. High-resolution digital images from the DIC system and photographs were also used as visual aids.

3.3.1 Uniaxial tension tests

FML is a complicated laminate system that requires an understanding of the constituent materials as well as how they perform together as a system. Therefore, a systematic approach was taken to isolate different aspects of failure by analysing behaviour from smaller components first. Tensile failure of

SRPP was analysed using 0.3 mm, 0.6 mm and 1.0 mm specimens, covering the range from the thinnest product available to the thicker SRPP used in making the SRPP/steel FML. Knowledge gathered from this was then used to analyse the failure behaviour of the FML. For in-depth analyses, behaviours at different reinforcement orientations with respect to the loading direction ($0^\circ/90^\circ$, $30^\circ/60^\circ$, $\pm 45^\circ$) were also investigated, for all SRPP and FML specimens.

Tensile tests were conducted using the Instron 8874 Axial-Torsion Servohydraulic Fatigue Testing System [213], following the ASTM A370 standard for sheet type [206] for steel and ASTM D3039 for SRPP and FML [205]. The testing of SRPP and FML required deviation from the standard, as explained in Table 3.4. It was confirmed that the stress-strain curves did not change due to the changed dimensions and speed. Drawings of the specimens are shown in Figures 3.7–3.9. Failure in this analysis is defined as the stage at which the material is no longer able to sustain a load as indicated by a drop in the load. The percentage drop in load which triggers a halt in the test is outlined in Table 3.4 so that microscopic analyses can be carried out at the earliest stage of fracture where possible.

Table 3.4 Modified parameters for SRPP and FML tensile tests.

Parameter	Specimens	Value	Reason
Crosshead speed (mm/minute)	All	20	To deform samples at a similar strain rate to the induced-biaxial deformation tests.
Specimen width (mm)	All	20	To ensure that the entire gauge area remains within the field of view of the optical strain measurement system up to maximum extension, while maintaining the desired level of precision.
Specimen gauge length (mm)	0.3 mm SRPP $30^\circ/60^\circ$ 0.3 mm SRPP $\pm 45^\circ$	44	
	all other specimens	66	
End of test (% drop in load)	0.6 mm SRPP $30^\circ/60^\circ$ 0.6 mm SRPP $\pm 45^\circ$ 1.0 mm SRPP $30^\circ/60^\circ$	2	
	1.0 mm SRPP $\pm 45^\circ$	3	
	FML $\pm 45^\circ$	7	
	0.3 mm SRPP $30^\circ/60^\circ$ FML $30^\circ/60^\circ$	10	
	0.3 mm SRPP $0^\circ/90^\circ$ 0.3 mm SRPP $\pm 45^\circ$ 0.6 mm SRPP $0^\circ/90^\circ$ 1.0 mm SRPP $0^\circ/90^\circ$ FML $0^\circ/90^\circ$	40	

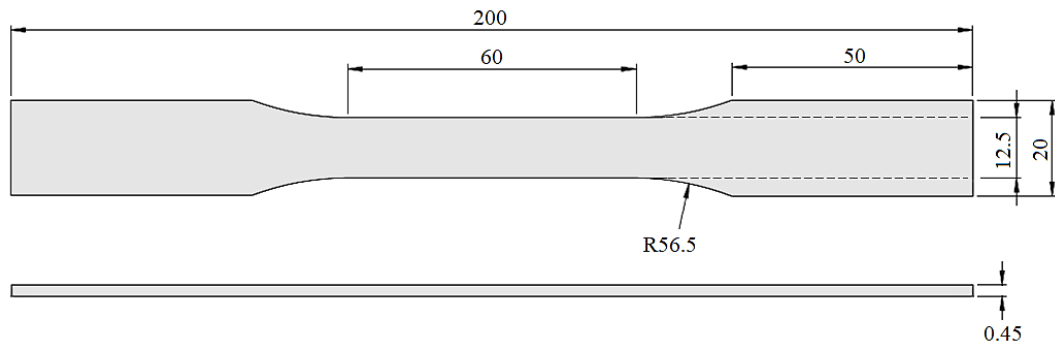


Figure 3.7 Steel tensile test specimen. All dimensions are in mm, not to scale.

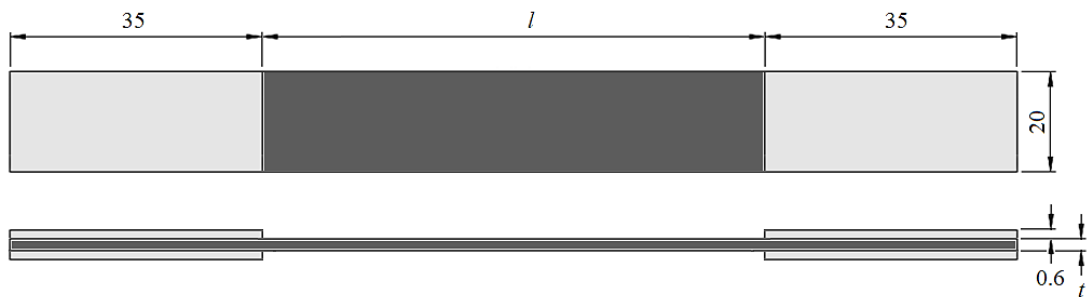


Figure 3.8 SRPP tensile test specimen with aluminium tabs. All dimensions are in mm, not to scale. Gauge length (l) is 44 mm for 0.3 mm specimens in $30^\circ/60^\circ$ and $\pm 45^\circ$ directions and 66 mm for all other samples. Thickness (t) is 0.3 mm, 0.6 mm or 1.0 mm. Direction of reinforcement in SRPP is $0^\circ/90^\circ$, $30^\circ/60^\circ$ or $\pm 45^\circ$.

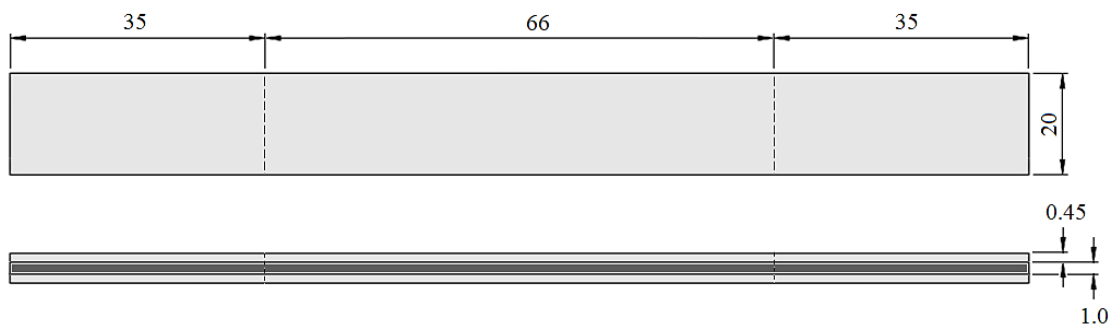


Figure 3.9 FML tensile test specimen. All dimensions are in mm, not to scale. SRPP is shown in black and steel is shown in grey. Gauge section is indicated by dotted lines. Direction of reinforcement in SRPP is $0^\circ/90^\circ$, $30^\circ/60^\circ$ or $\pm 45^\circ$.

3.3.2 Induced-biaxial deformation tests

Metal sheet forming is a manufacturing process which induces multi-directional deformations in metal sheets to form them into desired shapes. During the deformation, the state of stress and strain in 2D can be described by first and second principal stresses (σ_{p1} , σ_{p2}) and strains (ε_{p1} , ε_{p2}). These are given in Equations 3.1 and 3.2 in terms of normal stresses (σ_x , σ_y) and strains (ε_x , ε_y), and in-plane shear stress (τ_{xy}) and strain (γ_{xy}), in Cartesian coordinates.

$$\sigma_{p1, p2} = \frac{\sigma_x + \sigma_y}{2} \pm \sqrt{\left(\frac{\sigma_x - \sigma_y}{2}\right)^2 + \tau_{xy}^2}, \quad (\sigma_{p1} > \sigma_{p2}) \quad (3.1)$$

$$\varepsilon_{p1, p2} = \frac{\varepsilon_x + \varepsilon_y}{2} \pm \sqrt{\left(\frac{\varepsilon_x - \varepsilon_y}{2}\right)^2 + \left(\frac{\gamma_{xy}}{2}\right)^2}, \quad (\varepsilon_{p1} > \varepsilon_{p2}) \quad (3.2)$$

Ratios between the two principal stresses, $\alpha = \sigma_{p2} / \sigma_{p1}$, or strains, $\beta = \varepsilon_{p2} / \varepsilon_{p1}$, can be used to indicate the state of stress or deformation in a more meaningful way, with different values representing different deformation modes. This is illustrated in the strain and stress diagrams in Figure 3.10 with explanations for each mode given in Table 3.5.

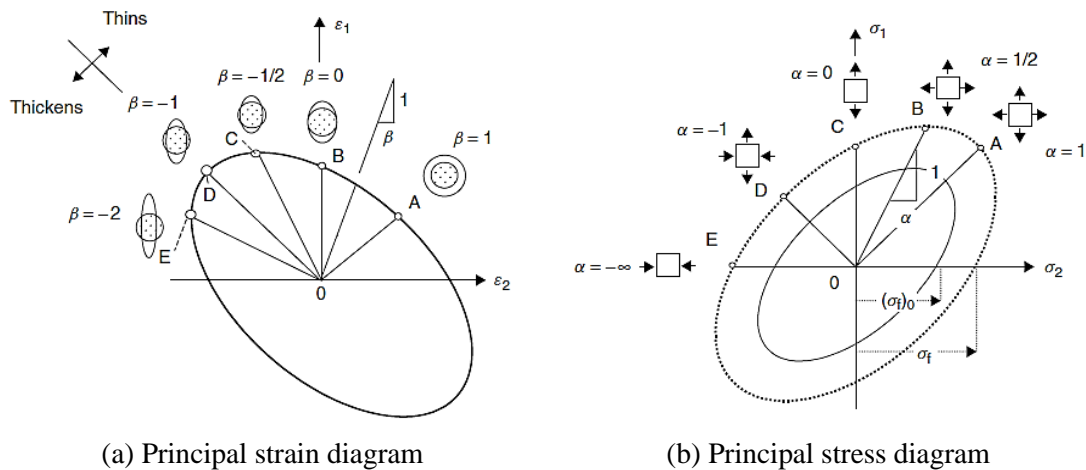


Figure 3.10 Deformation modes in sheet metal forming indicated on the a) strain diagram and b) stress diagram with contours of equal effective stress (yield loci). Principal directions are indicated by 1 and 2 in the diagrams. Yield loci for [214, pp. 33, 39].

Table 3.5 Brief explanation of deformation modes and the corresponding principal strain and stress ratios shown above in Figure 3.10.

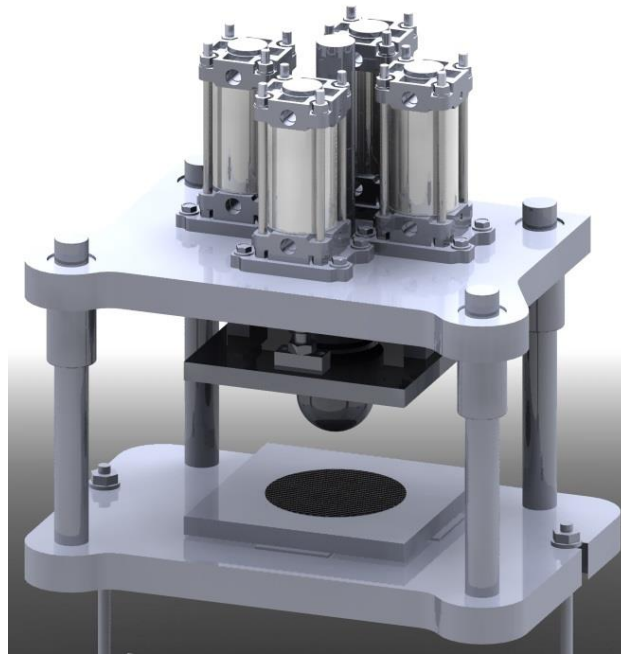
Deformation mode	Strain ratio, β	Stress ratio, α	State of metal sheet	Typically occurs in:
Equal biaxial stretching	1	1	Stresses and strains are equal in all directions.	Centre of sheet metal stretched over a hemispherical punch.
Plane strain	0	1/2	Stretches only in the first principal direction.	Side-wall of cup forming.
Uniaxial tension	-1/2	0	Stretches in the first principal direction and contracts in the second principal direction.	Free edge of an extruded hole.
Pure shear (or drawing)	-1	-1	Stresses and strains are equal and opposite. Sheet deforms without change in thickness.	Flange of a deep-drawn cup.
Uniaxial compression	-2	$-\infty$	Sheet thickens and can wrinkle.	Edge of a deep-drawn cup.

In traditional metal forming, a forming limit diagram (FLD) can be established which has a forming limit curve (FLC) on a principal strain diagram, indicating the upper limit beyond which further strains cause local necking and/or fracture. This is mostly done by experimenting with different specimen geometries to induce different deformation modes until failure⁴.

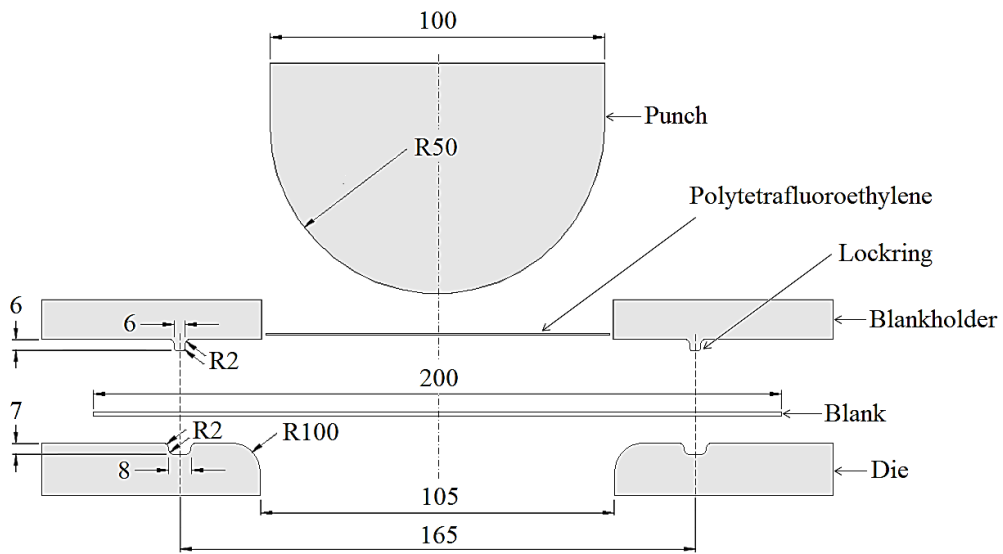
For this study, this method of using different specimen geometries in metal stamp forming to induce different deformation modes has been adapted, not for the purpose of establishing an FLD, but for the purpose of scrutinising the deformation and failure behaviours of SRPP and FML under combined in-plane biaxial deformations and out-of-plane bending. These tests will be referred to as induced-biaxial deformation (IBD) tests in this study.

IBD tests were carried out according to the ISO 12004-2 test standard [216] with some modifications. The specimen was held in a press machine against an open die using a blank holder, as illustrated in Figure 3.11, and then formed into a dome-shaped profile. Two different types of loading conditions were analysed on 1.0 mm SRPP and FML specimens using specimen geometries illustrated in Figure 3.12.

⁴ There are also methods by which an FLC can be calculated but the predicted limits deviate significantly from experimental observations [215].



(a)



(b)

Figure 3.11 Induced-biaxial deformation test setup; a) a 300 kN double-action mechanical press with hydraulic ram used in the test, and b) a cross-sectional schematic diagram. All dimensions are in mm, not to scale.

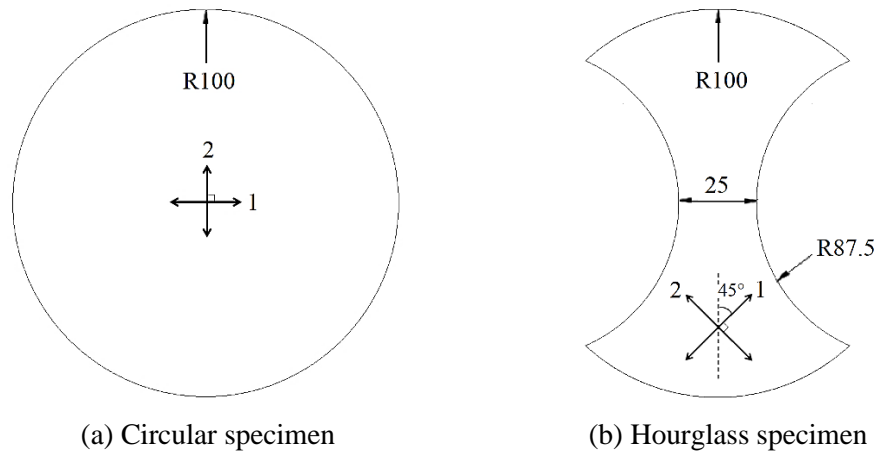


Figure 3.12 Induced-biaxial deformation test specimen geometries. Tape orientations are indicated by directions 1 and 2. All dimensions are in mm except the angle.

The first test used a circular specimen (Figure 3.12a) which was fixed around the edge by a lock-ring in the die and the blank holder. This creates an axisymmetric loading condition, which induces an equal biaxial stretching in both reinforcing directions at the centre of the specimen and varying types of deformations elsewhere. In the second type of test, an hourglass-shaped specimen similar to the Type I specimen in [217] was fixed at the two convex edges by the lock-ring, with the reinforcements oriented at $45^\circ/-45^\circ$ to the plane of symmetry (Figure 3.12b). This produces varying combinations of in-plane biaxial and shear deformations about the reinforcements in the specimen, including at the centre.

The punch velocity was modified from 1.5 mm/s to 10 mm/s because this was the minimum speed at which the press could maintain the stability in the applied load. This was not a concern since the measurements were taken at 15 Hz using the digital image correlation (DIC) system, allowing the state of the specimen to be captured and analysed over ample number of increments. Specimens were tested until failure as indicated by a sudden drop from the maximum load. For lubrication, two sheets of polytetrafluoroethylene (Teflon) were placed between the punch and the specimen.

3.3.3 Real-time surface strain analyses

To capture and analyse deformation characteristics leading up to a catastrophic failure of the material, a state-of-the-art DIC system called ARAMIS 5M [218], shown in Figure 3.13, was used. This system tracks real-time strains on specimen surfaces as they deform, using digital cameras that take high-resolution images at high speed. Based on a stochastic pattern that is inlaid on the surface during specimen preparation, it creates and tracks virtual gauge areas composed of an assigned number of pixels called facets (shown in Figure 3.14) and computes full-field strains by DIC. In this research, the resolution in the field of view was 2448×2050 pixels and the rates were set at 5–15 frames per second, using ARAMIS 5M.



Figure 3.13 ARAMIS, a commercial digital image correlation system provided by GOM GmbH [218].

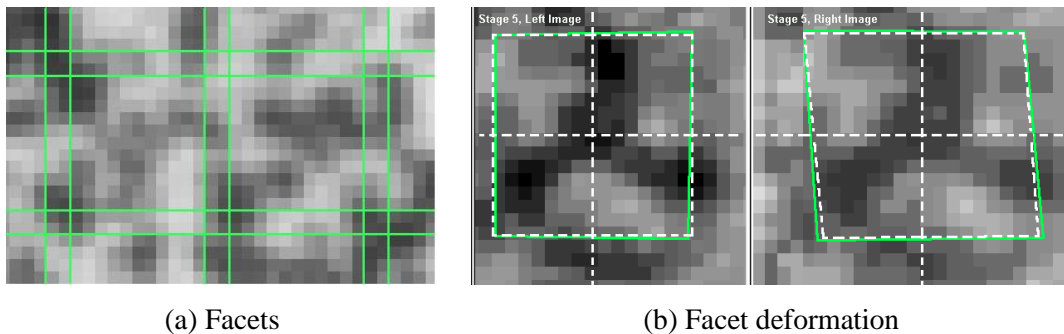


Figure 3.14 Example of facets in ARAMIS – a) 15×15 pixel facets with a facet step of 13 pixels [219, Ch. D, p. 3], b) facets shown on images captured by left and right cameras at a deformed state (green solid lines), with undeformed state shown as reference (white dashed lines) [219, Ch. A, p. 6].

It should be noted that the facet sizes and steps that were set in the DIC in the experiments in this study are to compute local strains over unit areas that are as small as possible without compromising accuracy. At such precision, any damage on the surface of SRPP can easily result in strains not being computable for the facet containing the damage, at the required accuracy. This can also compromise the accuracy of strains at points bordering such a facet, even if the DIC system has deemed it is accurate enough. This is not due to any error in the system, but rather to a combination of the facet size, fineness of the stochastic pattern, size of damage, and the fact that some types of damage can be confused with stochastic dots since both show up black in the black and white digital images.

As such, care must be taken to decide the validity of points around any damage on a case by case basis. This must be considered when reproducing the analyses and comparing to the results presented in this study, as it requires careful judgement on the analyst's part. The same applies to the use of interpolation around damaged areas in the SRPP, which is mostly best avoided at the level of precisions used in this study.

3.3.3.1 DIC system setup for tensile tests

In order to determine strains at the smallest scale possible with a high level of accuracy, a camera with a focal length of 50 mm was used, measuring areas of $80 \times 65 \text{ mm}^2$ or $100 \times 85 \text{ mm}^2$ (horizontal \times vertical) and a fine stochastic pattern created by spray-painting, such as one shown in Figure 3.15. This gives a pixel size of $32.7 \times 31.7 \text{ }\mu\text{m}^2$ – $40.9 \times 41.5 \text{ }\mu\text{m}^2$. The DIC system was calibrated to a deviation of 0.031 pixels, giving a maximum potential error in raw spatial coordinate values of $1.0 \text{ }\mu\text{m}$ and $1.3 \text{ }\mu\text{m}$ in horizontal and vertical directions, respectively.

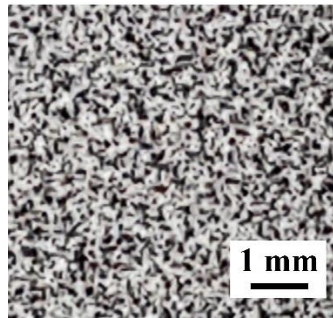


Figure 3.15 Stochastic pattern spray-painted on specimens for uniaxial tensile tests.

Optimal values of facet size and facet step⁵ were determined based on guidelines from the ARAMIS manual and existing studies on using DIC systems [219–223] and by experimenting with different values. Rectangular facet sizes and steps were varied between 5 to 15 pixels, and 4 to 13 pixels, respectively, and the resulting optimal parameters were determined per sample, as shown in Table 3.6 in the next page. The table also shows the measuring volumes used for each specimen type. Typically, larger measuring volumes, facet steps and facet sizes were required for specimens with high failure strains in order to keep the specimen in view. These parameters gave optimal results that capture small-scale strains without invalidating too many facets, which occurs when ARAMIS’s default accuracy limit of 0.04 pixels per facet is exceeded.

The mentioned accuracy limit of 0.04 pixels per facet refers to the stability of the centre of each facet between each captured deformation stage. Facets exceeding the set accuracy level are not presented in results by default and appear blanked out in surface strain images. This can occur at damage points that are larger than the stochastic dots or when there is a sudden large movement of facets, such as at specimen failure. It has been reported that, in practice, accuracy for in-plane displacement is likely to be several orders of magnitude better than the default value based on 3D measurements, approaching

⁵ Facet step is the distance from the left edge of one facet to that of the adjacent facet, and therefore determines the overlap of facets (overlap = facet size – facet step, in pixels). It is set based on the required spatial density of points, i.e. the distance between points in the point cloud.

Table 3.6 DIC system measuring volume, facet size and facet step for uniaxial tensile tests.

Specimens	Measuring area [mm ²]	Facet size	Facet step
0.3 mm SRPP 0°/90° 1.0 mm SRPP 0°/90° FML 0°/90°	80 x 65	12	8
0.6 mm SRPP 0°/90° 1.0 mm SRPP 0°/90° 1.0 mm SRPP ± 45° FML 30°/60°	100 x 85	12	8
0.3 mm SRPP 30°/60° 0.6 mm SRPP 30°/60° 1.0 mm SRPP 30°/60° 0.3 mm SRPP ± 45° 0.6 mm SRPP ± 45° FML ± 45°	100 x 85	13	9

0.001 pixels [223]. The DIC system was also used to cross-check the accuracy of the longitudinal strain values given by Instron and the accompanying software (Bluehill Universal Software). Two systems agreed to within 0.05% strains.

3.3.3.2 DIC system setup for induced-biaxial deformation tests

To study surface strains for IBD tests which have out-of-plane bending components, the 3D DIC system was set up beneath the press machine as shown in Figure 3.16. Two digital cameras, with focal lengths of 17 mm were placed 112 mm apart at the base⁶ and angled at 25° to each other to measure surface strains within a measuring volume of 150 × 130 × 80 mm² (horizontal × vertical × depth of field)⁷. Example digital images, strain grids and computed surface strains for a circular SRPP specimen are shown in Figure 3.17 in pages 58–59.

⁶ Slider distance in [219].

⁷ The depth of field (80 mm) is an approximate value.

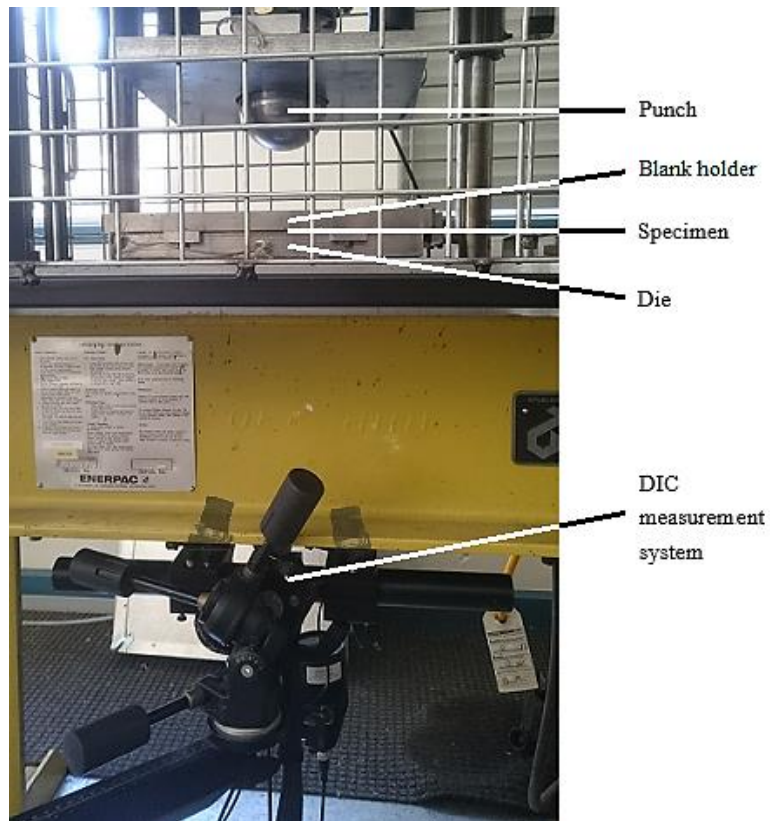
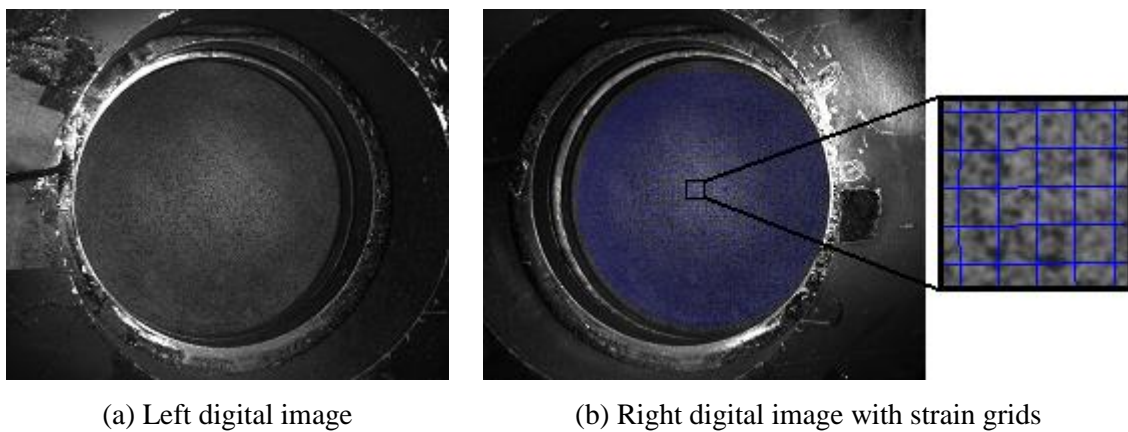


Figure 3.16 3D DIC system setup for induced-biaxial deformation tests. The digital cameras are behind the support structure of the press machine.



(a) Left digital image

(b) Right digital image with strain grids

Figure 3.17 Examples of DIC images for a deformed circular SRPP specimen, showing a) a digital image from the left camera, b) strain grids superimposed on a digital image from the right camera, and c) computed surface strains.

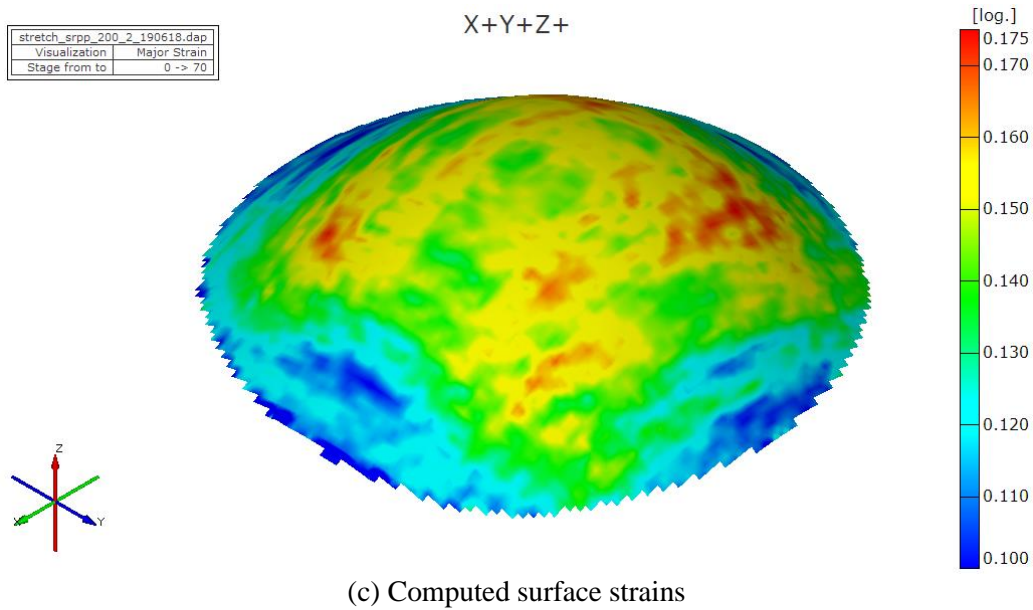


Figure 3.17 Examples of DIC images for a deformed circular SRPP specimen, showing a) a digital image from the left camera, b) strain grids superimposed on a digital image from the right camera, and c) computed surface strains.

The above setup gives a pixel size of $61.3 \times 63.4 \mu\text{m}^2$ with a $2.5 \mu\text{m}$ maximum potential error in raw spatial coordinate value under a calibration deviation of 0.04 pixels. Quadrangle facets were used with size and step of 19 and 15 pixels respectively, except for the SRPP hourglass specimens which required a smaller facet step of 13 pixels due to the extensive damage along the specimen edges. An example of the stochastic pattern spray-painted onto specimens is shown in Figure 3.18.

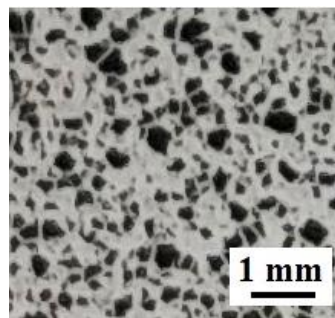


Figure 3.18 Stochastic pattern spray-painted on specimens for induced-biaxial deformation tests.

3.4 Summary

This chapter outlines the materials and methods used for investigating the deformation and failure behaviour of SRPP and SRPP/steel FML. Information on the materials include the material specifications for steel and SRPP, as well as the manufacturing process for the FML, so that the results

in this research can be reproduced using identical experimental procedures and analyses setups to those described herein, if required.

The methods outlined in this chapter will also help understand the results and discussions in the next three chapters, which are organised according to the test type. The first of the three results and discussion chapters will explain material behaviour using the tensile test results when the SRPP reinforcements are aligned to the loading direction. The second chapter will discuss results of the tensile tests when the reinforcements are aligned at off-axis angles to the loading direction. The last chapter on results and discussions will contain analyses on induced-biaxial deformation test results.

4 Failure Behaviour Under Uniaxial Tension (On-axis)

4.1 Introduction

In order to understand the failure mechanisms and related deformation behaviour of SRPP and SRPP/steel FML, uniaxial tensile tests were carried out, specifically in the direction of the reinforcement as these can provide information about the fundamental material behaviour without complicated load cases. As such, this is often the first type of test carried out when characterising a material. This chapter will elucidate the multiple damages and related mechanisms that occur in the materials and how they relate to material failure, many aspects of which have not been fully explained in the literature.

This chapter is divided into two main sections; the first on the behaviour of SRPP (Section 4.2) and the second on the FML (Section 4.3). The former is more detailed than the latter, partly because there is relatively less information about the behaviour of SRPP, and partly because the failure of the FML is largely dependent on the failure behaviour of its SRPP layer. Establishing how failure occurs in SRPP allows the SRPP-based FML system to be analysed with more ease.

With regard to the figures and the nomenclature, the following points should be noted:

- ‘ x° -tape’ denotes a tape that is at an angle of x° to the direction of applied load. For example, 0° -tape is a tape that is parallel to the loading direction and 90° -tape is a tape that is transverse to the load.
- The applied load is horizontal in micrographs, and vertical in photographs and DIC images, unless specified otherwise. Micrographs show surface sections unless specified otherwise.
- Strains are given as percentages, except for shear strain (γ_{xy}) which is given in degrees and the strains in DIC images which are given in non-percentage forms (mm/mm). All strains are given in logarithmic (true) strains and the notation ‘[log.]’ above the scale in DIC images simply denotes this.

4.2 Deformation and failure behaviour of self-reinforced polypropylene

In order to fully comprehend the behaviour of SRPP, three samples with different thicknesses were tested. It was found that 0.3 mm-thick specimens behave very differently to specimens that are 0.6 mm or 1.0 mm thick; this finding alone can provide valuable information about the failure mechanisms in

SRPP because it helps distinguish mechanisms that cause certain behaviours. For instance, it was found that the 0.3 mm specimens do not exhibit certain damage mechanisms that appear in thicker specimens, which allowed the critical damage that leads to failure to be identified for the first time using strain analysis. The difference in behaviour depending on the specimen thickness also allowed the toughening mechanisms in the thicker SRPP specimens to be identified, including crack arresting mechanisms which have not previously been identified in the literature for this type of material.

This section discusses the deformation and failure behaviour of SRPP in three subsections. The first subsection (Section 4.2.1) gives a brief overview of the stress-strain behaviour and failure behaviour at a macroscopic scale. This is a necessary first step that provides the context for understanding the damage mechanisms at a microscopic scale, which is discussed in the second subsection (Section 4.2.2).

The microscopic damage mechanisms discussed in the second subsection are less critical to the failure of the material. While less damaging, it is still important to analyse these to fully understand the material behaviour, as is identifying them as less critical to the failure of the material. It will also be shown that the microstructure of SRPP has a strong influence on the ways in which cracks are formed and propagated. This is an important aspect of the material behaviour, discussed in as it significantly affects the failure behaviour of SRPP specimens. This will be shown in Section 4.2.3, which discusses the most important aspects of the damage and toughening mechanisms that are related to the catastrophic failure of the material.

4.2.1 Stress-strain and macroscopic failure behaviour

This subsection will introduce the fact that there is a significant difference in the mechanical properties between the thin specimens (0.3 mm) and the thicker specimens (0.6 mm and 1.0 mm). This is an important aspect of the material behaviour because this thickness effect carries over to the damage characteristics and the specimen failure behaviour, which will be analysed in the subsequent sections.

The thickness effect is most pronounced in the stiffness and strength of different SRPP samples, as shown in Figure 4.1 and Table 4.1. The stiffness and strength increase with thickness in general but the 0.3 mm sample has much lower values than the 0.6 mm and 1.0 mm samples. The 0.6 mm and 1.0 mm samples exhibit strengths that are almost 5 and 6 times higher than that of the 0.3 mm sample, and tangential stiffnesses that are 63 and 70 times higher, respectively.

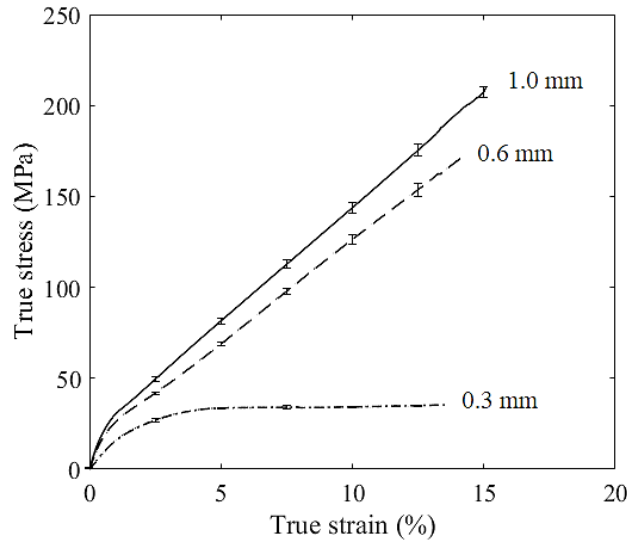


Figure 4.1 Tensile stress-strain curves of 0.3 mm, 0.6 mm and 1.0 mm SRPP samples. Failure strains portrayed are sample averages. Stress values are based on the averages of specimens that have not failed at given strains, and error bars indicate sample standard deviations.

Table 4.1 Summary of mechanical properties of 0.3 mm, 0.6 mm and 1.0 mm SRPP tensile test samples. Tensile failure strain (ϵ_t), strength (σ_t), chord modulus of elasticity (E^{chord} , stiffness between 0.1–0.3% strain), tangential stiffness ($E^{tangential}$, stiffness above 1% strain), transition strain ($\epsilon^{transition}$), and stress at transition strain ($\sigma^{transition}$) are given.

t (mm)	ϵ_t (%) ¹	σ_t (MPa) ²	E^{chord} (GPa) ³	$E^{tangential}$ (GPa) ³	$\epsilon^{transition}$ (%) ^{3,4}	$\sigma^{transition}$ (MPa) ^{3,4}
0.3	14 ± 5	35.4 ± 0.3	1.82	0.0180	1.86	23.3
0.6	14 ± 2	171 ± 4	3.79	1.13	0.492	16.9
1.0	15 ± 1	210 ± 3	4.32	1.26	0.569	15.6

¹ Failure strains given indicate sample means and standard deviations.

² Strengths are sample means and standard deviations at given average failure strain, calculated based on specimens that have not failed.

³ E^{chord} , $E^{tangential}$, $\epsilon^{transition}$, $\sigma^{transition}$ have been calculated according to the ASTM standard [205, Eq. 9], based on sample average stress-strain curves.

⁴ Transition point is where the stiffness changes in polymeric matrix composites, similar to yield point.

There is a small difference in the failure strain between samples. However, it is important to note that failure strains of the 0.3 mm specimens vary significantly from the sample average, unlike thicker samples. Failure strains in 0.3 mm specimens ranged from 8.05 – 19.5% and the sample had a standard deviation of 5% strain from the average. This equates to 36% in relative (percentage) standard deviation, which is larger than the relative standard deviations in the 0.6 mm sample (14%) and the 1.0 mm sample (7%) by more than 2 and 5 times, respectively. This large variation makes it especially difficult to predict when specimen failure will occur in a 0.3 mm specimen.

The types of damage that occurs at failure are also different in the 0.3 mm specimens compared to the 0.6 mm and 1.0 mm specimens, as shown in Figure 4.2. The 0.3 mm specimens fail without any fibrillation, delamination, tape or fibril pull-outs, whereas these are all present in the thicker specimens. The overall amount of damage also increases with the specimen thickness, with the largest difference observed between the 0.3 mm and 0.6 mm specimens. It should be noted that this is a similar trend to the variation in most mechanical properties depending on the thickness (e.g. strength). From this, it can be deduced that there is an association between the mechanical properties and the amount of damage that accumulates in SRPP specimens. Such a trend verifies the argument in the literature that more fibrillation and delamination in SRPP specimens is associated with the higher energy absorption of those specimens (i.e. compared to other specimens made with different manufacturing parameters).

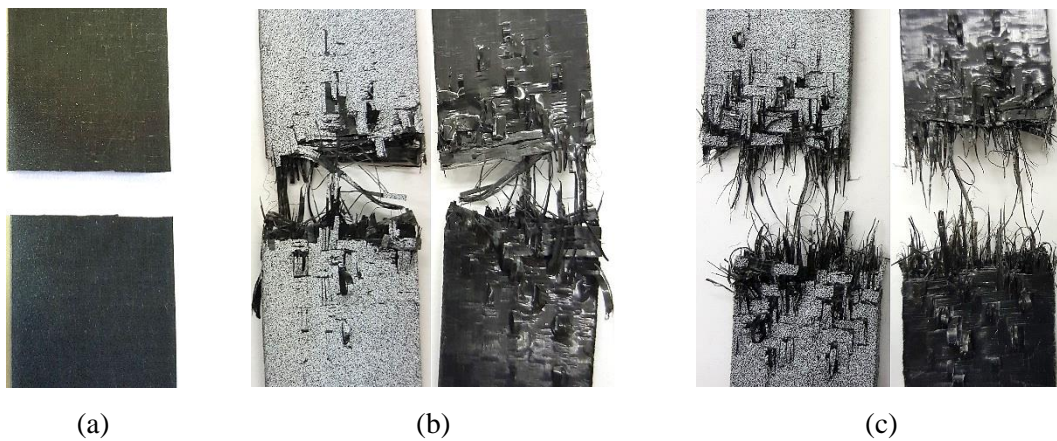


Figure 4.2 Typical specimen failure in a) 0.3 mm, b) 0.6 mm and c) 1.0 mm SRPP tensile samples. Spray painted sides are also shown for (b) and (c) for clarity.

The stress-strain and failure behaviour observed in the 1.0 mm specimens closely matched the behaviour of SRPP reported in the literature. In contrast, few studies on SRPP report behaviours similar to those seen in the 0.3 mm specimens. It can therefore be inferred that the difference in behaviour between specimens of different thicknesses has not been extensively studied in the literature, especially in the context of failure behaviour.

Nevertheless, a review of the literature suggests the following possible explanations for the different behaviour of 0.3 mm specimens:

- 1) Change in the relative amount of reinforcement in different directions with a change in specimen thickness. For example, in a study of a $0^\circ/90^\circ/0^\circ$ graphite/epoxy laminate in [224], there was a change in the failure strength with a change in the 90° -ply thickness.
- 2) Change in the reinforcement/matrix volume fraction due to processing conditions.

- 3) Relaxation of the reinforcement phase due to processing conditions being different or difficult to control in particularly thin sheets.
- 4) Change in ply thickness altering ply constraint on free surface ply and mid-ply, thereby changing the damage development [225].

The second and third explanations are the most likely considering the lower stiffness of 0.3 mm SRPP compared to thicker samples. The second case is likely because a similar reduction in post-yield stiffness has been observed in a hot compacted SRPP when compacted at a high temperature (191°C) [41]. Another study of hot compacted SRPP also found a significant decrease in strength at processing temperatures between 191°C and 194°C [71], although not as dramatically as observed in [41], or in the 0.3 mm specimens compared to the thicker specimens. In these studies, the authors conjectured that the mechanical properties decreased, and the interlayer bonding improved, due to more melting and molecular relaxation of the tape structure. It was also observed in [41] that the sample failed in a brittle fracture, which draws similarity to the failure behavior observed for 0.3 mm SRPP, as can be seen in Figure 4.2a above.

A similar case found in the literature is that of a film-stacked SRPP sample consolidated at 190°C which showed markedly different behaviour compared to other samples consolidated at lower temperatures [97]. In the sample consolidated at 190°C, the tapes have almost completely melted, resulting in a loss of the reinforcing effect. Furthermore, the sample did not exhibit fibrillation which the authors related to better fibre-matrix bonding. Due to this, a ‘fully bridged situation [226]’, which occurred in other samples, did not occur, and resulted in a significantly lower fracture toughness. It will be shown later that such ‘bridging’ phenomenon occurred only in the thicker specimens in the present study, showing the similarity of the 0.3 mm specimens of the present study to the significantly melted specimens in [97].

However, in the present study, microscopic analysis indicated that the tapes in the 0.3 mm specimens have not melted as substantially as described by [97] in their sample that was consolidated at 190°C. Also, even if a substantial part of tape has melted in the 0.3 mm SRPP, the fractional content of the reinforcement phase must still be higher than in the sample in [97]. The hot compacted SRPP used in this research ideally has reinforcement content of 70% vol. by design, whereas the sample in [97] had 50% wt. reinforcement which then further decreased through processing at 190°C.

Based on the above reflections, it is likely that the cause of the low tangential stiffness and strength of the 0.3 mm specimens are mostly due to the decrease in the molecular alignment in the tapes. This would be due to the manufacturing process being more difficult to control for thin specimens. It is also likely true that the tapes in the 0.3 mm specimens have melted more than in 0.6 mm or 1.0 mm specimens, although not substantially, and that this gave the 0.3 mm specimens better reinforcement–matrix bonding than was the case with the thicker specimens. This is supported by the fact that delamination

occurred in the thicker specimens but not in 0.3 mm specimens, and that other studies on SRPP have shown a reduction in delamination with an increase in the matrix volume fraction [70, 97].

It was mentioned earlier that there is an association between the amount of damage and the tensile limits of the SRPP samples of different thicknesses. In fact, it was found from microscopic analysis that not only the amount and size of the damage increase with specimen thickness, there are additional types of damages that occur in the 0.6 mm and 1.0 mm specimens but not in the 0.3 mm specimens. This will be elaborated upon in the next section.

4.2.2 Microscopic analysis of damage mechanisms

In a 2-phase FRP, failure typically initiates from micro-debonding at the fibre-matrix interface. The damage then leads to debonding at a larger scale, as well as fibre pull-outs, or to matrix crack and intralaminar delamination. In contrast, composites like SRPP exhibit many and significant damage instances co-occurring throughout the specimen well before failure, with no obvious division of damage mechanisms into separate phases. This can make it difficult to identify which damage mechanisms are related to the critical failure of the specimen.

Meanwhile, existing studies on SRPP and similar composite materials have mainly focused on the manufacturing process and the related impact on the overall mechanical properties. These are undoubtedly important as the manufacturing process can influence the material properties significantly and is the first step towards application. However, there has not been a comprehensive study of the different damage mechanisms that can occur in the consolidated SRPP, an understanding of which is necessary for manufacturing and applications after consolidation. It is therefore the aim of this section to give analyses of all observed damages in SRPP when subjected to tensile loading along one of the tape directions. Damage-related mechanisms that are closely linked to the failure behaviour will then be discussed in subsequent sections.

This section is divided into two parts; the first discusses damage mechanisms that occur in all specimens regardless of thickness, and the second discusses those that only occur in the 0.6 mm and 1.0 mm specimens. It should be mentioned that the different behaviours observed in different thicknesses offers certain advantages for the analysis of the material behaviour. For example, the fact that there is less damage in the 0.3mm specimens, and that there are fewer kinds of damage, facilitates identification of the more critical type of damage in the SRPP. This would have been difficult to identify by just looking at the thicker specimens. In addition, the deformation and failure behaviour of SRPP can be better explained by demonstrating the differences in damage characteristics, and how they impact the failure behaviour in different ways, depending on the thickness. Discussions related to the catastrophic failure of specimens appear in Section 4.2.3. This section will first explain the different types of damage present in SRPP specimens.

4.2.2.1 Damages common to SRPP specimens of all thicknesses

Microscopic examinations show that the following types of microscopic damage occur in all SRPP specimens regardless of the sample thickness. In general, the size and the amount of damage increase with specimen thickness. These damage types have been categorised by the nature and location of occurrences, with examples given in Figure 4.3 (except for fibril pull-outs):

- Tape-splits.
- Aligned crazing – craze-like cracks in the outer matrix.
- Crazing on the surface of the inner matrix, exposed by other damage.
- Fibril pull-outs
- Boundary cracks – cracks along the in-plane boundaries between two tapes.

The first four types of damage will be discussed next; however, since boundary cracks are very closely related to specimen failure, these are discussed later in Section 4.2.3.1.

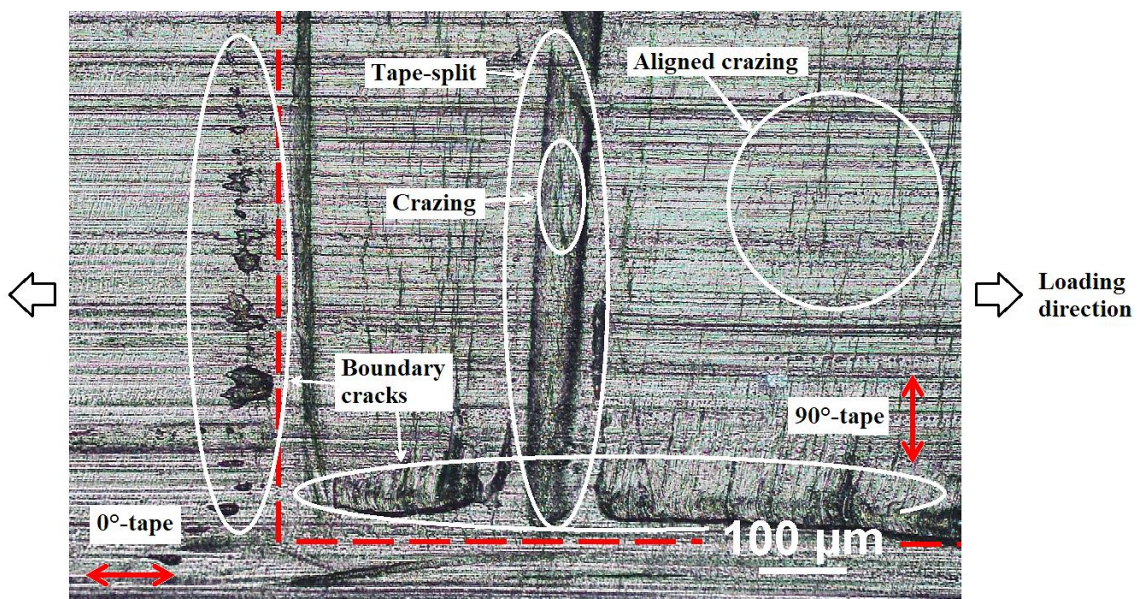


Figure 4.3 Optical micrograph showing different types of damage in a 0.3 mm SRPP tensile specimen. Dotted lines divide regions where surface tapes are at 0° and 90° to the applied load.

4.2.2.1.1 Tape-splits

Tape-splits are intra-tape cracks that split parts of the tape into smaller sections, as shown in Figure 4.4. These are very long and can sometimes be seen without a microscope, but typically they do not extend the entire length of the flat portion between the crimps in the weave.

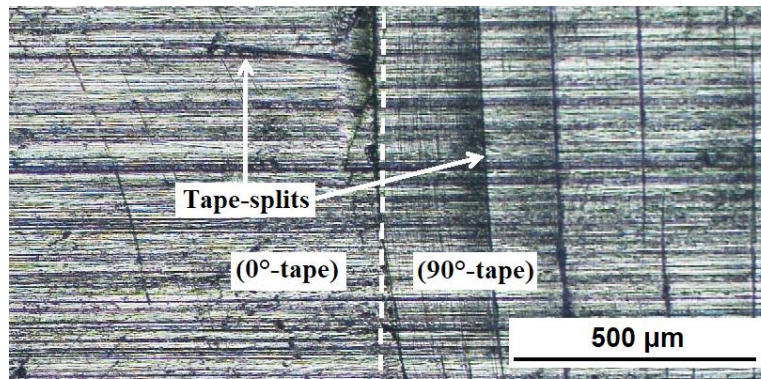


Figure 4.4 Optical micrograph of tape-splits in a 0°-tape and a 90°-tape on the surface of a 0.6 mm SRPP tensile specimen.

Cracks in SRPP tapes tend to propagate in the direction of the tape orientation because of the high degree of alignment of polymer chains in the tape. It takes less energy to break the Van der Waals forces between the molecular chains than to break the covalent bonds within the chains. As such, cracks propagate more easily between the chains, in the direction parallel to the tape orientation. Indeed, it is reported in the literature that tapes have weaker transverse strength than longitudinal strength [17].

In general, tape-splits occur more frequently in 90°-tapes than in 0°-tapes. This is because the 90°-tapes are loaded in the transverse direction to the tape orientation, which is weaker, whereas 0°-tapes are loaded along the tape orientation, which is stronger. Due to this behaviour, the density of tape-splits can be used to identify which are the 0°-tapes and which are the 90°-tapes under the microscope. An exception to this is that, after specimen failure, more tape-splits and fibrillation occur in 0°-tapes than in 90°-tapes near the site of the failure in 0.6 mm and 1.0 mm specimens.

The length and number of tape-splits in a specimen increase with the specimen thickness. In a 0.3 mm specimen, tape-splits are relatively infrequent compared to other types of damage. In comparison, tape-splits in 0.6 mm and 1.0 mm specimens are so frequent that these are most noticeable out of all types of damage during microscopic examinations.

4.2.2.1.2 Aligned crazes on the outer matrix

Aligned crazes are microscopic cracks in the surface matrix that occur over the entire gauge section of SRPP specimens. An example was shown above in Figure 4.3. At a low magnification, aligned crazes appear as fine lines on the surface that are transverse to the loading direction. This type of damage occurs more extensively in the thicker specimens than in the 0.3 mm specimens. It also occurs mostly on top of 90°-tapes, with only very few cracks occurring on top of 0°-tapes. This is similar to Jordan et al.'s [68] observation that a woven SRPP cracked predominantly in 90°-tapes under the tension generated during the peel test.

Aligned crazing is similar to typical crazing, which precedes fractures in brittle amorphous and some semi-crystalline polymers that are subjected to tensile loading. Cracks in typical crazing propagate transversely to the loading direction, as explained in the literature review. However, the aligned crazing observed in the surface matrix of the SRPP specimens propagate in the direction of the reinforcement beneath, regardless of the loading direction. On top of 0°-tapes, the microscopic cracks propagate in the direction of the applied load because the orientation of the tape underneath is parallel to the load.

Arguably, only the surface cracks on top of 90°-tapes are a type of crazing, since crazes by traditional definition form and propagate perpendicularly to the positive normal stress. However, as the cracks observed in the surface matrix do resemble typical crazing, this will be referred to from here on in as ‘aligned crazing’. The word ‘aligned’ is used to refer to two key differences when compared to typical crazing. The first difference is that the crazes are aligned to the direction of the tape underneath the surface matrix, as explained, and the second difference is that the aligned crazes have a *higher degree* of alignment, such that the cracks appear almost linear at high magnification. This is shown in Figure 4.5⁸ below. It should be noted that crazing has been reported in thermoplastic FRPs, for instance in a study of GFRPP [49], but there is no mention of the high alignment of crazes observed in this study. It will be seen that the aligned crazing observed here occurs due to the use of a large tape type of reinforcement that has a tendency to split along its orientation, which is rather unique among composites.

The micrograph in Figure 4.5 shows that the cracks form and propagate from microvoids forming collinearly and then coalescing into cracks. As can be seen from the image, the degree of alignment of the microvoids to a linear orientation is very high. Due to this, cracks in the aligned crazing appear straighter than those seen in typical crazing in amorphous PP, which is shown in Figure 2.12 and is reproduced in the next page.

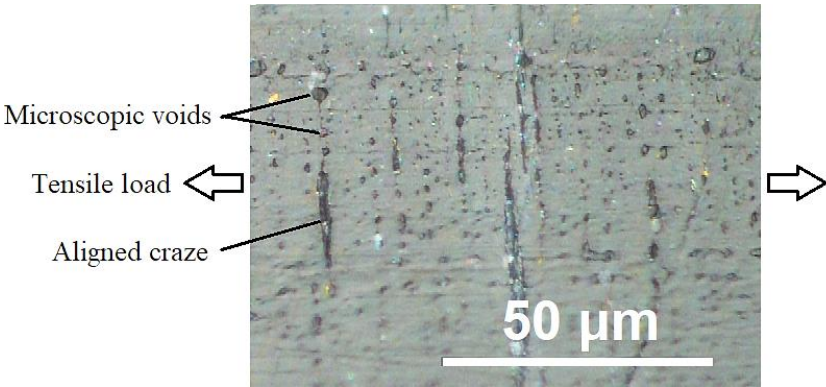


Figure 4.5 Optical micrograph of aligned crazes forming on the surface of a 0.3 mm SRPP tensile specimen.

⁸ White reflections in the image are stress whitening, as explained in the literature review.

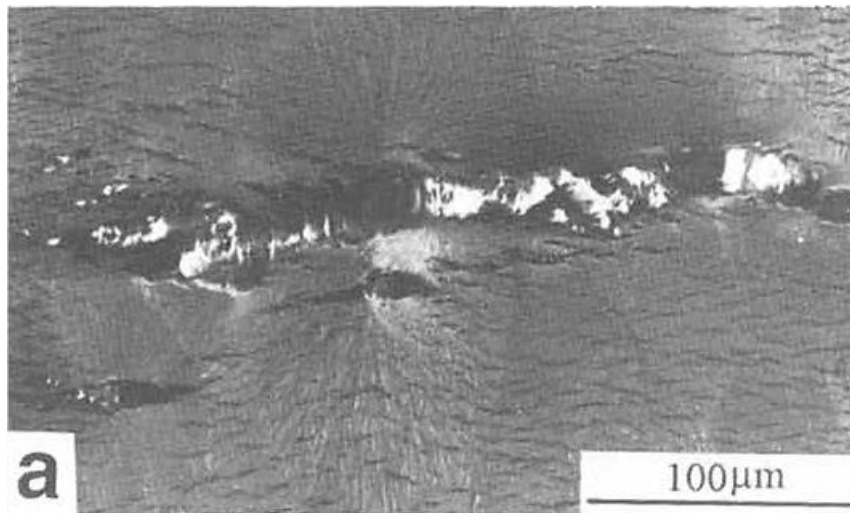


Figure 2.12 Crazing observed in polypropylene during a tensile test [133]. The applied load is vertical in this image.

The aligned crazes appear more linear than typical crazes because they are a manifestation of tape-splits beneath the surface matrix. As described previously, tape-splits are cracks that propagate between the molecular chains of the tape, which are highly aligned from the drawing process. The fact that the cracks between the chains in the tapes have propagated to the surface leads to the crazes in the surface matrix appearing aligned to such a high degree, in the direction of the underlying tape. An example that demonstrates this is shown in Figure 4.6.

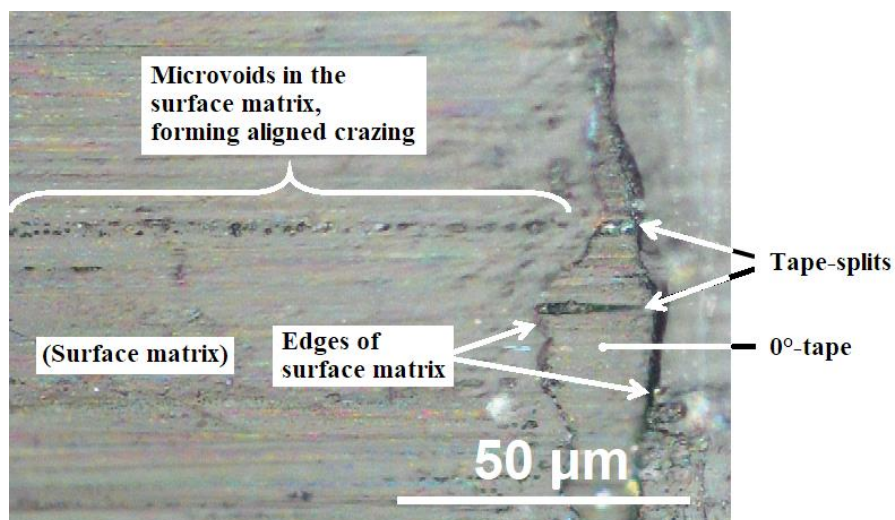


Figure 4.6 Optical micrograph of aligned crazes forming on the surface of a 0.6 mm SRPP tensile specimen.

The micrograph in Figure 4.6 shows a 0°-tape weaving underneath a 90°-tape, where the damage along the boundary has partially exposed the 0°-tape under the matrix. In the exposed part of the tape, there are two tape-splits. The top tape-split is aligned with microscopic voids in the surface matrix which are about to coalesce into an aligned craze. This shows the association between tape-splits and aligned crazing. The bottom tape-split has no associated damage in the attached surface matrix, showing the state at which, the tape-split has not yet propagated into the surface matrix. From this, it is likely that tape-splits induce aligned crazing.

There is another possibility that may contribute to the high alignment of aligned crazing to the tape orientation, namely that the matrix has orientations similar to the tape underneath and this manifests in the matrix damage. However, this would be possible only if the surface matrix is thin enough that the short-range order from the shish-kebab lamellar microstructure remains at the surface. As daughter kebab lamellae appear at around 300 nm away from the surface of the tape (see Figure 2.11), cracks on the surface are then likely to be propagating through stretched amorphous regions between neighbouring daughter kebab lamellae and between neighbouring parent kebab lamellae, and possibly through the crystalline parent kebab lamellae along c-axes⁹.

However, although it is possible for the matrix to have a considerable degree of internal order, this is at the sub-micro domain [109]. Optical micrographs on a cross-section of a 0.3 mm SRPP specimen shows there are two layers of weavings (four tapes through the thickness). Assuming that the tape volume fraction is 70%, a simple calculation gives approximately 10 µm of the matrix layer on each side of a tape. If the tapes and the matrix are evenly distributed through the thickness, the surface is more likely to be isotropic. In reality, this can be thinner on the surface depending on the manufacturing process, but the scenario would be possible only if the surface matrix is very much thinner. Hence, the likelihood of this hypothesis being correct is not very high, but it cannot be discarded entirely without an additional study of the microstructure, for example, via x-ray computed tomography. This is outside the scope of this research and is recommended for future research.

4.2.2.1.3 Crazing on the inner matrix

Apart from the aligned crazes seen on the outer surface, there is another type of crazing on the inner surfaces of the matrix, which is exposed by damage to the outer surface, such as tape-splits. An example is shown in Figure 4.7, which shows crazing in the internal matrix between two layers of tapes, exposed by a split in the tape on the surface. These microcracks are not aligned in the same way as the aligned crazes and always propagate perpendicularly to the loading direction, similar to crazes in plain PP (Figure 2.12).

⁹ While crazing mostly occurs in amorphous polymers, crazes have also been observed to propagate between lamellae through spherulite centres and between spherulites in crystalline polymers [109, 227, 228].

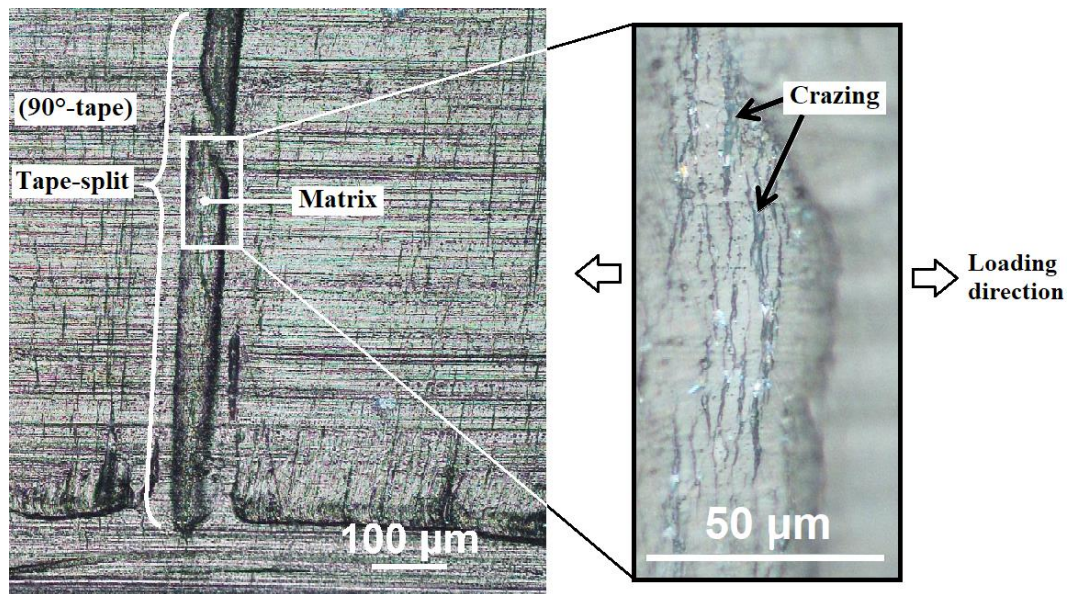


Figure 4.7 Optical micrograph of crazing on a surface exposed from a split in a 90°-tape of a 0.3 mm SRPP tensile specimen.

From the previous analysis of aligned crazing, it can be deduced that the crazing in the internal matrix must look different from the aligned crazing because it results from damage initiating in the matrix itself, as opposed to cracks propagating from tape-splits as in the case of aligned crazing. The question remains, then: why do tape-splits not cause matrix cracks in the same way as aligned crazing for the internal matrix? There are several possible causes.

One possible reason is that the hypothesis formed previously on the aligned crazing is true, that the matrix has a molecular orientation across a short range and this contributes to the aligned crazing occurring for a surface matrix layer that is thin enough. If this is true, and the internal matrix is thicker than the thickness over which the short-range order is retained, it would explain why the surface matrix exhibits aligned crazing whereas the internal matrix exhibits normal crazing. It is also possible that crazing initiates where matrices from different regions, formed from different tapes, meet, and the short-range orientation in lamellae are mismatched, causing cracks that are not aligned. Another possibility is that crazing occurs in the internal matrix before being exposed to the surface, and the absence of a free surface creates a different state of stress to that of the surface matrix.

4.2.2.1.4 Fibril pull-outs

Fibril pull-outs occur with noticeably different characteristics in the thicker specimens compared to the 0.3 mm specimens, unlike other damage mechanisms discussed before. Fibrillation and pull-outs occur in large amounts in thicker specimens, especially in 0°-tapes around the site of failure, mostly becoming

apparent post-failure. In comparison, fibril pull-outs in 0.3 mm specimens are not noticeable without microscopy. Fibril pull-outs in 0.6 mm and 1.0 mm specimens will be discussed first.

A fibril pull-out of the type that occur in 0.6 mm and 1.0 mm specimens is shown in Figure 4.8. Fibril, in this case, refers to a long and narrow section of a tape that is about 10–200 μm wide. The term ‘pull-out’ is used here because it appears as if a fibril of tape has been ‘pulled out’ from the composite. However, it is not the same as the commonly known fibre pull-out where one or more discrete units of fibre has separated from the matrix at the interface. The fibril in SRPP is a fraction of a reinforcement unit and is therefore not enclosed by the matrix or an interface, except at the perimeter. Therefore, ‘partial tape fracture’ or ‘fibril fracture’ may be more accurate descriptions than a ‘fibril pull-out’; however, fibril pull-out is used in this document as it conveys the imagery best and is consistent with existing research.

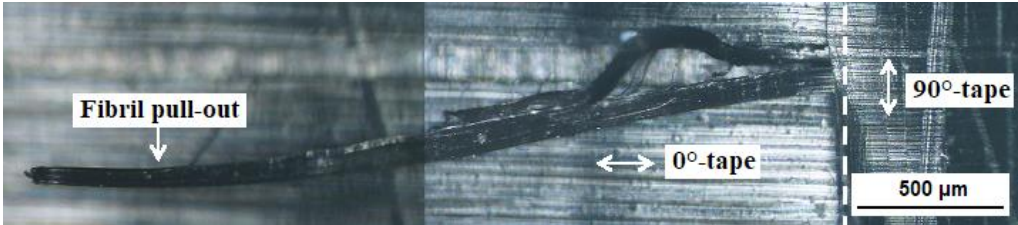


Figure 4.8 Optical micrographs of fibril pull-outs in a 1.0 mm SRPP tensile specimen.

The ends of fibril pull-outs mostly fracture across the lateral section in a ductile manner. This can be seen by the smooth morphology at the tip of the fibril in Figure 4.9, and the shear lip in Figure 4.10. This goes against the expectations set from studying the literature, as most studies report that drawn PP loaded in longitudinal or transverse directions fail in a brittle manner with fibrillation (for example, in [145]). Such statements must have been based on observations at a macroscopic level, so care must be taken to avoid any assumption that fibril ends break in a brittle manner at a microscopic scale.

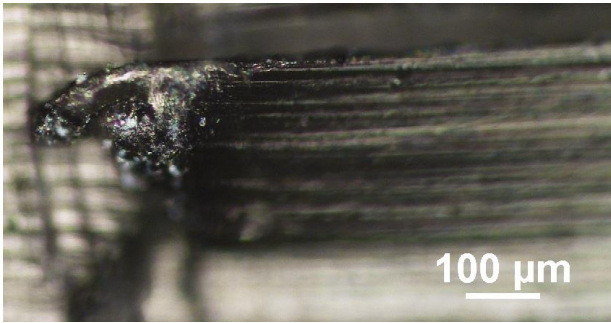


Figure 4.9 Optical micrograph of a fibril pull-out from a 0°-tape in a 0.6 mm SRPP tensile specimen.

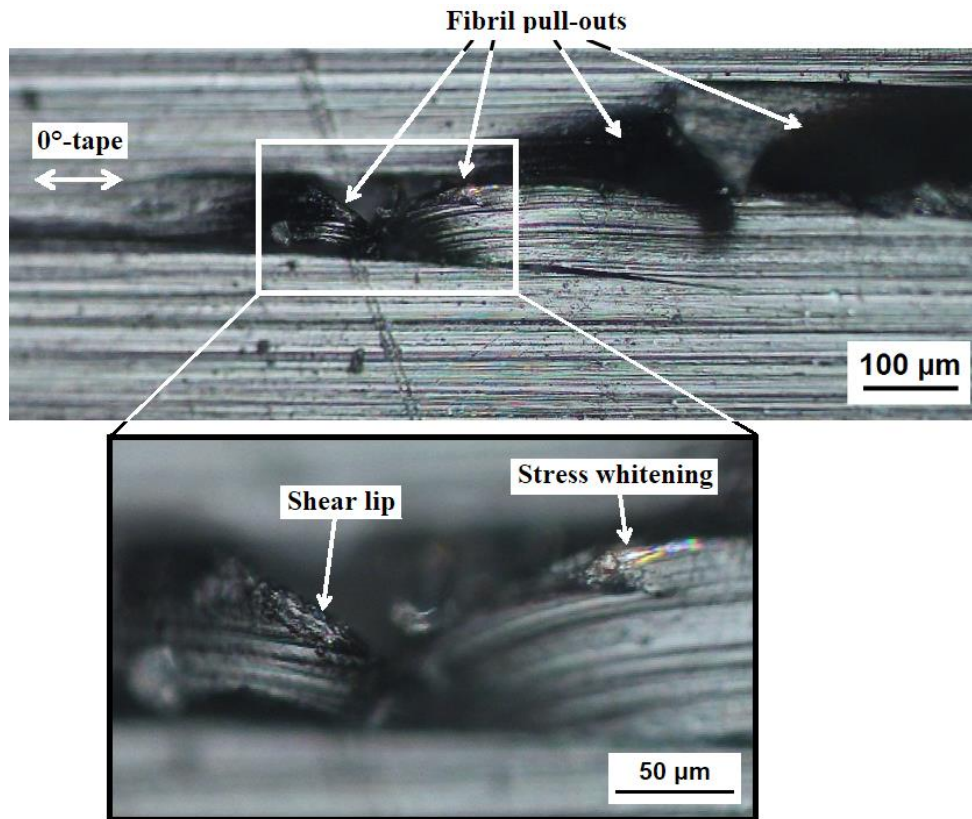


Figure 4.10 Optical micrographs of fibril pull-outs in a 1.0 mm SRPP tensile specimen.

Microscopic analyses of damages thus far indicate that cracks in SRPP tapes *tend* to propagate in a ductile manner (stable crack propagation) when they propagate in the direction perpendicular to the tape orientation, and in a brittle manner (unstable crack propagation) when they propagate in the direction of the tape orientation. This can be seen from the above observation that fibril ends fail in a ductile manner, in comparison to the tape-splits or sides of fibrils resulting from brittle crack propagations.

It must be stressed that the described behaviour is a tendency, not an absolute rule. An example is shown in Figure 4.11. It shows a crack transverse to the tape orientation that exhibits shear lip at the crack opening (Figure 4.11b) and a blunt crack tip at one end of the crack (Figure 4.11c), which are characteristics of a stable crack propagation and ductile failure. In the vicinity, there is another crack propagating along the tape orientation with a sharp tip, characteristic of unstable crack propagation and brittle failure. These observations are congruent with the general observation stated above; however, the upper image (Figure 4.11a) shows a sharp crack tip on the other end of the same transverse crack that has a blunt crack tip on one end. This goes against the general tendency. In this case, it seems likely that the crack initially formed and propagated in a brittle manner and the crack tip becomes blunted with further propagation, as there is evidence of crack tip blunting occurring in thicker specimens, which will be explained in a later section.

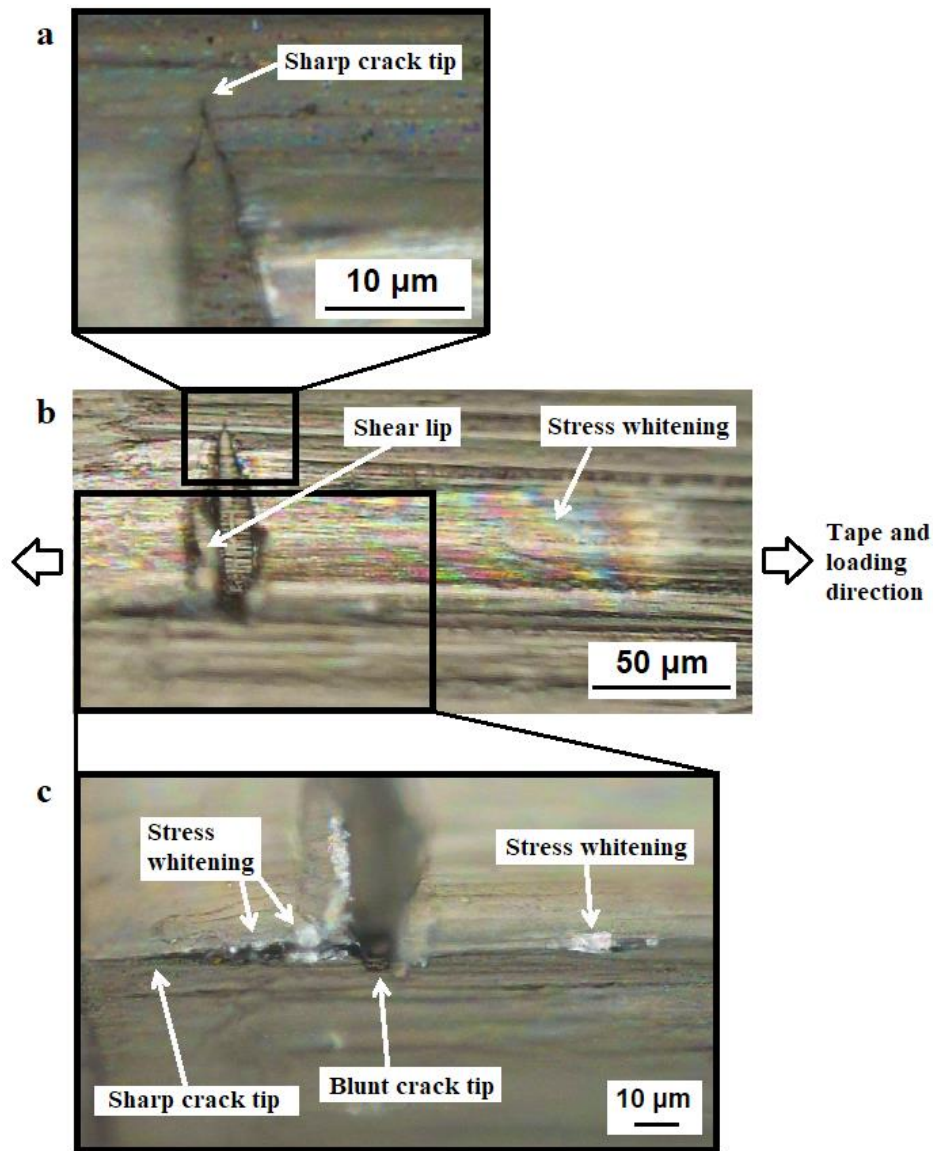


Figure 4.11 Optical micrographs of a 0°-tape of a 0.6 mm SRPP tensile specimen, showing different modes of crack propagation, indicated by the different crack tips.

It should be mentioned that the micrograph in Figure 4.11 has been shown in this section under the assumption that this represents an initiation stage of a fibril pull-out. This assumption was made because the stress whitening shown in Figures 4.11b and 4.11c suggests that cracks would have propagated along the sides of the crack opening and beneath it in the direction of the tape orientation, resulting in a fibril pull-out. If this is the case, it also shows that a fibril pull-out can occur from a tape that has partially delaminated within. It is possible that the assumption is wrong as this does not represent a case of a fibril pull-out. However, it still shows that a crack can propagate in a brittle manner even when it is not propagating in the direction of the tape orientation.

Fibril pull-outs in 0.3 mm specimens are different to those in the thicker specimens, and also to the common observations made on SRPP samples in the literature. For instance, fibril pull-outs in 0.3 mm

specimens occur in 90°-tapes instead of 0°-tapes, and only on the fracture surfaces, as shown in Figure 4.12. Also, the fibrils do not exceed 20 μm in their lateral dimension; at around 10–20 μm thick, they cannot be seen without a microscope. Due to this, 0.3 mm specimens appear to not exhibit any fibrillation at a macroscopic scale, in contrast to the thicker specimens.

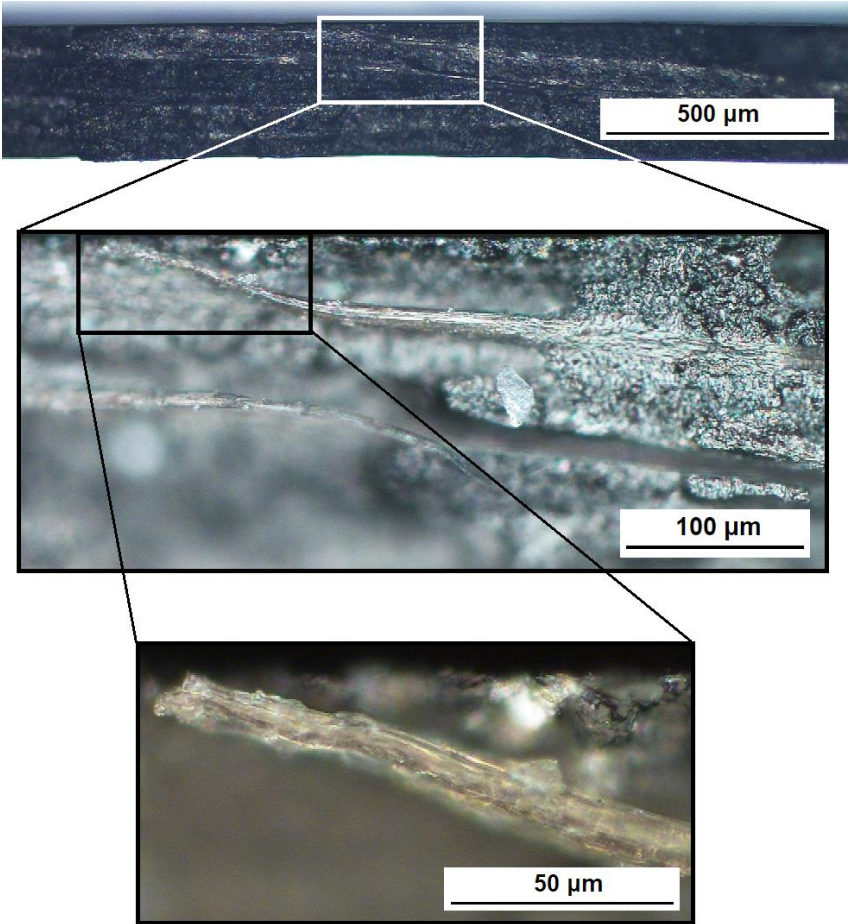


Figure 4.12 Optical micrograph of a fracture surface of a 0.3 mm SRPP tensile specimen. The direction of the applied load is orthogonal to the page.

Fibril pull-outs in 0.3 mm specimens occur specifically on the surface edge of the tapes. This can be seen at A and B in Figure 4.13, where the boundaries between the tape and matrix phases are shown more clearly than in Figure 4.12. The division between the constituent phases shows that fibrils, such as at C, occur within 90°-tapes, and on the edges.

The fact that fibril pull-outs occur on the edge of tapes indicates that failure can occur at the tape-matrix interface. However, this does not necessarily contradict existing studies that state that the interface is very strong in SRPP, since more crack propagation occurs within the tapes than at the interface overall. It also seems to be stronger than many 2-phase FRPs, considering that small portions of the tape and

matrix remain stuck on the fibrils in Figures 4.12 and 4.13 instead of debonding completely along the fibril as seen in many FRPs when fibres pull out of the matrix.

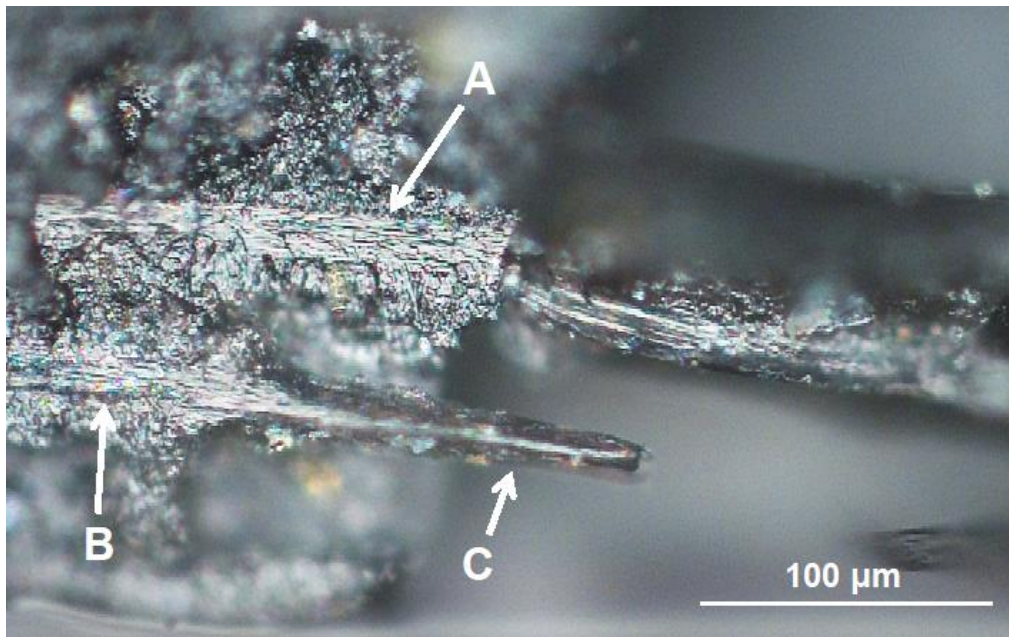


Figure 4.13 Optical micrograph of a fracture surface of a 0.3 mm SRPP tensile specimen, showing boundaries between 90°-tape and the matrix (A and B) and a fibril pull-out (C).

Thus far, types of damage that occur in all SRPP specimens, regardless of thickness, have been discussed. Of these, only fibril pull-outs display different characteristics depending on the thickness, other than the amount and size of the damage. The next section will discuss damage mechanisms that occur only in the thicker specimens.

4.2.2.2 Damages unique to thicker SRPP samples

In addition to the damages discussed in the previous section, there are additional mechanisms related to damage that occur only in the 0.6 mm and 1.0 mm specimens. These are:

- Microfibrillar crack bridging
- Tape kinking
- Oblique crack
- Delamination

This section will discuss the above mechanisms.

4.2.2.2.1 Microfibrillar crack bridging

Microfibrillar crack bridging occurs in tapes within 0.6 mm and 1.0 mm specimens, where small fibrils become partially detached from the sides of the opening of a tape-split and bridge the crack. Crack bridging toughens a material by impeding crack growth. Examples are shown in Figure 4.14 below and Figure 4.15 in the next page. The reason this is only observed in the thicker specimens is unclear. It is perhaps the case that the 0.3 mm specimens do not reach the level of strain required for the crack opening to be large enough for the microfibrillar bridging to be observed. As a similar example, spots of stress whitening occur inside crazes (e.g. Figures 4.5 and 4.7 above) but it is not clear whether or not these are crack bridging because the cracks are too narrow.

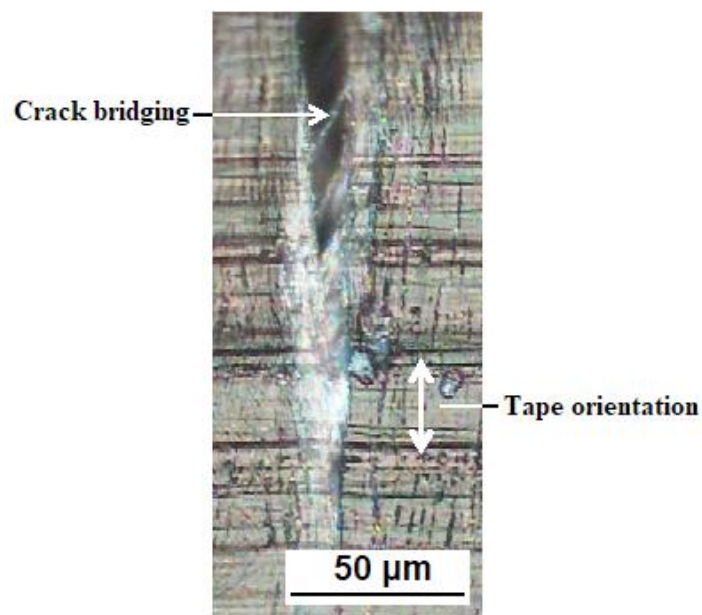
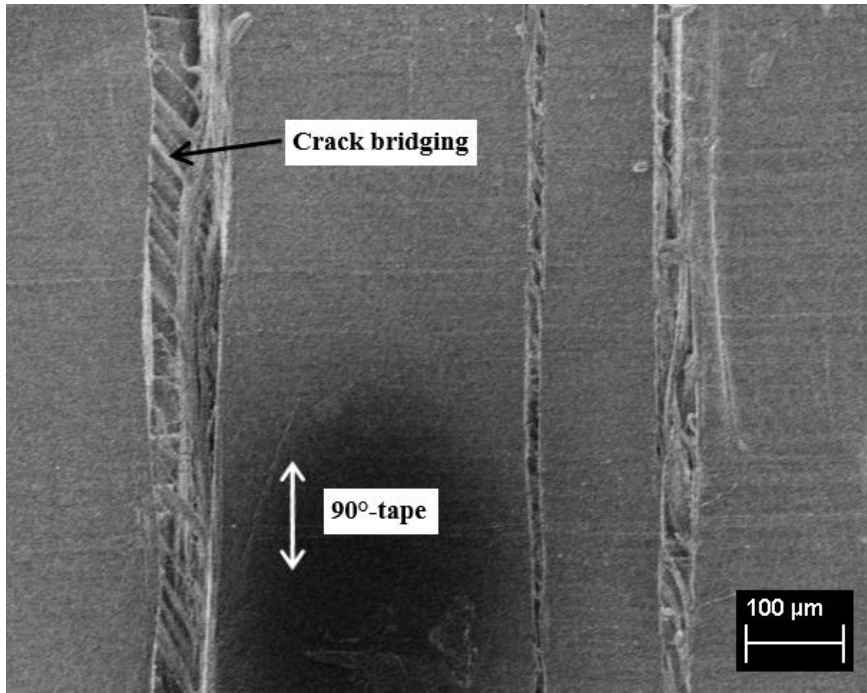


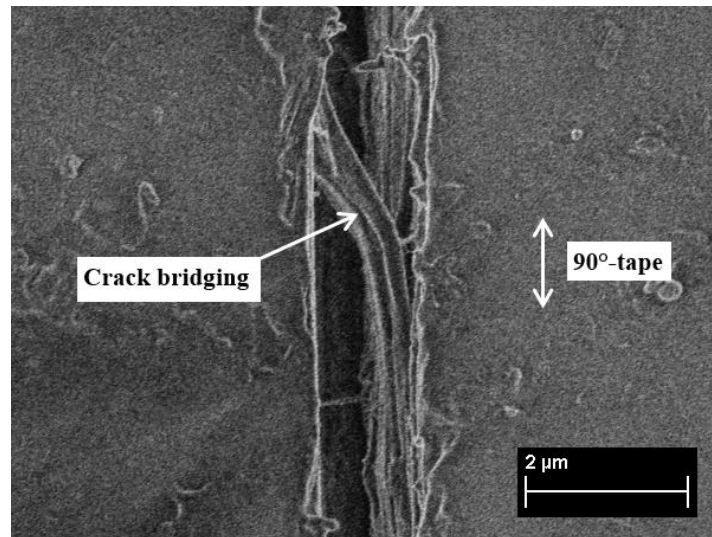
Figure 4.14 Optical micrograph of microfibrillar crack bridging in a 90°-tape of a 0.6 mm SRPP tensile specimen.

It is also possible that the chain molecules in the tapes within the 0.3 mm specimens are more entangled than in thicker specimens due to a higher molecular relaxation in the tapes when their surfaces are melted during the manufacturing process. If so, it may be that the entanglement creates stronger bonds between the molecular chains and, due to this, they tend to debond less from the bulk of the material. This would result in little or no crack bridging, as fibrils need to be separated from the bulk material for a crack bridging to occur.

In discussing the characteristics of micro-damages in SRPP in detail, a classification of fibrils into different categories by their lateral dimensions is desirable. This is because many different sized fibrils occur in the material, especially in the tape, and these can occur next to each other. This can lead to confusion as to which one is being referred to in discussing multiple types of fibrils. For example, there



(a)



(b)

Figure 4.15 Scanning electron micrographs of microfibrillar crack bridging in 90°-tapes of 0.6 mm SRPP tensile specimens. Magnification = 200x (a), = 20,000x (b). EHT = 1.00kV.

are often smaller fibrils around the edge of larger fibril pull-outs, as shown in Figure 4.16a. These are actually remnants of microfibrils from microfibrillar crack bridging, as can be seen by comparing Figure 4.16a to Figure 4.16b. Rather than providing a description of their relative sizes each time, it is suggested here that fibrils in SRPP and drawn PP be classified as a ‘fibril’, a ‘microfibril’ or a ‘nanofibril’, as illustrated in Figure 4.17.

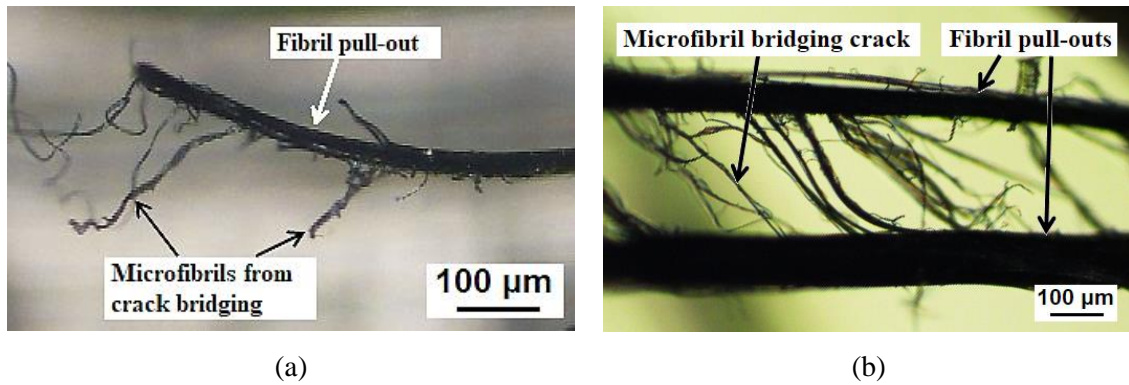


Figure 4.16 Micrographs of a) 1.0 mm and b) 0.6 mm SRPP tensile specimens showing smaller microfibrils from crack bridging attached around larger fibril pull-outs.

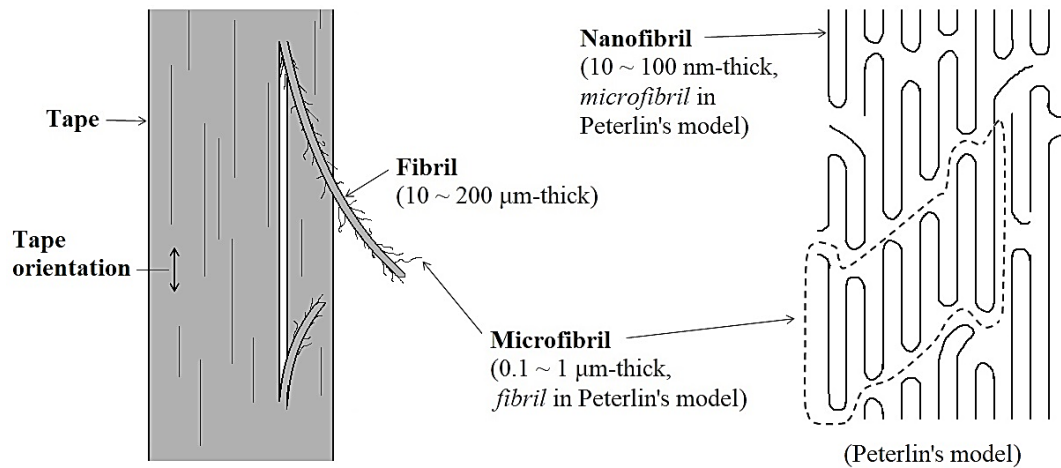


Figure 4.17 Different fibrils in SRPP according to the lateral dimension. The relationship to Peterlin's model [120, Fig. 12] is shown.

As denoted in Figure 4.17, there is a discrepancy between this definition and the definition in Peterlin's microfibrillar model [116–120]. Figure 4.15b showed that the microfibril in crack bridging is about 0.2–0.3 μm in width, similar to those in semi-crystalline polymers (around 0.2 μm [131, p. 2980]). Under Peterlin's microfibrillar model, this would then be a 'fibril' (a block of microfibrils, about 1 μm or less laterally [119]) and not 'microfibrils', which are only a few tens of nanometres thick [116]. However, since the lateral dimensions of what Peterlin refers to as 'fibrils' and 'microfibrils' are typically on the order of micrometres and nanometres, respectively, it seems more appropriate to rename them as 'microfibrils' and 'nanofibrils'. This is also more convenient considering that larger fibrils can occur in SRPP. These can then be referred to as 'fibrils'.

It can be seen from micrographs shown previously that the microfibrils in crack bridging are oblique to the direction of crack propagation. This is due to the crack bridging occurring in tapes which have a highly oriented structure. As a result, the appearance is closer to fibre bridging in double cantilever beam

(DCB) tests of unidirectional FRPs than to crack bridging in plain polymers. Fibrils that bridge crazes in plain polymers are typically polymer chains that have sheared perpendicularly to the crack propagation and are therefore aligned in the direction of tensile stress, as shown Figure 4.18. In contrast, fibre bridging in DCB tests of composites can exhibit slanted fibre ligaments when in shear, or when the crack propagates in the direction of the fibre. An example is shown in Figure 4.19 [229].

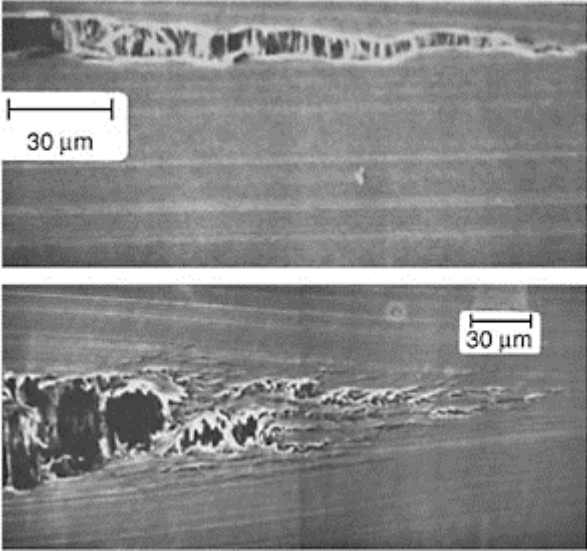


Figure 4.18 Crazing fibrils in polyethylene, reproduced from [132, p. 405]. The applied load is vertical in this image.

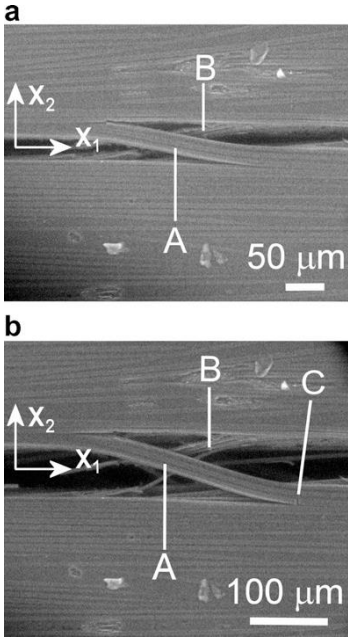


Figure 4.19 Crack bridged by single fibres and ligaments consisting of several fibres in a unidirectional carbon-fibre/epoxy composite. Reproduced from [229, p. 224].

Despite the similarity in appearance to FRPs, crack bridging in an SRPP tape occurs in a single, continuous phase. The microfibrils originate from the same medium the cracks propagate in, in contrast to the situation in FRPs where the fibres bridge cracks in the matrix or at the interface. This demonstrates how the tape in SRPP can behave like an FRP system while not really being a composite system itself. SRPP may be thought of as being comprised of smaller pseudo-FRPs (tapes) within a larger FRP system (tapes and matrix).

4.2.2.2.2 Tape kinking

The 90°-tapes in the thicker samples exhibit very few instances of a kinking behaviour at narrow sections created between tape-splits (< 100 µm), as shown in Figure 4.20. This behaviour is similar to fibre kinking, where compressive longitudinal stress creates a shear in the fibre in the presence of fibre misalignment to stress, waviness or voids. It is apparent this is caused by a combination of an applied tensile load, perpendicular to the transverse tape, and a resulting negative strain in the reinforcing direction from Poisson’s effect. Once again, this demonstrates that tapes can behave like fibre bundles at small scales. As these kinks are infrequent and small in scale, and do not propagate into larger, critical areas of damage, they do not play a significant role in ultimate failure under tensile loading.

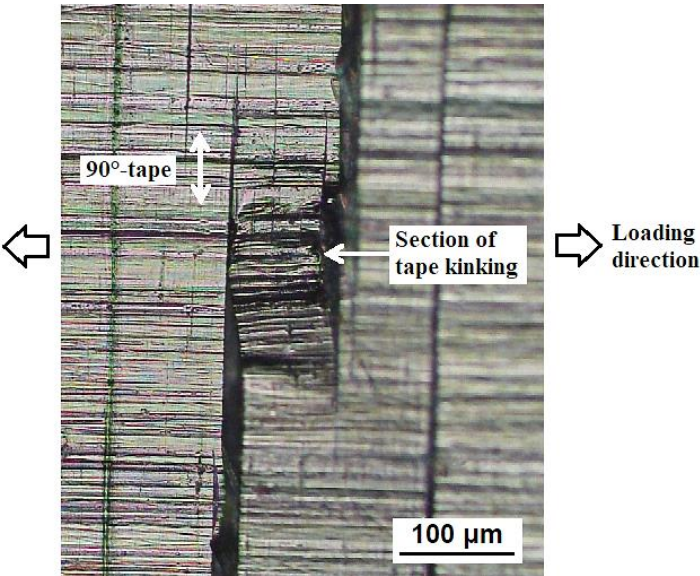


Figure 4.20 Optical micrograph of tape kinking in a 0.6 mm SRPP tensile specimen.

It is suspected that this does not occur in the 0.3 mm SRPP because the specimens fail before reaching the tensile strain required to induce tape kinking, similar to the way in which crack openings in crazing and tape-splits are much smaller than in thicker specimens.

4.2.2.2.3 Oblique cracks

In rare cases, cracks can propagate at an angle to the loading direction in larger fibrils, sections or the entire width of 0°-tapes. An example is shown in Figure 4.21. In the limited number of observations, oblique cracks occurred at approximately either 20° or 75° to the tape orientation and the loading direction. Such a crack initiates from the free edges and propagates across the tape or the section, as shown in Figure 4.21, and can result in the fracturing of the section.

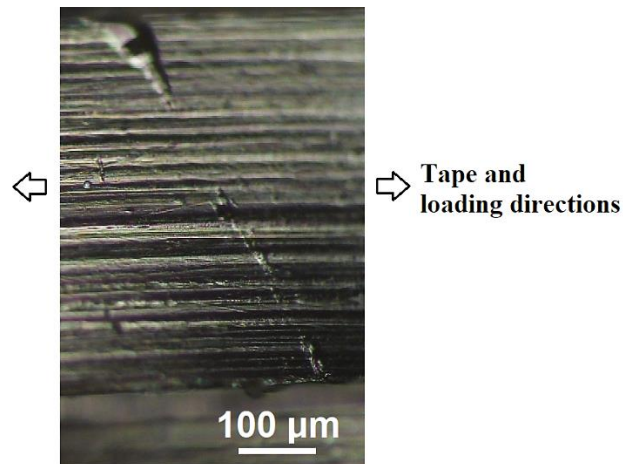


Figure 4.21 Optical micrograph of a 0.6 mm SRPP tensile specimen showing oblique crack initiation and propagation in a section of a 0°-tape.

The failure at an angle is not satisfactorily explainable from the existing literature. Shear zones or deformation bands, and the associated failure within those bands, are observed in polymers, but only in the presence of shear, compression or misalignment between tension and the initial drawing direction in oriented polymers [230]. Since SRPP was subjected to tensile load along one of the reinforcing directions, none of the mentioned cases apply in an ideal situation. It may then be that the local stress state was changed due to an irregularity, such as a defect or prior damage.

For example damage, such as a fibril pull-out, would cause unloading along the fibril. This would induce a strain gradient between the intact part of the material that is aligned to the damage and the surrounding material, near the root of the fibril pull-out, as illustrated in Figure 4.22 in the next page. It might then be that this then induces shear stress that is large enough to create a deformation band and local failure at an angle to the tape orientation.

Another possible cause is that, in the process of drawing PP, displacements in microstructural fibrils creates shear stress between the fibrils, resulting in shear in fibril shapes due to shear displacements between microfibrils within. This has been described previously in the literature review (see Figure 2.18). It may then be that the shear stress triggers a crack to propagate at an angle. It is also

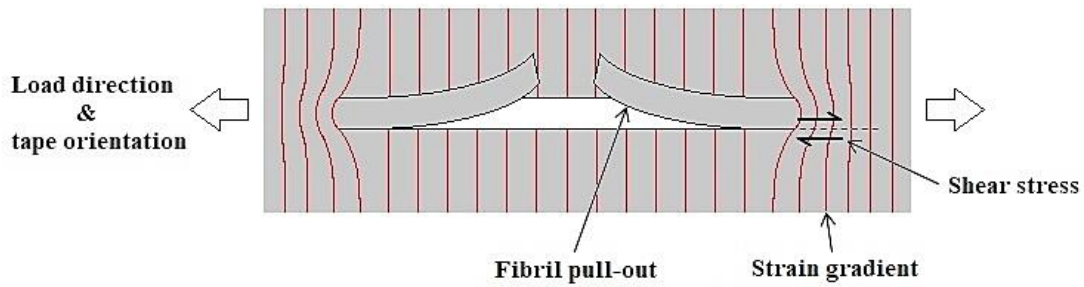


Figure 4.22 Possible deformation gradient and shear stress created around fibril pull-outs in an SRPP tape.

possible that oblique cracks are caused by surface scratches. Given that cracks seem to fail consistently around 20° or 75° to the tape orientation, it may be that only scratches close to these angles propagate further into the tape and cause local failure.

4.2.2.2.4 Delamination

As with other types of damage, the amount of delamination increases with specimen thickness. As mentioned earlier in Section 4.2.1, delamination does not occur in 0.3 mm specimens, probably due to the tapes' surface melting more during the manufacturing stage than in thicker specimens. This would have given the 0.3 mm specimens higher reinforcement–matrix bonding. Similar cases have been observed in other studies on SRPP, where additional matrix reduced delamination [70, 97]. Otherwise, it might be related to the fact that the stress in 0.3 mm specimens does not reach a threshold level for existing cracks (e.g. boundary cracks) to propagate to between tapes and cause delamination.

The most significant finding about delamination in 0.6 mm and 1.0 mm specimens is that delamination in SRPP specimens occurs at different levels. It can occur between two tapes (inter-tape delamination) or within a tape (intra-tape delamination), and the inter-tape delamination can occur between 0° and 90° -tapes in a single layer (intralaminar delamination), or between any two tapes of separate layers (interlaminar delamination). The different types of delamination can co-occur at a single location or occur within very close proximity to each other. This can be seen by studying the delaminated surfaces.

Figure 4.23 shows a surface of a 0° -tape which has delaminated from a 90° -tape on the surface. The delaminated surface exhibits damage in both longitudinal and transverse directions to the tape orientation. In the bottom image, fibril pull-outs in different directions can be seen. One fibril has been pulled out from the 0° -tape, whereas the other fibril has been pulled out from the 90° -tape and remains attached to the 0° -tape. Similarly, there are microcracks that are parallel to the tape orientation (region A) and perpendicular to it (region B). The microcracks are much thinner than tape-splits, somewhat resembling the aligned crazing that occurs on the surface matrix but longer and more densely packed.

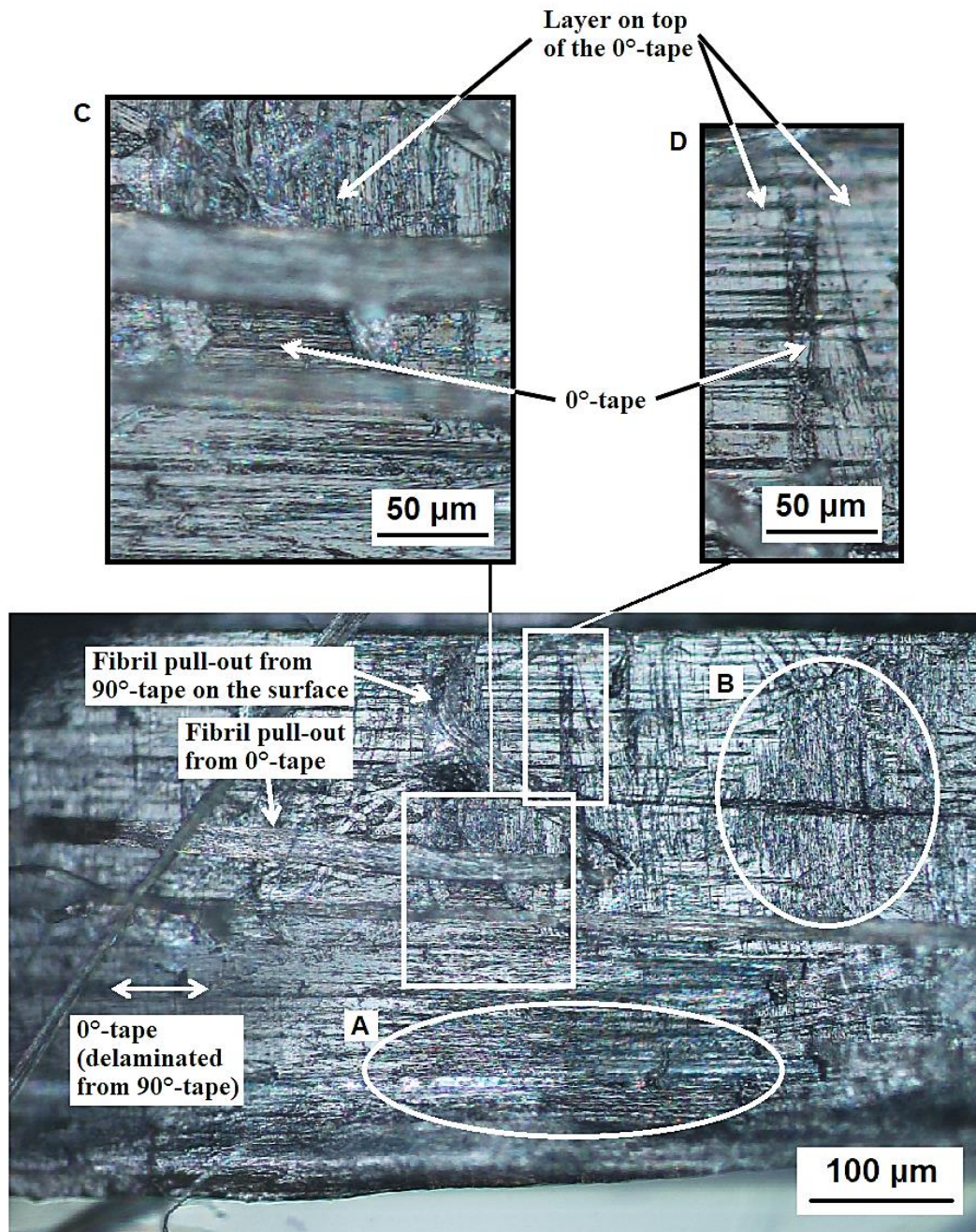


Figure 4.23 Optical micrograph of a 0.6 mm SRPP tensile specimen, showing a section of a 0°-tape that has been delaminated from the 90°-tape on the surface.

Such observation of damage occurring in both directions stems from the fact that delamination occurs at multiple levels – in the 0°-tape, the 90°-tape and in the matrix. For instance, by examining the material at varying depths through the thickness, it is possible to see that the damage transverse to the tape orientation, such as that seen in region A, is actually damage in the thin translucent or opaque layers on top of the 0°-tape. By recognising that cracks in SRPP tapes mostly propagate in the direction of the tape orientation, it can be deduced that the translucent layer is the matrix and the opaque layer is a

portion of the 90°-tape which has delaminated (intra-tape delamination). Example cases are shown in regions C and D, shown in the top two images.

In C, an opaque layer has partially peeled off from the base layer. The two layers can be distinguished from each other by the many microcracks that are oriented in different directions. Since cracks in tapes tend to propagate in the direction of the tape orientation, the top layer must be a thin portion of a 90°-tape that has delaminated, and the base layer must be the 0°-tape.

In D, there is an almost transparent layer with damage oriented in the transverse direction to the 0°-tape, on top of the base layer which has multiple cracks running parallel to the tape orientation. From the directionality of the damage, the base layer is the 0°-tape and the top layer is either the matrix or a portion of the 90°-tape. For reasons that will be explained in the next paragraph, the translucency of the layer indicates that the top layer is the matrix. Then, the damage that is transverse to the 0°-tape orientation must be a result of propagation or imprinting of cracks from the 90°-tape. In addition, the thin strip that does not have the matrix layer must have resulted from a fibril pull-out from the 90°-tape that has delaminated from the 0°-tape. In the process of delamination of the fibril, the matrix, and possibly a portion of the 0°-tape, has also delaminated from the 0°-tape.

An example demonstrating that the translucent layer is the matrix is shown in Figure 4.24 in the next page. The figure shows a 90°-tape that has delaminated from a 0°-tape. In the left of the lower image, the translucent layer exhibits shear flow. Shear flow here denotes the deformation or plastic flow in viscous solid materials, mostly when subjected to critical shear stress along their crystallographic slip planes. The deformed surface has a morphology that is continuous and smooth, as opposed to being rough, as shown in Figure 4.25 in the next page. Shear flow such as that shown in Figure 4.24 only occurs in the matrix at boundaries between 0° and 90°-tapes, as will be explained in a later section. Since the location where shear flow occurs in Figure 4.24 is indeed near a boundary between 0° and 90°-tapes, the translucent layer must be the matrix. The matrix appears almost transparent, probably due to the layer being much thinner than the tapes.

Since it is possible to discern the damage in the matrix from those in the tapes, it could be gathered from studying multiple delaminated surfaces that delamination occurs preferentially in 90°-tapes and matrix rather than in 0°-tapes. This points out that the tapes in SRPP have different resistance against intra-tape delamination depending on their orientation in relation to the loading direction.

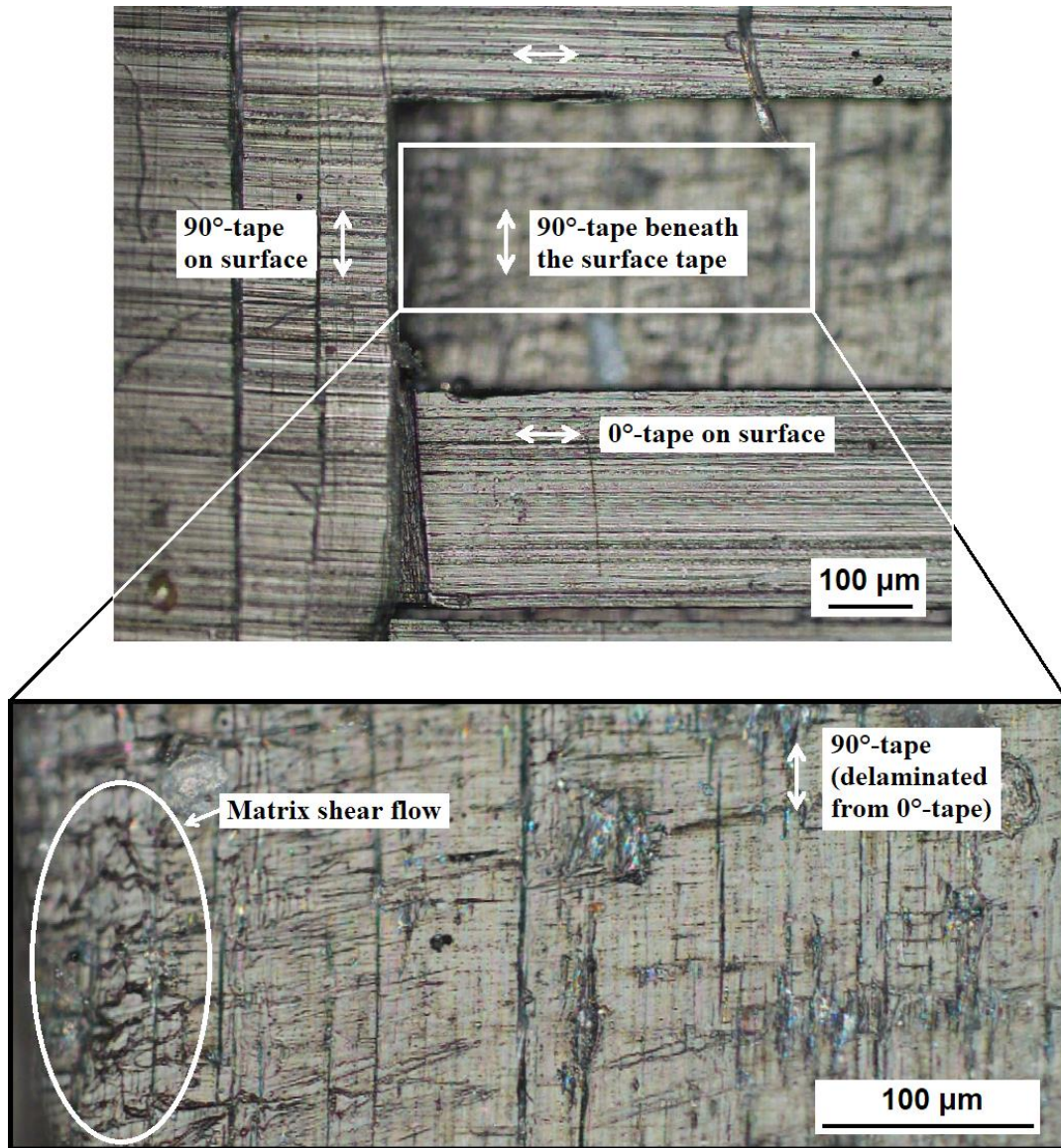


Figure 4.24 Optical micrograph of a 1.0 mm SRPP tensile specimen, showing a section of a 90°-tape that has delaminated from the 0°-tape on top.

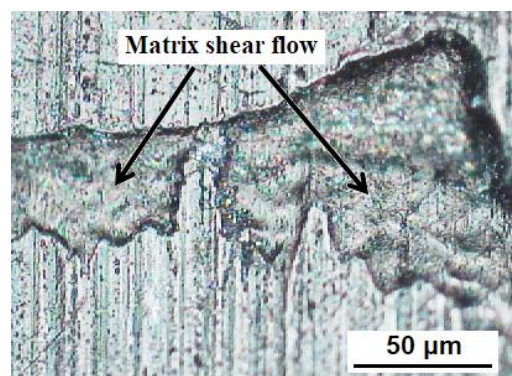


Figure 4.25 Example of shear flow in the matrix at a boundary crack between orthogonal tapes.

4.2.2.3 Summary of microscopic damage types

Different types of microscopic damage have been described and analysed in this section. Woven SRPP behaves quite differently to many other composites in that multiple kinds of damage can occur *simultaneously*, instead of occurring in separate phases. This makes it more challenging to identify the critical damage responsible for the failure of the material. Hence, all damage in the SRPP were examined using microscopy, as there has been no previous study providing such information. Three samples of different thicknesses have been analysed, as this gives the additional information required for an in-depth analysis of the failure behaviour of SRPP; this will be covered in the next section, together with a discussion of several damage-related mechanisms that have not been covered in this section because they are better explained in the context of the critical failure of specimens.

Before moving on to the failure behaviour, brief descriptions of the microscopic damages that have been analysed are given below. The amount and size of the damage are greater in thicker specimens, and also greater in 90°-tapes than in 0°-tapes. The following types of damage occur in all SRPP specimens regardless of the thickness:

- **Tape-splits:** Cracks in SRPP tapes that propagate along the tape orientation.
- **Aligned crazing:** Surface matrix cracks that are similar to crazes in polymers, except that they are aligned to a higher degree and occur in the direction of the tape underneath, due to being caused by tape-splits.
- **Crazing:** Observed on the inner matrix that has been exposed to the damage on the surface layer. These resemble typical crazing in polymers and propagate perpendicularly to the loading direction.
- **Fibril pull-outs:** Sections of tapes that are about 10 – 200 µm wide which have become separated from the surrounding material from one end.
- **(Boundary cracks:** This is discussed in the next section.)

The following types of damage are observed only in 0.6 mm and 1.0 mm SRPPs:

- **Microfibrillar crack bridging:** The phenomenon of microfibrils bridging the opening of tape-split type of cracks. The microfibrils are approximately 0.1–1 µm wide and form non-perpendicular angles to the direction of crack propagation.
- **Tape kinking:** Kinks that occur infrequently in small sections of 90°-tapes. These form under a combination of negative strain in the direction of the tape and positive strain in the direction of the load.

- **Oblique cracks:** Rare instances of cracks in tapes that propagate at around 20° or 75° to the orientation of the tape.
- **Delamination:** Separation of material into layers within a tape (intra-tape delamination), between tapes (inter-tape delamination). Intra-tape delamination can occur between 0° and 90°-tapes within a layer (intralaminar delamination) or between tapes of separate layers (interlaminar delamination). More delamination occurs within the 90°-tapes and the matrix than within the 0°-tapes.

4.2.3 Failure behaviour

This section discusses the failure behaviour of SRPP, where ‘failure’ refers to the sudden catastrophic failure of the specimen, after which it can no longer bear any load. This section is divided into two subsections.

The first subsection discusses the failure behaviour of 0.3 mm specimens. It includes a discussion on how failure initiates and whether there are ways to anticipate when and where failure will occur. This will help to develop an understanding of how failure occurs in thicker specimens as well, which may have been hard to identify without analysing the 0.3 mm specimens. The manner of crack propagation during failure will then be discussed. In the last part, it will be shown that cracks propagate in ways that have not been reported in the literature.

The second subsection discusses the failure behaviour of 0.6 mm and 1.0 mm specimens. It will be shown that they exhibit noticeably different failure behaviours compared to the 0.3 mm specimens because of various toughening mechanisms. It will be illustrated how they relate to the previously discussed damage mechanisms and stress-strain behaviour, as well as the mode of crack propagation. Finally, there will be a discussion of how the different failure behaviours observed in the 0.3 mm specimens might impact on the predictability of failure in thicker specimens.

4.2.3.1 Failure behaviour of 0.3 mm specimens

Failure in the 0.3 mm SRPP specimens is caused by the development of a particular type of damage called boundary cracks. This is the most important aspect of the catastrophic failure in the 0.3 mm specimens and, for this reason, it is discussed in this section, rather than being included in the previous analysis of all the other damage mechanisms.

This section discusses the failure behaviour of 0.3 mm specimens and is further divided into four parts;

1. A discussion of the different types of boundary cracks and their possible causes.

2. An explanation of how one specific type of boundary crack causes the development of critical damage that leads to specimen failure.
3. A discussion of the ways in which the onset of failure can be predicted using a surface strain analysis.
4. A consideration of the occurrence of different modes of crack propagation during the failure process.

4.2.3.1.1 Microscopic analysis of boundary cracks

There are four different types of boundaries and boundary cracks, as illustrated in Figure 4.26. To differentiate between each, they are denoted as $BC_y^{x^\circ}$. The superscript x° is either 0° to indicate boundaries or boundary cracks parallel to the loading direction, or 90° to indicate those that are perpendicular to the loading direction. The subscript y is either \parallel to indicate boundaries between parallel tapes or \perp to indicate boundaries between orthogonal tapes. The four types of boundaries are:

$BC_{\parallel}^{90^\circ}$: Boundary 90° to the loading direction, between two 90° -tapes.

$BC_{\perp}^{90^\circ}$: Boundary 90° to the loading direction, between orthogonal tapes where the 0° -tape weaves under the edge of a 90° -tape.

$BC_{\parallel}^{0^\circ}$: Boundary 0° to the loading direction, between two 0° -tapes.

$BC_{\perp}^{0^\circ}$: Boundary 0° to the loading direction, between orthogonal tapes where the 90° -tape weaves under the edge of a 0° -tape.

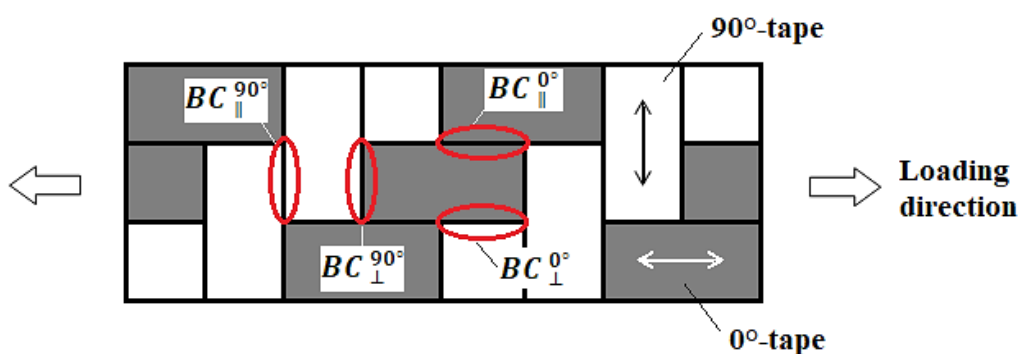


Figure 4.26 Illustration of the four types of boundaries and boundary cracks.

The most obvious difference between the boundary cracks is the difference in appearance, depending on whether the tapes at the boundary are parallel to each other ($BC_{\parallel}^{90^\circ}$ or $BC_{\parallel}^{0^\circ}$) or orthogonal to each other ($BC_{\perp}^{90^\circ}$ or $BC_{\perp}^{0^\circ}$). At $BC_{\parallel}^{90^\circ}$ and $BC_{\parallel}^{0^\circ}$, matrix cracks with sharp tips form and propagate in ways

that resemble tape-splits, as shown in Figure 4.27. In comparison, at $BC_{\perp}^{90^{\circ}}$ and $BC_{\perp}^{0^{\circ}}$, matrix damage starts with microvoids forming and coalescing along the boundary, with matrix shear flow and thinning occurring, as shown in Figure 4.28.

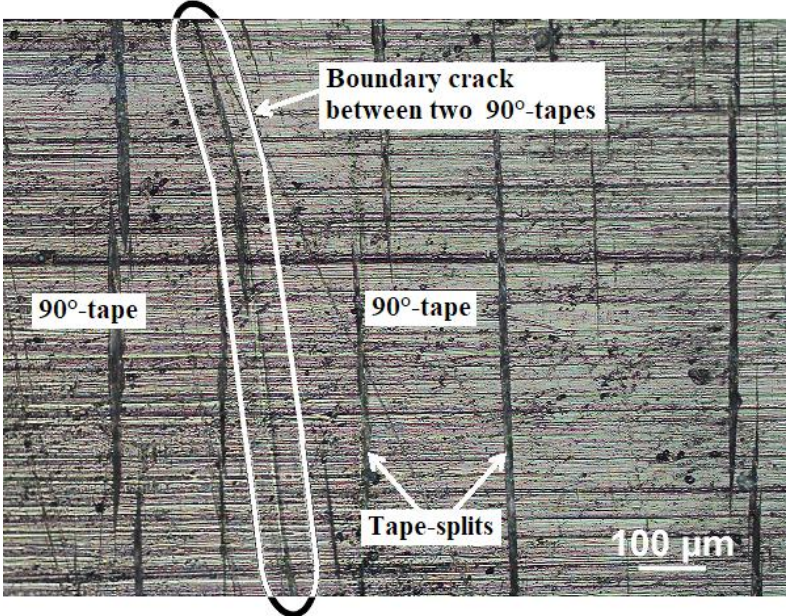


Figure 4.27 Boundary cracks between parallel tapes in a 0.6 mm SRPP tensile specimen, exhibiting matrix damage similar to tape-splits.

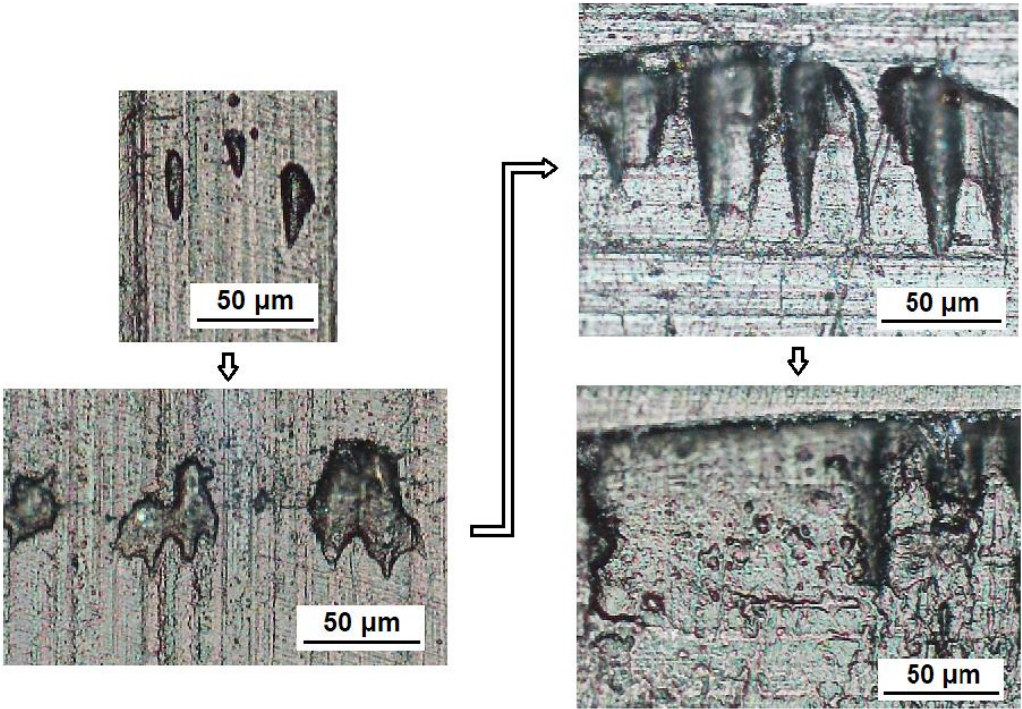
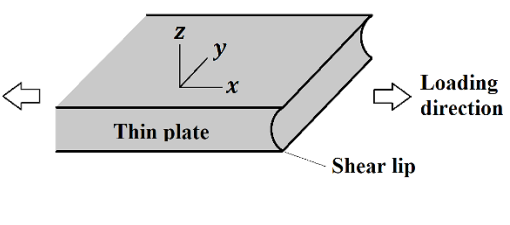
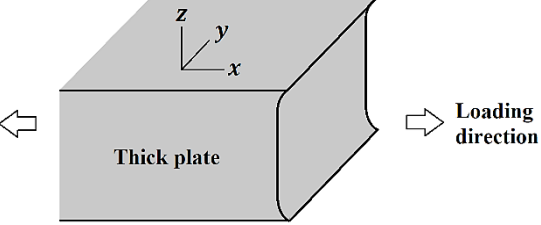


Figure 4.28 Boundary cracks between orthogonal tapes in 0.3 mm SRPP tensile specimens, depicting the process of the matrix damage development.

It was found that the characteristic appearance of boundary cracks is determined by the geometry of the weaving, not the loading direction. This can be deduced from the fact that there is little difference in the appearance between a boundary that is orientated at 0° to the loading direction ($BC_{\parallel}^{0^\circ}$ or $BC_{\perp}^{0^\circ}$) and a boundary that is at 90° to the loading direction ($BC_{\parallel}^{90^\circ}$ or $BC_{\perp}^{90^\circ}$). In the following paragraphs, this phenomenon will be explained by first considering what the different microscopic behaviours indicate about the mode of crack propagation and failure. This can then indicate what kind of stress and strain states are associated with each mode, and then this can be associated with the weaving geometry at each type of boundary crack.

Microscopic examinations show that $BC_{\parallel}^{90^\circ}$ and $BC_{\parallel}^{0^\circ}$ exhibit sharp crack tips, which is similar to tape-splits and crazing. In contrast, $BC_{\perp}^{90^\circ}$ and $BC_{\perp}^{0^\circ}$ have blunt crack tips. This indicates different types of crack propagation and failure occur at these boundary cracks. Sharp crack tips are related to unstable crack growth and brittle failure, observed when a material is in a plane strain condition, which typically occurs in thick plates. Conversely, blunt crack tips are characteristic of stable crack growth, shear flow and ductile failure, observed when a material is in a plane stress condition, in relatively thin plates. This relation is illustrated in Table 4.2.

Table 4.2 Plane stress and plane strain conditions and the associated modes of crack propagation and failure.	
	
Plane stress $\sigma_z = 0$ $\varepsilon_z \neq 0$	Plane strain $\sigma_z \neq 0$ $\varepsilon_z = 0$
Blunt crack tip	Sharp crack tip
Stable crack growth	Unstable crack growth
Ductile failure	Brittle failure
Smooth fracture surface	Rough fracture surface

To give a brief explanation, material close to the surface can deform easily in the out-of-plane direction (z -direction in Table 4.2) because the free surface is not constrained. In a thin plate where the stress cannot vary much through the thickness, there is approximately zero stress ($\sigma_z = 0$) and non-zero strain

in the z -direction ($\epsilon_z \neq 0$). This condition is known as plane stress and the material fails in a ductile manner, with shear lips occupying most of the thickness. A material away from the free surface in a thick plate is constrained in the z -direction ($\epsilon_z = 0$), and therefore, there is non-zero stress in the z -direction ($\sigma_z \neq 0$). This is known as plane strain condition. This puts a higher constraint on the plastic flow in the vicinity of the crack tip and results in a brittle fracture, which has little or no plastic deformation and low energy absorption during the fracture [231].

Based on the above explanation, the matrix at $BC_{\parallel}^{90^\circ}$ and $BC_{\parallel}^{0^\circ}$, which exhibit sharp crack tips, must be in a state of plane strain because the matrix is relatively thick in the z -direction; conversely, at $BC_{\perp}^{90^\circ}$ and $BC_{\perp}^{0^\circ}$, which exhibit blunt crack tips, the matrix must be in the plane stress condition because the matrix is much thinner in the z -direction. Indeed, the matrix is thicker at $BC_{\parallel}^{90^\circ}$ and $BC_{\parallel}^{0^\circ}$ than at $BC_{\perp}^{90^\circ}$ and $BC_{\perp}^{0^\circ}$ due to the local geometry from the weaving. This is shown in the simplified illustrations of $BC_{\parallel}^{90^\circ}$ and $BC_{\perp}^{90^\circ}$, shown in Figure 4.29, which depict cross-sections along the loading direction, near the free surface. In the cases of $BC_{\parallel}^{0^\circ}$ and $BC_{\perp}^{0^\circ}$, the direction of the load and displacement in the matrix are simply rotated by 90° , pointing in the direction orthogonal to the page.

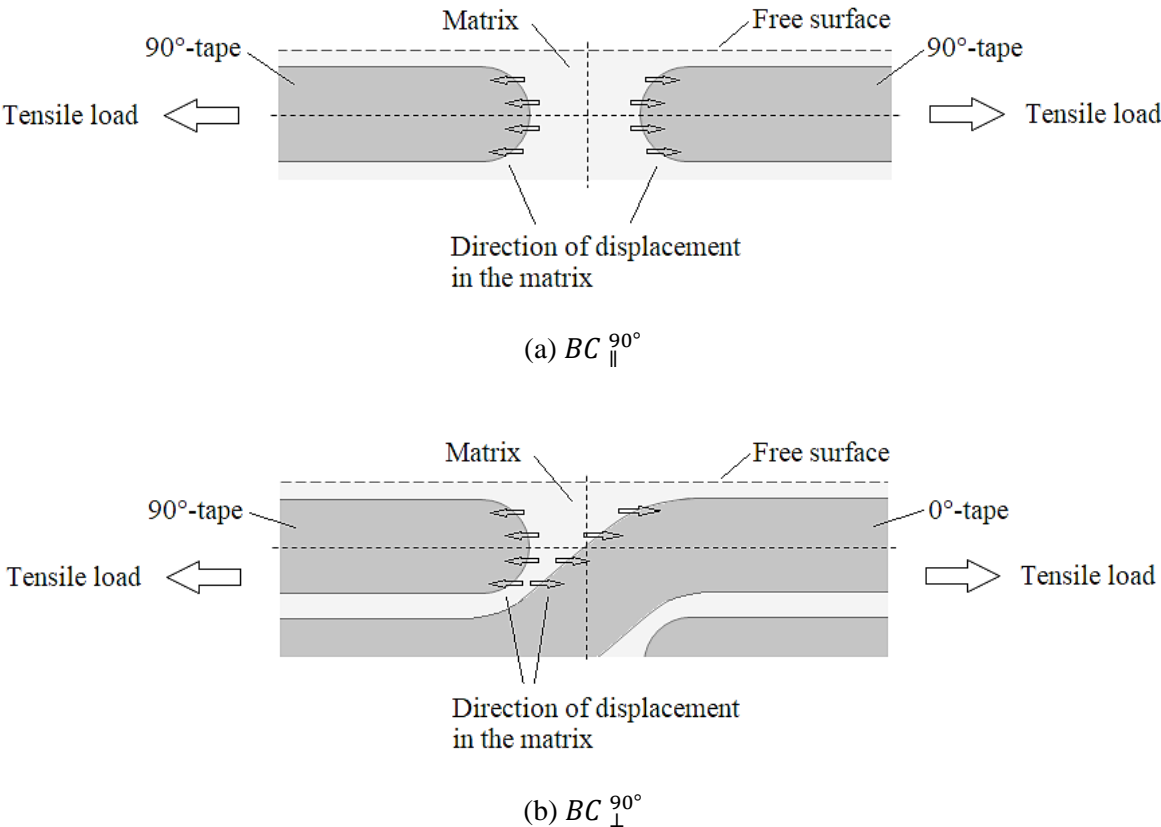


Figure 4.29 Cross-sections of boundary cracks on the surface that are oriented at 90° to the loading direction, a) between two 90° -tapes ($BC_{\parallel}^{90^\circ}$), and b) between 0° and 90° -tapes ($BC_{\perp}^{90^\circ}$).

From the above analysis, it can be seen that different types of boundary cracks have different modes of crack propagation and failure because the geometry of the weaving induces different states of stress and strain in the matrix. More specifically, boundary cracks between parallel tapes ($BC_{\parallel}^{90^\circ}$ and $BC_{\parallel}^{0^\circ}$) form and propagate in a brittle manner (cracks propagate *unstably* with *sharp crack tips*) under *plane strain* conditions, due to the matrix between the tapes being relatively thick in the out-of-plane direction. Boundary cracks between orthogonal tapes ($BC_{\perp}^{90^\circ}$ and $BC_{\perp}^{0^\circ}$) form and propagate in a ductile manner (cracks propagate *stably* with *blunt crack tips*) under *plane stress* conditions due to the matrix being relatively thin in the out-of-plane direction between the tapes.

From the matrix damage formed as described above, the boundary crack can then propagate into the tape as well. This can occur in two ways; either the crack propagates in the in-plane direction as shown in the example in Figure 4.30, which is relatively rare with limited propagation distances, or the boundary crack propagates into the tape in the out-of-plane direction through the thickness, as shown in Figure 4.31 in the next page.

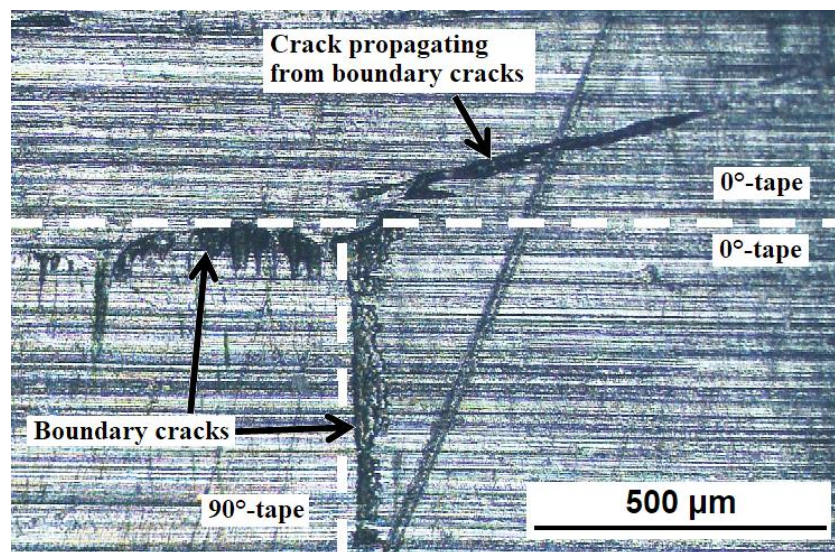


Figure 4.30 Optical micrograph of 0.3 mm SRPP tensile specimen, showing a crack propagating through the surface tape from boundary cracks.

From Figure 4.31, it may seem that such damage, where a $BC_{\perp}^{90^\circ}$ propagates into a 0° -tape, is critical, since this would lead to a reduction in the main reinforcing component if it results in a scission across the tape. In fact, such boundary cracks are not critical because the critical damage that leads to specimen failure occurs at a $BC_{\parallel}^{90^\circ}$ in 0.3 mm specimens, before any 0° -tape can fracture from a $BC_{\perp}^{90^\circ}$. This will be shown through the surface strain analysis in the next section.

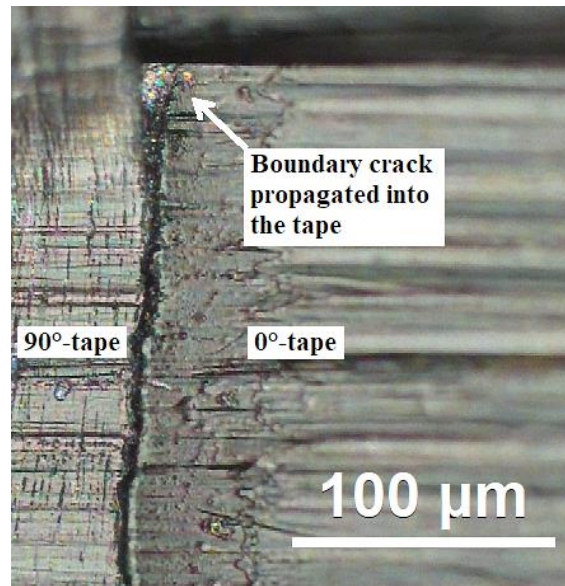


Figure 4.31 Optical micrograph of a boundary crack propagating into the tape in a 0.6 mm SRPP tensile specimen.

4.2.3.1.2 Development of boundary cracks into critical damage

In this section, surface strain analysis is used to illustrate how the boundary cracks between 90°-tapes ($BC_{\parallel}^{90^{\circ}}$) can lead to specimen failure. Figure 4.32 in the next page shows typical surface strain patterns at low to mid-ranges of applied strains (Figure 4.32a) and high applied strains (Figure 4.32b), captured using a DIC system. All SRPP specimens initially exhibit undulating surface strain patterns that match the weave pattern (Figure 4.32a), and then the weave pattern becomes less pronounced with further deformation, due to the emergence of strain localisation bands in which the strains get concentrated (Figure 4.32b). The strain localisation bands are similar to Lüders bands observed in metals, which are localised bands of plastic deformation on a macroscopic scale. However, the band fronts in SRPP are distinctively different to those seen in Lüders bands in that they are perpendicular to the loading direction, as opposed to being inclined at an angle to it.

The strain localisation bands likely promote the development of unusually high local strains that appear within the bands, or vice versa. Such an unusually high local strain will be referred to as a *high-strain concentration point (HSCP)* from now on, as indicated in Figure 4.32b. These points can reach strain values that are around double that of the average strain in the specimen. Due to such a high level of strain concentration, failure always initiates from an HSCP. This can be seen from the DIC system.

In the DIC system, the computed strains can be overlaid on top of the digital image of the specimen that was recorded by the system. From this, the HSCPs can be located in the stochastic pattern that was painted on the specimen. Then, by scrutinising the stochastic pattern on the actual specimen, it is possible to map the location of each HSCP shown in the system to a physical location on the specimen.

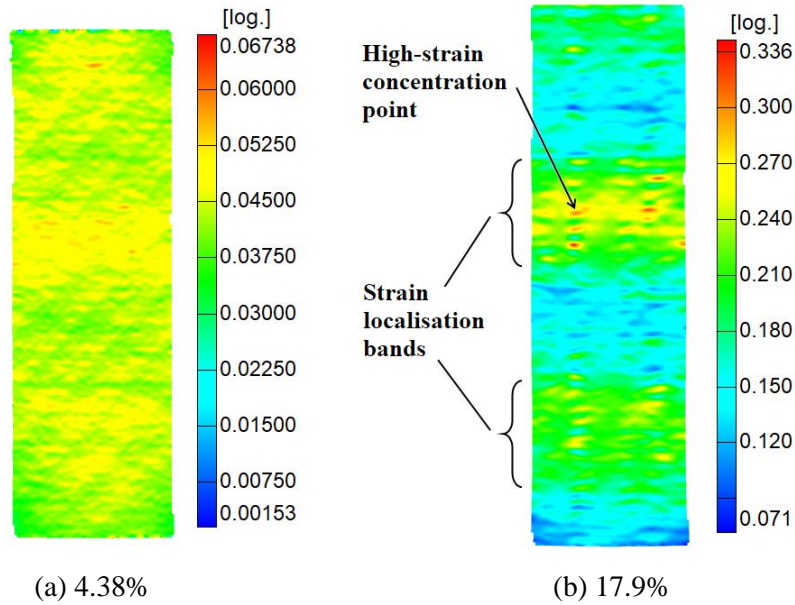


Figure 4.32 First principal strain of a 0.3 mm SRPP tensile specimen at applied strains of a) 4.38% and b) 17.9%.

It can then be seen by studying a failed specimen that the failure occurred across the specimen where there was at least one HSCP, as shown in Figure 4.33. Since this occurred in all specimens in the tested sample, it can be deduced that this is a consistent behaviour of the material.

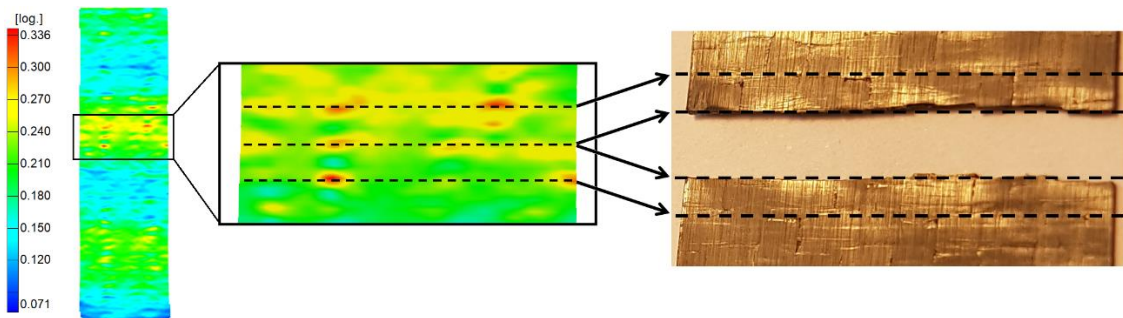


Figure 4.33 First principal strain on the front surface of a 0.3 mm SRPP tensile specimen at an applied strain of 19.4% (left) and a photograph of the back of the specimen after failure (right). Arrows and dotted lines indicate corresponding sections along the edges of 90°-tapes.

Using this method, it is also possible to see where in the weave structure each HSCP occurs. After identifying the location of the strain points of interest, the surface paint can be wiped off to reveal the weave structure on the front of the specimen, or the specimen can be flipped to show the weave structure on the reverse side. This shows that:

- All HSCPs occur along the edges of 90°-tapes, in one layer or the other, as shown in Figure 4.33.

- HSCPs on a $BC_{\parallel}^{90^{\circ}}$ boundary can induce other HSCPs to appear where there is no $BC_{\parallel}^{90^{\circ}}$ boundary. This can be deduced from the fact that some HSCPs that do not occur at a $BC_{\parallel}^{90^{\circ}}$ appear at locations above or below an HSCP that occurs at $BC_{\parallel}^{90^{\circ}}$, after the HSCP at $BC_{\parallel}^{90^{\circ}}$ appears.
- Failure only occurs across an HSCP that is on a $BC_{\parallel}^{90^{\circ}}$ boundary.

The above process of verifying where in the weave structure HSCPs occur is accurate but time consuming. Having verified that HSCPs always occur at locations coinciding with the edges of 90° -tapes, there is a quicker way of identifying which ones likely occur on a $BC_{\parallel}^{90^{\circ}}$ boundary. This can be done by first noting that strain patterns reflect that of the weave pattern when the applied strain is sufficiently low, because of the segments that display higher strains than the surrounding area. These *high-strain segments* are aligned to HSCPs, occurring along the edges of the 90° -tapes. An example is shown in Figure 4.34.

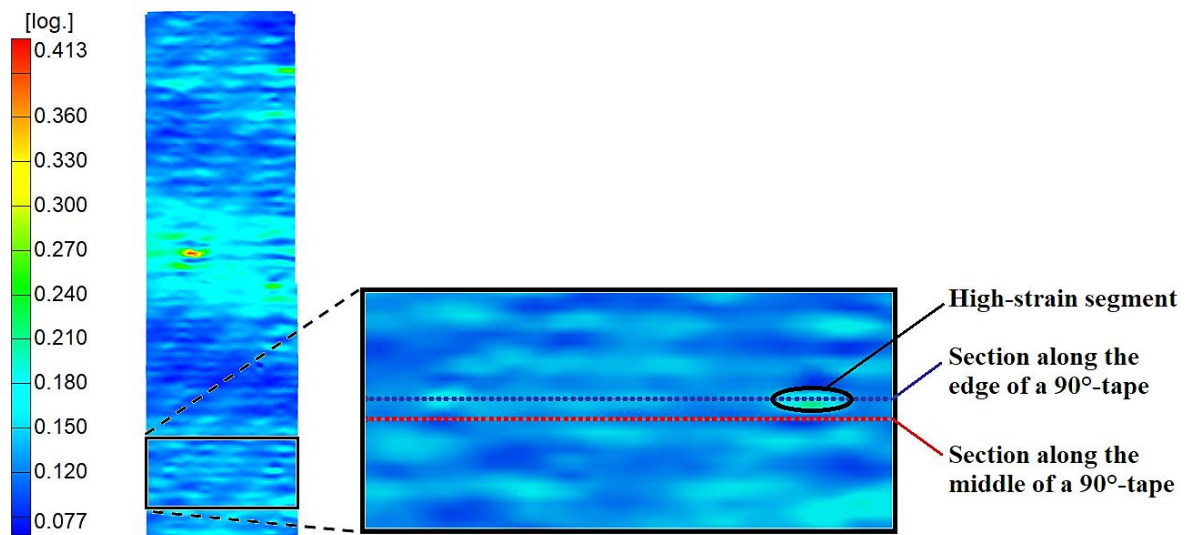


Figure 4.34 First principal strain on a surface of a 0.3 mm SRPP tensile specimen at an applied strain of 13.3%, showing an example of a high-strain segment and sections along the edge and the middle of a 90° -tape.

Given that the high-strain segments occur periodically along the edges of 90° -tapes, they must correspond to parts where the 90° -tapes are on the surface (Figure 4.35a), where 0° -tapes are on the surface (Figure 4.35b), or where 0° - and 90° -tapes meet (at $BC_{\perp}^{90^{\circ}}$, Figure 4.35c). From the length and the frequency of the segments, these cannot be occurring at $BC_{\perp}^{90^{\circ}}$ (Figure 4.35c), since $BC_{\perp}^{90^{\circ}}$ occur more frequently (every 2 x tape widths) than the high-strain segments (every 4 x tape widths).

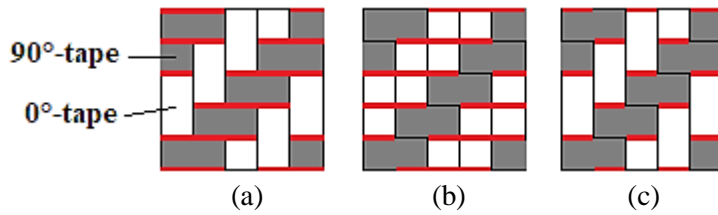


Figure 4.35 Possible locations where high-strain segments (red lines) occur, in relation to the weave structure.

Therefore, high-strain segments must correspond to strains peaking at $BC_{\parallel}^{90^\circ}$ on the surface, as illustrated in Figure 4.35a. This can be deduced from the congruency in geometry (the high-strain segments and edges of the 90° -tapes have the same alignment). Also, a matrix crack at $BC_{\parallel}^{90^\circ}$ is the most likely candidate for strain concentrations, as there is no evidence or valid reason for the strain to be high across the width of a 0° -tape. Therefore, surface strain must be high from $BC_{\parallel}^{90^\circ}$ and suppressed when 0° -tapes weave over 90° -tapes on the surface.

Based on the above finding, an HSCP can be identified as occurring on a $BC_{\parallel}^{90^\circ}$ on the surface if it develops from a high-strain segment. There is a limitation, however, that a high-strain segment can only give an approximate location of a $BC_{\perp}^{90^\circ}$ because there is no distinct boundary between a high-strain segment and the surrounding area, as could be seen from Figure 4.34. The precision of the DIC can be increased to combat this but this would limit the measuring area.

The fact that high-strain segments coincide with $BC_{\parallel}^{90^\circ}$ boundaries on the surface enables an analysis of how the surface strain fluctuates according to the weave geometry. An example is shown in Figure 4.36 in the next page, where strains along the edge and middle of a 90° -tape have been plotted (bottom), with a corresponding image of the weave pattern (top). Markers indicate peak strains occurring at $BC_{\parallel}^{90^\circ}$ and the trough strains in the tape near $BC_{\parallel}^{90^\circ}$.

Figure 4.36 shows that, in a low to mid-range level of applied strain, the single most influential factor that causes the fluctuation in the surface strain is the presence of $BC_{\parallel}^{90^\circ}$. This can be seen from the following observations:

- Large peaks occur at $BC_{\parallel}^{90^\circ}$ as expected, although not all $BC_{\parallel}^{90^\circ}$ cause significantly large strains.
- Peak strains at $BC_{\parallel}^{90^\circ}$ cause strains to be lower in the tapes above and below the $BC_{\parallel}^{90^\circ}$. This is because the total strain along any axis along the loading direction must be equal to the applied load. Due to this, strains along the tape are almost completely out of phase with strains along the edge.
- There is no significant difference in the strain that is caused by the difference in tape orientations.

These observations collectively indicate that it is $BC_{\parallel}^{90^\circ}$ that causes fluctuation in strains in SRPP, as opposed to the orientation of the tapes.

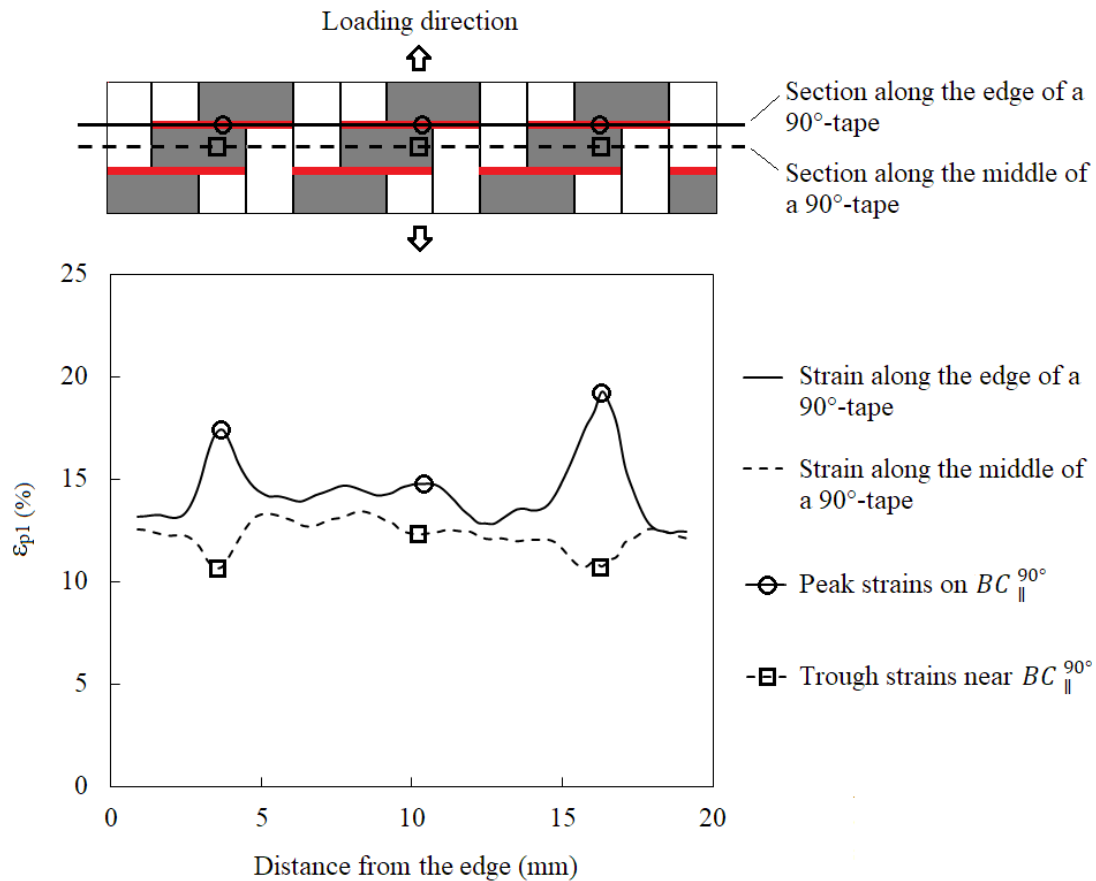


Figure 4.36 Plot of first principal strain (ϵ_{p1}) on sections along the edge and middle of a 90° -tape of a 0.3 mm SRPP specimen (bottom), and a diagram of the corresponding weave structure (top).

The above findings agree with the hypothesis of [183] but offer somewhat differing reasoning. [183] also used DIC to explain the undulation in the surface strains of a woven SRPP. The author suggested that the undulation is caused by the strains being higher in surface regions containing 90° -tapes and their boundaries, compared to regions containing 0° -tapes and their boundaries. The reason given was that a higher proportion of strain occurs in the matrix. The idea is illustrated in Figure 4.37. The surface strain analysis, however, shows that this reasoning is not quite correct.

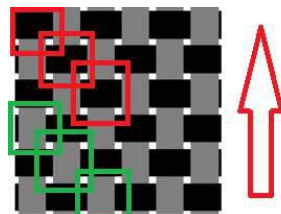


Figure 4.37 Cause of the textured surface strain according to [183, p. 202, Fig. 6.19], reproduced from the same literature.

The strain analysis shows that $BC_{\parallel}^{90^\circ}$ is the only factor that gives the fluctuating surface strain pattern that matches the weave style. The hypothesis by [183] is not incorrect, since $BC_{\parallel}^{90^\circ}$ occurs around 90° -tapes only. However, $BC_{\parallel}^{90^\circ}$ does not occur in *all* matrix regions around the perimeter of 90° -tapes as is implied in [183]'s illustration in Figure 4.37. There is actually no $BC_{\parallel}^{90^\circ}$ in Figure 4.37 because a plain weave pattern was used to demonstrate the point, despite the fact that 2/2 twill weave specimens were also used in [183]. This shows a lack of understanding of the correct cause of the phenomenon, likely due to the fact that a lower level of precision was used in [183]'s DIC setup, which has the effect of averaging the strains over wider areas.

Combining the above surface strain analysis and the microscopic analysis of boundary cracks from the previous section, the cause of failure in 0.3 mm SRPP specimens can be summed up as follows:

Concentration of strain occurs in the loading direction from the brittle damage in the matrix between the edges of two 90° -tapes. This induces lower strain levels in the surrounding tapes, such that the total strain along any axis parallel to the loading direction is equal to the applied strain.

Some strain concentration points grow particularly large (HSCPs) in the strain localisation band, where strains are generally higher than in other parts of the specimen. The HSCPs can promote further growth on damage at other points that are also on the edges of 90° -tapes but not necessarily where two 90° -tapes meet.

One of the HSCPs that occurs between two 90° -tapes becomes the critical point of failure. Once the strain concentration becomes large enough at the failure point, the surrounding 0° -tape(s) would break. Then, the damage propagates rapidly in an unstable manner, leading to a significant reduction in the load-bearing capacity. This results in an abrupt, macroscopically brittle failure across the specimen's width.

From this, it can be seen that boundary crack of type $BC_{\parallel}^{90^\circ}$ is the most critical type of damage that occurs in the 0.3 mm SRPP specimens. It will later be shown that this is also the case for thicker SRPP specimens, but the damage does not cause the same immediate failure of the specimen in the thicker specimens.

It should be noted that this finding does not agree with some of the literature on SRPP. One piece of research stated that failure occurred from reinforcement breakage which then led to subsequent matrix failure [108], whereas another suggested all damage occurred due to reinforcement or reinforcement-matrix interactions instead of damage occurring in the matrix [42]. As was pointed out in the literature review, such misconceptions probably arose due to the former study not focusing on the damage characteristics at a microscopic level, and the latter making the assumption that the matrix behaves in the same way as plain PP (which it does not, as shown in Section 2.3.2). It is also possible that the

difference in findings in [42] is due to the material having been manufactured using different techniques, which can affect the material behaviour rather significantly, as pointed out in the literature review.

On the other hand, [41] conjectured that matrix failure occurred at the yield point and that it is desirable to produce a matrix that remains as ductile as possible until failure in the reinforcement. Based on the findings in this chapter thus far, it is likely that this conjecture is accurate. This may also be due to the fact that the SRPP used in [41] was manufactured using the same techniques and reinforcement type as the SRPP used in this research, producing very similar microstructures and therefore material behaviour.

4.2.3.1.3 Prediction of failure in 0.3 mm specimens

The previous section showed that critical damage occurs at the boundary between 90°-tapes and cause the appearance of HSCPs. This section will build on this and analyse which of these can cause specimen failure. It will also discuss methods of predicting at what point in the process of deformation that failure is likely to occur.

It must first be realised that neither the failure strain nor the strength of material specifications are good indicators of failure for 0.3 mm SRPP, despite the fact that these are the most common measures used to predict when a material is likely to fail. Firstly, the failure strain is a statistical average value established from testing a sample of the material and there is simply too wide a variation in the sample ($14 \pm 5\%$). Secondly, there is less of a variation in the strength value but, given the low tangential stiffness of the 0.3 mm specimen after its yield point, a small deviation in stress results in a large deviation in strain. The result is that when using the average strength value, failure can be predicted to occur at a much earlier or later stage in the deformation process than the actual point at which the specimen fails. Hence, different ways of predicting when and where failure occurs in a 0.3 mm specimen are explored using the surface strain analysis.

The location of failure, or the failure point, can be identified using surface strain analysis. To explain, Figure 4.38 illustrates the progression of surface strains in a 0.3 mm specimen at different stages of deformation. The final image (Figure 4.38c) shows the state of the specimen immediately prior to specimen failure, which occurs along the dotted line. In this specimen, HSCPs A and B are the maximum ϵ_{p1} points during the mid-stage and final stage of deformation at applied strains of 4.2–11% and 11–13%, respectively. Strains at these points are plotted against the applied strain in Figure 4.39, with the average strain of the specimen shown for comparison.

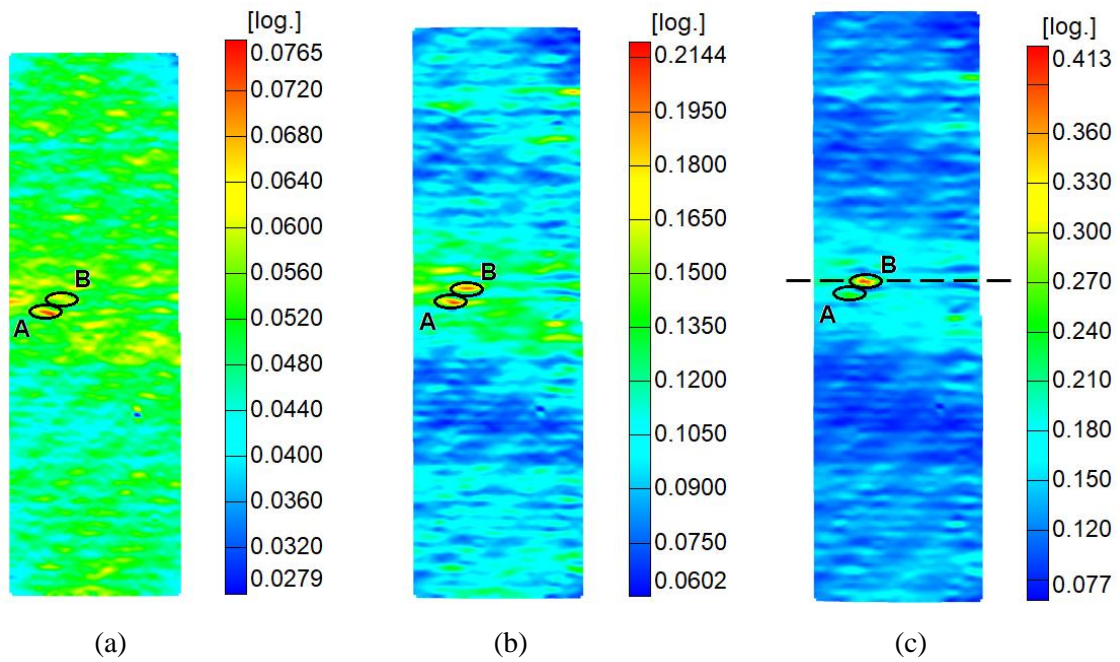


Figure 4.38 First principal strains of a 0.3 mm SRPP tensile specimen at applied strains of a) 5.0%, b) 10.0%, and c) 13.3% (last stage before specimen failure). Points A and B are points of maximum strain at different stages of deformation. Failure occurs along the dotted line in (c).

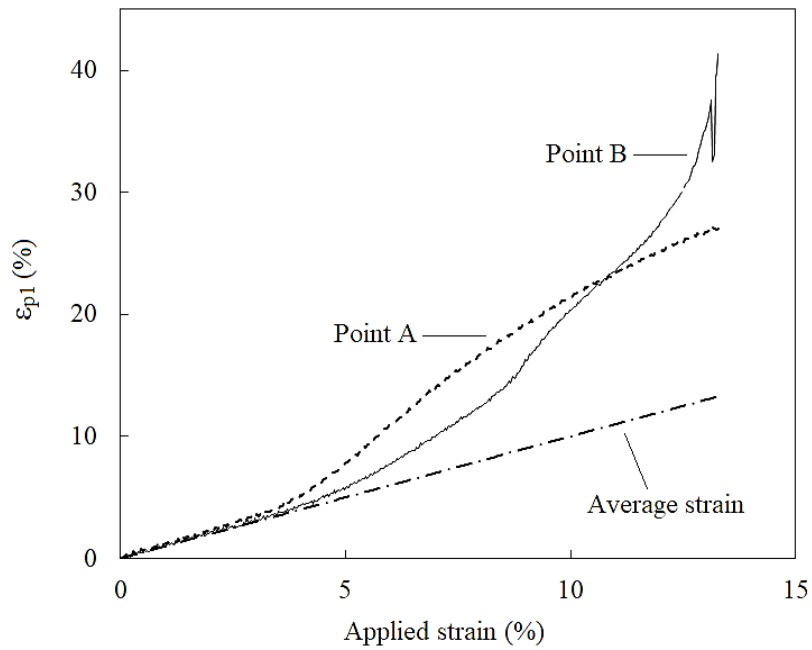


Figure 4.39 First principal strain (ϵ_{p1}) against the applied strain for points A, B and the average strain of the specimen in Figure 4.38.

From Figure 4.39, it can be seen that specimen failure initiates at point B, based on the rapid increase in strain before failure and the fact that failure occurs across point B. By failure, the maximum strain in the specimen occurs at point B (41.3%), which is triple that of the average strain or the applied strain (13.7%). From these observations, three possible indicators of specimen failure can be considered, where failure occurs when the indicator exceeds a threshold value: 1) Magnitude of the maximum strain ($|\epsilon_{max}|$), 2) rate of strain growth at HSCPs (gradient of strain increase, $F = \frac{d\epsilon_{HSCP}}{d\epsilon_{applied}}$), or 3) ratio between the maximum strain and the average or applied strain ($\iota = \frac{\epsilon_{max}}{\epsilon_{applied}}$).

As with the failure strain, these measures have very large variations between specimens, as shown by the sample statistics in Table 4.3 below. Relative standard deviations (standard deviation as a percentage) are given for comparison across the different measures. Due to this, it may appear that these are also unreliable measures for failure criteria. This is true for $|\epsilon_{max}|$. However, the threshold for F and ι can be set at low values to make them more reliable indicators, because the specimens will fail within a very narrow range of applied strain after reaching the threshold values.

Table 4.3 Sample statistics of 0.3 mm SRPP on possible indicators of failure.

Sample statistics	$ \epsilon_{max} $ (%)	F in the last 0.5% strain of the maximum strain point ¹	ι ²
Average \pm standard deviation	38 ± 14	18 ± 10	2.7 ± 0.5
Relative standard deviation	$\pm 37\%$	$\pm 55\%$	$\pm 19\%$
Range	32	24	0.9

¹ F is the gradient of strain increase at high strain concentration points in relation to the applied strain is increased. Secant gradient of the curve 'local strain versus applied strain', calculated based on the point of failure and a point at which the applied strain is 0.5% or 1.0% less than at failure.

² ι is a ratio between maximum strain and the applied strain.

³ Strains given are first principal strains.

For example, the F just before failure in this sample ranged between 8.0 and 32. If the threshold is set at 8.0, then all specimens fail within 0.5% applied strain after exceeding the threshold. This is possible because failure points exhibit such rapid increase in F . There is the caveat that only a very small window exists between detecting the onset of failure and the actual failure. In this sense, it is not a very robust indicator, but the threshold can be set lower for an additional margin of safety. For example, if the threshold gradient is 5, specimens will fail between 0.4 –1% applied strain after exceeding the threshold.

A similar concept applies to ι , the ratio between maximum strain and the applied strain. Although ι varies largely between specimens (in this case, between 2.2 and 3.1), the threshold can be set low and the specimens will fail soon after exceeding the threshold. For example, all specimens failed within 2.8% applied strain of reaching ι of 2.1. Because ι is normalised by the applied strain, the change in ι is less rapid and the variation within the sample is lower than other measures. It is also easier to detect in a sense that only the maximum strain at any applied strain is required, as opposed to requiring the strain history to work out F. Therefore, the ratio between the maximum strain and the applied strain (ι) appears to be the best indicator of *when* (at which stage of the deformation) failure is likely to occur.

In terms of detecting the *location* of failure, the increase in F (gradient of strain increase) is a better indicator than ι . ι is not a good indicator because multiple HSCPs can occur in a specimen which maintain similar levels of strain until failure, as shown in Figures 4.40 and 4.41. As can be seen, it is difficult to determine, just by looking at the magnitude of strain or the ratio to the applied strain, which will become the point of maximum strain that causes failure. The increasing F gives a more obvious indication as to which point will ultimately cause failure. However, a noticeable increase in F can appear very close to failure, as mentioned before. To combat this, another measure, strain path, can be used to give an earlier indication of where failure will occur.

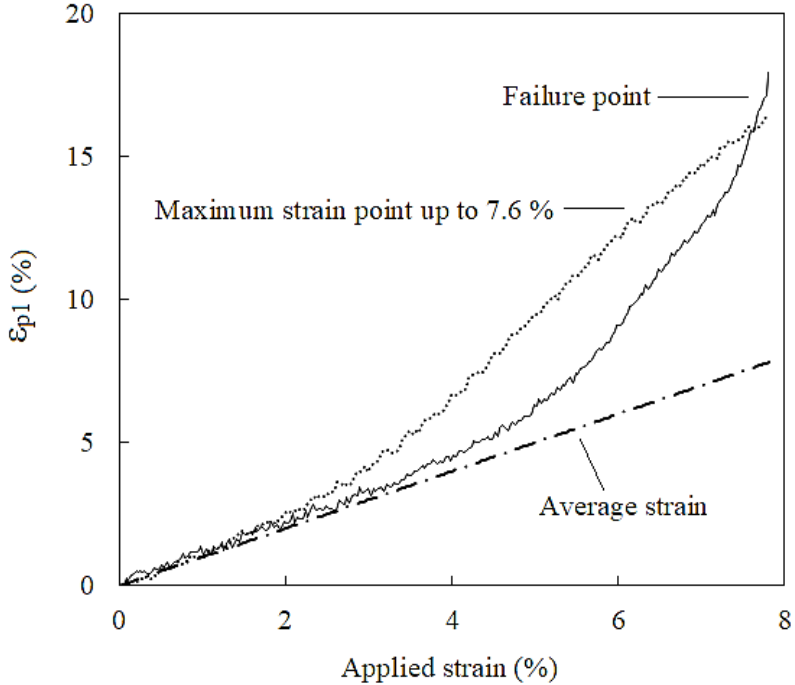


Figure 4.40 First principal strain (ϵ_{p1}) against the applied strain for a maximum strain point, failure point and the average strain in a 0.3 mm SRPP tensile specimen.

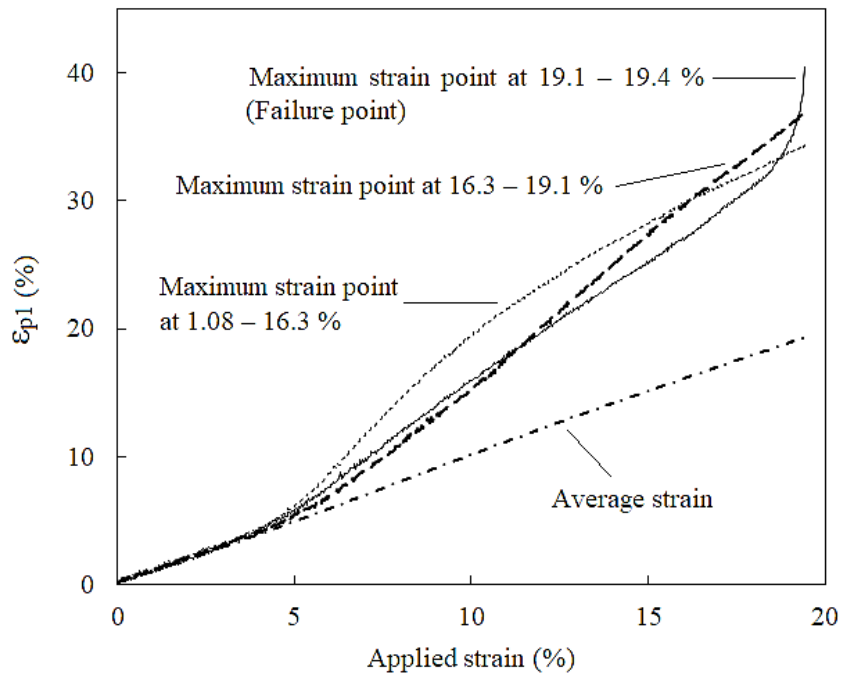


Figure 4.41 First principal strain (ϵ_{p1}) against the applied strain for maximum strain points and the average strain in a 0.3 mm SRPP tensile specimen.

In all 0.3 mm specimens, the failure point exhibited a strain path (of principle strains) that matched closely with that of the average strain of the specimen. This is illustrated in Figure 4.42a in the next page, for the specimen shown in Figure 4.38. As can be seen, point B, which was identified as the failure point, has a strain path that closely matches that of the average strain in the specimen. In contrast, the strain path at point A deviates from that of the average strain when the applied strain reaches approximately 5%. Due to the deviation, point B can be identified as the failure point by around 6% applied strain, as can be seen in Figure 4.42b. Using this approach, the strain path of HSCPs can indicate the failure point in 0.3 mm specimens by around 3–6% applied strain, which is around a quarter to a third of the applied strain to failure.

Interestingly, the strain path of the average strain of the specimen also changes from its original trajectory when the strain paths of non-failure points deviate from that of the average strain, at around 2–5% applied strain. The strain path of the specimen changes due to a decreased rate of reduction in the width. It is important to note this is also where HSCPs begin to appear. Given that the strain concentrations are caused by matrix damage at the tape boundaries, the change in the specimen's strain path likely reflects a widespread growth of such boundary cracks over the entire specimen. Interestingly, yielding phase in the stress-strain curve also occurs around 2–5% applied strain. This verifies Hine et al.'s theory [41] that yielding in SRPP must occur due to matrix failure, since plain PP yields around a similar strain. Although this does not negate postulation from other research; for example, that tie molecules in the amorphous phase start to flow at yield point, it does seem questionable whether both matrix failure and flow in tie molecules are likely to occur at the yield point.

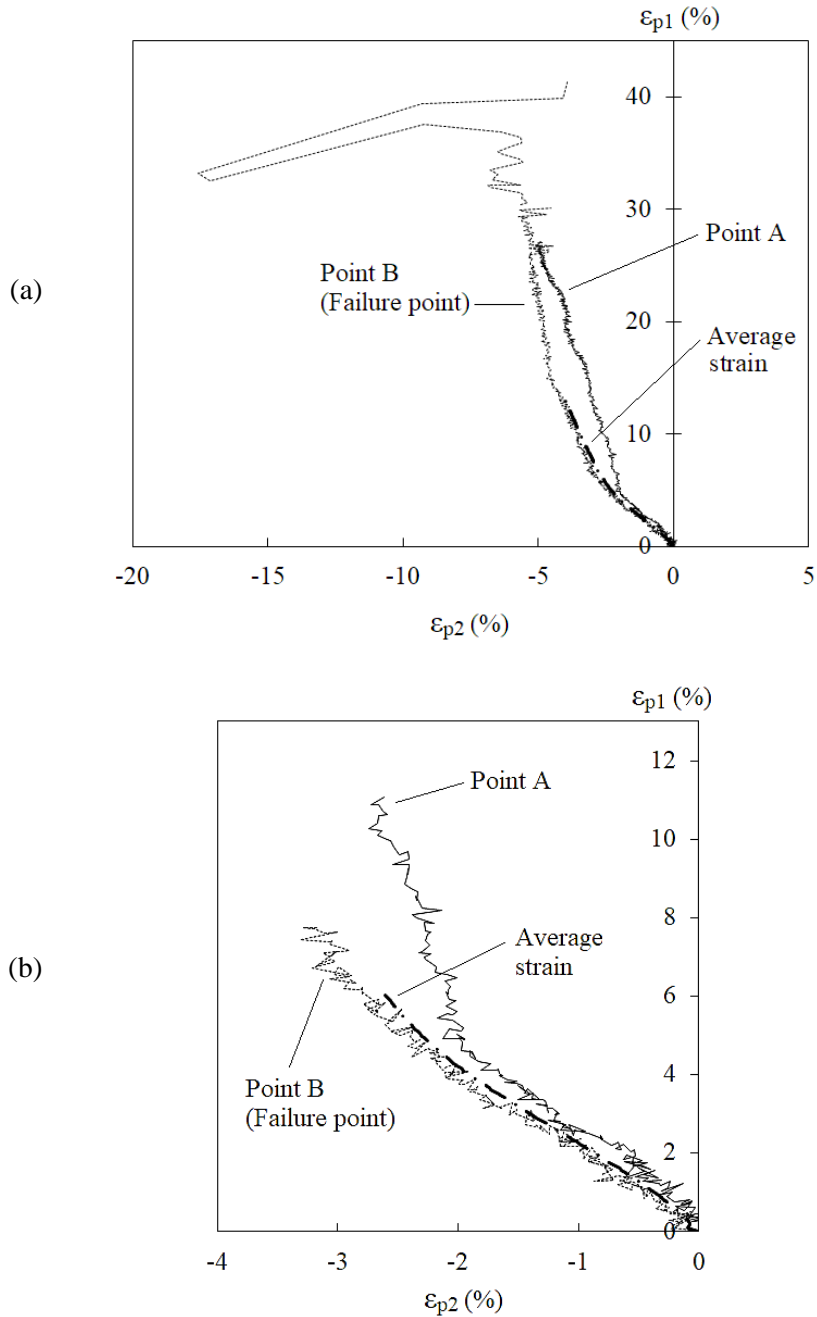


Figure 4.42 Strain paths of points A, B and the average strain of the specimen in Figure 4.38, a) up to failure, and b) up to 6% applied strain. Strains are given in first (ϵ_{p1}) and second (ϵ_{p2}) principal strains.

It can be seen from analysing the strain path that failure occurs at an HSCP whose strain path in the principal strain space closely follows that of the average strain of the specimen. However, there is an exception to the case, in that this does not apply when the failure point occurs on the edge of the specimen, as shown in Figure 4.43. Points A, B and C in the figure indicate locations of maximum strain when the applied strain is 1.08–16.3%, 16.3–19.1%, and 19.1–19.4%, respectively. As specimen failure occurs across points B and C, it is expected that one of these is the failure point. Evolution of strains at

these points against the applied strain were plotted earlier, in Figure 4.41. The plot showed that point C is the failure point, as the strain at this point increases rapidly and becomes the maximum strain point towards specimen failure. However, strain at point C does not exhibit a similar strain path to the average strain, as shown in Figure 4.44.

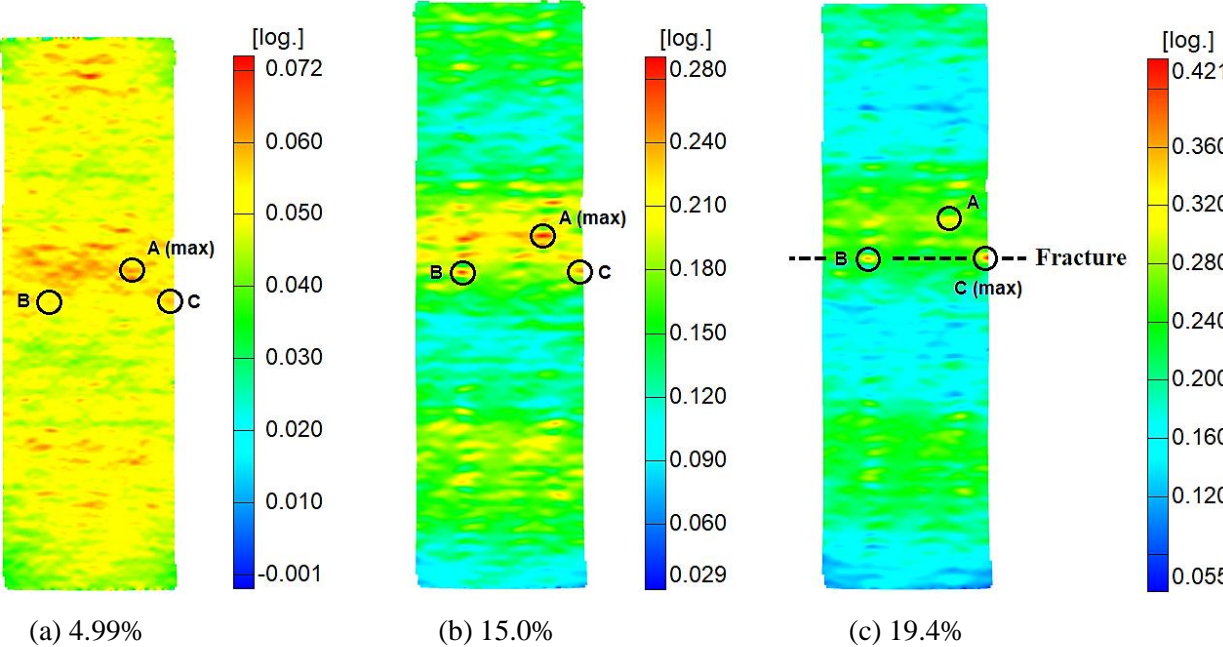


Figure 4.43 First principal strains of a 0.3 mm SRPP tensile specimen at applied strains of a) 4.99%, b) 15.0% and c) 19.4% (last stage before specimen failure). Points A, B, and C are points of maximum strains at different stages of deformation. Failure occurs along the dotted line in (c).

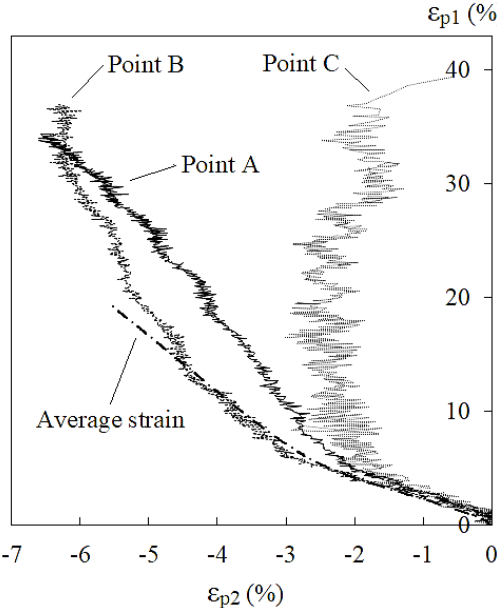


Figure 4.44 Strain paths of points A, B and C and the average strain in the 0.3 mm SRPP tensile specimen in Figure 4.43. Strains are given in first (ϵ_{p1}) and second (ϵ_{p2}) principal strains.

On a less important note, it may seem that failure occurred across points B and C due to the alignment of multiple HSCPs. However, this is unlikely. In the specimen shown in Figure 4.45, failure has occurred along a line where there is only one HSCP (point A), even when there is another line along which two HSCPs occur (points B and C). Therefore, failure must occur independently of the multiplicity of HSCPs that are collinear. In the specimen in Figure 4.45, the failure point (point A) had a similar strain path as the average strain of the specimen, an increasing strain growth before failure, and was the maximum strain before failure.

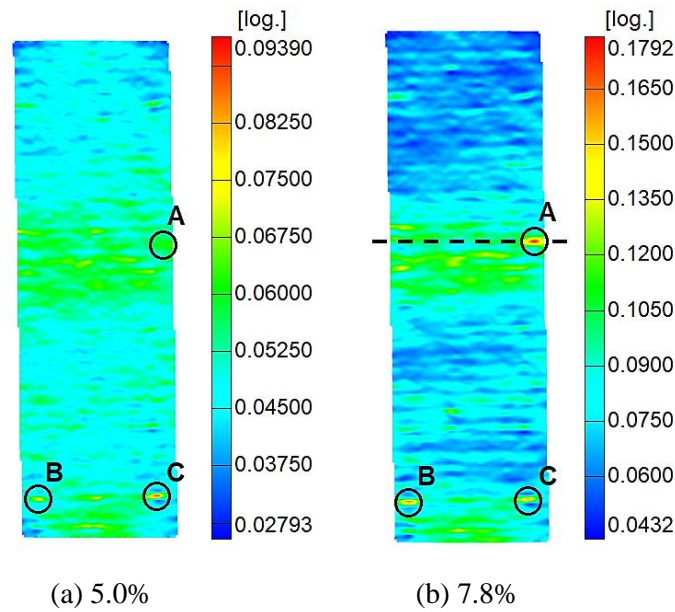


Figure 4.45 First principal strains of a 0.3 mm SRPP tensile specimen at applied strains of a) 5.0% and b) 7.8% (last stage before specimen failure). Points A and C are points of maximum strain at different stages of deformation, and point B is an HSCPs. Failure occurs along the dotted line in (b).

To sum up, failure of a 0.3 mm specimen can be predicted according to the following rules:

1. Failure occurs when the ratio between the maximum and average strains in the specimen $\left(r = \frac{\varepsilon_{max}}{\varepsilon_{applied}} \right)$ exceeds a threshold value.
2. Point of failure occurs at an HSCP that exhibits a strain path in the principal strain space that is close to the strain path of the average strain of the specimen, unless it occurs on the edge of the specimen.
3. If there is an HSCP on the edge of the specimen, the point of failure can be identified as the HSCP that exhibits a gradient of strain increase $\left(F = \frac{d\varepsilon_{HSCP}}{d\varepsilon_{applied}} \right)$ above a threshold value, which can be established experimentally.

This section showed that the above indicators derived from surface strain measurements can help predict when and where failure is most likely to occur. The significance of being able to predict when and where failure is likely to initiate is that a specimen can be unloaded at various stages of deformation to inspect the critical damage development. However, it should be noted that tracking down the exact point of damage would be a non-trivial task as it requires manual identification of a point in the fine stochastic pattern in both the DIC image and the specimen. Also, failure cannot realistically be predicted real-time, since DIC is typically carried out after digital images are taken. Computation of strains and calculations based on strains, such as the strain path, are not available real-time. Despite the limitations, it is still a useful method for analysing the failure behaviour.

The next section will discuss the ways in which cracks propagate in the failure process of 0.3 mm SRPP specimens. It will first discuss what phases cracks propagate through during fracture. It will then discuss how cracks propagate in ways that cause both brittle and ductile failure at a microscopic scale, in the same specimen.

4.2.3.1.4 Crack propagations during failure of 0.3 mm specimens

Although failure occurs at a boundary crack, not all boundaries between tapes are so weak as to create a preferential path through which a fracture can propagate. In 0.3 mm SRPP, it may first appear as if failure propagates preferentially along the edge of a 90°-tape because the fracture path seems to coincide with it. However, careful observation shows that failure initiates at a boundary between 90°-tapes and then propagates along a path approximately perpendicular to the load, which happens to coincide mostly with the edge of tapes.

However, this is not to say that a single crack originating from the boundary crack at a failure point makes up the entire fracture path in specimen failure. It appears that failure does initiate and propagate from the failure point but existing cracks in the general direction of the fracture path coalesce with the main crack that originated from the failure point. An example can be seen in the crack branching occurring on the fracture path, as shown at A and B in Figure 4.46. At these points, a crack continues to propagate for a short distance along the original trajectory of the fracture path, while the actual fracture path deviates from its original trajectory in a step-like discontinuity. Since this occurs in the opposite directions at A and B, three cracks likely initiated and then coalesced, one from below A, one from above B and one from between A and B.

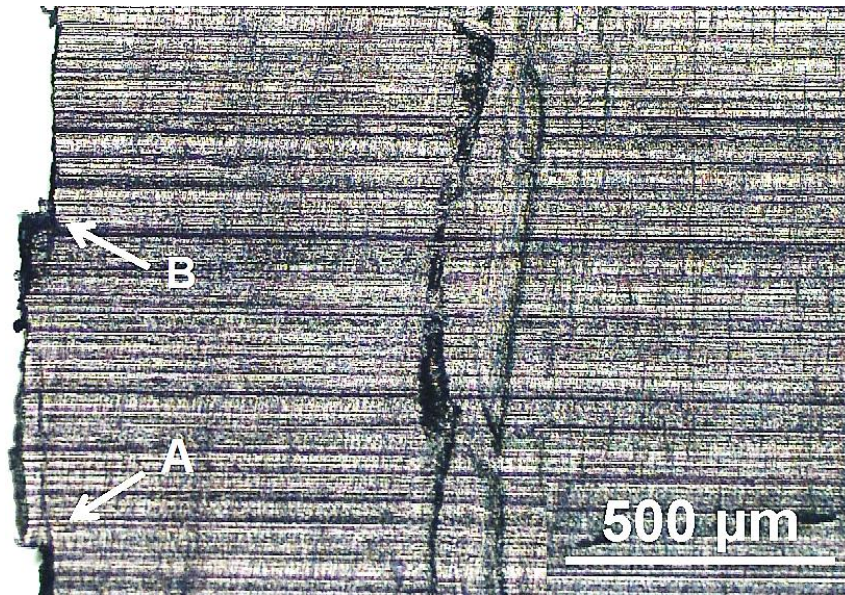


Figure 4.46 Optical micrograph showing brittle fracture in a 0.3 mm SRPP tensile specimen. A and B indicate crack branching.

Failure mostly propagates through the plane normal to the loading direction, as shown in Figure 4.46. However, it can also propagate through the plane of the specimen, as shown in Figure 4.47. This is somewhat like delamination but spans a broader range of depth over a shorter distance than the delamination in thicker specimens. It is therefore conjectured that the crack causing specimen failure propagated through multiple phases (tape and matrix). Since delamination in a composite implies a separation of two constituent layers by cracks propagating between the layers, instead of through the layers, this behaviour has not been classified as delamination.

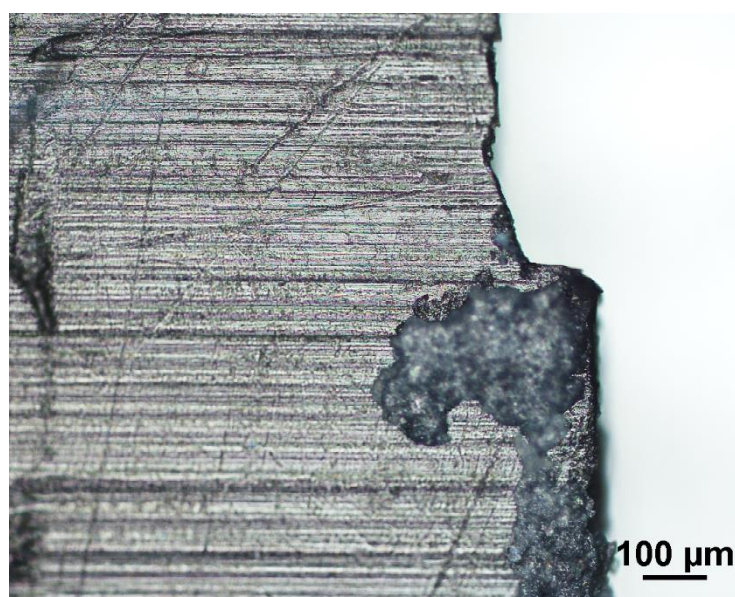


Figure 4.47 Optical micrograph of a 0.3 mm SRPP tensile specimen showing brittle fracture.

During the study of 0.3 mm specimens, a unique aspect of crack propagation during failure was observed that has not been observed in other studies of SRPP: The 0.3 mm specimen exhibits both brittle fracture surfaces and ductile fracture surfaces in a *single* specimen. Examples of fracture surfaces created from brittle and ductile failure are shown in Figures 4.48a and 4.48b, respectively, discernible by their rough or smooth morphologies.

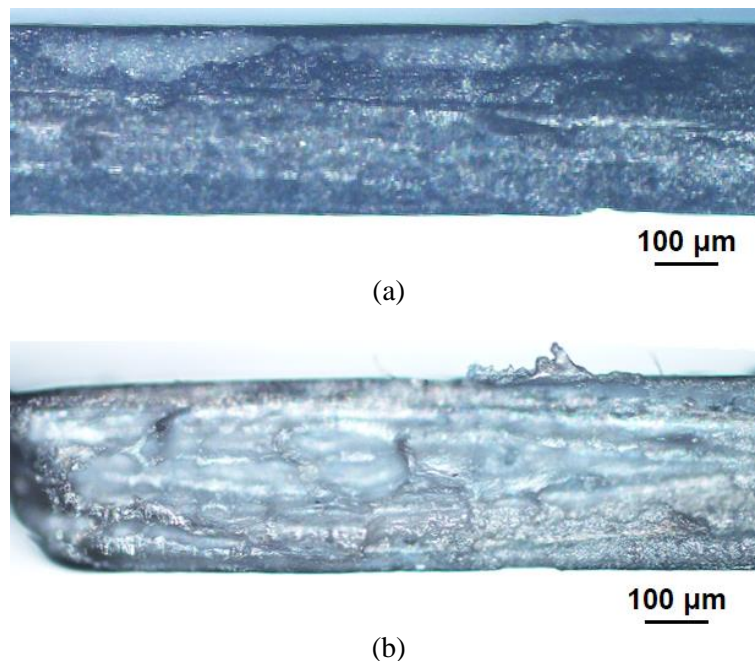


Figure 4.48 Optical micrographs of a) brittle and b) ductile fracture surfaces of 0.3 mm SRPP tensile specimens. The direction of the applied load is orthogonal to the page.

Brittle and ductile failures can actually *co-occur* in very close vicinity, as shown in Figure 4.49. It can be seen by focusing the microscope at different depths through the thickness that brittle fracture occurred on the top surface and ductile failure occurred on the bottom surface. This is an atypical observation. Although polymers can undergo both brittle and ductile failures, this mostly relates to the so-called Brittle-Ductile (BD) transitions¹⁰ where the mode of failure switches from one to another due to changes in temperature, strain rate, thickness, material composition, or thermal shock, instead of both modes occurring *concurrently*.

¹⁰ There are two Brittle-Ductile (BD) transition points in amorphous and semi-crystalline polymers. At the first BD transition point, crazing or brittle fracture occurs predominantly with the breaking of chains at low temperatures or with a high strain rate, but failure mode transitions to shear or ductile failure with an increase in temperature or a decrease in the strain rate [131]. The first transition occurs at around 0-20°C at 100%/minute in PP [232]. The second BD transition (or DB transition) occurs at a high temperature or at a lower strain rate than the first BD transition point. The second BD transition changes the failure mode from ductile to brittle with an increase in temperature or a decrease in strain rate. Crazing occurs again in this case but as a result of different mechanisms [131].

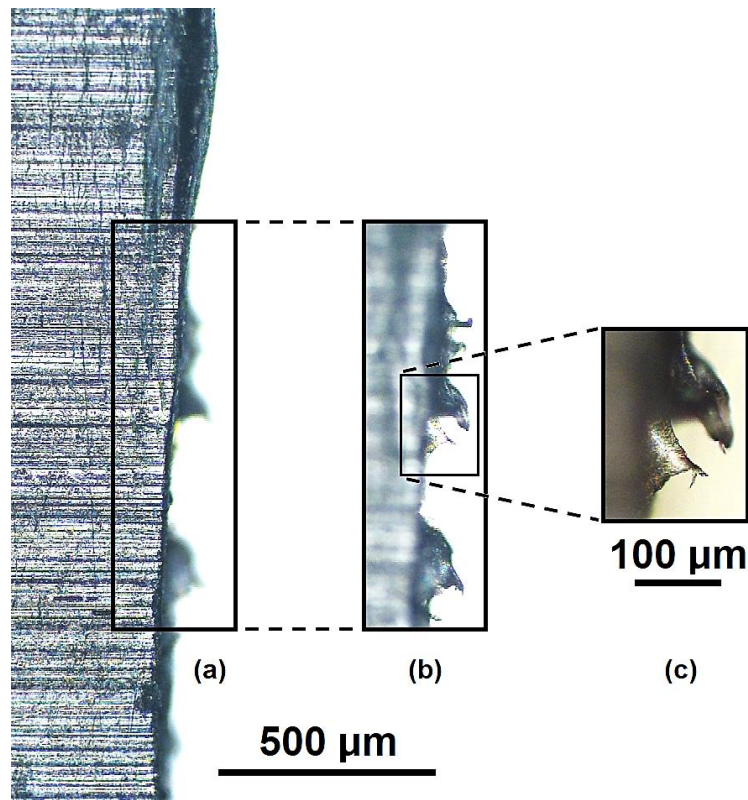


Figure 4.49 Optical micrograph of fracture in a 0.3 mm SRPP tensile specimen, showing both brittle and ductile characteristics. (a) is focused on the upper surface, (b) is focused further from surface, and (c) shows an area in (b) at a higher magnification.

There are very few studies that touch on the subject of different fracture modes in SRPP. One such study is on a hybrid carbon fibre/SRPP composite but on the subject of BD-transition with changes in the layup or the volume fraction of carbon fibres [190]. Another study reported that SRPPs consolidated at 190°C exhibited brittle fracture with no signs of plastic deformation in a sample with α -PP matrix, whereas a sample with β -PP matrix showed stable behaviour with fully yielded ligaments before crack propagation¹¹ [97]. However, it should be noted that both studies refer to changes in the fracture mode occurring when the material composition has been changed, effectively creating different material samples. In contrast, it is observed in the 0.3 mm SRPP that two different failure modes occur in the same specimen.

It may initially be postulated that the tape and matrix induce the different modes of failure because of the difference in their microstructures. An example of work that supports this is the study of an SRPE created by OPIM, in which a less-oriented core layer failed in a ductile manner and the outer layer that had a higher molecular alignment failed in a brittle manner [101]. However, it was shown earlier that ductile or brittle crack propagation can occur in both the tape and the matrix, depending on the direction

¹¹ This is similar to fracture modes in isotactic PP under tension at room temperature, where alpha- (α) spherulites exhibit brittle behaviour while beta- (β) spherulites go through extensive plastic deformation [133].

of crack propagation relative to the tape orientation and the weave geometry, respectively. Therefore, the phase difference alone does not influence the mode of failure.

The most convincing hypothesis is that the tape orientation and the weave geometry tend to induce a particular mode of crack propagation. If so, the influence of tape orientation would be higher than the weave geometry, since the tape volume fraction is higher than the matrix volume fraction.

If this hypothesis is correct, the phenomenon in Figure 4.49 can be explained. Brittle failure occurred in the 90°-tape on top (Figure 4.49a) and ductile failure occurred in the 0°-tape(s) below (Figure 4.49b), due to cracks propagating in parallel and perpendicular directions to the tape orientation, respectively. Figure 4.50 shows an example of brittle failure occurring in a 90°-tape and ductile failure in a 0°-tape due to the direction of crack propagation in relation to the tape orientation.

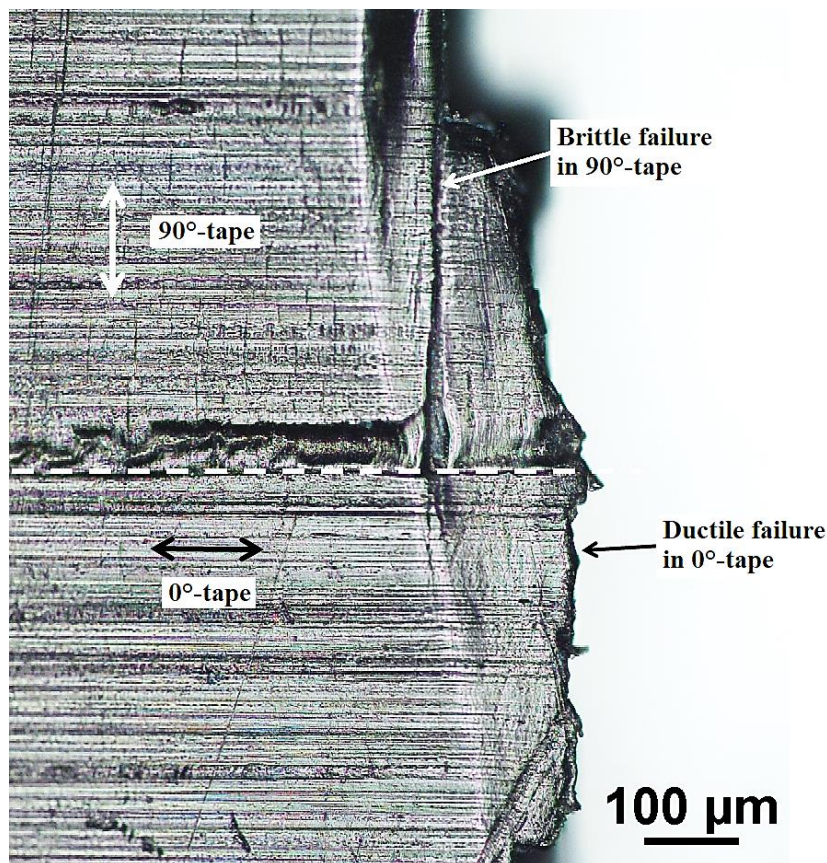


Figure 4.50 Optical micrograph of a 0.3 mm SRPP tensile specimen, pointing out brittle failure in 90°-tape and ductile failure in 0°-tape along the fracture path.

However, fracture surfaces that were shown in Figure 4.48 exhibited the same mode of failure through multiple tapes and matrix regions. This shows that the mode of failure does not always depend on the tape orientation or the weave geometry. The micrograph in Figure 4.50 also shows instances of ductile failure occurring in the 90°-tape and brittle crack propagation through the 0°-tape, as shown in

Figure 4.51. It appears from Figure 4.51 that this occurs when a crack propagates from one tape to another. This is quite clear in the case of a brittle crack propagating from a 90°-tape into a 0°-tape (left image of Figure 4.51). It may perhaps be that a crack propagates in a particular mode (brittle or ductile) *initially*, depending on factors such as the tape orientation or the weave geometry, but retains its mode of propagation in 0.3 mm SRPP as it propagates into a region that promotes a different mode of propagation.

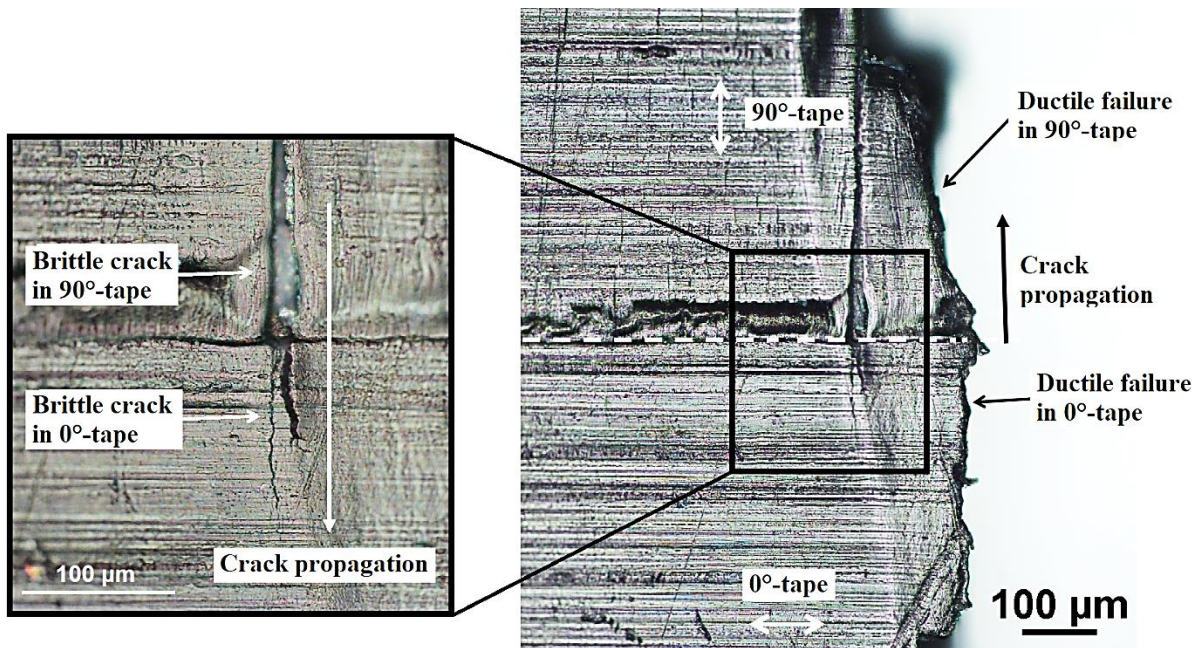


Figure 4.51 Optical micrograph of the 0.3 mm SRPP tensile specimen in Figure 4.50, showing propagation of a crack in the same brittle or ductile mode into 0° and 90°-tapes.

There is a further aspect that must be addressed in order for this hypothesis to be true. Microscopic examinations show that most of the fracture surface fail in a brittle manner, despite the fact that there is an equal number of 0°- and 90°-tapes and an equal number of different types of boundary cracks. This may be due to an unstable crack growth occurring at a faster speed than a stable crack growth under the same applied stress, since it requires very little or no additional stress to propagate. In the absence of any mechanism to impede unstable crack growth, it may propagate further than a stable one, causing the fracture surface to be mostly brittle. The fact that the critical failure initiates from a brittle matrix crack at a $BC_{\parallel}^{90^{\circ}}$ may also be a contributing factor.

It is also possible there are other influencing factors, such as local defects such as impurities, voids or surface scratches that can cause different modes of crack propagation and failure. For example, a semi-brittle or semi-ductile material can exhibit brittle or ductile fracture depending on the presence or the size of an inclusion or notch, due to changes in the local stress field [25, p. 2051–2064, 233]. However,

there was no direct evidence supporting this in the microscopic examinations. While this does not negate the possibility, it does make it seem less likely.

This section discussed the mode of crack propagation during failure in 0.3 mm specimens. The next section will build on this and show that 0.6 mm and 1.0 mm specimens also exhibit similar failure behaviours, and that the mode of crack propagation is influenced by the tape orientation. However, it will also show that the mode of crack propagation in the thicker specimens is not retained when propagating into another tape of different orientation. This difference to 0.3 mm specimens is instrumental in causing the failure behaviour of the thicker specimens to be different to that observed in the 0.3 mm specimens.

4.2.3.2 Failure behaviour of 0.6 mm and 1.0 mm specimens

This section discusses the failure behaviour of 0.6 mm and 1.0 mm specimens. The first part will explain the toughening mechanisms and how they affect the manner of crack propagation. It will then be explained how they cause the failure behaviour of the thicker specimens to be different to that of the 0.3 mm specimens.

4.2.3.2.1 Toughening mechanisms in 0.6 mm and 1.0 mm SRPPs

As was shown earlier, in Section 4.2.1, the failure characteristics in 0.6 mm and 1.0 mm specimens are distinctively different to those seen in the 0.3 mm specimens. For example, the thicker specimens exhibit microfibrillar crack bridging and delamination. These serve as toughening mechanisms by impeding crack growth, along with other mechanisms that will be explained later in this section. The presence of these toughening mechanisms is the primary cause of the difference in failure behaviour of thicker specimens compared to the 0.3 mm specimens.

Four toughening mechanisms were observed: 1) Microfibrillar crack bridging, 2) crack tip blunting, 3) crack arresting, and 4) macroscopic crack bridging by 0°-tapes.

1. Microfibrillar crack bridging

Microfibrillar crack bridging was described in Section 4.2.2.2.1. Microfibrils that are oblique to the crack opening connect the crack faces in tape-splits, in the wake of a crack. The effect of crack bridging is that it reduces the stress intensity at the crack tip and slows down the crack growth. This is an extrinsic toughening mechanism in that it occurs behind the crack tip.

2. Crack tip blunting

In general, crack tips can be blunted in fibre-reinforced composites by plastic relaxation in the matrix, by debonding at the fibre-matrix interface, by sub-crack damage parallel to the fibres, or by delamination,

either at the crack tip or ahead of it [234–236]. Crack tip blunting results in a considerable reduction in the tensile stress ahead of the crack, allowing the material to withstand a greater load [234].

In Mashinskaya and Perov’s study of organic FRP [237], it is explained that a crack can be blunted and arrested when colliding with a phase that has a lower elasticity modulus than the medium it is travelling in, but not the other way around. For instance, a matrix crack is not blunted or arrested in GFRP upon colliding with the fibre which is much stiffer than the matrix. However, the same concept does not apply as consistently in SRPP, in which the most influential factor that causes crack tip blunting is the orientation of tapes, rather than the phase difference.

In thicker SRPP specimens, a crack tip is blunted when it meets a neighbouring tape that is perpendicularly oriented to the direction of crack propagation, as shown in Figure 4.52. Here, cracks in tape-splits of a 90°-tape are blunted as they propagate into the neighbouring 0°-tape and are arrested as

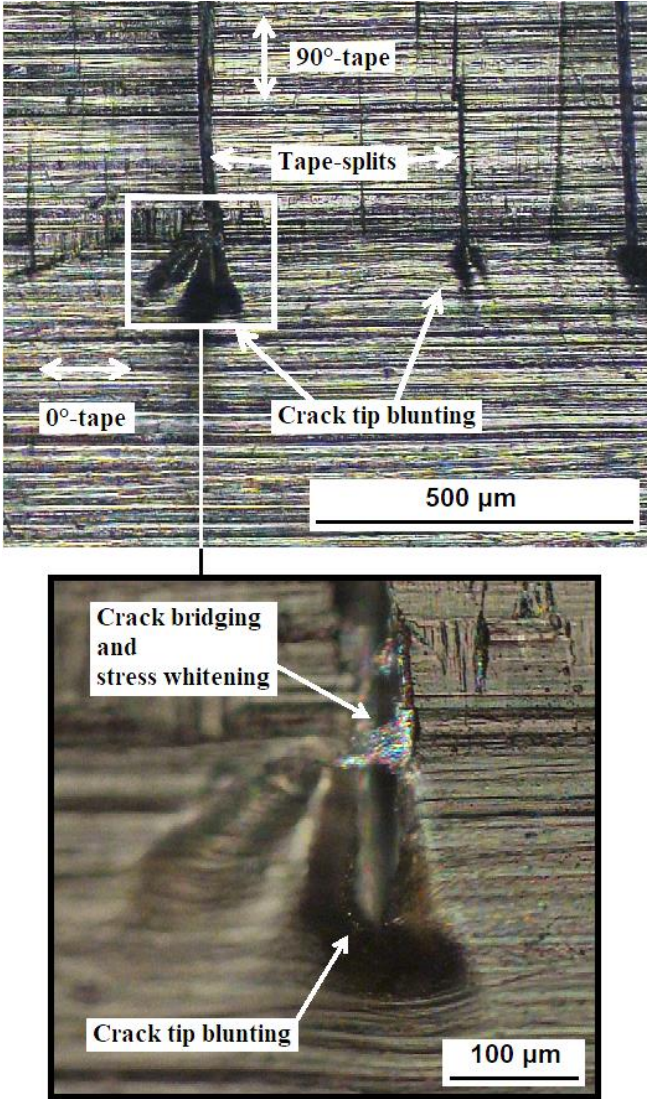


Figure 4.52 Optical micrograph of a 0.6 mm SRPP tensile specimen, showing crack tip blunting.

a result. Since the crack must obviously propagate through the matrix, it is blunted as it travels from a phase that has lower stiffness (matrix) into a phase that has higher stiffer (tape), which is the exact opposite of the case described in the literature.

The different behaviour of SRPP to FRPs is perhaps because of its reinforcement being very large and continuous while the matrix is comparatively small (tape volume fraction $\approx 70\%$), which is different to most FRPs (fibre volume fraction $\approx 20\text{--}30\%$). Due to this, it seems that the behaviour of crack propagation between the tapes is more important than the propagation between the phases. This demonstrates another behaviour of SRPP that is different to most FRPs due to its unique structure.

It should be noted that blunt crack tips are associated with stable crack growth and ductile failure. Therefore, the above observations of crack tip blunting show that when an unstable crack meets a tape that is perpendicularly oriented to the direction of its propagation, the mode of crack propagation changes to a stable mode, which can lead to ductile failure and/or an arresting of the crack. It can be recalled that there were other indicators of this behaviour from the previous analyses of the microscopic damage. For example, it was found that fibril ends tend to fail in a ductile manner against the tape orientation and that tape-splits in the direction of tape orientation always occurred in a brittle manner.

On a final note, it should be noted that multiple toughening mechanisms can co-occur. For instance, the bottom image in Figure 4.52 shows crack bridging occurring in conjunction with crack tip blunting.

3. Crack arresting

In SRPP, crack arresting can occur due to tape-splits occurring in the local zone in front of the crack, as it meets a tape that is perpendicularly oriented to the direction of crack propagation. An example is shown in Figure 4.53 in the next page. This is effectively what is known as microcrack toughening, but in the case of SRPP, the microcracks appear directly in front of the crack and occur only in the direction of the tape orientation, obviously due to the tape's microstructure.

Crack arresting resembles a crack deflection in some ways, for example, in Cook and Gordon's model [235] which is illustrated in diagrams 8–10 in Figure 4.54. The model depicts a plane of weakness in front of a crack that is perpendicular to the crack propagation (diagram 8). The plane of weakness splits up ahead of the crack (diagram 9) and the crack is effectively deflected as it joins the split (diagram 10). In the case of SRPP, the relatively weak Van der Waals forces between the microfibrils within the tape create the planes of weakness. However, the difference is that the SRPP tape is strong along its reinforcing direction and it resists crack propagation at the edge of the tape, before the crack can merge with the tape-splits.

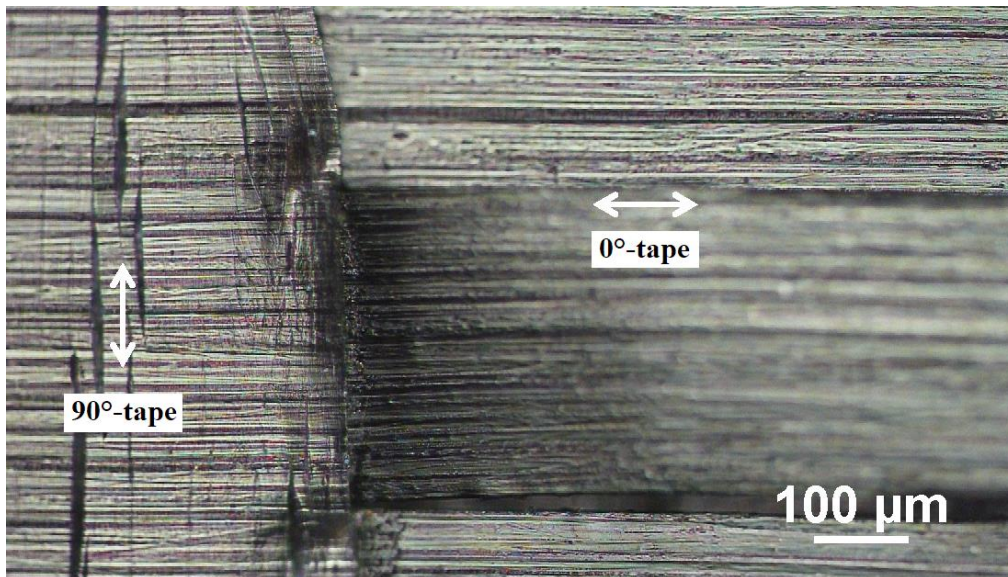


Figure 4.53 Optical micrograph of a 0.6 mm SRPP tensile specimen, showing crack arresting in a 90°-tape by developing tape-splits at local zones ahead of the cracks.

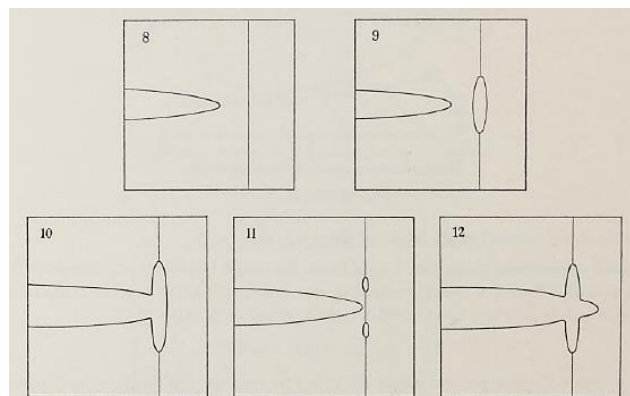


Figure 4.54 Cook and Gordon's crack deflection mechanism, showing interaction between an advancing crack and a plane of weakness under various conditions. Reproduced from [235, Fig. 8–12].

It is not clear whether a crack arrest affects its propagation along the tape it was propagating within. It is possible there is some impedance if the tapes have not delaminated. However, Figure 4.52 illustrates a case where the tape-split continues along the 90°-tape as it weaves underneath, at least in the vicinity of the crack for a short distance.

4. Macroscopic crack bridging by 0°-tapes

This crack bridging occurs at a larger scale than the microfibrillar crack bridging and is similar to fibre bridging in FRPs. Cracks that are transverse to the loading direction in 90°-tapes and matrix are bridged by 0°-tapes and sections of 0°-tapes, most of which remain unbroken in the loading direction until the

catastrophic failure of the specimen. The same toughening mechanism was observed in Stocchi et al.'s study of film-stacked SRPP specimens that were consolidated at different temperatures [97]. Some of their specimens failed in ways very similar to the thicker specimens, exhibiting a high degree of fibrillation, delamination and macroscopic crack bridging. These samples did indeed exhibit significantly higher fracture toughness than another sample which showed none of those failure characteristics, which is similar to the 0.3 mm specimens.

What has not been described in [97] is that this crack bridging is made possible due to the crack tip blunting and crack arresting. As explained, these mechanisms impede cracks from propagating into tapes that are perpendicularly oriented to the direction of crack propagation. This hinders propagation of transverse cracks into 0°-tapes, allowing them to remain intact in the direction of the applied load and bridge the cracks in 90°-tapes and the matrix. It is not clear if these microscopic toughening mechanisms do not occur in film stacked SRPP, or if they were simply not observed in previous studies because they occur much less frequently than other types of damage.

It should be mentioned that there is some ambiguity around whether or not macroscopic crack bridging should be considered as a separate toughening mechanism on its own, because it results from the crack tip blunting and crack arresting mechanisms. Nevertheless, it is discussed separately here as there is an existing study [97] which has identified it as a toughening mechanism. Also, while crack tip blunting and crack arresting mechanisms can occur in both tape directions, the macroscopic crack bridging by 0°-tapes represents a specific case, where only those that impede the crack growth in 0°-tapes are of real importance.

It is possible that there are additional toughening mechanisms in 0.6 mm and 1.0 mm specimens, on top of the four that are described above. For example, it is possible that a crack bifurcates into, or joins with, boundary cracks or inter-tape delamination that are perpendicular to the plane of the crack propagation, exactly as described in Cook and Gordon's crack deflection model. If crazes, tape-splits or boundary cracks open up in the vicinity of the crack tip during the crack propagation, *parallel* to the crack, this can slow down the crack growth by microcrack toughening. However, direct evidence of such additional toughening mechanisms has not been observed.

This section discussed different toughening mechanisms that exist in 0.6 mm and 1.0 mm specimens, namely the microfibrillar and macroscopic crack bridging, crack tip blunting and crack arresting mechanisms. The impact of the toughening mechanisms on SRPP can be made even clearer by comparing the failure behaviours of the thicker specimens against those of the 0.3 mm specimens. This is done in the next section.

4.2.3.2.2 Impact of toughening mechanisms on the failure behaviour of specimens of different thicknesses

The toughening mechanisms in 0.6 mm and 1.0 mm specimens are the primary cause of the different failure behaviour to 0.3 mm specimens. For instance, due to the toughening mechanisms, the tape orientation has a stronger influence in thicker specimens on the mode of crack propagation and the resulting mode of failure at a microscopic scale. Cracks propagate in an unstable manner and cause brittle failure, or propagate in a stable manner and cause ductile failure, when propagating in directions parallel or perpendicular to the tape orientation, respectively. In comparison, such behaviour was hypothesised to occur in 0.3 mm specimens under certain conditions, for example, in the initial phase of crack propagation.

The most significant effect of the above behaviour is that, in 0.6 mm and 1.0 mm specimens, transverse cracks to the loading direction are impeded from propagating in an unstable manner and continuously through multiple 0°-tapes at once, which is how failure occurs in 0.3 mm specimens. Even if a crack causes a tensile fracture of a 0°-tape in a 0.6 mm or 1.0 mm specimen, it is impeded from propagating directly into the surrounding 0°-tapes. This allows the load to be re-distributed to the remaining 0°-tapes, allowing the specimen to withstand further load, *if* the applied load has not exceeded the combined load-bearing capacity of the remaining reinforcements. An example is shown in Figure 4.55. A 0°-tape fractures from an oblique crack that can be detected as early as 13.2% applied strain, but this does not cause an immediate failure of the specimen, which occurs at 15.9% applied strain. Furthermore, the fracture of the tape does not cause any drop in the load.

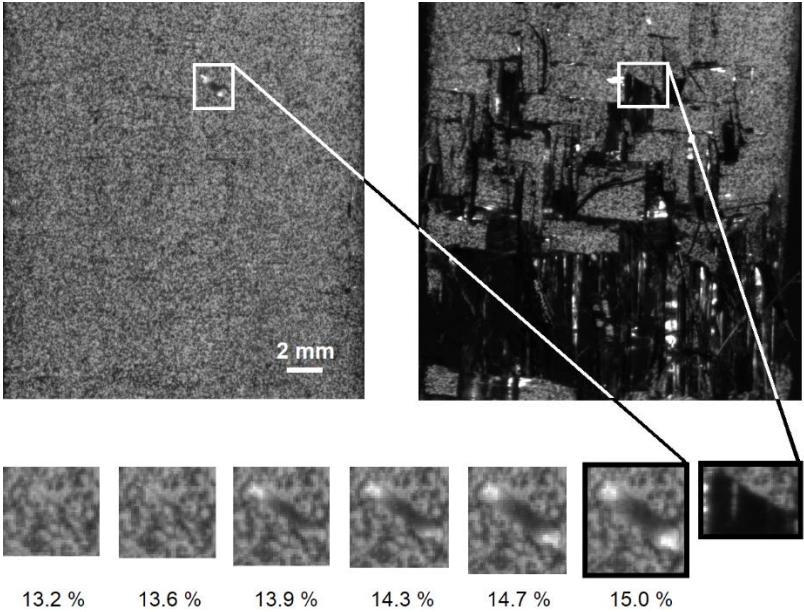


Figure 4.55 Growth of an oblique crack in a 0°-tape of a 1.0 mm SRPP tensile specimen, which does not lead to an immediate failure of the specimen. The applied strain at failure was 15.9%.

Failure occurs in thicker specimens when the combined resistance from the remaining 0° -tapes fails under the applied load. This means that failure of the 0.6 mm and 1.0 mm specimens is mostly dependent on the average stress of 0° -tapes in the specimen. As a result, specimens fail at relatively similar stresses and strains ($\epsilon_t = 14 \pm 2\%$, $15 \pm 1\%$). In contrast, 0.3 mm specimens lack the mechanisms which can impede unstable crack growth through the 0° -tapes. As a result, growth of the strain concentration at a $BC_{\parallel}^{90^\circ}$ that causes a 0° -tape or a portion of it to fracture leads to an almost immediate specimen failure. Therefore, failure of a 0.3 mm specimen is dependent on the magnitude of local damage, which can reach a critical threshold at widely varying applied strains. Due to this, 0.3 mm SRPP exhibits a large variation in the failure strain between specimens ($\epsilon_t = 14 \pm 5\%$).

The thicker specimens are less sensitive to local damage and fail at higher stresses, so they are able to withstand more damage prior to failure. In other words, 0.6 mm and 1.0 mm specimens have a higher damage tolerance under tension than 0.3 mm specimens. Furthermore, 1.0 mm specimens exhibit more damage than 0.6 mm specimens so it is likely that there is a general upwards trend in the damage tolerance with increases in thickness. However, there is an especially large difference between 0.3 mm and other specimens due to the different failure mechanisms. A greater amount of damage also mean that higher levels of energy are dissipated before failure in the thicker specimens, which would contribute to the toughness of 0.6 mm and 1.0 mm specimens being higher than that of 0.3 mm specimens.

It should be noted that the strength of SRPP also increases with thickness, in addition to the toughness. This is advantageous considering that so much attention is paid to strengthening materials, typically at the expense of toughness, despite the fact that both properties are crucial to many application [202]. It should be noted, however, that the largest difference exists in the 0.3 mm specimen, which is not expected to be used so frequently in applications due to its weaker mechanical properties.

The difference in failure behaviour between the thicker specimens and the 0.3 mm specimens also impacts the ways in which the onset of failure can be predicted. It was shown earlier in Section 4.2.3.1.3 that surface strain analysis can be used to identify HSCPs, which can then be used to predict at what stage a 0.3 mm specimen is likely to fail. In thicker specimens, this is not really necessary. The relatively small variation between specimens means that, for most applications, it suffices that the sample average strength or strain to failure be used to predict *when* a 0.6 mm or 1.0 mm specimen is likely to fail. This is the most common and simplest way of predicting failure under this loading condition.

It should be pointed out that serious damage still originates from HSCPs at $BC_{\parallel}^{90^\circ}$ in 0.6 mm and 1.0 mm specimens, as these can lead to fracture of 0° -tapes. As such, identifying the *location* of critical failure in a 0.6 mm or 1.0 mm specimen would involve identifying HSCPs, then determining 1) which of these can lead to a fracture of the 0° -tapes, and 2) whether or not the fracture of the tape would trigger

the catastrophic failure of the specimen. This would also give a more accurate prediction on when failure would occur, if necessary.

Although this has not been carried out in this study, part (1) would involve similar processes as those used to predict the failure point in the 0.3 mm specimens, such as identifying the maximum strain concentration point, $\frac{d\varepsilon_{HSCP}}{d\varepsilon_{applied}}$ or the strain path at HSCPs. Part (2) may involve processes such as modelling the energy release from the damage, and the load transfer and resulting stresses in other reinforcement units. Such a process may also need to account for other types of damage, crack density and saturation.

However, determining part (1) would face difficulties if the HSCPs are to be identified for real specimens using DIC measurements, as opposed to theoretical models because, in fact, not all HSCPs in a specimen can be detected, for several reasons. Firstly, in specimens thicker than 0.3 mm, there are additional layers in the middle of the specimen that cannot directly be observed. The effects of strain concentrations in these layers are reduced or may not even be reflected in the surface strains, and any local delamination would exacerbate this as well. Hence, it is difficult to identify HSCPs if they occur in the middle layers. Secondly, the number and size of damaged areas increases with specimen thickness. Not only does this increase the number of HSCPs that need to be analysed, as shown in Figure 4.56, it causes strain calculations to be invalid at some points. This typically occurs at points of large damages, such as shown in Figure 4.57, where the missing points on the right image represent points that could not be computed accurately enough at the set precision.

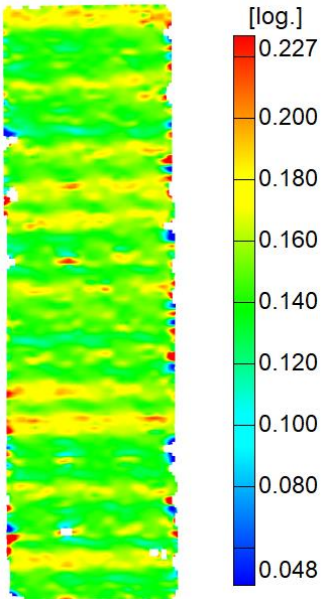


Figure 4.56 First principal strains of a 0.6 mm SRPP tensile specimen at the last stage just before specimen failure (15.1% applied strain).

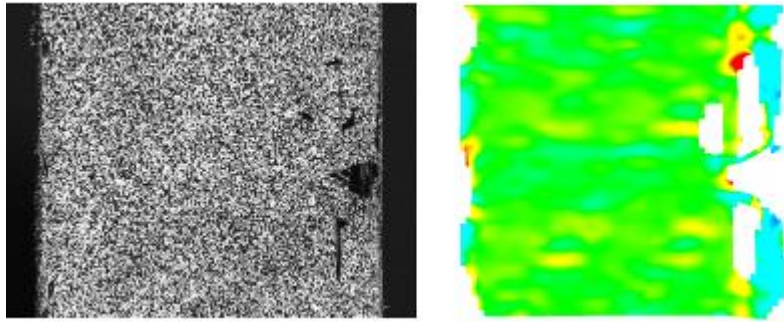


Figure 4.57 Digital image (left) and surface strain (right) of a section of a 1.0 mm SRPP tensile specimen, showing limitation in strain computation around large damages for a high-precision measurement.

Such loss of data can be prevented by using a coarser pattern with larger facet step and size. However, this gives strains that are averaged over wider areas, filtering out significant parts of local strain levels. Interpolation is possible but the precision is still lost due to the damage spanning several facets. This is most problematic along the free edges where damage occurs more extensively than in the middle of specimens, as shown in Figure 4.58. Due to these reasons, it is difficult to identify all the points of serious damage that can cause the fracture of 0° -tapes in thicker specimens. Thus, it is unrealistic to use surface strain measurements to identify the location of critical failure points in 0.6 mm and 1.0 mm specimens, unlike in 0.3 mm specimens.

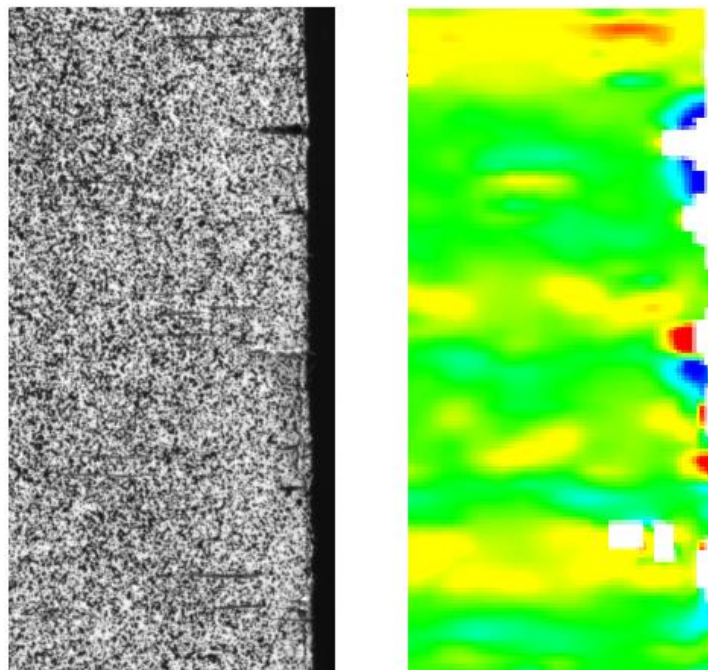


Figure 4.58 Digital image (left) and first principal strain (right) of a 0.6 mm SRPP tensile specimen, showing reduced accuracy of strain computation along the edge of the specimen.

4.2.4 Summary of failure behaviour of SRPP

Section 4.2 discussed various behaviours of SRPP, especially relating to its failure. In composites like SRPP, analysing the progression of failure is often made difficult by the multiple damages occurring simultaneously without separate phases of damage development. For this reason, damages in SRPP have been broken down and analysed one by one, some of which have not been reported in the literature. From this, it was found that one particular type of matrix damage, called boundary cracks, can be especially damaging. Boundary cracks between the edges of adjacent 90°-tapes can cause unusually high strain concentrations, which can then cause 0°-tapes to fracture. In specimens thin enough, this becomes a critical damage that rapidly propagates and causes specimen failure.

In addition, it was found that the development of critical damage in thin (0.3 mm) specimens can be tracked using a DIC system and surface strain analysis. This allows the onset of specimen failure to be predicted, with some limitations. This is useful because it is difficult to reliably predict the failure of such specimens based on the sample average strength or strain to failure, because they vary largely between specimens. The large variation is related to the lack of mechanisms that can impede unstable crack growth through the load-bearing 0°-tapes.

It was also found that the existence of certain damage-related toughening mechanisms can change the behaviour of SRPP. There is a general increase in the mechanical properties and the amount of damage with an increase in thickness, but this is most pronounced when the thickness is increased from 0.3 mm to 0.6 mm. This is due to the 0.6 mm and 1.0 mm specimens exhibiting microfibrillar bridging, crack tip blunting, crack arresting and macroscopic crack bridging. These are toughening mechanisms which impede cracks from propagating through tapes that are perpendicularly oriented to the crack. Such toughening mechanisms were determined to be the primary cause of the different failure behaviour between 0.3 mm and thicker specimens. Of the toughening mechanisms, only the macroscopic crack bridging was previously reported in the literature, and it was not understood that this occurred due to crack tip blunting and crack arresting mechanisms.

It was also found that the tape orientation in relation to the direction of crack propagation, and the local geometry from the weave structure, influence the mode of crack propagation (stable/unstable) and the resulting local failure (ductile/brittle). Due to this, the failure of an SRPP specimen occurs with a combination of ductile and brittle fractures at a microscopic scale, which has not been reported in the literature.

The macroscopic behaviour of SRPP is also rather unique, as it displays characteristics of brittle materials in some respects and of ductile materials in others. For example, SRPP fails in an abrupt manner with no reduction in the cross-section in a necking zone, and a considerable amount of damage occurs outside the strain localisation bands, which are characteristics of brittle materials. On the other

hand, SRPP exhibits large strain to failure, which is more typical of ductile materials than of brittle materials. In some ways, the material may be considered as semi-brittle or semi-ductile because local deformations around strain concentrations are sustained over a substantial amount of strain [25].

Section 4.2 thus discussed the various aspects of the behaviour of SRPP, some of which have not been analysed to the same depth in existing studies. The knowledge gathered from this will help understand the behaviour of an FML system that incorporates SRPP, which will be discussed in the next section.

4.3 Deformation and failure behaviour of self-reinforced polypropylene/steel fibre metal laminate

This section discusses the deformation and failure behaviour of SRPP/steel FML in two subsections; the first gives brief descriptions of stress-strain properties and damage characteristics, while the second gives surface strain analysis of the deformation and failure behaviour of the FML.

Knowledge of the deformation and failure behaviour of constituent materials is crucial to understanding the behaviour of an FML system. In the case of SRPP/steel FML subject to tensile loading, an understanding of the failure behaviour of SRPP is especially important because the FML fails as a result of a failure in the SRPP layer. This section will be brief, due to the fact that the behaviour of steel is well known and the SRPP has been analysed in depth in the previous section.

4.3.1 Stress-strain behaviour and damage characteristics

The tensile properties of SRPP/steel FML lie between those of steel and SRPP, as was shown by the stress-strain curve in Figure 3.1 (reproduced below) and as shown in Table 4.4. The stress-strain

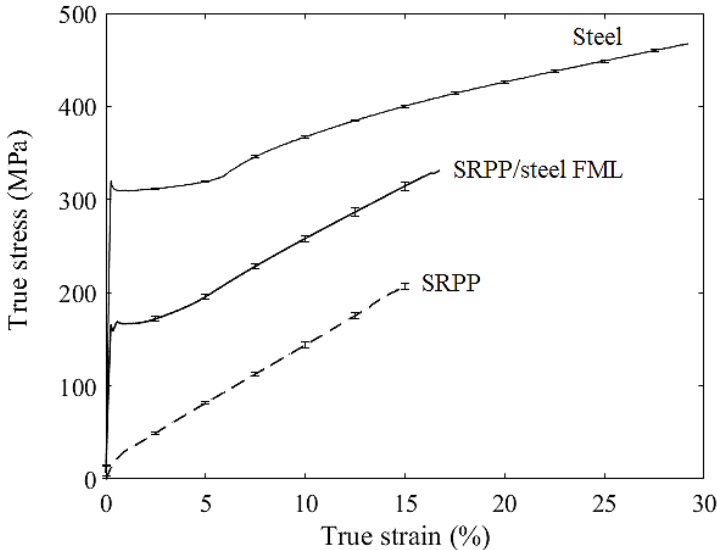


Figure 3.1 Measured stress-strain curves of steel, 1.0 mm SRPP and steel/SRPP FML.

Table 4.4 Tensile failure strain (ϵ_t), strength (σ_t) and upper yield strength (σ_y) or stress at transition strain ($\sigma^{transition}$) of steel, SRPP and SRPP/steel FML samples.

	ϵ_t (%) ¹	σ_t (MPa) ¹	σ_y (MPa)	$\sigma^{transition}$ (MPa)
Steel	29.2 ± 0.8	462.6 ± 0.8	331 ± 2	n/a ²
SRPP	15 ± 1	210 ± 3	n/a ²	16 ± 1
FML	17 ± 1	332 ± 3	176 ± 4	n/a ²

¹ Failure strains given indicate sample means and standard deviations. Strengths are sample means and standard deviations at given average failure strain, calculated based on specimens that have not failed.

² Not applicable.

behaviour of FML is closer to steel than to SRPP, mainly due to the strain hardening that is similar to steel. FML exhibits a yield point, and an increase in tangential stiffness after yielding, like that of steel, instead of a transition point as seen in SRPP. However, the tangential stiffness of FML after about 5% strain is very similar to SRPP, which is slightly higher than that of steel.

Such a mixture of behaviours of constituent materials agrees with the reported behaviour of many FMLs, including an SRPP/DP-steel FML in [149], which is the one used in the literature that is closest to the SRPP/steel FML. The stress-strain curve of the SRPP/steel FML is quite different to that of SRPP/DP-steel FML, but the fact that it has a similar profile to the steel, rather than the composite, is the same. Another difference is that the SRPP/DP-steel FML exhibited a higher failure strain than the SRPP/steel FML, but this was to be expected, considering that the failure strain of the SRPP used in [149] was much higher.

The SRPP/steel FML fails as a result of a failure in the SRPP layer. When the composite layer fails before the metal layers in an FML, it is typical that the load the laminate can withstand drops significantly and the metal layers then extend further until their strain to failure is reached [31, p. 73]. Tests are typically terminated after failure of the composite layer, as has been done in this study. The SRPP/steel FML was considered as ‘failed’ at this point because of the significant loss in the load-bearing capacity and the fact that more than half of the laminate’s volume fraction has failed.

The FML exhibits slightly higher strain to failure (17 ± 1%) than the SRPP layer (15 ± 1%), which is not unheard of (for example, see Figure 2 in [238]). It was, however, unexpected given that this is opposite to the behaviour observed in the SRPP/DP-steel FML in [149], which had lower strain to failure than its SRPP layer. The fact that the hybridisation of SRPP with steel sheets in an FML results in a slightly higher strain to failure and significantly higher stiffness than plain SRPP is similar to the behaviour observed when SRPP is hybridised with a low volume fraction of carbon fibres [198]. It is hypothesised that the SRPP/steel FML exhibits a higher failure strain than the plain SRPP due to the

steel layers impeding crack growth in the SRPP layer. Evidence that supports this hypothesis will later be shown, at the end of Section 4.3.2.

It can be recalled that there were crack impeding mechanisms in the 0.6 mm and 1.0 mm SRPP specimens that prevented immediate failure occurring from local damage, whereas the same damage would have caused failure in a 0.3 mm specimen. Similar mechanism may be working in the case of FML, where significant local damage in the SRPP layer, especially the boundary cracks between 90°-tapes on the surface layers, are bridged by the steel layers. This would impede the growth of cracks that lead to the fracture of 0°-tapes, thereby delaying the failure of the SRPP layer compared to plain SRPP specimens.

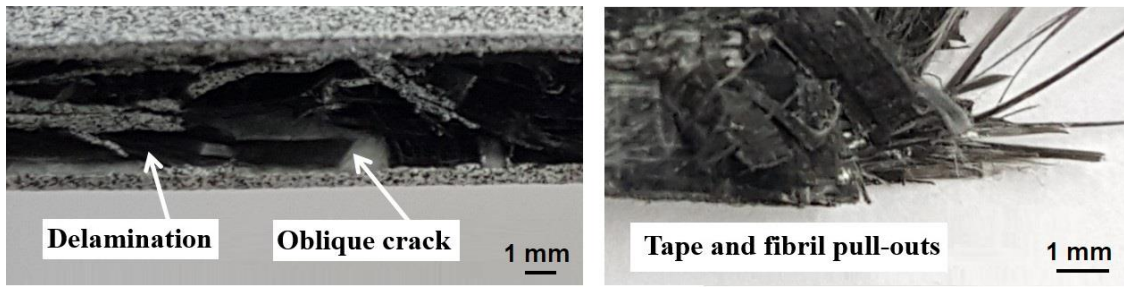
When an FML fails from the composite layer at a lower strain than the metal layer, its strength is typically predicted using a modified version of the well-known rule of mixture, given in Equation 4.1. The strength of the FML (σ_{FML}) is calculated based on the stress in the metal layer at the failure strain of the composite (σ'_m), metal volume fraction (V_m) and composite strength (σ_c). However, since the SRPP/steel FML fails at a higher strain than the plain SRPP, the modified rule of mixture does not exactly work for predicting its strength. Instead, further modification (given in Equation 4.2) can give a more accurate prediction of its strength, using an extrapolated value of the stress of the plain SRPP at the failure strain of the FML (σ'_c). Based on this, the predicted value for σ_{FML} is 317 MPa, which gives a 4.5% deviation from the measured value (332 MPa).

$$\sigma_{FML} = \sigma'_m V_m + \sigma_c (1 - V_m) \quad (4.3)$$

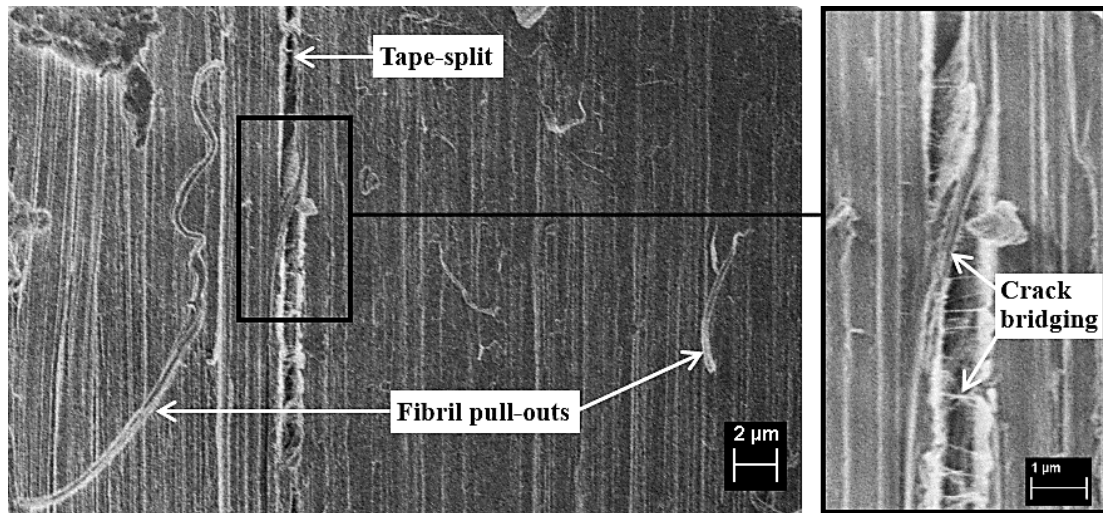
$$\sigma_{FML} = \sigma'_m V_m + \sigma'_c (1 - V_m) \quad (4.2)$$

There is no significant damage in the steel layers when the FML fails. In the SRPP layer, the damage characteristics are very similar to those in plain SRPP of the same thickness (1.0 mm). Examples of damage in the SRPP layer of the FML are shown in Figure 4.59 on the next page. There are minor differences compared to the plain SRPP specimens, such as larger amounts of delamination and tape/fibril pull-outs occurring on the surface, and that aligned crazing is not observed. These differences are caused by the fact that the SRPP layer has delaminated from the steel layers due to a larger reduction along the length from the unloading in the SRPP layer than in the steel layers, *after* failure. The difference in reduction in length from the unloading causes large delamination and damage along the gauge length. Since a significant portion of surface damage in the SRPP layer are related to post-failure events, it seems that there is no significant difference in damage characteristics of the SRPP layer of the FML compared to plain SRPP up to the point of failure.

It is therefore highly likely that a similar process of failure occurred in the SRPP layer as in the plain SRPP. Strain concentrations from boundary cracks would cause fracturing of the 0°-tapes in the vicinity, and when the applied load exceeds the combined resistance of the remaining 0°-tapes, the 0°-tapes



(a)



(b)

Figure 4.59 Photographs (a) and scanning electron micrographs (SEM) (b) showing typical damage in the SRPP layer of SRPP/steel-FML tensile specimens. SEM magnification = 5,000x (left), 20,000x (right), EHT = 1.00kV.

would fracture and lead to fracture in the SRPP layer. There are some minor differences to the plain SRPP, such as the additional crack impeding mechanism from the steel layers mentioned earlier, and how the location of damage growth is influenced by the steel layers. It will be shown in the next section that strain localisation bands form in the FML due to the influence of HSCPs in the SRPP layer and material properties of the steel layers. After the initial formation of strain localisation bands, it is likely that the strain growth promotes the concentrated growth of damage within the strain localisation band, and vice versa, during the deformation.

4.3.2 Surface strain analysis

Surface strain of a typical SRPP/steel FML specimen is shown in Figure 4.60. FML exhibits strain patterns from both steel and SRPP properties, transposed on top of one another. The first noticeable strain patterns from steel are diagonal strain localisation bands, forming across the width throughout the gauge length. These strain localisation bands are similar to those in SRPP except for few characteristics.

They are narrower, oblique to the loading direction, and have shear localisation along the bands as shown in Figure 4.61¹², which are similar to characteristics of Lüders band fronts in metals. However, the strain localisation bands in FML are different to typical Lüders bands in that they do not exhibit band fronts that propagate somewhat uniformly. Also, Lüders band fronts in mild steel sheets are oriented approximately 45° to the loading direction [239], whereas the strain localisation bands in FML are initially around 64–73° to the loading direction.

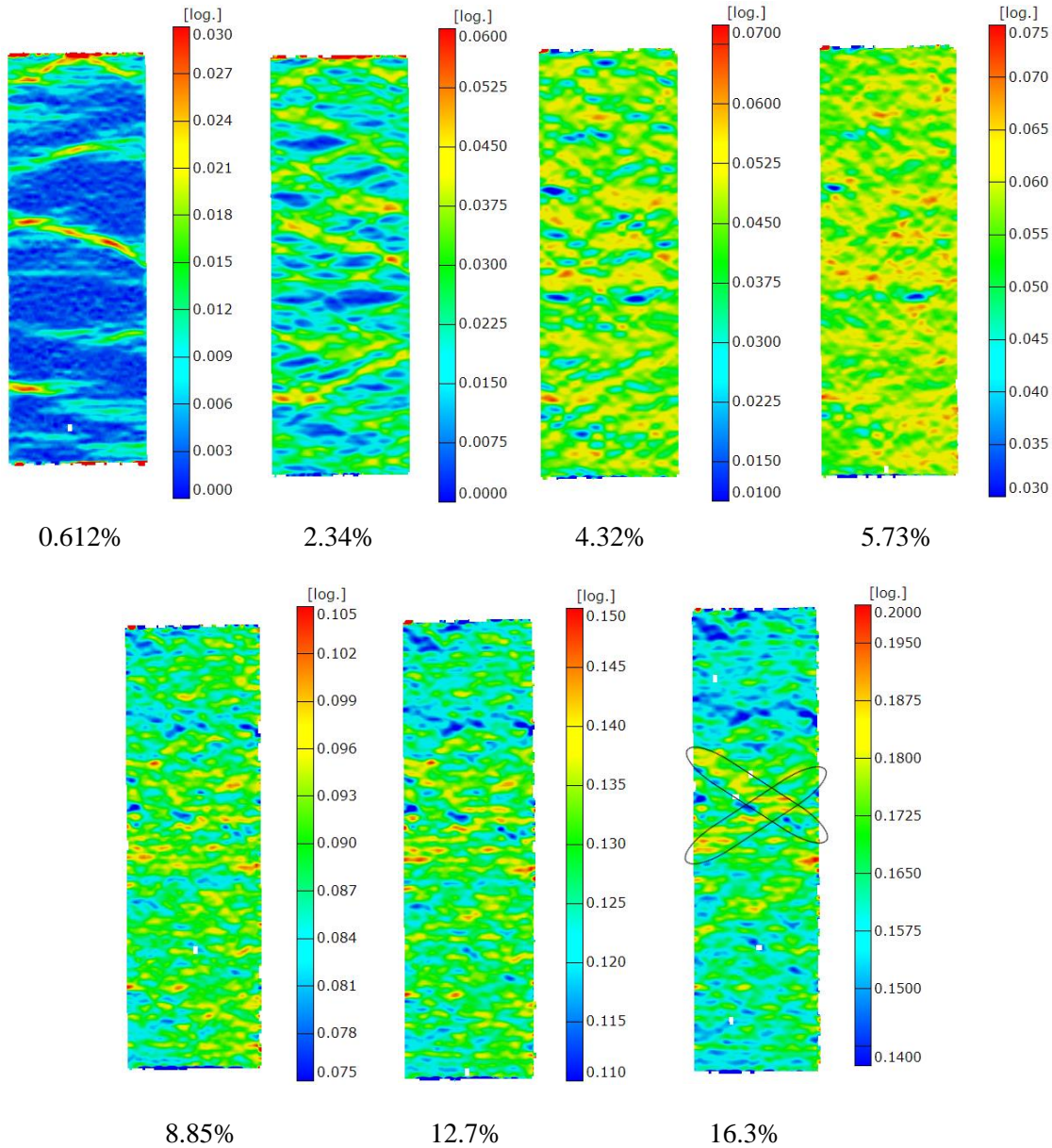


Figure 4.60 First principal strain of a SRPP/steel FML tensile specimen at the applied strains shown. The last image shows the stage just before failure and regions of higher strains are indicated. Scales have been manually adjusted to show strain patterns.

¹² Shear localisation along strain localisation bands are observed only at low strains.

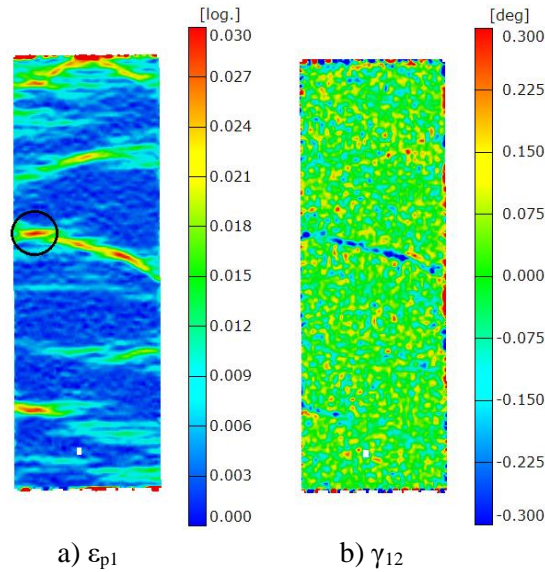


Figure 4.61 First principal strain (ϵ_{p1}) and shear strain (γ_{12}) in an SRPP/steel FML tensile specimen at 0.612% applied strain. Scales have been manually adjusted to emphasise strain patterns.

It can be seen from the surface strain pattern that strain concentrations occur in FML. These are likely to be caused by boundary cracks in the SRPP layer. The lines of strain concentrations can be seen more clearly at low applied strains when the strain localisation bands are relatively less pronounced, as indicated in Figure 4.61a. In the analysis of SRPP, similar high-strain concentration points (HSCPs) were observed and it was found that these are caused by the growth of matrix damage between the edges of neighbouring 90° -tapes ($BC_{\parallel}^{90^\circ}$). Given the similarity, and given that such HSCPs do not occur in plain steel, the strain concentrations in FML must arise due to HSCPs in the SRPP layer, which are caused by the $BC_{\parallel}^{90^\circ}$.

Assuming the above is correct, the boundary cracks – the inherent weaknesses in the SRPP layer – induce the initial formation of strain localisation bands in the FML. This can be deduced from observing that, at the very early stages of deformation, the oblique strain localisation bands form at the location of strain concentration points. Firstly, Figure 4.61a shows that all strain localisation bands occur across at least one strain concentration point. Secondly, there is one strain concentration point near the bottom left edge of the specimen where there is no strain localisation band. At a slightly higher strain, an oblique strain localisation band forms across this point, which is shown in the second image of Figure 4.60. These observations indicate that strain concentrations from boundary cracks in the SRPP layer induces formation of the strain localisation bands. After the initial formation, it is likely that the strain concentration within the bands promote concentrated growth of damage in the SRPP layer, and vice versa.

A failure in FML occurs as a result of a failure of the SRPP layer at a location within one of two fracture bands, which are strain localisation bands that exhibit higher strains than other strain localisation bands. Examples of fracture bands are indicated in the last image of Figure 4.60. An increase in strain levels within the fracture bands appear close to the stage of failure, after the strain localisation bands rotate slightly to approximately 57–63° to the loading direction. When two fracture bands occur, one is inclined at a positive angle and the other at a negative angle, and they cross each other.

The fracture bands appear as a result of necking in the steel layers, as can be seen by the fact that the necking bands in steel also form at approximately 57° to the loading direction [240]. It should also be mentioned that strain path of the FML specimen follows that of steel more closely than that of SRPP, as shown in Figure 4.62. This shows that the strain behaviour of FML is more heavily influenced by the properties of steel than SRPP (in this type of loading) even though the initial formation of strain localisation bands in FML are triggered by the boundary cracks in the SRPP layer.

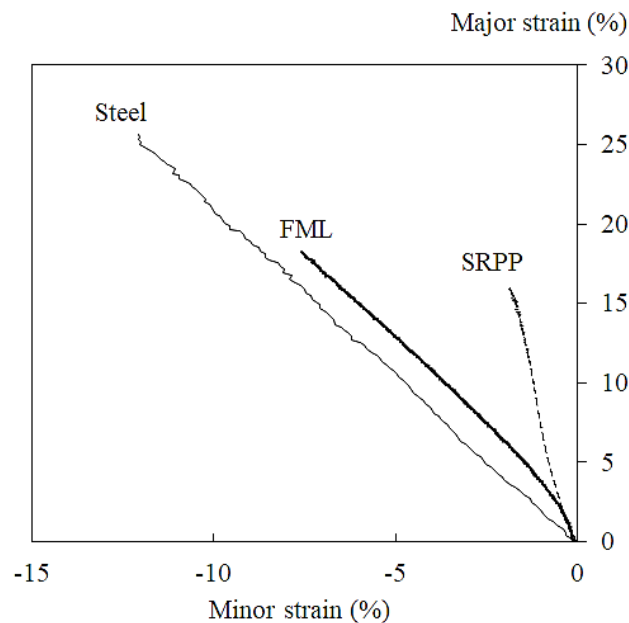


Figure 4.62 First principal strain (ϵ_{p1}) against second principal strain (ϵ_{p2}) for steel, SRPP and SRPP/steel FML tensile specimens.

The exact location of SRPP failure can be verified post-failure by peeling the layers apart or, for a more non-destructive evaluation, by examining the surface strains during or after failure. When the SRPP layer fails, the resulting increase in stress in the steel layers causes a sudden increase in strains along the fracture bands, as shown in Figure 4.63c. Also, if the digital images are taken at a sufficiently high rate, they can capture the exact moment of failure, as shown in Figure 4.63b. During failure, the stochastic patterns on the surface become blurred and causes errors in the strain computation on one side of the fracture, due to the sudden movement caused by the fracture in the SRPP layer. This conveniently allows the location of the SRPP failure to be identified without having to peel the layers apart.

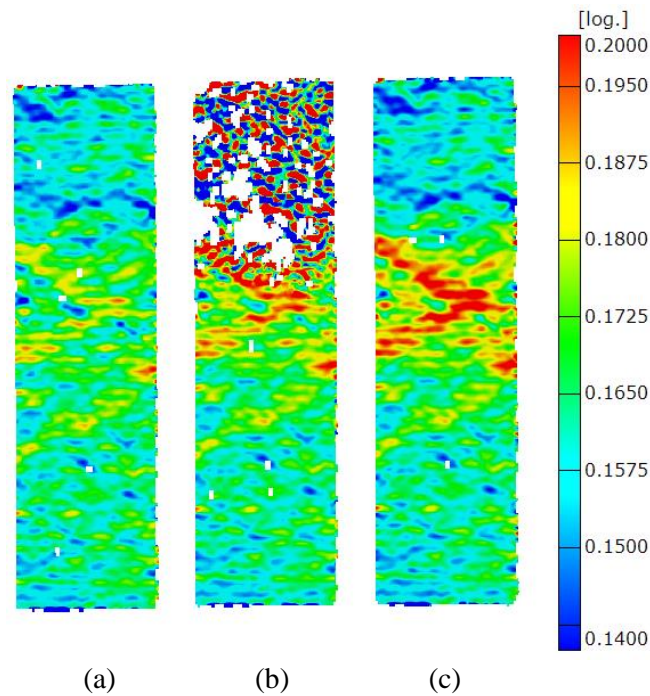


Figure 4.63 First principal strain of the SRPP/steel FML tensile specimen shown in Figure 4.60 a) before, b) during and c) after failure. Scale has been manually adjusted to show strain patterns.

The sudden increase in strain at the location of the SRPP failure is illustrated even more clearly in Figure 4.64 in the next page. The top image shows a section parallel to the loading direction on top of the surface strains at a stage just before failure. The bottom image shows a plot of strains along the section at different stages of deformation captured by the DIC system. The top black line shows strain after failure, the red line shows strain at the last stage before failure and other black lines indicate strains at every 100 stages before failure. This shows that strains in the specimen increase rather uniformly throughout the entire gauge section up until failure. Then, during failure, the strain increases suddenly only within the two fracture bands, which is where the SRPP layer fails.

It should be noted that the location of the failure can be identified with reasonable confidence only after the SRPP layer has failed. This is because many specimens exhibit multiple strain localisation bands with similar levels of strain concentration before failure, making it difficult to discern the fracture bands. The specimen shown in Figure 4.65 is a good example of this. The fracture band has been highlighted but the band is not so obvious until failure occurs.

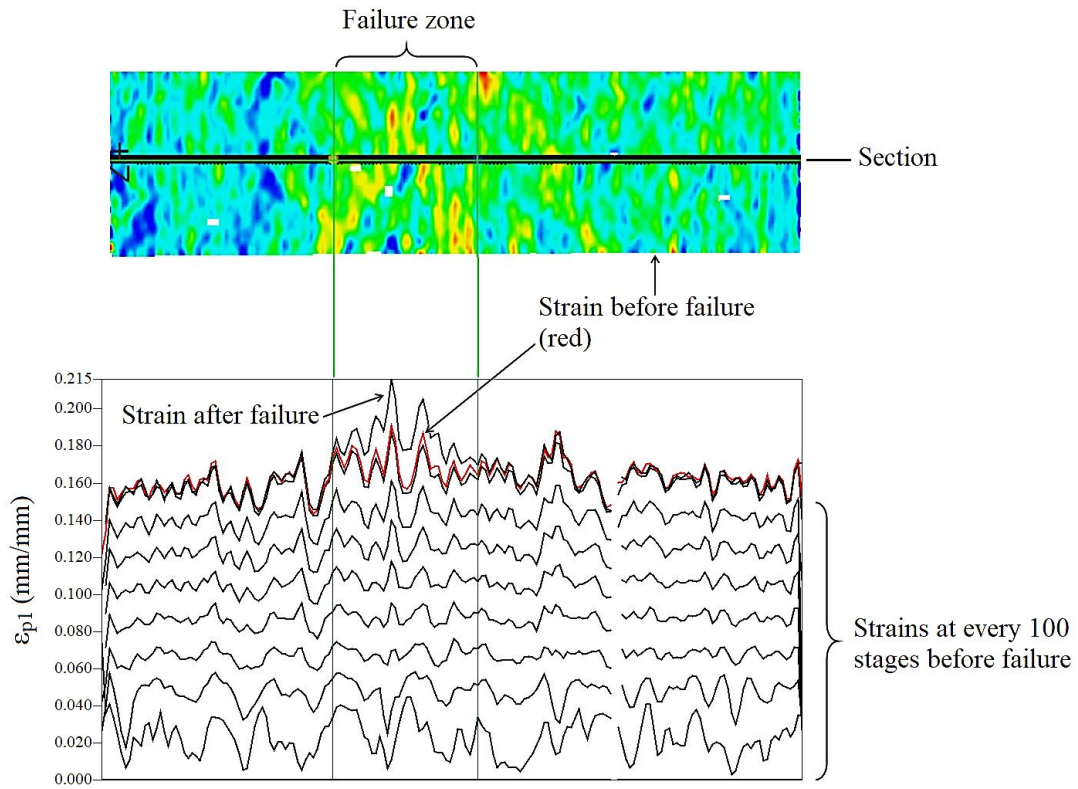


Figure 4.64 First principal strain (ϵ_{p1}) along a section of the SRPP/steel FML tensile specimen in Figure 4.63a, at different stages of deformation.

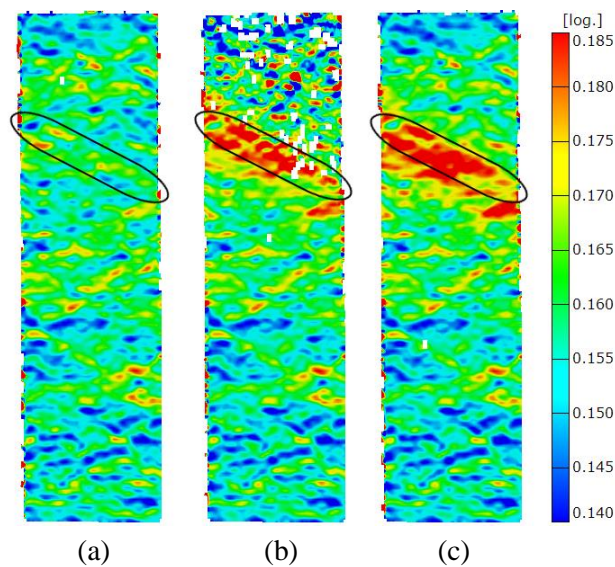


Figure 4.65 First principal strain of a SRPP/steel FML tensile specimen a) before, b) during and c) after failure. Scale has been manually adjusted to show strain patterns.

Also, the location of the failure cannot be predicted in the way it was done for 0.3 mm SRPP, for which the behaviour at HSCPs could indicate the point of failure. To illustrate the point, an example is given in Figure 4.66. Figure 4.66a (below) is a larger version of the image in Figure 4.65a (above) and shows

several strain concentration points; Figures 4.66b and 4.66c show plots of ϵ_{p1} at these points against the applied strain and ϵ_{p2} . It can be seen that unlike in the 0.3 mm SRPP specimens, there is no significant increase in F (gradient of strain increase relative to the applied strain), unique behaviour of the strain path, or any other noticeable characteristics that differentiate the strain concentration points in the fracture band (A, B and C in the figure) from those outside the fracture band (D and E). Therefore, the strain behaviour of individual local points does not indicate anything about the location of the failure in the FML specimen.

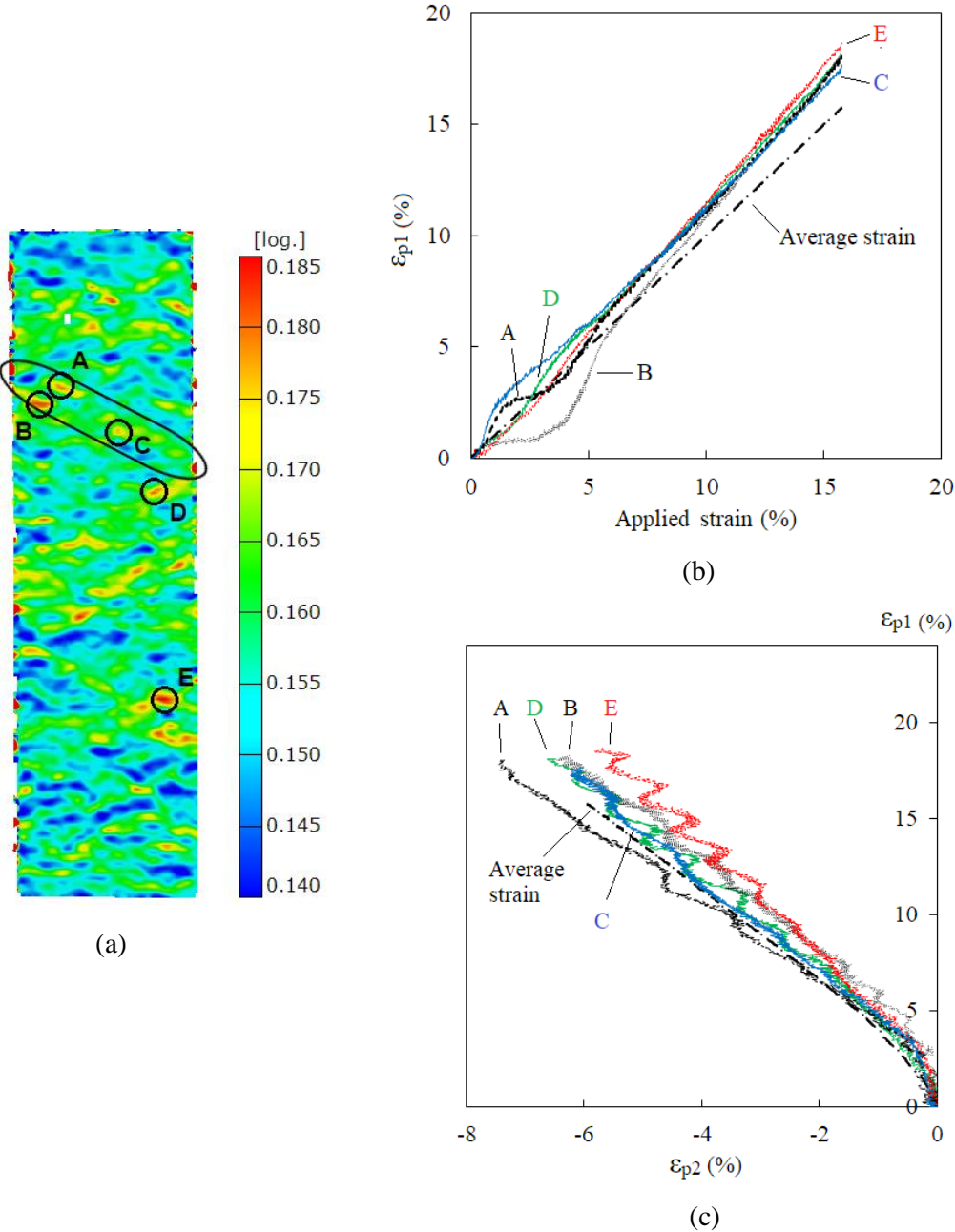


Figure 4.66 a) First principal strain (ϵ_{p1}) in the SRPP/steel FML tensile specimen in Figure 4.65a. ϵ_{p1} against b) the applied strain and c) the second principal strain (ϵ_{p2}), at strain concentration points shown in (a). Average strain in the specimen is also given for comparison.

In addition to the above, the level of strain concentration in FML is much smaller than in plain SRPP. This can be seen more clearly in Figure 4.67, shown below and in the next page, which gives examples of strain growth at various strain concentration points in 0.3 mm, 0.6 mm, 1.0 mm SRPP and FML specimens. Strains at HSCPs in SRPP specimens can often be twice as high (or more) than the average strain of the specimen. In comparison, there is a small difference between the strain concentration points and the average strain in the FML specimen.

The above observation supports the earlier conjecture, that the steel layers bridge and impede the growth of cracks in the SRPP layer of FML. This makes the FML even less sensitive to the growth of local damage than plain 1.0 mm SRPP specimens, in the same way that the thicker SRPP specimens are less sensitive to local damage than 0.3 mm SRPP specimens. It is likely from this that the toughness of the SRPP layer is increased by the adhesion to the steel layers in the FML, when compared to the plain SRPP.

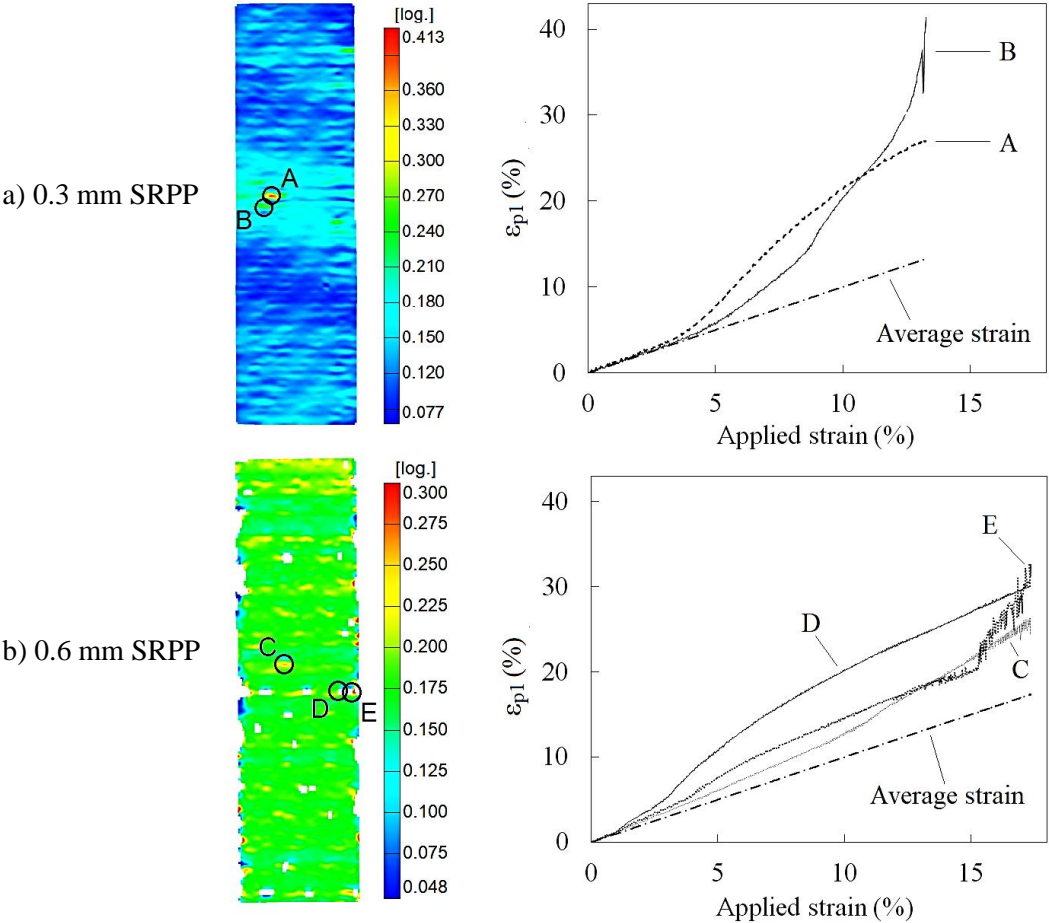


Figure 4.67 Comparison of strain growth at HSCPs in a) 0.3 mm, b) 0.6 mm, c) 1.0 mm SRPP and d) SRPP/steel FML specimens. Images on the left represent strains at the last stage before the specimens fail.

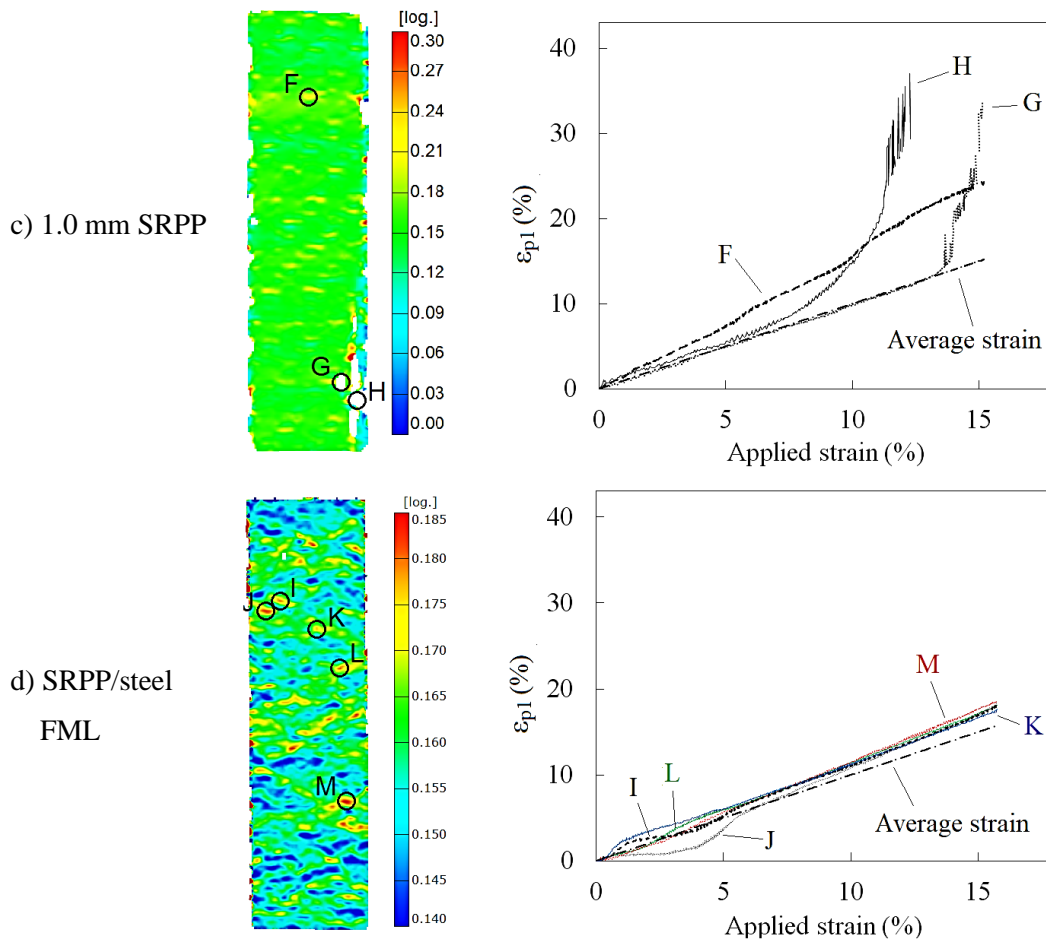


Figure 4.67 Comparison of strain growth at HSCPs in a) 0.3 mm, b) 0.6 mm, c) 1.0 mm SRPP and d) SRPP/steel FML specimens. Images on the left represent strains at the last stage before the specimens fail.

4.3.3 Summary of failure behaviour of FML

Section 4.3 investigated the behaviour of SRPP/steel FML when loaded under tension along one of the reinforcing directions of the SRPP layer. The knowledge gained from the earlier analysis of SRPP significantly helped explain the behaviour of the FML, since the FML exhibits a mixture of characteristics derived from both constituent materials. For example, the FML exhibits strain hardening and oblique strain localisation bands that are similar to steel, while also exhibiting strain concentrations that are similar to plain SRPP. FML derives its properties from its constituent materials, therefore its strength can be predicted relatively accurately with a modified rule of mixture.

The different material behaviours in the steel and SRPP layers also interact with each other. For instance, it was found that strain concentrations form in FML due to boundary cracks in the SRPP layer, which then trigger the formation of oblique strain localisation bands due to the properties of the steel. Then, the strain localisation bands induce concentrated growth of damage in the SRPP layer due to the strain

concentration within the bands, which then promotes further strain concentration, and so on. Eventually, the SRPP layer fails within one of the bands. At this point, the FML is deemed to have failed.

It is conjectured that the damage characteristics of the SRPP layer of the FML are the same as in plain SRPP, except that the cracks are bridged by the steel layers. The result is that crack growth in the SRPP layer is impeded and the level of strain concentration is much lower than in plain SRPP. This would make the FML less sensitive to local damage than the plain SRPP, similar to the way the toughening mechanisms in 0.6 mm and 1.0 mm SRPP specimens make them less sensitive to local damage than the 0.3 mm SRPP specimens.

4.4 Summary

As was described in the literature, SRPP and SRPP-based FML are relatively new classes of materials that have a lot of potential uses in various industries, mostly due to being lightweight, fully recyclable, highly impact resistant and thermoformable. There are some good studies on these, but they mostly focus on finding the optimal manufacturing techniques or investigating impact performance. While these definitely accelerated their use in many applications, less attention has been paid to the detailed analyses of their failure behaviour related to damage development, especially in SRPP. It is suspected, therefore, that the findings of this research are a valuable contribution to the literature.

Some findings of significance on the woven SRPP include analyses of damage types not previously reported in the literature, and discoveries about the initiation and progression of critical damage that leads to failure. It was also realised that the strain analysis used for tracking the critical damage growth can be used to predict the onset of failure in some cases, in a way that has not been done before. The SRPP was found to exhibit a distinctive manner of damage propagation and fracture due to its non-typical structures, such as the high internal microstructural alignment in the reinforcement and the unusually high reinforcement volume fraction. The thickness effect in the SRPP was also studied, which was found to be most significantly influenced by the extent of toughening mechanisms such as crack tip blunting, crack arresting and crack bridging.

Since the behaviour of an FML depends largely on the constituent materials, the findings regarding SRPP behaviour offer greater insights into the behaviour of SRPP/steel FML. It was found that the FML exhibited a mixture of material behaviours of SRPP and steel, which interact with each other to promote a unique damage growth and strain behaviour in the FML, from the early stages right up to failure. Ultimately, failure in the FML occurs in the SRPP layer, which exhibits similar damage progression to plain SRPP. It was, however, found that the steel layers change the strain behaviour, and therefore the damage distribution in the SRPP layer. Most significantly, the strain concentrations from the damage in the SRPP layer are suppressed significantly compared to those seen in plain SRPP.

The above findings relate to the tensile material behaviours when the reinforcements in SRPP are oriented parallel and perpendicular to the loading direction. In addition to this, it is important to understand their behaviours when the reinforcements are oriented off-axis to the loading direction, as anisotropic composites are known to behave differently when the reinforcements are loaded at different angles. This will be the subject of study in the next chapter.

5 Failure Behaviour Under Uniaxial Tension (Off-axis)

5.1 Introduction

An orthotropic composite material responds differently when loaded at an off-axis direction to its reinforcements, compared to when it is loaded along its reinforcements. This must also be understood in order to fully characterise a material, before the material behaviour under more complicated load conditions can be investigated. To understand how SRPP and SRPP/steel FML responds when loaded at an off-axis, uniaxial tensile tests have been carried out on the materials with SRPP tapes oriented at $30^\circ/60^\circ$ ¹³ and $\pm 45^\circ$ to the direction of the applied load.

It should be mentioned that the response of 2-phase FRPs under off-axis tensile tests is relatively well known. However, it was explained in the literature review and demonstrated through the findings in the last chapter that many aspects of SRPP behaviour differ from typical 2-phase FRPs. There are some studies that are relevant to the behaviour of SRPP at off-axis angles, most notably the works of [17, 40, 145], which were mentioned in the literature review. However, [17] and [145] are expected to give limited information on the type of SRPP studied in this research, as they study a UD form of SRPP [17] or just the reinforcement (drawn SRPP) [145]. [42] is of more relevance but focuses mainly on the effect of the processing conditions on the mechanical properties, the quality of consolidation (e.g. the amount of crimping and voids) and the difference in failure characteristics as observed visually. In this chapter, more attention is paid to the development of damage during the deformation and how this relates to the catastrophic failure of the material.

This chapter builds on the previous analyses of $0^\circ/90^\circ$ tensile tests and highlights the differences in deformation and failure characteristics arising from being loaded off-axis. This chapter is, once again, divided into two main sections, the first analysing the behaviour of plain SRPP and the second section analysing the behaviour of the FML.

In this chapter, the following apply with regard to the figures and nomenclature:

¹³ The accurate notation for a $30^\circ/60^\circ$ specimen is $30^\circ/-60^\circ$ or $-30^\circ/60^\circ$ since the tapes are orthogonal but the negative signs have been omitted for convenience.

- ‘ x° -tape’ denotes a tape that was originally at an angle of x° to the direction of applied load. For example, 30° -tape indicates a tape that was at 30° to the loading direction before loading, regardless of the angle after deformation.
- Directions 1 and 2 denote the reinforcement directions in the current state (i.e. along the changed tape directions when the material is deformed). ε_1 , ε_2 and γ_{12} denote strains in the direction of tapes and in-plane shear strain calculated about the original tape orientations. γ_{12} represents the change from 90° in the undeformed state to a new angle in the deformed state in degrees, as illustrated in Figure 5.1. The exception is 1 and 2 in ε_{p1} and ε_{p2} which indicate first and second principal strains.

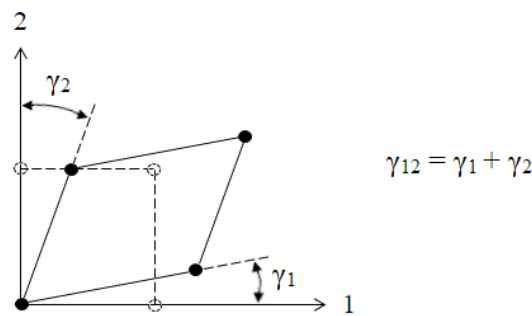


Figure 5.1 Shear strain (γ_{12}) definition. Dotted lines indicate the undeformed state, and solid lines indicate the deformed state.

- Double-sided arrows in images indicate the direction of tape orientations.
- The applied load is horizontal in optical micrographs, and vertical in photographs and DIC images, unless specified otherwise. In SEM images, tape orientations are indicated. Micrographs show surface sections unless specified otherwise.
- Several micrographs are combined in some images, with each micrograph focused on a different part of the image, to give more clarity.
- Strains are given in percentage, except γ_{12} which is given in degrees and the strains in DIC images which are given in non-percentage forms (mm/mm). All strains are given in logarithmic (true) strains and the notation ‘[log.]’ above the scale in DIC images simply denotes this.

5.2 Deformation and failure behaviour of off-axis self-reinforced polypropylene

This section discusses the behaviour of 0.3 mm, 0.6 mm and 1.0 mm thick SRPP specimens subjected to uniaxial tensile loading at $30^\circ/60^\circ$ and $\pm 45^\circ$ to tape orientations. Many aspects of the damage and

failure mechanisms in SRPP were explained in the previous chapter, and these will now help facilitate the analysis of its failure behaviour when loaded at off-axis directions to the reinforcing directions. Therefore, this section will focus on highlighting the differences to the 0°/90° specimens explained in the previous chapter.

This section is divided into three subsections. The first subsection describes the stress-strain and the macroscopic failure behaviour for each specimen type. An overview of the difference in deformation and failure behaviour depending on the orientation and specimen thickness will help understand the analyses in the following subsections. The second subsection discusses the microscopic damage characteristics, and the third subsection analyses the cause and development of failure in the off-axis specimens.

5.2.1 Stress-strain and macroscopic failure behaviour

In general, off-axis SRPP specimens behave similarly to each other but quite differently to the 0°/90° SRPP specimens. This can be seen from the stress-strain curves provided in Figures 5.2, 5.3 and 5.4 for 0.3 mm, 0.6 mm and 1.0 mm specimens, respectively. Each figure gives comparison of stress-strain curves when specimens are loaded at 0°/90°, 30°/60° and ± 45°. Stresses and strains at failure are summarised in Table 5.1.

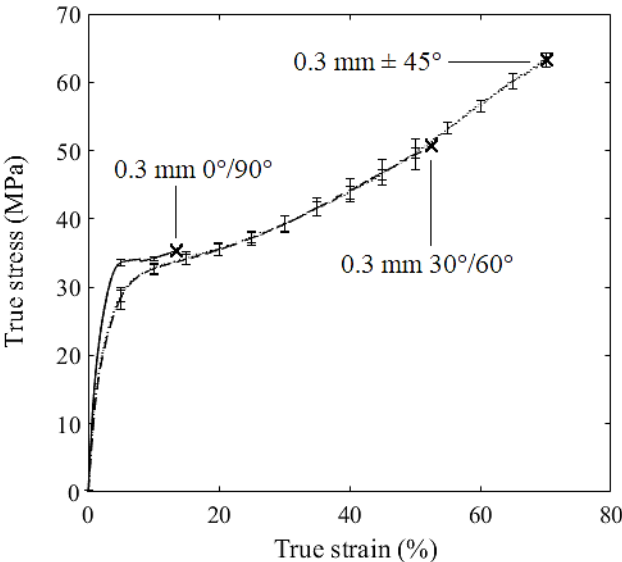


Figure 5.2 Tensile stress-strain curves of 0.3 mm SRPP loaded at 0°/90°, 30°/60° and ± 45°. Failure strains portrayed are sample averages, stress values are based on the average of specimens that have not failed at given strains, and error bars indicate sample standard deviations. Point of failure for each sample is indicated with a cross.

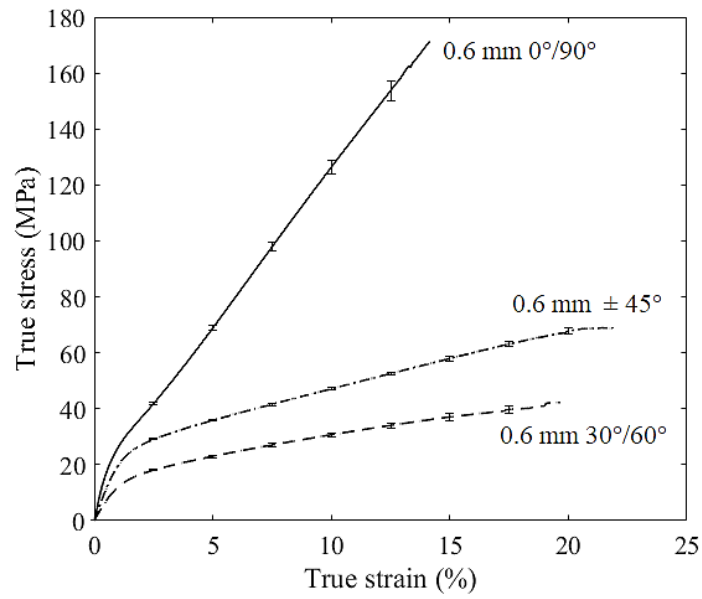


Figure 5.3 Tensile stress-strain curves of 0.6 mm SRPP loaded at $0^\circ/90^\circ$, $30^\circ/60^\circ$ and $\pm 45^\circ$. Failure strains portrayed are sample averages, stress values are based on the average of specimens that have not failed at given strains, and error bars indicate sample standard deviations.

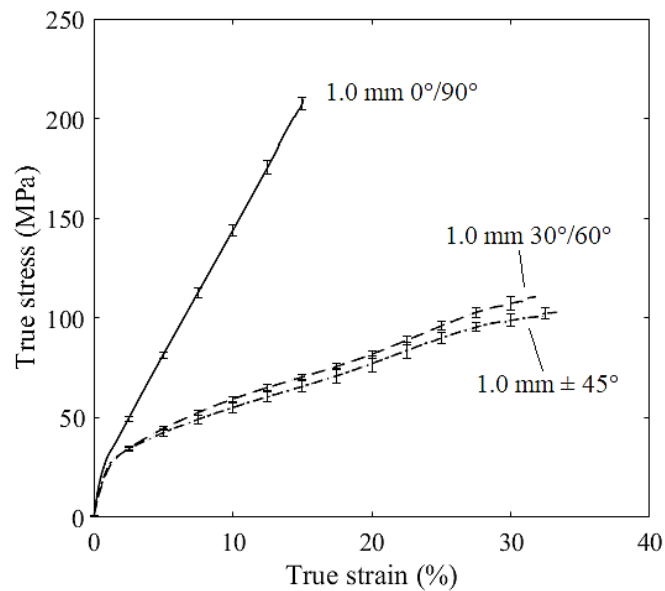


Figure 5.4 Tensile stress-strain curves of 1.0 mm SRPP loaded at $0^\circ/90^\circ$, $30^\circ/60^\circ$ and $\pm 45^\circ$. Failure strains portrayed are sample averages, stress values are based on the average of specimens that have not failed at given strains, and error bars indicate sample standard deviations.

Table 5.1 Tensile failure strength (σ_t), strains (ε_t) and relative standard deviation in failure strain (s_{ε_t}) of 0.3 mm, 0.6 mm and 1.0 mm SRPP specimens oriented at 0°/90°, 30°/60° and $\pm 45^\circ$ to the loading direction.

t (mm)	Orientation	σ_t (MPa) ¹	ε_t (%) ¹	s_{ε_t} ²
0.3	0°/90°	35.4 \pm 0.3	14 \pm 5	\pm 36%
0.3	30°/60°	51 \pm 3	53 \pm 10	\pm 19%
0.3	$\pm 45^\circ$	64 \pm 1	70 \pm 7	\pm 10%
0.6	0°/90°	171 \pm 4	14 \pm 2	\pm 14%
0.6	30°/60°	42 \pm 3	20 \pm 3	\pm 15%
0.6	$\pm 45^\circ$	70 \pm 2	22 \pm 1	\pm 5%
1.0	0°/90°	210 \pm 3	15 \pm 1	\pm 7%
1.0	30°/60°	111 \pm 4	32 \pm 2	\pm 6%
1.0	$\pm 45^\circ$	103 \pm 3	34 \pm 2	\pm 6%

¹ Failure strains given indicate sample means and standard deviations. Strengths are sample means and standard deviations at given average failure strain, calculated based on specimens that have not failed.

² Unit for this value is percentage (standard deviation) of percent (average) strains based on unrounded numbers.

From the above figures, it can also be seen that the 0.3 mm specimens behave very differently to the thicker specimens. For example, 0.6 mm and 1.0 mm off-axis specimens have much lower tangential stiffness and strengths and higher failure strains when tested in the off-axis direction compared to those exhibited when tested at 0°/90°. This is typical of FRP composite materials. In contrast, 0.3 mm specimens exhibit atypical behaviour and have higher strengths and only slightly lower stiffness in the off-axis directions than in the 0°/90° direction. The significantly higher strengths of the off-axis specimens (51–64 MPa) than the 0°/90° specimens (35.4 MPa) is mostly due to the off-axis specimens failing at unusually high strains (53–70%), about 3.8–5 times higher than the 0°/90° specimens (14 \pm 5%).

From the above, it can be seen that the thickness effect in the off-axis specimens differs from that in the 0°/90° specimens. To help compare, the stress-strain curves of 0°/90° and off-axis specimens have been given in Figure 4.1 (reproduced from Chapter 4) and Figure 5.5, with each graph showing the thickness effect.

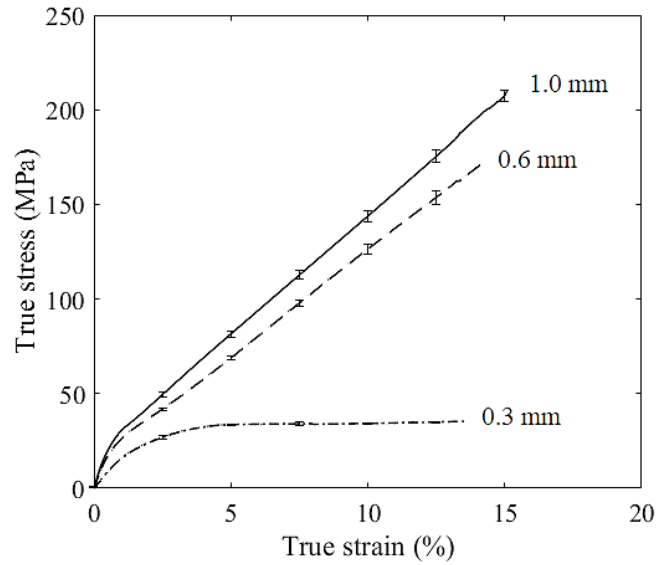


Figure 4.1 Tensile stress-strain curves of 0.3 mm, 0.6 mm and 1.0 mm SRPP samples. Failure strains portrayed are sample averages. Stress values are based on the averages of specimens that have not failed at given strains, and error bars indicate sample standard deviations.

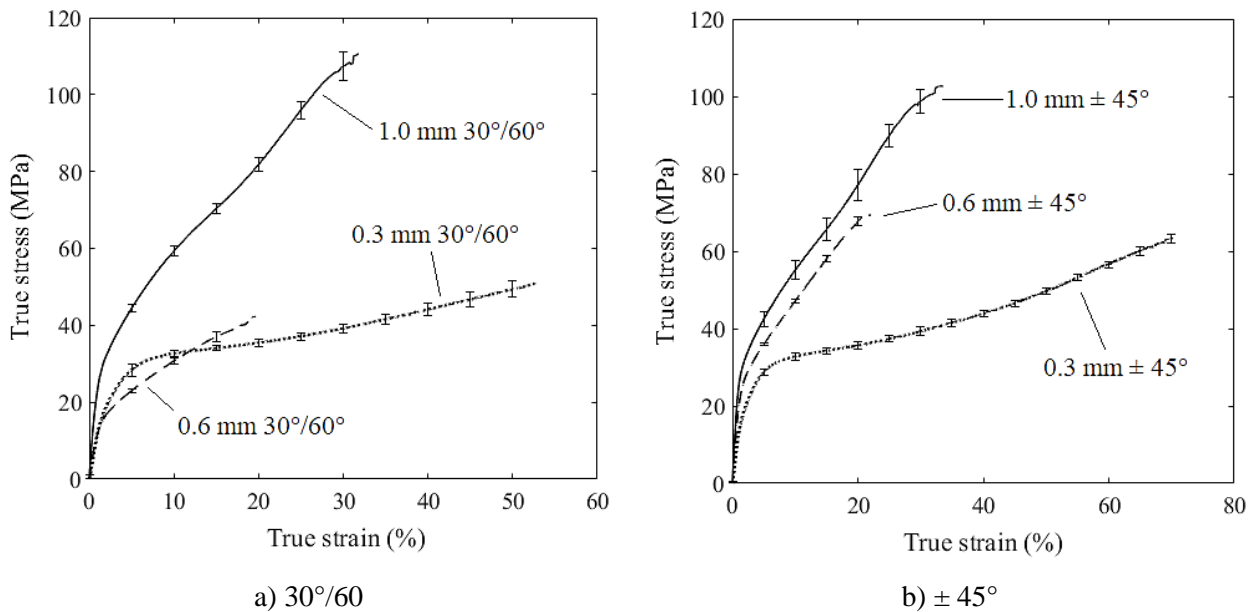


Figure 5.5 Tensile stress-strain curves of 0.3mm, 0.6 mm and 1.0 mm SRPPs loaded at a) 30°/60° and b) $\pm 45^\circ$. Failure strains portrayed are sample averages and the stress values are based on the average of specimens that have not failed. The error bars indicate sample standard deviations.

In addition to the mechanical properties, the visually observable damage characteristics at failure are also different depending on the thickness, as shown in Figures 5.6 and 5.7 for 30°/60° and $\pm 45^\circ$ specimens, respectively. Note that this is a similar trend to the 0°/90° specimens. Thicker specimens

exhibit fibrillation and tape/fibril pull-outs, as well as delamination (shown in Figure 5.8), none of which are observed in the 0.3 mm specimens. In addition, the 0.3 mm off-axis specimens occasionally exhibit wrinkling and high reduction across the width where failure occurs, which are not observed in the thicker specimens. The 1.0 mm specimens exhibit greater damage than the 0.6 mm specimens, sometimes over the entire gauge section. Thus, there is a general upwards trend in the amount of damage with each increase in thickness.

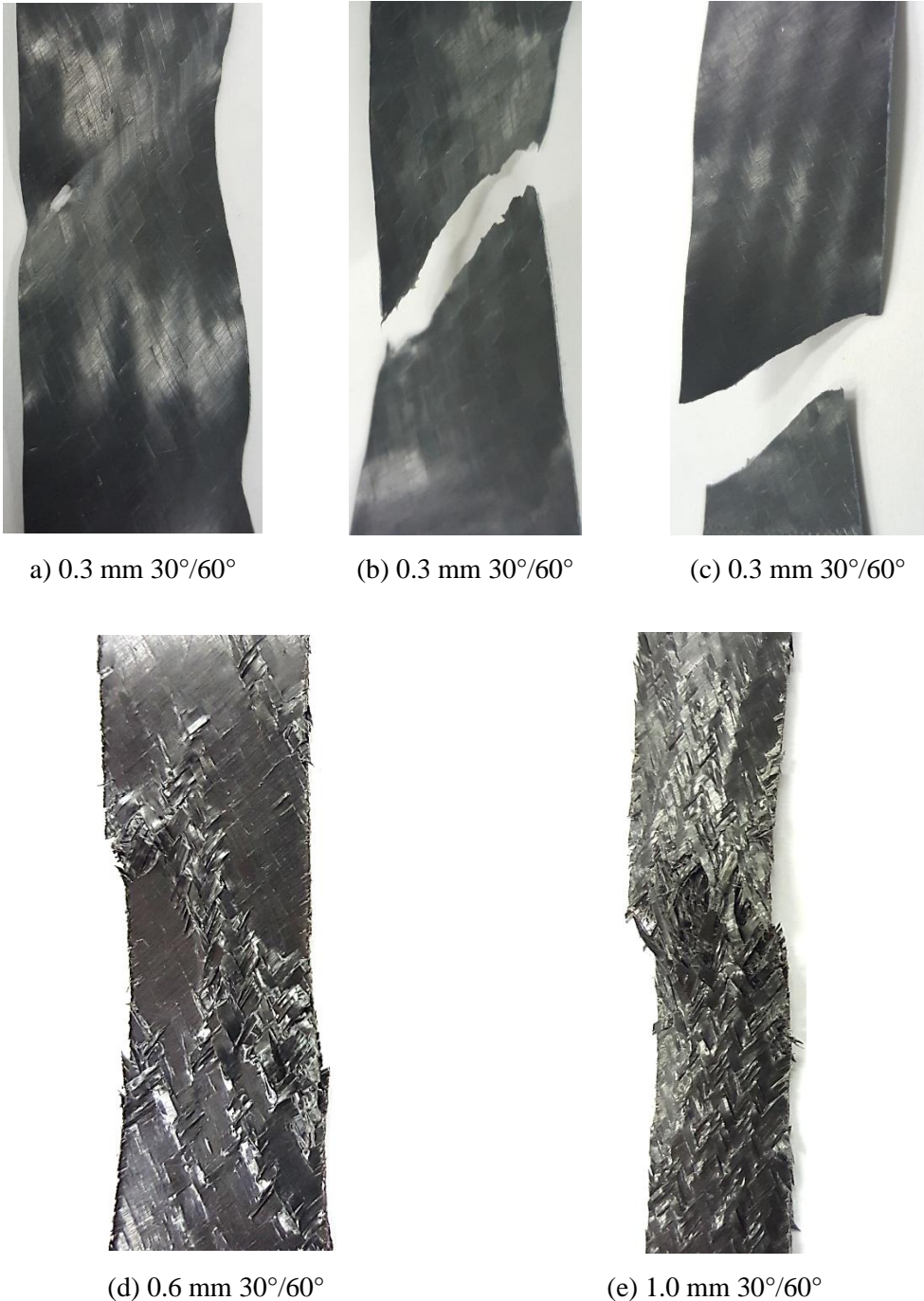


Figure 5.6 Photographs of 0.3 mm (a–c), 0.6 mm (d) and 1.0 mm (e) 30°/60° SRPP tensile test specimens at failure.

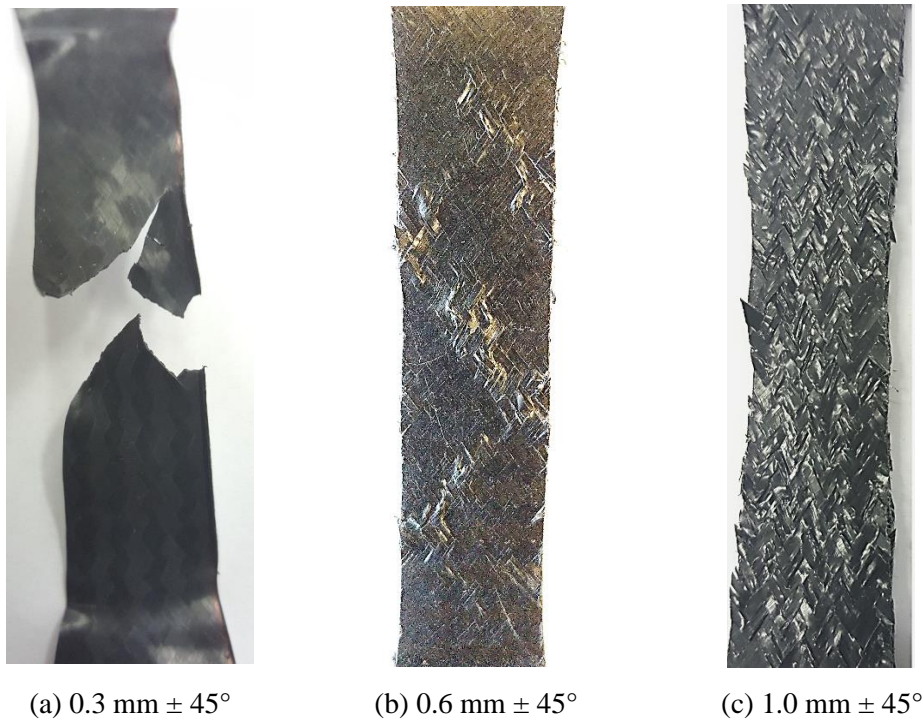


Figure 5.7 Photographs of 0.3 mm (a), 0.6 mm (b) and 1.0 mm (c) \pm 45° SRPP tensile test specimens at failure.

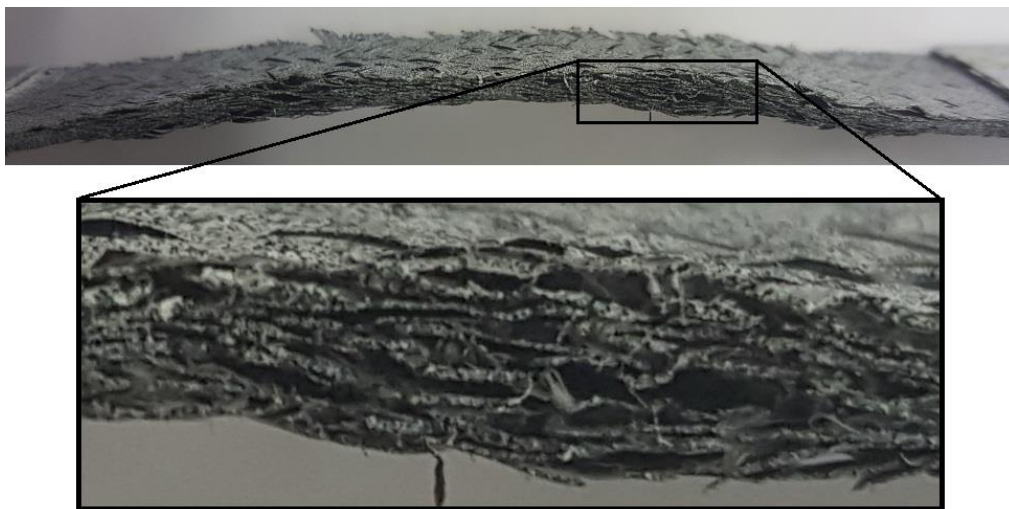


Figure 5.8 Delamination shown in a 1.0 mm \pm 45° SRPP tensile test specimen after failure. The direction of the applied load is horizontal in this image.

It should be mentioned that the photographs in Figures 5.6–5.8 represent specimens at failure, when the applied load has reached the maximum value and dropped by 2–3%. At this point, the thicker specimens have not separated completely into two pieces but are considered to have reached the failure point, since the specimen will be unable to carry any further load very shortly after this point. Further displacement

does separate the specimen into two pieces, as shown in Figure 5.9. Such behaviour contrasts to the separation of the $0^\circ/90^\circ$ specimens into two parts immediately upon reaching the maximum load.



Figure 5.9 Separation of a 0.6 mm $30^\circ/60^\circ$ specimen after failure.

The overall behaviour of both the $30^\circ/60^\circ$ and $\pm 45^\circ$ specimens is similar except for a few differences, which include the higher stiffness and strength of the 0.6 mm $\pm 45^\circ$ specimens than the 0.6 mm $30^\circ/60^\circ$ specimens, and the fact that the 0.3 mm $30^\circ/60^\circ$ specimens can sometimes fail with just a slit or a hole instead of separating into two pieces, as shown in Figure 5.6a. Both 0.3 mm $30^\circ/60^\circ$ and $\pm 45^\circ$ specimens fail approximately along their tape orientations, along 60° -tapes or in a zigzag-like path along $+45^\circ$ and -45° -tapes, respectively.

This section explained the stress-strain and macroscopic failure behaviour of various off-axis SRPP specimens, highlighting the similarities and differences to the $0^\circ/90^\circ$ specimens and between specimens of different thicknesses. It can be seen that there are some differences to the $0^\circ/90^\circ$ specimens that are commonly expected in an FRP when loaded at off-axis angles to the reinforcing directions, such as lower stiffness and strengths and higher failure strains, except in the 0.3 mm specimens. There was relatively little difference between the $30^\circ/60^\circ$ and $\pm 45^\circ$ specimens. Some trends in the behaviour due to the thickness differences that were observed in the $0^\circ/90^\circ$ specimens were also observed in the off-axis specimens, such as the increase in the amount and types of damage with thickness, and the strikingly different damage characteristics of the 0.3 mm specimens. The next section will show findings on the differences in the microscopic damage mechanisms as compared to the $0^\circ/90^\circ$ specimens.

5.2.2 Microscopic damage mechanisms

As with the $0^\circ/90^\circ$ SRPP specimens, multiple damage occur in the off-axis specimens throughout the deformation process. The types of damage that occur in the off-axis specimens are similar to those in the $0^\circ/90^\circ$ specimens although sometimes they manifest differently in terms of appearance and frequency due to the difference in the loading conditions. This subsection highlights these differences as analysed under the microscope.

It should be mentioned that no difference was found between the $30^\circ/60^\circ$ and $\pm 45^\circ$ specimens in terms of damage characteristics. Only a few differences between these specimens were found in terms of stress-strain behaviour and the catastrophic failure behaviour, part of which was mentioned in the previous subsection and part of which will be explained in Section 5.2.3.

This subsection is divided into two parts, the first covering damage that occur in all specimens, and the second covering damage observed only in the 0.6 mm and 1.0 mm specimens. One particular type of damage mechanism – boundary cracks – is discussed later under Section 5.2.3 due to its significant relevance in explaining the failure mechanisms in the 0.3 mm specimens. The direction of the applied load is horizontal in all micrographs except in Figures 5.29 and 5.20 and in the photograph in Figure 5.22.

5.2.2.1 Damage common to all thicknesses of SRPP specimens

The following types of damage mechanisms were observed in all specimens, regardless of thickness:

- Boundary cracks
- Tape-splits
- Aligned crazing
- Crazing

The characteristics of the above damage types will be analysed in this section. Since all of these have been discussed in detail during the analysis of the $0^\circ/90^\circ$ specimens in the previous chapter, only the differences to the $0^\circ/90^\circ$ specimens will be explained here.

5.2.2.1.1 Boundary cracks

Similar to observations in the $0^\circ/90^\circ$ specimens, damage occurs at boundaries that resemble tape-splits between tapes of the same orientation, as shown in Figure 5.10. At boundaries between differently oriented tapes, shear flow in the matrix occurs and the damage can propagate into the tapes along the boundary, as shown in Figures 5.11. (Shear flow here denotes deformation or flow in viscous solid materials like polymers in response to shear stress. The deformed surface has morphology that is

continuous and smooth, as opposed to being rough.) This is observed much more often in the 0.3 mm specimens than in the thicker ones.

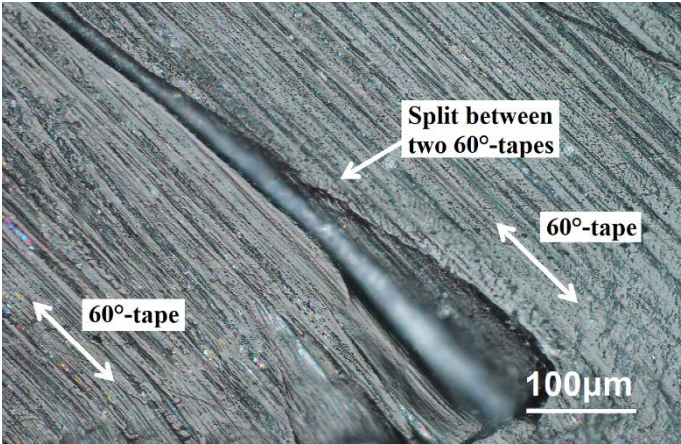


Figure 5.10 Optical micrograph of a boundary crack between two 60°-tapes in a 0.3 mm 30°/60° SRPP tensile test specimen, indicated with an arrow.

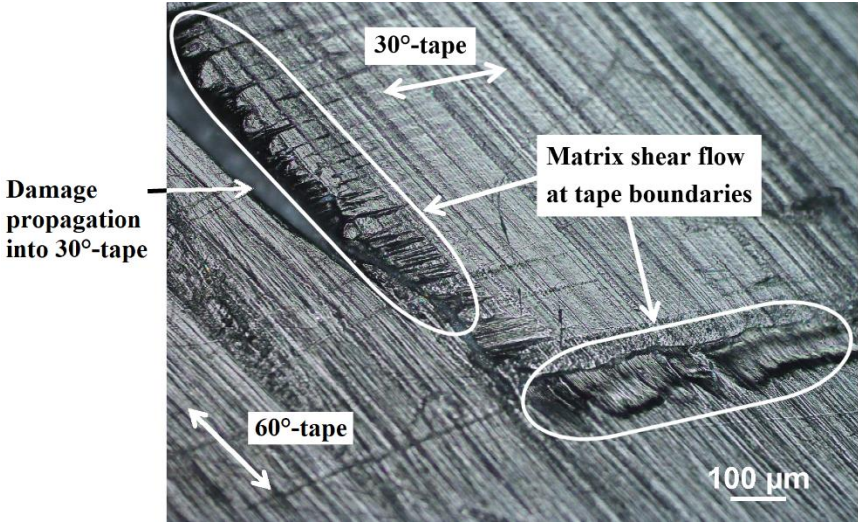


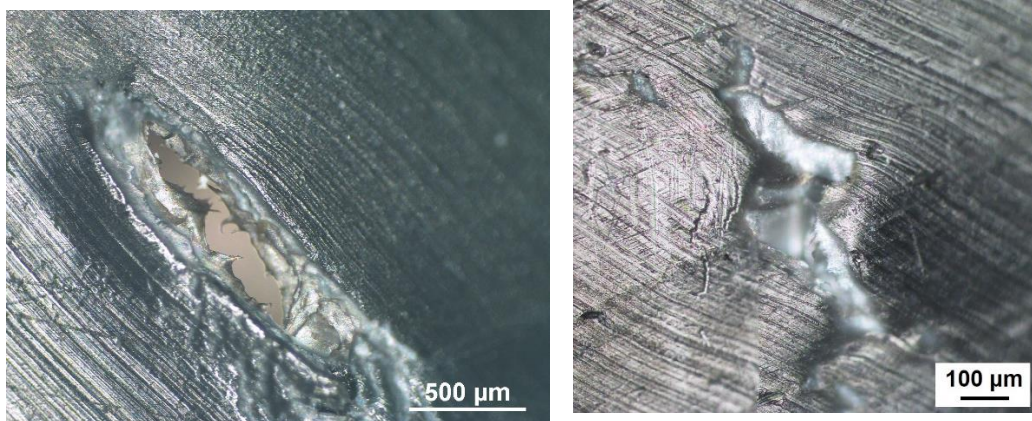
Figure 5.11 Optical micrograph of boundary cracks between 30° and 60°-tapes in a 0.3 mm 30°/60° SRPP tensile test specimen.

In off-axis specimens, boundary cracks can propagate under combined fracture modes of Mode I (tensile opening) and Mode II (in-plane shear), in contrast to the boundary cracks propagating only in Mode I in the 0°/90° specimens. An example is shown in Figure 5.12. This type of boundary crack occurs more frequently in $\pm 45^\circ$ specimens than in 30°/60° specimens.



Figure 5.12 Optical micrographs of boundary cracks in 0.3 mm $\pm 45^\circ$ SRPP tensile test specimens.

In 0.3 mm specimens, boundary cracks can propagate through the thickness, as shown in Figure 5.13. When this happens, a boundary crack can become the critical damage that causes specimen failure. The fact that failure initiates from boundary cracks is similar to the failure behaviour seen in the $0^\circ/90^\circ$ specimens. However, the type of critical boundary cracks found in off-axis specimens are those between tapes of different orientations, in contrast to the $0^\circ/90^\circ$ specimens in which the critical boundary cracks occurred between tapes of the same orientation. This will be explained in more detail in Section 5.2.3.



(a) 0.3 mm $30^\circ/60^\circ$

(b) 0.3 mm $\pm 45^\circ$

Figure 5.13 Optical micrographs showing ductile damage in a) 0.3 mm $30^\circ/60^\circ$ and b) 0.3 mm $\pm 45^\circ$ SRPP tensile test specimens.

In 0.6 mm and 1.0 mm specimens, boundary cracks can propagate to between tapes and cause delamination, which will be explained in more detail in Section 5.2.2.2.1. Where delamination does not occur, the edges of tapes can exhibit curved profiles, as shown Figure 5.14. Due to this, boundary cracks can propagate into the tape instead of between the tapes, tangentially to the curved edge, as depicted in

the figure. This is possible because the SRPP has very wide and ductile reinforcements and good bonding between reinforcements compared to typical FRPs, such as a glass fibre-reinforced composite, which would have delaminated or had fibre breakages before such shape changes could be seen in the fibres.

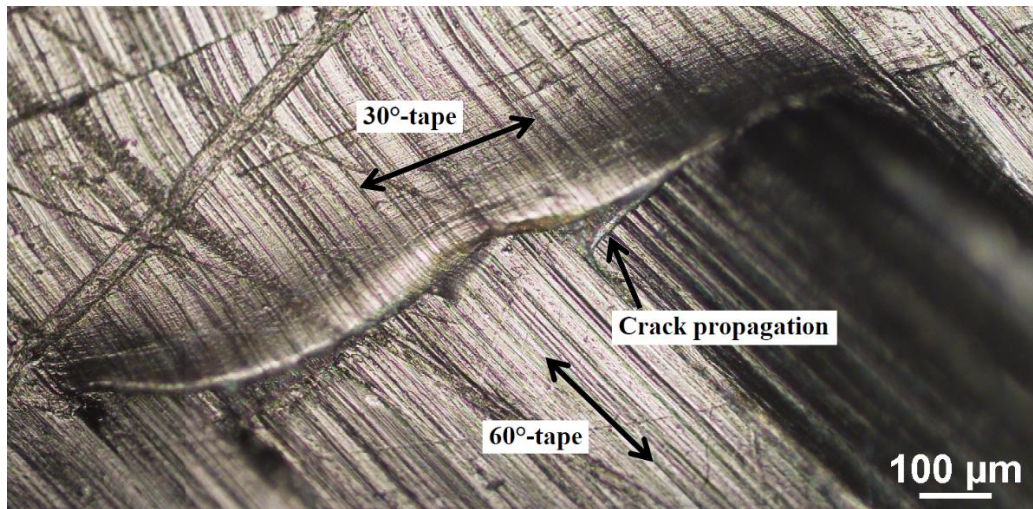


Figure 5.14 Optical micrograph of a curved edge of a 30°-tape in a 0.6 mm 30°/60° SRPP tensile test specimen.

5.2.2.1.2 Tape-splits

Similar to the 0°/90° specimens, tape-splits occur in all off-axis specimens and the amount of damage increases with thickness. However, there is not much difference in the number of tape-splits depending on the orientation of tape, except in one case. In relatively badly damaged areas of 0.6 mm and 1.0 mm 30°/60° specimens close to failure, more tape-splits occur in the 60°-tapes than in the 30°-tapes, as shown in Figure 5.15. This is obviously due to the higher alignment of the 30°-tapes to the direction of the applied load than the 60°-tapes. When the tape orientation is closer to a transverse direction to the loading direction, the tape suffers more tape-splits because the tapes are weaker in the transverse direction than in the reinforcing direction. This was also seen in the case of 0°/90° specimens which had far more tape-splits in the 90°-tapes (transverse to the loading direction) than the 0°-tapes (aligned to the loading direction).

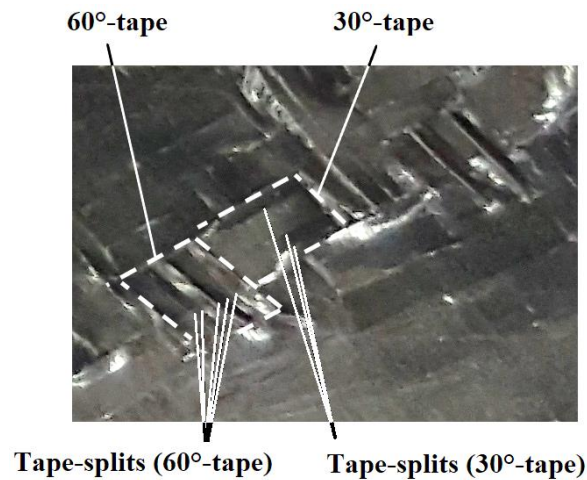


Figure 5.15 Tape-splits in a 0.6 mm 30°/60° SRPP tensile test specimen.

In the off-axis specimens, tape-splits promote the in-plane shear strains in the material as the tape-splits create smaller sections of tapes which can slide relative to one another, as shown in Figure 5.16. In addition, the in-plane shear strain *within* the unbroken sections of the tapes also contributes to the increase in shear strain of the material. This can cause slight wrinkling in some cases, as shown in Figure 5.16. This is only observed in 0.6 mm and 1.0 mm specimens because the tape-splits do not occur sufficiently extensively in the 0.3 mm specimens to cause wrinkling.

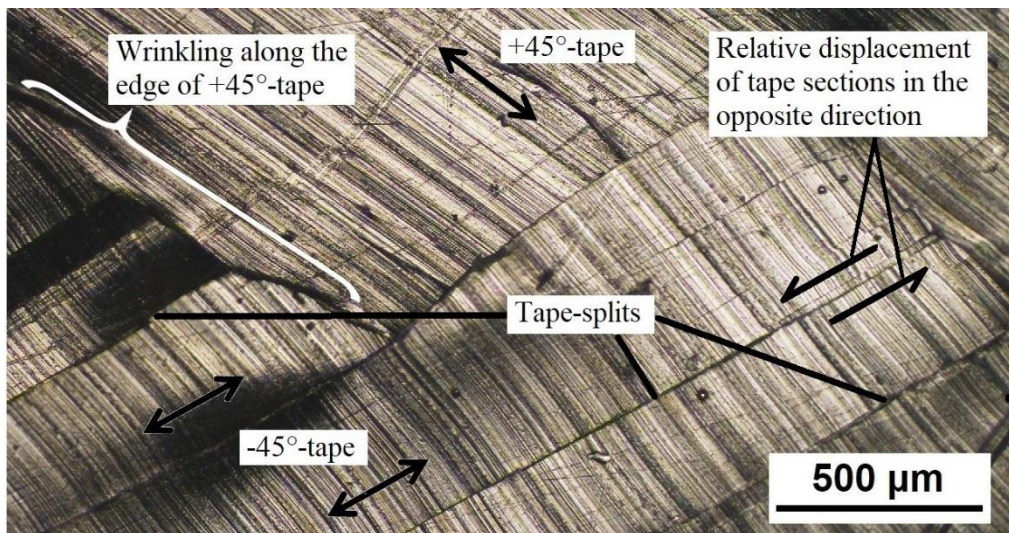


Figure 5.16 Optical micrograph of tape-splits in a 1.0 mm $\pm 45^\circ$ SRPP tensile test specimen.

5.2.2.1.3 Aligned crazing

Aligned crazing occurs in off-axis specimens in the same way as in the $0^\circ/90^\circ$ specimens, where collinear microscopic voids join to form cracks on the surface along tape orientations. However, the aligned crazing does not occur as much as in the 90° -tapes in the $0^\circ/90^\circ$ specimens. This is due to the off-axis specimens deforming predominantly by in-plane shear ($\gamma_{12} > 0$), and the reduction in tensile strain in the transverse direction to the tape orientation. (In comparison, 90° -tapes in $0^\circ/90^\circ$ specimens are deformed along the weaker lateral dimension which promotes the growth of aligned crazing). In the off-axis specimens, there is no noticeable difference in the amount of damage due to tape orientation.

5.2.2.1.4 Crazing

Crazing also occurs in the off-axis specimens. As explained in the previous chapter, crazing is a type of matrix cracks that form in response to tensile stress. It occurs much less frequently than in $0^\circ/90^\circ$ specimens, probably due to the matrix deforming under a combination of tensile strain (due to the applied load) and in-plane shear strain (due to tapes on either side of the matrix moving in different directions). Note that crazes form when cracks form and propagate in Mode I fracture mode (tensile opening).

Crazing occurs in two instances. In the first instance, it occurs in the matrix between the edges of two tapes, as shown in Figure 5.17. Crazes are approximately transverse to the direction of normal stress and only propagate within the matrix. As such, cracks are shorter than in the $0^\circ/90^\circ$ specimens, in which matrix cracks between tapes can extend the entire length between the weave boundaries and form boundary cracks.

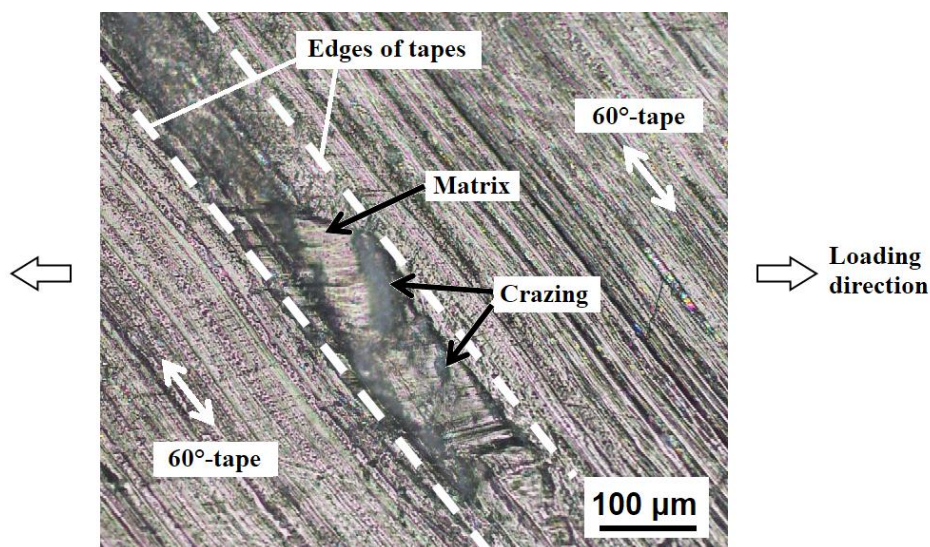


Figure 5.17 Optical micrograph of matrix crazing between neighbouring 60° -tapes in a 0.3 mm $30^\circ/60^\circ$ SRPP tensile test specimen.

The second instance where crazing occurs is in the matrix on the surface of the material, as shown in Figure 5.18. This contrasts to $0^\circ/90^\circ$ specimens which exhibit only *aligned crazing* in the surface matrix (Section 4.2.2.1.2). It may be recalled that aligned crazing in the $0^\circ/90^\circ$ specimens occurs from the coalescing of microvoids that form along the underlying splits in the tapes beneath the surface matrix. Due to this, the aligned crazes are highly linear and aligned to the tape orientation. In contrast, crazing in the surface matrix of off-axis specimens resembles typical crazing in polymers where the microcracks propagate transversely to the direction of the applied load. This is not aligned to the orientation of the tape underneath the matrix and, as such, the cracks do not exhibit a high degree of linearity. In the case of off-axis specimens, it is apparent that the crazes in the surface matrix do not derive from tape-splits underneath.

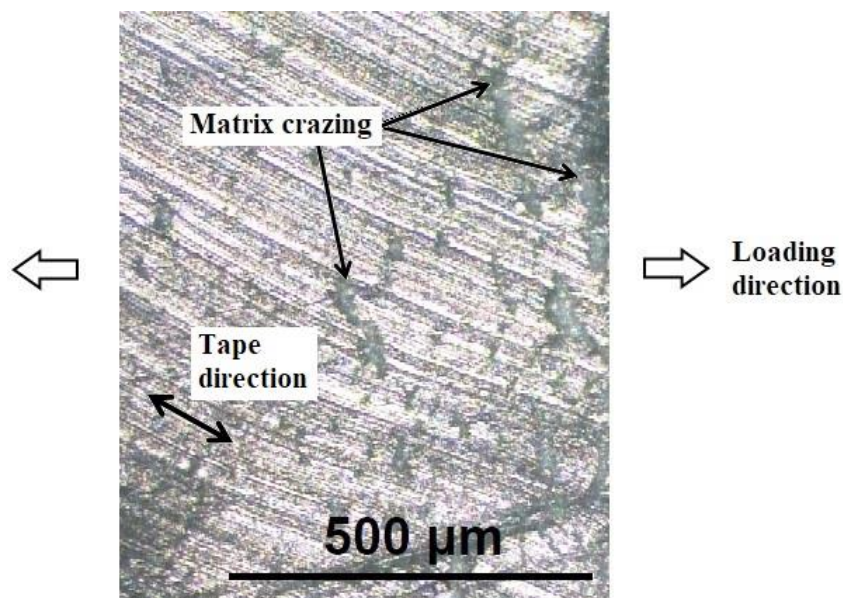


Figure 5.18 Optical micrograph of surface matrix crazing in a $0.3 \text{ mm} \pm 45^\circ$ SRPP tensile test specimen.

Cracks within crazing of the surface matrix in the vicinity of large areas of damage can propagate much further than those shown in Figure 5.18, as shown in Figure 5.19a. Also, crazing can occur on top of other damage. In the case shown in Figure 5.19b, crazing has occurred in the surface matrix and failure has occurred in the tape underneath. As can be seen, cracks propagated in a brittle manner in crazing and the tape has failed in a ductile manner. This demonstrates that both brittle and ductile damage can occur in the same region in SRPP specimens due to the different damage mechanisms occurring in the reinforcement and the matrix.

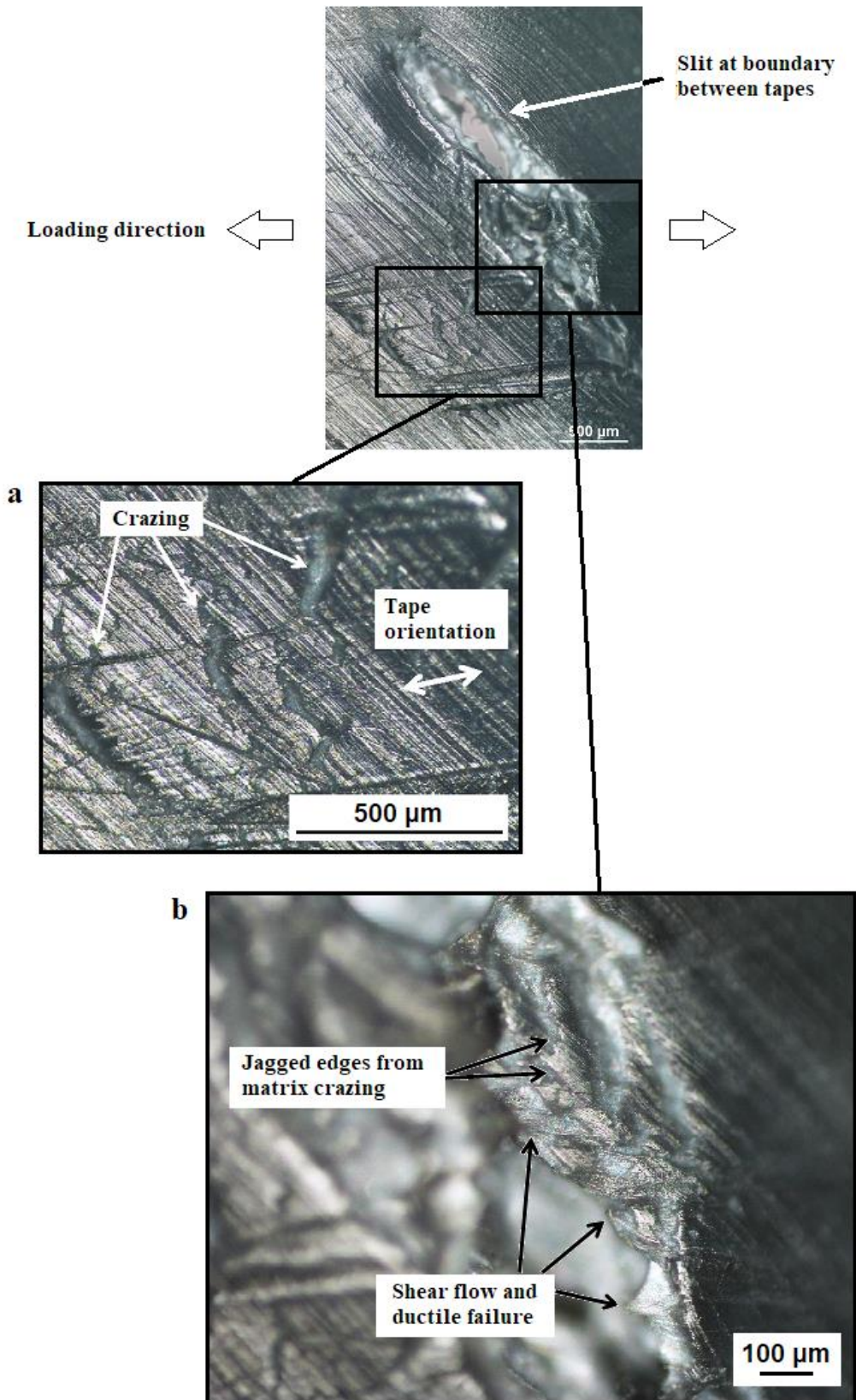


Figure 5.19 Optical micrograph of a 0.3 mm 30°/60° SRPP tensile test specimen near a slit, showing a mixture of crazing on the surface matrix and shear flow and ductile failure in the tape.

5.2.2.2 Damage unique to thicker SRPP specimens

The following subsections will discuss the characteristics of damage mechanisms that were observed in 0.6 mm and 1.0 mm specimens but not in 0.3 mm specimens. Specifically, these are:

- Delamination
- Tape and fibril pull-outs
- Fibrillar crack bridging
- Tape-fold
- Oblique crack

These types of damage all occurred in thicker specimens when the SRPP was tested at the $0^\circ/90^\circ$ direction, again showing similarity to the $0^\circ/90^\circ$ specimens. An exception is that tape-folds are only observed in off-axis specimens. There is an additional minor difference in that tape and fibril pull-outs were observed in all $0^\circ/90^\circ$ specimens regardless of thickness, whereas this was observed only in thicker off-axis specimens. The damage characteristics listed above will be explained in the following sections.

5.2.2.2.1 Delamination

Delamination in the off-axis 0.6 mm and 1.0 mm specimens occur with mostly similar characteristics to the $0^\circ/90^\circ$ specimens of the same thickness. The difference is that it occurs more abundantly throughout the entire gauge section in the 1.0 mm off-axis specimens, and in only a few regions spread throughout the gauge section in the 0.6 mm specimens (this was shown earlier in Figures 5.6–5.8). In contrast, delamination in the 0.6 mm and 1.0 mm $0^\circ/90^\circ$ specimens were concentrated around the region of failure. In addition, delamination in off-axis specimens becomes very visible well before failure, whereas visible delamination in the $0^\circ/90^\circ$ specimens mostly appeared at failure.

Delamination probably does not occur in the off-axis 0.3 mm specimens for the same reason it does not occur in the 0.3 mm $0^\circ/90^\circ$ specimens. It was conjectured earlier this is due to a greater degree of melting of the matrix occurring in the 0.3 mm $0^\circ/90^\circ$ specimens than in the thicker specimens during the manufacturing process, which would have increased the reinforcement–matrix bonding (Sections 4.2.1 and 4.2.2.2.4).

Delamination in the off-axis specimens occurs mostly within the tapes near the surface with a lot of fibrillation, as shown in Figure 5.20, which is similar to that seen in the $0^\circ/90^\circ$ specimens. However, unlike the $0^\circ/90^\circ$ specimens, there is no noticeable trend of delamination occurring preferentially within tapes of one orientation over another. The fact that delamination occurs more often in the tapes than in the matrix indicates that the adhesion between the tapes is quite strong in SRPP when compared to many other FRPs, as reported in the literature.

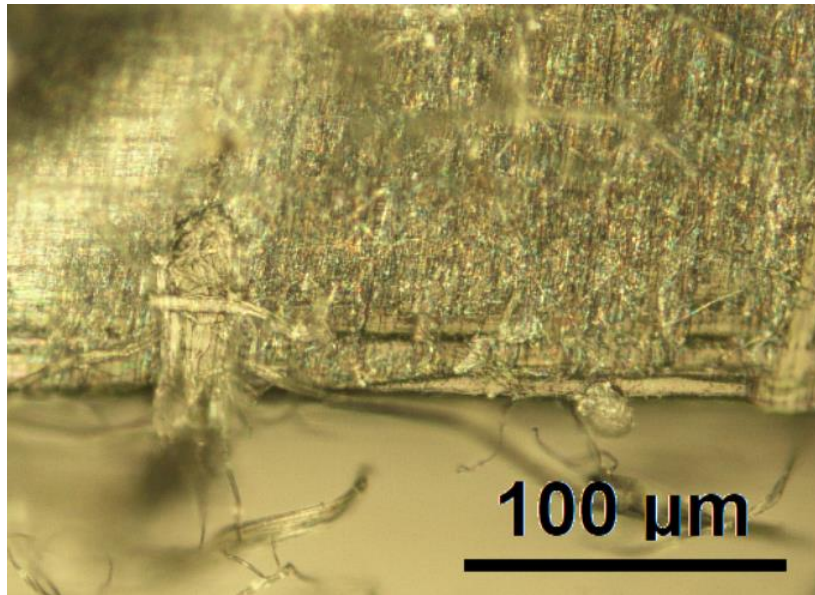


Figure 5.20 Optical micrograph of a delaminated tape in a 1.0 mm \pm 45° SRPP tensile test specimen. Direction of the applied load is 45° to the horizontal direction.

From microscopic analysis, it appears that delamination occurs from the propagation of a boundary crack between tapes that are oriented in different directions (crack along an edge of a tape where it meets another tape that weaves underneath it). An example is shown in Figure 5.21, where local delamination between a section of a 30°-tape and a 60°-tape has resulted from the propagation of a boundary crack between them.

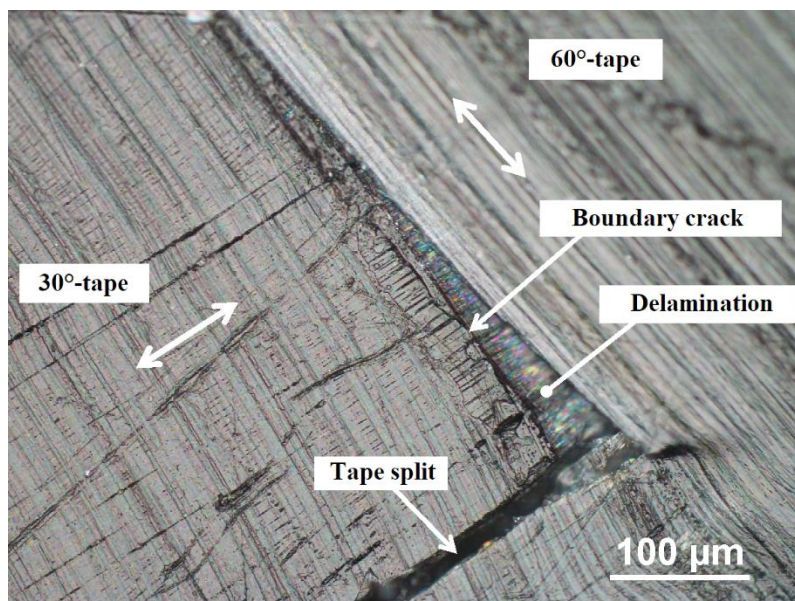


Figure 5.21 Optical micrograph of delamination occurring from a boundary between 30° and 60°-tapes in a 0.6 mm 30°/60° SRPP tensile test specimen.

Microscopic analysis also suggests that a boundary crack propagates into delamination from a point where it joins with a tape-split or another boundary crack. This is suspected to be due to a free edge being created along the side of the tape or its section when it is separated from the surrounding material via a tape-split or a boundary crack. As delaminations occur easily from free edges, the combination of a tape-split or a boundary crack with another boundary crack likely promotes easier crack propagation into a delamination.

It can also be seen from Figure 5.21 that the 30°-tape section has pulled out from underneath the 60°-tape unevenly, from the side where the boundary crack joins with a tape-split. This is due to the tapes rotating towards the direction of the load when subjected to loading at off-axis angles to their orientations. As the delamination propagates, the separated regions of the tapes rotate more easily in opposite directions, towards the loading direction, which would further accelerate the propagation of delamination. This may explain why delamination in off-axis specimens occurred earlier than in the 0°/90° specimens, well before the failure stage, as well as throughout the gauge section.

When the tapes have completely delaminated from each other between the weave boundaries, they rotate freely in the opposite direction in the region, which is known as trellising. The correlation between damage and trellising is quite obvious when comparing between regions of small and large amounts of damage in 0.6 mm specimens, as shown in Figure 5.22.

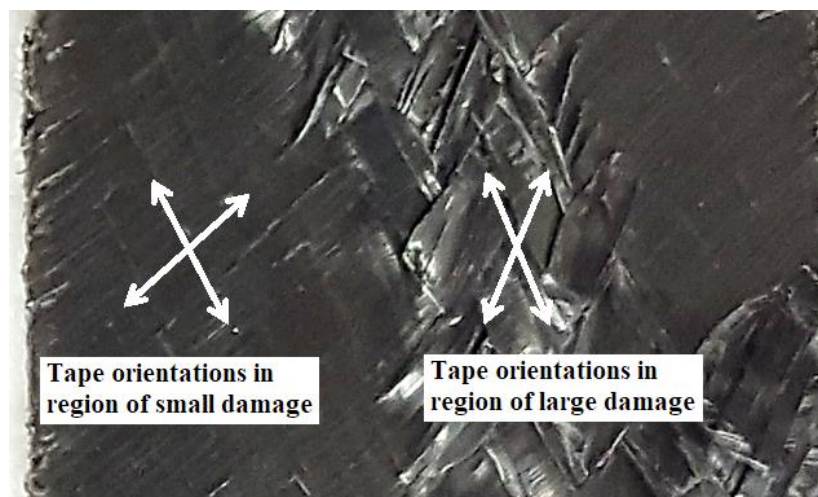


Figure 5.22 Comparison of tape orientations in regions of small and large amounts of damage in a 0.6 mm 30°/60° SRPP tensile test specimen.

5.2.2.2.2 Tape and fibril pull-outs

More tape and fibril pull-outs occur in 0.6 mm and 1.0 mm off-axis specimens than in 0°/90° specimens, mostly along the edges. In comparison, no tape pull-out is observed in 0.3 mm specimens. This is shown

in Figure 5.23. From surveying the ends of the tape pull-outs in thicker specimens, it can be seen that they form an angle to the edge of the specimen (Figure 5.23a). This is due to the decrease in γ_{12} within the tapes due to the unloading when the tapes become separated from the surrounding material. In comparison, the ends of the tapes in 0.3 mm specimens are aligned to the edge of the specimen because γ_{12} within the tapes are not recovered, as the adhesion holds the tapes together (Figure 5.23b).

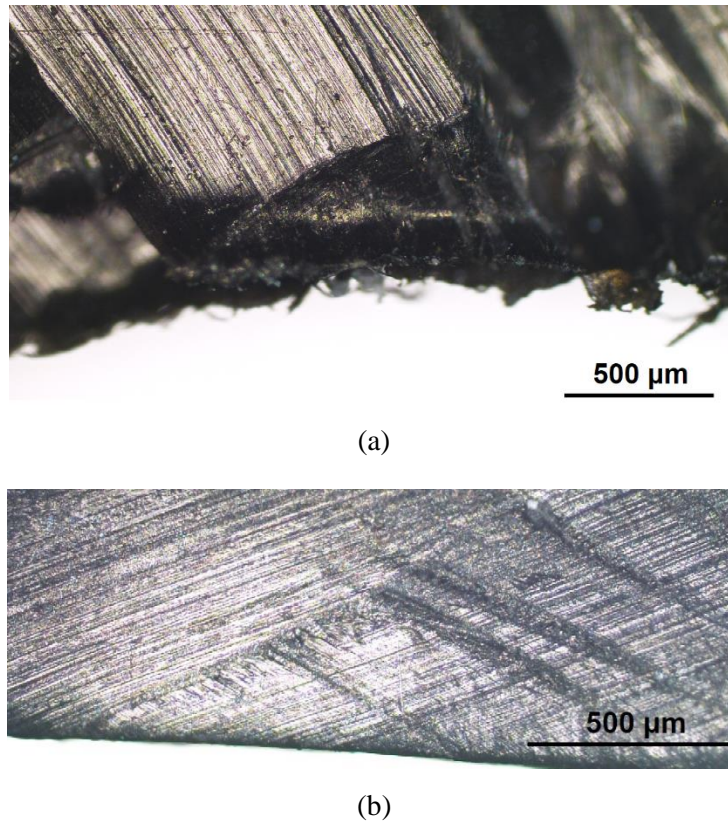


Figure 5.23 Optical micrograph of the edges of a) 0.6 mm 30°/60° and b) 0.3 mm $\pm 45^\circ$ SRPP tensile test specimens.

In the off-axis specimens, the majority of the tape and fibril pull-outs occur from the edges of the specimens, and only small amount fracture laterally, as shown in Figure 5.24 in the next page. This is because one or both ends of all tapes in the specimen are on the edge of the specimen, which are only constrained by the adhesion to the surrounding material. A pull-out occurs when the interfacial shear strength at the tape–matrix interface, or the matrix shear strength, are overcome. This requires less stress than is required to break the tape or the fibril laterally (strength in the reinforcing direction must be overcome). Therefore, tapes and fibrils pull out from the edges far more often than they fracture laterally in the tape.

This contrasts to the behaviour of the 0°/90° specimens, in which most fibril pull-outs occur in 0°-tapes when they fracture at the point of specimen failure. The difference arises due to the 0°-tapes in 0°/90°



Figure 5.24 Pull-outs and fracture of tapes and fibrils in a 1.0 mm $\pm 45^\circ$ SRPP tensile test specimen after failure. Examples of fractured tapes and fibrils are highlighted. Direction of load is horizontal in the image.

specimens being fixed at both ends by mechanical grips. In this case, fibrils' longitudinal strength must be overcome for them to fracture first, before they can pull out. As such, fibril pull-outs in $0^\circ/90^\circ$ specimens occurred at much higher levels of applied stress, mostly at specimen failure. In comparison, tape and fibril pull-outs in the off-axis specimens occurred before specimen failure.

When tape and fibril pull-outs do fracture laterally in the off-axis specimens, the ends tend to exhibit characteristics of brittle fracture, as shown in Figure 5.25. This is a behaviour not commonly seen in 0.6 mm and 1.0 mm $0^\circ/90^\circ$ specimens, although it may be due to fractures in the lateral direction to tape orientation mostly occurring in thin fibrils instead of wide sections of tapes.

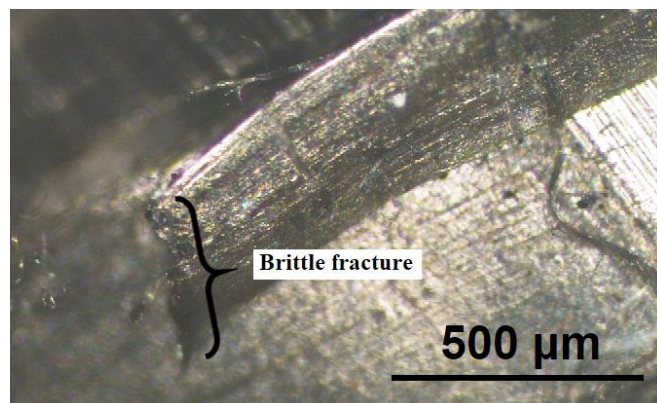


Figure 5.25 End of a fibril that has fractured in a brittle manner in a 0.6 mm $30^\circ/60^\circ$ SRPP tensile test specimen.

Smaller fibrils in the 0.6 mm and 1.0 mm off-axis specimens do tend to fail in a ductile manner at their ends, which is similar to the behaviour of the 0.6 mm and 1.0 mm 0°/90° specimens. However, the failed ends of thin fibrils in the off-axis specimens shear off in a jagged manner as shown in Figure 5.26, in contrast to the more linear profile of fibril ends in the 0°/90° specimens (see Figures 4.9 and 4.10). This demonstrates that the tapes in SRPP fracture with different characteristics when subjected to a combination of in-plane shear and normal strains in relation to the reinforcing directions, in comparison to when they are only subjected to normal strains.

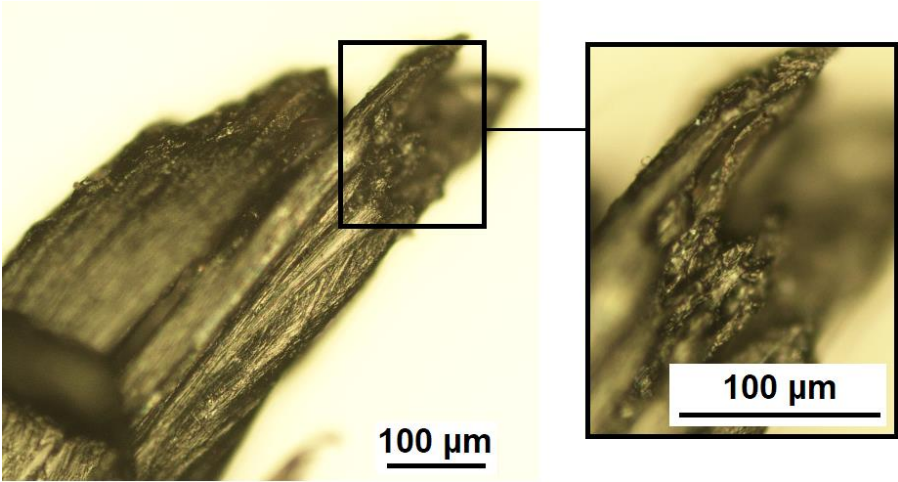


Figure 5.26 Optical micrographs of the end of a fibril pull-out in a 1.0 mm ± 45° SRPP tensile test specimen at different magnifications.

Another difference with the 0.6 mm and 1.0 mm 0°/90° specimens is that, in 0.6 mm and 1.0 mm off-axis specimens, both brittle and ductile fractures *can* co-occur when cracks propagate in directions not aligned to the tape orientation, as shown in Figure 5.27, although this is not observed very often. This

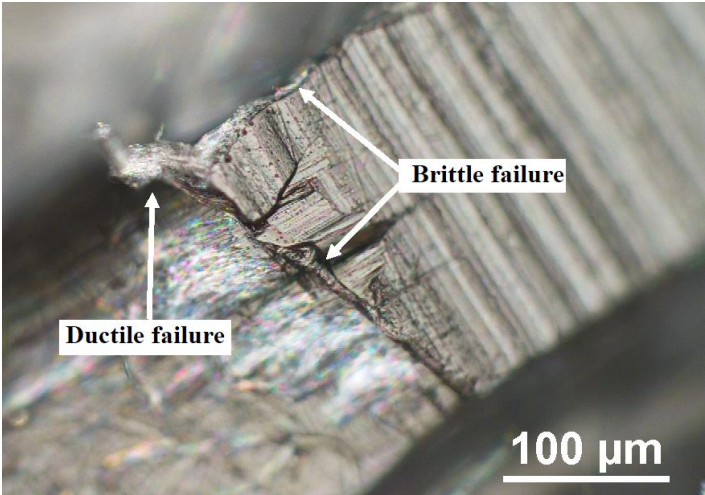


Figure 5.27 Optical micrograph of a tape section in a 0.6 mm 30°/60° SRPP tensile test specimen, exhibiting both brittle and ductile failure.

is closer to the failure behaviour in 0.3 mm 0°/90° specimens than in 0.6 mm and 1.0 mm 0°/90° specimens. Although both brittle and ductile failure modes can also occur in 0.6 mm and 1.0 mm 0°/90° specimens, they occurred in separate instances in that brittle failure occurred in the direction of the tape, and ductile failure occurred otherwise. In the fibril shown in Figure 5.27, brittle failure occurred from a crack not propagating in the reinforcing direction, as well as ductile failure.

To sum up, fractured ends of tapes and wider fibrils tend to exhibit brittle failure while the ends of small fibrils tend to exhibit ductile failure, and both brittle and ductile failures can occur in any size of tapes/fibrils and they can also co-occur right next to each other in a single tape/fibril.

5.2.2.2.3 Fibrillar crack bridging

Fibrillar crack bridging occurs in tape-splits of 0.6 mm and 1.0 mm off-axis specimens as shown in Figures 5.28 and 5.29. In comparison to the 0°/90° specimens, there are more fibrils, as well as more variation in sizes of fibrils, in the off-axis specimens. Fibrils can be thicker than 10 µm (Figure 5.28) or thinner than 100 nm (Figure 5.29). According to the classification previously defined (Figure 4.17), fibrils (> 10 µm), microfibrils (0.1–1 µm) and nanofibrils (10–100 nm) can appear in a single crack in off-axis specimens, whereas only microfibrils were observed in crack bridging in the 0°/90° specimens. This means that SRPP tapes can be separated down to the smallest building block of Peterlin's model of drawn semi-crystalline polymers (see Section 4.2.2.2.1), in the form of crack bridging, when they are loaded at an angle to their orientations.

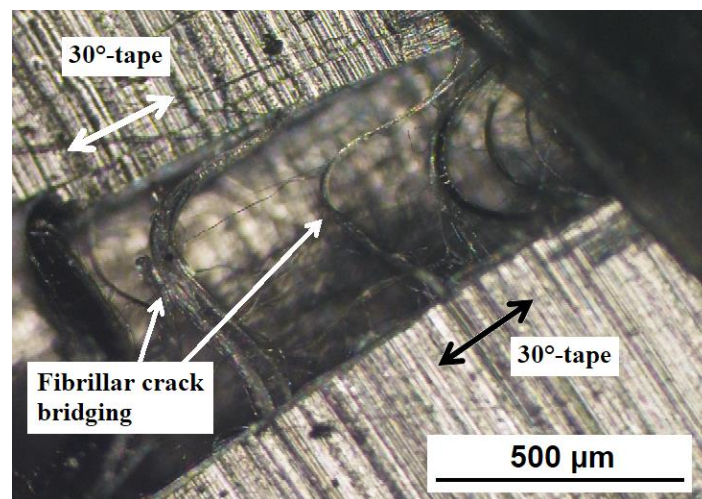


Figure 5.28 Optical micrograph of a fibrillar crack bridging in a tape-split of a 0.6 mm 30°/60° SRPP tensile test specimen.

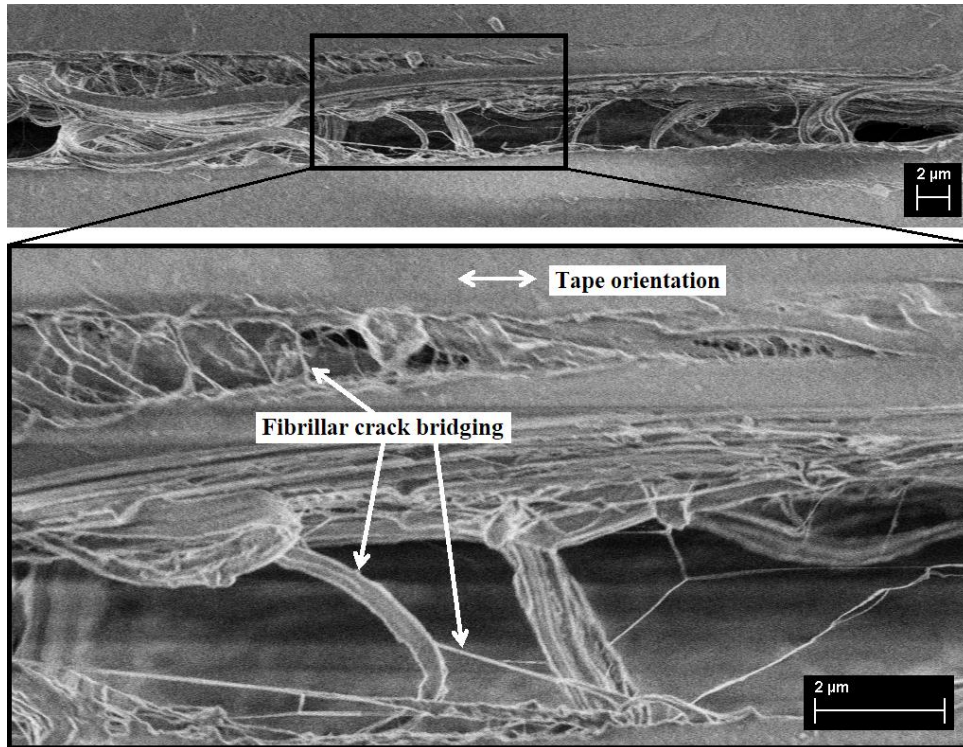


Figure 5.29 Scanning electron micrographs of fibrillar crack bridging in a tape-split of a 0.6 mm 30°/60° SRPP tensile test specimen. Magnification = 5,000x (top), 20,000x (bottom), EHT = 1.00kV. Direction of the load is at 60° to the tape orientation shown.

It is worth noting that fibrils are oblique to the direction of crack propagation, which is similar to those observed in the 0°/90° specimens and dissimilar plain polymers (where fibrils are perpendicular to cracks). Although the fibrils in Figures 5.28 and 5.29 are curved, this is due to the decrease of γ_{12} in the tapes from the unloading, which can occur when the tapes pull out and when the specimen is unloaded after the test. (The case of a decrease in γ_{12} from the unloading from tape pull-outs was described earlier in Section 5.2.2.2.2.) Prior to this, fibrils would have been taut and straight, as shown in Figure 5.30. Along with decrease of γ_{12} from the unloading, sections on either side of a tape-split would have moved in the opposite direction to one another, as illustrated by arrows in Figure 5.31, causing the fibrils bend.

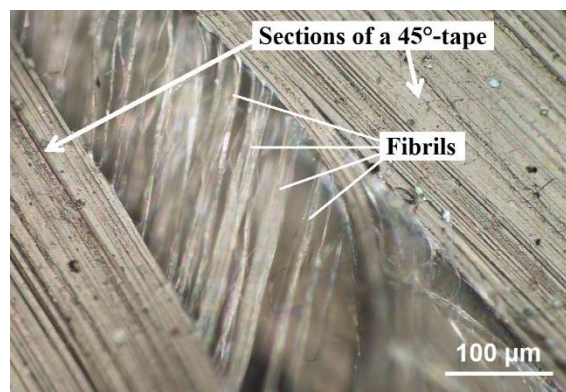


Figure 5.30 Optical micrograph of fibrillar crack bridging in a tape-split of a 1.0 mm $\pm 45^\circ$ SRPP tensile test specimen.

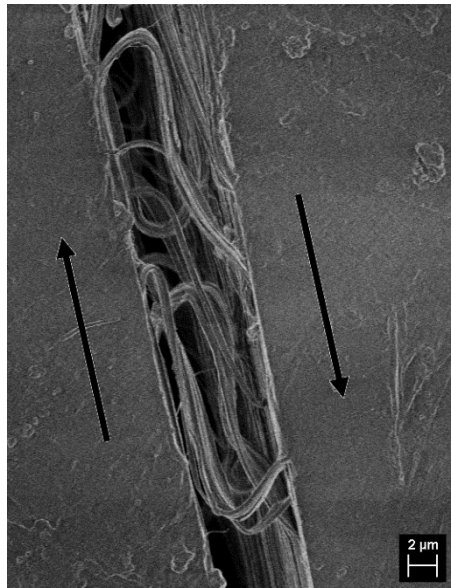


Figure 5.31 Scanning electron micrograph of fibrillar crack bridging in a tape-split of a 1.0 mm \pm 45° SRPP tensile test specimen. Magnification = 5,000x, EHT = 1.00kV. The tape is orientated along the arrows in the image.

In addition to the above differences, crack bridging in the off-axis specimens can occur across larger crack openings, as well as across delamination between tapes as shown in Figure 5.32. Crack bridging across delamination occurs more frequently in 1.0 mm specimens than in 0.6 mm specimens. It should be noted that 1.0 mm specimens sustain more damage before failure than do the 0.6 mm specimens. From this, it is hypothesised that the crack bridging might increase damage tolerance and fracture toughness similar to the toughening mechanisms in 0.6 mm and 1.0 mm 0°/90° specimens, although they have not been measured.

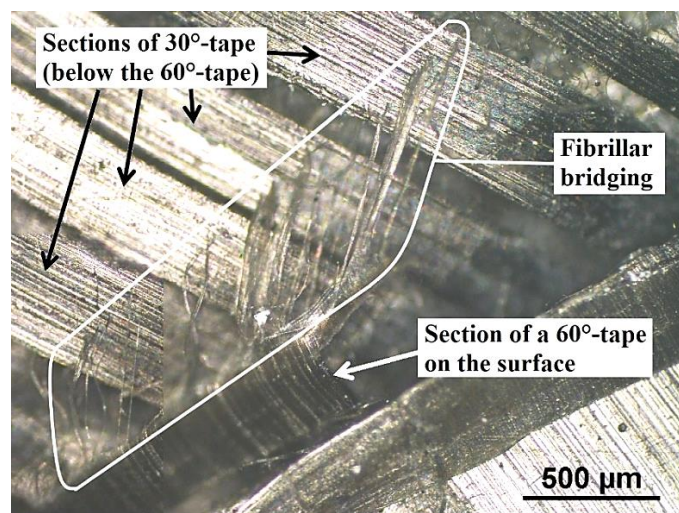


Figure 5.32 Optical micrograph of fibrils bridging inter-tape delamination in a 0.6 mm 30°/60° SRPP tensile test specimen.

Fibrillation and crack bridging can also occur in the matrix between the edges of two tapes, as shown in Figure 5.33. The fibrils created in the matrix have a lower degree of alignment than the fibrils created from the tapes due to little or no molecular alignment in the matrix. The matrix here can be thought of as being in the process of drawing under the applied load, whereas the tapes are already highly drawn from the manufacturing stage.

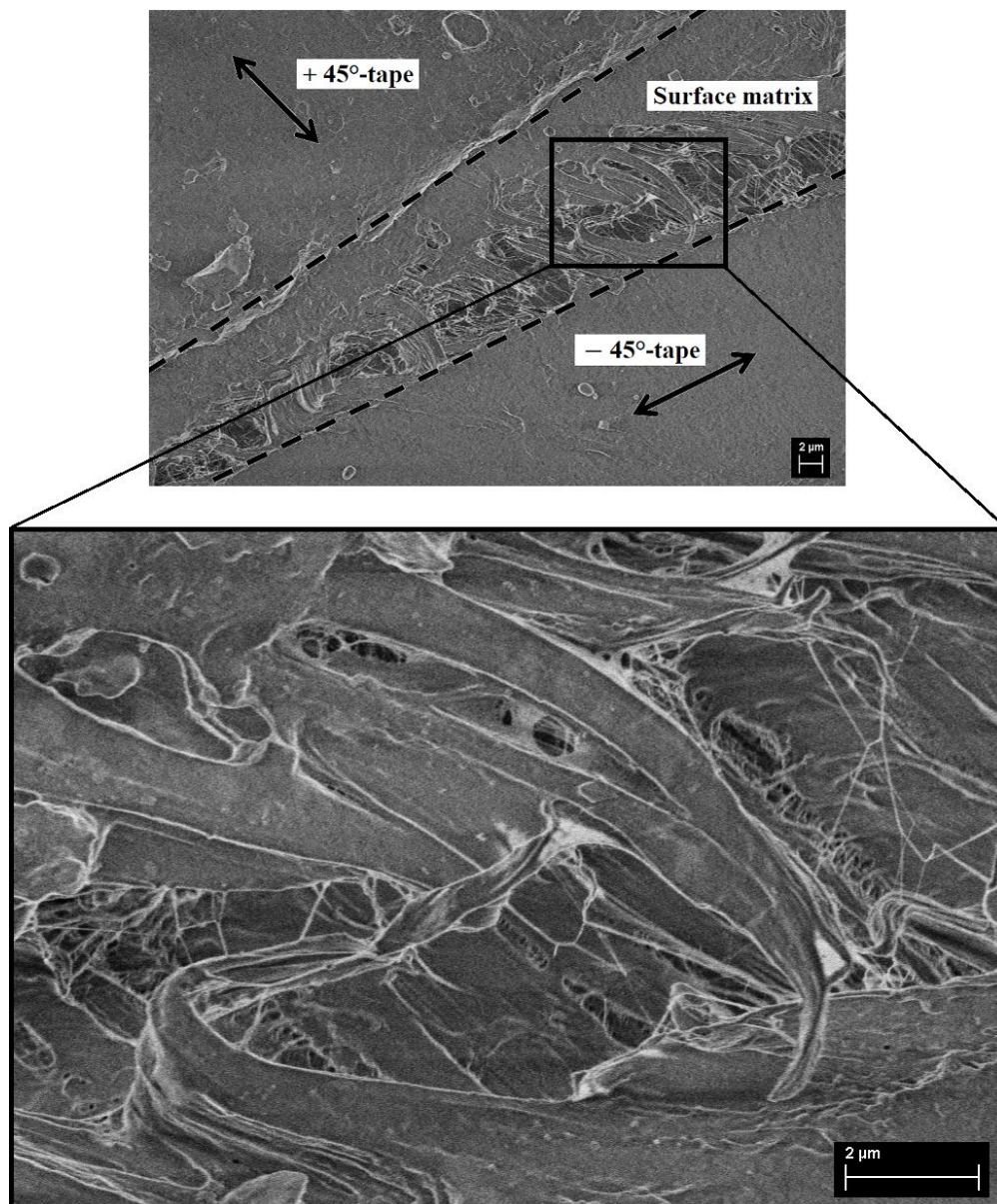


Figure 5.33 Scanning electron micrographs of matrix damage at a boundary between +45° and -45°-tapes of a 0.6 mm \pm 45° SRPP tensile test specimen. Magnification = 5,000x (top), 20,000x (bottom), EHT = 1.00kV.

5.2.2.2.4 Tape-fold

A partial folding of tapes on the edges occurs in the 0.6 mm and 1.0 mm off-axis specimens, as shown in Figure 5.34. This occurs due to a combination of *partial* delamination and trellising. When adjacent tapes with different orientations rotate in opposite directions, delaminated parts of the tapes can rotate further than the parts that have not delaminated. Due to this, a tape can fold over itself on the edge. This behaviour does not occur in the 0.3 mm specimens as they do not delaminate, and not does it occur in the $0^\circ/90^\circ$ specimens as there is no γ_{12} .

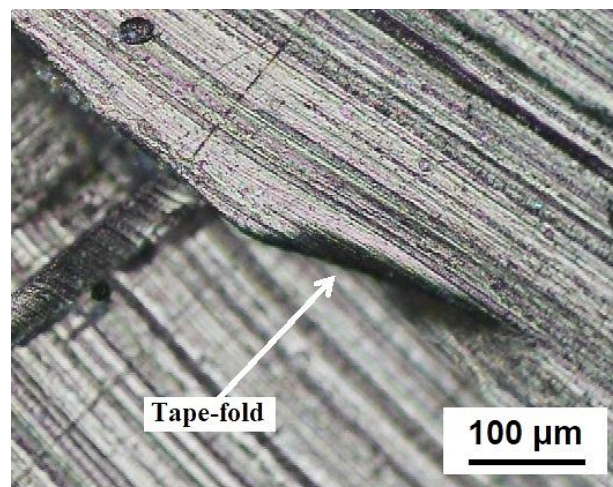


Figure 5.34 Optical micrograph of a tape-fold in a 0.6 mm $\pm 45^\circ$ SRPP tensile test specimen.

5.2.2.2.5 Oblique cracks

It was shown that 0° -tapes or tape sections in the 0.6 mm and 1.0 mm $0^\circ/90^\circ$ specimens can fail at approximately 20° or 75° to the tape orientation (Section 4.2.2.2.3). It was explained that this is rather unusual and possible hypotheses were given. Oblique cracks were also observed in the off-axis specimens, with tapes fracturing at around 25° or 75° to tape orientations, as shown in Figure 5.35 in the next page. In the off-axis specimens, these occurred more frequently than in the $0^\circ/90^\circ$ specimens.

In contrast to observations in the $0^\circ/90^\circ$ specimens, failure occurring at an angle to the tape orientation has been observed before in other polymers and there have been attempts to explain the underlying cause in the literature, for instance, in [230]. It is explained in the study that when polymers with molecular alignment are deformed at an off-axis angle to their initial drawing directions, they form narrow deformation bands. These bands are either nearly parallel to the polymer orientation and resemble shear bands in metals, or they form larger angles to the drawing direction and resemble kink bands in metals. Based on other studies reviewed in [230], the former might be caused by a combination of (001) slip

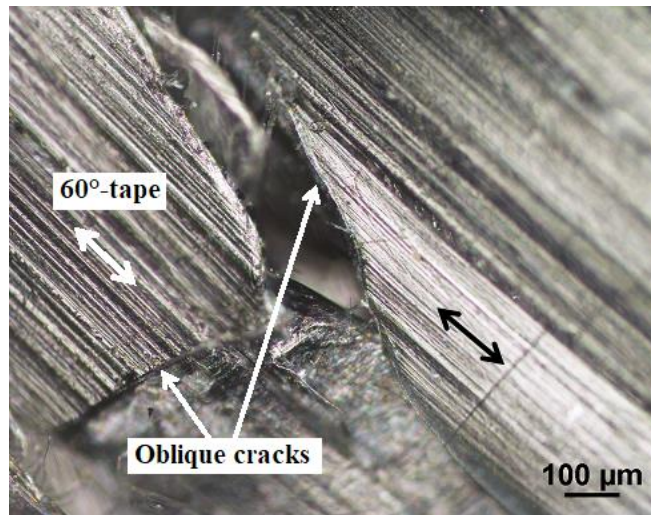


Figure 5.35 Optical micrograph of a fractured tape section in a 0.6 mm 30°/60° SRPP tensile test specimen.

system and mechanical twinning and the latter might be caused by gross reorientation of lamellae in the deformation band with a number of slip planes acting on a lamella.

The explanation in [230] may be the reason behind much of the oblique cracks observed in SRPP. However, the question still remains as to why oblique cracks were observed in tapes of the 0°/90° specimens, as these were not loaded at an angle to their drawing directions. Therefore, clear conclusions cannot be reached at this stage and the hypotheses made in Section 4.2.2.2.3 cannot be ruled out.

5.2.2.3 Summary of microscopic damage

Section 5.2.2 analysed various damage mechanisms that occur in SRPP specimens when deformed at 30°/60° and $\pm 45^\circ$ to the tape orientations. It was found that the same *types* of damage mechanisms occur whether the direction of load is applied along the reinforcement or at an angle, with a few exceptions. (Tape-folds only occur in off-axis specimens and tape kinking was only observed in the 0°/90° specimens.)

Although the types of damage are similar in off-axis and 0°/90° specimens, there are differences in their characteristics. For example, matrix shear flow was observed in boundary cracks between tapes that are oriented in different directions. The number of tape-splits in a tape increased as the angle between the tape and the load approached 90°, which is obviously related to the tape having weaker transverse strength than longitudinal strength. Compared to the 0°/90° specimens, less aligned crazing, crazing, and tape/fibril fractures occurred in the off-axis specimens, while more delamination and tape/fibril pull-outs occurred in the 1.0 mm off-axis specimens. More fibrillar crack bridging was observed in off-axis specimens as well, with a wider range of fibril types, ranging from nanofibrils to macro-fibrils.

In addition, it was found that the rotation of tapes towards the loading direction assisted the propagation of boundary cracks into delamination, which caused delamination to occur throughout the gauge sections well before failure. Due to the in-plane shear strain about the tape orientation, a tape can trellis, exhibit curved edges, warp, or fold over itself along the edges, depending on the extent of damage in the region.

5.2.3 Failure behaviour

This subsection on SRPP discusses the failure behaviour of the off-axis specimens. Failure in this case refers to the point at which the maximum load has been reached, as described earlier in Section 5.2.1. Failure behaviour of the 0.3 mm specimens is discussed first in Section 5.2.3.1. This will cover an analysis of critical damage and its propagation and strain analysis of the failure point. In the following Section 5.2.3.2, the failure behaviour of 0.6 mm and 1.0 mm specimens will be discussed, initially the initiation and progression of damage mechanisms that ultimately lead to failure of 0.6 mm 30°/60° specimens. This gives significant insight into how failure occurs in 0.6 mm \pm 45° and 1.0 mm specimens, which do not consequently require a long explanation. There will then be a brief discussion on the information offered by strain analysis using a DIC system regarding the failure behaviour of these specimens.

5.2.3.1 Failure behaviour of 0.3 mm specimens

The discussion on the failure behaviour of 0.3 mm off-axis specimens will start with how the critical damage initiates at a boundary crack and propagates. Then, Section 5.2.3.1.2 will show that surface strain analysis can be used to identify the point of failure, using some of the methods developed for 0.3 mm 0°/90° specimens in Section 4.2.3.1.3.

5.2.3.1.1 Initiation and propagation of critical damage

Failure in off-axis 0.3 mm specimens appears to initiate from a boundary crack, as in the case of 0°/90° specimens. However, critical boundary cracks in off-axis 0.3 mm specimens occur between tapes of different orientations and they propagate through the thickness, causing slits or holes to appear, as shown in Figures 5.36 and 5.37. As can be seen, the critical boundary cracks exhibit blunt crack tips and cause a ductile type of failure in the tapes, which must be due to the weave geometry based on the analysis of 0°/90° specimens in Chapter 4. (Interestingly, there are rare instances where slits do not occur along tape boundaries, as shown in Figure 5.38 but they are not related to specimen failure.) The fact that critical boundary cracks occur between differently oriented tapes indicates that damage development

from the warp and weft tapes rotating in the opposite directions is more damaging than matrix cracks between parallel tapes in 0.3 mm off-axis specimens.



Figure 5.36 Failures along a boundary between 30° and 60°-tapes in a 0.3 mm 30°/60° SRPP tensile test specimen. White lines indicate boundaries between 30° and 60°-tapes and red lines on either side of the damage represent the same tape boundary.

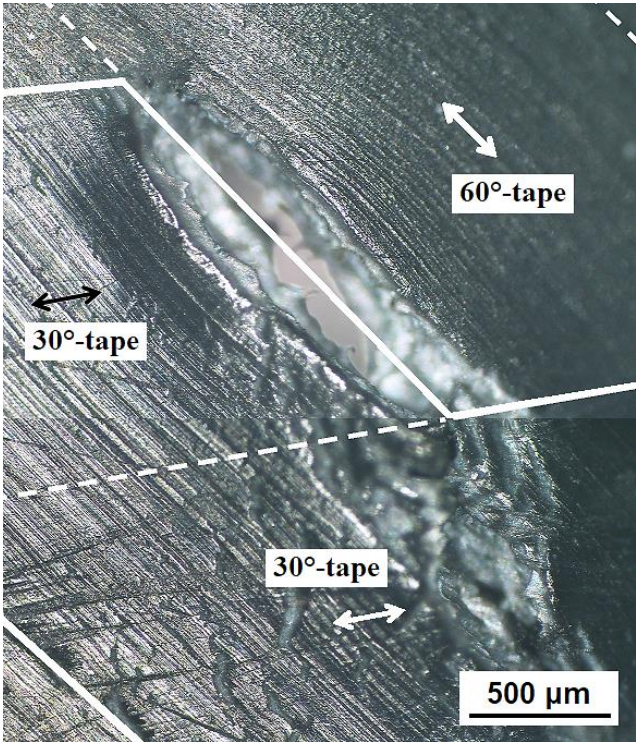


Figure 5.37 Optical micrograph of a slit at a boundary between 30° and 60°-tapes in a 0.3 mm 30°/60° SRPP tensile test specimen. Solid lines indicate boundaries between 30° and 60°-tapes and dotted lines indicate boundaries between tapes oriented in the same direction. Arrows indicate tape orientations.

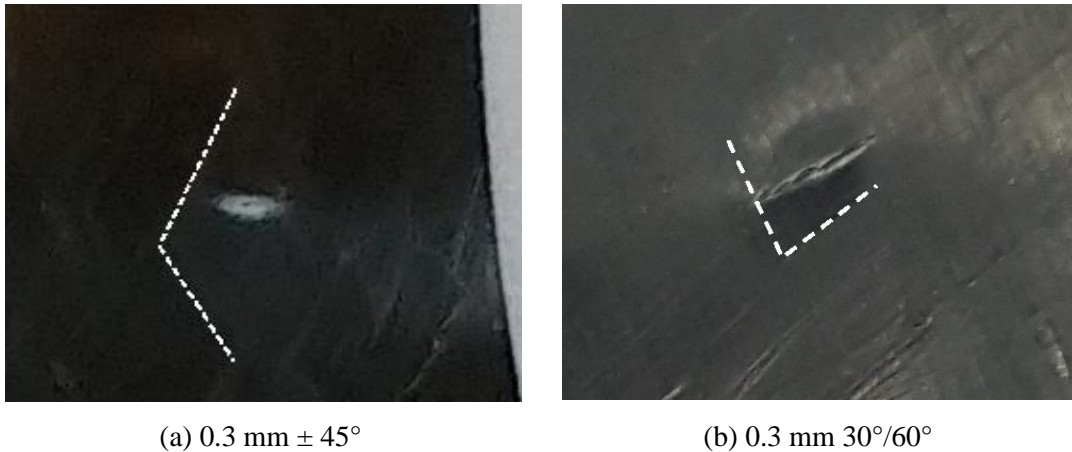


Figure 5.38 Slits occurring away from fracture sites and not along tape boundaries in 0.3 mm SRPP tensile test specimens tested at a) $\pm 45^\circ$ and b) $30^\circ/60^\circ$. Nearby tape boundaries between weft and warp tapes are indicated with dotted lines for clarity.

The described failure behaviour in 0.3 mm off-axis specimens contrasts to the 0.3 mm $0^\circ/90^\circ$ specimens, in which critical failure initiated between parallel tapes. This indicates that different type of stress and strain states drive the failure in the off-axis specimens, obviously due to the presence of in-plane shear strain about the tape directions. It is suspected that cracks in off-axis specimens propagate in both Modes I (tensile opening) and II (in-plane shear), whereas $0^\circ/90^\circ$ specimens fail via cracks propagating in Mode I only.

Failure in the $30^\circ/60^\circ$ specimens always occur from boundary cracks that are at 60° to the loading direction. This is because they are closer to being perpendicular to the loading direction than the boundary cracks that are at 30° to the loading direction, which would promote faster crack propagation. In $\pm 45^\circ$ specimens, there is no such difference between boundary cracks at $+45^\circ$ or -45° to the loading direction, so failure can occur from either.

The fact that 0.3 mm off-axis specimens fail at much higher applied strains ($53 \pm 10\%$, $70 \pm 7\%$) than 0.3 mm $0^\circ/90^\circ$ specimens ($14 \pm 5\%$) might be due to critical cracks in the 0.3 mm off-axis specimens initially propagating in a stable manner. This can be seen from the blunt crack tip and ductile failure at the critical boundary crack. Cracks propagating in a stable manner propagate more slowly than unstable ones, leading to failure occurring at a much later stage of deformation in the 0.3 mm off-axis specimens than in the 0.3 mm $0^\circ/90^\circ$ specimens. It is probable that crack arresting occurs in the 0.3 mm off-axis specimens, as the critical boundary cracks span one width of a tape initially, before propagating faster. Figures 5.39 is likely showing an example of a crack tip blunting.

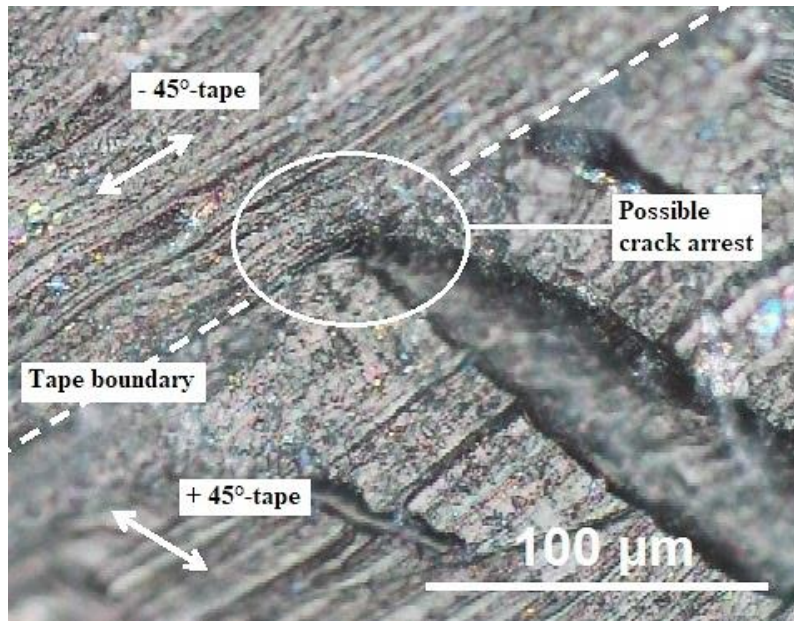


Figure 5.39 Optical micrograph of a possible crack tip blunting in a 0.3 mm $\pm 45^\circ$ SRPP tensile test specimen.

Regardless of whether crack tip blunting occurs, crack tips of critical damage in an off-axis 0.3 mm specimen are initially blunt. However, when the crack propagates rapidly at failure, it can propagate in either a ductile or a brittle manner, as shown in Figure 5.40, which is a rather peculiar phenomenon that was also observed in the $0^\circ/90^\circ$ specimens (Section 4.2.3.1.4).

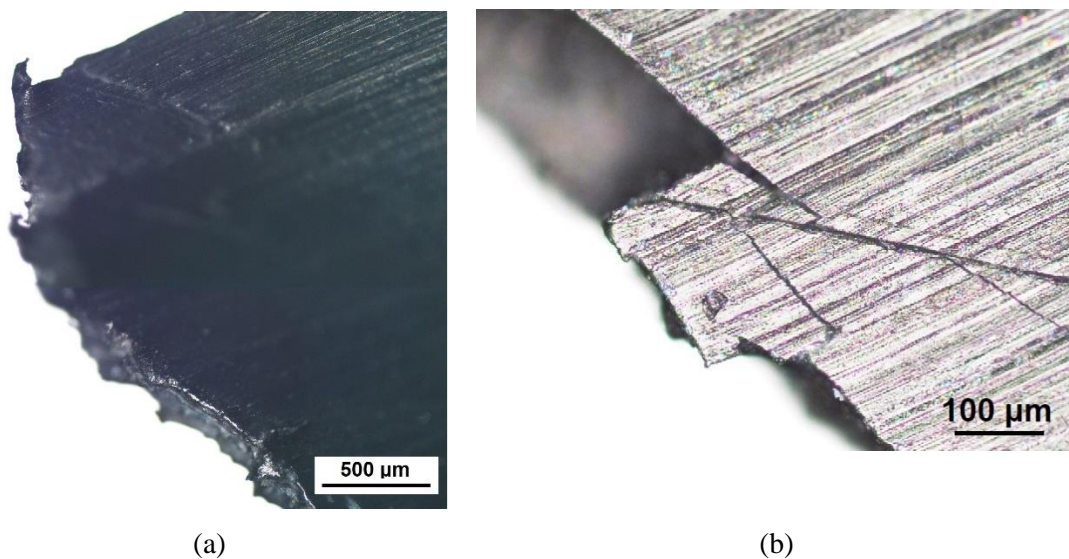


Figure 5.40 Optical micrographs of fractured edges of a 0.3 mm $30^\circ/60^\circ$ SRPP tensile test specimen.

During the rapid propagation of a crack at failure, the crack does not necessarily propagate along the boundaries between tapes. Failure mostly occurs at a slightly wider angle to the loading direction than 60° and $\pm 45^\circ$, as shown in Figure 5.41. However, there is always at least one section along the fracture path which occurs exactly along a tape boundary between differently oriented tapes, as indicated by the circles in Figure 5.41. These typically span one width of the tape and occur on the boundary between weft and warp tapes.

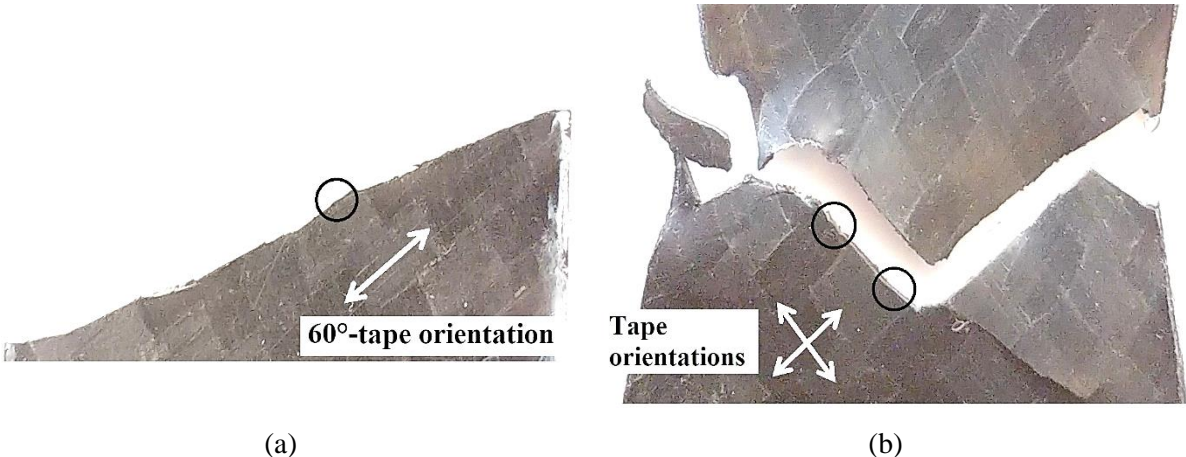


Figure 5.41 Fractures in 0.3 mm SRPP tensile test specimens with failure along the indicated tape boundaries, tested in a) $30^\circ/60^\circ$ and b) $\pm 45^\circ$ directions.

The above behaviour shows that few boundaries between differently oriented tapes provide weak points along which critical damage initiates, propagates or coalesces. Given that $\pm 45^\circ$ specimens fracture along both boundaries oriented at 45° or -45° to the loading direction, it is more likely that multiple boundary cracks initiate throughout the specimen and coalesce when one of them propagates rapidly across the width during failure. An example that illustrates this is shown in Figure 5.42 in the next page, where cracks at A–E most likely occurred separately from each other. It is still possible that cracks have bifurcated but evidence of such was not found.

From the analysis in this section, it can be seen that the failure behaviour of the off-axis 0.3 mm specimens is similar to the 0.3 mm $0^\circ/90^\circ$ specimens in many ways. They fail without delamination or large fibrillation, and boundary cracks were yet again found to be the critical damage that causes specimen failure. The critical boundary crack could propagate in both ductile and brittle manners during failure. However, there were also differences seen in the 0.3 mm $0^\circ/90^\circ$. For instance, the critical type of boundary crack was always found to occur between tapes of different orientations, instead of between parallel tapes. Also, the cracks propagated through the thickness first, causing a ductile failure of tapes, before propagating sideways in a rapid manner. In some $30^\circ/60^\circ$ specimens, the crack has not even propagated all the way across the width when the maximum load was reached, which is not observed in any other specimen.

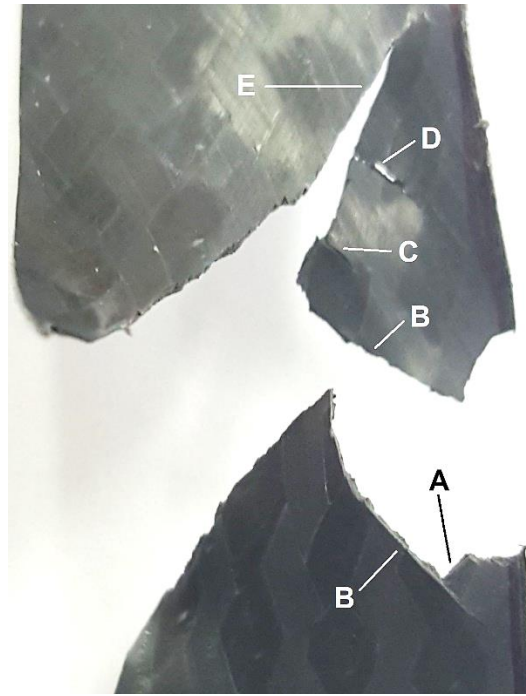


Figure 5.42 Crack propagation and coalescence in a 0.3 mm $\pm 45^\circ$ SRPP tensile test specimen.

5.2.3.1.2 Surface strain analysis of failure

This section will continue with the analysis of the failure behaviour of off-axis 0.3 mm specimens, this time using surface strain analysis. Similar to the analysis carried out on the $0^\circ/90^\circ$ specimens, this will show ways in which the surface strains can help identify failure points and decipher underlying behaviour. This will show that the deformation and failure of off-axis specimens are different to those in the $0^\circ/90^\circ$ specimens and that the same technique used for predicting the failure point and stage in the $0^\circ/90^\circ$ specimens cannot therefore be applied to some off-axis specimens.

Surface strain analyses of 0.3 mm off-axis specimens make it apparent that their deformation and failure behaviour are heavily influenced by the in-plane shear strain. Therefore, γ_{12} is a good strain measure to use for analysing deformation and failure behaviour. Figure 5.43 in the next page illustrates that ϵ_{p1} can also be used in identifying critical damage points from large strain points. For the purpose of analysing the failure points and their behaviour, both ϵ_{p1} and γ_{12} can be used.

An interesting observation of 0.3 mm $30^\circ/60^\circ$ specimens is that, in contrast to $0^\circ/90^\circ$ and $\pm 45^\circ$ specimens, none of the specimens failed from an HSCP that is exactly on the edge. The closest observation to failure occurring from an edge is shown in Figure 5.44 where failure initiates from a hole very close to the edge at point A. The hole becomes visible in the digital image at an applied strain of 41.6% and ruptures at 42.3% applied strain. The split grows until the specimen fractures at an applied strain of 42.8%.

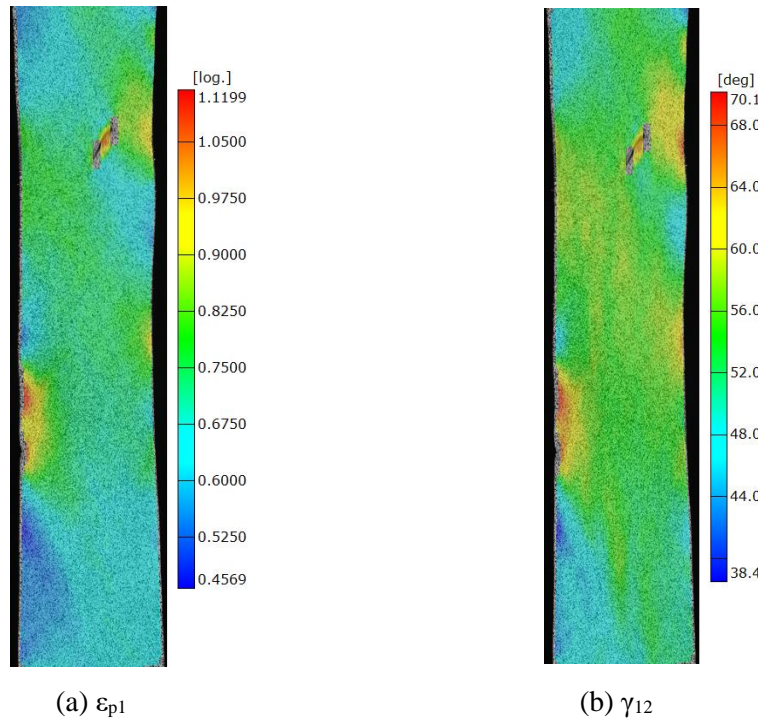


Figure 5.43 a) First principal strain (ϵ_{p1}) and b) shear strain (γ_{12}) in a 0.3 mm $\pm 45^\circ$ SRPP tensile test specimen just before fracture.

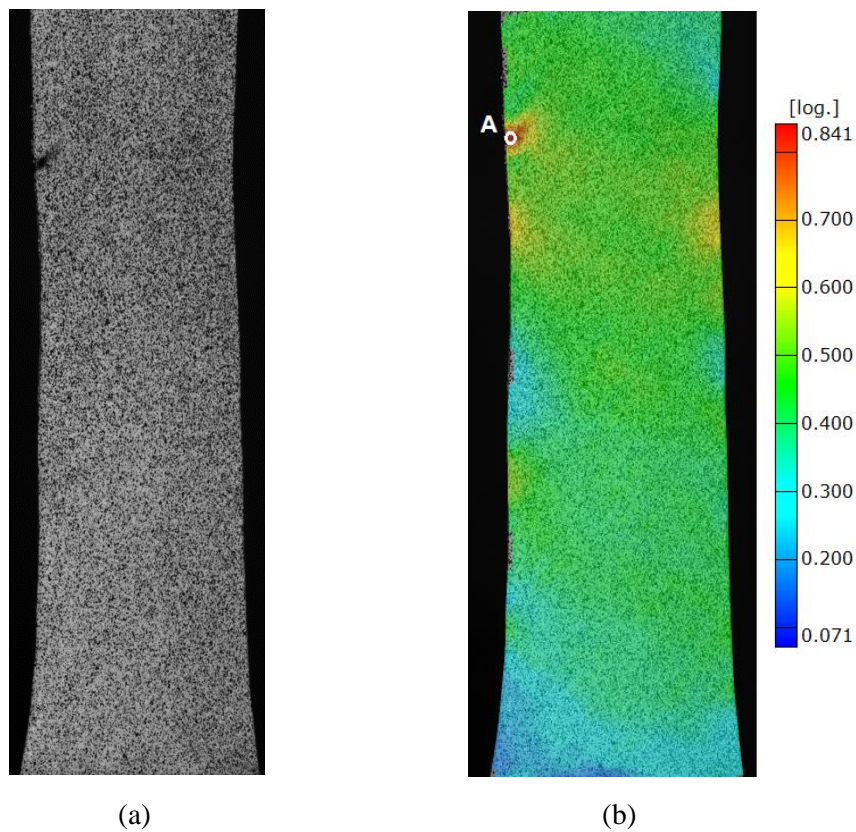


Figure 5.44 a) Photograph and b) first principal strain (ϵ_{p1}) in a 0.3 mm $30^\circ/60^\circ$ SRPP tensile test specimen at an applied strain of 41.5%.

Certain aspects of the strain behaviour in off-axis specimens are similar to those seen in 0°/90° specimens. For example, off-axis specimens also fail at HSCPs. Also, ± 45° specimens often fail within strain localisation bands, at least partly. An example that shows this is in Figure 5.45. Such behaviours show similarities to the 0°/90° specimens. However, failure points in 30°/60° specimens were often outside the strain localisation bands, or the specimens sometimes exhibit wide regions of high strains instead of a localisation of strains along narrow bands, as was the case in Figures 5.43. It should be noted that the mentioned behaviours are tendencies and some specimens do not follow this trend.

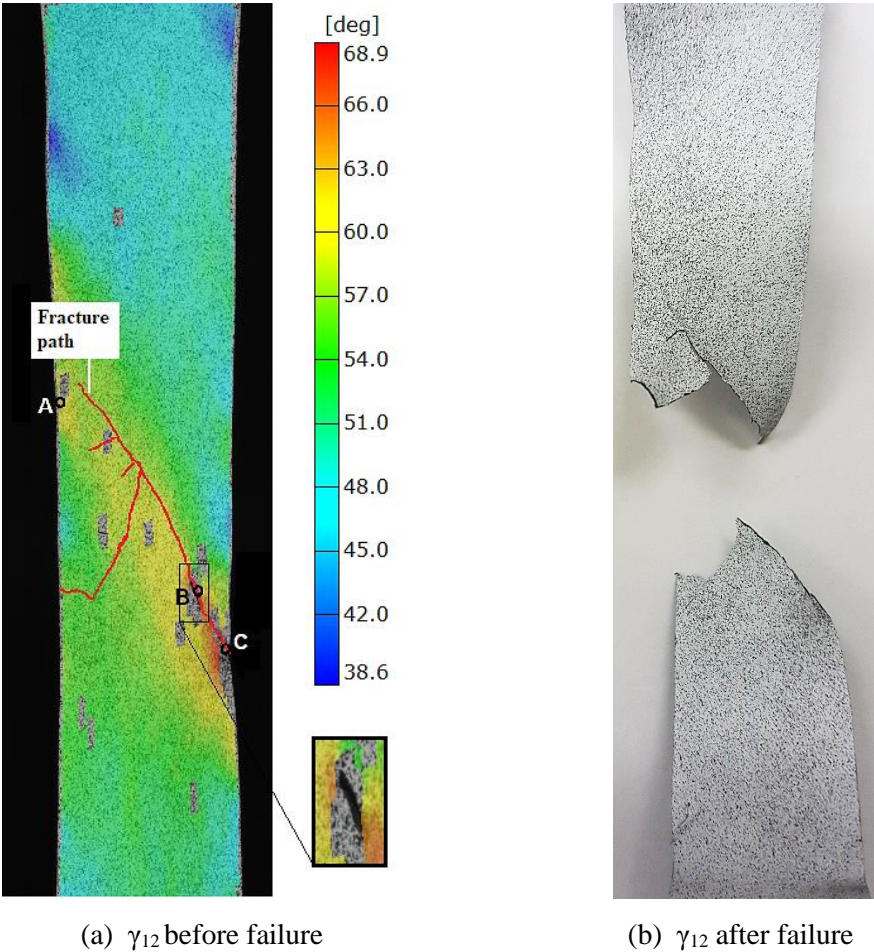


Figure 5.45 a) Shear strain (γ_{12}) before failure in a 0.3 mm $\pm 45^\circ$ SRPP tensile test specimen. Fracture paths are indicated by red lines in (a) and a photograph of the specimen after failure is shown in (b) for reference.

The methods for predicting where and at what stage of deformation failure is likely to occur in 0.3 mm 0°/90° specimens can be applied partly to 0.3 mm off-axis specimens. As to which methods apply, it depends on the tape orientations to the loading direction. In 0.3 mm 30°/60° specimens, failure occurs at an HSCP that becomes the maximum strain point and exhibits an increase in the gradient of strain increase $\left(F = \frac{d\varepsilon_{HSCP}}{d\varepsilon_{applied}}\right)$ before specimen failure. However, the strain path of the failure point is

dissimilar to that of the average strain of the specimen. In $0.3 \text{ mm} \pm 45^\circ$ specimens, the strain path of failure points does follow that of the average strain of the specimen. It also exhibits an increase in F . However, the failure point does not necessarily become the maximum strain point before failure. This contrasts with the $30^\circ/60^\circ$ specimens. Example specimens that demonstrate these behaviours are shown below.

An example of a $0.3 \text{ mm} \pm 45^\circ$ specimen, in which the failure point follows the same strain path as the average strain of the specimen and exhibits an increase in F but does not necessarily become the maximum strain point before failure, was shown in Figure 5.45. There are three HSCPs in the specimen shown in Figure 5.45a¹⁴, two occurring on the edges (A and C) and one inside the specimen (B). Failure occurs through points B and C and it appears to initiate from point B. The slit at B appears at a boundary crack between $+45^\circ$ and -45° -tapes, as shown in Figure 5.46. Based on the previous analysis, the strain concentration caused by the boundary crack would have led to failure of tapes through the thickness, causing the slit to appear, which would then have propagated across the specimen. Failure is unlikely to have initiated from point C. A noticeable reduction in the width of the specimen can be seen at this point. This is characteristic of specimens that fail from a slit (boundary crack) inside the specimen, instead of from an edge. As shown in Figure 5.47, the failure point (B) does not become the maximum strain point but still exhibits the increase in F near the failure stage.

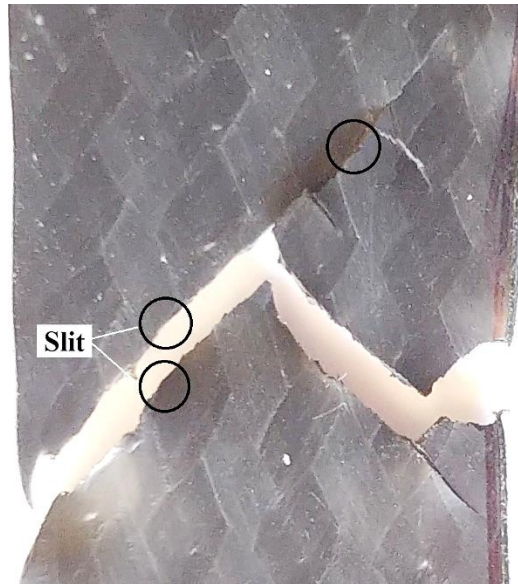


Figure 5.46 Fracture along tape boundaries (encircled) in the $0.3 \text{ mm} \pm 45^\circ$ SRPP tensile test specimen in Figure 5.45. Fracture along the boundary labelled ‘slit’ indicates the slit at B in Figure 5.45a.

¹⁴ Strains at points B and C are not shown in Figure 5.45a because the damage had grown so large by this stage (last stage before failure) that strains could not be computed at the required precision and accuracy. Strains at B and C have been computed up to applied strains of 68.7% and 70.0%. Considering that the specimen failed at the applied strain of 72.5%, the loss of data due to the damage is not significant.

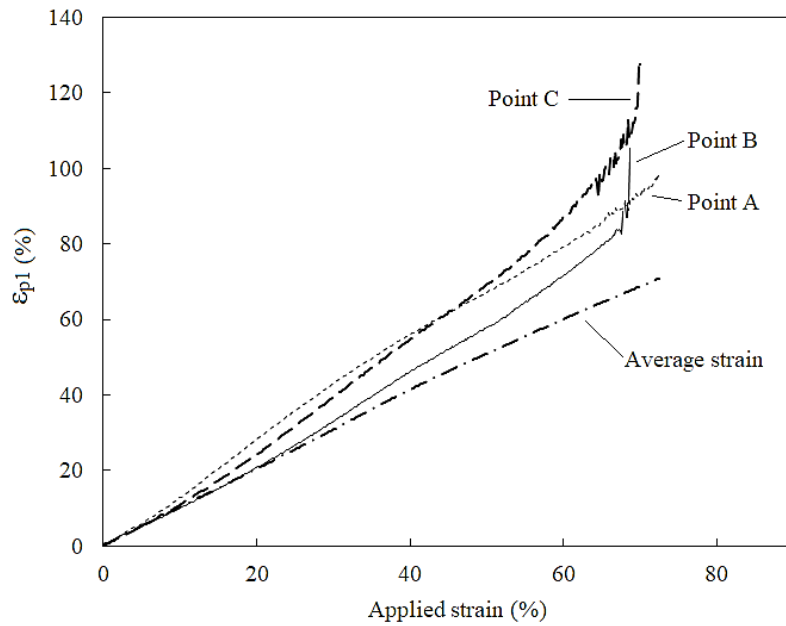


Figure 5.47 First principal strain (ϵ_{p1}) against the applied strain for points A, B, C and the average strain in the $0.3 \text{ mm} \pm 45^\circ$ SRPP tensile test specimen in Figure 5.45.

However, in the analysis of the $0^\circ/90^\circ$ specimens, there was another indicator of the point at which failure initiated. Failure initiated from a point which closely followed a strain path of the average strain of the specimen, unless failure initiated from the edge. This could be determined from a plot of ϵ_{p1} against ϵ_{p2} of HSCPs and the average strain. A similar plot for the $\pm 45^\circ$ specimen shown in Figure 5.48

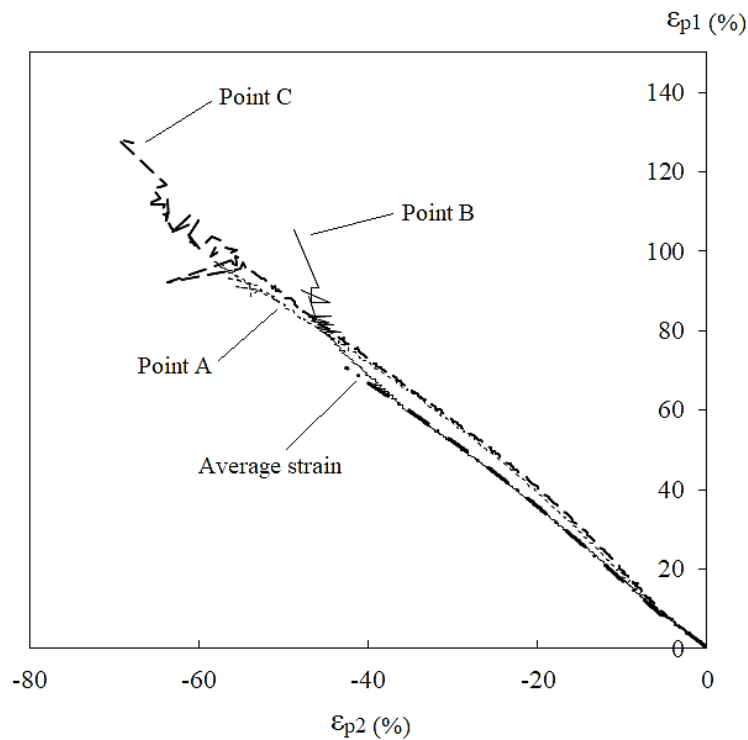


Figure 5.48 Strain paths of points A, B, C and the average strain in the $0.3 \text{ mm} \pm 45^\circ$ SRPP tensile test specimen in Figure 5.45.

demonstrates that the same guideline applies to the $\pm 45^\circ$ specimens as well. It can be seen that strain path of point B (at which failure occurs) closely adheres to that of the specimen average, whereas those at points A and C do not. This becomes more distinguishable if ϵ_{p1} are plotted against strain ratio $\left(\beta = \frac{\epsilon_{p2}}{\epsilon_{p1}}\right)$, as shown in Figure 5.49. The result is the same using γ_{12} , as shown in Figure 5.50, because these strains are closely correlated with ϵ_{p1} in the off-axis specimens, as mentioned earlier.

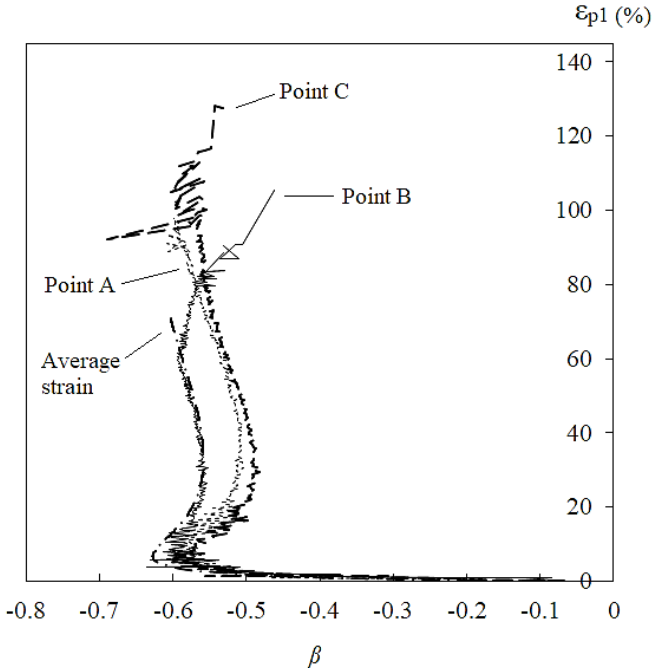


Figure 5.49 First principal strain (ϵ_{p1}) against strain ratio ($\beta = \epsilon_{p2}/\epsilon_{p1}$) for points A, B, C and the average strain in the 0.3 mm $\pm 45^\circ$ SRPP tensile test specimen in Figure 5.45.

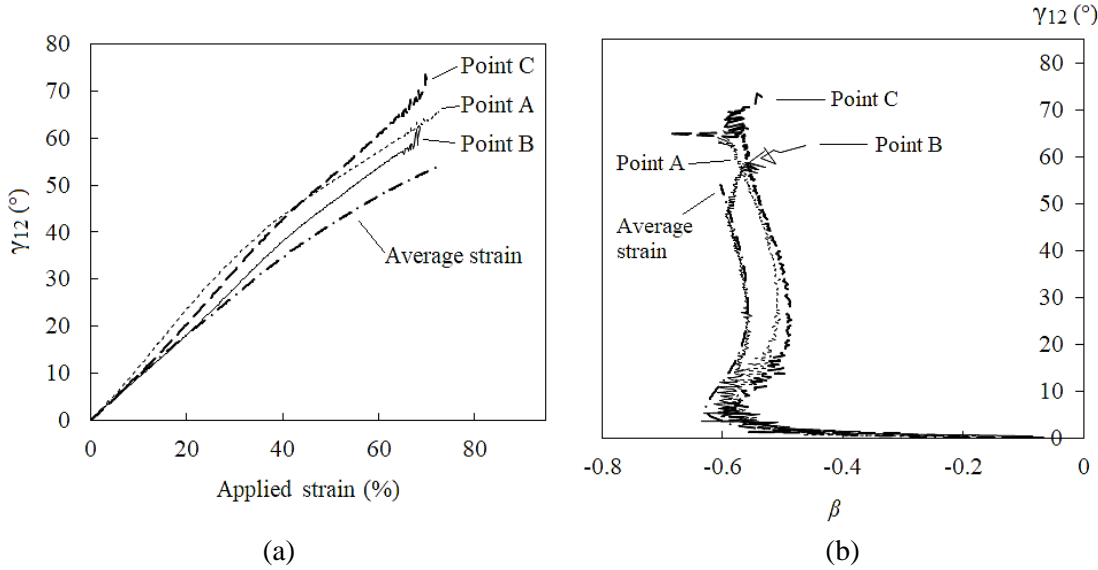


Figure 5.50 Strain behaviour for points A, B, C and the average strain in the 0.3 mm $\pm 45^\circ$ SRPP tensile test specimen in Figure 5.45. a) Shear strain (γ_{12}) against applied strain and b) γ_{12} against strain ratio ($\beta = \epsilon_{p2}/\epsilon_{p1}$).

In contrast to the $0.3\text{ mm} \pm 45^\circ$ specimens, the failure point in a $0.3\text{ mm } 30^\circ/60^\circ$ specimen does become the point of maximum strain before failure but does not have the same strain path as the average strain of the specimen. (Failure point does show an increase in F towards the failure stage, which is still similar to the $0^\circ/90^\circ$ and $\pm 45^\circ$ specimens.) An example is shown in Figure 5.51. The $0.3\text{ mm } 30^\circ/60^\circ$ specimen shown fractures between HSCPs A and B, starting from the slit at A. It should be mentioned that point A represents a point that is close to the edge of the specimen, not on the edge. As can be seen from Figure 5.51b, strains at both points A and B exhibit an increase in F and the strain at point A becomes the point of maximum strain just before failure. However, Figure 5.51c shows that the strain paths at both points are different to that of the average strain of the specimen.

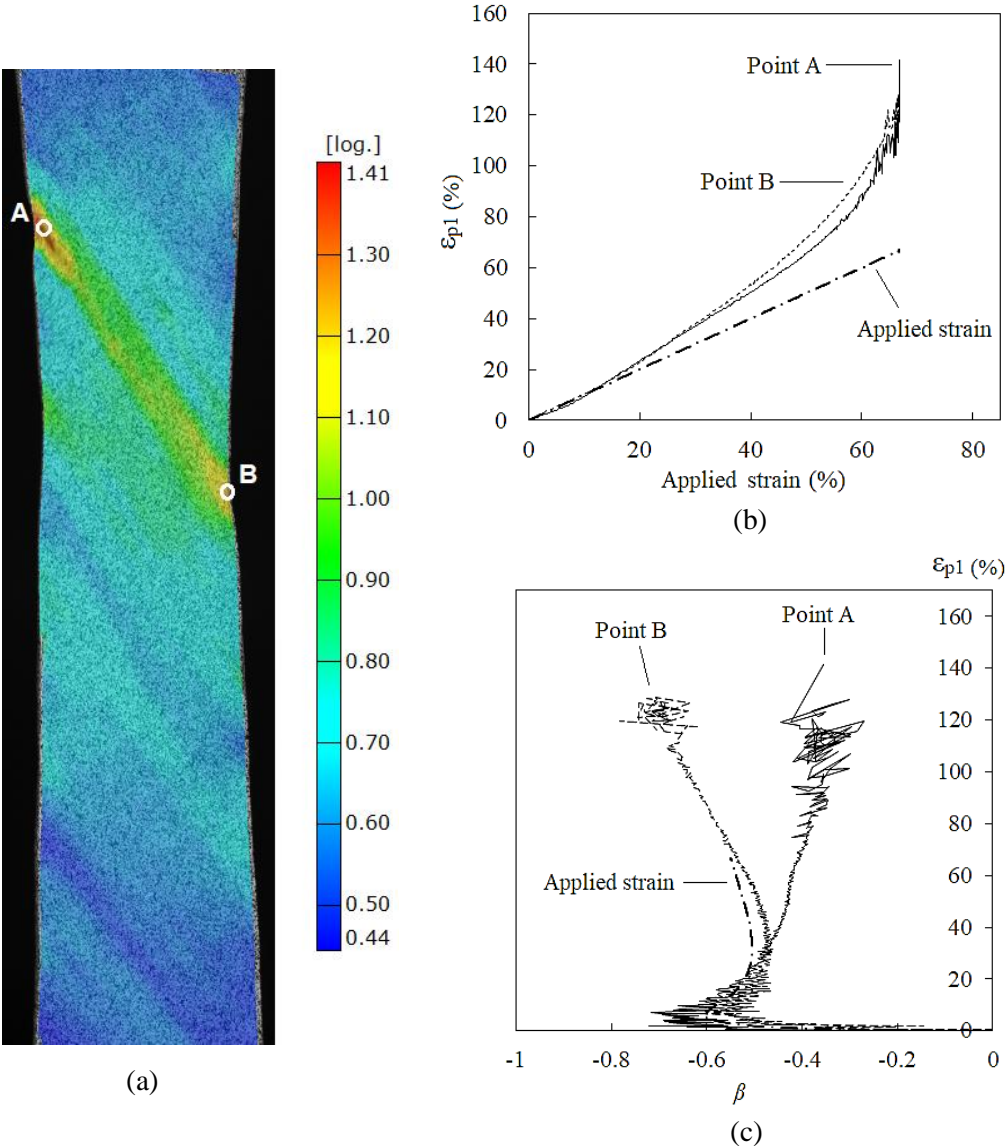


Figure 5.51 a) First principal strain (ϵ_{p1}) in a $0.3\text{ mm } 30^\circ/60^\circ$ SRPP tensile test specimen before fracture. Points A and B indicate strain concentration points along the fracture path. ϵ_{p1} against b) applied strain and c) strain ratio ($\beta = \epsilon_{p2}/\epsilon_{p1}$) for strain concentration points and the average strain in the specimen.

From the surface strain analysis of the 0.3 mm off-axis specimens above, it is apparent that guidelines established for locating or predicting failure initiation points based on the analysis of 0°/90° specimens apply only *partially*. The best means of detecting the failure point in $\pm 45^\circ$ specimens is to monitor the strain paths of HSCPs compared to the average strain in the principal strain space, for instance, by plotting ϵ_{p1} against β . The specimen is then likely to fail at the location that has a similar strain path as the average strain, except when failure occurs from a HSCP at the edge of the specimen. Failure will occur around the time at which the applied strain has reached the sample mean of failure strains. The sample mean of the 0.3 mm $\pm 45^\circ$ specimens had a relative standard deviation of 10% and is more precise than in the case of the 0.3 mm 0°/90° or 30°/60° specimens, which had relative standard deviations of 36% and 19%, respectively.

Failure points in the 30°/60° specimens can be detected from monitoring the ϵ_{p1} of the HSCPs, as the failure point will exhibit a noticeable rise in the rate of strain increase and become the point of maximum strain, as with the 0°/90° specimens. Hence, the most reliable way to predict when failure is likely to occur is to statistically determine a threshold using measures such as F or the ratio between maximum strain and average/applied strain ($\iota = \frac{\epsilon_{max}}{\epsilon_{applied}}$) in the specimen, as was mentioned in the analysis of 0°/90° SRPP. The latter is recommended over the former because the change in F can appear late in the deformation process, sometimes very close to failure. The appropriate threshold for the ι , above which failure is likely to occur, is around 2.2 for the 0.3 mm 30°/60° specimens.

It is not clear what causes the different response in the 30°/60° and $\pm 45^\circ$ specimens, as the microscopic analysis showed very similar damage characteristics. The behaviour of the failure point in the 30°/60° specimens that did not go through the same state of strain as the majority of points in the specimen may be related to asymmetry in tape orientations, as this is the obvious difference compared to the 0°/90° and $\pm 45^\circ$ specimens.

5.2.3.2 Failure behaviour of 0.6 mm and 1.0 mm specimens

This section will explain the progression of damage that lead to the failure of 0.6 mm and 1.0 mm off-axis specimens. It will also be shown that missing points from surface strains computed by the DIC system can be used to identify areas of critical microscopic damage before failure occurs.

In 0.6 mm and 1.0 mm off-axis specimens, specimen failure does not occur along a single crack, or a combination of a few cracks, as is the case in the 0.3 mm specimens. They instead exhibit multiple damage along the failure path as was observed in the 0.6 mm and 1.0 mm 0°/90° specimens (specifically extensive tape-splits, boundary cracks, and additional delamination, fibrillation, and tape and fibril pull-outs). As with the 0°/90° specimens, this makes it difficult to pinpoint the exact initiation point of critical damage in thicker specimens. However, the large amount of damage and failure in the off-axis

specimens occurs more slowly with differently characteristics to the 0.6 mm and 1.0 mm 0°/90° specimens, such that their progression can be observed.

The initiation of failure in a 0.6 mm 30°/60° specimen is shown in Figure 5.52a. Failure here initiates with tape and fibril pull-outs at the edges of the specimen, mostly in tapes that are not restrained by the grips at both ends of the tape. The phenomenon of tape and fibril pull-outs was explained in Section 5.2.2.2.2. Based on the analyses thus far, it is possible that some tape pull-outs initiate from boundary cracks which propagate into local delamination between tapes. An observation from the strain analysis that supports this is shown in Figure 5.53 in the next page. In this specimen, an HSCP occurs along the edge of a tape which pulls out from the edge of the specimen.

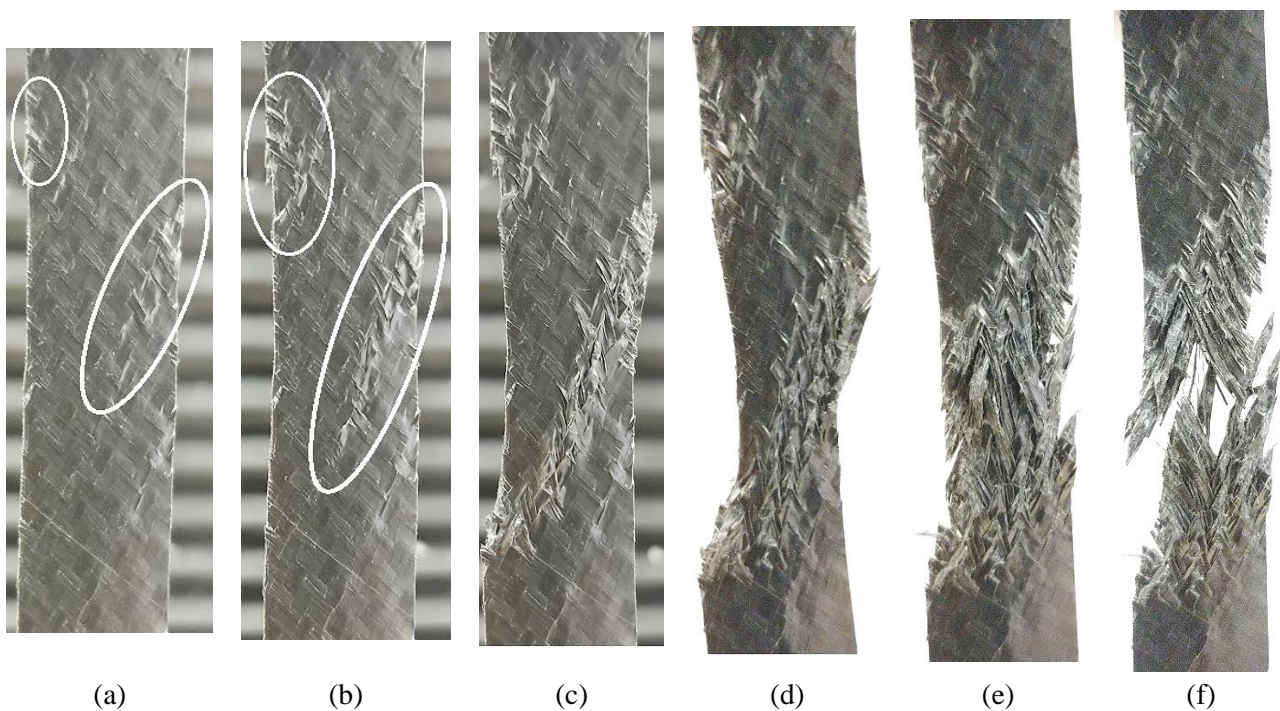


Figure 5.52 Progression of damage until failure (a–c) and after failure (d–f) in a 0.6 mm 30°/60° SRPP specimen.

Subsequent propagation of damage that leads to failure of the 0.6 mm 30°/60° specimen is shown in Figures 5.52b and c. After tape and fibrils pull out from the edges, a cluster of various types of damage, including tape-splits, boundary cracks and delamination, propagates from the pull-outs, most often in the direction of the 30°-tapes, as shown in Figure 5.52b. The reason that the cluster of damage propagates in the direction of the 30°-tapes is probably due to the stress in the reinforcing direction being higher in the 30°-tapes than the 60°-tapes, causing faster propagation of delamination along the 30°-tapes (from the end of the pull-outs at the edge of the specimen). In the cluster of damage, tapes and fibrils trellis towards the loading direction.

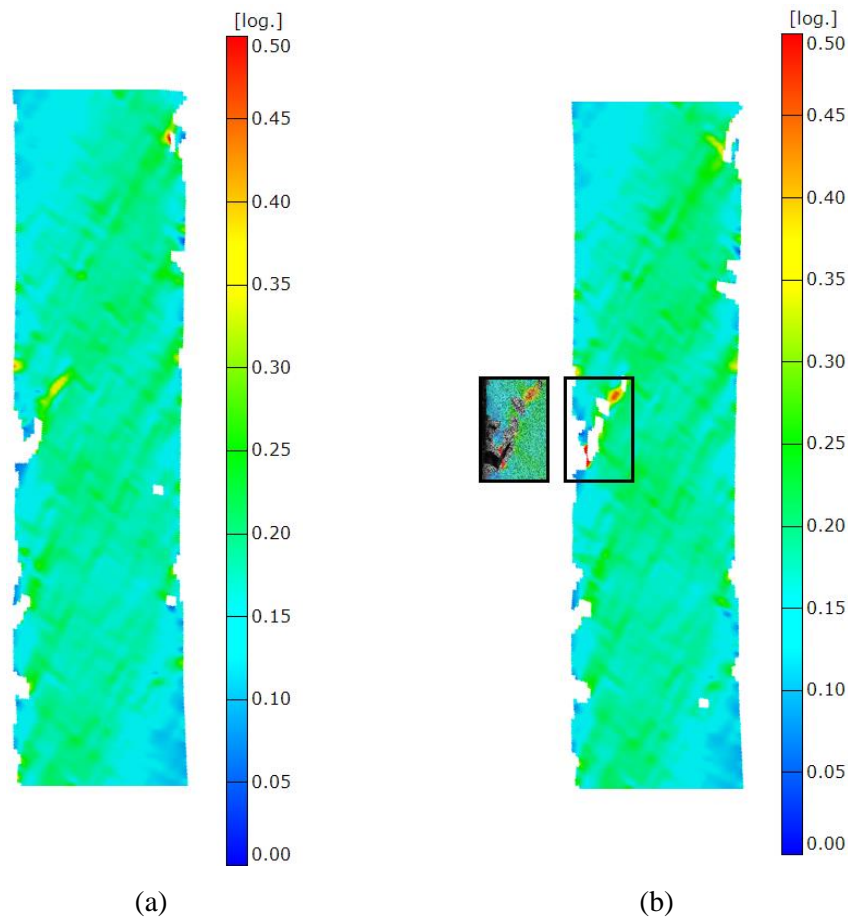


Figure 5.53 First principal strain (ϵ_{p1}) in a 0.6 mm 30°/60° SRPP tensile test specimen at applied strains of a) 17.5% and c) 17.8%, showing strain concentration at the edge of a tape which pulls out from the edge of the specimen.

Failure occurs in the 0.6 mm 30°/60° specimen when the cluster of damage has propagated from one edge to the other edge, as shown in Figure 5.52c. At this stage, enough tapes have pulled out to reduce the amount of load the specimen can support, and the specimen is considered to have failed. Figures 5.52d and c show the subsequent progression of damage when the grips continue to pull the specimen in opposite directions until it is separated into two parts. The two parts of the specimen are seen to slide past each other along the cluster of damage (Figure 5.52d) before finally separating (Figures 5.52e and f).

Similar damage progression and failure occurs in 0.6 mm $\pm 45^\circ$ specimens, except that in these cases, the cluster of damage propagates in +45°-tape direction as easily as in -45°-tape direction, as shown in Figure 5.54a. In some specimens, however, pull-outs seem to occur preferentially along the warp direction first, rather than along the weft direction, as seen in Figure 5.54b.



Figure 5.54 0.6 mm \pm 45° SRPP tensile test specimens at failure with cluster of damages propagating along a) both tape directions and b) a single tape direction.

There are a few differences in the damage and failure behaviour of 1.0 mm off-axis specimens compared to 0.6 mm specimens. The 1.0 mm specimens fail with damage occurring more evenly throughout the entire gauge section. For example, most tapes at the specimen edges that are not held by the grips pull out, instead of just few, as shown in Figure 5.55 in the next page. Tape pull-outs promote damage along the tapes, similar to those seen in the 0.6 mm specimens, but because all tapes at the edges pull out, there is no concentration of damage. Also, more tapes trellis in 1.0 mm specimens due to damage occurring over a larger area. This, and the fact that the damage is not as concentrated as in the 0.6 mm specimens, allows the 1.0 mm specimens to fail at higher applied strains than the 0.6 mm specimens.

In 0.6 mm off-axis specimens, surface strains are harder to analyse than in 0.3 mm specimens, due to large areas of damage disrupting the surface stochastic patterns that enable the computation of strains. This is especially the case where critical damage occurs, as the critical damage is extensive in the 0.6 mm off-axis specimens (e.g. tape/fibril pull-outs, cluster of damage). However, the missing strains can be used to identify the location of critical microscopic damage before it become apparent from visual observations, as shown in Figure 5.56. A cluster of damage, and eventual failure, occur where strains are missing, in the direction of the 30°-tape. It should be noted that this does not apply in 1.0 mm off-axis specimens where damage occurs more evenly throughout the specimen.

The average strength and strain at failure can be used to identify when failure is likely to occur in 0.6 mm and 1.0 mm off-axis specimens as these are sufficiently consistent across specimens (5–15% relative standard deviations, shown in Table 5.1).

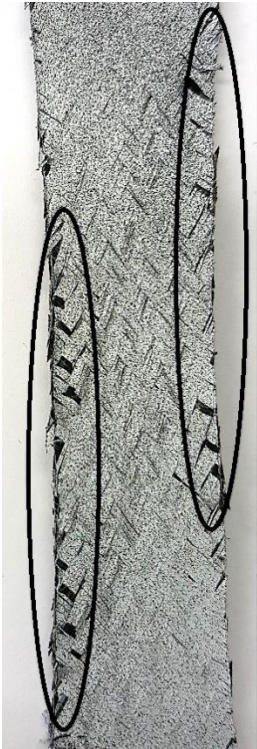
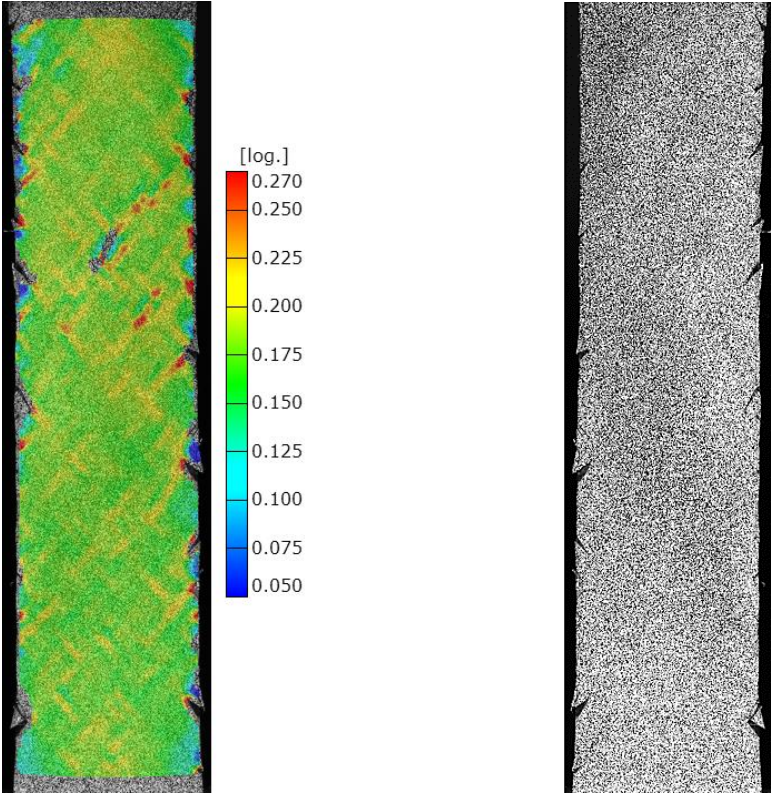


Figure 5.55 Tape pull-outs in a 1.0 mm 30°/60° SRPP tensile test specimen at failure.



(a)

(b)

Figure 5.56 0.6 mm $\pm 45^\circ$ SRPP tensile test specimen with (a) and without (b) a translucent layer of first principal strain (ϵ_{p1}) transposed on top, at 17.7% applied strain. (Applied strain at failure = 19.2%).

5.2.4 Summary of failure behaviour of off-axis SRPP

Section 5.2 discussed the findings on the deformation and failure behaviour of 0.3 mm, 0.6 mm and 1.0 mm SRPP specimens when subjected to uniaxial tension at $30^\circ/60^\circ$ and $\pm 45^\circ$ to the reinforcing directions. It was shown that SRPP exhibits similar behaviours, in general, when subjected to the load at $30^\circ/60^\circ$ and $\pm 45^\circ$ directions. There were also some similarities to the $0^\circ/90^\circ$ specimens, such as the absence of extensive fibrillation and delamination in 0.3 mm specimens and the increase in the amount of damage with the increase in specimen thickness. Also, similar types of damage occurred, depending on the thickness and regardless of the loading direction, with a few exceptions.

However, the characteristics of each damage type were found to be different in off-axis specimens compared to the $0^\circ/90^\circ$ specimens, mostly due to the in-plane shear strain in relation to the tape orientation. For example, boundary cracks propagated more easily into delamination, tape and fibril pull-outs mostly occurred from the edges without fracturing, the influence of tape orientation on the mode of crack propagation (stable or unstable) and microscopic failure mode (ductile or brittle) changed slightly, and more and finer fibrils bridged the cracks, not just in tape-splits but also in delamination. The various types of damage could significantly affect the deformation behaviour and mechanical properties. For example, trellising occurred where damage allowed tapes and fibrils to rotate more towards the loading direction. This occurred more in the 1.0 mm specimens, in which damage occurred throughout the gauge section, compared to the 0.6 mm specimens, which had a smaller degree of damage occurring in fewer regions. This caused the failure strain of the 1.0 mm specimens to be higher than those of the 0.6 mm specimens, despite the failure mechanisms being similar.

Critical damage, and their progression, was identified for each specimen. It was found that the boundary crack is again the critical damage that causes failure in 0.3 mm off-axis specimens, but between tapes of different orientations. This causes the mode of crack propagation (stable) and the resulting failure (ductile) to be different to those in the 0.3 mm $0^\circ/90^\circ$ specimens, initially. This is likely to be the reason why the 0.3 mm off-axis specimens fail at high strains. Failure in 0.6 mm and 1.0 mm off-axis specimens was found to initiate from tape and fibril pull-outs from the edges of specimens. The pull-outs generated propagation of a cluster of damage along the 30° -tapes, which occurred along few tapes in the 0.6 mm and in most tapes in the 1.0 mm specimens. The specimens then failed from extensive tape and fibril pull-outs from the edges of the specimens. It was also found that failure points, or regions, can be detected using surface strains, with some limitations.

5.3 Deformation and failure behaviour of off-axis self-reinforced polypropylene/steel fibre metal laminate

This section discusses the deformation and failure behaviour of off-axis SRPP/steel FML. Analysis of the failure behaviour of off-axis FML specimens is facilitated by the fact that the behaviour of SRPP at off-axis directions and the behaviour of the FML at a $0^\circ/90^\circ$ loading direction have previously been analysed.

This section is divided into two subsections. The first subsection outlines the stress-strain behaviour with some comments on how some of the different behaviours at off-axis directions may affect design considerations using the FML. It then briefly explains that the microscopic damage in the SRPP layer is very similar to those in plain SRPP (1.0 mm). The second subsection discusses the strain behaviour of off-axis FML specimens. This will show that strain localisation and fracture bands form in similar ways to those seen in the $0^\circ/90^\circ$ FML specimens, though failure occurs differently. Findings regarding how the adhesion to steel affects the behaviour of the SRPP layer will also be given.

5.3.1 Stress-strain behaviour and microscopic damage in the SRPP layer

SRPP/steel FMLs tested with tapes in the SRPP layer oriented at $30^\circ/60^\circ$ and $\pm 45^\circ$ to the applied load exhibit stress-strain behaviours shown in Figures 5.57, 5.58 and Table 5.2. The stress-strain curves and properties of $0^\circ/90^\circ$ FML, steel, $30^\circ/60^\circ$ SRPP and $\pm 45^\circ$ SRPP have also been provided for comparison.

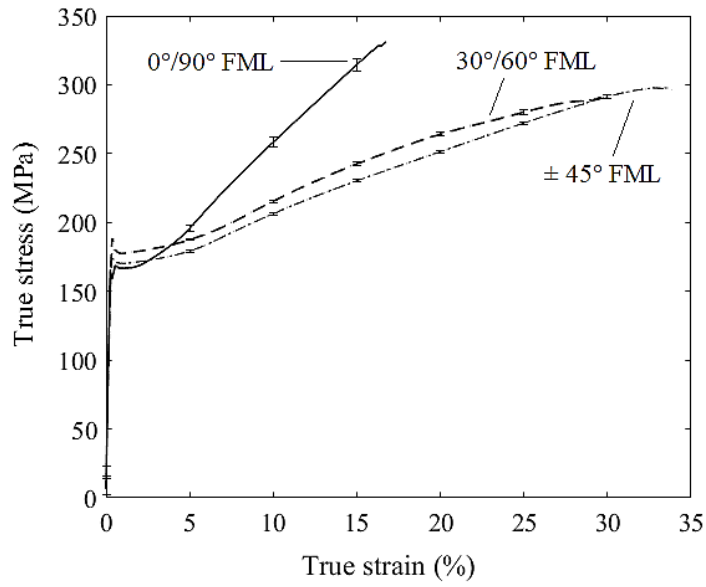
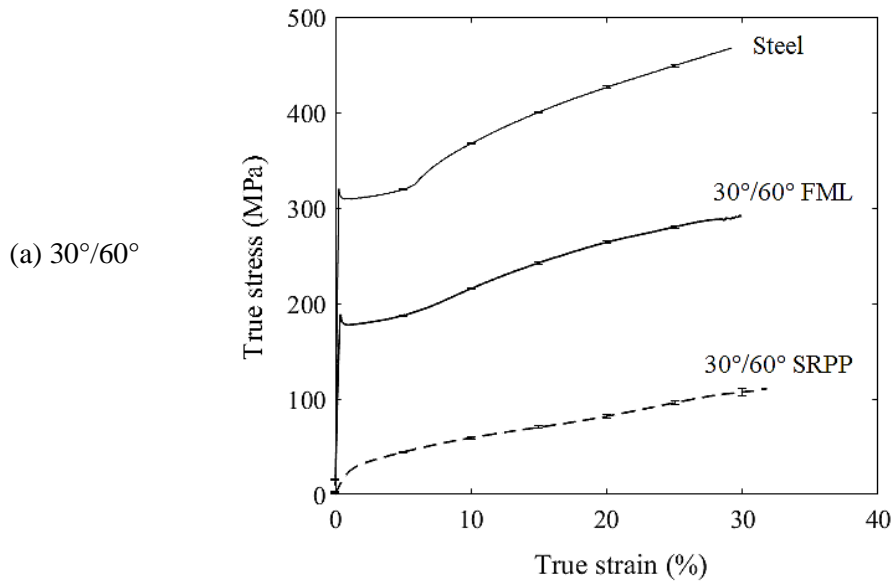


Figure 5.57 Tensile stress-strain curves of 30°/60° and ±45° SRPP/steel FMLs in comparison to 0°/90° FML.



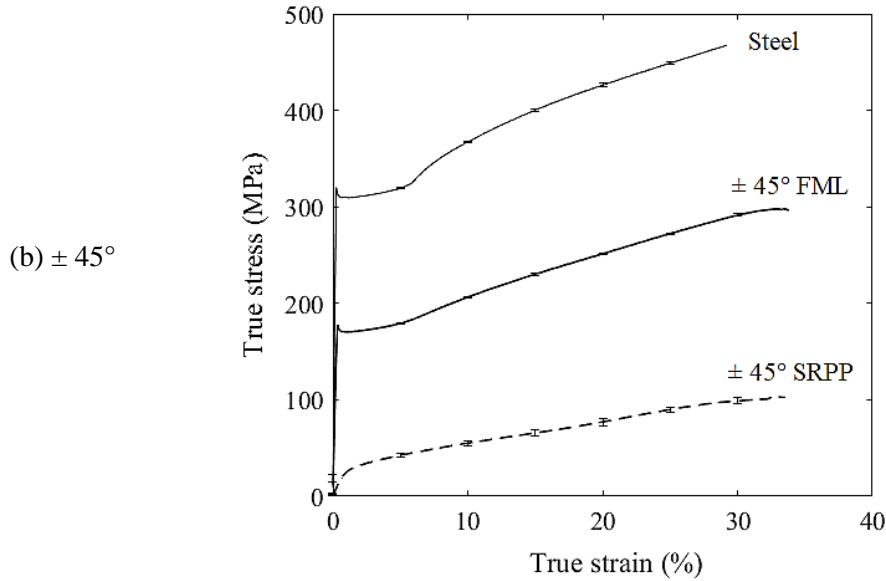


Figure 5.58 Tensile stress-strain curves of a) $30^\circ/60^\circ$ and b) $\pm 45^\circ$ SRPP/steel FMLs in comparison to steel and 1.0 mm SRPPs of corresponding orientations.

Table 5.2 Tensile failure strains (ϵ_t), strengths (σ_t) and upper yield strength (σ_y) or stress at transition strain ($\sigma^{transition}$) of steel, $0^\circ/90^\circ$, $30^\circ/60^\circ$ and $\pm 45^\circ$ SRPP/steel FMLs, $30^\circ/60^\circ$ and $\pm 45^\circ$ 1.0 mm SRPP specimens.

Material	ϵ_t (%) ¹	σ_t (MPa) ¹	σ_y (MPa)	$\sigma^{transition}$ (MPa)
Steel	29.2 ± 0.8	462.6 ± 0.8	331 ± 2	n/a ²
$0^\circ/90^\circ$ FML	17 ± 1	332 ± 3	176 ± 4	n/a ²
$30^\circ/60^\circ$ FML	30 ± 1	291 ± 1	195 ± 8	n/a ²
$\pm 45^\circ$ FML	34 ± 1	296 ± 4	179 ± 6	n/a ²
$30^\circ/60^\circ$ SRPP	32 ± 2	111 ± 4	n/a ²	24 ± 1
$\pm 45^\circ$ SRPP	34 ± 2	103 ± 3	n/a ²	24 ± 1

¹ Failure strains given indicate sample means and standard deviations. Strengths are sample means and standard deviations at given average failure strain, calculated based on specimens that have not failed.

² Not applicable.

From these, it can be seen that FML exhibits similar effects of tape orientation as the SRPP. For instance, $30^\circ/60^\circ$ and $\pm 45^\circ$ FML specimens have significantly larger failure strains compared to the $0^\circ/90^\circ$ specimens (by 76% and 100%, respectively) and lower tangential stiffnesses. It can also be seen that the off-axis FML specimens exhibit similarities to the $0^\circ/90^\circ$ FML specimens in some respects. For example, they exhibit stress-strain behaviours that are between those of the constituent layers. In contrast to the $0^\circ/90^\circ$ FML specimens, failure in the off-axis FML specimens occurs with ductile failure in the steel

layers. Interestingly, the average failure strain of the $\pm 45^\circ$ FML specimens ($34 \pm 1\%$) is higher than that of the steel specimens ($29.2 \pm 0.8\%$), while the $30^\circ/60^\circ$ FML specimens failed at the same failure strain as plain steel.

The significantly larger failure strain at off-axis directions can be leveraged in scenarios where the FML has to be pre-consolidated and subsequently deformed to desired shapes. However, it should be noted that the residual stress in the SRPP layer may be significantly higher than in the steel layers, especially at large strains. This can be seen from the fact that, when an off-axis FML is unloaded after testing, steel layers delaminate from the SRPP layer and buckle due to a higher reduction in length occurring in the SRPP layer, as shown in Figure 5.59 in the next page. This may or may not serve the desired end result.

Another factor to consider is that the FML exhibits out-of-plane bending about the longitudinal axis of the specimen due to the larger reduction in width in SRPP than in steel, which creates compressive stress in steel layers in the width direction. This is more pronounced in the off-axis FML than in $0^\circ/90^\circ$ FML specimens because Poisson's ratio of the SRPP layer is higher at off-axis direction to the load than at $0^\circ/90^\circ$. In some specimens, steel layers can bend in the opposite direction such that the edges of the steel layers bend away from each other. This causes delamination within the SRPP layer at the edges, as shown in Figure 5.60. (The centre of the specimen has suffered greater delamination because the ends were constrained by the grips). Therefore, although the FML can be deformed far more in the off-axis directions, there might be a limit in the extent to which this behaviour can be utilised. Studies of springback and buckling of are not the subject of this study but are required before any real applications for this FML are considered. Study on deformation at elevated temperatures is also recommended as it is likely to alleviate the aforementioned problems.

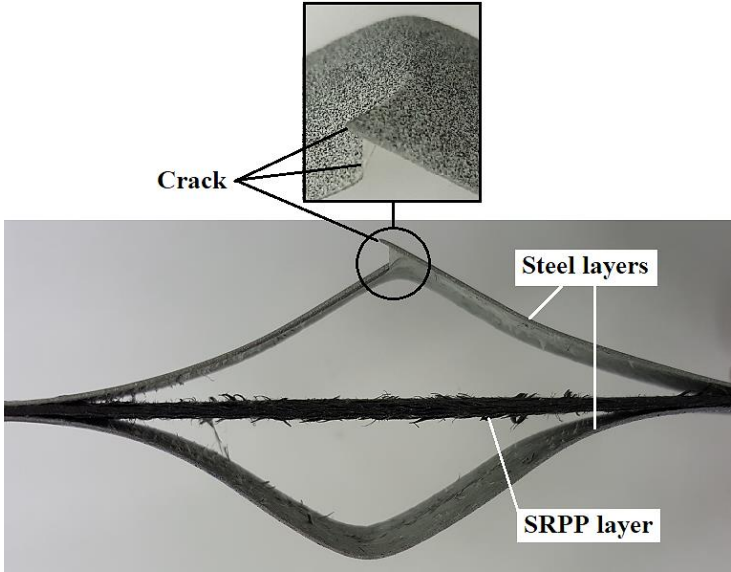


Figure 5.59 Buckled steel layers in an unloaded $30^\circ/60^\circ$ SRPP/steel FML tensile test specimen, post-failure. Direction of the applied load is horizontal in the image.

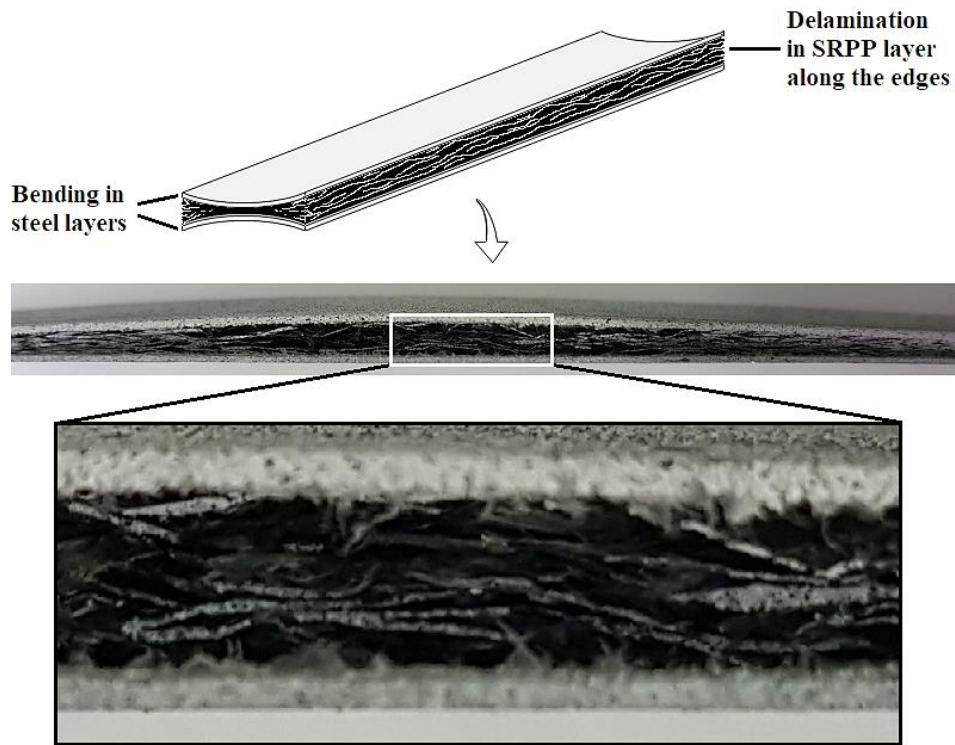


Figure 5.60 Delamination within the SRPP layer of a $\pm 45^\circ$ SRPP/steel FML tensile test specimen caused by out-of-plane bending in the steel layers. Direction of the applied load is horizontal in the image.

The SRPP layer in off-axis FML specimens exhibit similar microscopic damage characteristics to corresponding 1.0 mm SRPP specimens. There are a few differences to plain SRPP specimens relating to the fact that the surface of the SRPP layer is glued to steel, as opposed to being a free surface. For instance, aligned crazing on the surface matrix of the SRPP layer is not observed, as in the case of $0^\circ/90^\circ$ FML. There are also more tape and fibril pull-outs than in SRPP specimens, though these are due to the damage from delamination from the steel after failure. Additionally, the SRPP layer of off-axis FMLs exhibits more shear flow in the surface matrix than in $0^\circ/90^\circ$ FML, as shown in Figure 5.61, likely from out-of-plane shear (γ_{13} and γ_{23}) between the steel and SRPP layers created from the rotation in the SRPP tapes. Apart from these, there is no difference in damage observed under the microscopes compared to the SRPP specimens.

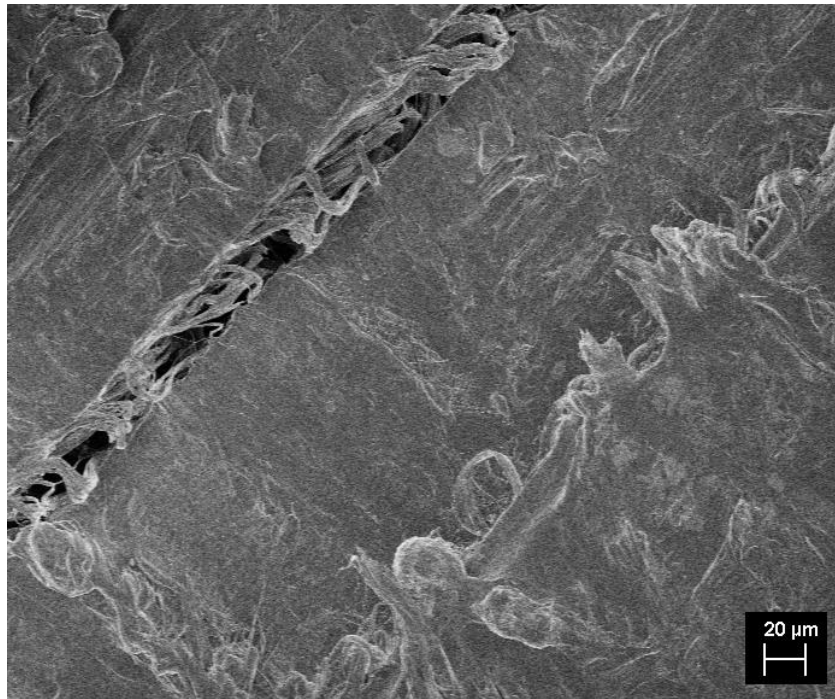


Figure 5.61 Scanning electron micrograph of the surface of a delaminated SRPP layer in a $\pm 45^\circ$ SRPP/steel FML tensile test specimen. Magnification = 500x, EHT = 1.00kV.

5.3.2 Surface strain analysis

Strain distribution of off-axis FMLs shows the influence of both SRPP and steel layers, which is similar to the $0^\circ/90^\circ$ specimens. Examples of surface strains of a $30^\circ/60^\circ$ FML are shown in Figure 5.62. Strain patterns along the tape directions are less obvious in the off-axis FMLs than in $0^\circ/90^\circ$ FML because the variations in strain are small compared to the strains along the strain localisation bands, but can be seen faintly at higher applied strains, away from strain localisation bands. Narrow strain localisation bands also appear in the off-axis FMLs from what appears to be the HSCPs at boundary cracks in the SRPP layer, similar to those observed in the $0^\circ/90^\circ$ specimens. However, unlike the $0^\circ/90^\circ$ specimens, the strain localisation bands are initially oriented at 45° to the loading direction and in only one direction ($+45^\circ$ or -45°), not both.

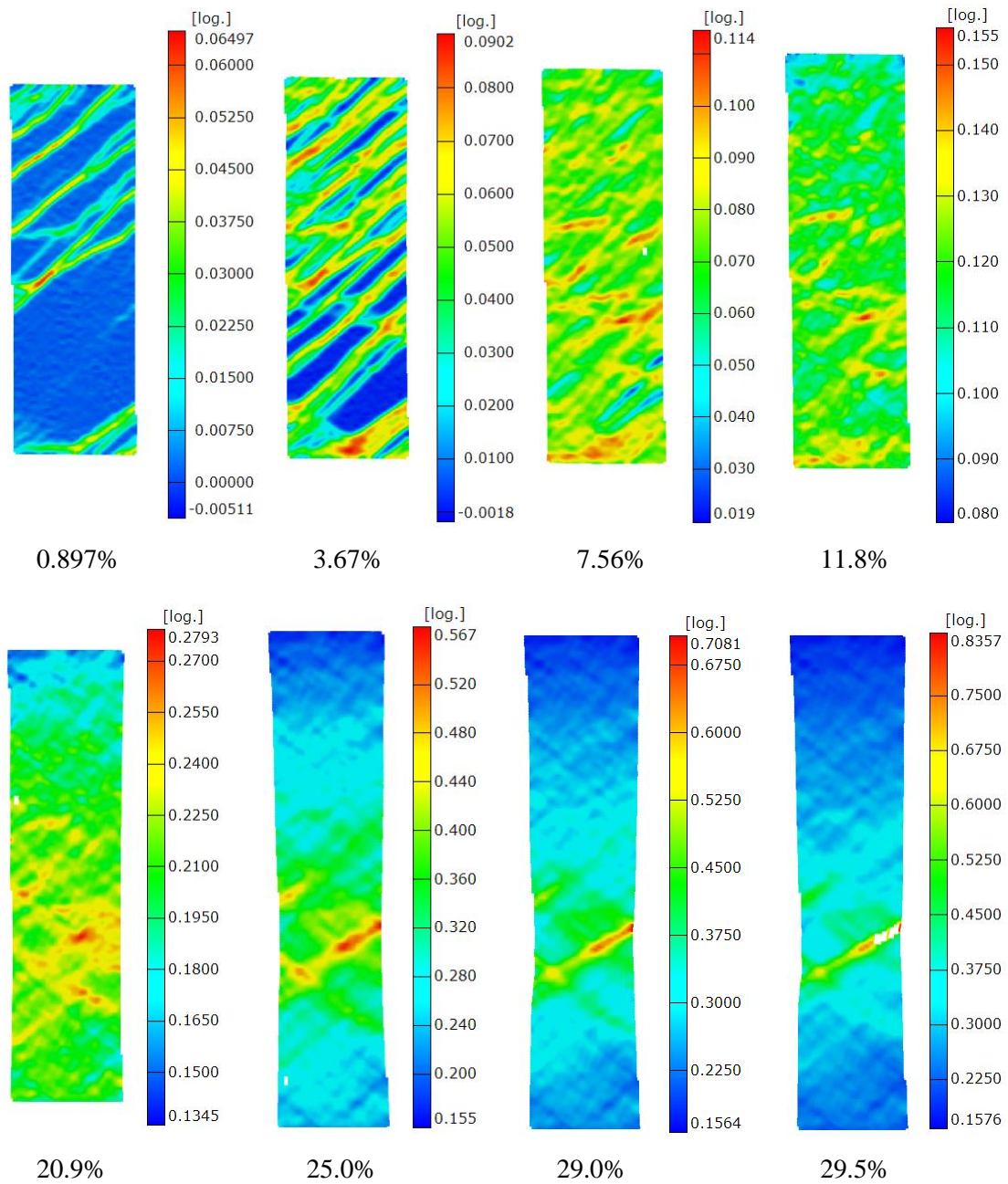


Figure 5.62 First principal strain (ϵ_{p1}) of a $30^\circ/60^\circ$ SRPP/steel FML tensile test specimen at applied strains shown. The final image shows strains just before failure.

In addition to the strain patterns mentioned above, horizontal bands can appear from the start of the deformation in rare cases, as shown in Figure 5.63. This is possibly due to a defect inherent in the material. Such bands disappear at higher strains as the strains become more homogenised over the gauge section other than along the oblique strain localisation bands.

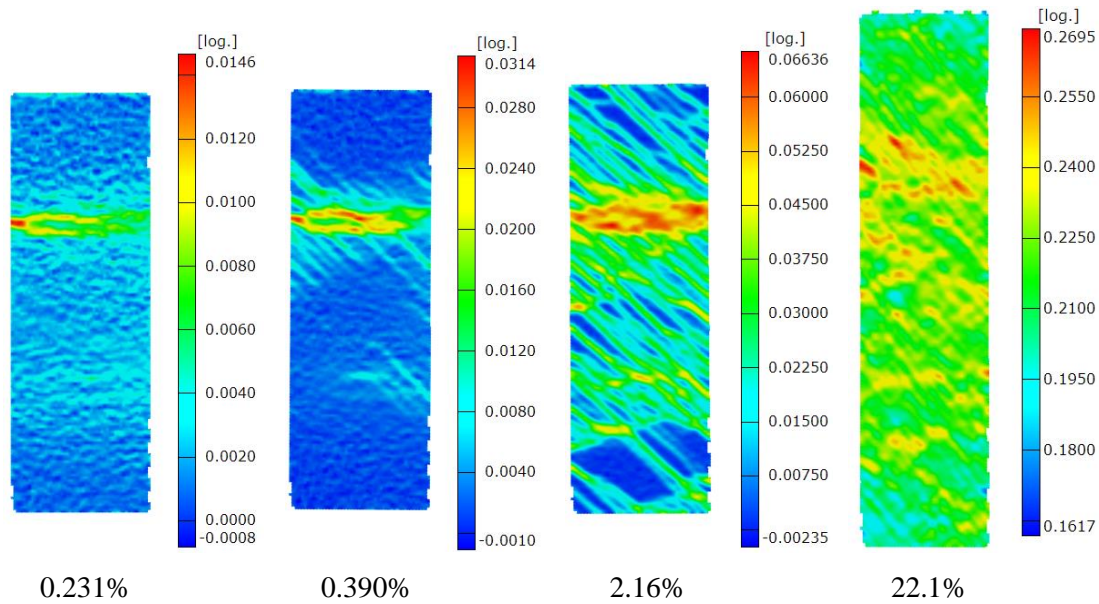


Figure 5.63 First principal strain (ϵ_{p1}) of a $\pm 45^\circ$ SRPP/steel FML tensile test specimen at applied strains shown.

At higher strains, the oblique strain localisation bands rotate and the strain becomes concentrated along fewer bands, or new strain localisation bands form in smaller numbers, in both \pm directions, as shown in Figure 5.62. The strain localisation bands are approximately $51\text{--}55^\circ$ to the loading direction, varying slightly depending on the tape orientations (higher in $30^\circ/60^\circ$ specimens than in $\pm 45^\circ$ specimens) and their positions along the gauge length (higher angles form towards the middle of the gauge length).

Very close to failure, the strain gets further concentrated along the strain localisation bands that have rotated further from the loading direction. Some of these bands become fracture bands, along which the steel undergoes localised necking, as shown in Figure 5.64b. The localised necking and failure in steel layers causes the failure of the FML at off-axis directions. An example of localised necking and failure in the steel layer is shown in Figure 5.65. The angle the fracture band makes with the loading direction is around $57\text{--}59^\circ$ which is, once again, close to the fracture angle of steel (57°), and similar to the case in the $0^\circ/90^\circ$ FML specimens. However, the fracture bands in off-axis specimens are much narrower and exhibit higher strains. This contrasts to failures occurring in the SRPP layer within fracture bands that are much wider in the $0^\circ/90^\circ$ specimens.

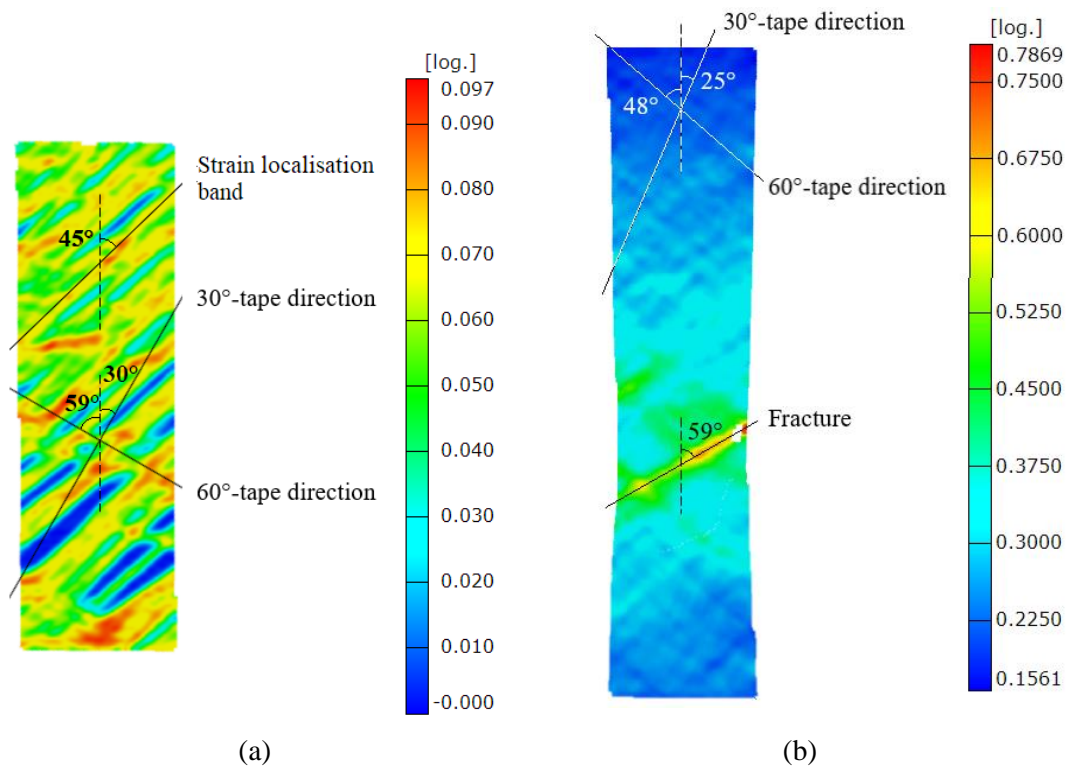


Figure 5.64 First principal strain (ϵ_{p1}) of the 30°/60° SRPP/steel FML tensile test specimen in Figure 5.62 at applied strains of a) 5.53% and b) 29.4%, showing strain localisation bands, tape directions and the fracture band.

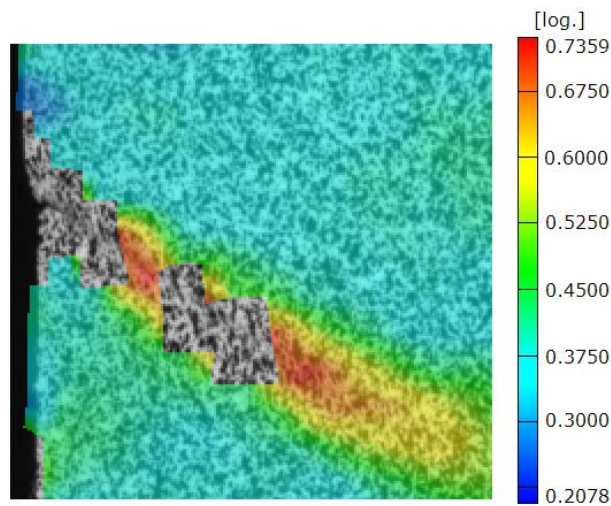


Figure 5.65 Example of localised necking and failure occurring in the steel layer of a $\pm 45^\circ$ SRPP/steel FML tensile test specimen, where the surface strain is highest. (First principal strain is shown).

Examples were shown using 30°/60° specimens in Figures 5.62 and 5.64, but similar phenomenon occur in $\pm 45^\circ$ specimens with slightly different angles, as shown in Figure 5.66. This can also be seen by comparing the angles that strain localisation bands, fracture bands and tapes form to the loading direction

in 0°/90°, 30°/60° and ± 45° specimens, which are shown in Table 5.3. From the table, it can be seen that the behaviour of off-axis specimens is very similar. In comparison, their behaviours are slightly different to that of 0°/90° specimens, except for the fact the fracture bands form similar angles to the fracture angle of plain steel in all specimens.

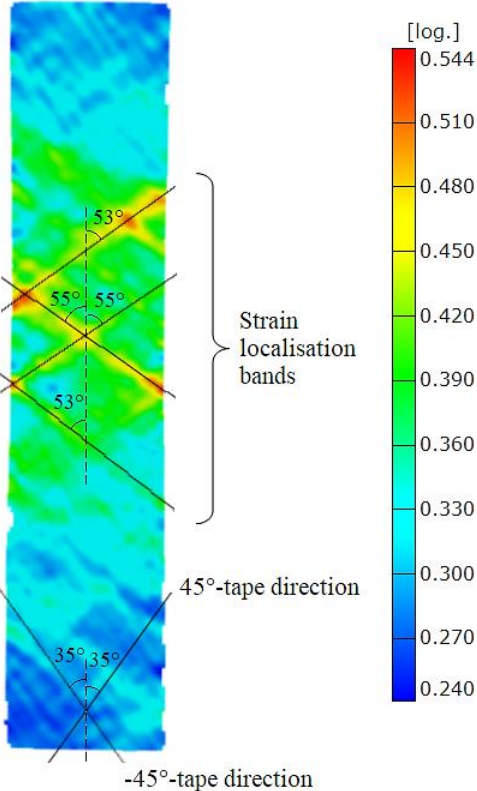


Figure 5.66 First principal strain (ϵ_{p1}) of a ± 45° SRPP/steel FML tensile test specimen at an applied strain of 34.2%, showing strain localisation bands and tape directions.

Table 5.3 Approximate angles of tape orientations, strain localisation bands and fracture bands to the loading direction in 0°/90°, 30°/60° and ± 45° tensile SRPP/steel FML specimens.

FML orientation	Initial strain localisation bands	Strain localisation bands at high strains	Fracture band	Final tape orientations	Change in tape orientations
0°/90°	64 ~ 73°	Not applicable	57 ~ 63°	0°, 90°	0°
30°/60°	45°	53 ~ 55°	57°	± 22 ~ 25° (30°-tape),	± 5 ~ 8° (30°-tape),
				∓ 46° ~ 50° (60°-tape)	∓ 10° ~ 14° (60°-tape)
± 45°	45°	51 ~ 52°	57 ~ 59°	± 30 ~ 35°	± 10 ~ 15°

The above strain analysis shows that some deformation behaviours of off-axis specimens are similar to those observed in the 0°/90° specimens; for instance, strain localisation bands and fracture bands form as a result of interacting material behaviours of the steel and SRPP layers. Also, looking at high strain points compared to the applied strains, cracks in the SRPP must be impeded from growing due to the adhesion to the steel layers, similar to the 0°/90° specimens. However, there are key differences such as the angles of strain localisation bands being different and that SRPP tapes rotate towards the loading direction in off-axis specimens and not in the 0°/90° specimens. The most crucial difference between off-axis and 0°/90° specimens is that the final failure of the FML occurs due to the failure in the steel layers in the off-axis specimens, whereas the 0°/90° specimens fail from a failure in the SRPP layer.

There is no evidence to suggest that the final failure in the steel layer of the FML results directly from damage in the SRPP layer. It is likely that the only direct cause is the localised necking due to the properties of steel. Even if certain types of damage in the SRPP are related to the failure – for instance, by inducing necking to occur at the point of the damage in the SRPP layer – no indication was found in the surface strain analysis through DIC that could capture the process. However, it should be recalled that strain localisation bands that turn into fracture bands and ultimately lead to failure are initially generated from strain concentration points, which are likely to be boundary cracks in the SRPP layer.

Laminating steel sheets with SRPP has an interesting effect on the behaviour of the SRPP layer when loaded at off-axis. Despite plain SRPP and FML specimens failing at similar applied strains, as shown in Figure 5.67a, the FML specimens exhibit a far lower γ_{12} than SRPP specimens, as shown in Figure 5.67b. At 30°/60° to the loading direction, the maximum γ_{12} in FML is almost half of that in SRPP. This indicates that the SRPP tapes in the FML do not rotate towards the loading direction as much as in the plain SRPP. This shows that steel layers have the effect of reducing the amount of rotation

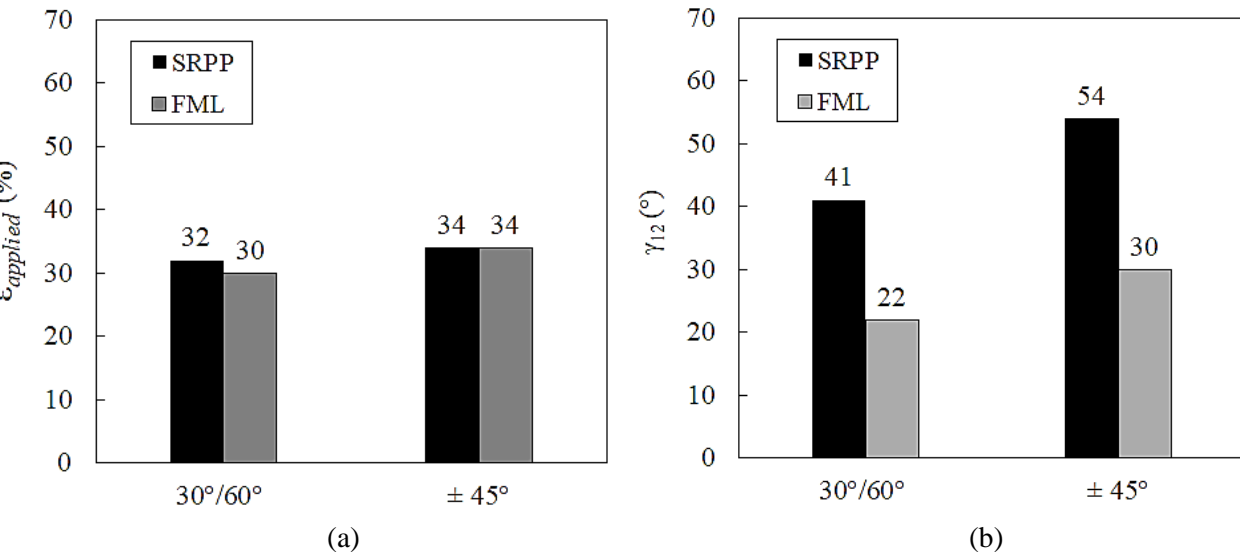


Figure 5.67 a) Applied strain in the loading direction ($\epsilon_{applied}$) and b) maximum shear angle (γ_{12}) at failure of 1.0 mm SRPP and SRPP/steel FML specimens, tested at 30°/60° and ± 45° to the applied load

of the SRPP tapes towards the loading direction and increasing the strain in the reinforcing direction in the tapes. This must be due to the smaller magnitude of Poisson's ratio in the steel layers limiting the amount of reduction in width in the SRPP layer.

It was shown earlier that larger trellising is correlated to a larger amount of damage occurring throughout the gauge section in the 1.0 mm off-axis SRPP specimens. From this, it can be conjectured that steel layers have the effect of delaying the growth of damage in the SRPP layer, and this reduces the amount of trellising, which is related to the reduced degree by which the tapes rotate towards the loading direction.

It is also possible that tape pull-outs from specimen edges occur less easily in the SRPP layer of the FML than in plain SRPP, due to the damage being impeded by the adhesion to the steel. Consider that tape pull-outs would occur more easily when SRPP tapes are under a higher strain along the reinforcing direction, as is the case in FML in comparison to plain SRPP. Furthermore, tape pull-outs have been shown to initiate failure in 1.0 mm off-axis SRPP specimens. However, the SRPP layer does not fail in the FML at the same applied strain that causes plain SRPP to fail. This suggests that fewer tape pull-outs occur, or that the damage propagating from tape pull-outs is less in the SRPP layer of the FML than in plain SRPP specimens at the same applied strain. It is therefore likely that damage is suppressed in the SRPP layer in the FML due to the adhesion to the steel layers, to the effect that failure in the SRPP layer is delayed, as compared to plain SRPP.

Considering the above conjecture, an FML using a metal that has a higher failure strain than the steel used here may allow the FML to deform even further, beyond the strain to failure of plain SRPP. However, prior to its use in any practical applications, the aforementioned issue of bending, and the possible delamination that could result from the bending, would need to be addressed.

5.3.3 Summary of failure behaviour of off-axis FML

Section 5.3 discussed the deformation and failure behaviour of SRPP/steel FML when it is deformed in the off-axis directions ($30^\circ/60^\circ$ and $\pm 45^\circ$) to the reinforcing directions of the SRPP layer. It was found that the $30^\circ/60^\circ$ and $\pm 45^\circ$ specimens generally exhibited similar behaviour. In comparison, the off-axis specimens exhibited a mixture of similarities and differences to the material behaviour when loaded at $0^\circ/90^\circ$ directions.

Similarities between the off-axis FML and $0^\circ/90^\circ$ FML specimens included the fact that the damage characteristics in the SRPP layer of the FML were similar to those in plain SRPP. (The *actual* damage characteristics in the SRPP layer, when comparing off-axis and $0^\circ/90^\circ$ FML specimens, were obviously different but the *behaviour* that the damage characteristics of the FML did not change significantly from plain SRPP when it was laminated with steel layers, were similar). The observations that strain

localisation bands formed at an angle to the loading direction from suspected damage in the SRPP layer, and that fracture bands formed at the same angle of fracture as in plain steel, were also similar to 0°/90° FML specimens.

However, there were some important differences between the off-axis and 0°/90° FML specimens. For example, strain to failure increased when loaded in the off-axis directions compared to the 0°/90° directions, as was seen in the case of plain SRPP. Another important difference was that failure occurred from localised necking and failure in the steel layers, whereas 0°/90° FML was shown previously to fail as a result of a failure in the SRPP layer.

It was found that laminating SRPP with steel produced interesting effects in the FML at off-axis directions. It appears this generated less trellising and higher strain in the tape directions in the SRPP layer compared to plain SRPP. Also, the damage growth and propagation in the SRPP layer are likely impeded by the adhesion to the steel layers, similar to the case of 0°/90° FML. This is conjectured to be part of the reason why the SRPP layer in FML fails at higher strains than in plain SRPP, when loaded in the off-axis directions.

5.4 Summary

Chapter 5 discussed the findings on the deformation and failure behaviour of SRPP and SRPP/steel FML, when subjected to uniaxial tension at 30°/60° and $\pm 45^\circ$ to the reinforcing directions. The behaviour was compared with SRPP specimens of corresponding orientations and with 0°/90° FML specimens. This included findings on whether and how damage characteristics are different in the off-axis SRPP and FML specimens, both from each other and when compared to corresponding 0°/90° specimens. The types of damage in off-axis specimens were similar to 0°/90° specimens, but their characteristics were different in many ways. Between plain SRPP and an SRPP layer in FML, the damage characteristics were similar, except for the fact that large damage in the SRPP layer of the FML were impeded from growing larger due to the adhesion to the steel layers. Much of the behaviour of the 30°/60° and $\pm 45^\circ$ specimens were found to be similar, for both the SRPP and FML.

Critical damage that caused specimen failure, and their progression up to the point of failure, were identified for each material. It was also discussed how this influenced surface strains. Again, it was found that boundary cracks cause failure in 0.3 mm off-axis specimens, which is similar to the 0.3 mm 0°/90° SRPP specimens. However, the type of boundary crack that is critical to the failure of the specimen, and the manner in which it propagates and causes failure, were found to be different. In addition, 0.6 mm and 1.0 mm off-axis specimens ultimately failed due to tape and fibril pull-outs from the edges of specimens, in contrast to the 0.6 mm and 1.0 mm 0°/90° specimens which failed from the fracture of tapes and fibrils.

The cause of failure of off-axis FML specimens was found to be different to the cause found in the $0^\circ/90^\circ$ FML specimens. Off-axis FML failed from localised necking and a resulting tearing in the steel layers, in contrast to $0^\circ/90^\circ$ FML which was shown in the previous chapter to fail as a result of a failure in the SRPP layer. This was despite the fact that the manner in which strain localisation bands and fracture bands developed were similar (from interacting material behaviours of the steel and SRPP layers). The effect of laminating SRPP with steel had similar effects in off-axis FMLs to $0^\circ/90^\circ$ FML, in terms of damage in the SRPP layer being impeded by the steel layers, but with some additional effects, such as an increasing strain in the tape directions and a reduction in the rotation of tapes towards the loading direction.

6 Failure Behaviour Under Biaxial Deformation

6.1 Introduction

In order to find out how SRPP and SRPP/steel FML behaves and fails when subject to a combination of in-plane deformation and out-of-plane bending, induced-biaxial deformation (IBD) tests were carried out.

The first section discusses the material behaviour in circular specimens. This experiment found that damage development, failure initiation and propagation differ to when the materials are subjected to uniaxial tension. Through strain analysis, critical damage that causes failure has been identified for each material, as well as the conditions under which the critical damage and failure occurs. It will also be shown that failure behaviour can differ between specimens for both SRPP and FML, and that the likely cause of this is the quality of consolidation or material imperfections in the SRPP.

The second section discusses the results of the IBD tests using hourglass specimens with SRPP tapes orientated at 45° – -45° to the line of symmetry (along the y -axis). It was found that specimens deformed and failed in ways similar to that of $\pm 45^\circ$ tensile test specimens. This allowed confirmation of the findings from the off-axis tensile test experiments, that failure in SRPP subjected to large in-plane shear strain occurs with propagation of specific micro-damage that leads to tape pull-outs from the free edges. Through analysis of FML specimens, it was found that the surface strain analysis can be used to identify how critical failure arises in the FML, when compared with the behaviour exhibited by the constituent materials.

In this chapter, the following applies with regard to the figures and nomenclature:

- x -axis is horizontal and y -axis is vertical in all images except in those showing side-views of specimens. Local coordinates and strains along x and y axes (ε_x and ε_y) are tangential to the surface.
- Directions 1 and 2 denote the reinforcement directions in the current state (i.e. along the changed tape directions when the material is deformed). Initial tape orientations in the undeformed state are shown in Figures 6.1a and b. ε_1 , ε_2 and γ_{12} denote strains in the direction of tapes and in-

plane shear strain about the original tape orientations. The exception is 1 and 2 in ϵ_{p1} and ϵ_{p2} which indicate first and second principal strains.

- Meridian lines denote lines along the curvature of the surface that pass through the centre of the specimen and are aligned with the reinforcing directions. In an undeformed state, the meridians are aligned with the x and y axes.
- The outer surface is the surface that is furthest from the punch and visible to the DIC measurement system, as illustrated in Figure 6.1c.
- Strains are given as percentages, except for γ_{12} and γ_{xy} which are given in degrees, and strains in DIC and finite element analysis images which are given in non-percentage forms (mm/mm). All strains are given in logarithmic (true) strains and the notation '[log.]' above the scale in DIC images simply denotes this.

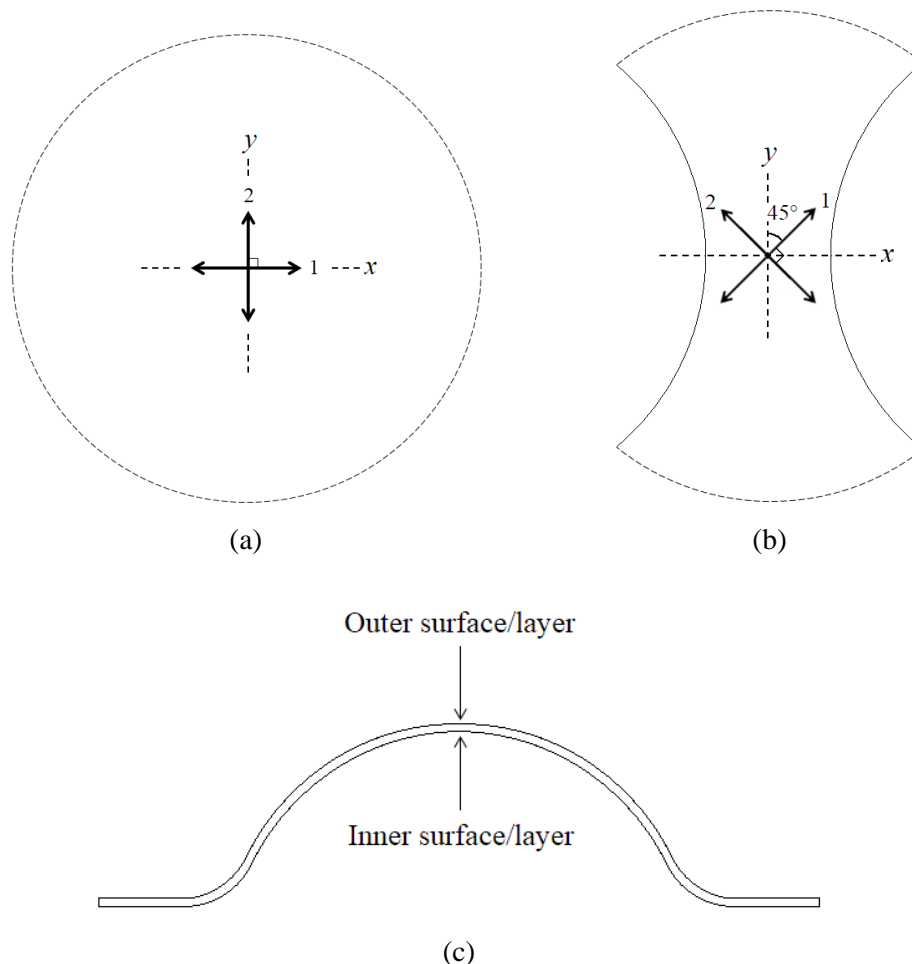


Figure 6.1 Local x - y coordinates and tape orientations 1 and 2 in the undeformed state, for a) circular and b) hourglass specimens in induced-biaxial deformation tests. Dotted perimeters represent approximate boundaries for areas visible to the DIC system. c) Outer and inner surfaces or layers shown on a cross-section of a deformed specimen.

6.2 Deformation and failure behaviour of circular specimens

This section analyses the failure behaviour and the relevant deformation behaviour of SRPP and SRPP/steel FML when subjected to equal deformation in the two tape directions in the middle and varying degrees of biaxial deformation elsewhere, on top of out-of-plane bending deformation. This was done using circular specimens which are fixed around the perimeters and deformed by a semi-hemispherical punch through an open die, as described in Section 3.3.2.

The behaviour of SRPP is discussed in the first subsection. First, the damage characteristics of fractured SRPP specimens is examined, and then the ways in which the critical damage develops is analysed, utilising the digital images captured at small increments of deformation and the computed strains from the DIC system. It will be shown that failure in circular SRPP IBD test specimens is caused by fibril pull-outs in the centre region of the outer layer; how this occurs, and how surface strains indicate such failure, will be analysed. It will also be shown that specimens can exhibit slight differences in the failure behaviour, which are likely due to the consolidation quality.

The second subsection discusses the behaviour of SRPP/steel FML, based on the knowledge gathered regarding the behaviour of SRPP, strain analysis and FEA. Circular FML IBD test specimens exhibit two types of fracture paths, both of which are different to those found in the SRPP specimens. It will be shown the fracture path differs due to the failure initiating in different layers. Depending on whether the SRPP or the outer layer fails first, the detected strain behaviour of the specimen also differs towards the failure event. This can therefore be used to indicate in which layer the failure initiated.

6.2.1 SRPP

The critical failure in circular SRPP IBD test specimens occur as shown in Figure 6.2, where the critical failure refers to the state of a specimen which cannot bear further load. For IBD tests, this occurs with a sharp drop in the load. The propagation of cracks and fractures during the failure process occurs almost instantaneously, to the point where the process cannot be captured using a frame rate of 15 frames per second. However, it is not hard to predict, from examining various specimens, that failure initiates from the fracture of tapes in the centre region of the specimen. It is also possible to categorise the failure process into five stages, as shown in Figure 6.2e, from the initiation of failure at stage 1, to the propagation of failure in stages 2–5. The following paragraphs will analyse the failure behaviour through stages 2–5, before the initiation of failure (stage 1) is explained later on.



(a)



(b)



(c)



(d)



(e)

Figure 6.2 Inner surfaces of failed circular SRPP induced-biaxial deformation test specimens. Corners of the images are located on the die bend. Stages of critical failure initiation (1) and propagation (2 – 5) are indicated in (e).

As can be seen in Figure 6.2, most specimens exhibit roughly equal amounts of fibril pull-outs in both tape directions at the centre. However, the specimen in Figure 6.2e exhibits an additional phase of failure propagation (stage 2), where the failure path extends in one of the tape orientations (direction 2) and causes more fibril pull-outs in one tape direction (direction 1). A close-up photo of the fibril pull-outs is shown in Figure 6.3. It can be seen from the figure that the damage characteristics resemble those of failure of the $0^\circ/90^\circ$ tensile specimens, which suggests that the critical failure in circular IBD test specimens occurs from fibrillation and fracture of tapes in the middle, due to the tension in the reinforcing direction.



Figure 6.3 Close up of failure at the centre of the specimen shown in Figure 6.2e.

At stage 3, the tapes oriented in the other direction fibrillate and fracture in a similar manner. Inferring from the failure process exhibited by the specimen in Figure 6.1e, it is likely that in all specimens, critical failure starts with the fracture of tapes in one direction, and then *subsequently* propagates into the fracture of tapes oriented in the other direction, as opposed to tapes fracturing in both directions *simultaneously*.

At stage 4, failure propagates outwards from the centre along diagonals that are, in most cases, oriented at approximately 45° to the reinforcing directions. Damage along some diagonals may not result in noticeable tape fracture and pull-outs, as shown in Figures 6.1c and d. It is hypothesised that the failure propagates diagonally to the tape directions because the initial fracture of tapes at the centre causes the unloading of tapes along the meridian lines. The reductions in tapes along their lengths in both directions would cause stretching of the material between the meridian lines, causing the material to shear about the tape orientations, as shown in Figure 6.4. Then, the tapes would fracture due to the tensile stress built-up along the tapes. Unloading also occurs in fractured tapes, causing further tensile fracture of tapes between the meridian lines, and so on, causing the fracture to propagate diagonally to the tape

directions. Hence, the failure along the diagonals also exhibit characteristics of tensile failure of the tapes, as shown in Figure 6.5.

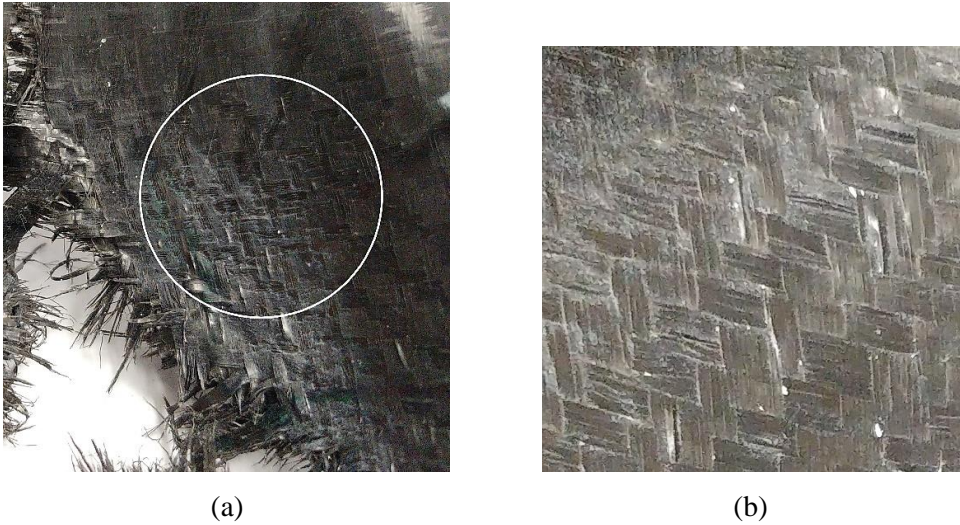


Figure 6.4 Combination of deformation in the tape directions and in-plane shear deformations at locations diagonal to the tape direction from the centre.



Figure 6.5 Fibril pull-outs along a diagonal failure path from the centre of a specimen.

At stage 5, failure can additionally propagate in the direction of one or both tape orientations, as indicated by stage 5 shown in Figure 6.2e and as shown in Figure 6.6. Cracks propagate along the boundary between the tapes as shown. This verifies earlier findings from tensile tests that tape boundaries are the ‘weak’ parts of SRPP, along which damage tends to propagate.



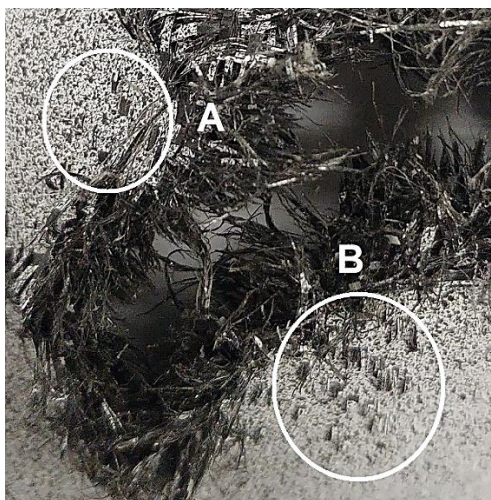
(a)



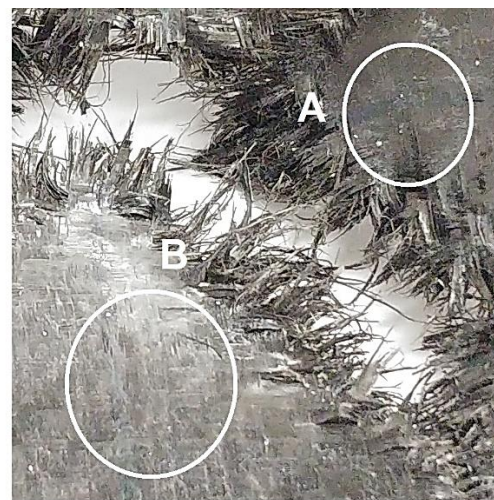
(b)

Figure 6.6 Propagation of failure in the direction of tape orientation.

It can be clearly seen in failed specimens that more tape and fibril pull-outs tend to occur on the outer surface. An example is shown in Figure 6.7 where areas marked A and B exhibit tape and fibril pull-outs on the outer surface but not on the inner surface. Also, the pull-outs jut outwards, as shown in Figure 6.8, more than jutting inwards or tangentially to the curvature of the specimen. This demonstrates that the increases in stress and strain in the tapes towards the outer layer due to the bending are not insignificant. From this, it is likely that critical damage that leads to specimen failure initiates in the outer layer. Since the DIC system captures the state of the outer surface, the digital images and strain analysis from the DIC system yield critical information on the specimen failure in IBD tests.



(a)



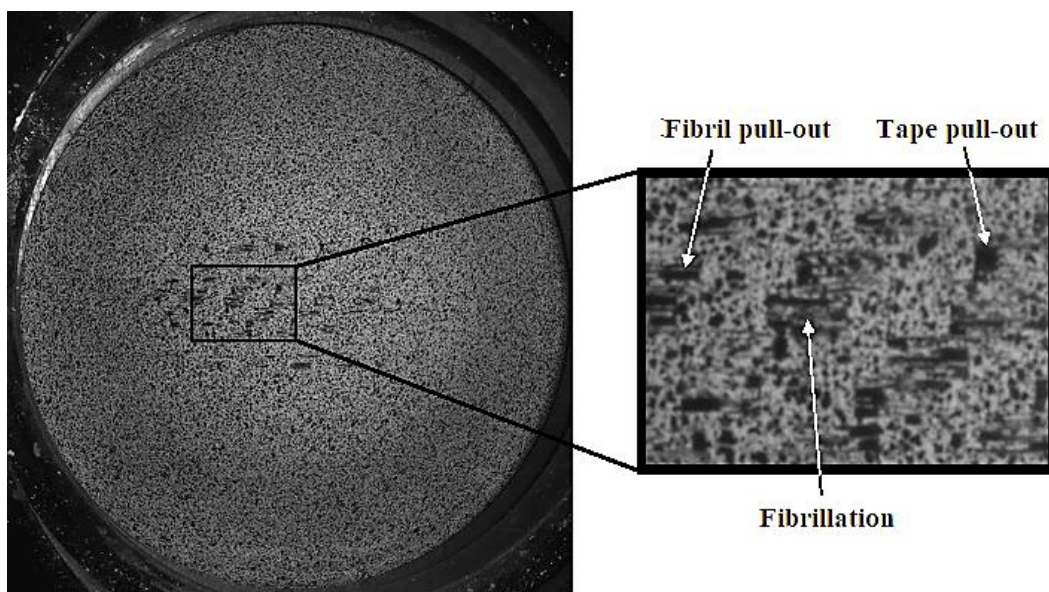
(b)

Figure 6.7 Larger amount of tape and fibril pull-outs occurring on the outer surface (a) of a specimen compared to the inner surface (b), in same regions (A and B).



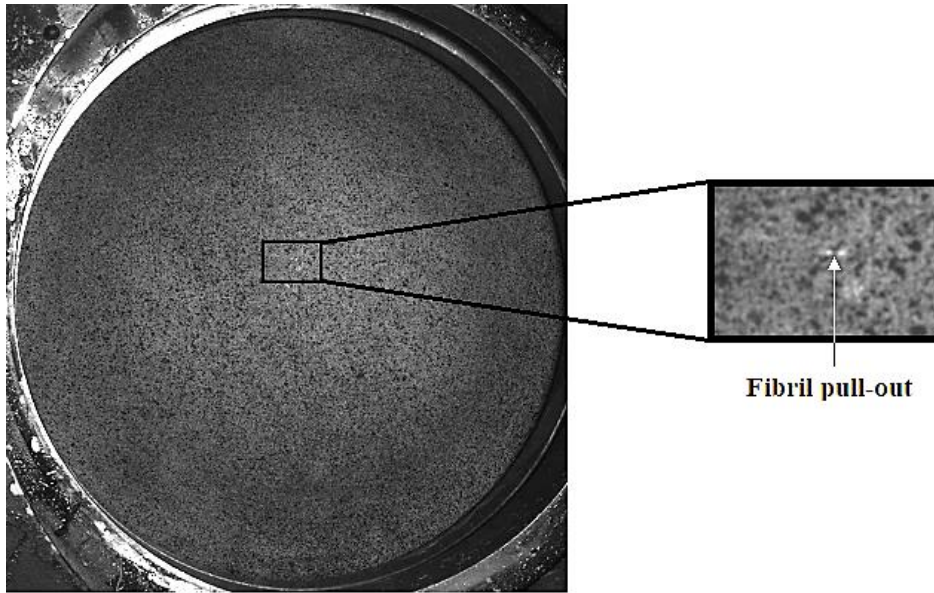
Figure 6.8 Side-view of the outer surface of a specimen, showing fibril pull-outs.

Careful observation of the digital images from the DIC system shows that certain specimens exhibit greater damage from a couple of stages before failure, as shown in Figure 6.9a, in comparison to other specimens that exhibit just one or two visible instances of damage just before failure, as shown in Figure 6.9b. Specimens that exhibit more damage before failure fail at slightly lower punch depths (34.0 ± 0.2 mm) and loads (22 ± 1 kN) than those that exhibit just one or two noticeable instances of damage prior to failure (36.0 ± 0.7 mm, 26.14 ± 0.09 kN). This suggests that the SRPP specimens with a higher quality of consolidation exhibit less damage before failure and are able to withstand slightly higher loads.



(a)

Figure 6.9 Comparison of circular SRPP induced-biaxial deformation test specimens that exhibit different amounts of damage before failure.



(b)

Figure 6.9 Comparison of circular SRPP induced-biaxial deformation test specimens that exhibit different amounts of damage before failure.

The implication from the above, in any future research on developing failure criteria for SRPP, is that the quality of consolidation also needs to be considered if a criterion is to be developed based on the density of damage, as is sometimes the case. For other types of failure criteria, such as the failure limit curve established in [111], it suffices that certain metrics, such as average stress or strain derived over a region, be used as a failure limit, since the specimens still fail at relatively consistent loads, depths and average strains. The region over which the data is derived must be larger than the size of the damage.

The critical damage that leads to failure in a circular SRPP IBD test specimen is a fibril pull-out on the outer surface in the centre region. This leads to specimen failure in a well-consolidated specimen almost immediately, or very shortly after the fibril pull-out occurs. In the case of a less well-consolidated specimen, the fibril pull-out occurs at a lower depth and several more fibril pull-outs are observed before it fails, as mentioned previously.

The process of initiation of the critical fibril pull-out is illustrated in Figure 6.10. Well before the failure of the specimen, there are many tape-splits and boundary cracks on the surface (Figure 6.10a). A digital image is also given in Figure 6.10a for clarity. The critical damage initiates from a boundary crack between tapes on the surface (Figure 6.10b-c). The boundary crack propagates between the surfaces of a surface tape and the tape beneath it, causing local delamination between them (Figure 6.10d). The combination of the local delamination and the existing tape-splits result in fibrillation of the surface tape (Figure 6.10e). Then, a fibril fractures under tension, resulting in a local fibril pull-out (Figure 6.10f). Note that the transition of boundary cracks to local delamination is somewhat similar to the transition

of transverse cracks in a transverse ply into interlaminar delamination in a three-point bending test of a GFRPP [48], although no corresponding drops in load were observed in the IBD test of SRPP.

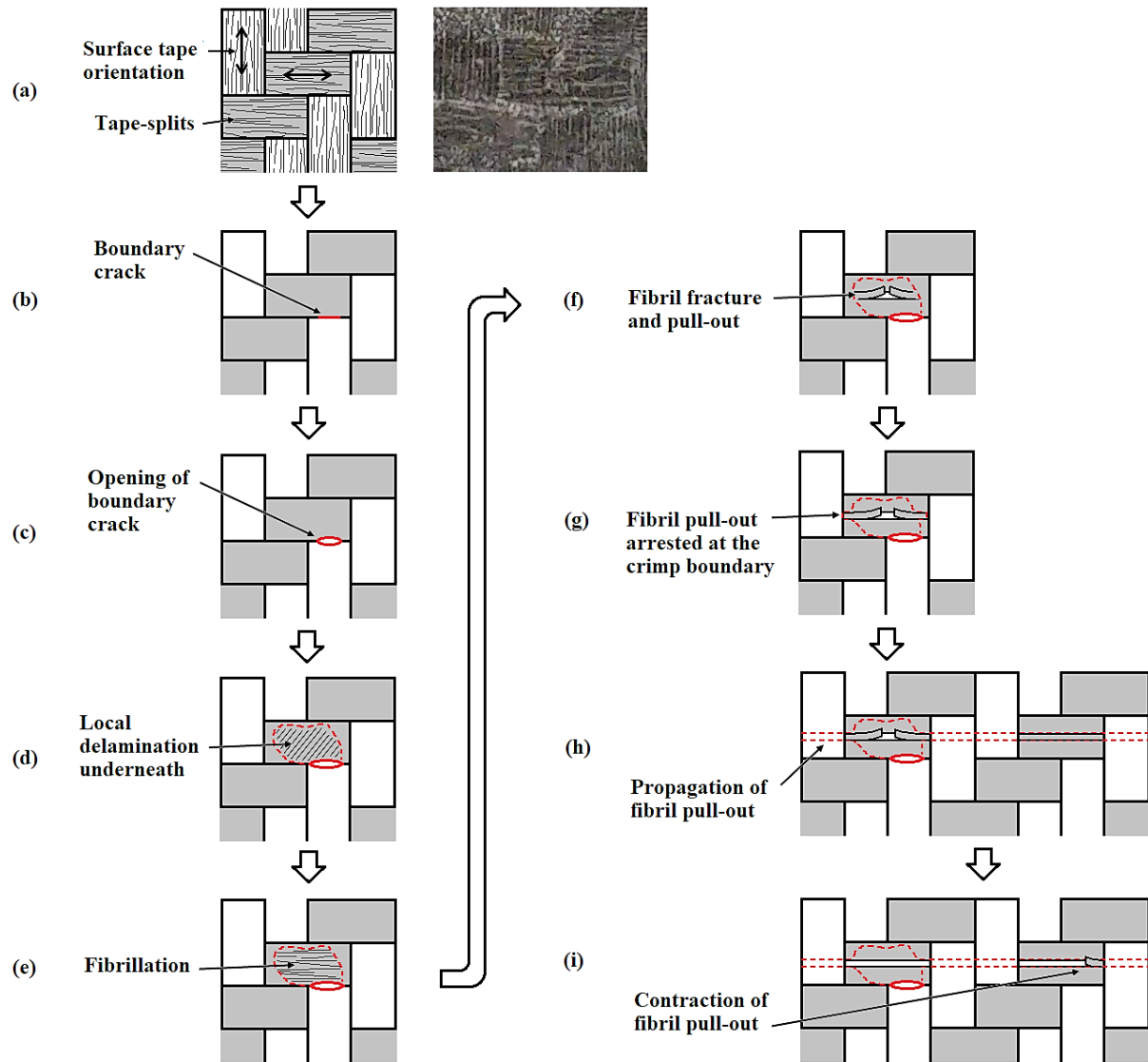


Figure 6.10 Fibril pull-out process in circular SRPP induced-biaxial deformation test specimens.

The fibril pull-out is initially arrested from propagating at the weave boundary (Figure 6.10g). It is likely that a toughening mechanism, similar to those found in the tensile specimens, occurs, where tape-splits in a tape are bridged by the orthogonal tape that crosses on top of it and prevents the tape-splits from opening further. This is similar to the behaviour of other woven FRPs, in which local delaminations, triggered from the shear stress between transverse cracks and longitudinal yarns, are initially confined by the crimp boundaries. The local delaminations can then propagate further, causing fibre breakages in the surrounding bundles and interlaminar delamination [24, pp. 41–56].

A fibril pull-out triggers specimen failure in a well-consolidated specimen, likely due to the strain concentration in the remaining layers. Less well-consolidated specimens do not fail so soon after a fibril pull-out, so it is possible to observe how the damage propagates after the initial fibril pull-out.

In specimens with poorer consolidation, the fibril pull-out propagates beyond the weave boundary with further deformation (Figure 6.10h). Since the fibril is unconstrained by the surrounding material, the fibril pull-out reduces in length due to unloading (Figure 6.10h). This shows that fibril pull-outs propagate more easily in a less well-consolidated specimen than in a well-consolidated specimen deformed to the same depth. This is because a specimen with poorer consolidation has lower adhesive strength between the tapes, making the propagation of local delamination easier. Finally, the specimen fails after multiple pull-outs occur. This is, once again, likely due to the increased strain concentration at points of fibril pull-outs in the centre region. Hence, it is conjectured that failure occurs earlier in a less well-consolidated specimens due to the critical fibril pull-out (near the centre) occurring earlier.

A fibril fracture and pull-outs can initiate on its own or occur as a result of a fracture in the neighbouring fibril. This can be deduced by tracking the progression of cracks in a specimen with poorer consolidation by scrutinising the stochastic pattern on the surface of the specimen through incremental stages of deformation. An example is illustrated in Figure 6.11 in the next page, showing noticeable tape-splits (red), boundary cracks (yellow) and fractures across fibrils (white) in a region of a specimen. Black regions in fibrils with missing surface patterns are either a region that is bared due to a fibril pull-out on the surface (A in Figure 6.11), or part of a fibril pull-out that was originally underneath the surface (and hence not painted on the surface) but has become exposed due to the movement of the fibril as it reduced in length from unloading (B in Figure 6.11). Fibril fractures that triggered fibril pull-outs are numbered in the order of appearance.

There are four points that can be ascertained from Figure 6.11.

1. Fibril fractures and pull-outs can initiate at different places at the same time, as indicated by two fibril fractures that are labelled '1' in the figure.
2. A fracture of a fibril triggers subsequent breakages in the neighbouring fibrils of the same tape, as can be seen by the fibril fractures labelled 1, 3, 4 and 5, which all occur in a single tape at the top of the image. The fibrils break at different places along the length of the tape, as opposed to a single crack propagating across multiple fibrils and breaking them. This shows that the tape was fibrillated and delaminated from the surrounding tapes before the fibrils broke, with each fibril deforming as an unconstrained and discontinuous unit. If the tape was not fibrillated and delaminated before the fibril fractures, it is likely that a propagation of a single crack across multiple fibrils would have been observed.

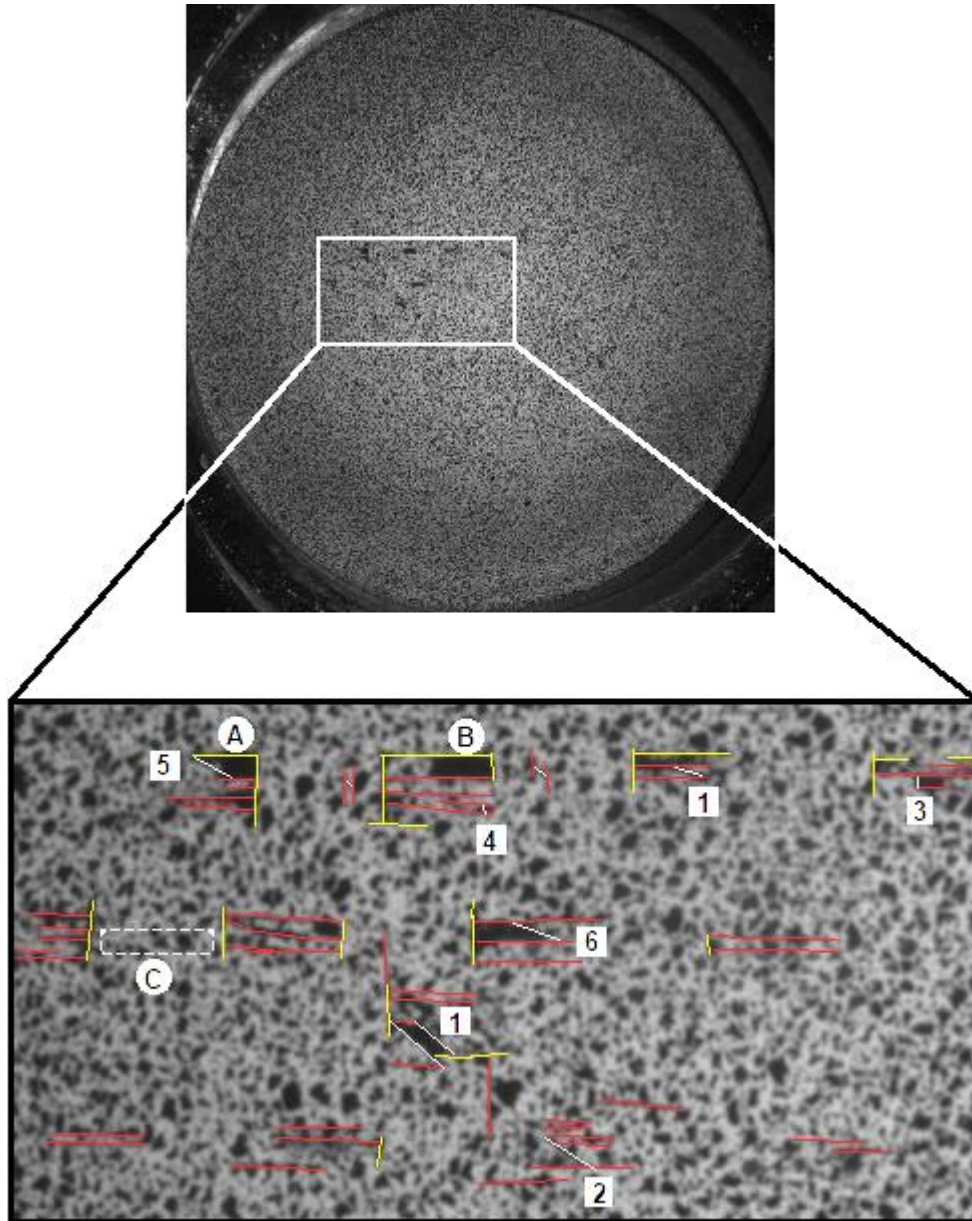


Figure 6.11 Digital image of a region in a circular SRPP induced-biaxial deformation test specimen before failure. Red lines indicate large tape-splits, yellow lines indicate boundary cracks and white lines indicate fractures across fibrils. Fibril fractures that triggered fibril pull-outs are numbered in the order of appearance.

3. Fibrils beneath the surface tape can also fracture and cause pull-outs. This is the case at the region marked C in Figure 6.11. The movement of surface fibrils away from C in regions to the left and right of C indicates that a fibril fracture occurred somewhere in region C, under the surface tape, and caused the fibril to pull-out. This then triggered the fracture and pull-out of the neighbouring fibril, at the point labelled '6'. The observation that a fibril has fractured and pulled out from beneath the surface tape also supports the likelihood that the tapes were delaminated before the fibril fracture.

- Fibrils often fracture at an oblique angle to the reinforcing direction. It will be recalled that such oblique cracks were observed in rare instances in tensile test specimens. This shows that oblique cracks can form when a tape deforms under tensile stress in the reinforcing direction ($\epsilon_1 > 0$ and $\sigma_1 > 0$), regardless of whether it experiences positive strain in the transverse direction due to tensile stress ($\epsilon_2 > 0$ and $\sigma_2 > 0$ in the IBD test) or negative strain in the transverse direction due to Poisson's effect ($\epsilon_2 < 0$ and $\sigma_2 = 0$ in $0^\circ/90^\circ$ tensile tests). It is still not exactly clear what causes oblique cracks to form, although several hypotheses were made earlier. What can be said for now is that oblique cracks occur more frequently under biaxial stretch deformation mode (in-plane principal strain ratio, $\beta > 0$) than under uniaxial tension mode ($\beta \approx -0.5$).

It was mentioned earlier that the critical damage that causes specimen failure occurs in the centre region of the specimens. This was deduced from observing that large cracks can occur away from the centre region, in a well-consolidated specimen, but do not cause specimen failure. In comparison, a fibril pull-out near the centre is followed very shortly by specimen failure. An example is shown in Figure 6.12, where a large fibril pull-out occurs away from centre, at B, at a punch depth of 31.0 mm. However, the specimen does not fail until it reaches a punch depth of 35.5 mm, right after another fibril pull-out near the centre becomes noticeable (marked A in Figure 6.12), at a punch depth of 34.7 mm. Careful observation shows that the pull-out at B is arrested at the weave boundary.

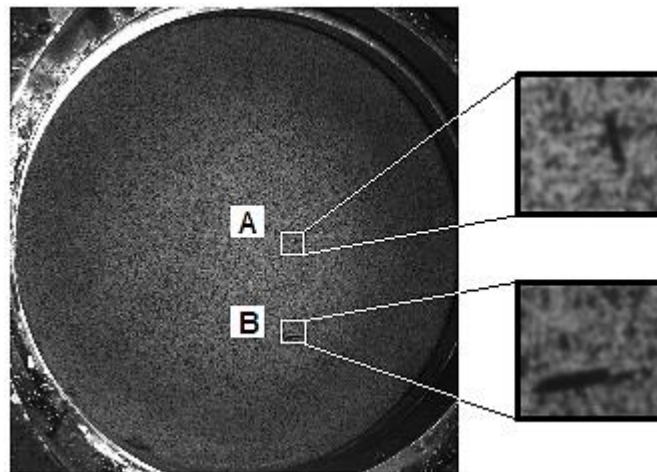


Figure 6.12 Digital image of a circular SRPP induced-biaxial deformation test specimen before failure, showing a critical fibril pull-out near the centre (A) and a non-critical fibril pull-out away from the centre region (B).

In the case of specimens with poorer consolidation, the specimen fails after multiple fibril pull-outs which can extend far along the length of the fibril, away from centre region. However, it was observed that fibril fractures start from the centre region. This observation, in addition to the observation of the well consolidated specimens, indicate that only the fibril fracture and pull-outs from the centre region

are critical to the failure of circular SRPP IBD test specimens. The reason behind this phenomenon laid out below.

The amount of strain in the tape direction is higher in the centre region and along the meridian lines, as shown by ϵ_x and ϵ_y distributions in Figure 6.13a and b. In comparison, tapes in regions diagonal to the centre are subject to a smaller strain component along the tape orientation and a non-zero in-plane shear strain about the tape orientation, as can be seen by the γ_{xy} distribution in Figure 6.13c. Therefore, fibril pull-outs tend to occur in the centre region, and near the meridian lines, but not in other regions.

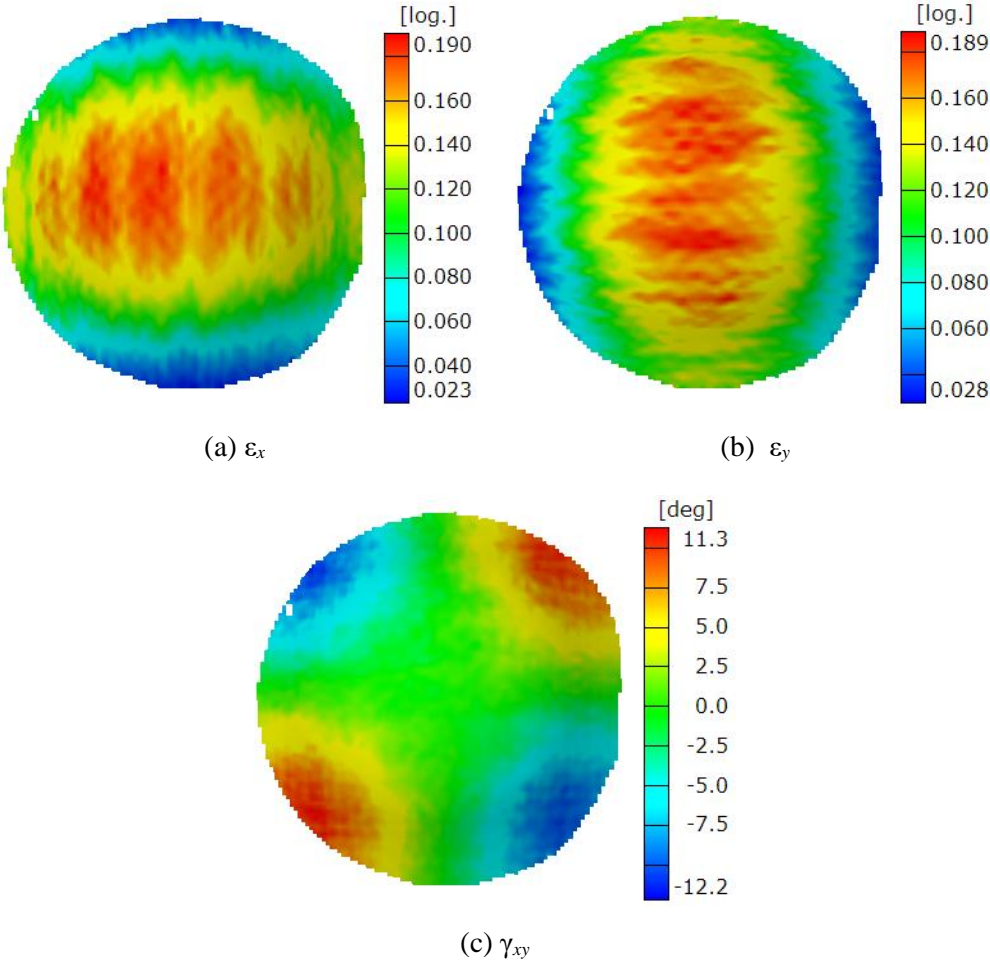


Figure 6.13 a) Strain in x -direction (ϵ_x), b) strain in y -direction (ϵ_y), and c) shear angle about x - y directions in a circular SRPP induced-biaxial deformation test specimen before failure.

When a fibril pull-out occurs, it causes strain concentration in the region of the pull-out. The effect of this is most relevant for the tape directly underneath the fibril pull-out, which experiences a higher strain than the inner layers due to the effects of bending. The tape then fractures when the strain in its

reinforcing direction reaches the limit. When the tape fractures, the surrounding material rapidly fails and causes specimen failure.

It should be noted that the tape underneath the fibril pull-out is orthogonally oriented to the fibril pull-out, meaning that the strain in the tape, in the orthogonal direction to the reinforcing direction of the fibril pull-out, is of importance. This strain is higher in the centre region than outside the region as illustrated in Figure 6.14 by points A and B. Hence, only the fibril pull-outs in the centre region are considered critical.

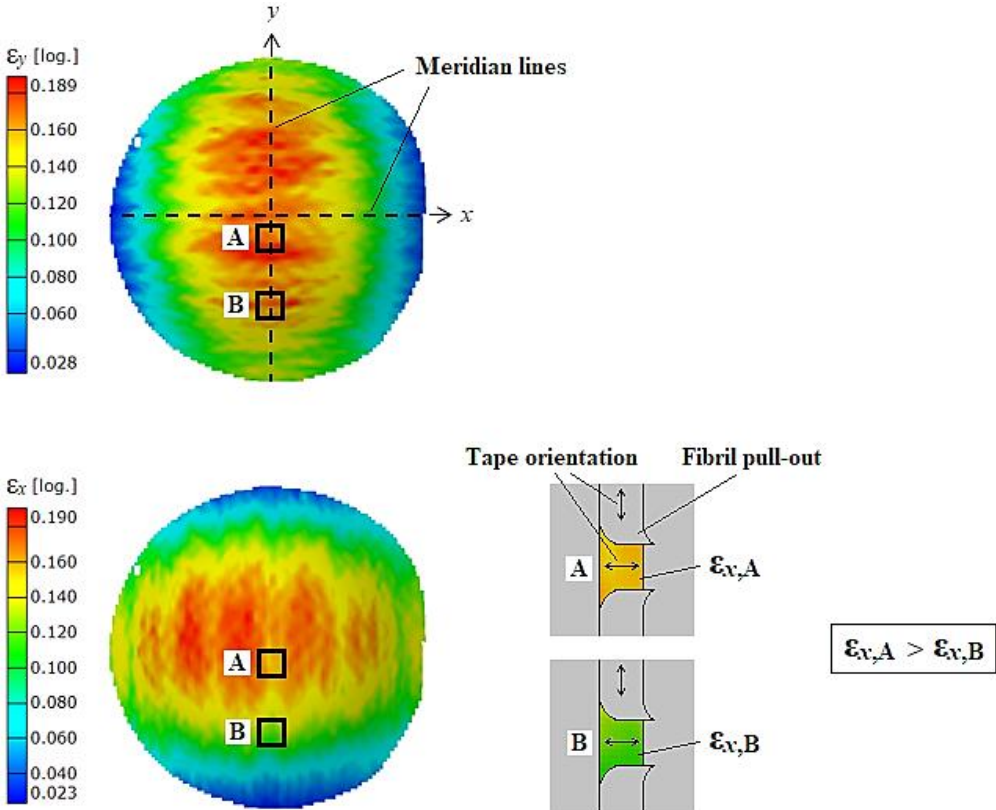


Figure 6.14 Comparison of strains underneath fibril pull-outs in the centre region of the specimen (A) and outside the centre region (B), in the direction of tape orientation, of a circular SRPP induced-biaxial deformation test specimen.

From the above analysis, it is clear that strain along the tape directions should be used for strain analysis of the critical damage point, or the failure point. Since the failure point occurs in the centre region where the tapes exhibit negligible γ_{12} , analysis using ϵ_x and ϵ_y needs to be considered.

In IBD test specimens, the modes of deformation vary widely throughout the specimen (approximately $-0.3 < \beta \leq 1$ in circular specimens) because the internal forces in the specimen vary, depending on the distance from the centre, due to the applied load conditions, and the material response also varies

depending on the reinforcement directions. Therefore, a strain measure should be used that reflects the mode of failure at the failure point.

The benefit of surface strain analysis is that it can detect a fibril pull-out, which can then become critical damage. When a fibril fractures, the two parts of the fibril separate away from each other due to the unloading. This causes a strain concentration at the point of fibril fracture, as shown at A in Figures 6.15a and b, and a strain decrease next to it, as shown at B in Figure 6.15a and b. The contrast

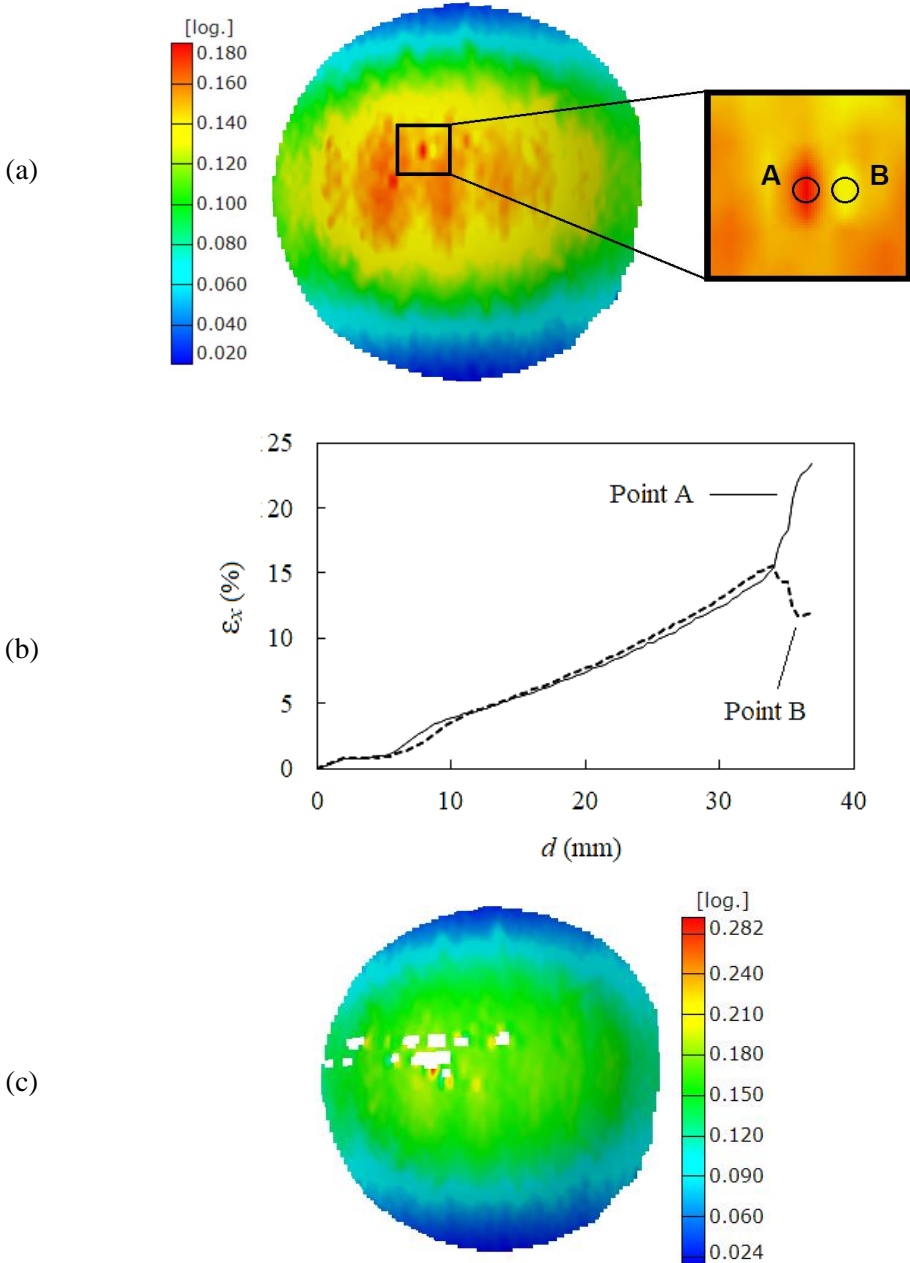


Figure 6.15 Strain in x -direction (ϵ_x) in a circular SRPP induced-biaxial deformation test specimen: a) ϵ_x distribution after a fibril pull-out occurs in the x -direction at point A at a punch depth (d) of 34.0 mm, b) plot of ϵ_x against d at points A and B, c) ϵ_x distribution after the fibril pull-outs propagate further and the fibrils unload ($d = 36.9$ mm).

between these points makes the point of fibril pull-out stand out in the ϵ_x distribution, as shown in Figure 6.15a. In specimens with poorer consolidation, the pull-outs propagate further, beyond the weave boundary, and the fibrils experience a reduction in their lengths from unloading. This causes a large change in the pattern that was painted on the surface along the fibril, causing strains along the fibril pull-out to become incomputable, as shown in Figure 6.15c. In addition, fibril pull-outs can cause sudden changes to the principal strain directions when they occur, as shown in Figure 6.16.

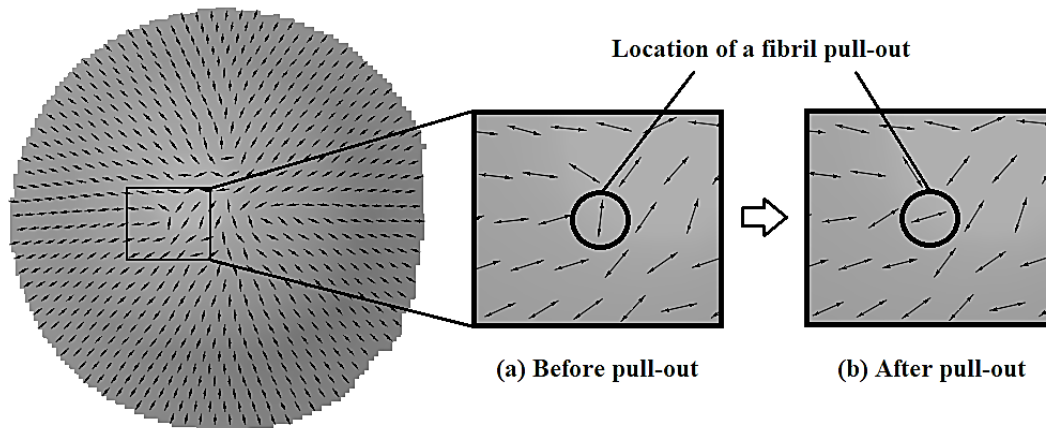


Figure 6.16 First principal strain directions in a circular SRPP induced-biaxial deformation test specimen indicated with arrows, before (a) and after (b) a fibril pull-out.

It should be noted that it is only possible to detect a fibril pull-out by observing the strain behaviour *after* it occurs. Therefore, it can be challenging to find the location of the failure point in a well-consolidated specimen because it can fail almost immediately after a fibril pull-out occurs at the centre. In a less well-consolidated specimen, it is relatively easy to detect where fibril pull-outs have occurred, but it is still difficult to predict the exact location of the failure point. However, it was found from strain analysis that the critical fibril pull-out occurs when it reaches approximately $20 \pm 1\%$ strain in the direction of the fibril (ϵ_1 or ϵ_2) in the centre region of the specimen, at which the strain in the transverse direction is approximately $17 \pm 1\%$. This can help predict or detect the failure point. Furthermore, it was found that failure in circular SRPP IBD test specimens occurs at relatively consistent depths, loads and strains, as shown in Table 6.1 in the next page.

It is interesting that a single, local damage can cause the failure of the circular SRPP IBD test specimen. In a sense, this is similar to the 0.3 mm tensile test specimens, which fail when the strain concentration from a boundary crack reaches a very high value. This sensitivity to local damage is not observed in 0.6 mm and 1.0 mm tensile test specimens. However, the critical fibril pull-out in IBD test specimens occurs at a consistent strain, and the resulting specimen failure also occurs at a consistent depth, load and strains, which is similar to the behaviour of the thicker tensile test specimens and different to the

Table 6.1 Punch depth (d), load (P) and strains in circular SRPP induced-biaxial deformation test specimens. For strains, average (avg.) and maximum (max.) values are given for first principal strain (ϵ_{p1}), second principal strain (ϵ_{p2}), strains in x and y directions ($\epsilon_{x,y}$), and shear angle (γ_{12}).

d (mm)	P (kN)	ϵ_{p1} (%)		ϵ_{p2} (%)		$\epsilon_{x,y}$ (%)		γ_{12} (deg)
		avg.	max.	avg.	max.	avg.	max.	max.
35 ± 1	24 ± 2	16 ± 1	21 ± 1	6.9 ± 0.8	18 ± 1	11 ± 1	20 ± 2	11.9 ± 0.6

0.3 mm tensile test specimens. This is possibly because the IBD test specimens do not exhibit unusually high strain concentrations caused by the boundary cracks, although why that is the case is not clear. In the absence of such, there is no particular fibril that develops unusually high strains, which can cause it to fail much earlier than other fibrils in the centre region. Therefore, the IBD test specimens can fail from a single local instance of damage but do not exhibit the same variation in failure limits as the 0.3 mm tensile test specimens.

In this section, it was analysed how critical failure initiates and propagates when SRPP is subjected to in-plane biaxial and out-of-plane bending deformations using circular IBD test specimens. It was shown that failure occurs from fibril pull-outs in the centre region of the outer layer, which triggers an outward propagation of damage, causing many fibril fractures and pull-outs. The critical fibril pull-outs occurred after they fracture at a specific strain in the reinforcing directions, which then causes strain concentrations to appear from the damage. It was also shown that specimens can exhibit slight differences in the failure behaviour that are likely related to differences in the consolidation quality. In the next section, the deformation and failure behaviour of circular FML IBD test specimens will be discussed.

6.2.2 FML

Combining steel and SRPP layers to create an FML allows the laminate to withstand higher loads in IBD tests, as can be seen in Figure 6.17. (Punch depths and loads at failure are given in Table 6.2.) This is a phenomenon that is simple to understand, similar to how the modified rule of mixture could be applied for determining the strength of FML tensile test specimens. The maximum load in FML before failure (87 ± 2 kN) is slightly higher than the sum of the maximum loads in the constitutive layers, in proportion ($28 \times 2 + 24 = 81$ kN).

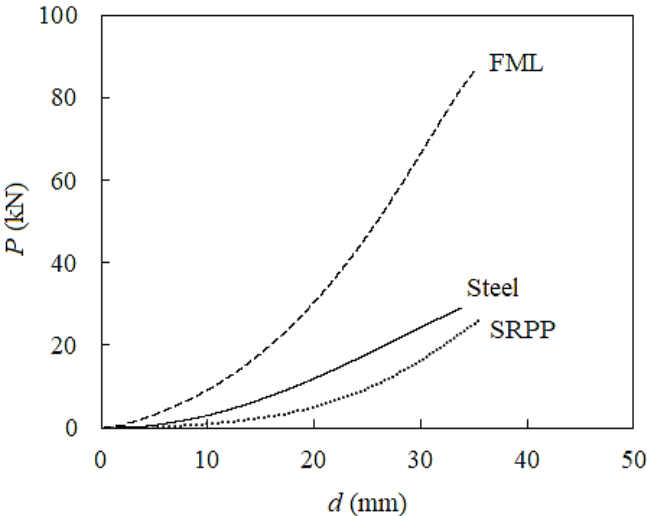


Figure 6.17 Typical curves of applied load (P) against specimen depth (d) of circular induced-biaxial deformation tests specimens for steel, SRPP and SRPP/steel FML.

Table 6.2 Sample statistics of circular induced-biaxial deformation tests specimens for steel, SRPP and SRPP/steel FML before failure: applied load (P), depth (d), average first principal strain ($\overline{\epsilon_{p1}}$), and average strain in x -direction ($\overline{\epsilon_x}$).

	P (kN)	d (mm)	$\overline{\epsilon_{p1}}$ (%)	$\overline{\epsilon_x}$ (%)
Steel	28 ± 2	33 ± 1	15.3 ± 0.9	32 ± 3
SRPP	24 ± 2	35 ± 1	16 ± 1	21 ± 1
FML	87 ± 2	35.3 ± 0.6	16 ± 1	27 ± 6

In comparison, determining how failures occur in FML IBD test specimens is more difficult. It is difficult to discern from the load curves, or from visual examinations of the failed FML specimens, whether it is the steel or the SRPP layer that causes the failure, due to that fact that all the layers fail suddenly at the same time, in the same places. It is also difficult to estimate by comparing depths or average strains before failure because they are similar for plain steel, plain SRPP and FML specimens,

as shown in Table 6.2 and Figure 6.18. In fact, a careful analysis will show that the steel layer or the SRPP layer can both fail first in the FML. It will also be shown that the appearance of the failure path can indicate whether the failure was triggered by a failure in the outer steel or the SRPP layer.

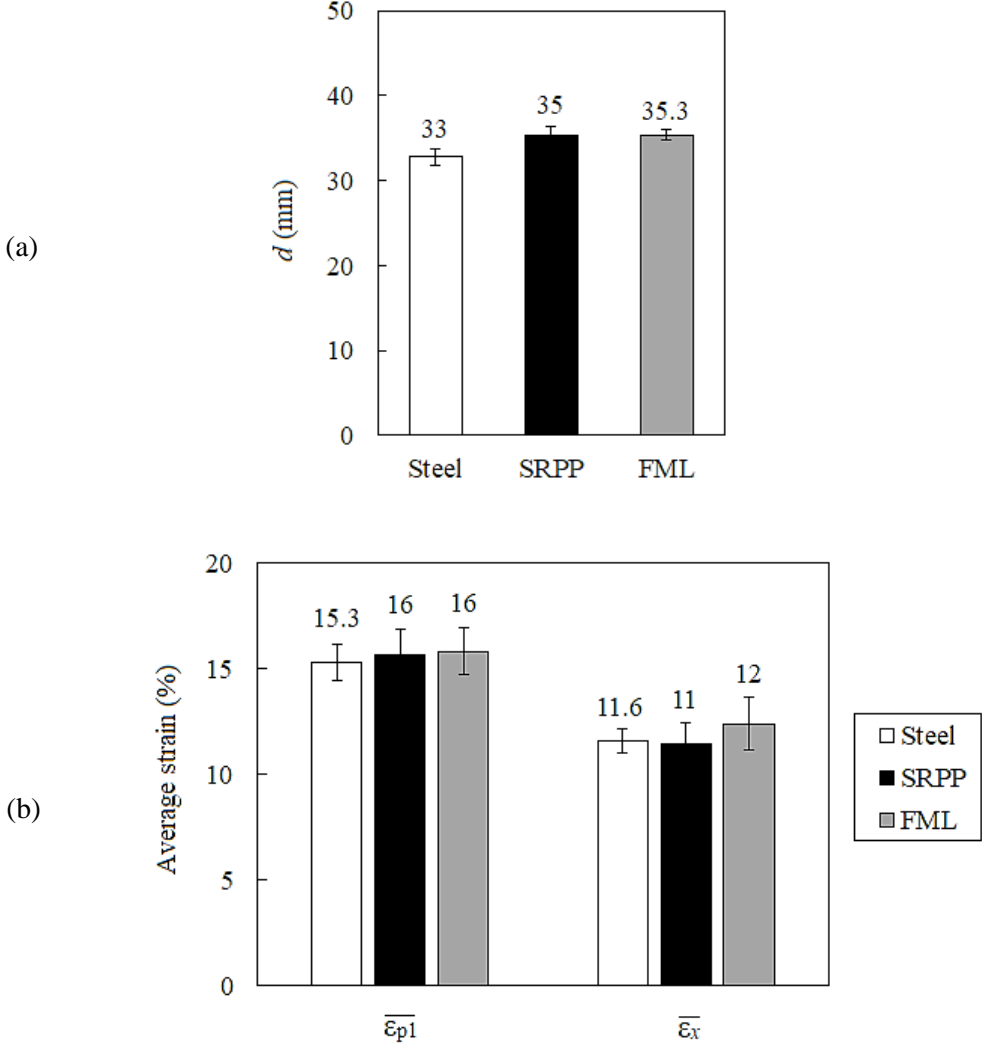
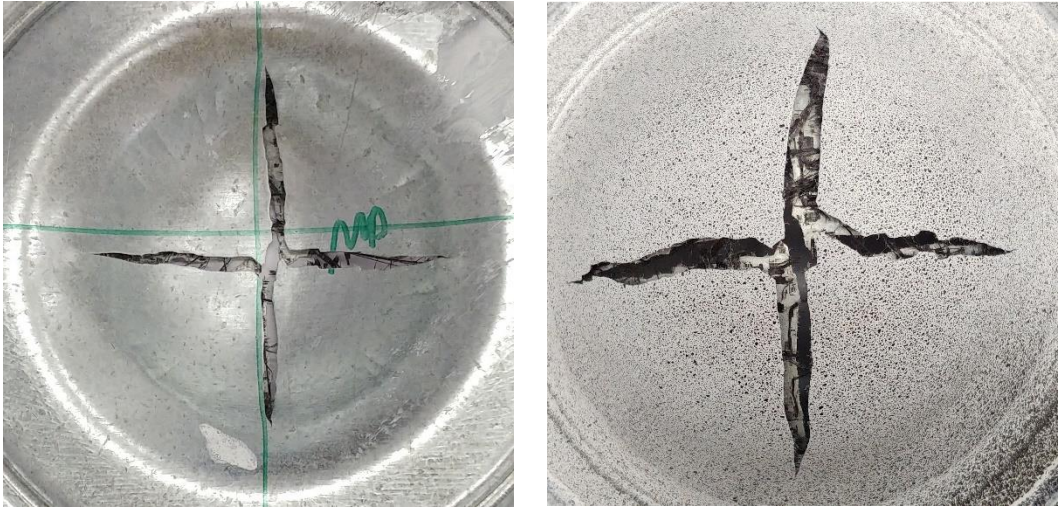


Figure 6.18 a) Punch depth (d), b) average first principal strain ($\overline{\epsilon_{p1}}$) and average strain in x -direction ($\overline{\epsilon_x}$) in circular induced-biaxial deformation tests specimens for steel, SRPP and SRPP/steel FML before failure.

Circular FML IBD test specimens can fail either along the meridian lines, as shown in Figure 6.19, or in the side-wall region, as shown in Figure 6.20. In the former case, the SRPP layer fails first and, in the latter case, the outer steel layer fails first, which then triggers failure in other layers. This can be gathered from studying the strain distributions in both types of FML specimens in comparison to each other and to plain steel and SRPP specimens. As mentioned previously, ϵ_x and ϵ_y are the most appropriate strain measures to use for analysing the failure behaviour of plain SRPP. For steel, analysis based on ϵ_{p1} is

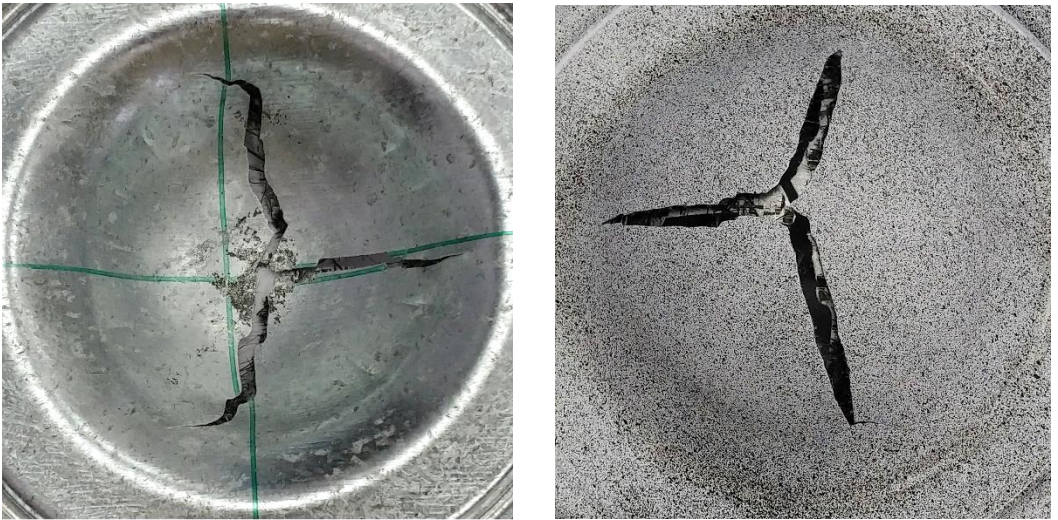
more appropriate since its strain distribution is axisymmetric, due to the loading condition being axisymmetric and the material being isotropic. Therefore, both ϵ_{p1} and ϵ_x or ϵ_y are used for comparing the strain behaviour across different specimens.



Inner surface

Outer surface

(a)

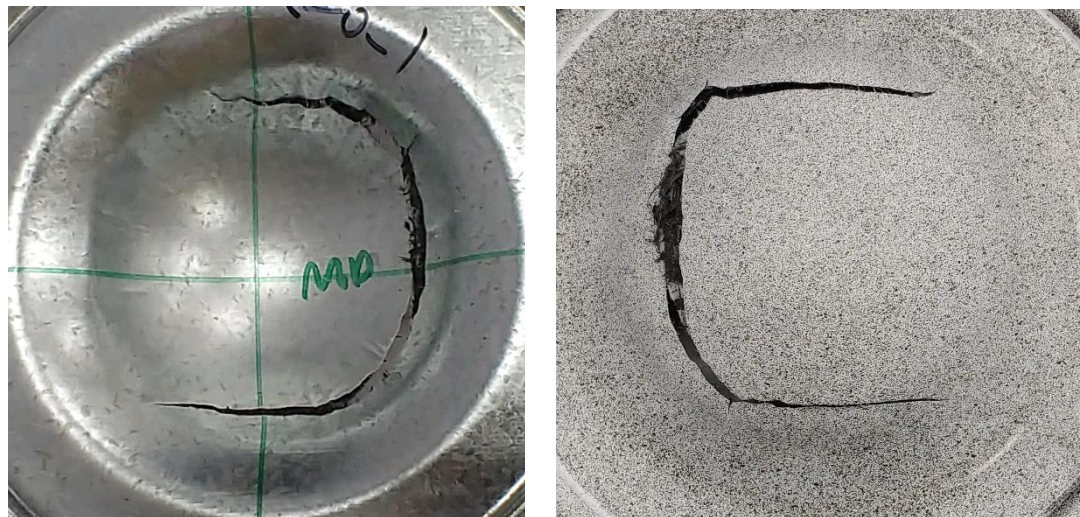


Inner surface

Outer surface

(b)

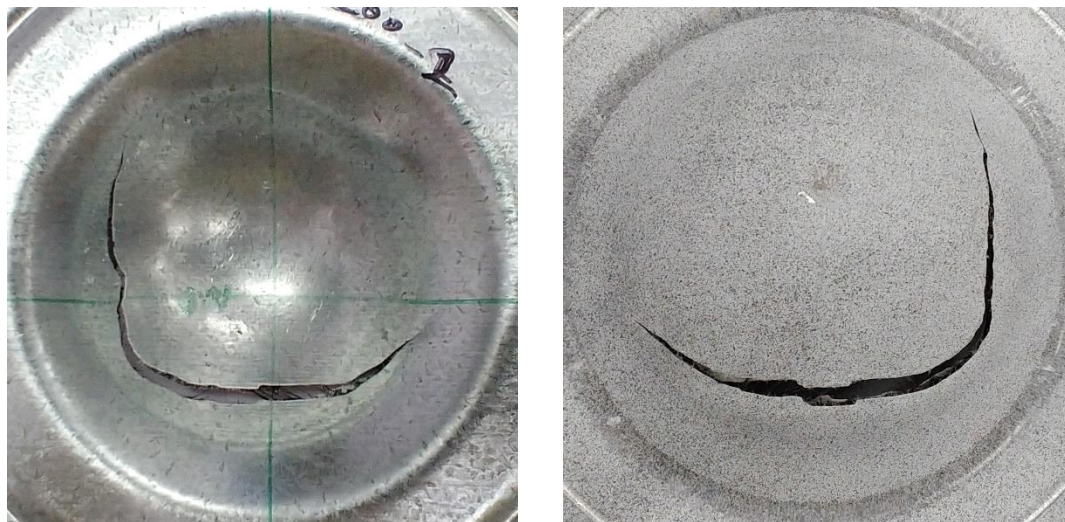
Figure 6.19 Circular SRPP/steel FML induced-biaxial deformation test specimens that have failed a) along meridian lines or b) partially along the meridian lines. Corners of the images are located on the lock-ring. Horizontal and vertical lines marked on the inner surface depict tape directions in the SRPP layer, not meridian lines.



Inner surface

Outer surface

(a)



Inner surface

Outer surface

(b)

Figure 6.20 Circular SRPP/steel FML induced-biaxial deformation test specimens that have failed in the side-wall regions. Corners of the images are located on the lock-ring. Horizontal and vertical lines marked on the inner surface depict tape directions in the SRPP layer, not meridian lines.

Comparison of ε_{p1} and ε_y distributions in steel, SRPP and the FML specimens are shown in the left, centre and right columns of Figures 6.21 and 6.22, respectively, at approximately every 10 mm punch depths. The FML specimen in the figure is the specimen that was shown in Figure 6.19a, which failed along the meridian lines. ε_x distributions are not shown but these are very similar to ε_y distributions rotated by 90° , at the punch depths shown in the figures. Strain distributions at the start of the deformation are given for ε_{p1} in Figure 6.21 but omitted for ε_y in Figure 6.22 because these are similar to one another.

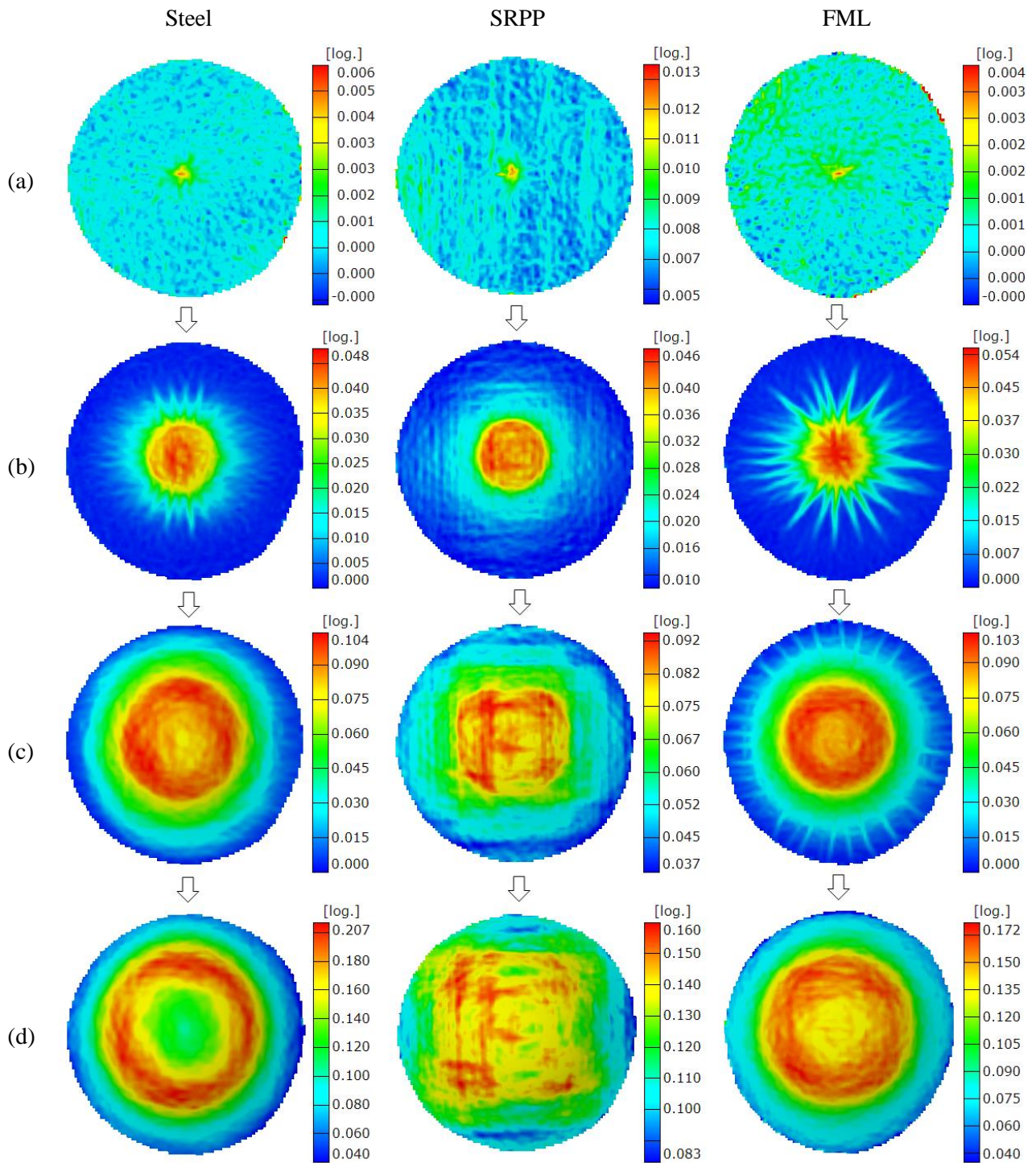


Figure 6.21 Comparison of first principal strains in circular induced-biaxial deformation test specimens for steel (left), SRPP (centre) and SRPP/steel FML (specimen in Figure 6.19a, right), at punch depths of approximately a) 0 – 1 mm, b) 10 mm, c) 20 mm, and d) 30 mm.

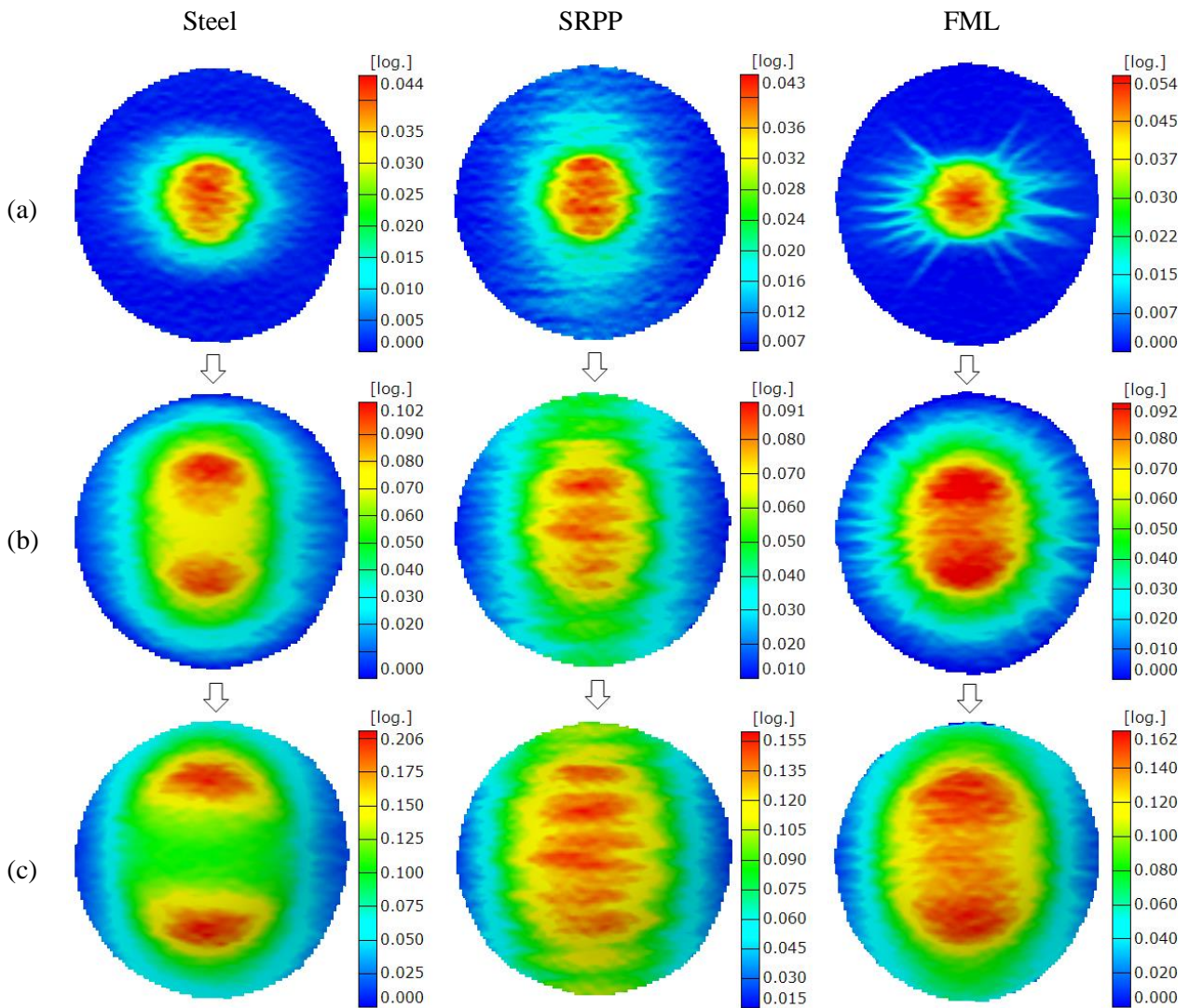


Figure 6.22 Comparison of strain in the y-direction in circular induced-biaxial deformation test specimens for steel (left), SRPP (centre) and SRPP/steel FML (specimen in Figure 6.19a, right), at punch depths of approximately a) 10 mm, b) 20 mm, and c) 30 mm.

First looking at Figures 6.21a and b, it can be seen that the ϵ_{p1} distributions in steel, SRPP and FML specimens are initially similar to each other. In each specimen, strain is concentrated in the centre region and the region spreads outwards with increase in punch depth. There are minor differences such as the undulation in the strain pattern in the SRPP specimen. Based on the previous findings from tensile test experiments, it can be deduced that this is caused by higher strains occurring at boundary cracks in the matrix between the tapes.

Then, the rate of strain growth increases in the side-wall region until strains are higher in the side-wall region, as shown in Figure 6.21c. With further deformation, the degree of strain concentration increases and the region of strain concentration shifts outwards, as shown in Figure 6.21d. During these stages, the strain distribution in SRPP deviate noticeably from that of steel due to the effects of tape

directionality. It changes from being axisymmetric to being just symmetric about x and y axes, and ε_{p1} gets concentrated in four regions that are diagonal to the centre point and the meridian lines. The FML specimen exhibits a strain distribution that is a mixture of steel and SRPP's properties. Its strain distribution is more concentric than SRPP, showing the influence of the steel layer. It also exhibits a slight undulation in the strain pattern, as well as regions of slightly higher strains along the diagonals than along the meridians, which shows the effects of SRPP properties on the FML.

Figure 6.22 shows ε_y distributions. Similar to ε_{p1} , ε_y gets concentrated in the side-wall region in the steel specimen. In comparison, ε_y in the SRPP specimen is concentrated more evenly around the meridian line at the centre and the side-wall regions. Again, FML specimen exhibits a strain distribution that is a combination of the two constitutive materials. Its ε_y distribution is higher in the side-wall regions like steel. However, the level of strain concentration is much lower than in steel because the strain in the centre region is similar to that in the SRPP specimen, which is higher than in the steel specimen.

An FML specimen that fails along the meridians was given as an example in the above figures. FML specimens that fail in the side-wall region (Figure 6.20) exhibit similar strain behaviour until around a punch depth of 27 mm, after which the strain gradually gets more concentrated in a section of the side-wall region. In contrast, the strains in FML specimens that fail along the meridians are much more evenly distributed. This difference is demonstrated in Figure 6.23 in the next page, which shows ε_{p1} in the two types of specimens couple of stages before failure (Figure 6.23a) and just before failure (Figure 6.23b).

In specimens that fail in the side-wall regions, localised necking occurs in the outer steel layer and causes failure. This can be seen from the evolution of strain in the last few stages of deformation before failure, as shown in Figure 6.24 in pages 225–226. ε_{p1} distribution is shown along the left side of the figure from punch depth of 35.7 mm until failure, at increments of 0.1 mm. Along the right side of the figure, ε_{p1} along a horizontal section through the point of maximum ε_{p1} is plotted. Numerous lines in the plots represent ε_{p1} along the section at each stage of deformation captured by the DIC system. Red lines indicate ε_{p1} at the stage corresponding to the strain distribution shown on the left. From this figure, it can be seen that ε_{p1} increases at especially high rates in the last few stages of deformation around the point of maximum ε_{p1} . This is also where the outer steel layer fails.

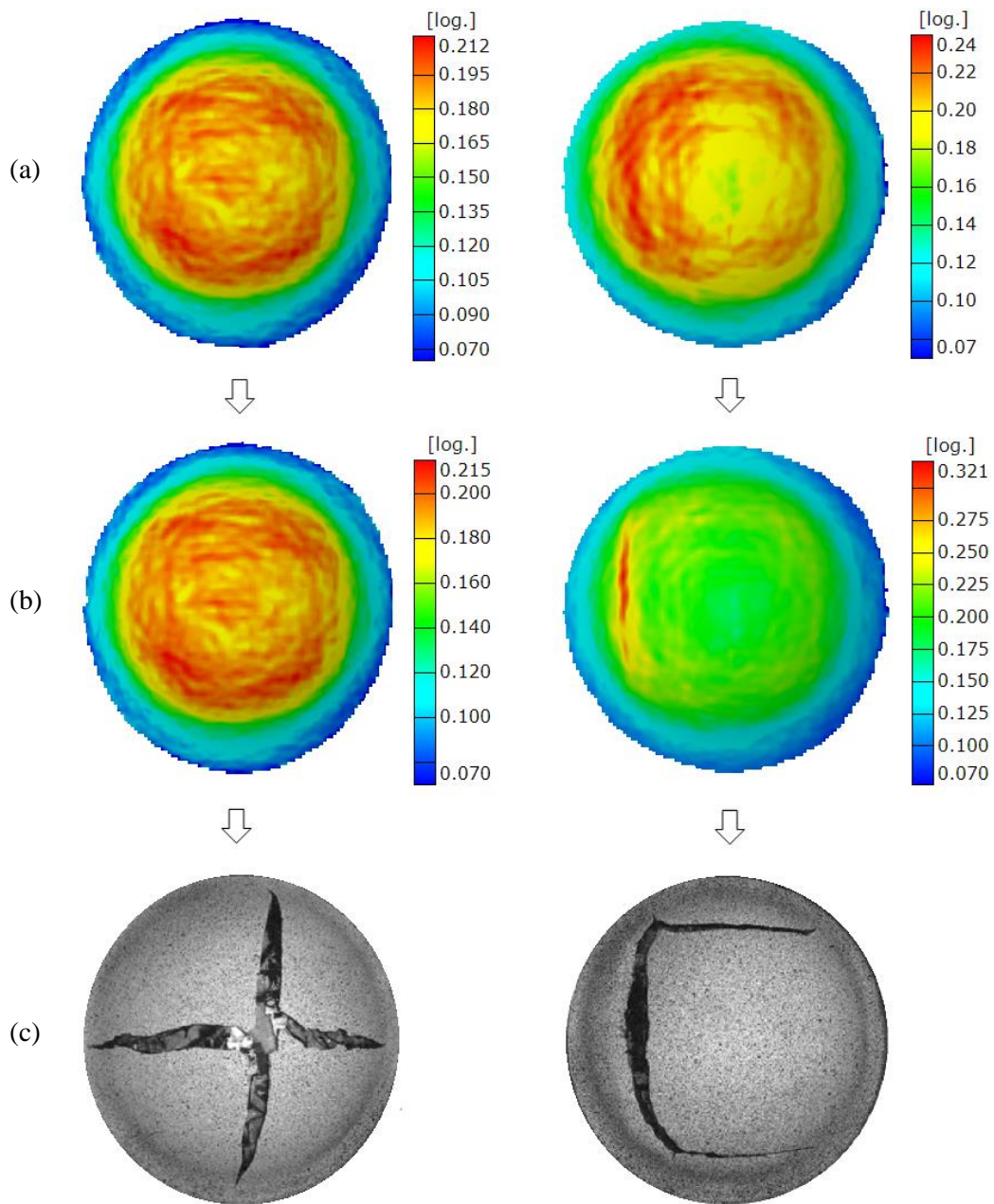


Figure 6.23 First principal strains in circular SRPP/steel FML induced-biaxial deformation test specimens that fail along the meridians (left) and in the side-wall region (right), a) at a punch depth of 35.7 mm and b) just before failure (punch depths of 36.2 mm, 36.0 mm). Digital images of specimens after failure are shown for reference in (c).

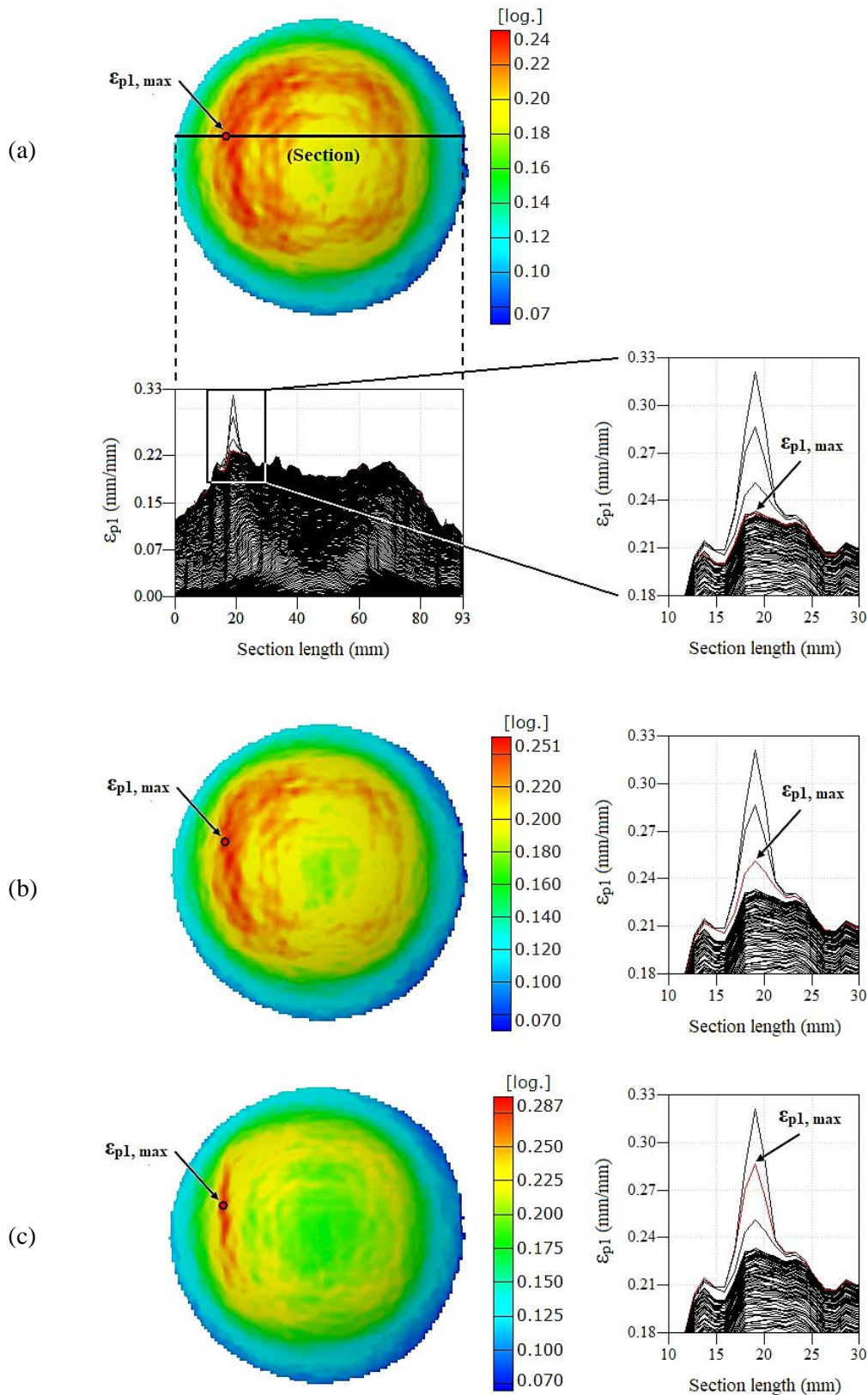


Figure 6.24 First principal strain (ϵ_{p1}) of a circular steel/SRPP FML induced-biaxial deformation test specimen at punch depths of a) 35.7 mm, b) 35.8 mm, c) 35.9 mm, and d) 36.0 mm (last stage before failure). Images on the left depict surface strain distributions. Plots on the right depict strains along a horizontal section through the point of maximum strain ($\epsilon_{p1, \max}$), with red lines indicating strains at the stage corresponding to the left image.

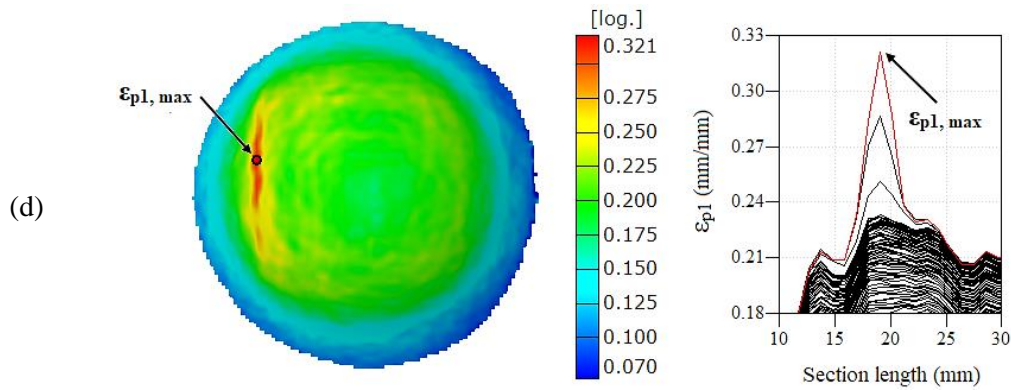


Figure 6.24 First principal strain (ϵ_{p1}) of a circular steel/SRPP FML induced-biaxial deformation test specimen at punch depths of a) 35.7 mm, b) 35.8 mm, c) 35.9 mm, and d) 36.0 mm (last stage before failure). Images on the left depict surface strain distributions. Plots on the right depict strains along a horizontal section through the point of maximum strain ($\epsilon_{p1, \max}$), with red lines indicating strains at the stage corresponding to the left image.

The described behaviour of FML specimens that fail in the side-wall region is very similar to that of plain steel. Steel also fails at the point of maximum ϵ_{p1} in the side-wall region where localised necking occurs, as shown in Figure 6.25. The figure also shows that the failure paths in the steel and FML specimens are similar. In addition, these specimens have the same maximum ϵ_{p1} before failure, which are $32 \pm 3\%$ and $32.2 \pm 0.1\%$ for the steel and FML specimens, respectively.

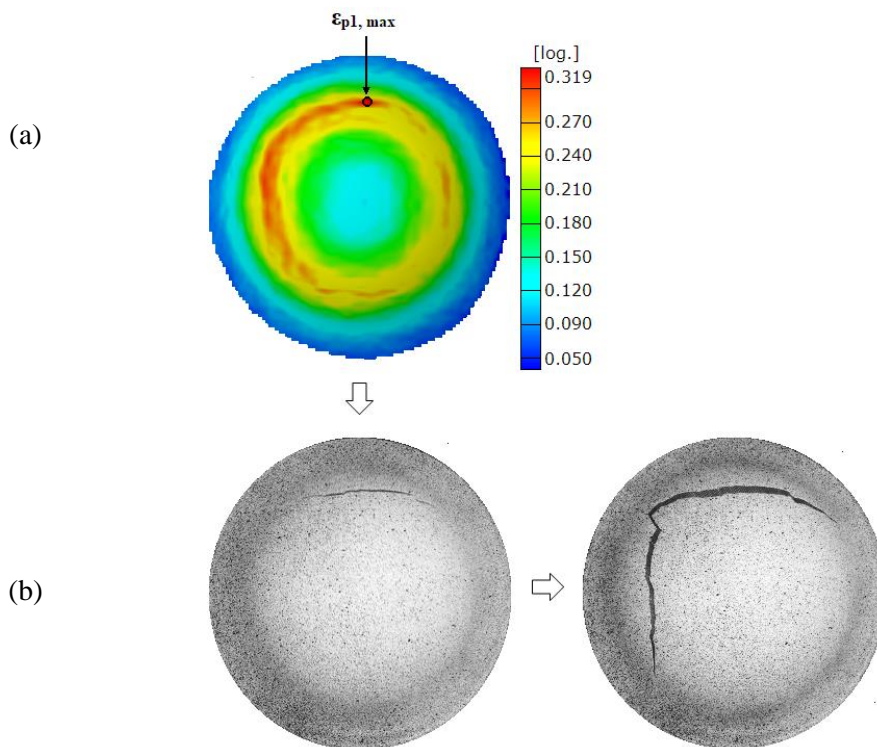


Figure 6.25 Failure in a circular steel induced-biaxial deformation test specimen: a) first principal strain distribution and maximum strain point ($\epsilon_{p1, \max}$) at the last stage before failure, b) tearing (left) and propagation of crack (right) upon failure.

In comparison, the FML specimens that fail along the meridian lines show more similarities to plain SRPP specimens than to plain steel specimens, and they fail abruptly with no sign of localised necking. For example, the maximum ϵ_{p1} is only $22 \pm 1\%$, which is very close to the maximum ϵ_{p1} in plain SRPP specimens ($21 \pm 1\%$) and much lower than the maximum ϵ_{p1} in steel ($32 \pm 3\%$). These FML specimens also exhibit ϵ_x and ϵ_y distributions that are more similar to SRPP specimens than the FML specimens that fail in the side-wall region.

Figures 6.26 and 6.27 summarise more clearly the above similarities of each type of FML specimens to steel and SRPP specimens. These figures show ϵ_{p1} , ϵ_x and ϵ_y distributions in FML specimens that fail along the meridians and in the side-wall region, respectively. Points of maximum ϵ_{p1} , ϵ_x and ϵ_y are also shown, and points where ϵ_x or ϵ_y are larger than 20.0% are indicated with a translucent grey colour in the ϵ_x and ϵ_y distributions. These figures elucidate the crucial difference between the two types of FML specimens that fail in different ways.

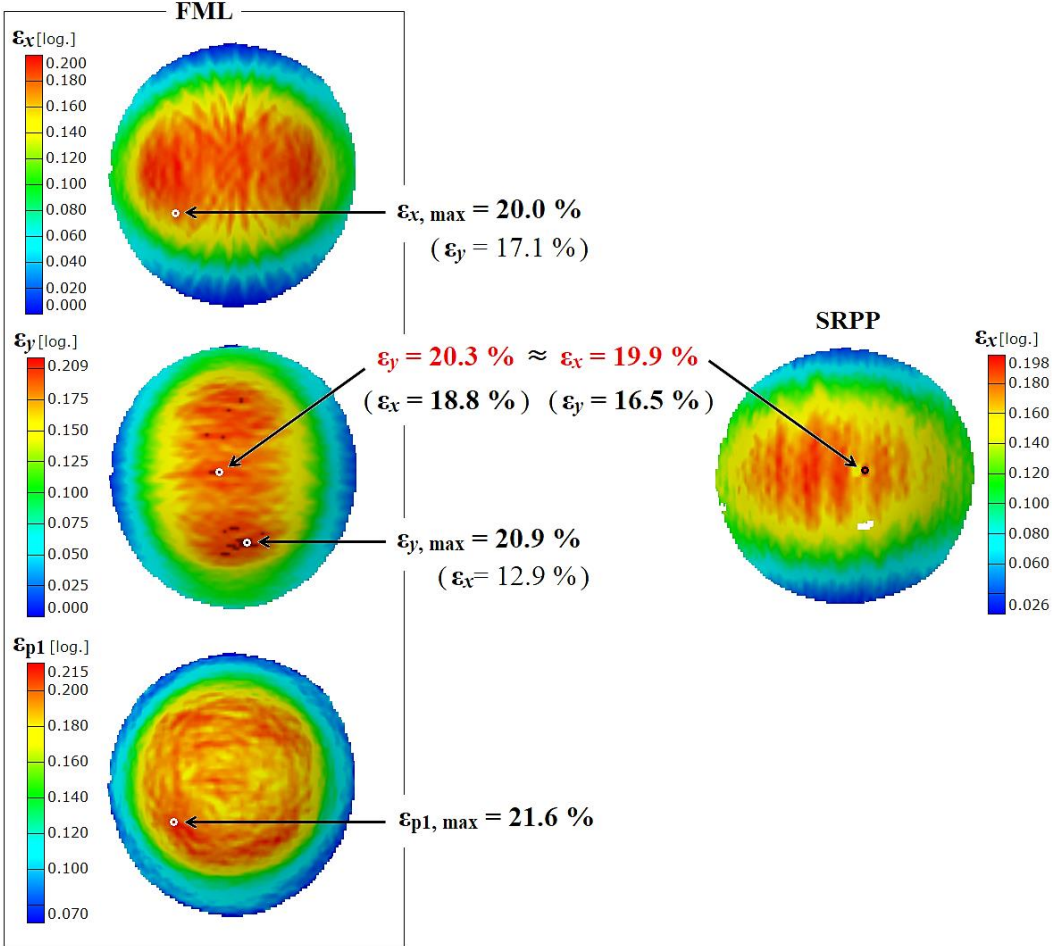


Figure 6.26 First principal strain (ϵ_{p1}) and strains in x and y directions (ϵ_x , ϵ_y) in a circular steel/SRPP FML induced-biaxial deformation test specimen that fails along the meridian lines, at the last stage before failure. Points in ϵ_y distribution that are highlighted in a translucent grey colour represent strains above 20.0%. ϵ_x in an SRPP specimen at the last stage before failure is given for comparison.

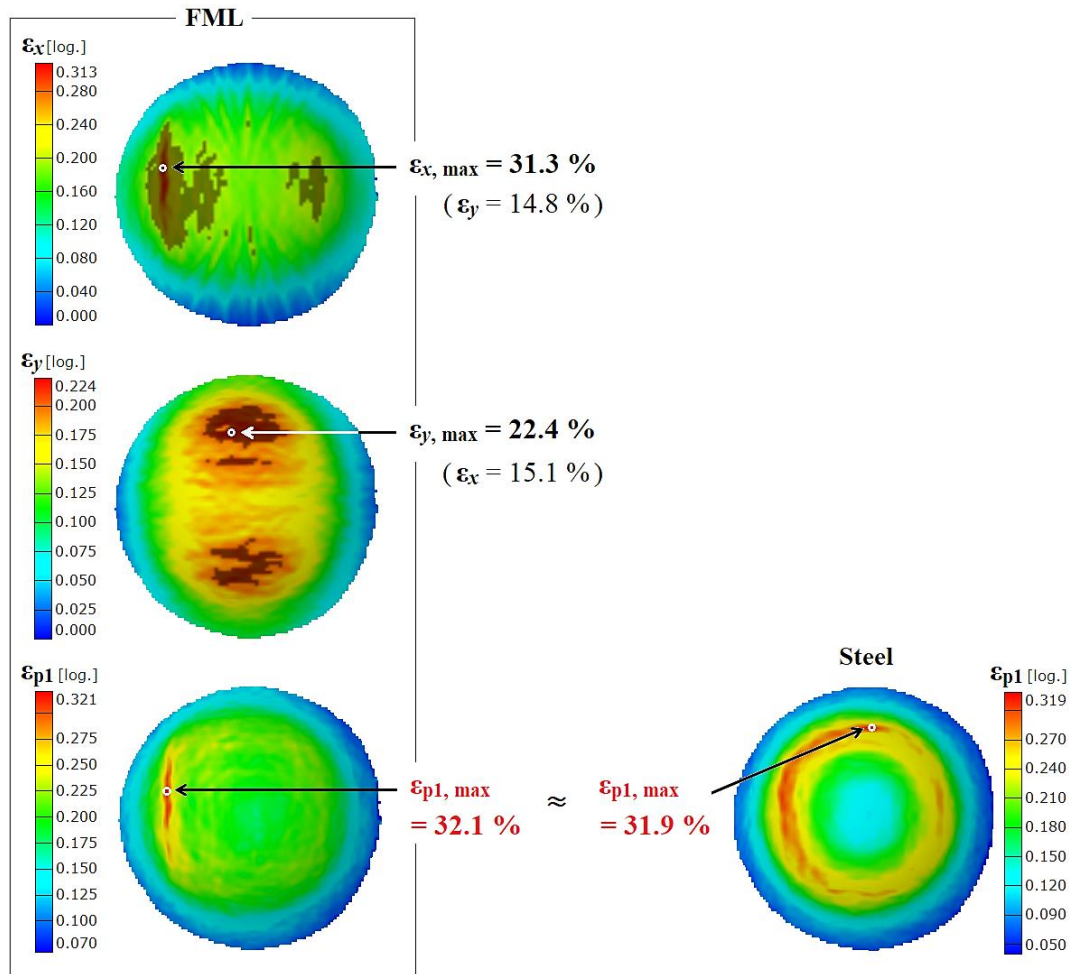


Figure 6.27 First principal strain (ϵ_{p1}) and strains in x and y directions (ϵ_x , ϵ_y) in a circular steel/SRPP FML induced-biaxial deformation test specimen that fails in the side-wall region, at the last stage before failure (left). Points in ϵ_x and ϵ_y distributions that are highlighted in a translucent grey colour represent strains above 20.0%. ϵ_{p1} in a steel specimen at the last stage before failure is given for comparison (right).

In the FML specimen that fails along the meridians (Figure 6.26), ϵ_y at a point near the centre is 20.3%. This is the same level of strain that occurs along the critical fibril pull-outs that cause failure in plain SRPP specimens ($20 \pm 1\%$) that also occur in the centre region. Strain in the transverse direction at this point is 18.8%, which is also very close to the transverse strain at the critical fibril pull-out ($17 \pm 1\%$). To give an example, strain distribution in a plain SRPP specimen is shown in the figure, with ϵ_x and ϵ_y shown at the critical fibril pull-out before failure. (ϵ_x distribution is shown because the fibril pull-out occurs in the x -direction.) Based on this observation, it is likely that a fibril pull-out occurred in the SRPP layer near the centre of the FML specimen and caused failure.

It should be noted that the point near the centre in the FML specimen is not the point of maximum ϵ_x or ϵ_y . Maximum ϵ_x and ϵ_y occur elsewhere, and there are other points where ϵ_y is higher than 20%. However, these points are located in the side-wall region, where the strain in the transverse direction (ϵ_x) is much

lower than 17%. Based on this, it is likely that fibril pull-outs that could cause failure of the SRPP layer did not occur at these points, despite the high level of strain in the direction of tape orientation.

In contrast to the above FML specimen, the FML specimen that fails in the side-wall region exhibits ϵ_x and ϵ_y below 20% in the centre region, as shown in Figure 6.27. Although this FML specimen has a larger number of points where the ϵ_x or ϵ_y is higher than 20%, these points all occur in the side-wall regions. This is a result of strains getting more concentrated in the side-wall regions during the deformation, as in the steel specimens, as opposed to being more evenly distributed around the centre and side-wall regions as seen in the SRPP specimens. This was described previously. Such strain behaviour suggests that critical fibril pull-outs would not have occurred in the SRPP layer of this FML specimen.

From the above observations, it can be conjectured that the FML specimens which failed in the side-wall regions failed from localised necking occurring in the outer steel layer, and that the FML specimens which failed along the meridian lines failed from a critical fibril pull-out occurring in the centre region of the SRPP layer. In the former case, the localised necking would have led to thinning and tearing in the outer steel layer in the side-wall region, causing other layers to fail subsequently. The SRPP layer failed in the direction of tape orientation, as can be seen in Figure 6.28. This is likely to be along the boundary crack, based on previous analyses of failure in SRPP.

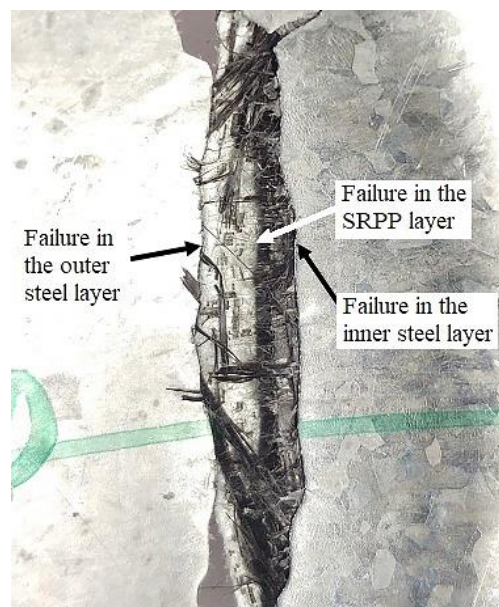


Figure 6.28 Inner surface of a circular steel/SRPP FML induced-biaxial deformation test specimen, showing propagation of failure in the constituent layers.

In the latter case of the FML failing along the meridian lines, the fibril pull-out would have caused failure in the SRPP layer, as abruptly as in plain SRPP specimens. This would have caused both steel

layers to fail abruptly as well, along where the SRPP layer failed. The steel layers would have been intact before the failure initiated in the SRPP layer since no localised necking was observed.

The reason for the failure path of these FML specimens being different that of plain SRPP specimens is probably due to the adhesion between the steel and SRPP layers. As was explained earlier, the reason SRPP specimens fail in the diagonal directions is likely due to the unloading of fractured tapes in the reinforcing direction (Section 6.2.1). In the FML specimen, the unloading of tapes is likely hindered due to the adhesion to the steel layers. Therefore, the fracture of a tape leads to a fracture in the neighbouring tape at the weak point in the material, which is along the boundary between the tapes that are transverse to the fracturing tapes. This would cause the fracture to propagate in the direction of tape orientations, along the meridian lines.

The reason the FML specimens can fail in two different ways is not certain. One might think this is due to the quality of adhesion between the steel and SRPP layers being stronger or poorer in some specimens. However, this seems unlikely considering that failure in each of the constitutive layers occurred within very close proximity of each other. Instead, it may be that there is an effect of material imperfection on the deformation and failure behaviour, similar to how the different failure behaviours of SRPP specimens were conjectured to be caused by the difference in the consolidation quality. For example, it may be that damage occurred in the side-wall region of the SRPP layer of an FML specimen, which then caused the development of higher strains in the region, and eventually the localised necking in the steel layer.

An ideal FML specimen modelled using finite element analysis (FEA) can give an estimate of when the hypothetical material imperfections would have caused deviation in the behaviour of the two FML specimens. To do this, the moment when the strain behaviour of the actual FML specimens starts to deviate from that of the ideal FML simulated with FEA should be observed. To demonstrate, Figure 6.29¹⁵ has been given, where the images show ϵ_{p1} distribution in an FML specimen that failed along the meridians from the SRPP layer (left), in an FML specimen that failed in the side-wall region from the outer steel layer (centre), and in an FML specimen simulated with FEA (right), at different stages of deformation up until failure.

¹⁵ Images for FML simulated using finite element analysis were produced using the method outlined in Appendix C.

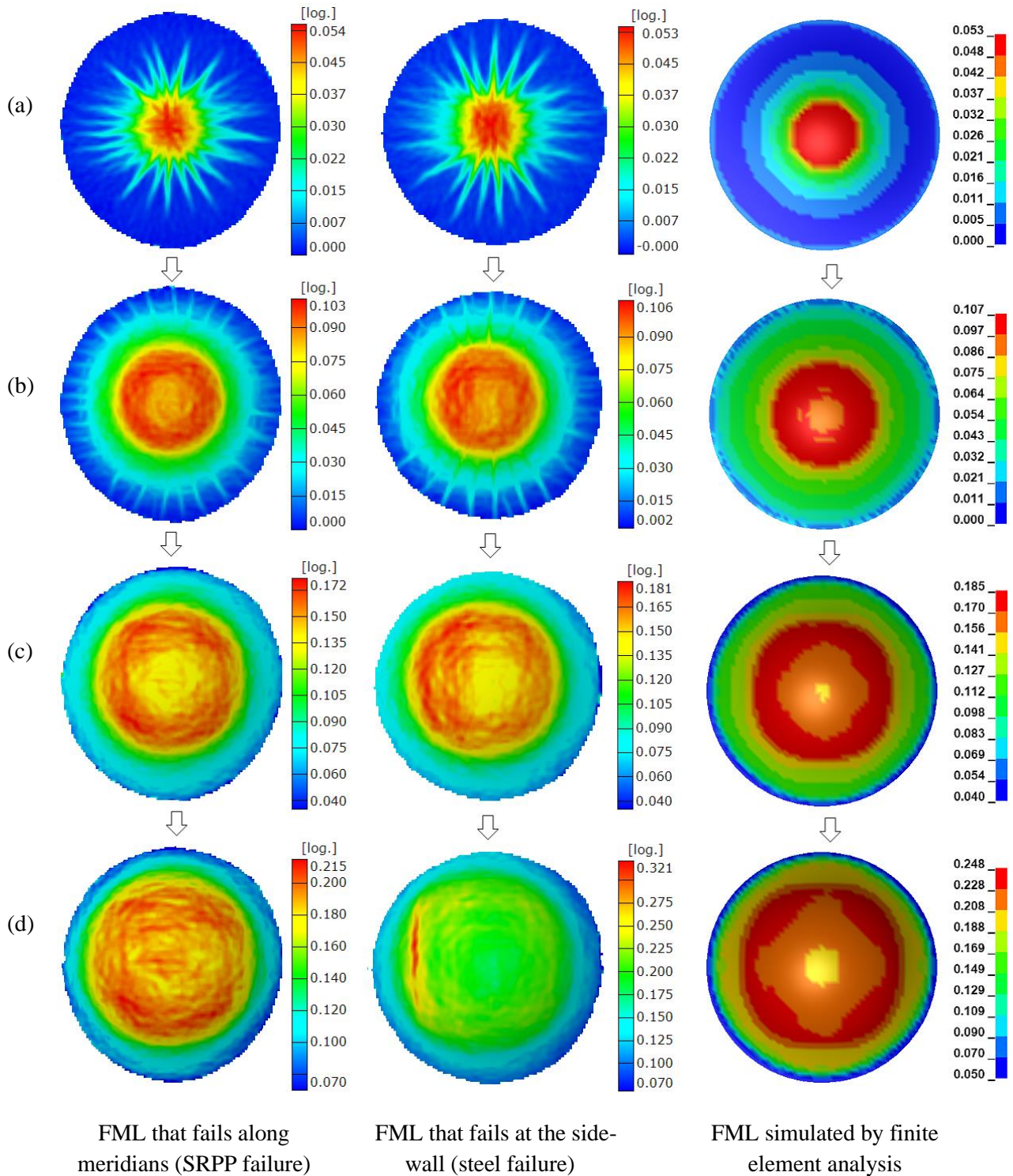


Figure 6.29 Comparison of first principal strain in circular steel/SRPP FML induced-biaxial deformation test specimens that fail at the side-wall (left) and along the meridians (right), and in FML specimen simulated using finite element analysis (right), at punch depths of approximately a) 10 mm, b) 20 mm, c) 30 mm, and d) 35 mm (close to failure).

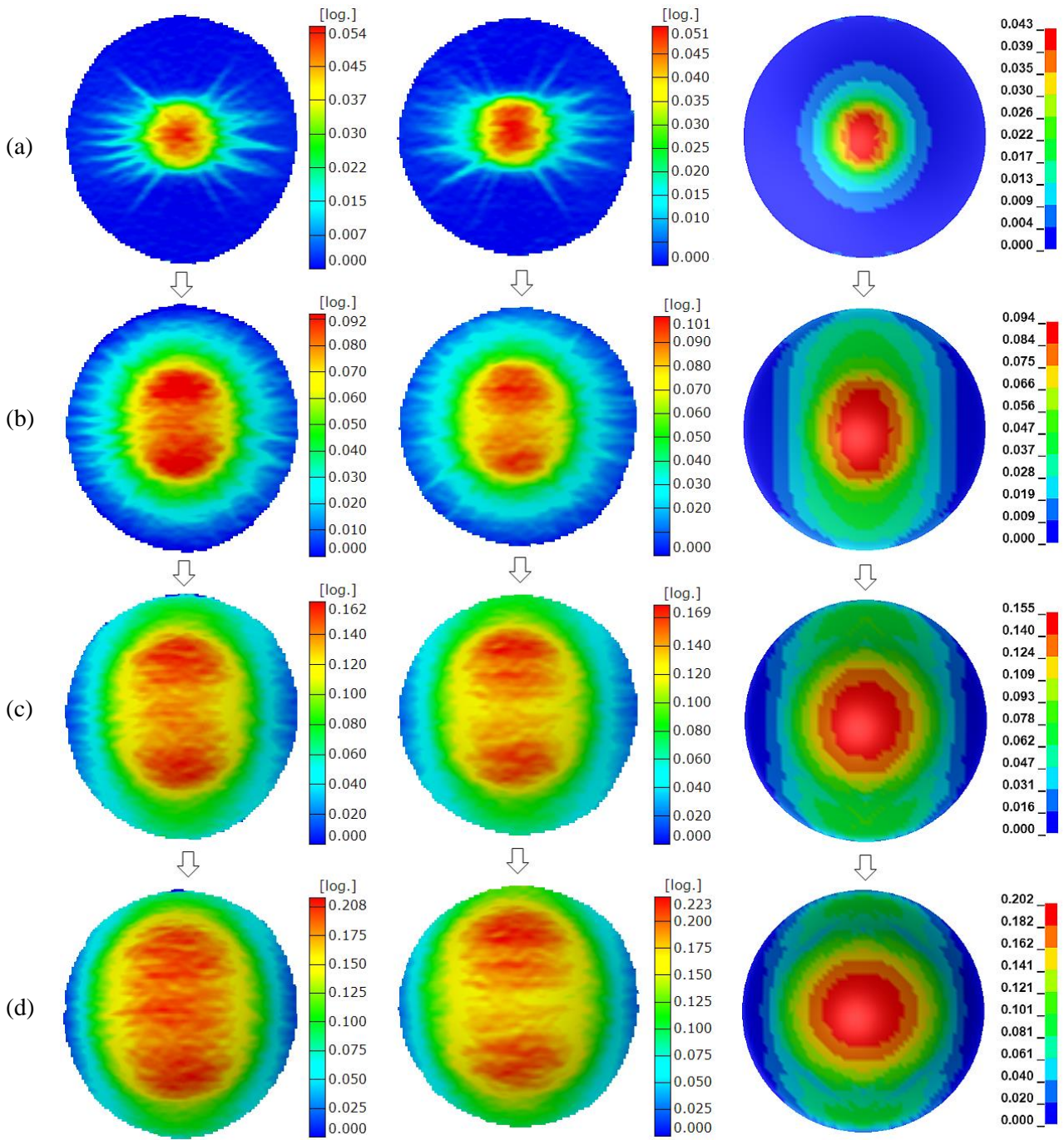
Comparing the FML specimens in Figure 6.29d, it can be seen that the ideal FML (shown on the right) does not reflect the localised necking in the steel layer, which occurs in the actual FML specimen that is shown in the centre column. This is because the model has been developed assuming a perfect material without any material imperfection. In order to model localised necking, an instability such as geometric imperfection has to be introduced into the model.

Similarly, the ideal FML specimen also differs to the actual FML specimen that fails from the SRPP layer (left column of Figure 6.29d). The strain at the centre is lower in the ideal FML than in the actual FML specimen. This may be related to the fact that in the actual FML specimen, a fibril fracture, and probably a pull-out, would have occurred before failure (at the stage shown in Figure 6.29d) and caused the strain to increase at the centre. Then, the higher strain at the centre of the actual FML specimen depicts the development of damage that caused instability in the specimen, which would not occur in an ideal FML specimen without any material imperfection. The distributions of ϵ_{p1} of the actual FML specimens in the left and centre columns of Figure 6.29 deviate from the ideal FML from around punch depths of 31 mm and 27 mm, respectively.

Similar deviations occur in ϵ_y distributions, shown in Figure 6.30 in the next page. There are two stages at which ϵ_y distributions in FML specimens deviate from each other. The first deviation occurs at a punch depth of around of 10 mm, where the ϵ_y in the side-wall regions of the actual FML specimens become higher than at the centre, whereas ϵ_y remains higher at the centre in an ideal FML. The second deviation occurs at a punch depth of around 31 mm, where the FML specimen in the left column exhibits an increase in ϵ_y at the centre until the strains become more evenly distributed in the centre and side-wall regions. Although the reason for the first deviation is unclear, the second deviation is probably due to a fibril fracturing at the centre and starting to pull out.

Putting the above observations together, it can be seen that the strain behaviour of the FML specimen which fails from the SRPP layer (left columns in Figures 6.29 and 6.30) starts to deviate from the ideal or perfect FML from a punch depth of around 31 mm. This would be due to initiation of fibril pull-outs in the centre region of the SRPP layer.

For the FML that fails from localised necking in the steel layer (centre columns in Figures 6.29 and 6.30), the strain behaviour starts to deviate from the ideal FML from a punch depth of around 27 mm. Strain starts to get concentrated in a part of the side-wall region where localised necking occurs later. Although the reason is not clear, it can be hypothesised that the higher strains develop in the region due to the occurrence of fibril pull-outs or other damage in the SRPP layer in this region. It is also possible that microscopic damage occurred in the steel layer (e.g. at the grain boundary) but this seems less likely, given that SRPP has been shown to exhibit a great deal of sizeable damage from very early stages of deformation.



FML that fails along meridians (SRPP fails first)

FML that fails at the side-wall (steel fails first)

FML simulated by finite element analysis

Figure 6.30 Comparison of strain in the y-direction in circular steel/SRPP FML induced-biaxial deformation test specimens that fail at the side-wall (left) and along the meridians (right), and in FML specimen simulated using finite element analysis (right), at punch depths of approximately a) 10 mm, b) 20 mm, c) 30 mm, and d) 35 mm (close to failure).

Based on the hypotheses proposed earlier, non-critical damage may develop relatively early in the deformation process and then later cause critical damage to develop, and this manifests in the surface strain behaviour of the FML. It can be noticed from the ϵ_{p1} and ϵ_y in the ideal FML at the last stage before failure (in Figures 6.29d and 6.30d) that its maximum ϵ_{p1} (24.8%) is very close to the ϵ_{p1} value that triggers localised necking in steel (24%), and that its maximum ϵ_y (20.2%) is very close to the ϵ_y value that causes critical fibril pull-outs in SRPP (20%). Hence, the FML is sensitive to small deviations in these maximum strain values, which would explain why the material system can fail from failure of either the SRPP or the outer steel layers. The small deviations in strain values may occur depending on the locations of possible damage in the SRPP layer, which are not critical in and of themselves, but can affect how the critical damage develops. The occurrence of such non-critical damage might depend on the consolidation quality, or simply on the random material imperfections inherent in the material.

In summary, Section 6.2 investigated the behaviour of SRPP and SRPP/steel FML when subjected to in-plane biaxial deformation and out-of-plane bending. It was demonstrated, once again, that surface strains can be used to detect and analyse the critical damage that leads to the failure of the specimen. It was found that the critical type of damage in circular SRPP IBD test specimens is fibril pull-out in the centre region of the specimen, in the outermost layer. Analyses showed that this occurs from a combination of micro-damage and fracture of fibrils due to the positive strain in the reinforcing direction. It was also found that specimens can exhibit different amounts of fibril pull-outs before failure, likely depending on the quality of consolidation.

An interesting phenomenon was observed for FML specimens, where failure could occur either along the meridian lines or in the side-wall region. This was found to be due to the failure occurring from the SRPP layer in the former case and from the outer steel layer in the latter case. The reason failure can occur from failure of either the SRPP or the steel layer is possibly due to non-critical damage occurring in the SRPP layer at different locations, which affects how the critical damage occurs later on. The occurrence (or not) of non-critical damage may depend on the consolidation quality in the SRPP layer, or on random occurrences of material imperfections. It was also found in this study that the layer that causes failure in the specimen fails in similar ways, and at similar strains, to the failure of the material when tested by itself (plain steel or plain SRPP). Due to this, surface strains could be used to indicate which layer caused failure in the FML specimen.

6.3 Deformation and failure behaviour of hourglass specimens

This section discusses the behaviour of SRPP and SRPP/steel FML hourglass IBD specimens, which are shaped like an hourglass, with tapes oriented at $\pm 45^\circ$ to the axis of symmetry (y -axis). They are fixed around the convex edges and punched with a semi-hemispherical punch, which produces a combination of positive strains along the specimen length, negative strains across the width, as well as in-plane shear strains in relation to tape orientations and out-of-plane bending. This section is relatively brief because the specimens behave in similar ways to $\pm 45^\circ$ tensile test specimens in many respects.

The first subsection explains the behaviour of SRPP specimens. Due to the similarity to the off-axis tensile test specimens, the IBD tests could confirm the findings from the previous chapter on the material behaviour when subjected to large in-plane shear deformations; failure in the SRPP occurs from the propagation of boundary cracks into local delaminations, which cause tape pull-outs to occur from the free edges, which then leads to specimen failure. The section will also highlight that maximum surface strain points can be used identify where the critical tape pull-out, and therefore failure, occurs.

The second subsection discusses the behaviour of FML specimens. It was found, through the IBD test, that the FML's strain behaviour under this type of deformation is more heavily influenced by the behaviour of the steel layers. This applies to the strain distribution during deformation, as well as the fact that failure occurs from localised necking in the outer steel layer, at the same limiting strain. The difference in behaviour as compared to that of the plain SRPP specimens arises from the different proportion of in-plane shear strains contributing to the overall strain of the specimen. This section will demonstrate that analysis of strains in constituent materials can lead to conclusions on how failure initiates in the FML.

6.3.1 SRPP

SRPP hourglass IBD test specimens fail in the narrow section at the centre, with similar damage characteristics as $1.0 \text{ mm } \pm 45^\circ$ tensile test specimens. The similarity arises due to a large γ_{12} in the specimen, which is shown in Figure 6.31a. A difference with regard to the tensile specimens is that damage is concentrated in the narrow section in the middle, as shown in Figure 6.32, in contrast to the tensile test specimens, in which the damage occurred evenly throughout the gauge section. This difference is due to larger strains occurring in the narrow section of the IBD test specimens, as can be seen by γ_{12} , ε_{p1} and ε_{p2} strain distributions shown in Figures 6.31a–c.

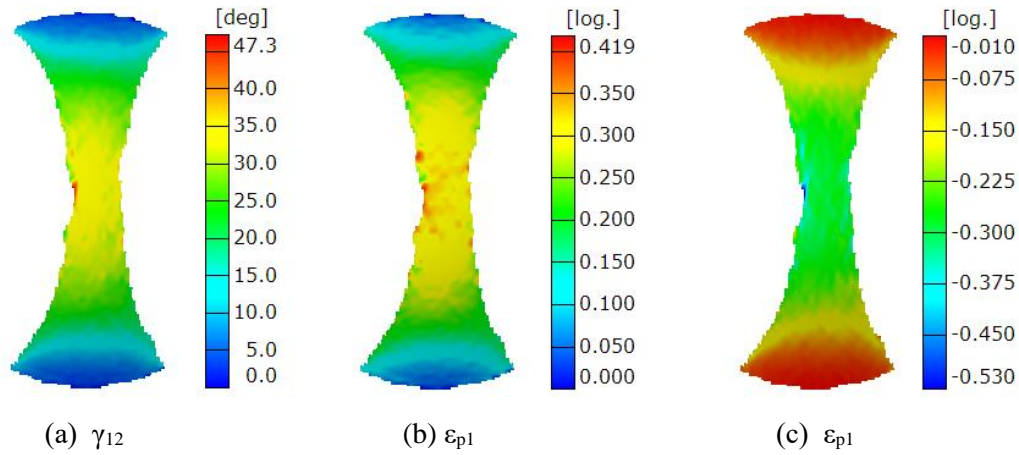


Figure 6.31 a) Shear angle about tape orientations (γ_{12}), b) first principal strain (ϵ_{p1}), and c) second principal strain (ϵ_{p2}) in an SRPP hourglass induced-biaxial deformation test specimen before failure.

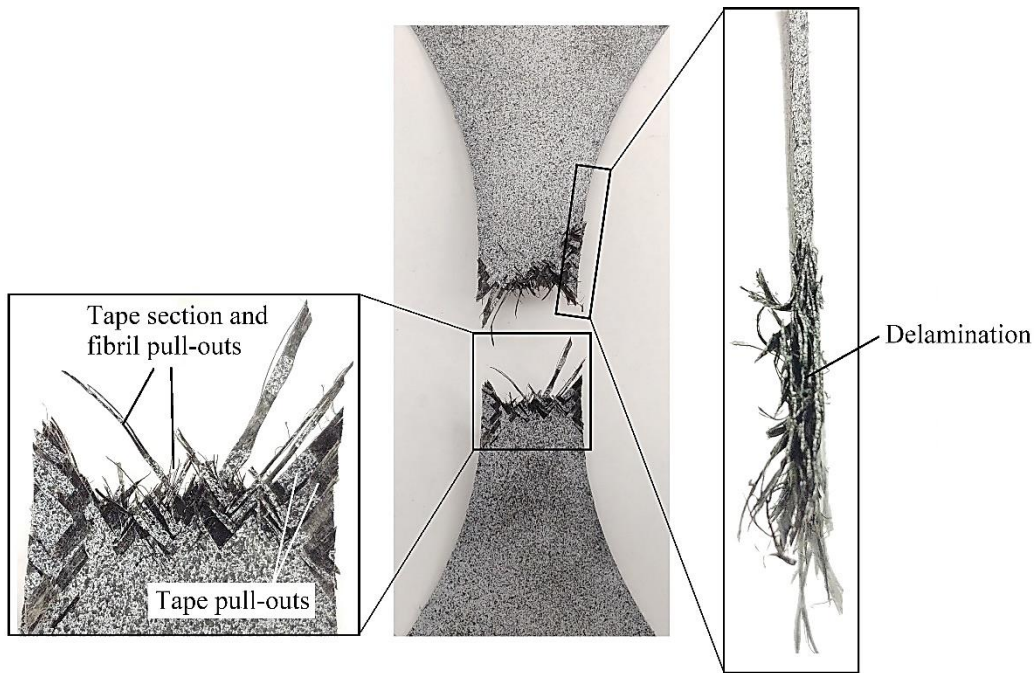


Figure 6.32 Damage in an SRPP hourglass induced-biaxial deformation test specimen shown after failure.

It is likely that failure initiates in the outer layer of the SRPP due to the bending causing higher strain in the outermost surface. This allows the development of critical damage to be observed more easily than in tensile test specimens. By examining the high-resolution digital images at a high frame rate of 15 frames per second, it can be seen that the progression of the critical damage is also very similar to that observed in the $1.0 \text{ mm} \pm 45^\circ$ tensile test specimens. An example of the development of critical damage in a specimen is shown in Figure 6.33, with an image of the surface on the left and the corresponding ϵ_{p1} on the right.

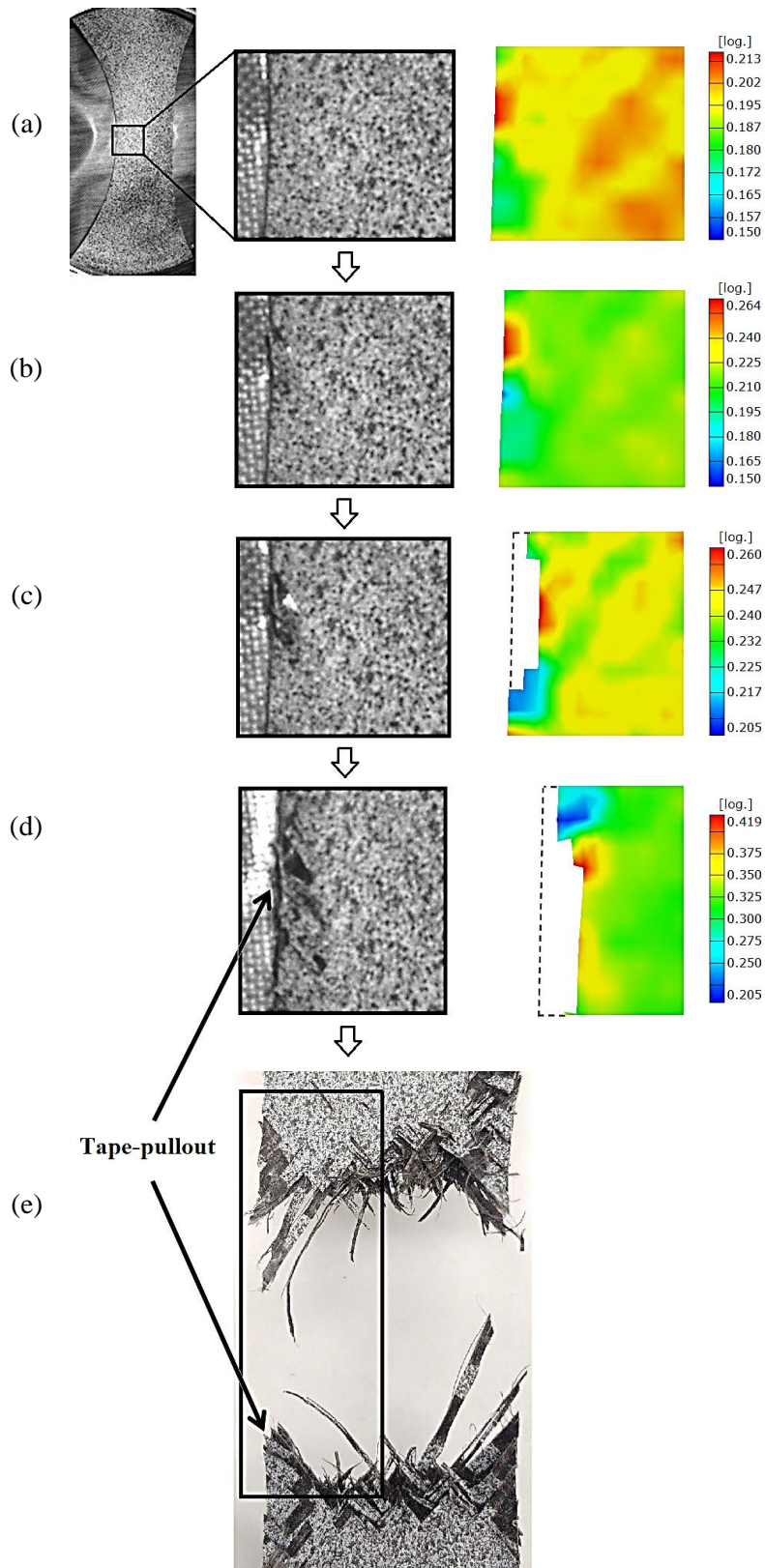


Figure 6.33 Development of a critical tape pull-out in an SRPP hourglass induced-biaxial deformation test specimen at punch depths of a) 22.5 mm, b) 24.4 mm, c) 26.8 mm, d) 34.3 mm (last stage before failure), and e) after failure. Photographs are shown on the left and ϵ_{p1} are shown on the right. The dotted lines indicate areas where the strain cannot be computed.

Failure in an SRPP hourglass IBD test specimen occurs as a result of micro-damage causing a tape pull-out at an edge in the narrow section. This can be seen in the images on the left in Figure 6.33. The critical damage initiates with the widening of a boundary crack at the edge. (This is visible at a higher magnification than can be shown in Figure 6.33.) The crack then propagates into a local delamination of the surface tape (Figure 6.33b). The local delamination joins with another boundary crack on the other side of the tape, causing the tape to pull out (Figure 6.33c). The tape pull-out is initially short as it is arrested at the weave boundary. With further deformation, the micro-damage, and hence the pull-out, propagates out to the surrounding areas (Figure 6.33d). Finally, failure occurs across a section through the point of the tape pull-out, as shown in Figure 6.33e. Similar damage also appears elsewhere, along both edges.

The maximum strain point can reflect the location and development of the critical damage. The maximum ϵ_{p1} of the specimen occurs at the point of the tape pull-out, as shown by the images on the right side in Figure 6.33. This occurs before the boundary crack becomes noticeable from the digital images (Figure 6.33a), which means that the strain concentration reflects the location of the boundary crack as it grows at a microscopic scale. When the tape pull-out occurs, strains become incomputable due to the scale of the damage being larger than the specified precision of the experiment (Figures 6.33c and d). However, the maximum ϵ_{p1} appears right beside the pull-out in the computable part. Therefore, the maximum strain point can indicate the approximate location of the largest damage that occurs in the specimen, which then causes the failure of the specimen (Figure 6.33e). The maximum ϵ_{p1} point is given as an example, but this is also the point of maximum γ_{12} and ϵ_{p2} (in magnitude), as was shown in Figure 6.31.

As can be seen from the above, the cause and process of failure in an SRPP hourglass IBD test specimen is quite similar to that of a $1.0 \text{ mm} \pm 45^\circ$ tensile test specimen. There are some differences, however, such as that fact that the failure occurs sooner in the IBD test specimens after tape pull-outs occur because strains are higher in the outer layer in the narrow section of the specimen, due to the hourglass shape of the specimen, creating higher internal forces in this section. However, the fundamental failure behaviour is the same between the hourglass IBD test specimens and the off-axis tensile test specimens.

6.3.2 FML

FML hourglass IBD test specimens fail with damage characteristics that are similar to FML $\pm 45^\circ$ tensile test specimens, as shown in Figure 6.34. The SRPP layer fails with the same types of damage that occur in the plain SRPP IBD test specimens and the steel layers fracture at angles of around $\pm 57 \pm 4^{16}$, close to the typical fracture angles of plain steel (57°). Failure occurs across the narrow, middle section, where the damage is concentrated, in a similar way to that seen in the plain SRPP IBD test specimens.

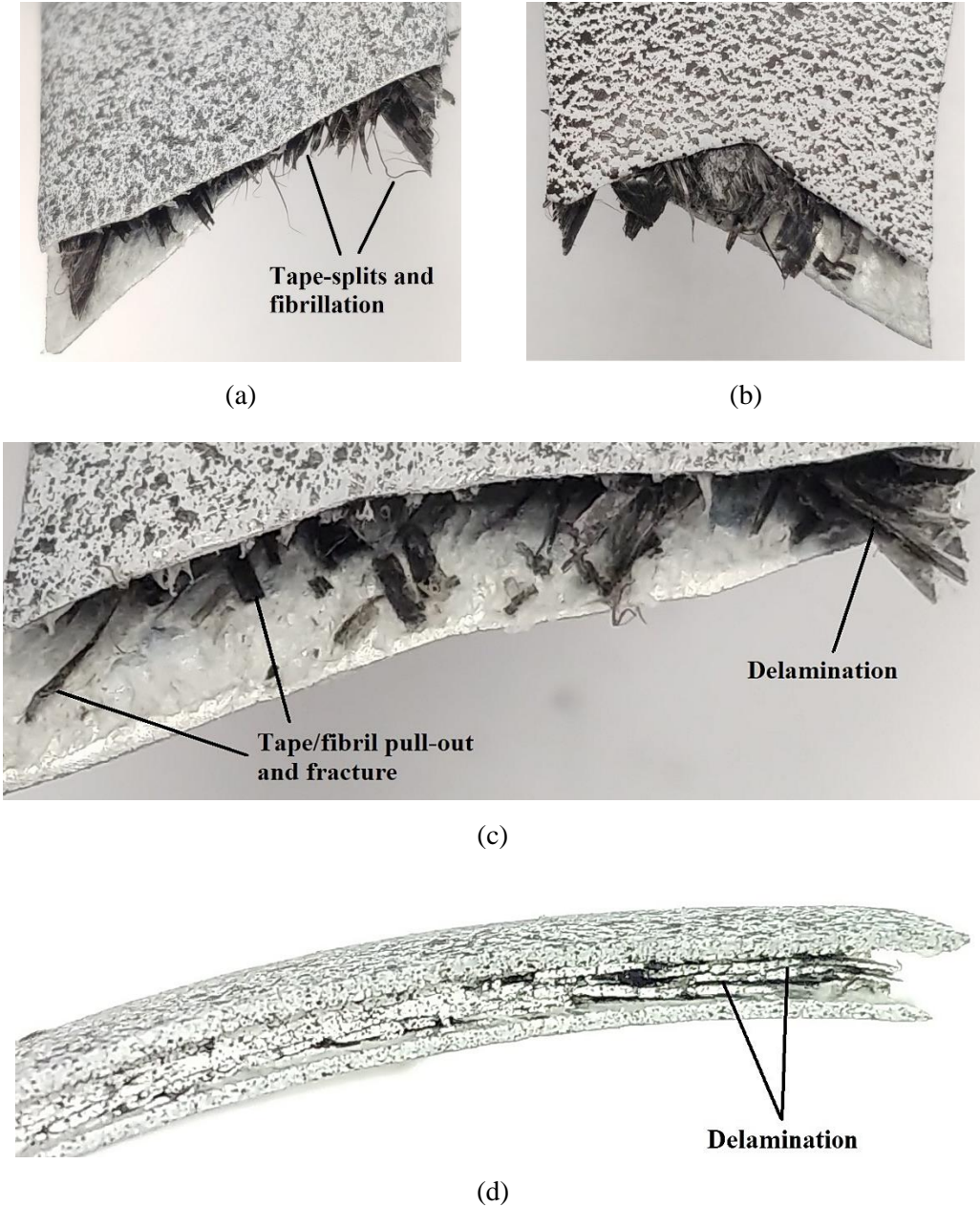


Figure 6.34 Damage in SRPP/steel FML hourglass induced-biaxial deformation test specimens shown after failure.

¹⁶ $\pm 4^\circ$ is sample standard deviation.

Failure in FML hourglass IBD test specimens is triggered by the failure of the outer steel layer. To show this, strain analysis is required because it is difficult to see where failure initiated from through purely visual inspection. It is clear that failure does not initiate in the inner steel layer since its internal stress would be lower than in the outer steel layer due to bending. As such, one specimen, shown in Figure 6.35, failed in the outer steel and SRPP layers only. However, the outer steel and SRPP layers fail simultaneously in all specimens when the maximum load is reached.

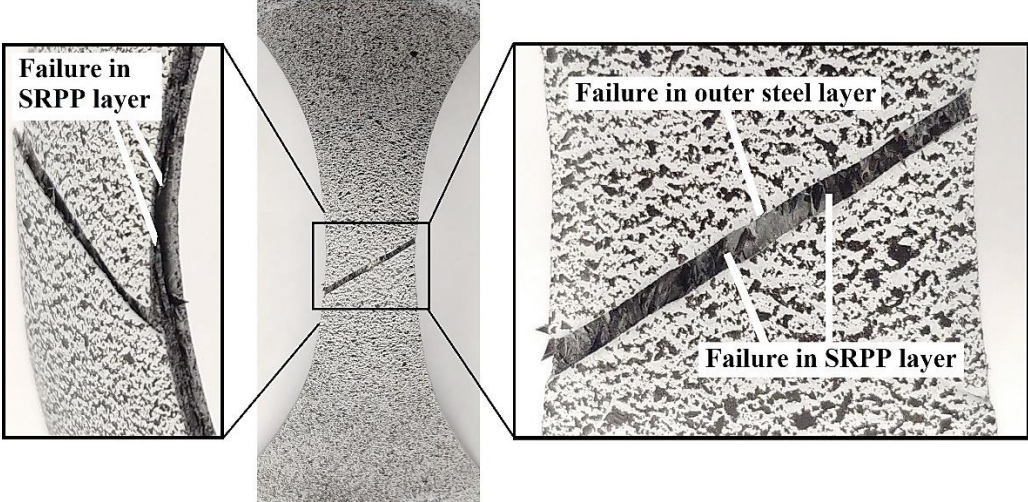


Figure 6.35 Failure in the outer steel and SRPP layers in an SRPP/steel FML hourglass induced-biaxial deformation test specimen.

The strain behaviour of FML specimens is more significantly influenced by the material behaviour of the steel layers than the SRPP layer, despite their respective total thicknesses being similar. This can be seen from comparison of ϵ_{p1} distributions at the same depths, as shown in Figure 6.36 in the next page. Steel and FML specimens exhibit more concentrated strains in the middle section and steeper strain gradients than seen in the SRPP. In addition, steel and FML exhibit similar maximum ϵ_{p1} values, whereas the maximum ϵ_{p1} in SRPP is only about 76–77% of maximum ϵ_{p1} in steel and FML at around a punch depth of 30 mm.

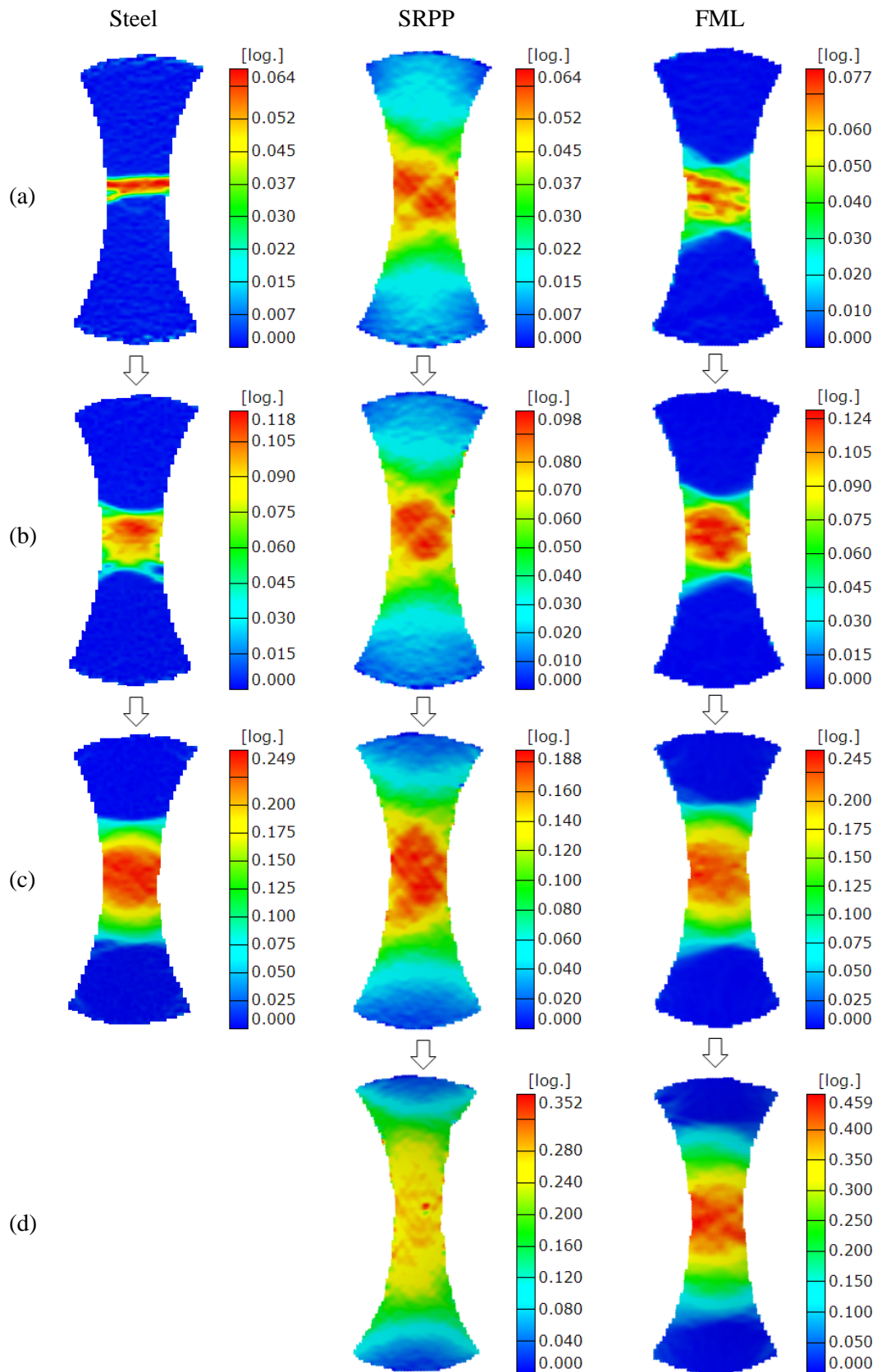


Figure 6.36 Comparison of first principal strains in steel (left), SRPP (centre) and SRPP/steel FML (right) hourglass induced-biaxial deformation test specimens, at punch depths of approximately a) 0 – 1 mm, b) 10 mm, c) 20 mm, and d) 30 mm, except for the steel specimen at a punch depth of around 30 mm.

The similarity between FML and steel specimens, and their dissimilarity to SRPP specimens, can also be seen from their strain paths. Figure 6.37 shows a plot of ϵ_{p1} against ϵ_{p2} for maximum ϵ_{p1} point and average strain in centre region, for each specimen. This shows that strain ratios (β) for steel and FML in the middle sections are approximately -0.36 and -0.42, which is closer to uniaxial tensile deformation mode ($\beta = -0.5$), whereas the β in SRPP is approximately -1.3 for the average strain, which is closer to pure shear mode of deformation ($\beta = -1$).

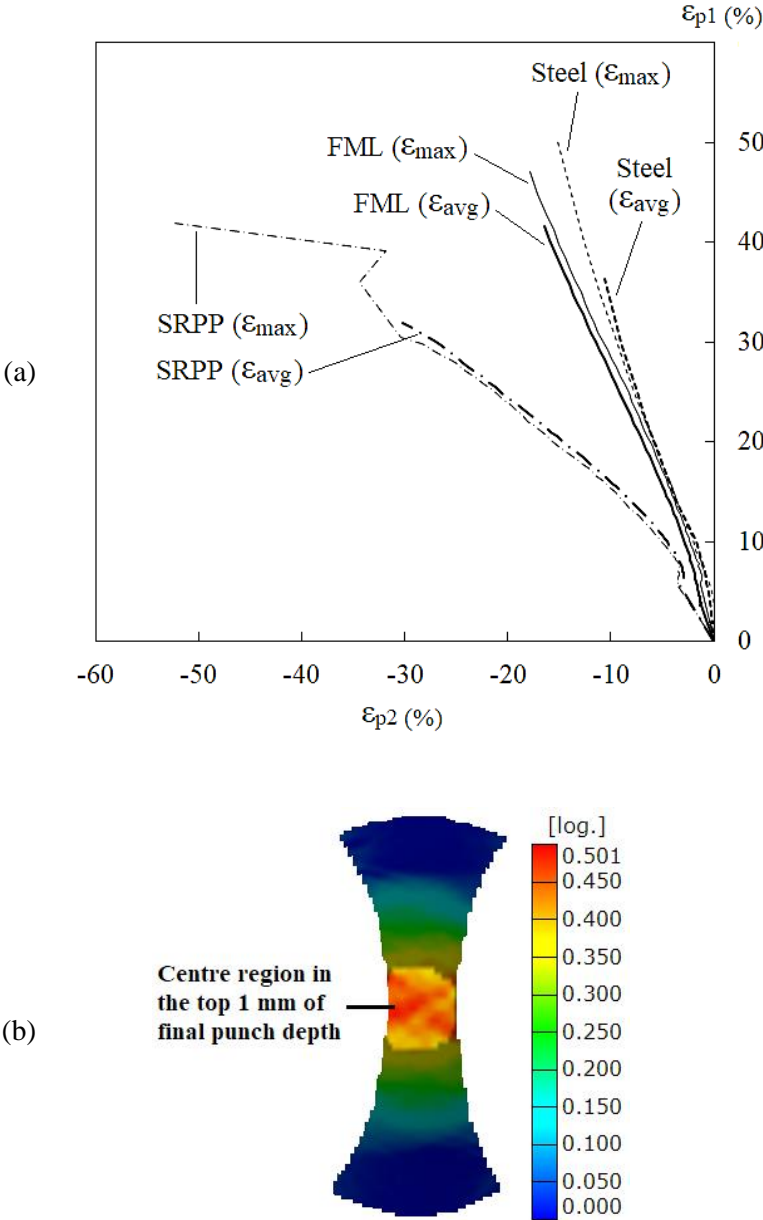


Figure 6.37 a) Comparison of strain paths in steel, SRPP and SRPP/steel FML hourglass induced-biaxial deformation test specimens, in a plot of first principal strain (ϵ_{p1}) against second principal strain (ϵ_{p2}). For each material, the maximum ϵ_{p1} point (ϵ_{max}) and the average strain in the centre region (ϵ_{avg}) are given, where the centre region is the top 1 mm of the final punch depth (example given in b).

The discrepancy in the deformation modes of SRPP and FML specimens is caused due to a larger *proportion* of overall deformation occurring by means of γ_{12} in the SRPP specimens than in the FML specimens. In both SRPP and FML specimens, γ_{12} has a significant effect on the deformation, as can be seen from the fact that their γ_{12} distributions (Figure 6.38, pp. 243–244) are similar to their respective ε_{p1} distributions (Figure 6.36, p. 241). Yet, the magnitudes of average and maximum ε_{p1} are much higher in FML than in SRPP, whereas the average and maximum γ_{12} are somewhat similar between the two materials, as shown in Figure 6.39. SRPP therefore has a higher proportion of its deformation occurring by means of in-plane shear deformation about the tape orientations. Due to this, the deformation mode (β) is close to uniaxial tension mode in FML and pure shear mode in SRPP in the centre regions.

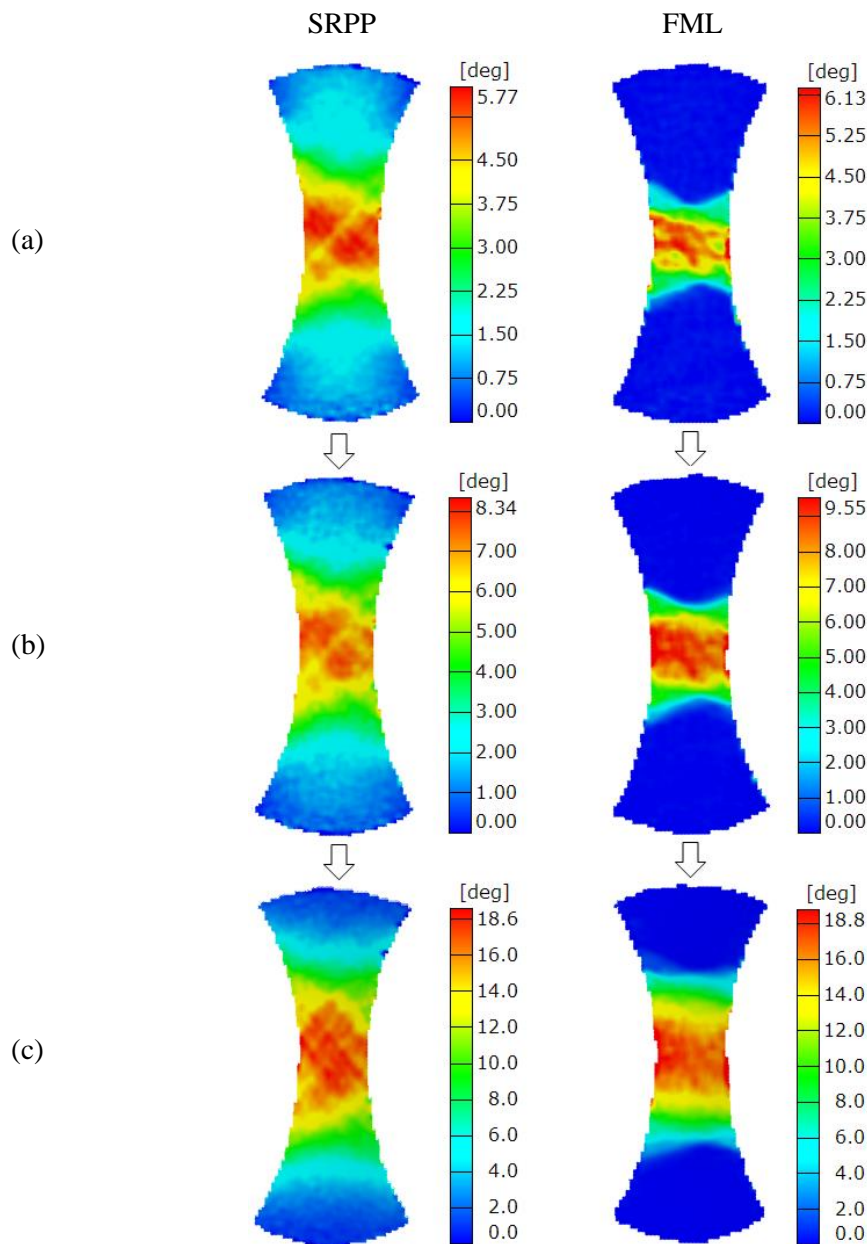


Figure 6.38 Comparison of shear angles in SRPP (left) and SRPP/steel FML (right) hourglass induced-biaxial deformation test specimens in Figure 6.36, at punch depths of approximately a) 0 – 1 mm, b) 10 mm, c) 20 mm, and d) 30 mm.

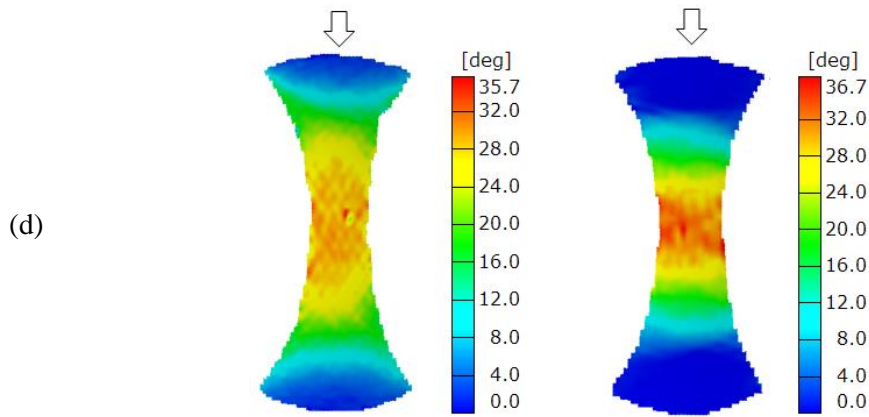


Figure 6.38 Comparison of shear angles in SRPP (left) and SRPP/steel FML (right) hourglass induced-biaxial deformation test specimens in Figure 6.36, at punch depths of approximately a) 0 – 1 mm, b) 10 mm, c) 20 mm, and d) 30 mm.

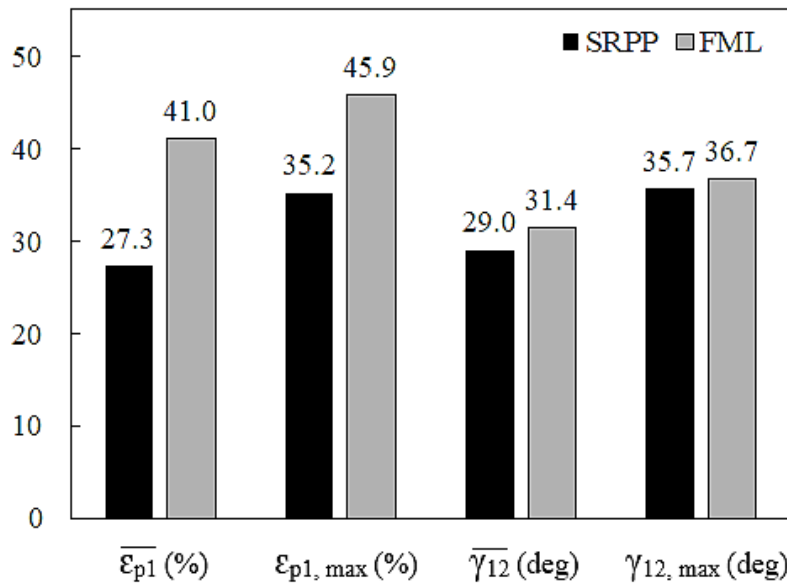


Figure 6.39 Comparison of first principal strain (ε_{p1}) and shear angle (γ_{12}) in SRPP and SRPP/steel FML hourglass induced-biaxial deformation test specimens shown in Figure 6.38, at a punch depth of 30 mm. Average strains in the centre regions ($\overline{\varepsilon_{p1}}$, $\overline{\gamma_{12}}$) and maximum strains ($\varepsilon_{p1, \max}$, $\gamma_{12, \max}$) are given, where the centre region is the top 1 mm of the punch depth.

The following observations on maximum strains in steel, SRPP and FML before failure show that the outer steel layer fails before the SRPP layer and causes failure of the FML specimens. To help illustrate the point, ε_{p1} and γ_{12} distributions and values at the last stage before failure are shown in Figure 6.40 and Table 6.3. FML hourglass IBD test specimens fail through the point of maximum ε_{p1} and γ_{12} – which occur at the same point, or right next to each other – in both the outer steel and the SRPP layers. Before failure, the maximum ε_{p1} in FML is $49 \pm 4\%$. This is very close to the maximum ε_{p1} in steel specimens

($49.5 \pm 0.8\%$), which fail from localised necking occurring through the point of maximum ϵ_{p1} . The signs of localised necking occurring in the steel layer of the FML can be seen by the strain concentrations along the fracture angles through the point of maximum ϵ_{p1} , shown in Figure 6.40a.

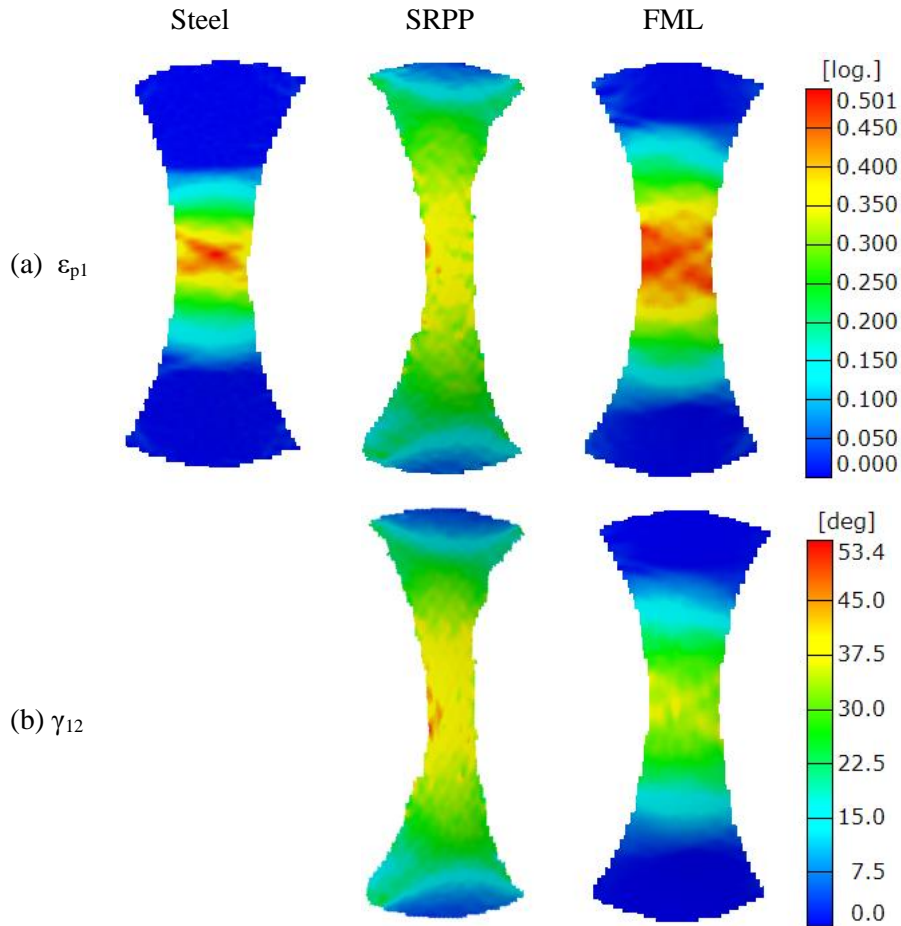


Figure 6.40 Comparison of first principal strain (ϵ_{p1}) and shear angle (γ_{12}) in steel (left), SRPP (centre) and SRPP/steel FML (right) hourglass induced-biaxial deformation test specimens at the last stage before failure.

Table 6.3 Comparison of punch depth (d), average and maximum first principal strains (ϵ_{p1}) and shear angles (γ_{12}) in steel, SRPP and SRPP/steel FML hourglass induced-biaxial deformation test specimens before failure. Average strains are based on the centre region, in the top 1 mm of the punch depth.

	d (mm)	$\overline{\epsilon_{p1}}$ (%)	$\epsilon_{p1, \max}$ (%)	$\overline{\gamma_{12}}$ (deg)	$\gamma_{12, \max}$ (deg)
Steel	25 ± 0.8	36 ± 0.8	49.5 ± 0.8	n/a	n/a
SRPP	36 ± 1	33 ± 1	43 ± 1	37 ± 2	50 ± 3
FML	30 ± 1	40 ± 6	49 ± 4	31 ± 2	37 ± 2

In contrast, the maximum ε_{p1} in SRPP specimens before failure is $43 \pm 1\%$, which is lower than the maximum ε_{p1} in FML at failure ($49 \pm 4\%$), which suggests that the maximum ε_{p1} in FML is indeed caused by localised necking in the steel layer, rather than a critical tape pull-out in the SRPP layer. The conjecture that a large tape pull-out has not occurred in the SRPP layer of the FML is also supported by the fact that the maximum γ_{12} in FML before failure ($37 \pm 2^\circ$) is much lower than the maximum γ_{12} observed in plain SRPP before failure ($50 \pm 3^\circ$).

Large tape pull-outs probably did not occur in the SRPP layer of the FML due to the damage in the SRPP layer being suppressed by the adherence to the steel layers. The adhesion between the layers likely has two effects, the first of which is that the steel layers restrict the γ_{12} in the SRPP layer compared to plain SRPP specimens, in which a large γ_{12} exacerbates the extent of the damage, as was shown in Chapter 5. The second effect is that the cracks are hindered from enlarging, similar to the crack arresting mechanisms hypothesised to occur in the analyses of tensile test specimens.

The fact that damage in the SRPP layer of FML is suppressed by the steel layers can be seen by comparing the level of strain concentrations in the SRPP and FML specimens shown in Figure 6.40. The level of strain at the maximum strain point compared to the surrounding region is lower in the FML specimen than in the plain SRPP specimen. Since strain concentrations in SRPP reflect the growth of the damage, as shown in previous chapters, this indicates that damage growth is suppressed in the SRPP layer of the FML, as compared to plain SRPP, due to the adherence of the SRPP to the steel layers.

Another observation which shows that the outer steel layer must have failed, rather than the SRPP layer in the FML specimen, is that the maximum ε_{p1} and γ_{12} points can occur at *or* away from the edges. This behaviour is similar to the way in which the point of maximum ε_{p1} in steel specimens can occur at *or* away from the edges, and contrasts to the behaviour of SRPP specimens, in which the maximum ε_{p1} and γ_{12} points always occur at the edges, due to the critical tape pull-outs occurring from the edges. This observation supports the finding that failure in the FML specimens is triggered by localised necking in the outer steel layer at the point of maximum ε_{p1} , as opposed to tape pull-outs in the SRPP layer.

It should be noted that the FML specimens fail at a deeper punch depth (30 ± 1 mm) than steel specimens (25 ± 0.8 mm), despite the fact that failure in the FML occurs due to a failure in the outer steel layer. This is a good example that demonstrates how the failure limit of a constituent material of a laminate can increase in terms of total length, depth or average strain, due to the hybridisation that changes the strain distribution in the layer. On the other hand, the failure limit of a constituent layer can also be reduced due to laminate failure being caused by failure in another layer, as is obviously the case with the SRPP layer in the FML. (Plain SRPP fails at deeper punch depth than FML, at 36 ± 1 mm.)

In this section, it was found that the hourglass IBD test specimens exhibit similar behaviours to off-axis tensile test specimens. The difference is that, in the hourglass IBD test specimens, by nature of the loading conditions imposed, failure occurs in the outer layer and in the narrow region at the centre. This

allows the damage and strain development that are relevant to the failure of the material to be observed using the DIC system. From this, it can be confirmed that SRPP fails from tape and fibril pull-outs from the free edges, and FML fails from localised necking of the steel layer, when the materials are deformed at off-axis angles to the reinforcing directions.

It was also shown that laminating SRPP with steel had similar effects to the off-axis tensile test specimens. The damage in the SRPP layer of the FML was suppressed by the steel layers, and a different proportion of the total deformation occurred from the in-plane shear deformation in the FML compared to plain SRPP. Again, it was shown that strain analysis from the in-situ DIC system can indicate the failure location within the material, as well as analyse in which layer the failure occurred in the FML.

6.4 Summary

In this chapter, the failure behaviours of SRPP and SRPP/steel FML were analysed when the materials are subjected to a combination of in-plane biaxial deformation and out-of-plane bending.

It can be recalled that, in tensile tests of SRPP, the progression of damage that caused failure in the 1.0 mm specimens had to be ascertained through a combination of microscopic and strain analysis and different specimen thicknesses because the development of critical damage is obscured by myriad of non-critical damage. In the case of the IBD tests, larger overall strain – and therefore failure – is induced in the outer layer at the centre of the specimen. Due to this, some of the damage progression that is relevant to the SRPP failure could be observed directly using high-resolution digital images captured by the DIC system. In addition, it was demonstrated, once again, that strain analysis can be used to investigate where the failure occurred and the possible reasons behind the failure.

Using the above, it was confirmed that failure in the SRPP occurred from tape and fibril pull-outs from the free edges, and that the FML failed from necking in the steel layer, when the materials are loaded at off-axis to their reinforcing directions. It was also confirmed that laminating SRPP with steel had the effect of inducing different amounts of γ_{12} when compared to plain SRPP, as well as suppressing the damage in the SRPP layer.

When the SRPP is subjected to equal biaxial deformation at the centre, it was found that failure occurs from different types of fibril pull-outs. In this case, micro-damage mechanisms cause fibrillation in the tapes, and the fibrils subsequently fracture from reaching their limiting strains in the direction of the reinforcement. This causes fibril pull-out and additional failure of the tape in the layer underneath, after which the material failure ensues. The same failure process can occur in the FML, when the SRPP layer fails first. However, it was found that the FML can also fail from localised necking and the resulting failure in the outer steel layer, despite the loading conditions being identical. This also changed the failure path. This phenomenon of the FML exhibiting two different failure behaviours is conjectured to

be due to material imperfections, or the variation of the consolidation quality of the SRPP layer, which was also conjectured to be the cause of slight variations observed in the failure behaviour of the plain SRPP specimens.

7 Conclusion and Future Work

This thesis elucidated the failure behaviour and the related deformation behaviour of self-reinforced polypropylene (SRPP) and SRPP/steel fibre metal laminate (FML). The research project was motivated from the perspective that different industries can exploit the benefits of these materials beyond their current uses. However, a review of the literature showed that there is limited research that details the failure process of the materials, an understanding of which is desirable before expanding their field of applications. For instance, it was unclear what kinds of damage are directly related to the failure of the material, the causes and the processes of their development, how or whether these change under different loading conditions and whether they can be detected.

The reason why such factors were unclear is because many of the existing studies of SRPP focused on the manufacturing methods, the effect of processing parameters on the mechanical properties, and impact behaviour, and the research in the area of its failure behaviour is far from mature. Since a clear understanding of the material behaviour of an FML is largely dependent on its constituent materials, the failure behaviours of SRPP-based FMLs are also largely unknown. It should also be reiterated here that single polymer composites (SPCs) like SRPP behave and fail quite differently to the more well understood 2-phase fibre-reinforced polymers (FRPs) and, as a result, very little of the knowledge about the material behaviour of 2-phase FRPs is transferrable to SPCs.

The current research therefore set out to investigate the failure behaviour of SRPP and SRPP/steel FML in more depth, using various loading conditions, material thicknesses, material orientations, and methods of analyses. The findings were discussed in detail in Chapters 4–6, with summaries given at the end of each large section and every chapter. This concluding chapter will focus more on highlighting the significance of the findings, in the context of their implications on the existing knowledge and design considerations.

One of the most significant aspects of the research is related to the approach used to investigate the failure behaviour. Firstly, it was found that the thickness effect can be used to uncover the different damage mechanisms and how they relate to the catastrophic failure of SRPP. From this, the cause of the failure of FML could also be identified, based on the knowledge gained from studying the behaviour of SRPP. Secondly, it was demonstrated that a combination of microscopic analysis and strain analysis using a DIC system can effectively be used to identify the critical damage and related mechanisms that

cause specific failure behaviours under various loading conditions, as well as their progression during the deformation process up to the point of failure. It was also demonstrated that strain analysis can be used to indicate where and when failure is likely to occur or has occurred. This includes the identification of which constituent layer of the FML failed first, thereby causing the failure of the system.

From studying SRPP, it was found that the progression of damage that leads to its failure is similar to that of typical woven FRPs, in which failure often occurs from cracks at transverse yarn boundaries, which then propagate into local delamination, which then causes failure in the surrounding fibres. Cracks can also be arrested at crimp or weave boundaries. Similar behaviours were observed in woven SRPP, where transverse boundary cracks (or boundary cracks that are at the largest angle to the loading direction, in the case of off-axis specimens) between tapes were often found to lead to other types of damage such as delamination, pull-outs or the fracture of tapes or fibrils, which led to specimen failure. Also, cracks were arrested at the weave boundaries under certain circumstances.

However, there were also important differences in the ways in which damage in SRPP led to failure, as compared to typical woven FRPs. For example, cracks at the transverse yarn boundaries in woven FRPs tend to occur from micro-debonding at the interface between the fibre and the matrix. In contrast, boundary cracks in SRPP occur in the matrix. Interfacial debonding can occur, but only in very limited cases and only in certain circumstances (e.g. on the fracture surface of a 0.3 mm $0^\circ/90^\circ$ specimen). Interfacial debonding occurs much less frequently in SRPP than in 2-phase FRPs due to a stronger bond forming between reinforcement and matrix phases that are chemically identical, as reported by other studies. An example that demonstrates this in the current research is the finding that delamination in thicker specimens preferentially occurs within the tapes, for which the interface must be strong enough to induce failure in the tape before the interfacial bond fails.

In addition to the above difference to the FRPs, SRPP was also found to exhibit extremely high strain concentration points at some boundary cracks, which has not been reported in existing studies. This was found to be a very important behaviour, as this was identified as the critical damage that caused failure in many cases. It was also discovered that the unique strain behaviour of such high strain concentration points can be used to indicate, track or predict when and where failure occurs, under certain circumstances. This was found to be useful in cases where specimen failure is difficult to predict using conventional means, such as in 0.3 mm tensile test specimens.

It should be mentioned that many of the types of damage and related mechanisms identified in this study have not been reported in the literature on SRPP, with some of them exhibiting characteristics that were not previously observed for any FRPs. This includes boundary cracks, aligned crazing, crack bridging in tapes by micro- and nanofibrils, crack arresting mechanisms, crack tip blunting, and oblique cracks. Some of them were named, as appropriate, where reference to the phenomena could not be found in the

literature. The ways in which the characteristics of each damage mechanisms vary, or do not vary, depending on the loading angle, material and thickness, were also identified.

It was also discovered that cracks can propagate in both stable or unstable manners and cause ductile or brittle fractures at a microscopic scale in the SRPP. It was found that these can co-occur in the same specimen, which is an interesting phenomenon that has not been reported before in this type of material. It was found that the different modes of crack formation and propagation occurred depending on various factors, such as phase difference (reinforcement or matrix), directionality of the reinforcement, geometry of the weave structure, presence of other damage, and specimen thickness.

Damage of various types was found to have some interesting effects on the failure limits of SRPP, depending on the loading scenarios. Uniaxial tensile test of SRPP along the reinforcing directions at different thicknesses showed that the extra damage mechanisms in 0.6 mm and 1.0 mm specimens introduced toughening mechanisms that are not present in the 0.3 mm specimens. This allowed the thicker specimens to fail at more consistent applied strains, which is a desirable characteristic for design purposes. When SRPP specimens are subjected to loading at off-axis to the reinforcing directions, the larger amount of damage occurring in the 1.0 mm specimens than in 0.6 mm specimens caused a larger amount of trellising of the tapes, which ultimately caused the 1.0 mm specimens to fail at higher applied strains.

During the study of materials under induced biaxial deformations, it was found that the consolidation quality or material imperfections can change the failure behaviour of the material systems. For example, some SRPP specimens failed at deeper punch depths and exhibited substantially less fibril pull-outs before failure, and it was hypothesised that such specimens have a better quality of consolidation. For FML specimens, it was conjectured that the consolidation quality or the inherent material imperfections affects the way in which strains develops in the specimen, to the point where they can affect the layer in which the failure initiates so that it can either be the SRPP or the outer steel layer. The critical damage that leads to failure, and the failure path of the FML, differ depending on which constituent layer fails first.

The above findings suggest that deriving the optimal processing parameters to control the material quality is incredibly important for SRPP, similar to the SPCs and other hybrid materials that are based on them. This highlights the significance of existing studies on SPCs that explore different manufacturing techniques and parameters. It also suggests that desirable characteristics may be achieved for the intended design at the material manufacturing stage through carefully controlling the level of consolidation. This will affect the amount and types of damage and deformation, as well as the failure behaviours, all of which can be taken advantage of, depending on the expected loading conditions. This is similar to the fact that a lower consolidation quality and the resulting higher amount of damage can be exploited to achieve higher energy absorption in impact scenarios. These reflections also highlight

the importance of understanding the failure behaviour of these materials before using them in any specific application.

The findings regarding the effect of material quality also suggests that different manufacturing methods (e.g. film stacking as opposed to hot compaction) might change the micro-damage development and failure behaviour of SPCs. Future study on whether or not this is the case is recommended, as this would help understand the link between the manufacturing process, its impact on the microstructure of the material, micro-damage development, and critical failure behaviour at a macroscopic level. This would be of benefit to those trying to understand the underlying causes of the failure behaviour of SPCs. By extension, this would benefit those studying the failure behaviour of thermoplastic-based FRPs and their hybridisations, and the designers within various industries who are looking to incorporate these materials. It would also be of interest to investigate how much of the findings from this research on SRPP and SRPP-based FML apply to other types of SPCs (e.g. self-reinforced polyethylene) and other types of hybrid materials based on such materials.

On the form factor of SRPP, it was mentioned in the literature review that the use of a tape type of reinforcement with a 2/2 twill weave pattern created the least amount of crimping when compared to other reinforcement and weave types, and were therefore most desirable [41, 68, 70]. It should be noted that the SRPP used in this research also used a tape type of reinforcement woven in a 2/2 twill weave pattern. It was shown that matrix cracks between tapes of the same orientation, which have no crimping, can be especially damaging under uniaxial tensile loading. In addition, it was found that some critical damage can be initially arrested at the weave boundary where there is crimping. This does not necessarily negate the fact that minimal crimping is desirable. Boundary cracks that propagated into local delamination and promoted critical fibril pull-outs in circular IBD test specimens likely occurred at the weave boundary, where there was crimping. However, this does beg the question as to whether the reduced crimping always has the desired effect on the failure behaviour, or whether it depends on the specific loading conditions.

With regards to the behaviour of FML, an important finding was that the material behaviours of the steel and SRPP layers interacted with each other during the deformation process up to the point of failure. A good example is the case of tensile test specimens with the SRPP reinforcements oriented at 0°/90° to the loading direction. In these specimens, multiple strain localisation bands form at an oblique angle to the loading direction, some of which develop into fracture bands, which form the same angle as the fracture angle of plain steel. This clearly reveals the influence of the material behaviour of steel. What is interesting is that the strain localisation bands initially form from strain concentration points which are likely caused by boundary cracks in the SRPP layer. Also, while failure occurs within the fracture bands, it is actually the SRPP layer which fails first, causing failure of the FML.

Another important aspect of the FML behaviour that was discovered was that the steel layers significantly reduce strain concentrations from the SRPP layer, indicating that large crack growth in the SRPP layer is impeded by the adhesion to the steel layer. On top of this, the SRPP layer in an FML can endure higher strains in the off-axis directions than plain SRPP due to the damage being inhibited by the steel layers. This is partly related to the in-plane shear strain being reduced when the SRPP is laminated with steel, which reduces the degree of rotation of the tapes towards the loading direction at the same applied strain. Overall, these behaviours show the potential for SRPP to be deformed beyond its limiting strain when laminated with other materials, which could be useful in manufacturing. However, making use of such behaviours would require consideration of other factors that may or may not be desirable, such as out-of-plane warping of the steel layers at large strains, or large differences in the residual stress of SRPP and steel layers.

The findings from this research has many implications regarding the predictability of failure of this SRPP or similar materials, as will be explained in the following paragraphs. In the case of metals, failure limits based on the state of principal strains can be determined experimentally for sheet metal forming applications, as was explained in Chapter 3. There is a precedence of similar limits being established for SRPP [111]. However, the findings from the tensile tests in the current study shows that, when using such failure limits for SRPP, considerations about how the limits were established need to be understood. For instance, it was shown that different failure criteria would apply for 0.3 mm SRPP compared to 0.6 mm or 1.0 mm SRPP under uniaxial tension. Failure of 0.6 mm and 1.0 mm specimens can be predicted with ease, based on the average or applied stress or strain, but doing so for 0.3 mm SRPP would give inaccurate predications for many specimens. Therefore, the failure limits in [111] would not apply well to 0.3 mm SRPP specimens under tension, since these limits were established without considering the presence of the high strain concentrations that occur in these specimens. This demonstrates the importance of understanding the underlying failure behaviour of the materials.

In the literature review, it was mentioned that the failure of a coextruded tape-reinforced UD SRPP [17] under tensile loading was dominated by tape strength between $0^\circ < \theta < 2^\circ$, by shear between $2^\circ < \theta < 23^\circ$, and by transverse strength of the tape above this angle. It is clear that the SRPP studied in the current research behaves differently, likely because it is woven and / or because it was manufactured using a different method. In this hot compacted SRPP, the transverse strength was found to be of little relevance due to the additional reinforcements in the perpendicular direction. Between $30^\circ < \theta < 60^\circ$ (where θ is one of the reinforcing directions), it was found that, while in-plane shear strains about the reinforcing directions have a large effect on the damage behaviour, the critical damage occurs from boundary cracks propagating into tape fractures (in 0.3 mm specimens) or tape and fibril pull-outs from the free edges causing multiple instances of damage (in 0.6 mm and 1.0 mm specimens).

The SRPP behaviour under tension for the range $0^\circ < \theta < 30^\circ$ (which is same as $60^\circ < \theta < 90^\circ$ in this case) is unknown, but is expected to be very similar to the $30^\circ/60^\circ$ and $\pm 45^\circ$ specimens for thicker specimens. For thinner specimens, such as the 0.3 mm specimens used in this study, there would be a sharp transition point somewhere in $0^\circ < \theta < 30^\circ$ where the mode of crack formation and initial propagation of the critical boundary crack changes from being unstable to stable (with an increase in angle), which determines the failure behaviour.

From the above observations, it can be seen that neither shear strength nor transverse strength of the tape dominates the tensile failure behaviour of the hot compacted woven SRPP, unlike in the coextruded UD SRPP. This is also the case for biaxial deformation, in which the critical failure depended on fibril pull-outs, which occurred from various micro-damage mechanisms but most crucially, from a fracture in the reinforcing direction and delamination. Consolidation quality also influenced its failure, which is also the possible cause for the different behaviour of 0.3 mm specimens under tensile loading compared to the thicker specimens.

Based on the findings from this research, a comprehensive failure criterion for the woven SRPP may have to account for factors such as tape strength in the reinforcing direction, influence of the weave pattern, fracture toughness as a variable of consolidation quality, the angle between the tape and the load, damage tolerance and damage density, among others. This is due to the complex nature of the damage mechanisms that lead to failure of this type of composite.

However, predicting the failure of SRPP, or similar materials, may be simplified if multiple separate failure criteria are developed depending on the primary cause of failure and the material condition. For instance, it can be recalled that few studies found that failure in flax-fibre/PP [60] and GFRPP [61] were dominated by fibre failure and that this could be used to predict the failure limits of the composites subjected to various load scenarios similar to the IBD tests. It was questioned in the literature review whether the same concept would apply to SRPP. The study on the circular IBD test and the 0.6 mm and 1.0 mm $0^\circ/90^\circ$ tensile tests suggest that such failure criterion would be applicable for deformation modes ranging between equal biaxial deformation and uniaxial tension, since critical damage occurs with the fracture of tapes or fibrils at consistent strains in the reinforcing directions.

However, when 0.6 mm or 1.0 mm specimens are subjected to in-plane shear in off-axis tensile tests, the same failure criterion would not apply since failure occurs from the delamination and pull-outs of tapes from the free edges, not tape fractures. Also, in cases of 0.3 mm $0^\circ/90^\circ$ tensile test specimens, failure occurs at widely varying applied strains. In this case, even though the specimen ultimately fails with a fracture of the reinforcement, high strain concentrations from boundary cracks and the lack of toughening mechanisms heavily influence the failure behaviour, such that failure cannot be predicted accurately enough using the magnitude of strain in the reinforcing direction. Therefore, it is hypothesised

that a relatively simple failure criterion may be developed *if* there are multiple sub-criteria separating the instances where the fundamental causes of failure are different.

The above reflections demonstrate the importance of understanding the exact phenomenon behind the cause of material failure under different types of load conditions. It also demonstrates the very different failure behaviour of SRPP in comparison to 2-phase FRPs, even those based on the same matrix (PP). This can be attributed to the rather unique choice of reinforcement material, size, shape and molecular structure in SRPP, as well as the woven structure.

Also, it can be seen that a natural progression for future works would be to use the data and the insights generated from this research to design a failure criterion for this woven SRPP. This would then hopefully expand into the generation of failure criteria of SPCs and perhaps thermoplastic FRPs, as well as FMLs based on such materials. In addition to those already suggested, studies in the following areas are recommended, in order for researchers and designers to benefit from a better understanding of the behaviour of SRPP, SRPP-based FMLs and similar material systems.

Firstly, it is recommended that similar research be carried out at elevated temperatures, up to the melting point of SRPP, to see how the material behaviours found in this study changes. Depending on the potential applications of SRPP, FML or similar materials, it may also be of benefit to investigate their material behaviour at lower temperatures. For example, if they are to be used as automotive parts, any changes in the behaviour at temperatures similar to cold regions of the world should be accounted for and fully understood. For design purposes, it is also recommended that buckling behaviour, and behaviour around joints of SRPP-based FML, is investigated. For research on the subject of failure behaviour and failure criteria of SRPP, it is recommended that additional types of tests be carried out under different loading conditions, including compression, pure bending, pure shear, and uniaxial tension at between $0^\circ < \theta < 30^\circ$ using 0.3 mm specimens, as well as characterisation on the fracture toughness. It is also recommended that additional methods of analyses be incorporated, such as in-situ scanning electron microscopy and mesoscale modelling.

References

- [1] A. Vlot, L. B. Voegesang, and T. J. de Vries, "Towards application of fibre metal laminates in large aircraft," *Aircraft Engineering and Aerospace Technology*, vol. 71, no. 6, pp. 558–570, 1999.
- [2] B. Borgonje, and M. S. Ypma, "Long term behaviour of Glare," *Applied Composite Materials*, vol. 10, no. 4–5, pp. 243–255, 2003.
- [3] AGY, "GLARE Laminate with S-2 Glass Fiber," 2013. [Online]. Available: https://www.agy.com/agy_documents/glare-laminate/. [Accessed Oct. 10, 2018].
- [4] R. J. H. Wanhill, "GLARE®: A Versatile Fibre Metal Laminate (FML) Concept," in *Aerospace Materials and Material Technologie: Volume 1: Aerospace Materials*, N. Prasad, and R. J. J. Wanhill, Eds. Springer Singapore, 2017, pp. 291–307.
- [5] C. A. J. R. Vermeeren, "An historic overview of the development of fibre metal laminates," *Applied Composite Materials*, vol. 10, no. 4–5, pp. 189–205, 2003.
- [6] A. K. Vlot, E. Kroon, and G. La Rocca, "Impact response of fiber metal laminates," *Key Engineering Materials*, vols. 141–143, pp. 235–276, 1998.
- [7] H. J. Fleisher, "Design and explosive testing of a blast resistant luggage container," In Proc. Structures under Shock and Impact Conference IV, 1996, pp. 51-59.
- [8] McLaren Automotive, "Super series: the next generation," 2017. [Online]. Available: <http://cars.mclaren.com/featured-articles/1>. [Accessed Sep. 25, 2018].
- [9] Volvo Car Group, Public Affairs, "Volvo XC90 body structure," Jan. 22, 2014. [Online]. Available: <https://www.media.volvocars.com/global/en-gb/media/photos/148215/volvo-xc90-body-structure>. [Accessed Oct. 10, 2018].
- [10] S. Davey, R. Das, W.J. Cantwell, and S. Kalyanasundaram, "Forming studies of carbon fibre composite sheets in dome forming processes," *Composite Structures*, vol. 97, pp. 310-316, 2013.
- [11] B. Behrens, A. Raatz, S. Hübner, C. Bonk, F. Bohne, C. Bruns, M. and Micke-Camuz, "Automated Stamp Forming of Continuous Fiber Reinforced Thermoplastics for Complex Shell Geometries," *Procedia CIRP*, vol. 66, pp. 113-118, 2017.
- [12] J. Fleischer, J. Nieschlag, "Introduction to CFRP-metal hybrids for lightweight structures," *Production Engineering*, vol. 12, pp. 109–111, 2018.

- [13] C. Froemder, K. Kirwan, N. Reynolds, P. R. Wilson, F. C. Fernandes, and S. R. Coles, "Investigation of the Processability of Hybrid Thermoplastic Nonwoven including Recycled Carbon Fibre through Fast Stamping," In Proc. SAMPE Europe Conference 2018 Southampton, Southampton, 2018.
- [14] T. Mattner, J. Popp, T. Kleffel, C. Gröschel, and D. Drummer, "High-Speed Forming of Continuous Fiber Reinforced Thermoplastics," *Applied Composite Materials*, 2020.
- [15] W. Wang, A. Lowe and S. Kalyanasundaram, "A study on continuous flax fibre reinforced polypropylene composite in stamp forming process," *Advanced Composites Letters*, vol. 22, pp. 86-89, 2013.
- [16] T. Peijis, *Materials Today*, "Composites for recyclability," *Materials Today*, vol. 6, no. 4, pp. 3035, 2003.
- [17] B. Alcock, N. O. Cabrera, N.-M. Barkoula, J. Loos, and T. Peijs, "The mechanical properties of unidirectional all-polypropylene composites," *Composites Part A: Applied Science and Manufacturing*, vol. 37, pp. 716–726, 2006.
- [18] B. Alcock, N. O. Cabrera, N.-M. Barkoula, T. Peijs, "Low velocity impact performance of recyclable all-polypropylene composites," *Composites Science and Technology*, vol. 66, pp. 1724–1737, 2006.
- [19] N. Cabrera, B. Alcock, J. Loos, and T. Peijs, "Processing of all-polypropylene composites for ultimate recyclability," In Proc. Institution of Mechanical Engineers Part L Journal of Materials Design and Applications, 218, 2004, pp. 145–156.
- [20] A. Kmetty, T. Bárány, and J. Karger-Kocsis, "Self-reinforced polymeric materials: A review," *Progress in Polymer Science*, vol. 35, no. 10, pp. 1288–1310, 2010.
- [21] I. M. Ward and P. J. Hine, "The science and technology of hot compaction," *Polymer*, vol. 45, pp. 1413–1427, 2004.
- [22] Propex Fabrics GmbH & Co.KG, "Applications," 2018. [Online]. Available: <https://www.curvonline.com/products-services/applications.html#c252>. [Accessed Sep. 18, 2018].
- [23] S. Fakirov, "Nano- and Microfibrillar Single-Polymer Composites: A Review," *Macromolecular Materials and Engineering*, vol. 298, no. 1, pp. 9–32, 2013.
- [24] R. Talreja and J. Varna, Eds., *Modeling Damage, Fatigue and Failure of Composite Materials*. Cambridge, UK: Woodhead Publishing, 2016.
- [25] D. Arencón and J. I. Velasco, "Fracture Toughness of Polypropylene-Based Particulate Composites," *Materials*, vol. 2, pp. 2046-2094, 2009.
- [26] G. Reyes Villanueva and W. J. Cantwell, "The high velocity impact response of composite and FML-reinforced sandwich structures," *Composites Science and Technology*, vol. 64, no. 1, pp. 35–54, 2004.

- [27] J. Fan, W. J. Cantwell and Z. W. Guan, “The low-velocity impact response of fiber-metal laminates,” *Journal of Reinforced Plastics and Composites*, vol. 30, no. 1, pp. 26–35, 2011.
- [28] R. Marissen, “Fatigue crack growth predictions in Aramid reinforced aluminium laminates (ARALL),” *Journal of Aircraft*, vol. 25, no. 2, pp. 135–140, 1988.
- [29] R. O. Ritchie, W. Yu and R. J. Bucci, “Fatigue crack propagation in ARALL® LAMINATES: measurement of the effect of crack-tip shielding from crack bridging,” *Engineering Fracture Mechanics*, vol. 32, no. 3, pp. 361–377, 1989.
- [30] L. B. Vogelesang and J. W. Gunnink, “ARALL: A Materials Challenge for the next Generation of Aircraft,” *Materials and Design*, vol. 7, no. 6, pp. 287–300, 1986.
- [31] R. Alderliesten, *Fatigue and Fracture of Fibre Metal Laminates*, Cham, Switzerland: Springer International Publishing, 2017, pp. 7–25.
- [32] M. J. Hinton, A. S. Kaddour and P. D. Soden, *Failure criteria in fibre reinforced polymer composites: the world-wide failure exercise*, Oxford, UK: Elsevier Science Ltd., 2004.
- [33] A. S. Kaddour and M. J. Hinton, “Benchmarking of triaxial failure criteria for composite laminates: Comparison between models of Part (A) of ‘WWFE-II’,” *Journal of Composite Materials (special issue)*, vol. 46, pp. 2595–2634, 2012.
- [34] A. S. Kaddour and M. J. Hinton, “Evaluation of theories for predicting failure in polymer composite laminates under 3-D states of stress: Part A of the second worldwide failure exercise (WWFE-II),” *Journal of Composite Materials (special issue)*, vol. 46, pp. 19–20, 2012.
- [35] A. S. Kaddour and M. J. Hinton, “Evaluation of theories for predicting failure in polymer composite laminates under 3-D states of stress: Part B of the second worldwide failure exercise (WWFE-II),” *Journal of Composite Materials (special issue)*, vol. 47, pp. 6–7, 2013.
- [36] A. S. Kaddour, M. J. Hinton, P. A. Smith, and S. Li, “The background to the third world-wide failure exercise,” *Journal of Composite Materials*, vol. 47, no. 20–21, pp. 2417–2426, 2013.
- [37] A. S. Kaddour, M. J. Hinton, S. Li, and P. A. Smith, “The world-wide failure exercises: How can composites design and manufacture communities build their strength,” In Proc. 16th European Conference on Composite Materials, Seville, Spain, 2014.
- [38] J. R. Reeder, “An evaluation of mixed-mode delamination failure criteria,” NASA Langley Research Center; Hampton, VA, United States, Tech. Report. NASA-TM-104210, 1 Feb. 1992.
- [39] N. J. Capiati and R. S. Porter, “Concept of one polymer composites modelled with high density polyethylene,” *Journal of Materials Science*, vol. 10, no. 10, pp. 1671–1677, 1975.
- [40] B. Alcock, N. O. Cabrera, N.-M. Barkoula, A. B. Spoelstra, J. Loos, and T. Peijs, “The mechanical properties of woven tape all-polypropylene composites,” *Composites Part A: Applied Science and Manufacturing*, vol. 38, no. 1, pp. 147–161, 2007.

- [41] P. J. Hine, I. M. Ward, N. D. Jordan, R. Olley, and D. C. Bassett, "The hot compaction behaviour of woven oriented polypropylene fibres and tapes. I. Mechanical properties," *Polymer*, vol. 44, no. 4, pp. 1117–1131, 2003.
- [42] A. Izer, A. Stocchi, T. Bárány, V. Pettarin, C. Bernal, and T. Czigány, "Effect of the consolidation degree on the fracture and failure behavior of self-reinforced polypropylene composites as assessed by acoustic emission," *Polymer Engineering and Science*, vol. 50, no. 11, pp. 2106–2113, 2010.
- [43] G. Romhány, T. Bárány, T. Czigány, and J. Karger-Kocsis, "Fracture and failure behaviour of fabric-reinforced all-poly(propylene) composite (Curv®)," *Polymers for Advanced Technologies*, vol. 18, no. 2, pp. 90–96, 2007.
- [44] N. A. Zanjani and S. Kalyanasundaram, "A Comparison between Forming Behaviours of Two Pre-Consolidated Woven Thermoplastic Composites," *Journal of Materials Science and Chemical Engineering*, vol. 3, pp. 180-189, 2015.
- [45] G. Nicoletto and E. Riva, "Failure mechanisms in twill-weave laminates: FEM predictions vs. experiments," *Composites Part A: Applied Science and Manufacturing*, vol. 35, pp. 787–795, 2004.
- [46] G. A. Bibo, and P. J. Hogg, "The role of reinforcement architecture on impact damage mechanisms and post-impact compression behaviour," *Journal of Materials Science*, vol. 31, pp. 1115-1137, 1996.
- [47] D. Hull and T. W. Clyne *An Introduction to Composite Materials*, 2nd ed. Cambridge, UK: Cambridge University Press, 1996.
- [48] A. Pupurs, "Micro-Crack Initiation and Propagation in Fiber Reinforced Composites," PhD thesis, Luleå University of Technology, Luleå, 2015.
- [49] H. Wafai, A. Yudhanto, G. Lubineau, R. Yaldiz, and N. Verghese, "An experimental approach that assesses in-situ microscale damage mechanisms and fracture toughness in thermoplastic laminates under out-of-plane loading," *Composite Structures*, vol. 207, pp. 546-559, 2019.
- [50] D Cai, G Zhou, X. Wang, C. Li, and J. Deng, "Experimental investigation on mechanical properties of unidirectional and woven fabric glass/epoxy composites under off-axis tensile loading," *Polymer Testing*, vol. 58, pp. 142–152, 2017.
- [51] H. Nishid, V. Carvelli, T. Fujii, and K. Okubo, "Thermoplastic vs. thermoset epoxy carbon textile composites," *IOP Conference Series: Materials Science and Engineering*, vol. 406, 012043, 2018.
- [52] Committee on Thermoplastic Composites as Structural Components, "The Place for Thermoplastic Composites in Structural Components," National Materials Advisory Board, National Research Council, Virginia, USA, Tech. Report. NMAB-4 34, 1 Dec. 1987.
- [53] V. Dikshit, S. Bhudolia and S. Joshi, "Multiscale Polymer Composites: A Review of the Interlaminar Fracture Toughness Improvement," *Fibers*, vol. 5, 38, 2017.

- [54] K. Kim, L. Ye and K. Phoa, “Interlaminar Fracture Toughness of CF/PEI and GF/PEI Composites at Elevated Temperatures,” *Applied Composite Materials*, vol. 11, pp. 173–190, 2004.
- [55] B. Vieille, J. Aucher and L. Taleb, “Comparative study on the behavior of woven-ply reinforced thermoplastic or thermosetting laminates under severe environmental conditions,” *Materials and Design*, vol. 35, pp. 707–719, 2012.
- [56] Y. Ma, M. Ueda, T. Yokozeki, T. Sugahara, Y. Yang, and H. Hamada, “A comparative study of the mechanical properties and failure behavior of carbon fiber/epoxy and carbon fiber/polyamide 6 unidirectional composites,” *Composite Structures*, vol. 160, pp. 89–99, 2017.
- [57] M. C. Lafarie-Frenot and F. Touchard, “Comparative in-plane shear behaviour of long-carbon-fibre composites with thermoset or thermoplastic matrix,” *Composites Science and Technology*, vol. 52, pp. 417-425, 1994.
- [58] A. Bourmaud, G. Ausias, G. Lebrun, M. -L. Tachon, and C. Baley, “Observation of the structure of a composite polypropylene/flax and damage mechanisms under stress,” *Industrial Crops and Products*, vol. 43, pp. 225– 236, 2013.
- [59] W. Hufenbach, M. Gude, M. Thieme, and R. Böhm, “Failure behaviour of textile reinforced thermoplastic composites made of hybrid yarns - I: Probabilistically based damage models,” In Proc. 12th International Conference on Fracture, Ottawa, Canada, 2009.
- [60] W. Wang, “Forming Analysis of Natural Fibre Composites,” PhD thesis, Australian National University, Canberra, 2015.
- [61] J. Liang, “Investigation of failure behaviour of a glass-fibre reinforced thermoplastic composite,” MPhil thesis, Australian National University, Canberra, 2017.
- [62] Propex Fabrics GmbH & Co.KG, “This is Curv®,” 2018. [Online]. Available: <https://www.curvonline.com/products-services/this-is-curvr.html>. [Accessed Oct. 12, 2018].
- [63] BJE Kunststoffe, “A New Generation Thermoplastic Composite,” [Online]. Available: http://www.bje-kunststoffe.com/en/technical_curv.html. [Accessed Dec. 1, 2018].
- [64] M. Bonner, B. Elfering and I.M. Ward, “The mechanical properties of high stiffness hot-compacted polypropylene: a new development,” *Journal of Materials Science*, vol. 49, pp. 1606–1611, 2014.
- [65] M. I. Abo El-Maaty, D. C. Bassett, R. H. Olley, P. J. Hine, and I. M. Ward, “The hot compaction of polypropylene fibres,” *Journal of Materials Science*, vol. 31, pp. 1157–1163, 1996.
- [66] P. J. Hine, I. M. Ward, R. H. Olley, and D. C. Bassett, “The hot compaction of high modulus melt-spun polyethylene fibres,” *Journal of Materials Science*, vol. 28, pp. 316–324, 1993.
- [67] P. J. Hine, I. M. Ward, and J. Teckoe, “The hot compaction of woven polypropylene tapes,” *Journal of Materials Science*, vol. 33, pp. 2725–2733, 1998.

- [68] N. D. Jordan, D. C. Bassett, R. H. Olley, P. J. Hine, and I. M. Ward, "The hot compaction behaviour of woven oriented polypropylene fibres and tapes. II. Morphology of cloths before and after compaction," *Polymer*, vol. 44, pp. 1133–1143, 2003.
- [69] Y. Meerten, Y. Swolfs, J. Baets, L. Gorbatikh, and I. Verpoest, "Penetration impact testing of self-reinforced composites," *Composites Part A: Applied Science and Manufacturing*, vol. 68, pp. 289–295, 2015.
- [70] Y. Swolfs, L. Crauwels, L. Gorbatikh, and I. Verpoest, "The influence of weave architecture on the mechanical properties of self-reinforced polypropylene," *Composites Part A: Applied Science and Manufacturing*, vol. 53, pp. 129–136, 2013.
- [71] Y. Swolfs, Q. Zhang, J. Baets, and I. Verpoest, "The influence of process parameters on the properties of hot compacted self-reinforced polypropylene composites," *Composites Part A: Applied Science and Manufacturing*, vol. 65, pp. 38–46, 2014.
- [72] Y. Swolfs, W. Van den fonteyne, J. Baets, and I. Verpoest, "Failure behaviour of self-reinforced polypropylene at and below room temperature," *Composites Part A: Applied Science and Manufacturing*, vol. 65, pp. 100–107, 2014.
- [73] J. Teckoe J, R. H. Olley, D. C. Bassett, P. J. Hine, and I. M. Ward, "The morphology of woven polypropylene tapes compacted at temperatures above and below optimum," *Journal of Materials Science*, vol. 34, no. 9, pp. 2065–2073, 1999.
- [74] J. Karger-Kocsis and S. Siengchin, "Single-Polymer Composites: Concepts, Realization and Outlook: Review," *KMUTNB International Journal of Applied Science and Technology*, vol. 7, no. 1, pp. 1-9, 2014.
- [75] B. Alcock, N. O. Cabrera, N.-M. Barkoula, C. T. Reynolds, L. E. Govaert, and T. Peijs, "The effect of temperature and strain rate on the mechanical properties of highly oriented polypropylene tapes and all-polypropylene composites," *Composites Science and Technology*, vol. 67, no. 10, pp. 2061–2070, 2007.
- [76] B. Alcock, N. O. Cabrera, N.-M. Barkoula, N. M. Wang, and T. Peijs, "The effect of temperature and strain rate on the impact performance of recyclable allpolypropylene composites," *Composites Part B: Engineering*, vol. 39 no. 3, pp. 537–47, 2008.
- [77] K. Banik T. N. Abraham and J. Karger-Kocsis, "Flexural creep behavior of unidirectional and cross-ply all-poly(propylene) (PURE®) composites," *Macromolecular Materials and Engineering*, vol. 292, no. 12, pp.1280–1288, 2007.
- [78] K. Banik, J. Karger-Kocsis and T. N. Abraham, "Flexural creep of all-polypropylene composites: model analysis," *Polymer Engineering & Science*, vol. 48, no. 5, pp. 941–948, 2008.
- [79] N. M. Barkoula, B. Alcock, N. O. Cabrera T. Peijs, "Fatigue properties of highly oriented polypropylene tapes and all-polypropylene composites," *Polymers and Polymer Composites*, vol. 16, no. 2, pp. 101–113, 2008.
- [80] N. O. Cabrera, "Recyclable all-polypropylene composites: concept, properties and manufacturing," PhD thesis, Technische Universiteit Eindhoven, Eindhoven, 2004.

- [81] K. J. Kim, W. R. Yu and P. Harrison, "Optimum consolidation of self-reinforced polypropylene composite and its time-dependent deformation behaviour," *Composites Part A: Applied Science and Manufacturing*, vol. 39, no. 10, pp. 1597–605, 2008.
- [82] T. N. Abraham, S. Wanjale, T. Bárány, and J. Karger-Kocsis, "Tensile mechanical and perforation impact behavior of all-PP composites containing random PP copolymer as matrix and stretched PP homopolymer as reinforcement: effect of [beta] nucleation of the matrix," *Composites Part A: Applied Science and Manufacturing*, vol. 40, no. 5, pp. 662-668, 2009.
- [83] T. N. Abraham, S. Siengchin, and J. Karger-Kocsis, "Dynamic Mechanical and Perforation Impact Behavior of All-PP Composites Containing Beta-Nucleated Random PP Copolymer as Matrix and Stretched PP Homopolymer Tape as Reinforcement: Effect of Draw Ratio of the Tape," *Journal of Thermoplastic Composites Materials*, vol. 24, pp. 377–388, 2011.
- [84] T. Bárány, A. Izer, and T. Czigány, "On consolidation of self-reinforced polypropylene composites," *Plastics, Rubber and Composites*, vol. 35, no. 9, pp. 375–379, 2006.
- [85] T. Bárány, A. Izer, and J. Karger-Kocsis, "Impact resistance of all-polypropylene composites composed of alpha and beta modifications," *Polymer Testing*, vol. 28, no. 2, pp. 176–182, 2009.
- [86] T. Bárány, J. Karger-Kocsis and T. Czigány, "Development and characterization of self-reinforced poly(propylene) composites: carded mat reinforcement," *Polymers for Advanced Technologies*, vol. 17, pp. 818–824, 2006.
- [87] S. Houshyar and R. A. Shanks, "Morphology, Thermal and Mechanical Properties of Poly(propylene) Fibre-Matrix Composites," *Macromolecular Materials and Engineering*, vol. 288, pp. 599–606, 2003.
- [88] S. Houshyar and R. A. Shanks, "Tensile properties and creep response of polypropylene fibre composites with variation of fibre diameter," *Polymer International*, vol. 53, pp.1752–1759, 2004.
- [89] S. Houshyar and R. A. Shanks, "Mechanical and thermal properties of toughened polypropylene composites," *Journal of Applied Polymer Science*, vol. 105, no. 2, pp. 390–397, 2007.
- [90] S. Houshyar, R. A. Shanks and A. Hodzic, "Influence of different woven geometry in poly(propylene) woven composites," *Macromolecular Materials and Engineering*, vol. 290, no. 1, pp. 45–52, 2005.
- [91] S. Houshyar, R. A. Shanks and A. Hodzic, "Tensile creep behaviour of polypropylene fibre reinforced polypropylene composites," *Polymer Testing*, vol. 24, pp. 257–264, 2005.
- [92] S. Houshyar, R. A. Shanks and A. Hodzic, "The effect of fiber concentration on mechanical and thermal properties of fiber-reinforced polypropylene composites," *Journal of Applied Polymer Science*, vol. 96, np. 6, pp. 2260–72, 2005.
- [93] A. Izer, "Development and investigation of self-reinforced polypropylene composites based on the polymorphism of PP," PhD thesis, Budapest University of Technology and Economics, Budapest, 2010.

- [94] A. Izer, T. Bárány and J. Varga, “Development of woven fabric reinforced all-polypropylene composites with beta nucleated homo- and copolymer matrices,” *Composites Science and Technology*, vol. 69, no. 13, pp. 2185–2192, 2009.
- [95] T. Kitayama, S. Utsumi, H. Hamada, T. Nishino, T. Kikutani, and H. Ito, “Interfacial properties of PP/PP composites,” *Journal of Applied Polymer Science*, vol. 88, pp. 2875–2883, 2003.
- [96] J. Loos, T. Schimanski, J. Hofman, T. Peijs, and P. J. Lemstra, “Morphological investigations of polypropylene single-fibre reinforced polypropylene model composites,” *Polymer*, vol. 42, pp. 3827–3834, 2001.
- [97] A. Stocchi, V. Pettarin, A. Izer, T. Bárány, T. Czigány, and C. Bernal, “Fracture Behavior of Recyclable All-Polypropylene Composites Composed of α - and β -Modifications,” *Journal of Thermoplastic Composite Materials*, vol. 24, pp. 805–814, 2011.
- [98] H. Li, S. Jiang, J. Wang, D. Wang, and S. Yan, “Optical microscopic study on the morphologies of isotactic polypropylene induced by its homogeneity fibers,” *Macromolecules*, vol. 36, pp. 2802–2807, 2003.
- [99] H. Li, X. Zhang, X. Kuang, J. Wang, D. Wang, and L. Li, “A scanning electron microscopy study on the morphologies of isotactic polypropylene induced by its own fibers,” *Macromolecules*, vol. 37, no. 8, pp. 2847–2853, 2004.
- [100] H. Li, X. Q. Zhang, Y. X. Duan, D. J. Wang, L. Li, and S. K. Yan, “Influence of crystallization temperature on the morphologies of isotactic polypropylene single-polymer composite,” *Polymer*, vol. 45, no. 23, pp. 8059–8065, 2004.
- [101] G. Zhang, L. Jiang, K. Z. Shen, and Q. Guan, “Self-reinforcement of high-density polyethylene low density polyethylene prepared by oscillating packing injection molding under low pressure,” *Journal of Applied Polymer Science*, vol. 71, pp. 799–804, 1999.
- [102] Q. Guan, X. G. Zhu, D. Chiu, K. Z. Shen, F. S. Lai, and S. P. McCarthy, “Self-reinforcement of polypropylene by oscillating packing injection molding under low pressure,” *Journal of Applied Polymer Science*, vol. 62, pp. 755–762, 1996.
- [103] L. M. Chen and K. Z. Shen, “Biaxial self-reinforcement of isotactic polypropylene prepared in uniaxial oscillating stress field by injection molding, I. Processing conditions and mechanical properties,” *Journal of Applied Polymer Science*, vol. 78, pp. 1906–1910, 2000.
- [104] L. M. Chen and K. Z. Shen, “Biaxial self-reinforcement of isotactic polypropylene prepared in uniaxial oscillating stress field by injection molding, II. Morphology,” *Journal of Applied Polymer Science*, vol. 78, pp. 1911–1917, 2000.
- [105] Lankhorst Yarns, “Pure®,” [Online]. Available: <https://www.lankhorstyarns.com/product-groups/pure/>. [Accessed Dec. 5, 2018].
- [106] Milliken & Company, “Tegris® Thermoplastic Composites,” 2018. [Online]. Available: <http://tegris.milliken.com/en-us/Pages/default.aspx>. [Accessed Dec. 5, 2018].

- [107] Don & Low Ltd., “Torodon®, Advanced Composite Materials,” 2018. [Online]. Available: <https://www.donlow.co.uk/gb/en/markets/torodon/>. [Accessed Dec. 5, 2018].
- [108] S. Venkatesan, “Stamp forming of composite materials: an experimental and analytical study,” PhD thesis, Australian National University, Canberra, 2012.
- [109] A. Galeski, “Strength and toughness of crystalline polymer systems,” *Progress in Polymer Science*, vol. 28, pp. 1643-1699, 2003.
- [110] N. A. Zanjani and S. Kalyanasundaram, “Stretch Forming Simulation of Woven Composites Based on an Orthotropic Non-Linear Material Model,” *Journal of Materials Science and Chemical Engineering*, vol. 3, pp. 168–179, 2015.
- [111] N. A. Zanjani, A. Sexton and S. Kalyanasundaram, “Induced forming modes in a pre-consolidated woven polypropylene composite during stretch forming process at room temperature: I. Experimental studies,” *Composites Part A, Applied Science and Manufacturing*, vol. 68, pp. 251–263, 2015.
- [112] N. A. Zanjani, W. Wang and S. Kalyanasundaram, “The effect of fiber orientation on the formability and failure behavior of a woven self-reinforced composite,” *Journal of Manufacturing Science and Engineering*, vol. 137, no. 5, pp. 2015.
- [113] M. Z. Hassan, R. Umer, S. Balawi, and W. J. Cantwell, “The impact response of environmental-friendly sandwich structures,” *Journal of Composite Materials*, vol. 48, no. 25, pp. 3083–3090, 2014.
- [114] J. Karger-Kocsis, T. Harmia and T. Czigány, “Comparison of the fracture and failure behavior of polypropylene composites reinforced by long glass fiber and by glass mats,” *Composites Science and Technology*, vol. 54, pp. 287–298, 1995.
- [115] J. Varna, R. Joffe and L. Berglund, “Effects of voids on failure mechanisms in RTM laminates,” *Composites Science and Technology*, vol. 53, pp. 241–249, 1995.
- [116] A. Peterlin, “Molecular Model of Drawing Polyethylene and Polypropylene,” *Journal of Materials Science*, vol. 6, pp. 490–508, 1971.
- [117] A. Peterlin, “Radical formation and fracture of highly drawn crystalline polymers,” *Journal of Macromolecular Science, Part B: Physics*, vol. 6, no.4, pp. 583–597, 1972.
- [118] A. Peterlin, “Morphology and fracture of drawn crystalline polymers,” *Journal of Macromolecular Science, Part B: Physics*, vol. 8, pp. 83–100, 1973.
- [119] A. Peterlin, “Plastic Deformation of Crystalline Polymers,” *Polymer Engineering and Science*, vol. 17, no. 3, pp. 183–193, 1977.
- [120] A. Peterlin, “Leading Contribution, Drawing and extrusion of semi-crystalline polymers,” *Colloid & Polymer Science, Colloid and Polymer Science*, vol. 265, pp. 357–382, 1987.

- [121] X. Sun, H. Li, X. Zhang, J. Wang, D. Wang, and S. Yan, "Effect of Fiber Molecular Weight on the Interfacial Morphology of iPP Fiber/Matrix Single Polymer Composites," *Macromolecules*, vol. 39, pp. 1087-1092, 2006.
- [122] W. Callister, *Material Science and Engineering, An Introduction*. New York, NY: John Wiley & Sons, Inc., 2007.
- [123] T. Nagasawa and Y. Shimomura, "Mechanism of Formation of Shish Kebab Structures," *Journal of Polymer Science, Polymer Physics Edition*, vol. 12, pp. 2291–2308, 1974.
- [124] P. C. Roozmond, Z. Ma, K. Cui, L. Li, and G. W. M. Peters, "Multimorphological Crystallization of Shish-Kebab Structures in Isotactic Polypropylene: Quantitative Modeling of Parent–Daughter Crystallization Kinetics," *Macromolecules*, vol. 47, pp. 5152–5162, 2014.
- [125] K. Wang, M. Guo, D. Zhao, Q. Zhang, R. Du, Q. Fu, X. Dong, and C. C. Han, "Facilitating transcrystallization of polypropylene/glass fiber composites by imposed shear during injection molding," *Polymer*, vol. 47, pp. 8374–8379, 2006.
- [126] G. Ellis, M. A. Gómez and C. Marco, "Synchrotron Infrared Microscopy Study of the Crystalline Morphology of the Interphase in Polypropylene/LCP-Fiber Model Composites," *Journal of Macromolecular Science Part B–Physics*, vol. B43, no. 1, pp. 191–206, 2004.
- [127] J. M. Felix and P. Gatenholm, "Effect of transcrystalline morphology on interfacial adhesion in cellulose/polypropylene composites," *Journal of Materials Science*, vol. 29, pp. 3043-3049, 1994.
- [128] F. Hoecker and J. Karger-Kocsis, "Effects of crystallinity and supermolecular formations on the interfacial shear strength and adhesion in GF/PP composites," *Polymer Bulletin*, vol. 31, pp. 707-714, 1993.
- [129] C. Moon, "The effect of interfacial microstructure on the interfacial strength of glass fiber/polypropylene resin composites," *Journal of Materials Science*, vol. 54, no. 1, pp. 73–82, 1994.
- [130] C. Y. Yue and W. L. Cheung, "Interfacial properties of fibrous composites, Part II Determination of interracial shear strength, interracial coefficient of friction, and the shrinkage pressure on the fibre," *Journal of Materials Science*, vol. 27, pp. 3181-3191, 1992.
- [131] R. A. C. Deblieck, D.J.M. van Beek, K. Remerie, and I. M. Ward, "Failure mechanisms in polyolefines: The role of crazing, shear yielding and the entanglement network," *Polymers*, vol. 52, pp. 2979–2990, 2011.
- [132] S. Lampman, Eds., *Characterization and Failure Analysis of Plastics*. Materials Park, OH: ASN International, 2003, pp 404-406.
- [133] M. Aboulfaraj, C. G. Sell, B. Ulrich, and A. Dahoun, "In situ observation of the plastic deformation of polypropylene spherulites under uniaxial tension and simple shear in the scanning electron microscope," *Polymer*, vol. 36, no. 4, pp. 731–742, 1995.

- [134] Z. Bartczak and E. Martuscelli, "Orientation and properties of sequentially drawn films of an isotactic polypropylene; hydrogenated oligocyclopentadiene blends," *Polymer*, vol. 38, pp. 4139–4149, 1997.
- [135] P. B. Bowden and R. J. Young, "Critical resolved shear stress for [001] slip in polyethylene," *Nature Physical Science*, vol. 229, pp. 23–25, 1971.
- [136] P. B. Bowden, R. J. Young, J. M. Ritchie, and J. G. Rider, "Deformation mechanisms in oriented high-density polyethylene," *Journal of Materials Science*, vol. 8, pp. 23–36, 1973.
- [137] P. B. Bowden and R. J. Young, "Review, Deformation mechanisms in crystalline polymers," *Journal of Materials Science*, vol. 9, pp. 2034–2051, 1974.
- [138] R. J. Young, "A dislocation model for yield in polyethylene," *The Philosophical Magazine: A Journal of Theoretical Experimental and Applied Physics*, vol. 30, no. 1, pp. 85–94, 1974.
- [139] R. J. Young, "Screw dislocation model for yield in polyethylene," *Materials Forum*, vol. 11, pp. 210–216, 1988.
- [140] L. Lin and A. S. Argon, "Review, Structure and plastic deformation of polyethylene," *Journal of Materials Science*, vol. 29, pp. 294–323, 1994.
- [141] R. Hiss, S. Hobeika, C. Lynn, and G. Strobl, "Network Stretching, Slip Processes, and Fragmentation of Crystallites during Uniaxial Drawing of Polyethylene and Related Copolymers. A Comparative Study," *Macromolecules*, vol. 32, pp. 4390–4403, 1999.
- [142] X. Chen, F. Lv, F. Su, Y. Ji, L. Meng, C. Wan, Y. Lin, X. Li, and L. Li, "Deformation mechanism of iPP under uniaxial stretching over a wide temperature range: An in-situ synchrotron radiation SAXS/WAXS study," *Polymer*, vol. 118, pp. 12–21, 2017.
- [143] S. Fakirov, "Nano-/microfibrillar polymer–polymer and single polymer composites: The converting instead of adding concept," *Composites Science and Technology*, vol. 89, pp. 211–225, 2013.
- [144] S. Fakirov, M. Duhovic, P. Maitrot, and D. Bhattacharyya, "From PET Nanofibrils to Nanofibrillar Single-Polymer Composites," *Macromolecular Materials and Engineering*, vol. 295, no. 6, pp. 515–518, 2010.
- [145] D. Shinozaki and G. W. Groves, "The plastic deformation of oriented polypropylene: tensile and compressive yield criteria," *Journal of Material Science*, vol. 8, pp. 71–78, 1973.
- [146] A. Kelly and G. J. Davies, "The principles of the fiber reinforcement of metals," *Metallurgical Review*, vol. 10, pp. 1–77, 1965.
- [147] M. S. Hoo Fatt, C. Lin, D. M. Revilock Jr., and D. A. Hopkins, "Ballistic impact of GLAREe fiber–metal laminates," *Composite Structures*, vol. 61, pp. 73–88, 2003.
- [148] G. S. Langdon and L. A. Rowe, "The response of steel-based Fibre-metal laminates to localised blast loading," In Proc. 17th International Conference on Composite Materials, Edinburgh, UK, 2009.

- [149] G. Reyes and S. Gupta, “Manufacturing and mechanical properties of thermoplastic hybrid laminates based on DP500 steel,” *Composites Part A, Applied Science and Manufacturing*, vol. 40, pp. 176–183, 2009.
- [150] J. G. Carrillo and W. J. Cantwell, “Mechanical properties of a novel fiber–metal laminate based on a polypropylene composite,” *Mechanics of Materials*, vol. 41, pp. 828–838, 2009.
- [151] E. S. Haji & Co., “Mild Steel (MS) vs Stainless Steel,” 22 May 2012. [Online]. Available: <http://eshaji.in/technical-info/ms-vs-ss/>. [Accessed Dec. 12, 2018].
- [152] S.M.R. Khalili, R.K. Mittal and S. Gharibi Kalibar, “A study of the mechanical properties of steel/aluminium/GRP laminates,” *Journal of Materials Science and Engineering: A*, vol. 412, pp. 137–140, 2005.
- [153] Q. Liu, J. Ma, L. Kang, G. Sun, and Q. Li, “An experimental study on fatigue characteristics of CFRP-steel hybrid laminates,” *Materials and Design*, vol. 88, pp. 643–650, 2015.
- [154] T. Pärnänen, M. Kanerva, E. Sarlin, and O. Saarela, “Debonding and impact damage in stainless steel fibre metal laminates prior to metal fracture”, *Composite Structures*, vol. 119, pp. 777–786, 2015.
- [155] T. Pärnänen, A. Vanttinen, M. Kanerva, J. Jokinen, and O. Saarela, “The Effects of Debonding on the Low-Velocity Impact Response of Steel-CFRP Fibre Metal Laminates,” *Applied Composite Materials*, vol. 23, pp. 1151–1166, 2016.
- [156] R. G. J. van Rooijen, J. Sinke and S. Van der Zwaag, “Improving the adhesion of thin stainless steel sheets for fibre metal laminate (FML) applications,” *Journal of Adhesion Science and Technology*, vol. 19, no. 16, pp. 1387–1396, 2005.
- [157] C. Xu, K. Ramani, and G. Kumar, “Thermoplastic adhesive bonding of galvanized steel to polypropylene composite and its durability,” *International Journal of Adhesion and Adhesives*, vol. 22, pp. 187–195, 2002.
- [158] M. Harhash, A. Carrado and H. Palkowski, “Forming Limit Diagram of Steel/Polymer/Steel Sandwich Systems for the Automotive Industry,” in *Advanced Composites for Aerospace, Marine, and Land Applications*, T. Sano, T. S. Srivatsan and M. W. Peretti, Eds. Springer, Cham, 2014, pp. 243-254.
- [159] M. Harhash, A. Carrado and H. Palkowski, “Deep- and stretch-forming of steel/polymer/steel laminates,” In Proc. 2nd Euro Hybrid Materials and Structures, Kaiserslautern, Germany, 2016.
- [160] M. Harhash, O. Sokolova, A. Carrado and H. Palkowski, “Mechanical properties and forming behaviour of laminated steel/polymer sandwich systems with local inlays – Part 1,” *Composite Structures*, vol. 118, pp. 112–120, 2014.
- [161] M. Harhash, A. Carrado and H. Palkowski, “Mechanical properties and forming behaviour of laminated steel/polymer sandwich systems with local inlays – Part 2: Stretching and deep drawing,” *Composite Structures*, vol. 160, pp. 1084–1094, 2017.

- [162] T. M. Van Velze, “Thermoplastics in ARALL laminates—Development, production and testing of ARALL laminates with a thermoplastic matrix,” MSc thesis, Delft University of Technology, Delft, Netherlands, 1988.
- [163] W. van der Hoeven, “Preliminary evaluation of a high temperature Fibre Metal Laminate,” National Aerospace Laboratory; Amsterdam, Netherlands, Tech. Report. NLR-CR-2007-596, 2007.
- [164] W. J. Cantwell, N. Jones, G. A. Wade, G. Reyes, J. F. Guillen, and P. Compston, “The impact response of novel fibre metal laminates,” in *High Performance Structures and Composites*, C. A. Brebbia and W. P. de Wilde, Eds. Southampton, UK: WIT Press, 2002.
- [165] P. Compston, W. J. Cantwell, C. Jones, and N. Jones, “Impact perforation resistance and fracture mechanisms of a thermoplastic based fiber-metal laminate,” *Journal of Materials Science Letter*, vol. 20, pp. 597–599, 2001.
- [166] G. S. Langdon, W. J. Cantwell and G. N. Nurick, “The blast response of novel thermoplastic-based fibre-metal laminates—some preliminary results and observations,” *Composites Science and Technology*, vol. 65, pp. 861–872, 2005.
- [167] G. S. Langdon, W. J. Cantwell and G. N. Nurick, “Localised blast loading of fibre–metal laminates with a polyamide matrix,” *Composites Part B: Engineering*, vol. 38, pp. 902–913, 2007.
- [168] P. Cortes and W. J. Cantwell, “The prediction of tensile failure in titanium-based thermoplastic fibre-metal laminates,” *Composites Science and Technology*, vol. 66, pp. 2306–2316, 2006.
- [169] K. Friedrich and M. Hou, “On stamp forming of curved and flexible geometry components from continuous glass fibre/polypropylene composites,” *Composites Part A, Applied Science and Manufacturing*, vol. 29, no. 3, pp. 217–226, 1998.
- [170] M. Hou, “Stamp forming of fabric-reinforced thermoplastic composites,” *Polymer Composites*, vol. 17, pp. 596–603, 1996.
- [171] M. Hou, “Stamp forming of continuous glass fibre reinforced polypropylene,” *Composites Part A, Applied Science and Manufacturing*, vol. 28, pp. 695–702, 1997.
- [172] M. Hou and K. Friedrich, “Stamp forming of continuous carbon fibre/polypropylene composites,” *Composites Manufacturing*, vol. 2, no. 3, pp. 3–9, 1991.
- [173] M. R. Abdullah and W. J. Cantwell, “The high velocity impact response of self-reinforced polypropylene fibre metal laminates,” in *Damage and Fracture of Composite Materials and Structures*, M. N. Tamin, Eds. Springer-Verlag Berlin Heidelberg, 2012, pp. 219–240.
- [174] P. Compston, W.J. Cantwell, M.J. Cardew-Hall, S. Kalyanasundaram, and L. Mosse, “Comparison of surface strain for stamp formed aluminium and an aluminium polypropylene laminate,” *Journal of Materials Science*, vol. 39, pp. 6087–6088, 2004.

- [175] L. Mosse, P. Compston, W.J. Cantwell, M. Cardew-Hall, and S. Kalyanasundaram, “The effect of process temperature on the formability of polypropylene based fibre–metal laminates,” *Composites Part A: Applied Science and Manufacturing*, vol. 36, pp. 1158-1166, 2005.
- [176] L. Mosse, P. Compston, W.J. Cantwell, M. Cardew-Hall, and S. Kalyanasundaram, “Stamp forming of polypropylene based fibre–metal laminates: the effect of process variables on formability,” *Journal of Materials Processing Technology*, vol. 172, pp. 163-168, 2006.
- [177] L. Mosse, “Stamp forming of fibre-metal laminates,” PhD thesis, Australian National University, Canberra, 2006.
- [178] L. Mosse, W.J. Cantwell, M. Cardew-Hall, P. Compston, and S. Kalyanasundaram, “A study of the effect of process variables on the stamp forming of rectangular cups using fibre–metal laminate systems,” *Advanced Materials Research*, vol. 6-8, pp. 649–656, 2005.
- [179] S. Dhar Malingam, “An investigation into the forming behaviour of metal composite hybrids,” PhD thesis, Australian National University, Canberra, 2011.
- [180] J. Gresham, “Influence of temperature on the stamp forming of fibre-metal laminate systems,” MPhil thesis, Australian National University, Canberra, 2006.
- [181] J. Gresham, W. Cantwell, M. J. Cardew-Hall, P. Compston, and S. Kalyanasundaram, “Drawing behaviour of metal-composite sandwich structures,” *Composite Structures*, vol. 75, pp. 305–312, 2006.
- [182] S. Kalyanasundaram, S. DharMalingam, S. Venkatesan, and A. Sexton, “Effects of process parameters during forming of self reinforced-PP based fibre metal laminate,” *Composite Structures*, vol. 97, pp. 332-337, 2013.
- [183] A. Sexton, “Stretch forming of thermoplastic fibre-metal laminates,” PhD thesis, Australian National University, Canberra, 2014.
- [184] A. Sexton, W. Cantwell and S. Kalyanasundaram, “Stretch Forming Studies on a Fibre Metal Laminate based on a Self-Reinforcing Polypropylene Composite,” *Composite Structures*, vol. 94, pp. 431-437, 2012.
- [185] J. Cao, R. Akkerman, P. Boisse, J. Chen, H. S. Cheng, et al., “Characterization of mechanical behavior of woven fabrics: experimental methods and benchmark results,” *Composites Part A, Applied Science and Manufacturing*, vol. 39, no. 6, pp. 1037–1053, 2008.
- [186] J. Iriondo, L. Aretxabaleta and A. Aizpuru, “Characterisation of the elastic and damping properties of traditional FML and FML based on a self-reinforced polypropylene,” *Composite Structures*, vol. 131, 47–54, 2015.
- [187] P. J. Hine, M. J. Bonner, I. M. Ward, Y. Swolfs, and I. Verpoest, “The influence of the hybridisation configuration on the mechanical properties of hybrid self reinforced polyamide 12/carbon fibre composites,” *Composites Part A, Applied Science and Manufacturing*, vol. 95, pp. 141–151, 2017.

- [188] L. Mencattelli, J. Tang, Y. Swolfs, L. Gorbatiikh, and S. T. Pinho, “Bio-inspired design for enhanced damage tolerance of self-reinforced polypropylene/carbon fibre polypropylene hybrid composites,” *Composites Part A, Applied Science and Manufacturing*, vol. 121, pp. 341–352, 2019.
- [189] F. Mesquita, A. van Gysel, M. Selezneva, Y. Swolfs, S. V. Lomov, and L. Gorbatiikh, “Flexural behaviour of corrugated panels of self-reinforced polypropylene hybridised with carbon fibre: An experimental and modelling study,” *Composites Part B: Engineering*, vol. 153, pp. 437–444, 2018.
- [190] M. Selezneva, Y. Swolfs, A. Katalagianakis, T. Ichikawa, N. Hirano, I. Taketa, T. Karaki, I. Verpoest, and L. Gorbatiikh, “The brittle-to-ductile transition in tensile and impact behavior of hybrid carbon fibre/self-reinforced polypropylene composites,” *Composites Part A: Applied Science and Manufacturing*, vol. 109, pp. 20–30, 2018.
- [191] S. A. Tabatabaei, Y. Swolfs, H. Wu, and S. V. Lomov, “Full-field strain measurements and meso-FE modelling of hybrid carbon/self-reinforced polypropylene,” *Composite Structures*, vol. 132, pp. 864–873, 2015.
- [192] I. Taketa, J. Ustarroz, L. Gorbatiikh, S. V. Lomov, and I. Verpoest, “Interply hybrid composites with carbon fiber reinforced polypropylene and self-reinforced polypropylene,” *Composites Part A, Applied Science and Manufacturing*, vol. 41, no. 8, pp. 927–932, 2010.
- [193] J. Tang, Y. Swolfs, M. Yang, K. Michielsen, J. Ivens, V. Lomov, and L. Gorbatiikh, “Discontinuities as a way to influence the failure mechanisms and tensile performance of hybrid carbon fiber/self-reinforced polypropylene composites,” *Composites Part A, Applied Science and Manufacturing*, vol. 107, pp. 354–365, 2018.
- [194] J. Tang, Y. Swolfs, M. L. Longana, H. Yu, M. R. Wisnom, S. V. Lomov, and L. Gorbatiikh, “Hybrid composites of aligned discontinuous carbon fibers and selfreinforced polypropylene under tensile loading,” *Composites Part A, Applied Science and Manufacturing*, vol. 123, pp. 97–107, 2019.
- [195] J. Tang, A. Aslani, Y. Swolfs, G. Bullegas, S. T. Pinho, S. V. Lomov, and L. Gorbatiikh, “Staggered ply discontinuities for tailoring the tensile behavior of hybrid carbon fiber/self-reinforced polypropylene composites: A study of pattern parameters,” *Composites Part A, Applied Science and Manufacturing*, vol. 125, 105551, 2019.
- [196] J. Tang, Y. Swolfs, A. Aslani, L. Mencattelli, G. Bullegas, S. T. Pinho, S. V. Lomov, and L. Gorbatiikh, “Engineering tensile behavior of hybrid carbon fiber/self-reinforced polypropylene composites by bio-inspired fiber discontinuities,” *Composites Part B: Engineering*, vol. 178, 107502, 2019.
- [197] Y. Swolfs, L. Crauwels, E. Van Breda, L. Gorbatiikh, P. Hine, I. Ward, and I. Verpoest, “Tensile behaviour of intralayer hybrid composites of carbon fibre and self-reinforced polypropylene,” *Composites Part A, Applied Science and Manufacturing*, vol. 59, pp. 78–84, 2014.

- [198] Y. Swolfs, J. Shi, Y. Meerten, P. Hine, I. Ward, I. Verpoest, and L. Gorbatikh, “The importance of bonding in intralayer carbon fibre/self-reinforced polypropylene hybrid composites,” *Composites Part A, Applied Science and Manufacturing*, vol. 76, pp. 299–308, 2015.
- [199] Y. Swolfs, Y. Meerten, P. Hine, I. Ward, I. Verpoest, and L. Gorbatikh, “Introducing ductility in hybrid carbon fibre/self-reinforced composites through control of the damage mechanisms,” *Composite Structures*, vol. 131, pp. 259–265, 2015.
- [200] Y. Swolfs, “Hybridisation of self-reinforced composites: Modelling and verifying a novel hybrid concept,” PhD thesis, KU Leuven, Leuven, 2015.
- [201] Y. Swolfs, P. De Cuyper, M.G. Callens, I. Verpoest, and L. Gorbatikh, “Hybridisation of two ductile materials – Steel fibre and self-reinforced polypropylene composites,” *Composites Part A, Applied Science and Manufacturing*, vol. 100, pp. 48–54, 2017.
- [202] M. E. Launey and R. O. Ritchie, “On the Fracture Toughness of Advanced Materials,” *Advanced Materials*, vol. 21, pp. 2103–2110, 2009.
- [203] BlueScope Steel Limited, “Metallic Coated Formable GALVABOND®, G2/G2S steel” GALVABOND G2/G2S datasheet. [Revised Nov. 2003].
- [204] Amoco Fabrics, “Curv™ 100 – Technical Data Sheet,” Curv datasheet. [Revised Feb. 2003].
- [205] *Standard Test Method for Tensile Properties of Polymer Matrix Composite Materials*, ASTM D3039/D3039M-14, 2014.
- [206] *Standard Test Methods and Definitions for Mechanical Testing of Steel Products*, ASTM A370-77, International, 1977.
- [207] Collano AG, “Collano – Contact,” [Online]. Available: <https://www.collano.com/en/service/contact>. [Accessed Oct. 12, 2018].
- [208] *Standard Test Method for Lap Shear Adhesion for Fiber Reinforced Plastic (FRP) Bonding*, ASTM D5868-01-14, 2014.
- [209] S. W. Tsui, H. M. White, and A. F. Johnson, “Enhanced Bonding of Polypropylene to Polypropylene and other Materials with Novel Thermoplastic Heat Activated Adhesives,” presented at 2nd Annual Society of Plastics Engineers Automotive Composites Conference, Troy, MI, 2002.
- [210] T. Sinmazçelik, E. Avcu, M. Ö. Bora, and O. Çoban, “A review: Fibre metal laminates, background, bonding types and applied test methods,” *Materials and Design*, vol. 32, no. 7, pp. 3671–3685, 2011.
- [211] M. Fedel, M. Olivier, M. Poelman, F. Deflorian, S. Rossi, and M.-E. Druart, “Corrosion protection properties of silane pre-treated powder coated galvanized steel,” *Progress in Organic Coatings*, vol. 66, no. 2, pp. 118–128, 2009.
- [212] N. Parhizkar, B. Ramezanzadeh, and T. Shahrabi, “Corrosion protection and adhesion properties of the epoxy coating applied on the steel substrate pre-treated by a sol-gel based

- silane coating filled with amino and isocyanate silane functionalized graphene oxide nanosheets,” *Applied Surface Science*, vol. 439, pp. 45–59, 2018.
- [213] Instron, “8874 (25kN/100Nm) Axial-Torsion System,” [Online]. Available: <http://www.instron.us/en-us/products/testing-systems/dynamic-and-fatigue-systems/servo-hydraulic-fatigue/8874-axial-torsion>. [Accessed Oct. 12, 2018].
- [214] Z. Marciniak, J. L. Duncan and S. J. Hu, *Mechanics of Sheet Metal Forming*, 2nd ed. Woburn, MA: Butterworth-Heinemann, 2002.
- [215] W. F. Hosford and J. L. Duncan, “Sheet metal forming: A review,” *Journal of Minerals, Metals and Materials Society*, vol. 51, no. 11, pp. 39–44, 1999.
- [216] *Metallic materials -- Sheet and strip -- Determination of forming-limit curves -- Part 2: Determination of forming-limit curves in the laboratory*, ISO 12004-2:2008, 2008.
- [217] K. S. Raghavan, “A simple technique to generate in-plane forming limit curves and selected applications,” *Metallurgical and Materials Transactions A*, vol. 26, no. 8, pp. 2075–2084, 1995.
- [218] GOM, “ARAMIS – 3D Motion and Deformation Sensor,” 2018. [Online]. Available: <https://www.gom.com/metrology-systems/aramis.html>. [Accessed Oct. 12, 2018].
- [219] *ARAMIS User Manual – Software, ARAMIS v6.3 and higher*, rev-a, GOM mbH, Braunschweig, Germany, 2011.
- [220] J. P. M. Hoefnagels, B. G. Vossen, and C. C. Tasan, “Electron Micrographic Digital Image Correlation: Method Optimization and Microstructural banding Case Study,” in *Application of Imaging Techniques to Mechanics of Materials and Structures, Volume 4: Proceedings of the 2010 Annual Conference on Experimental and Applied Mechanics*, Springer Science & Business Media, T. Proulx, Eds. New York: Springer, 2012, pp. 71-77.
- [221] J. Kang, “Microscopic strain mapping based on digital image correlation,” In Proc. XIth International Congress and Exposition, Orlando, FL, 2008.
- [222] V. Pickerd, “Optimisation and Validation of the ARAMIS Digital Image Correlation System for use in Large-scale High Strain-rate Events,” Maritime Division, Defence Science and Technology Organisation, VIC, Australia, Tech. Report. DSTO-TN-1203, Aug., 2013.
- [223] T. Schmidt, “3D ARAMIS, Sensitivity Accuracy and Data Validity Considerations,” Trillion Quality Systems LLC, West Conshohocken, PA, Tech. Report. May, 2009.
- [224] H. Fukunaga and T. Chou, “Probabilistic failure strength analyses of graphite/epoxy cross-ply laminates,” *Journal of Composite Materials*, vol. 18, pp. 339-356, 1984.
- [225] S. Kellas and J. Morton, “Scaling effects in angle-ply laminates,” NASA Langley Research Center; Hampton, VA, United States, Tech. Report. NASA CR-4423, Feb. 1992.
- [226] E. Smith, “A Discussion of Results from Models Simulating Crack Tip Reinforcement: Fully Bridged Situation,” *International Journal of Engineering Science*, vol. 27, pp. 1473–1477, 1989.

- [227] J. J. Horst and J. L. Spormaker, "Mechanism of fatigue in short glass fiber reinforced polyamide 6," *Polymer Engineering and Science*, vol. 36, pp. 2718–2726, 1996.
- [228] H. G. Olf and A. Peterlin, "Cryogenic crazing of crystalline, isotactic polypropylene," *Journal of Colloid and Interface Science*, vol. 47, pp. 628–635, 1974.
- [229] B. F. Sørensen, E. K. Gamstedt, R. C. Østergaard, S. Goutianos, "Micromechanical model of cross-over fibre bridging – Prediction of mixed mode bridging laws," *Mechanics of Materials*, vol. 40, pp. 220–234, 2008.
- [230] I. M. Ward, "Review: The Yield Behaviour of Polymers," *Journal of Materials Science*, vol. 6, pp. 1397–1417, 1971.
- [231] P. L. Fernando and J. G. Williams, "Plane Stress and Plain Strain Fractures in Polypropylene," *Polymer Engineering and Science*, vol. 20, pp. 215–220, 1980.
- [232] Y. Lin, V. Yakovleva, H. Chen, A. Hiltner, and E. Baer, "Comparison of Olefin Copolymers as Compatibilizers for Polypropylene and High-Density Polyethylene," *Journal of Applied Polymer Science*, vol. 113, pp. 1945–1952, 2009.
- [233] K. Liu and M. R. Piggott, "Fracture Failure Processes in Polymers. I: Mechanical Tests and Results," *Polymer Engineering and Science*, vol. 38, pp. 60–68, 1998.
- [234] J. Tirosh, "The Effect of Plasticity and Crack Blunting on the Stress Distribution in Orthotropic Composite Materials," *Journal of Applied Mechanics*, vol. 4, pp. 785–790, 1973.
- [235] J. Cook and J. E. Gordon, "A mechanism for the control of crack propagation in all-brittle systems," *Proceedings of the Royal Society of London. Series A. Mathematical and Physical Sciences*, vol. 282, pp. 508–520, 1964.
- [236] J. F. McGarry, J. F. Mandell and S. S. Wang, "Fracture of Fiber Reinforced Composites," *Polymer Engineering and Science*, vol. 16, pp. 609–614, 1976.
- [237] G. P. Mashinskaya and B. V. Perov, "Principles of Developing Organic Fibre-Reinforced Plastics for Aircraft Engineering," in *Polymer Matrix Composites, Volume 4 of Soviet Advanced Composites Technology Series*, R. E. Shalin, Ed. London, UK: Chapman & Hall, 1995.
- [238] H.T.N. Kuan, W. J. Cantwell, Md. A. Hazizan, and C. Santulli, "The fracture properties of environmental-friendly fiber metal laminates," *Journal of Reinforced Plastics and Composites*, vol. 30, no. 6, pp. 499–508, 2011.
- [239] N. Srinivasan, N. Raghu and B. Venkatraman, "Study On The Deformation Band Characteristics In Mild Steel Using Digital Image Correlation," *Journal of Multidisciplinary Engineering Science and Technology*, vol. 5, pp. 400–403, 2014.
- [240] C. Li, D. E and N. Yi, "Analysis on fracture initiation and fracture angle in ductile sheet metal under uniaxial tension by experiments and finite element simulations," *Journal of Materials Research*, vol. 31, pp. 3991–3999, 2016.

- [241] Collano, “Collano 22.100_22.101, Technical Data Sheet,” Collano 22.010, 22.011 datasheet. [Revised Jun. 2007].
- [242] *LS-DYNA® Keyword User’s Manual, Volume II, Material Models*, LS-DYNA R7.1, revision: 5442, Livermore Software Technology Corporation, Livermore, CA, 2014.
- [243] *LS-DYNA® Theory Manual*, Livermore Software Technology Corporation, Livermore, CA, 2006.
- [244] *LS-DYNA® Keyword User’s Manual, Volume I*, LS-DYNA R7.1, revision: 5471, Livermore Software Technology Corporation, Livermore, CA, 2014.
- [245] O. Cousigné, D. Moncayo, D. Coutellier, P. Camanho, H. Naceur, and S. Hampel, “Development of a new nonlinear numerical material model for woven composite materials accounting for permanent deformation and damage,” *Composite Structures*, vol. 106, no. 1, pp. 601–614, 2013.
- [246] LSTC and DYNAmore GmbH, “SOFT option,” rev. 16, May 2003. [Online]. Available: <https://www.dynasupport.com/howtos/contact/soft-option>. [Accessed Nov. 17, 2018].
- [247] T. Belytschko and I. Leviathan, “Projection schemes for one-point quadrature shell elements,” *Computer Methods in Applied Mechanics and Engineering*, vol. 115, pp. 277–286, 1994.
- [248] T. Belytschko and C. S. Tsay, “A stabilization procedure for the quadrilateral plate element with one-point-quadrature,” *International Journal for Numerical Methods in Engineering*, vol. 19, pp. 405–419, 1983.
- [249] T. Belytschko, J. I. Lin, and C. S. Tsay, “Explicit algorithms for nonlinear dynamics of shells,” *Computer Methods in Applied Mechanics and Engineering*, vol. 42, pp. 225–251, 1984.
- [250] Y. Dewang, M. S. Hora and S. K. Panthi, “Review on finite element analysis of sheet metal stretch flanging process,” *APRN Journal of Engineering and Applied Science*, vol. 9, no. 9, pp. 1565–1579, 2014.
- [251] T. J. R. Hughes and W. K. Liu, “Nonlinear finite element analysis of shells: Part I. Three-dimensional shells,” *Computer Methods in Applied Mechanics and Engineering*, vol. 26, no. 3, pp. 331–362, 1981.
- [252] T. J. R. Hughes and W. K. Liu, “Nonlinear finite element analysis of shells: Part II. Two-dimensional shells,” *Computer Methods in Applied Mechanics and Engineering*, vol. 27, no. 2, pp. 167–181, 1981.
- [253] LSTC and DYNAmore GmbH, “Contact stiffness calculation,” 2001. [Online]. Available: <https://www.dynasupport.com/tutorial/contact-modeling-in-ls-dyna/contact-stiffness-calculation>. [Accessed Nov. 17, 2018].

Appendix A – Collano® 22.100 datasheet



Collano 22.100_22.101

Technical Data Sheet

Description

Usage:

This adhesive film is suitable for bonding textiles, foams, skins, metals and polyamides. Preliminary tests are necessary for other materials.

Processing:

Can be processed with all established calendering, lamination and bonding techniques except high frequency welding.

Working safety:

Please observe the instructions on the safety data sheet.

Product data

Base:

Thermoplastic adhesive film based on modified polyolefines

Colour:

Slightly opaque

Smell:

Odorless prior to processing.

Density: (DIN 53479)

0.92 g/cm³

Melting range: (Kofler bench)

120-130 °C

Melt flow rate: (DIN ISO 1133)

2-6 g/10 min (190 °C / 21.2 N)

Heat deflection temperature: (internal method)

110 °C

Washing resistance: (in accordance with DIN 53920)

60 °C

Dry cleaning resistance: (internal method)

Yes

Special properties:

May be safely used in direct contact with food, except oils, fats and fatty products, according to FDA regulations and the "Lebensmittel- und Bedarfsgegenständegesetz".

Storage:

Do not store below 0 °C (32 °F) or above 40 °C (104 °F). Store in a cool, dry place away from direct sunlight. Under appropriate storage conditions at least 1 year after delivery.

Delivery form:

Slitted or unslitted film without carrier

Application data

Temperature range:

Avoid temperatures above 220 °C (430 °F).

Minimal bondline temperature:

140 °C

Disposal:

Dispose of according to local and national regulations, e.g. dispose of preferably in a incineration plant suitable for plastics.

Requirements

Chemical resistance:

Resistance to PVC plasticizers: none

Contact

T +41 41 469 91 11

F +41 41 469 91 12

collano@collano.com

Guarantee

We guarantee the consistency and faultless quality of this product, manufactured in accordance with ISO quality standards, which has been developed on the basis of our long-standing experience with the recommended applications under the specified conditions. Material, processing, and application conditions may significantly influence product properties. Pre-application tests by the user are therefore essential. For non-specified applications or deviations in application conditions, we recommend that Collano's technical support service be consulted first. Collano's general sales and delivery terms and conditions shall apply.

Reference: [241]

Appendix B – Lap shear test summary

Table B.1 Lap shear test configurations and resulting maximum loads, used to determine optimal conditions for consolidating SRPP/steel FML.

Temperature (°C)	Number of adhesive films	Surface abrasion – silicon carbide (grit size)		Load (kN)
		SRPP	Steel	
165	1	none	none	1.95
165	2	none	none	1.93
165	3	none	none	2.06
170	1	none	none	1.77
170	2	none	none	2.07
170	3	none	none	2.2 ± 0.1
170	3	120	none	2.27
170	3	80	none	2.45
175	1	none	none	2.05
175	2	none	none	2.2 ± 0.3
175	2	none	320	1.93
175	2	none	80	2.03
175	2	320	none	2.04
175	2	320	320	2.17
175	2	80	none	2.21
175	2	80	80	2.07
175	3	none	none	2.2 ± 0.3
175	3	120	none	2.30
175	3	120	120	2.05
175	3	80	80	2.10
176 ¹	1	none	none	1.77
176 ¹	2	none	none	1.97
176 ¹	3	none	none	2.07
180	1	none	none	1.70
180	2	none	none	1.90
180	3	none	none	2.01

¹ Temperature fluctuated between 174 – 178 °C during consolidation.

Appendix C – Finite element analysis setup

Finite element analysis (FEA) was used in the analysis of FML IBD test specimens in addition to the surface strain analysis, in order to gain additional information about the SRPP layer. FEA was carried out using explicit analysis in LS-DYNA software. License and resources were provided by National Computational Infrastructure, supercomputing facility in Australia. Setups used for FEA are outlined in this section.

C.1 Material modeling

C.1.1 Steel

Steel was modelled using Material Type 24, Piecewise Linear Isotropic Plasticity, in LS-DYNA [242, p. 2-154-2-160]. It is an elasto-plastic material based on the von Mises yield criteria where the hardening function in terms of effective plastic strain can be defined by the user [243, pp. 19.46–19.47].

C.1.2 SRPP

SRPP was modelled using a User-Defined Material (UMAT) subroutine in LS-DYNA [244]. There are other material models provided in LS-DYNA for composite materials that can model nonlinearity via plasticity or damage theories and/or by direct data input. However, the full customisation of material behaviour given by UMAT makes it the preferred option for the modelling of many composites. This was also the case for SRPP studied in this research, for which [110] found that the highly nonlinear material can be modelled more accurately by defining the Poisson's ratios as nonlinear variants rather than as average, constant values as many models assume.

SRPP is an orthotropic composite which has three mutually orthogonal planes of symmetry with orthogonal axes 1, 2 and 3. For thin sheets, the effects of stress components in the out-of-plane direction ($\sigma_3, \tau_{23}, \tau_{13}$) are negligible compared to the in-plane components ($\sigma_1, \sigma_2, \tau_{12}$). The generalised Hooke's Law can then be simplified to Equation C1, where E_i is the longitudinal modulus of elasticity in direction i , and ν_{ij} is the Poisson's ratio ($= -\varepsilon_j/\varepsilon_i$), where $i, j=1,2$, denoting directions.

$$\begin{Bmatrix} \sigma_1 \\ \sigma_2 \\ \tau_{12} \end{Bmatrix} = \begin{bmatrix} \frac{E_1}{1 - \nu_{12}\nu_{21}} & \frac{\nu_{12}E_2}{1 - \nu_{12}\nu_{21}} & 0 \\ \frac{\nu_{12}E_2}{1 - \nu_{12}\nu_{21}} & \frac{E_2}{1 - \nu_{12}\nu_{21}} & 0 \\ 0 & 0 & G_{12} \end{bmatrix} \begin{Bmatrix} \varepsilon_1 \\ \varepsilon_2 \\ \gamma_{12} \end{Bmatrix} \quad (C1)$$

Similar to the works of [245], the nonlinear behaviour was considered as a macroscopic behaviour independent from the damage evolution as this requires a limited number of inputs and provides a very practical approach. Using such a tangential modulus method based on the works of [110], the experimentally-obtained longitudinal tangential modulus in Figure 3.1 was used as instantaneous moduli of the material in directions 1 and 2 as functions of strains in the corresponding directions ($E_i^t(\varepsilon_i)$, $i = 1,2$), given in Equation C2. Experimentally obtained curves of Poisson's ratios, $\nu_{ij}(\varepsilon_i)$ ($i = 1,2, i \neq j$), and shear modulus, $G_{12}(\tau_{12})$, are given in Equations C3 and C4. The exponential curve fit for the mechanical properties was found to capture the experimental data better than a polynomial curve fit.

$$E_i^t(\varepsilon_i) = \left. \frac{d\sigma}{d\varepsilon} \right|_{\varepsilon=\varepsilon_i} = A_1 e^{a_1|\varepsilon_i|} + A_2 e^{a_2|\varepsilon_i|} \quad (C2)$$

where

$$\begin{aligned} A_1 &= 1.3 \times 10^9 \\ a_1 &= -7.05 \times 10^{-5} \\ A_2 &= 2.997 \times 10^9 \\ a_2 &= -119 \end{aligned}$$

$$\nu_{ij}(\varepsilon_i) = -\frac{\varepsilon_j}{\varepsilon_i} = B_1 e^{b_1|\varepsilon_i|} + B_2 e^{b_2|\varepsilon_i|} \quad (C3)$$

where

$$\begin{aligned} B_1 &= 0.05 \\ b_1 &= -0.926 \\ B_2 &= 0.5 \\ b_2 &= -111 \end{aligned}$$

$$G_{12} = G_{21} = \frac{\tau_{12}}{\gamma_{12}} = C_1 + C_2 e^{c_3|\gamma_{12}|} \quad (C4)$$

where

$$\begin{aligned} C_1 &= 1.18 \times 10^8 \\ C_2 &= 3.29 \times 10^8 \\ c_3 &= -28.4 \end{aligned}$$

The subroutine was used for updating the stresses and strains to current state for each time increment. At each increment, the material constants E_i , ν_{ij} and G_{12} for current time are calculated according to Equations C2–C4 using the strain states from the previous time increment. These are used to find the current Q_{ij} components, which can then be used to calculate stress increments given strain increments, according to Equation C1. Stresses are updated by adding the calculated incremental stresses to stresses from the previous state.

C.1.3 FML

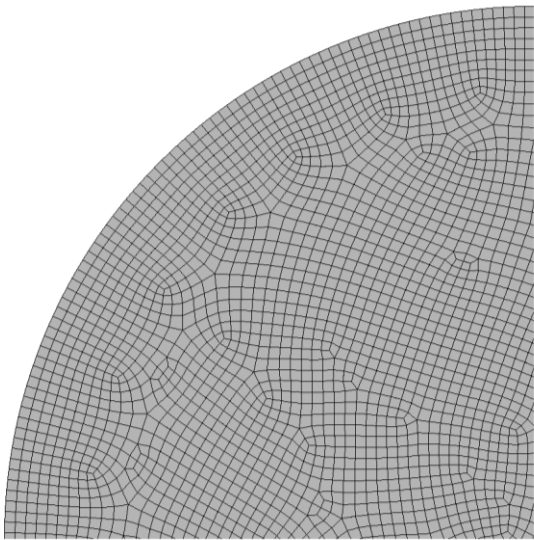
FML was modelled by representing steel and SRPP sheets as separate layers of shell elements that are tied together at an offset using a contact type ‘Tied edge to surface’ in LS-DYNA. An additional ‘beam offset’ option was used which allows the contact to be penalty-based where the forces and corresponding moments are transmitted between the slave nodes and master segments by discrete, beam-like spring elements [244, p. 11-5]. In contrast to the node-constraint method, the penalty method induces little, if any, hourglassing [243, p. 26.2]. In addition, the soft constraint penalty method was used. This calculates two stiffnesses – one based on the standard penalty method and the other based on additional stability conditions – and applies the higher value [244, pp. 11-61, 11-64, 246]. This was more effective for dealing with contact between surfaces with different material stiffnesses.

C.2 Elements and Mesh

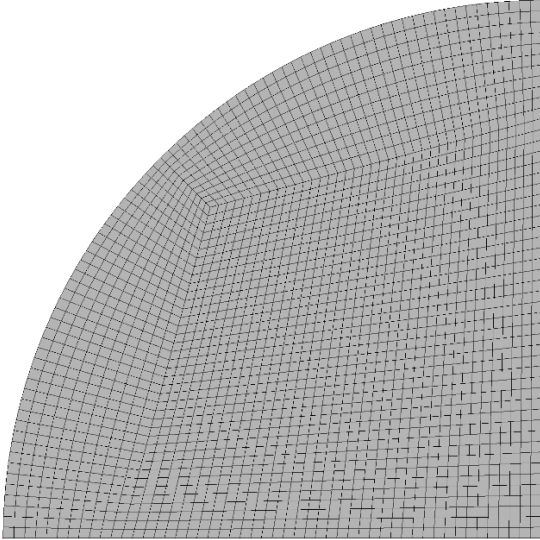
Belytschko-Leviathan (BL) shells [247] (Type 8 in LS-DYNA) were used to model the steel and SRPP sheets. These are four-node quadrilateral shell elements with one-point quadrature based on the Belytschko-Tsay (BT) formulation [248, 249]. A BT type shell was not used, even though it is fast, robust and widely used in FEA, because it can be problematic under warping and is not free of hourglassing. To address the shortcomings of the BT shell, BL shells were used at a small additional computational cost ($\times 1.08$ – 1.25 [244, p. 2-24, 250]) and the hourglass energy was maintained below 10% of peak internal energy of the system. Hughes-Liu shell types [251, 252] were also considered but these were much more computationally expensive (including co-rotational and selectively-reduced integrated forms) and unnecessary, since the BL shells gave results that are accurate enough.

Specimens were modelled accounting for the material thicknesses. Five integration points based on Gauss quadrature rule were used, where the position of integration points in relation to the mid-plane ($x_{mid} = 0$) and the outermost surfaces ($x_{surface} = \pm 1$) are ± 0.9062 , ± 0.5385 , 0. A shear correction factor of $5/6$, which is the recommended default value, was used. Tools (open die, blank holder, punch) were modelled as simple rigid bodies (Material Type 20) with BT shell elements, moving only in the out-of-plane direction in relation to the specimen.

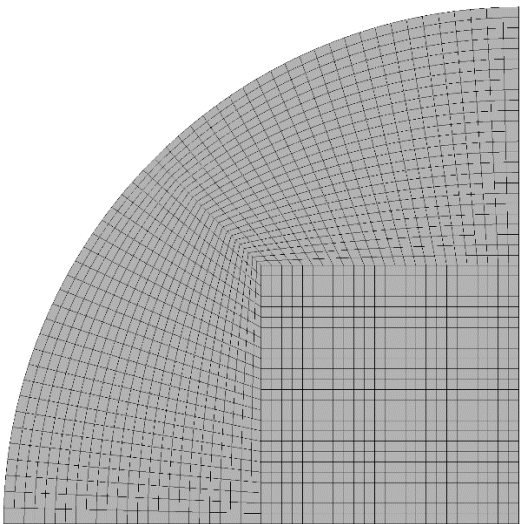
Several mesh shapes shown in Figure C1 were trialled for the specimen. The best option was Figure C1d, where a structured mesh with square elements was used except around the curved edge, which required a non-structured mesh. For SRPP, element sizes and aspect ratios were controlled to avoid degenerate element shapes that can cause erroneous stress and strain concentrations. For each specimen type, the mesh was refined over a few attempts such that the model was accurate enough (when surface strains were compared to experimental results) without being unnecessarily computationally expensive. A mesh size of around 1 mm was required for SRPP ($\approx 3.2k$ elements in a circular specimen).



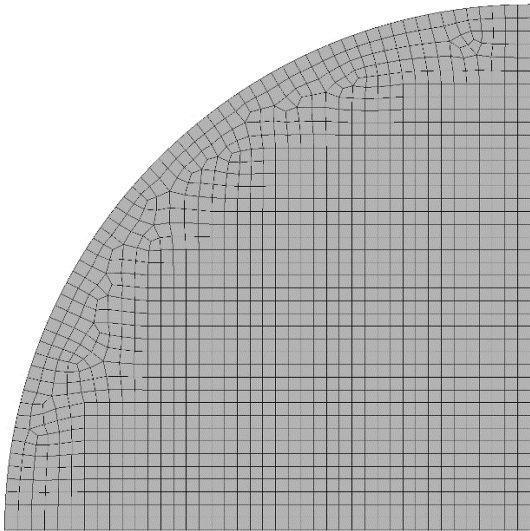
(a) Non-structured mesh



(b) Structured mesh



(c) Structured mesh with square elements in the middle



(d) Structured mesh with square elements in the middle and along x and y meridians and non-structured mesh elsewhere

Figure C.1 Mesh patterns tried on full-circle blanks in FEA models. Only a quarter of the blanks are shown.

C.3 Model setup

Geometries for FEA simulation of a circular IBD test are shown in Figure C2. A lock-ring was initially modelled but required much finer meshes around the lock-ring to avoid penetration error, as shown in Figure C3. Consequently, it was replaced by fixing the edges of the specimens, which gave similar results while significantly reducing the computational cost.

It should still be noted that clamping the specimen using the lock-ring pre-stretches the specimen due to the material drawing into the lock-ring. This induces ϵ_{p1} of about 1% in circular specimens, which is very small compared to the level of strain at the final stages of deformation. In the hourglass specimens, the induced strain reaches about 6% in the narrow central region and an average ϵ_{p1} of approximately 1.3%, as shown in Figure C4. This was not of great concern since using a slightly higher punch depth could easily simulate the effect of pre-stretch and only general strain distributions were of importance.

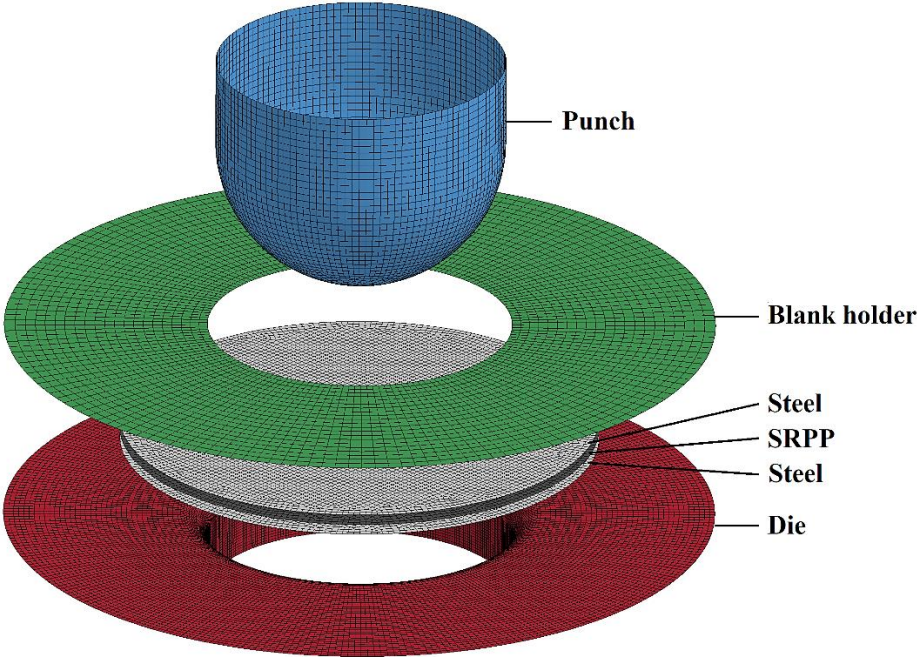


Figure C.2 FEA model geometry for a circular FML induced-biaxial deformation test.

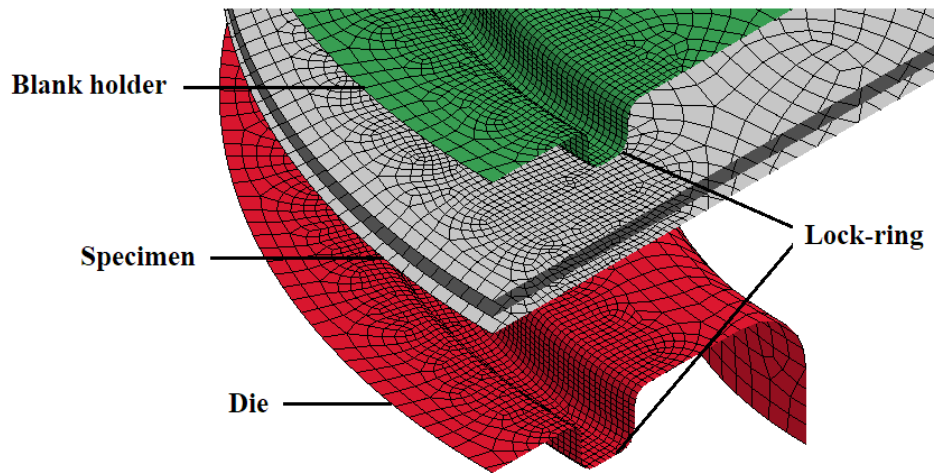


Figure C.3 Half-section of an FEA model with lock-ring.

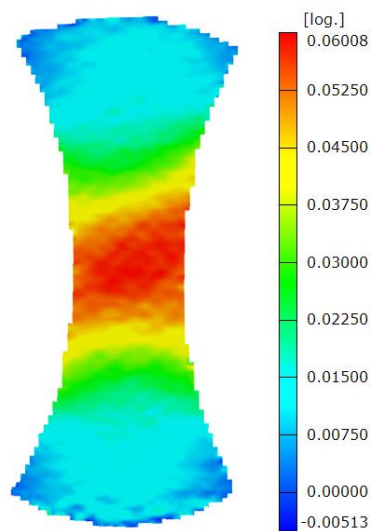


Figure C.4 First principal strain in a SRPP hourglass test specimen prior to induced-biaxial deformation test, induced from fixing the convex edges with a lock-ring.

The IBD tests were simulated as quasi-static, where the applied load is slow enough that the inertial effects are negligible and can be ignored. Accordingly, contact and pressure were established between the blank holder, specimen and die, before ramping up the velocity of the punch to a constant speed. Kinetic energy of the system was kept below 5% of the potential energy, close to zero in most cases. Convergence was checked for each simulation by reducing the time step size until further reduction produced a negligible difference in results.

‘Forming one-way surface to surface’ contact was used between the specimen and tools, with the specimen as slave surfaces and tools as master surfaces. For contact between the SRPP specimen and

tools, the additional option of a segment-based penalty method was used, which is effective for materials with dissimilar stiffness or mesh densities [253]. In addition, a smooth curve-fitted surface was used to represent the master segment (SMOOTH option in LS-DYNA). This allows a more accurate representation of the actual surface, reduce contact noise and produce smoother results with coarser mesh [244, p. 11-7].

Contact forces can introduce oscillatory noise into the response so a viscous contact damping has also been applied in all contact options in LS-DYNA with VDC parameter set at 20 [244, p. 11-19]. Depending on the contacting surfaces, coefficients for static and dynamic frictions varied from 0.1 (between SRPP sheets and the punch with Teflon) to 0.7 (maximum coefficient of static friction between the steel sheets and tools without any lubrication).